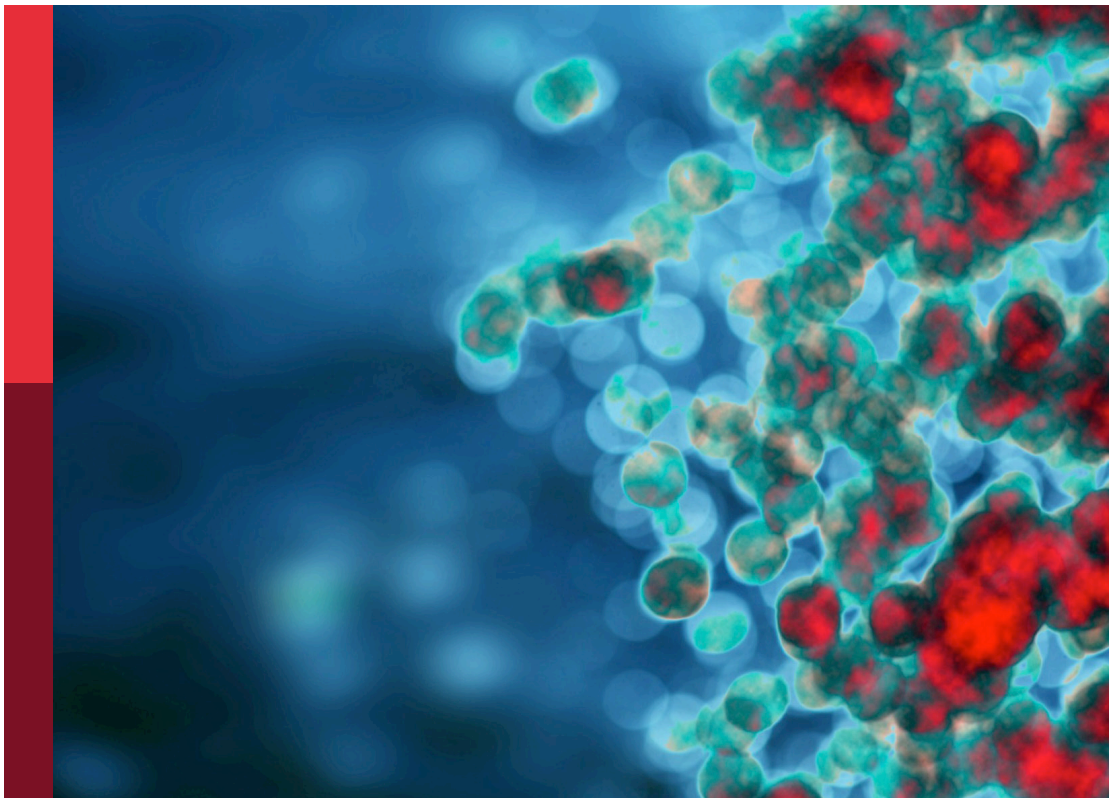
frontiers | Research Topics

Immunosenescence in the cancer microenvironment

Edited by
Elena Ciaglia, Giulia Accardi, Annibale Alessandro Puca, Tamas Fulop and Daniela Cesselli

Published in
Frontiers in Immunology



FRONTIERS EBOOK COPYRIGHT STATEMENT

The copyright in the text of individual articles in this ebook is the property of their respective authors or their respective institutions or funders. The copyright in graphics and images within each article may be subject to copyright of other parties. In both cases this is subject to a license granted to Frontiers.

The compilation of articles constituting this ebook is the property of Frontiers.

Each article within this ebook, and the ebook itself, are published under the most recent version of the Creative Commons CC-BY licence. The version current at the date of publication of this ebook is CC-BY 4.0. If the CC-BY licence is updated, the licence granted by Frontiers is automatically updated to the new version.

When exercising any right under the CC-BY licence, Frontiers must be attributed as the original publisher of the article or ebook, as applicable.

Authors have the responsibility of ensuring that any graphics or other materials which are the property of others may be included in the CC-BY licence, but this should be checked before relying on the CC-BY licence to reproduce those materials. Any copyright notices relating to those materials must be complied with.

Copyright and source acknowledgement notices may not be removed and must be displayed in any copy, derivative work or partial copy which includes the elements in question.

All copyright, and all rights therein, are protected by national and international copyright laws. The above represents a summary only. For further information please read Frontiers' Conditions for Website Use and Copyright Statement, and the applicable CC-BY licence.

ISSN 1664-8714
ISBN 978-2-83251-892-2
DOI 10.3389/978-2-83251-892-2

About Frontiers

Frontiers is more than just an open access publisher of scholarly articles: it is a pioneering approach to the world of academia, radically improving the way scholarly research is managed. The grand vision of Frontiers is a world where all people have an equal opportunity to seek, share and generate knowledge. Frontiers provides immediate and permanent online open access to all its publications, but this alone is not enough to realize our grand goals.

Frontiers journal series

The Frontiers journal series is a multi-tier and interdisciplinary set of open-access, online journals, promising a paradigm shift from the current review, selection and dissemination processes in academic publishing. All Frontiers journals are driven by researchers for researchers; therefore, they constitute a service to the scholarly community. At the same time, the *Frontiers journal series* operates on a revolutionary invention, the tiered publishing system, initially addressing specific communities of scholars, and gradually climbing up to broader public understanding, thus serving the interests of the lay society, too.

Dedication to quality

Each Frontiers article is a landmark of the highest quality, thanks to genuinely collaborative interactions between authors and review editors, who include some of the world's best academicians. Research must be certified by peers before entering a stream of knowledge that may eventually reach the public - and shape society; therefore, Frontiers only applies the most rigorous and unbiased reviews. Frontiers revolutionizes research publishing by freely delivering the most outstanding research, evaluated with no bias from both the academic and social point of view. By applying the most advanced information technologies, Frontiers is catapulting scholarly publishing into a new generation.

What are Frontiers Research Topics?

Frontiers Research Topics are very popular trademarks of the *Frontiers journals series*: they are collections of at least ten articles, all centered on a particular subject. With their unique mix of varied contributions from Original Research to Review Articles, Frontiers Research Topics unify the most influential researchers, the latest key findings and historical advances in a hot research area.

Find out more on how to host your own Frontiers Research Topic or contribute to one as an author by contacting the Frontiers editorial office: frontiersin.org/about/contact

Immunosenescence in the cancer microenvironment

Topic editors

Elena Ciaglia — University of Salerno, Italy
Giulia Accardi — University of Palermo, Italy
Annibale Alessandro Puca — MultiMedica Holding SpA (IRCCS), Italy
Tamas Fulop — Université de Sherbrooke, Canada
Daniela Cesselli — University of Udine, Italy

Citation

Ciaglia, E., Accardi, G., Puca, A. A., Fulop, T., Cesselli, D., eds. (2023). *Immunosenescence in the cancer microenvironment*. Lausanne: Frontiers Media SA. doi: 10.3389/978-2-83251-892-2

Table of contents

05 Editorial: Immunosenescence in the cancer microenvironment
Annibale Alessandro Puca and Elena Ciaglia

08 The Role of the Tumor Microenvironment and Treatment Strategies in Colorectal Cancer
Yaping Chen, Xiao Zheng and Changping Wu

29 Establishing a Prognostic Signature Based on Epithelial–Mesenchymal Transition-Related Genes for Endometrial Cancer Patients
Jinhui Liu, Guoliang Cui, Shuning Shen, Feng Gao, Hongjun Zhu and Yinghua Xu

45 Identifying a Novel Defined Pyroptosis-Associated Long Noncoding RNA Signature Contributes to Predicting Prognosis and Tumor Microenvironment of Bladder Cancer
Hongcheng Lu, Jiajin Wu, Linghui Liang, Xinwei Wang and Hongzhou Cai

56 A Novel m1A-Score Model Correlated With the Immune Microenvironment Predicts Prognosis in Hepatocellular Carcinoma
Mingxing Zhao, Shen Shen and Chen Xue

68 Characteristics of Prognostic Programmed Cell Death–Related Long Noncoding RNAs Associated With Immune Infiltration and Therapeutic Responses to Colon Cancer
Yan Chen, Yue Zhang, Jiayi Lu, Zhongchen Liu, Shasha Zhao, Mengmei Zhang, Mingzhi Lu, Wen Xu, Fenyong Sun, Qi Wu, Qi Zhong and Zhongqi Cui

86 Comprehensive Analysis of Senescence Characteristics Defines a Novel Prognostic Signature to Guide Personalized Treatment for Clear Cell Renal Cell Carcinoma
Peng Zhou, Zheng Liu, Henglong Hu, Yuchao Lu, Jun Xiao, Yanan Wang, Yang Xun, Qidong Xia, Chenqian Liu, Jia Hu and Shaogang Wang

101 Endogenous Retroviruses (ERVs): Does RLR (RIG-I-Like Receptors)-MAVS Pathway Directly Control Senescence and Aging as a Consequence of ERV De-Repression?
Eros Di Giorgio and Luigi E. Xodo

114 Senescent Tumor Cells in the Peritoneal Carcinomatosis Drive Immunosenescence in the Tumor Microenvironment
Heidi Braumüller, Bernhard Mauerer, Christopher Berlin, Dorothea Plundrich, Patrick Marbach, Pierre Cauchy, Claudia Laessle, Esther Biesel, Philipp Anton Holzner and Rebecca Kesselring

130 A Four-Cell-Senescence-Regulator-Gene Prognostic Index Verified by Genome-Wide CRISPR Can Depict the Tumor Microenvironment and Guide Clinical Treatment of Bladder Cancer
Jian-Xuan Sun, Chen-Qian Liu, Jin-Zhou Xu, Ye An, Meng-Yao Xu, Xing-Yu Zhong, Na Zeng, Si-Yang Ma, Hao-Dong He, Zong-Biao Zhang, Shao-Gang Wang and Qi-Dong Xia

148 MS4A6A is a new prognostic biomarker produced by macrophages in glioma patients
Chunyu Zhang, Haitao Liu, Yinqiu Tan, Yang Xu, Yuntao Li, Shiao Tong, Sheng Qiu, Qianxue Chen, Zhongzhou Su, Daofeng Tian, Wei Zhou and Chunlong Zhong

164 Aging-based molecular classification and score system in ccRCC uncovers distinct prognosis, tumor immunogenicity, and treatment sensitivity
Maoshu Zhu, Chaoqun Huang, Xinhong Wu, Ying Gu, Xiaoxu Hu, Dongna Ma and Weimin Zhong

182 RNA m^5C regulator-mediated modification patterns and the cross-talk between tumor microenvironment infiltration in gastric cancer
Qiang Zhang, Xiangfei Sun, Jianyi Sun, Jiangshen Lu, Xiaodong Gao, Kuntang Shen and Xinyu Qin

196 Identify the immune characteristics and immunotherapy value of CD93 in the pan-cancer based on the public data sets
Aiyuan Guo, Jingwei Zhang, Yuqiu Tian, Yun Peng, Peng Luo, Jian Zhang, Zaoqu Liu, Wantao Wu, Hao Zhang and Quan Cheng

213 Single-cell RNA datasets and bulk RNA datasets analysis demonstrated *C1Q*+ tumor-associated macrophage as a major and antitumor immune cell population in osteosarcoma
Jihao Tu, Duo Wang, XiaoTian Zheng and Bin Liu

frontiers | Frontiers in Immunology

TYPE Editorial
PUBLISHED 27 February 2023
DOI 10.3389/fimmu.2023.1161110

Check for updates

OPEN ACCESS

EDITED AND REVIEWED BY
Enrico Capobianco,
Jackson Laboratory, United States

*CORRESPONDENCE
Elena Ciaglia
eciaglia@unisa.it

SPECIALTY SECTION
This article was submitted to Cancer Immunity and Immunotherapy, a section of the journal Frontiers in Immunology

RECEIVED 07 February 2023
ACCEPTED 16 February 2023
PUBLISHED 27 February 2023

CITATION
Puca AA and Ciaglia E (2023) Editorial: Immunosenescence in the cancer microenvironment. *Front. Immunol.* 14:1161110. doi: 10.3389/fimmu.2023.1161110

COPYRIGHT
© 2023 Puca and Ciaglia. This is an open-access article distributed under the terms of the Creative Commons Attribution License (CC BY). The use, distribution or reproduction in other forums is permitted, provided the original author(s) and the copyright owner(s) are credited and that the original publication in this journal is cited, in accordance with accepted academic practice. No use, distribution or reproduction is permitted which does not comply with these terms.

Editorial: Immunosenescence in the cancer microenvironment

Annibale Alessandro Puca[1,2] and Elena Ciaglia[1]*

[1]Department of Medicine, Surgery and Dentistry "Scuola Medica Salernitana", University of Salerno, Salerno, Italy, [2]Cardiovascular Research Unit, IRCCS MultiMedica, Milan, Italy

KEYWORDS

senescence, therapy resistance, immune-suppression, aberrant crosstalk, biomarker

Editorial on the Research Topic
Immunosenescence in the cancer microenvironment

Senescence is thought to be a major barrier to the tumor formation, as it limits the replicative potential of many tumors including melanoma, hepatocellular carcinoma, and medulloblastoma. In glioblastoma, despite the promising therapeutic effect of temozolomide or etoposide, the therapy-induced cancer senescent cells remain metabolically active, and this brings attention to the potential side effects of cancer cell senescence, mainly evasion from therapy-induced senescence and resistance occurrence. Further the spreading of senescence to the neighboring cells, mainly immune cells can both enhance and dampen antitumor response.

Based on these premises, the understanding of senescence signature in cancer microenvironment may be a valuable indicator for patients' prognosis and therapy response.

The present collection includes original contributions highlighting the role of the cellular senescence and the peculiar immune status in osteosarcoma, peritoneal carcinomatosis, gastric and color cancer, cell renal cell and hepatocellular carcinomas, gliomas and in a set of bladder and endometrial cancers with particular attention to the senescence-based molecular features and the perturbation of the immune profile of the tumor microenvironment (TME).

The selected manuscripts took advantage of the rapid progress in the development of next-generation sequencing (NGS) technologies and in available bioinformatics tools which in recent years are greatly facilitating both the basic science and the clinical approaches by providing many valuable insights into complex cancer genomics.

The Cancer Genome Atlas (TCGA) and Gene Expression Omnibus (GEO) database were the main source of multi-omics data and clinical informations used by the authors to describe several score models, which are not only a robust prognostic indicator for patients' prognosis but also provides a new reference basis for personalized treatment selection.

- Based on the widespread application of single-cell RNA sequencing (scRNA-seq) technology Zhang et al. reported that aging-related MS4A6A is overexpressed in glioma tissue at both transcriptional and protein levels, and it is related to the degree of suppressing macrophage infiltration and to the significant decrease in overall survival (OS).

- Through a combination of bulk-sequencing and single-cell sequencing technology, Tu et al. demonstrated that a peculiar subpopulation of tissue-resident macrophages (*C1Q*+ TAMs), which often expresses *CD206*, *HLA-DR*, *SEPP1*, *FOLR2*, and *APO* associated with the overall survival of osteosarcoma patients and that most of the high expression of immune infiltration-related genes links to better survival. As authors stated, this study provided evidence of how immune cells influence prognosis in osteosarcoma and that *C1Q*+ TAMs can be therapeutic target cells to improve the osteosarcoma treatment.

With the advancement of next-generation sequencing technologies, RNA modifications have gained much attention because they participate in several physiological and pathological processes.

- A comprehensive analysis of RNA sequencing (RNA-seq) data and clinical information using TCGA and GEO databases led Zhao et al. to discover that the RNA methylation, e.g. N^1-methyladenosine (m1A) modifications, have a potential role in the prognosis of hepatocellular carcinoma (HCC) as these modifications clearly associated with different overall survival, TNM stage and tumor immune microenvironment (TIME) characteristics, mainly impacting prognosis and therapy response.
- Similarly Zhang et al. assessed the RNA 5-methylcytosine (m5C) modification pattern for individual gastric cancer patients and the association with the degree of immune infiltration and the most favorable prognosis in terms of tumor recurrence and immune checkpoint sensitivity.
- Lu et al. applied a novel modelling algorithm to construct a pyroptosis-related lncRNA signature in the bladder cancer. Long noncoding RNAs (lncRNAs) contribute to regulating immune microenvironment in many diseases and here the authors disclosed that this pyroptosis-related lncRNA risk model possessed good prognostic value, and the ability to predict the outcome of immunotherapy. Mechanism analysis revealed that high risk group was characterized by a higher proportion of M0 macrophages and M2 macrophages than those in the low-risk score group. However, the proportion of CD8+ T cells was significantly lower in the high-risk score group. Patients with lower risk score were characterized by higher immune checkpoint gene expression and Tumor Mutation Burden (TMB) and display a better response to immunotherapy and chemotherapy compared with patients with high-risk score.
- Similarly Chen et al. analyzed the role of Programmed Cell Death-related lncRNAs in the prognosis of colon cancer patients and their correlations with clinicopathological characteristics, the TME, the immune checkpoint genes, TMB and both immunotherapy and chemotherapeutic drug sensitivity, mainly focusing on the biological functions of the lncRNA U62317.4
- Starting from EMT-related genes (ERGs) expression and clinical data from TCGA Liu et al. develop Epithelial-mesenchymal transition (EMT)-related prognostic signature for endometrial cancer patients among which the low-risk group showed more immune activities, higher TMB and better therapy response. On the contrary, the high-risk group had higher m6A RNA expression, microsatellite instability level and stemness indices.
- Interestingly, Zhou et al. by screening RNA-seq data of the TCG-Kidney renal clear cell carcinoma (KIRC) cohort identified senescence subtypes in tumor samples. Using the adaptive lasso regression, they established a senescence score and demonstrated it was negatively correlated with immune infiltration. Furthermore, signatures from different gene expression profiles suggested that the senescence program is closely correlated with CAFs of the tumor stroma, self-limited antitumor immunity, and drug sensitivity. Consequently, a senescence score was applied to predict patients' prognosis and to properly distinguish anti–PD-1 responders in Clear Cell Renal Cell Carcinoma -ccRCC.
- At the same way, Sun et al. identified a four-cell-senescence-regulator-gene prognostic index in bladder cancer and investigated its relationship with TMB, the immune landscape of TME and response to immunotherapy and chemotherapy.
- A computational approach by Zhu et al. offered for the first time interaction between aging-associated genes in ccRCC and remodeling of the TME, providing a novel insight into the molecular drivers underlying ccRCC initiation and development.

Of note, the special issue also reported the discover of valuable biomarkers such as the predictive value of CD93 in pan-cancer. CD93 is a transmembrane receptor that is mainly expressed on endothelial cells and macrophages and Guo et al. here characterized the association between its mRNA level and immune scores, stromal scores, immune infiltrates, immune checkpoints, and prognosis in most cancer which might suggest to targeting it as a promising therapeutic strategy.

Interestingly in a murine orthotopic transplantation model for peritoneal carcinomatosis (PC), Braumüller et al. showed that the tumor cells senescence in PC is associated with a senescence-associated secretory phenotype (SASP) influencing the tumor microenvironment of PC. SASP factors can induce a senescence phenotype in neighboring cells mainly determing immunosenescence in the TME of PC. According to the focus of our special issue, these results provide a new immunoescape mechanism in PC of colorectal cancer explaining the resistance of PC to known chemo- and immunotherapeutics. Therefore, senolytic approaches may represent a valuable therapeutic opportunity to threat this terminal stage of CRC.

Finally Chen et al. reviewed the latest research progress in the immune microenvironment and strategies related to immunotherapy for colorectal cancer for the proper selection of treatment strategies for CRC patients.

Overall, we hope that all manuscripts enclosed in this Research Topic may be of interest for the readership who constantly look for useful references to optimize cancer prevention, early detection, prognosis as well as therapy.

Author contributions

All authors listed have made a substantial, direct, and intellectual contribution to the work and approved it for publication.

Conflict of interest

The authors declare that the research was conducted in the absence of any commercial or financial relationships that could be construed as a potential conflict of interest.

Publisher's note

All claims expressed in this article are solely those of the authors and do not necessarily represent those of their affiliated organizations, or those of the publisher, the editors and the reviewers. Any product that may be evaluated in this article, or claim that may be made by its manufacturer, is not guaranteed or endorsed by the publisher.

frontiers in Immunology

REVIEW
published: 02 December 2021
doi: 10.3389/fimmu.2021.792691

The Role of the Tumor Microenvironment and Treatment Strategies in Colorectal Cancer

Yaping Chen[1], *Xiao Zheng*[1] *and Changping Wu*[1,2*]

[1] Department of Tumor Biological Treatment, The Third Affiliated Hospital of Soochow University, Changzhou, China,
[2] Department of Oncology, The Third Affiliated Hospital of Soochow University, Changzhou, China

Colorectal cancer (CRC) has the second highest mortality rate among all cancers worldwide. Surgery, chemotherapy, radiotherapy, molecular targeting and other treatment methods have significantly prolonged the survival of patients with CRC. Recently, the emergence of tumor immunotherapy represented by immune checkpoint inhibitors (ICIs) has brought new immunotherapy options for the treatment of advanced CRC. As the efficacy of ICIs is closely related to the tumor immune microenvironment (TME), it is necessary to clarify the relationship between the immune microenvironment of CRC and the efficacy of immunotherapy to ensure that the appropriate drugs are selected. We herein review the latest research progress in the immune microenvironment and strategies related to immunotherapy for CRC. We hope that this review helps in the selection of appropriate treatment strategies for CRC patients.

Keywords: immunotherapy, immune microenvironment, bevacizumab, PD-1, colorectal cancer

OPEN ACCESS

Edited by:
Elena Ciaglia,
University of Salerno, Italy

Reviewed by:
Valentina Lopardo,
University of Salerno, Italy
Biao Yang,
Sichuan University, China
José Medina-Echeverz,
Affimed Therapeutics, Germany

****Correspondence:***
Changping Wu
wcpjjt@163.com

Specialty section:
This article was submitted to Cancer Immunity and Immunotherapy, a section of the journal Frontiers in Immunology

Received: *11 October 2021*
Accepted: *15 November 2021*
Published: *02 December 2021*

Citation:
Chen Y, Zheng X and Wu C (2021) The Role of the Tumor Microenvironment and Treatment Strategies in Colorectal Cancer. Front. Immunol. 12:792691. doi: 10.3389/fimmu.2021.792691

INTRODUCTION

Colorectal cancer (CRC) is a common malignant tumor of the digestive system. Worldwide, CRC ranks third in the incidence rate and second in the mortality rate among malignant tumors (1). The incidence of CRC is related to many factors, such as heredity, a low-fiber diet, smoking, lack of exercise, and obesity. At present, changes in the intestinal microbiome and metabolites are also considered risk factors for CRC (2). Traditionally, the treatment of CRC includes surgery, chemotherapy and radiotherapy. In recent years, along with the continuous research on the embryonic origin, anatomical structure, tumor clinical manifestations and genes of the left and right colon, there have been different targeted therapies for "left and right CRC dispute", namely, cetuximab and bevacizumab, respectively. Furthermore, the advent of the small molecule anti-

Abbreviations: CRC, colorectal cancer; ICIs, immune checkpoint inhibitors; TME, tumor immune microenvironment; DCs, dendritic cells; ECM, extracellular matrix; VEGF, vascular endothelial growth factor; VEFGR, vascular endothelial growth factor receptor; TGF-β, transformation and growth factors-β; PDGF, platelet-derived growth factor, CAF, cancer associated fibroblasts; TAM, tumor-associated macrophage; TAN, tumor-associated neutrophil; MDSC, myeloid-derived suppressor cell; TILs, tumor-infiltrating lymphocytes; mCRC, metastatic CRC; NK, Natural killer; OS, overall survival; PD-1, programmed cell death 1; CTLA-4, cytotoxic T-lymphocyte-associated antigen 4; ACT, adoptive cell therapy; MSS, microsatellite stable; dMMR, mismatch repair deficieny; MSI-H, high microsatellite instability; CAR, chimeric antigen receptor-modified; CIK, cytokine-induced killer; OS, overall survival; PFS, progression-free survival; DFS, disease-free survival; RFS, recurrence-free survival rate.

vascular oral drug, apatinib mesylate, has diversified the CRC treatment. Nevertheless, the prognosis of CRC depends on the stage of the tumor. The mortality of stage I/II is 8-13%, that of stage III is 11-47%, and that of stage IV is as high as 89% (3). Early detection of tumors and early effective treatment can reduce the mortality of CRC. In addition to the small molecule anti-vascular oral drugs, new therapeutic strategies for the treatment of advanced CRC based on immune checkpoint inhibitors (ICIs) have progressed. Overall, advancements in research on the tumor immune microenvironment (TME) and strategies related to immunotherapy are expected to provide more treatment choices for CRC patients.

CRC is a typical tumor infiltrated by effector memory lymphocytes, yet there have been no major breakthroughs in clinical prognosis and immunotherapy (4). It is essential to elucidate the immune environment of CRC to improve current treatment strategies and prognosis for CRC patients. The TME refers to the environment of tumor cells or tumor stem cells, which is closely related to tumor occurrence, development and metastasis of tumors. In the TME, angiogenesis is induced, and regulatory T cells (Tregs) and myeloid-derived suppressor cells (MDSCs) are recruited, which helps suppress the antitumor immune response and promote tumor progression. Furthermore, cytokines within the TME manipulate immune functions and are involved in muted immune responses that guide tumor progression (5). Therefore, the TME of CRC is an important factor affecting cancer immunotherapy. It is necessary to develop a comprehensive understanding of the TME of CRC and extend this knowledge to current treatment strategies that target dysfunctional components in the TME. This paper reviews the interaction of various components of the CRC microenvironment and related treatment strategies, with the goal of finding more effective treatment methods through a better understanding of the interaction of CRC microenvironment.

THE COLORECTUM COMPOSITION AND MICROENVIRONMENT

The colorectum is not only the main digestive organ but also an important immune organ, participating in innate and adaptive immunity. The colorectum includes the intestinal epithelium, intestinal intraepithelial lymphocytes and lamina propria lymphocytes. The intestinal epithelium digests and absorbs nutrients and forms a mucosal barrier, which effectively prevents the invasion of harmful bacteria in the intestine (6, 7). The intestinal epithelium is mainly composed of absorptive columnar epithelial cells, goblet cells and endocrine cells. Goblet cells secrete a variety of mucus proteins to form a mucus barrier to limit the invasion of bacteria into the intestinal mucosa. If the intestinal tract lacks mucus, long-term exposure to the bacterial environment may cause chronic inflammation similar to ulcerative colitis, possibly leading to cancer (8, 9). Intestinal epithelial cells also participate in the immune response. These cells obtain lumen antigens and present them to dendritic cells (DCs) in the intestinal lamina propria, which is called the goblet cell associated antigen channel (gap cells) (10, 11). McDonald et al. found that interfering with the interaction between APCs and intestinal epithelial cells *via* CCR6- deficiency in mice reduces the transfer of goblet cell products to APCs and induces the mucosal response (12). Goblet cells also regulate the immune response by secreting various cytokines, such as IL25, IL18, IL17, IL15, IL13, IL7 and IL6, as well as the chemokine exotoxins CCL6, CCL9 and CCL20 (10). Therefore, goblet cells play a unique and indispensable role in maintaining intestinal immune homeostasis by interacting with immune cells. Many endocrine cells are distributed in the colon and rectum and act as the sensory sentinels of the intestinal environment and coordinators of mucosal immunity (13). Intestinal endocrine cells can secrete cholecystokinin secretin, somatostatin, and histamine, among others, under the stimulation of chemicals or other molecules. Intestinal endocrine cells are the key receptors of metabolites of intestinal flora. Indeed, endocrine cells recognize pathogen-associated molecular patterns (PAMPs) and release cytokines and peptide hormones, which directly affect the function of the intestinal barrier. In the immune system, peptide hormones such as GLP-1 can regulate the activation of intestinal immune cells (14–16). M cells, also called microfold cells or membranous cells, are located between the lymphoid follicular epithelium and scattered among intestinal mucosal epithelial cells. M cells actively transport a variety of substances, such as soluble antigens and microorganisms, *via* liquid pinocytosis and receptor-mediated endocytosis. Recently, it was found that M cells play a specialized antigen transport role in the mucosal immune system, transporting antigens from the intestinal cavity to the subepithelial lymphoid tissue, so as to induce an immune mucosal immune response or immune tolerance (17, 18). M cell-dependent antigen uptake is mediated by specific receptors, such as β1 integrin, cellular prion protein and glycoprotein-2 (GP2) (17).

The immune cells involved in colorectal mainly include intestinal intraepithelial lymphocytes (IELs) and lamina propria lymphocytes which play an immunomodulatory role in maintaining colorectal homeostasis. The former cells express a variety of receptors, such as chemokine receptor CCR9 and integrin αEβ7. CCR9 interacts with CCL25 produced by the intestinal epithelial cells to help recruit IELs to the intestinal mucosa. Integrin αEβ7 (αE, also known as CD103) interacts with E-cadherin on intestinal cells to promote entry and retention in the intestinal epithelium (19). Approximately 90% of IELs are T cell receptor (TCR) positive, although a small number are TCR negative (20).

Lamina propria lymphocytes include DCs, intestinal T cells and plasma cells. DCs are antigen-presenting cells that are not evenly distributed in the intestine. $CD11c^+CD11b^-CD103^+$ DCs are commonly found in the colon of mice, whereas $CD11b^+CD103^+$ DCs are commonly found in the small intestine (21). Human intestinal DCs display more complex markers than mouse intestinal DCs. Human $CD103^+$ signal regulatory protein α $(SIRPα)^-$ intestinal DCs are associated with mouse intestinal $CD11b^-CD103^+$ DCs, whereas human

$CD103^+$ $SIRP\alpha^+$ DCs are closely related to mouse intestinal $CD103^+CD11b^+$ DCs, which regulate the induction of T cells (22). In recent years, it has been found that DCs and goblet cells can interact and participate in the immune response. $CD11c^+CD103^+$ DC subsets present antigens from goblet cells (23). Intestinal T cells include γδ T and αβ T cells. On the one hand, intestinal T cells secrete IFN-γ, TNF-α and other cytokines participating in the immune response against infection and resisting intestinal bacterial immersion. On the other hand, they secrete a variety of factors such as IL-4, IL-5, IL-10, IL-17 and IL-22, to maintain intestinal immune balance. There are also special Treg cells in the intestinal lamina propria that produce IL-10 and TGF-β to negatively regulate the activation of effector T cells and suppress the intestinal inflammation. Plasma cells are distributed in the lamina propria of colorectal tissue and produce different antibodies. In the duodenum/jejunum, 79% of plasma cells express IgA, 18% of plasma cells express IgM and 3% of plasma cells express IgG, while the corresponding numbers in the colon are 90%, 6 and 4%, respectively (24).

TME IN CRC

The components of the TME in CRC include tumor cells, blood vessels, the extracellular matrix, fibroblasts, lymphocytes, bone marrow-derived suppressor cells and signaling molecules.

Extracellular Matrix (ECM)

The ECM is composed of glycoprotein, collagen, elastin, proteoglycan and other macromolecules, which support and connect tissues and maintain normal physiological functions (25). Compared with normal tissue, the ECM structure of tumor tissue is disordered, and the process by which the infiltration of fibroblasts/myofibroblasts and the subsequent accumulation of significant amounts of collagenous ECM is observed in the TME is called desmoplasia (26). Desmoplasia is connected with poor prognosis and resistance to therapy (27). Furthermore, an abnormal ECM regulates the epithelial-mesenchymal transition (EMT) and affects cancer progression by directly promoting cell transformation and metastasis (28). Wei et al. found that increasing the stiffness of the surrounding ECM drives the EMT in breast cancer cells by promoting TWIST1 translocalization into the nucleus (29). ECM abnormalities also affect the efficacy of immunotherapy *via* dense EMC, preventing not only immune cells from reaching the tumor cells but also immunotherapeutic drugs from reaching the tumor. In addition, the shielding diffusion barrier that the ECM forms result in hypoxia, which directly enhances immune escape by upregulating immunomodulatory factors and increasing angiogenic signals (30). In general, ECM abnormalities relieve the behavioral regulation of stromal cells and promote tumor-related angiogenesis and inflammation, resulting in resistance to immunotherapy in the TME (31).

Peptidylarginine deiminase 4 (PAD4) is a member of the PAD family including calcium dependent isozymes (PADs 1-4 and 6) (32). PAD4 overexpression is typically involved in elevated tumor citrullination and hypercitrullination alters cell-matrix adhesion and enhances metastasis (33). Yuzhalin et al. found that citrullination of the ECM and expression of PAD4 promote liver metastasis of human CRC, which may create opportunities for the development of biomarkers and therapeutic targeting (34). Tenascin C (TNC) is a glycoprotein in the extracellular matrix, and plays a role in promoting metastasis, modulating adhesion and motility, developing angiogenesis, and establishing immune tolerance (35). In addition, Murakami et al. reported that the TNC on the CRC interstitial ECM is a factor driving liver metastasis (36), and differences in the expression of ECM-related proteins, such as the upregulated expression of TNC, exist in patients with liver metastasis and CRC recurrence (37).

Angiogenesis

Angiogenesis refers to the production of new blood vessels, while tumor angiogenesis is an endless vicious cycle that cannot be self-regulated. After tumorigenesis, cells proliferate rapidly, and the tumor becomes ischemic and hypoxic. Ischemic and hypoxic cancer cells secrete vascular endothelial growth factor (VEGF), which binds to vascular endothelial growth factor receptors (VEGFRs) on the adjacent vascular endothelium to directly stimulate tumor angiogenesis and promote the migration of endothelial cells (38). The basement membrane cells degrade, and the surrounding vascular endothelial cells proliferate rapidly and migrate to the tumor tissue *via* angiogenesis. Angiogenesis of tumor tissue is the result of the joint action of cancer cells, various tumor-related cells and their bioactive products, such as cytokines, growth factors and microbubbles. Various immune cells such as macrophages, neutrophils, immature myelocytes, B cells, T cells and peripheral cells interact in tumor angiogenesis (39).

VEGF is the most important growth factor regulating angiogenesis in colon cancer and is expressed in all colon carcinoma surgical specimens, including normal mucosa, primary colon cancers and metastatic tumors, as well as in human colorectal cancer cell lines (40, 41). Colon cancer patients with high VEGF expression had a significantly worse prognosis than those with low VEGF expression (41). Furthermore, VEGF has three receptors on CRC cells. VEGFR-1 is associated with tumor grade, Dukes stage and lymph node involvement, and VEGFR-2 is correlated with lymph node involvement while no correlation with any of the clinicopathological variables was found for VEGFR-3 (42). Witte et al. found that the expression of VEGFR-3 in >25% of colorectal cancer cells was associated with a significantly poorer overall survival, but not with lymph node metastasis or depth of tumor invasion (43). Overall, angiogenesis is an important mechanism for the occurrence and development of CRC. Tumor cells secrete VEGF and promote tumor-related angiogenesis which further promotes proliferation and distant metastasis, seriously affecting the prognosis of tumor patients.

Cancer-Associated Fibroblasts (CAFs)

Fibroblasts are nonepithelial, nonvascular and nonhematopoietic cells in connective tissue that are mainly responsible for the

formation of extracellular stroma. Fibroblasts maintain the epithelial homeostasis of normal tissues and play an important role in wound healing. When mechanical injury occurs or radiation, temperature, toxins and pathogens cause acute injury, body cells stimulate the protective system, macrophages produce transformation and growth factor-β (TGF-β) and platelet-derived growth factor (PDGF), and fibroblasts and immune cells proliferate and promote angiogenesis (44). CAFs are important components of the TME and play an essential role in tumorigenesis and development. CAFs have many potential origins, but most are considered to originate from local ancestors (45). Tumor cells are usually derived from fibroblasts in tissues, which are induced and activated by tumor cells in the microenvironment (46–48). CAFs interact with tumor cells to promote tumor growth and maintain their malignant tendency. Tumor cells affect the recruitment of CAF precursors and induce normal fibroblasts to differentiate into CAFs, which secrete a variety of growth factors such as TGF-β, VEGF, chemokines and cytokines, such as CXCL12 (SDF-1), CXCL14, CXCL16, CCL2, CCL5, IL-4, and IL-6, and metalloproteinases, such as MMP-1, MMP-2, MMP-3, MMP-9, MMP-13 and MMP-14. These factors stimulate tumor growth, angiogenesis, invasion and metastasis through a variety of mechanisms, thus affecting tumor prognosis.

Endoglin, which is expressed in CAFs in CRC specimens, metastatic lymph nodes and liver metastases, is a member of the TGF-β family of co-receptors and is involved in CAFs-mediated invasion and metastasis through TGF-β signaling pathway activation (49). Hu et al. found that CAFs can directly secrete exosomes to enhance the cell stemness and epithelial-mesenchymal transformation in CRC cells to promote CRC metastasis and chemotherapy resistance. The mechanism is dependent on increased expression of miR-92a-3p, which directly inhibits Fbxw7 and moap1 and activates Wnt/β-Catenin pathway to inhibit mitochondrial apoptosis and promote stem cell differentiation, the EMT, metastasis and 5-FU/L-OHP resistance in CRC cells (50). According to Heichler et al., CAFs secrete IL-6/IL-11 by activating STAT3 signaling pathway to promote tumor development. Moreover, the expression of pSTAT in CRC correlates with patient survival (51). CAFs are related to resistance in gastrointestinal tumors. The fibroproliferative response induced by CAFs interferes with the delivery of drugs to gastrointestinal cancer cells and causes drug resistance to chemotherapy (52).

Tumor-Associated Macrophages (TAMs)

Macrophages are resident phagocytes in lymphoid and nonlymphoid tissues that participate in steady-state tissue homeostasis by scavenging apoptotic cells and growth factors. Macrophages have a wide range of pathogen recognition receptors, which enable them to effectively phagocytize and induce the production of inflammatory cytokines. It is well known that the TME is rich in macrophages, and TAMs are considered the most abundant immune cell population in solid tumor tissues (53). TAMs are mainly recruited from the periphery by chemokines released from tumor tissues, including CCL2, CCL3, CCL4, CCL5 and CXCL12. These factors bind to corresponding receptors for recruitment of monocytes/macrophages (54). TAMs play an important role in promoting tumor angiogenesis and express a variety of growth factors (such as VEGF, PDGF and bFGF), membrane binding molecules and soluble proteases (including MMPs and cathepsin), inflammatory cytokines (TNF-α, IL-1β, IL-6), cyclooxygenase 2 (COX2) and CXC-chemokine ligand 8 (CXCL8) to promote sustained cell activation and proliferation, promoting ECM remodeling and recruitment and activation of angiogenic cells (55–57).

In CRC, TAMs are enriched in the high incidence site of the epithelial mesenchymal transformation (EMT). TAMs promote the growth and invasion of colon cancer cells through EMT remodeling (58). When HT-29 or HCT116 cells are co-cultured with TAMs (THP-1 cells stimulated by conditioned medium from a CRC cell line), TAM derived IL-6 activates the JAK2/STAT3 pathway, which results in increased FoxQ1 expression, leads to the production of CCL2 and promotes the recruitment of macrophages, thus enhancing the migration and invasion of CRC cells (59). TAMs are the main cells in the tumor EMT (60). TAMs are related to the vascular system of CRC and can be used as markers of angiogenesis-mediated CRC. By studying 76 CRC patients, Marech et al. showed a significant correlation between macrophage infiltration and microvessel density (61). Furthermore, a large total number of TAMs is favorable for the CRC prognosis. Indeed, Nakayama et al. detected high levels of TAMs in patients with a good prognosis (62). Koelzer et al. found that $CD68^+$ TAMs predicted longer OS (63). Similarly, Cavnar et al. reported a significant positive correlation between DFS and $CD68^+$ cells in 188 patients with CRC liver metastasis (64). Compared with the total number of macrophages determined by CD68 markers, the M2-like phenotype of macrophages can better predict the adverse prognosis in CRC. In the study of Wei et al., high-level expression of interstitial CD163 at the front of tumor invasion was significantly correlated with tumor grade, lymphatic vascular invasion, tumor invasion, lymph node metastasis and TNM stage, and was associated with poor recurrence survival rate (RFS), as based on IHC analysis of 81 Chinese CRC patients (59). Yang et al. found that in 81 CRC patients, a high $CD163^+/CD68^+$ ratio at the front of tumor invasion (rather than at the tumor stroma) was closely related to enhance lymphatic vascular invasion, tumor invasion, TNM stage, RFS and OS in CRC patients (65).

Myeloid-Derived Suppressor Cells (MDSCs)

Myeloid cells are composed of mononuclear myeloid cells and granulocytes, while mononuclear myeloid cells are mainly composed of monocytes, final differentiated macrophages and DCs. Granulocytes include neutrophils, eosinophils and basophils (66–68). In the early 1980s, these cells were found to be immunosuppressive. Therefore, to unify this group of cells, they were named bone marrow-derived suppressor cells in 2007 (69).

MDSCs interact with the TME, and tumor and stromal cells secrete TGF-β, MMP9, BV8, IL-6, IL-1β, β-FGF and VEFG through autocrine and paracrine mechanisms, mobilizing and expanding MDSCs and further promoting tumor growth (70). The TME can secrete chemokines, cause MDSCs to migrate to the tumor site, inhibit immune function and accelerate tumor

progression (71, 72). CCL2 recruits MDSCs to the CRC TME (73), enhancing the immunosuppressive function by inhibiting T cell proliferation and stimulating Treg development (74). In a mouse model, reducing CXCL4 in CRC tumor tissue promoted the recruitment of MDSCs, resulting in an immunosuppressive environment and progression of CRC (75). Ouyang et al. found increased levels of $CD33^+$ $CD11b^+HLA\text{-}DR^-$MDSCs in primary tumor tissues of CRC patients, which was related to advanced TNM stage and lymph node metastasis. At the same time, it was found that tumor cells induce the expansion of MDSCs through a variety of inflammatory factors. These tumor-derived MDSCs inhibit T cell proliferation and promote tumor cell growth through oxidative metabolism (76).

Tumor-Associated Neutrophils (TANs)

Neutrophils are effector cells of the innate immune system. Unlike macrophages, neutrophils are not antigen-presenting cells but act as killer cells in the blood. Neutrophils are mainly produced in the bone marrow, accounting for 50-70% of human circulating leukocytes, with a half-life of only 5 days; however, they are the only immune cells that can dissolve cells and tissues (77). When the body releases chemokines after infection, neutrophils tend to migrate and recognize pathogens (78). In cancer, tumor cells and TAMs release the chemokines CXCL1/2/3/6/8 and CCL3/5, which induce neutrophils in peripheral blood to enter the TME and polarize into different TANs (79, 80).

A few studies on the relationship between TANs and the survival rate of CRC patients have been conducted (81). Rao et al. found that an increase in neutrophils in tumors is associated with a malignant phenotype and can predict poor prognosis in CRC (82). Galdiero et al. evaluated CRC patients receiving 5-FU chemotherapy and found that a higher TAN concentration was associated with better treatment efficacy. TANs are important immune cell infiltration components in CRC. In fact, evaluating TAN infiltration may help to identify patients who will benefit from 5-FU chemotherapy (83). Berry et al. analyzed the number of neutrophils in CRC tissues. Due to the lack of neutrophil-specific antibodies, neutrophils were counted manually according to their morphology, and high levels of TANs were associated with better overall survival (OS) in patients with stage II CRC (84). Furthermore, the combination of the neutrophil lymphocyte ratio and platelet count is able to predict the future clinical course of CRC (85). A high neutrophil to lymphocyte ratio (NLR) has also been shown to be a poor prognostic factor in CRC patients. Li et al. retrospectively analyzed a cohort of 354 patients with stage I-III CRC and observed a close relationship between dynamic changes in the NLR and the OS rate (86). Additionally, a high NLR has an adverse effect on the OS of CRC patients undergoing radical surgery (87).

Tumor-Infiltrating Lymphocytes (TILs)

Lymphocytes are the main immune cells of tumors, including T, B, NK, and NKT cells, and these subsets can reflect tumor immunotherapy and serve as clinical biomarkers. T cells are the most abundant and characteristic immune cells in the TME and are divided into cytotoxic T cells, helper T cells, inhibitory T cells and NKT cells, in contrast to traditional T cells (88). T cells prevent tumor growth by targeting tumor cells. Tregs are a specific group of $CD4^+$T cells related to the overreaction of immunosuppression, inflammation and allergic diseases (89). In cancers, Tregs are considered to inhibit immunity in most cases, and Treg infiltration is associated with poor prognosis (90–92). Marshall et al. found that Treg cells promote lung cancer metastasis (93). High $FoxP3^+$ Treg infiltration exhibits a significant correlation with shorter OS patients with other solid tumors, including ovarian cancer, gastric cancer, renal cell carcinoma, melanoma, hepatocellular carcinoma, oral squamous cell carcinoma and breast cancer (94–97). However, in some tumors with chronic inflammatory infiltration, the accumulation of Tregs correlates positively with good prognosis. Frey et al. found that patients with mismatch repair deficiency (dMMR) CRC had high-level infiltration of $Foxp3^+$ Tregs, with an increased survival rate (98). According to Hanke et al., high-level infiltration of $Foxp3^+$ Tregs in early lymph node-negative CRC has a good prognosis (99). Vlad et al. also found that an increased $Foxp3^+$ Treg density is associated with improved survival in CRC and is an independent prognostic factor (100). The relationship between Treg infiltration and tumor prognosis seems to be closely related to tumor type. Treg regulation plays the dual or multiple roles in antitumor immunity and the tumor treatment response, maintaining immune homeostasis and preventing autoimmunity (101, 102).

B lymphocytes participate in immune regulation mainly by producing immunoglobulin, presenting antigen secreting cytokines. B lymphocytes produce antibodies in the tumor microenvironment, which promotes tumor development (103, 104). B cells also inhibit tumor growth. Mouse B cells can promote antitumor activity through T cell-mediated immunity, inhibiting tumor development, and CD20-deficient mice show T cell antitumor inhibition (105–107). In malignant melanoma, enhanced patient survival is related to the simultaneous presence of tumor-related $CD8^+$ T cells and $CD20^+$ B cells but not to other clinical features (108). Research on the progression of CRC by B cells is limited, and views are inconsistent. There are differences between the B cell subsets in the peripheral blood, mesenteric lymph nodes and primary tumors of patients with CRC and those of healthy people, and B cells are activated in tumor-related tissues (109). After activation, B cells in patients with CRC differentiate into mature types, resulting in a specific response to tumors. On the other hand, the number of B cells in patients with metastatic CRC (mCRC) is small and the proportion of regulatory B cells is increased, which may be involved in immune escape (110, 111). Nevertheless, Berntsson et al. found that the survival time of CRC patients with B cell infiltration was prolonged (112). Through multiple-regions single-cell sequencing of tumors, normal mucosal tissue, liver metastases, and pairs of noncancerous tissues in CRC patients, a recent study showed that the contradictory effect of B cells on tumors in the past was due to the existence of multiple subtypes of B cells. IgA^+IGCL2^+ plasma cells are associated with poor prognosis of CRC, whereas highly proliferated $GLC2^+$ plasma cells and circulating B cells are associated with a better prognosis (113).

Natural killer (NK) cells are effector cells of the immune system. When cells are infected or mutated by the virus, the expression of MHC-1 on their surface is lacking or abnormal. NK cells bind to NKG2D interaction ligands through antibody-dependent cell-mediated cytotoxicity (ADCC) or receptors, degranulate and release cytotoxic perforin and granzyme, induce signal transduction, and kill virus-infected cells and tumor cells (114). However, compared with those in adjacent normal tissues, NK cell levels in CRC tissues are low, suggesting that less NK cell infiltration may be one of the mechanisms of TME immune escape (115). The phenotype of peripheral NK cells in CRC patients changes, which promotes tumor progression (116). In CRC patients with curative tumor resection, the expression of NKp44 and NKG2D on circulating NK and NKT cells is increased, suggesting that the primary tumor and TME have an inhibitory effect on the phenotype of NK and NKT cells in CRC (117). *In vitro*, NK cells can enhance the cytotoxicity of cetuximab and the killing effect on RAS and BRAF mutant CRC cells (118). A phase I clinical trial observed NK cells to be closely related to the therapeutic effect of CRC. Cetuximab was significantly effective in patients with NK cell infiltration, though there was no significant correlation in patients who did not receive cetuximab (119). NK cell therapy has played a key role in hematological diseases and resulted in the use of NK cells in solid tumors. Initial results for chimeric antigen receptor-NK (CAR-NK) in the treatment of CRC patients have been obtained and NKG2D-CAR-modified NK cells showed antitumor effects in mouse models. At the same time, the standard CAR-NK was used in three CRC patients, who reached the safe end point (120). NK cells are also a prognostic factor for CRC recurrence (121).

In addition to NK cells and T cells, there is a special group of cells with the common characteristics of NK and T cells, called NKT cells. NKT cells have $CD4^+$ $CD8^+$ thymocytes, which develop in the thymus and migrate to peripheral organs such as the liver, spleen, lung and intestine (122, 123). Although NKT cells exert cytotoxicity, they mainly secrete a large number of helper T cytokines Th1-, Th2-, Th17-, Treg- or helper follicular cytokine (TFH)-cell related cytokines to play a regulatory role in innate or acquired immunity (124, 125). Type I NKT cells recognize glycosphingolipids α- galactose ceramide or its analogs (126, 127). α-Galactose ceramide (α-galcer) increases NKT expression and PD-1 in combination with α-galce increases the activity of NKT cells, enhances the antitumor response, and significantly reduces the occurrence of small and large intestinal tumors (128). Compared with the normal mucosa, the expression of CD69L and FasL is increased in infiltrating type I NKT cells in CRC tumor tissue, IFN- γ and granzyme B are also increased, and the OS rate of CRC patients with high-level NKT cell infiltration is higher than that of patients with low NKT cell infiltration (129). Intratumoral infiltration of NKT cells can be used as a prognostic factor for CRC.

Exosomes

In the process of tumor cell growth, invasion and metastasis, tumor cells and interstitial fine cells located in the TME can not only secrete various soluble molecules, including cytokines and chemokines, but also release various vesicles. These vesicle structures are extracellular vesicle structures (130) that can be divided into exosomes (20-100 nm), microbubbles (100-1000 nm) and apoptotic bodies (1-5 μm) according to their size. Exosomes are different in size from microbubbles and apoptotic bodies and have specific surface molecular characteristics, such as CD9 and CD63 expression. Exosomes are present in almost all body fluids, including plasma/serum, saliva, breast milk, cerebrospinal fluid, urine and semen (131–141). Exosomes are also distributed in the TME and carry cargo including a variety of proteins, DNA, mRNA, miRNA, long noncoding RNA, and even virus/prion genetic material (142–146). Exosomes play a key role in local and remote intercellular communication in cancer and are an important part of the TME. Almost all kinds of cells in tumors can secrete exosomes, including tumor cells, tumor-associated adipocytes, TAFs, TAMs and vascular endothelial cells. Exosomes can be ingested by recipient cells to participate in intercellular signal exchange (130).

Zeng et al. found that in CRC, cancer-derived exosomal miR-25-3p promotes vascular permeability and angiogenesis by regulating the expression of VEGFR2, ZO-1, occludin and claudin-5 in endothelial cells by targeting KLF2 and KLF4. And miR-25-3p from CRC cells enhances CRC metastasis in the mouse liver and lungs. In addition, the expression of miR-25-3p in circulating exosomes is significantly higher in CRC patients with metastasis than in those without metastasis, and exosomes can be used as blood biomarkers (147). CRC-derived exosomal miR-106b-3p promotes tumor metastasis by downregulating DLC-1 expression (148). Exosomal miR-200c-3p negatively regulates the migration and invasion of CRC stimulated by lipopolysaccharide (LPS) (149). The CRC-derived exosomal circRNA, circPACR can be induced by miR-142-3p/miR-506-3p-TGF-β1 to promote CRC cell proliferation, migration and invasion (150). CAFs are the main components of the TME and promote cancer development through tumor matrix interactions. Bhome et al. compared the exosomes of normal and TAFs in CRC patients and found that CAFs were enriched in microRNAs 329, 181a, 199b, 382, 215 and 21, with microRNA 21 being the most abundant. After establishing the original transplanted tumor model with miR-21-overexpressing fibroblasts, liver metastasis increased (151). Exosomal miR-21 is expressed by stromal fibroblasts and promotes tumor cell metastasis. MiR-21 is involved in the progression of CRC. Exosomes secreted by CAFs are also involved in CRC metastasis and chemoresistance. Hu et al. found that CAFs secrete exosomes, resulting in a significant increase in the level of miR-92a-3p in CRC cells, activating the Wnt/β- catenin pathway and inhibiting mitochondrial apoptosis by directly inhibiting FBXW7 and MOAP1; the effect is to promote stemness, EMT, metastasis and 5-FU/L-OHP resistance in CRC (50). This finding provides an alternative way to predict and treat CRC metastasis and chemoresistance by inhibiting exosomal miR-92a-3p. Exosomes can also be used as diagnostic markers in CRC. Maminezhad et al. detected CRC cell lines and patient serum,

and found increased levels of miR19a, miR-20a, miR-150 and let-7a but decreased levels of miR-143 and miR-145, with expression being related to TNM stage (152). Clinically, many miRNAs secreted by exosomes, such as let-7a, miR-1229, miR-1246, miR-150, miR-21, miR-223, and miR-23a have been used as diagnostic and prognostic markers for screening and predicting CRC tumors (153).

Immunosenescence

Immunosenescence is a process of immune dysfunction that tend to cause inflammation and an immunosuppressive microenvironment leading to tumorigenesis and cancer metastasis (154). Senescence might become an obstacle to achieve efficacious immunotherapy in the TME, since senescent cells secret proinflammatory cytokines and growth factors, known as the senescence associated secretory phenotype (SASP), and this secretion has been implicated in both aging and cancer development (155). Giunco et al. found that in elderly CRC patients, senescent CD8 cells, but not CD4, displayed a significant relationship with disease outcome. Furthermore, the CD4/CD8 ratio was a prognostic marker of disease relapse in stage I-III CRC patients (156). In the TME of CRC, immunosenescent cells can influence the therapeutic effect since the majority of CRC patients with microsatellite stability (MSS) do not benefit from current anti-PD-1 therapy. A recent study found that in 18 MSS CRC patients, the number of immunosuppressive/exhausted T-cell phenotypes at tumor lesions were increased and $CD8^+$ $CD28^-$ immunosenescent T cells were accumulated according to single-cell mass cytometry analysis. Moreover, the TME of CRC hosts chemokines/cytokines that likely recruit immunosuppressive/exhausted T cell subsets to regulate the immune system (157). It is necessary to comprehensively understand the immunosenescence to help boost the immune response in patients with MSS CRC.

CURRENT STRATEGIES RELATED TO IMMUNOTHERAPY IN CRC

Antiangiogenic Therapy

Bevacizumab, an immunoglobulin G monoclonal antibody against humanized vascular growth factor A, selectively binds to vascular endothelial factor subtype A (VEGF-A), hinders the binding of vascular endothelial growth factor to receptor tyrosine kinases (VEGFR), and initiates signaling to inhibit tumor angiogenesis (158, 159). Bevacizumab has been approved for first-line and second-line treatment of mCRC (160). An Italian randomized, open, multicenter, phase 3 clinical trial (NCT00719797) compared the efficacies of FOLFIRI combined with bevacizumab and FOLFIRI alone, and the median survival time of the FOLFIRI combined with bevacizumab group was greater than that of the FOLFIRI group (29.8 months *vs.* 25.8 months, HR = 0.80, $P = 0.03$) (161). Additionally, the combined use of bevacizumab did not significantly increase side effects but did enhance effective PFS and OS (162). The latest study found that bevacizumab combined with capecitabine was also effective as an advanced treatment for previously irinotecan-, oxaliplatin- and fluoropyrimidine-resistant mCRC (163). VEGF plays an important role in the CRC immune microenvironment, which can inhibit DC maturation, reduce T cell tumor infiltration and increase inhibitory cells in the TME (164–167). We found that the level of VEGF was increased in tumors. Moreover, bevacizumab inhibited the VEGF-VEGFR1 binding signal on DCs, NF-κB signaling, and DC cell maturation, prevented the increase in the amount of MHC and other molecules, and suppressed T cell activation. In CRC patients, bevacizumab elevated the number of mature DCs in the peripheral blood (168). Limagne et al. found that the amount pf MDSCs of patients decreased with FOLFOX in combination with bevacizumab, which was related to longer survival (169).

Ramucirumab, a humanized monoclonal antibody, mainly acts on the extracellular region of VEGF receptor 2 and has a beneficial role in gastric cancer, lung cancer and CRC (170–175). In the RAISE trial, after first-line oxaliplatin/fluoropyrimidine chemotherapy combined with bevacizumab for progressed CRC, ramucirumab was added to FOLFIRI, and the OS rate and progression-free survival(PFS) rate of patients were significantly improved (176).

Aflibercept is a monoclonal antibody composed of the extracellular segments of human VEGFR-1 and VEGFR-2 fused with the vascular endothelial growth factor-binding region and human immunoglobulin G1 FC region. Aflibercept β combined with FOLFIRI was approved for second-line treatment of mCRC in 2017 (177). A high-quality double-blind randomized controlled trial (RCT), the VELOUR trial, compared the efficacy of aflibercept plus FOLFIRI with that of placebo plus FOLFIRI, and the median OS, OS and PFS were higher than those in the former group (178). However, aflibercept in elderly patients (> 65 years old) shows a controllable increase in toxicity (179).

In addition to using monoclonal antibodies to inhibit the VEGFA pathway, some small molecule inhibitors have been applied in anti-VEGF therapy, such as regorafenib, sorafenib, sunitinib, pazopanib and axitinib. An international, multicenter, placebo-controlled phase III clinical trial (CORRECT) found that the median survival time of mCRC patients in the regorafenib group was longer than that in the placebo group (6.4 months *vs.* 5.0 months, HR = 0.77, $P = 0.00052$) (180). Regorafenib combined with nivolumab also has good applicability for the treatment of MSS chemotherapy-resistant mCRC (181). Sorafenib, a multi-kinase inhibitor that targets serine threonine and tyrosine kinases involved in tumor progression and angiogenesis, including all VEGFRs and PDGFR-β, RET, FLT3 and c-KIT (182), is used to treat advanced renal cell carcinoma, unresectable hepatocellular carcinoma and thyroid cancer (183–186). In CRC, a phase I clinical trial (RESPECT) found that the first-line combined use of sorafenib and oxaliplatin, folic acid and fluorouracil (mFOLFOX6) did not prolong PFS (187). In a multicenter, randomized phase II clinical trial (NEXIRI-2/PRODIGE 27), mCRC patients carrying RAS mutations had a prolonged 2-month no-progression rate and median PFS with the use of sorafenib combined with irinotecan after oxaliplatin, irinotecan, fluoropyrimidines and bevacizumab failed (188). Sunitinib is a

small molecule multi-target receptor tyrosine kinase inhibitor. However, for patients with unresectable/advanced mCRC, the first-line combination of sunitinib and FOLFIRI did not lead to significant clinical benefits (189). A randomized, phase III clinical trial found no significant difference in median PFS between sunitinib combined with FOLFIRI and FOLFIRI combined with placebo (190). Fruquintinib, a small molecule selective VEGFR inhibitor independently developed in China, significantly prolonged the median OS of patients after three-line use of fruquintinib compared with that of patients receiving the placebo (9.3 months vs. 6.6 months, HR = 0.65) (191). The major antiangiogenic therapy agents under clinical investigation in CRC are summarized in **Table 1**.

Anti-EGFR Therapy

EGFR is a membrane-bound receptor tyrosine kinase protein that activates downstream intracellular signaling pathways, including MAPK (RAS/RAF/MEK/ERK), PI3K/AKT, and JAK/STAT3 signaling, and plays a role in tumor cell growth, proliferation and differentiation (206, 207). EGFR promotes tumor progression when overexpressed. CRC patients exhibit high-level expression of EGFR. Therefore, targeting EGFR and its downstream pathways has become a new strategy for the treatment of CRC (208). Cetuximab is a human/mouse chimeric IgG1 monoclonal antibody that mainly binds to EGFR on the surface of tumor cells and competitively blocks EGFR signaling to inhibit tumor cell proliferation. Cetuximab also inhibits the development of neovascularization by reducing the production of VEGF and activates the human anti- chimeric antibody (HACA) (209). Initial multiple clinical phase II trials found that among EGFR-positive patients, cetuximab combined with irinotecan had a better clinical effect than chemotherapy alone (210–212). Despite no significant difference between the PFS risk ratios and OS rates of mCRC patients receiving cetuximab combined with FOLFIRI and mCRC patients receiving FOLFIRI alone, cetuximab combined with FOLFIRI benefited KRAS wild-type patients (213). KRAS is an effector molecule responsible for signal transduction from ligand-bound EGFR to the nucleus. Activation of KRAS mutations often leads to CRC resistance to the EGFR targeted monoclonal antibodies (214). Therefore, EGFR-positive wild-type KRAS CRC responds to cetuximab (215). The CEBIFOX study found an ORR of 70.3%, a median PFS of 10.9 months (95% CI 9.0-12.9), and an OS of 33.8 months (95% CI 21.4-45.5) for fortnightly use of cetuximab combined with FOLFOX6 in patients with RAS wild-type mCRC (216).

Panitumumab, the first fully humanized IgG2 monoclonal antibody, displays a high affinity for EGFR, and its mechanism of

TABLE 1 | Summary of antiangiogenic therapy for colorectal cancer (CRC).

Regimen	Target population	Design	Treatment	Registration number	Reference
Bevacizumab	mCRC	Phase II	FOLFIRI+ Bevacizumab	NCT00467142	(192)
	mCRC	Phase II	Oxaliplatin + Bevacizumab + Capecitabine	NCT00159432	(193)
	mCRC	Phase II	FOLFOX + Bevacizumab FOLFOX + Bevacizumab + Irinotecan	NCT01321957	(194)
	mCRC	Phase II	Perioperative FOLFOXIRI + Bevacizumab Postoperative FOLFOX	NCT01540435	(195)
	mCRC	Phase III	FOLFOXIRI + Bevacizumab FOLFIRI + Bevacizumab	NCT00719797	(161)
	mCRC	Phase III	Capecitabine + Bevacizumab Capecitabine	NCT00484939	(196)
	mCRC	Phase III	Chemotherapy + Bevacizumab Chemotherapy + Cetuximab	NCT00265850	(197)
	mCRC	Phase III	Bevacizumab + Xelox	NCT00384176	(198)
	mCRC	Phase III	Bevacizumab + Chemotherapy Chemotherapy	NCT00112918	(199)
	mCRC	Phase III	Bevacizumab + Xelox	NCT00577031	(200)
Ramucirumab	mCRC	Phase III	Ramucirumab + FOLFIRI Placebo+ FOLFIRI	NCT01183780	(176)
Aflibercept	mCRC	Phase III	Aflibercept + FOLFIRI Placebo	NCT01661270	(201)
	mCRC	Phase III	Aflibercept + FOLFIRI Placebo	NCT00561470	(178, 202)
Regorafenib	mCRC	Phase III	Regorafenib Placebo	NCT01103323	(180)
	mCRC	Phase III	Regorafenib	NCT01853319	(203)
	mCRC	Phase III	Regorafenib Placebo	NCT01584830	(204)
Sorafenib	mCRC	Phase II	Sorafenib + Bevacizumab	NCT00826540	(182)
	mCRC	Phase II	Sorafenib + Irinotecan	NCT01715441	(188)
Sunitinib	mCRC	Phase II	Sunitinib + FOLFIRI	NCT00668863	(189)
	mCRC	Phase III	Sunitinib + FOLFIRI Placebo +FOLFIRI	NCT00457691	(190)
Fruquintinib	mCRC	Phase III	Fruquintinib Placebo	NCT02314819	(191, 205)

action in CRC treatment is similar to that of cetuximab. Clinical phase II and III trials have shown that panitumumab can significantly prolong the PFS of patients with refractory CRC, with good tolerance (212, 217). In a randomized phase III trial (PRIME), the PFS of patients with wild-type KRAS was prolonged with mCRC first-line use of panitumumab combined with fluorouracil, folic acid and oxaliplatin (FOLFOX4) compared with that of patients receiving FOLFOX4 alone, though there was no significant difference in OS (218). In the randomized, open, phase II VOLFI study (AIO KRK0109), FOLFOXIRI combined with panitumumab was used as the first-line treatment for Ras wild-type mCRC improving the ORR and secondary surgical resection rate (219). In a phase II trial of locally advanced rectal cancer, FOLFOXIRI combined with panitumumab/cetuximab was used as a new adjuvant chemotherapy for patients with wild-type RAS-BRAF rectal cancer, with good clinical efficacy and tolerance (220). The major agents targeting EGFR therapy under clinical investigation in CRC are summarized in **Table 2**.

Immune Checkpoint Inhibitors (ICIs)

Immune checkpoints are molecules that express and regulate the activation of immune cells. When the immune response is too strong, the immune checkpoint acts as a key regulator for attenuation (222). However, in cancer, immune checkpoints are highly activated and overexpressed; thus, antigens cannot be presented to T cells, inhibiting their immune function and resulting in malignant cell proliferation and tumor immune escape (223, 224). ICIs restore immune function mainly by targeting and/or blocking immune checkpoint protein ligands on the surface of T cells or other immune cell subsets (225). ICIs constitute a mature monoclonal antibody immunotherapy. The most widely studied immune checkpoint targets are programmed cell death 1 (PD-1) and cytotoxic T -lymphocyte-associated antigen 4 (CTLA-4), which are used for a variety of solid tumors (226–228). There are also studies on the potential role of other checkpoints in tumor immune regulation, such as lymphocyte activation gene-3 (LAG-3), T cell immunoglobulin-3 (Tim-3), T cell immunoglobulin and the ITIM domain (TIGIT) (229–233). CTLA-4 is a transmembrane protein that is mainly expressed on activated T cells and was first cloned in 1987 (234). CTLA-4 binds the B7 molecule to reduce T cell activity and inhibit T cell activation channels, with an immunosuppressive function (235, 236). In 2010, the CTLA-4 inhibitor ipilimumab was demonstrated to improve the long-term prognosis of patients with unresectable malignant melanoma (237). In 2011, ipilimumab became the first ICI approved by the FDA for cancer treatment. PD-1, a new member of the immunoglobulin gene superfamily, is expressed by various immune cells, such as CD4 and CD8 T cells, B cells, macrophages, DCs and tumor-infiltrating lymphocytes (TILs) (238, 239). PD-1 is a negative regulatory molecule that inhibits T cell activation and limits autoimmunity (240, 241). The use of PD-1/PD-L1 pathway inhibitors can restore the function of effector T cells, playing an antitumor role (242). At present, a variety of PD-1 and PD-L1 inhibitors have been approved by the FDA to treat a variety of tumors.

There are currently three PD-1 and CTLA-4 inhibitors approved by the FDA for CRC: pembrolizumab, nivolumab and ipilimumab (**Table 3**).

Pembrolizumab (Keytruda®) is the first PD-1 inhibitor approved by the FDA for metastatic malignant melanoma (252). In recent years, pembrolizumab has been used for non-small-cell lung cancer (253, 254), Hodgkin's lymphoma (255, 256), HNSCC (257), urothelial carcinoma (258, 259), gastric cancer (260) and CRC (243, 244). The landmark clinical trial NCT01876511 for the treatment of CRC with pembrolizumab is noteworthy. The clinical trial included 11 dMMR CRC patients and 21 pMMR CRC patients and 9 patients with dMMR in other cancers. The immune-related objective response rate and immune-related PFS rate were 40% and 78% in dMMR CRC patients, and 0% and 11% in pMMR CRC patients, respectively. The median PFS and OS in the dMMR group were not achieved, and the median PFS and OS in the pMMR CRC group were 2.2 months and 5.0 months, respectively (HR = 0.1, $P < 0.001$) (245). Based on these data, pembrolizumab (Keytruda®) was approved to treat unresectable or metastatic dMMR and high microsatellite instability (MSI-H) CRC by the FDA on May 23, 2017 (261). KEYNOTE-164 is a phase II clinical trial for evaluating pembrolizumab in the treatment of refractory, MSI-H/dMMR metastatic CRC. At the end of the trial data, the median follow-up time of group A (previously received ≥ 2-line treatment) was 31.3 months (range of 0.2-35.6 months), the objective response rate was 33% (95% CI, 21% - 46%), and the median PFS was 2.3 months (95% CI, 2.1-8.1 months). The median follow-up time of CRC in group B (previous ≥ 1-line treatment) was 24.2 months (range of 0.1-27.1 months), the objective response rate was 33% (95% CI, 22% - 46%) and the median PFS was 4.1 months (95%

TABLE 2 | Summary of anti-EGFR therapy for colorectal cancer (CRC).

Regimen	Target population	Design	Treatment	Registration number	Reference
Cetuximab	mCRC	Phase II	Cetuximab + FOLFOX-6	NCT01051167	(216)
	mCRC	Phase III	Chemotherapy + Bevacizumab Chemotherapy + Bevacizumab + Cetuximab	NCT00208546	(221)
	mCRC	Phase III	Cetuximab + FOLFIRI FOLFIRI	NCT00154102	(213)
Panitumumab	mCRC	Phase III	Panitumumab + FOLFOX4 FOLFOX4	NCT00364013	(218)
	mCRC	Phase II	Panitumumab + FOLFOXIFI FOLFOXIFI	NCT01328171	(219)

TABLE 3 | FDA approved main agents of immune checkpoint inhibitors (ICIs) for colorectal cancer (CRC).

Regimen	Target population	FDA approved date	Registration number	Reference
PD-1 inhibitor				
Pembrolizumab	Unresectable or metastatic dMMR and high microsatellite instability (MSI-H) CRC	23 May 2017	NCT01876511 KEYNOTE-164 KEYNOTE-177 (NCT02563002)	(243–245)
Nivolumab	DMMR and MSI-H mCRC	1 August 2017	CheckMate 037 CheckMate 066 CheckMate 142 (NCT02060188)	(246–248)
PD-1 + CTLA-4 inhibitor				
Nivolumab + Ipilimumab	DMMR and MSI-H mCRC	10 July 2018	CheckMate 142	(249–251)

CI, 2.1-18.9 months). The incidence of treatment-related grade 3-4 adverse events was 16% in group A and 13% in group B. Thus, pembrolizumab can be safely used in patients with MSI-H/dMMR CRC (244). KEYNOTE-177 (NCT02563002) is a phase III clinical trial in which patients with metastatic MSI-H/dMMR CRC were randomly assigned to the pembrolizumab arm, though patients receiving chemotherapy could switch to pembrolizumab if disease progression occurred. The PFSs of the pembrolizumab and chemotherapy groups were 16.5 months and 8.2 months, respectively (HR = 0.60; 95% CI, 0.45-0.80; $P = 0.0002$) (243).

Another successful PD-1 inhibitor is nivolumab (Opdivo®). Based on the CheckMate 037 and CheckMate 066 trials, nivolumab has also been approved for the first time to treat unresectable or metastatic melanoma (246, 247). Nivolumab showed a good therapeutic effect in mCRC patients with dMMR/MSI-H. CheckMate 142 (NCT02060188) found that 23/74 patients achieved objective remission, and 68.9% (51/74) of patients received > 12 weeks of disease control; the safety of dMMR/MSI-H mCRC was tolerable (248). Nivolumab was approved on August 1, 2017, for dMMR and MSI-H mCRC. Interestingly, the CTLA inhibitor ipilimumab has also shows a certain therapeutic effect in CRC. Ipilimumab combined with nivolumab as the treatment for dMMR/MSI-H mCRC patients was effective at 9 months in 94% of patients; the PFS rates at 12 months were 76% and 71% for dMMR and MSI-H mCRC patients, respectively, and the OS rates at 12 months were 87% and 85% for dMMR and MSI-H mCRC patients, respectively (249). Moreover, ipilimumab combined with nivolumab did not significantly increase toxicity or side effects (250). Therefore, ipilimumab and nivolumab were approved for dMMR and MSI-H mCRC on July 10, 2018. Furthermore, a recent phase II CheckMate 142 study found that first-line nivolumab plus low-dose ipilimumab had robust and durable clinical benefit and was well tolerated as a first-line treatment for MSI-H/dMMR mCRC patients (251).

Adoptive Cell Therapy (ACT)

Adoptive cell therapy utilizes the immune cells, such as T cells, DCs, NK cells or cytokine-induced killer (CIK) cells, of patients or other donors for tumor patients to achieve anti-tumor effects. ACT for CRC treatment includes TILs, CIK cell therapy and chimeric antigen receptor-modified (CAR) T cell therapy (**Table 4**). In a clinical study on TILs combined with IL-2 in CRC, patients in the ACT group received TILs extracted from metastatic tumors, as stimulated and amplified with high-dose IL-2, whereas the control group received traditional chemotherapy. Although no significant difference in disease-free survival (DFS) was observed between the two groups after 1, 3 and 5 years, TCRε chain expression increased significantly in disease-free patients

TABLE 4 | Summary of adoptive cell therapy (ACT) for colorectal cancer (CRC).

Regimen	Target population	Design	Registration number	Status
TILs	Malignant Solid Neoplasm including MCRC Adenocarcinoma, Metastatic Ovarian Carcinoma	Phase II	NCT03610490	Active, not recruiting
	CRC stage III	Phase I/II	NCT03904537	Recruiting
	CRC	/	NCT02980146	Completed
CEA-CAR-T	CRC stage III, CRC liver metastasis	Phase I	NCT04513431	Not yet recruiting
	Solid cancers including CRC	Phase I, II	NCT04348643	Recruiting
	CRC Peritoneal Carcinomatosis Peritoneal Metastases Gastric Cancer Breast Cancer Pancreas Cancer	Phase I	NCT03682744	Active, not recruiting
CART72	mCRC	Phase I	CC-9701 and CC-9702 clinical trials by Cell Genesys and Aventis Pharmaceuticals	Completed
CIK	CRC	Phase IV	NCT03084809	Completed
DC-CIK	CRC	Phase II, III	NCT02419677	Completed
	CRC	Phase II, III	NCT02415699	Unknown
	CRC	Phase II	NCT02202928	Unknown

compared with that in patients with recurrence (P = 0.04), suggesting that TILs play a role in the immune response (262). Sentinel lymph node (SLN)-T cells are also used for ACT in the treatment of CRC. A preliminary study found that after 16 CRC patients were injected with SLN T cells, 4 of 9 patients with stage IV CRC experienced complete remission, with a median survival time of 2.6 years, which was much greater than the median survival time of 0.8 years in the control group (263). In another I/II clinical study of 55 patients with CRC with SLN metastasis, the median OS of the experimental group that received expanded lymphocytes was 28 months, whereas that of the control group was 14 months, and no obvious toxicity or side effects was observed (264).

Many clinical trials using TILs or SLN T cells as a treatment for CRC (NCT03610490, NCT03904537, and NCT02980146) are being performed. NK cells have natural cytotoxicity toward tumor cells, with antibody dependent cytotoxicity (ADCC), and can secrete a variety of cytokines and chemokines for an immunomodulatory role. Therefore, NK cells can also be used for adoptive therapy. In a phase I clinical trial, expanded NK cells combined with IgG1 antibody were used to treat patients with gastric cancer or CRC. Among 6 evaluable patients, 4 were in stable condition (SD), and disease progression occurred in two patients (119). As TILs have the limitation of needing to be expanded from a tumor, exogenous T cell receptors (TCRs) have been expressed on cells by genetic engineering technology. Carcinoembryonic antigen (CEA) levels are often elevated in the tissues and serum of patients with gastrointestinal tumors. Therefore, genetically engineered autologous T lymphocytes that express mouse TCR against human CEA have been used for CRC treatment. In a phase I clinical trial, three patients with refractory mCRC were administered TCR targeting CEA, and their serum CEA levels were significantly decreased (74–99%). One patient showed reduced liver and lung metastases, but all three patients experienced severe transient inflammatory colitis (265). CAR-T cells have achieved remarkable results in B-cell leukemia and lymphoma, although the development of solid tumors is lagging (266, 267). A phase I clinical trial of targeted CEA-CAR-T cells for CRC treatment found that 7 of the 10 CEA^+ patients were in stable condition after CAR-T cell treatment, with 2 patients maintaining this state for more than 30 weeks, and 2 patients underwent tumor regression (268). Another study on CAR-T cells targeting tumor-associated glycoprotein (TAG)-72 (CART72 cells) in the treatment of mCRC found that a very short duration of CART72 cells in the blood (≤14 weeks), suggesting that CART72 cells have a limited role in mCRC (269). A CAR-NK study targeting NKG2D found that after three mCRC patients received local infusion of CAR-NK cells, ascites production decreased and tumor cells in ascites samples decreased significantly. In addition, the method using RNA to make CAR can enhance the specificity of NK cells to NKG2DL and their tumor cell killing activity (120).

CIK cells treatment is a part of ACT and is induced by mononuclear cells cultured with CD3 monoclonal antibody and cytokines such as IFN-γ, IL-1 and IL-2. CIK cells include activated NKT cells, $CD3^-/CD56^+$ NK cells and $CD3^+/CD56^-$ CTLs. CIK cells have the characteristics of rapid proliferation, strong antitumor activity, wide spectrum and low toxicity. They have been used in the treatment of various solid tumors, such as hepatocellular carcinoma, renal cell carcinoma, gastric cancer, breast cancer, ovarian cancer, non-small-cell lung cancer and nasopharyngeal carcinoma. The efficacy of somatic CIK cells in patients with mCRC was examined in a phase II clinical trial. MCRC patients in the experimental group received chemotherapy combined with CIK cells, whereas the control group received chemotherapy alone. The median OS rates of the experimental and the control groups were 36 months and 16 months, respectively (P < 0.001), and the PFS rates were 16 months and10 months (P = 0.072), respectively. Although there was no significant difference, there was an increasing trend (270). A retrospective study using CIK cells to treat postoperative CRC patients reported a median PFS and median OS in the CIK group of 25.8 months and 41.3 months, respectively, while the median PFS and median OS in the control group were 12.0 months and 30.8 months, respectively (271). Another retrospective study on the efficacy of postoperative adjuvant infusion of CIK cells combined with chemotherapy for CRC observed a significantly longer DFS in the group than in the control group [HR = 0.28, 95% CI (0.09, 0.91), P = 0.034]. The 2-year DFS rates of the CIK group and control group were 59.65 ± 24.80% and 29.35 ± 6.39%, respectively. Moreover, CIK cell infusion was not associated with immediate adverse reactions (272). Dendritic cytokine-induced killer cells (DC-CIK) were observed in the combined first-line treatment of advanced CRC. The 5-year OS rates of the DC-CIK group and non-DC-CIK group were 41.3% and 19.4% (P = 0.001), and the 5-year PFS rates of the DC-CIK group and non-DC-CIK group were 57.4% and 33.6% (P = 0.022), respectively (273). Overall, DC-CIK immunotherapy combined with first-line treatment can significantly prolong the 5-year OS and PFS rates in patients with advanced CRC.

Cancer Vaccine and Oncolytic Virus Therapy

Cancer vaccines are another method of immunotherapy for CRC (**Table 5**). Tumor cells express tumor-associated antigen (TAA), and by expressing specific tumor antigens, cancer vaccines can stimulate the body to produce a specific immune response. However, the results obtained for vaccines in the treatment of CRC are not consistent. Initially, a prospective randomized controlled clinical trial was conducted in CRC patients, and an autologous tumor cell BCG vaccine that induced active specific immunotherapy (ASI) was used. The study found that there was no statistically significant difference in the survival rate or disease-free survival rate of 80 eligible patients (279). A randomized phase III clinical trial of adjuvant ASI with autologous tumor cell BCG reported no significant difference in DFS and OS rates between the surgical resection plus ASI group and the simple resection group of stage II and III CRC patients (280). In another study of stage II and III CRC patients, despite no clinical benefit of autologous tumor cell BCG immunotherapy for stage III CRC after surgery, the recurrence-free period of autologous tumor cell BCG adjuvant ASI after surgical resection was significantly longer

TABLE 5 | Summary of cancer vaccine and oncolytic virus therapies for colorectal cancer (CRC).

Regimen	Target population	Design	Registration number	Reference
AD5 CEA Vaccine	CRC Lung Cancer Breast Cancer	Phase I, II	NCT01147965	(274)
CEA (6D) VRP Vaccine (AVX701)	CRC Lung Cancer Breast Cancer Pancreatic Cancer Colon Cancer	Phase I, II	NCT00529984	Completed
	CRC stage III	Phase I	NCT01890213	Completed
DC/PANVAC or GM-CSF	CRC Metastasis Cancers	Phase II	NCT00103142	(275)
Modified vaccine Ankara–5T	mCRC	/	ISRCTN54669986	(276)
GVAX Colon Vaccine	mCRC	Phase II	NCT02981524	Completed
MVA-Brachyury-TRICOM	CRC	Phase I	NCT02179515	(277)
Bavarian Nordic (BN)-CV301	CRC	Phase I	/	(278)

than that of simple resection (P = 0.011), and recurrence-free survival was significantly prolonged (P = 0.032) (281). As antigen-presenting cells, DCs are also often modified to produce vaccines. A randomized trial for CRC patients on the activation of CD40L by DC vaccines *in vitro* found that 15 of 24 patients had immune induction reactions. The five-year recurrence-free survival rate (RFS) of those who had tumor-specific T cell proliferation or IFN-γ induced by the vaccine that appeared at one week after vaccination was significantly higher than that of patients without a response (63% *vs*. 18%, P = 0.037) (282). The randomized phase II clinical trial on administering DC vaccines after complete resection of CRC liver metastasis showed a significantly longer median DFS for the vaccine group was than for the observation group (25.6 months *vs*. 9.53 months) (283).

Guanylcyclase C (GUCY2C), which is selectively expressed by intestinal epithelial cells and some neurons, is almost universally overexpressed in CRC (284). According to a phase I study using the Ad5-GUCY2C-PADRE vaccine in the treatment of stage I or II (pN0) colon cancer (NCT01972737), the vaccine can stimulate the immune response of T cells and has certain safety (285). CEA is overexpressed in CRC and acts as a tumor antigen marker. A phase I/II trial using the Ad5[E1-, e2b-]-CEA (6D) vaccine for advanced CRC reported a median survival time for the 32 patients included in the study of 11 months, and the Ad5 [E1-, e2b -] - CEA (6D) vaccine was well tolerated and induced an immune response (286). In the phase I study of patients with stage III CRC treated with virus-like replicator particle (VRP)-CEA, 12 CRC patients completed standard postoperative adjuvant chemotherapy and received VRP-CEA immunization 4 times every 3 weeks. The 5-year RFS rate was 75% (95% CI 40-91%), and no deaths were observed during the period. After vaccination, levels of $CD8^+$ TEMs increased (10/12), $Foxp3^+$ Tregs decreased (10/12), and specific CEA and IFN-γ produced by $CD8^+$ granzyme B^+ TCM cells increased (287).

Several CRC clinical trials of CEA-modified tumor vaccines have been carried out, such as NCT01147965, NCT00529984, and NCT01890213 (274). MUC1 is abnormally expressed in tumors and is also a tumor-associated antigen. DCs and poxvirus vectors act as immune stimulants against tumor antigens. A randomized phase II trial (NCT00103142) compared whether two vaccines based on DCs and pox vectors encoding CEA and MUC1 (PANVAC) can prolong the survival of mCRC patients after resection (275). Seventy-four mCRC patients after resection and perioperative chemotherapy were randomly treated with autologous modified PANVAC with DC (DC/PANVAC) or GM-CSF (granulocyte macrophage colony-stimulating factor) every time. The 2-year RFS rates of the two groups were similar, and the DC and poxvirus vectors had similar activity. As a treatment for mCRC, the modified vaccine Ankara-5T4 and low-dose cyclophosphamide improved the antitumor immune response and prolonged survival, with no safety problems (276). Furthermore, a phase I trial (NCT02179515) was performed to test the safety and tolerability of a modified vaccinia Ankara (MVA)-based vaccine modified to express brachyury and T-cell costimulatory molecules (MVA-Brachyury-TRICOM) in advanced patients including colon cancer patients. Heery et al. found that the MVA-brachyury-TRICOM vaccine directed against a transcription factor known to mediate EMT can be administered safely in patients with advanced cancer and can activate brachyury-specific T cells *in vitro* and in patients (277). Recently, a phase I dose-escalation trial of Bavarian Nordic (BN)-CV301, which is a recombinant poxviral vaccine targeting MUC-1 and CEA with costimulatory molecules, was conducted to test the safety and immune response of the vaccine. The trial found that the BN-CV301 vaccine was safely administered to patients with advanced cancer (278).

GVAX is a cellular immunotherapy induced by an allogeneic, whole-cell, granulocyte macrophage colony-stimulating factor that can induce the immune response of T cells to TAAs. A phase 2 study (NCT02981524) of the colon GVAX vaccine, cyclophosphamide and pembrolizumab in 17 patients with pMMR advanced CRC was carried out. The median PFS was 82 days (95% CI 48-97 days), and the median OS was 213 days (95% CI 179-441 days) (288). Although GVAX/Cy plus PD-1 did not achieve the main outcome expected in pMMR CRC, biochemical reactions were observed in patients, providing a certain method to cause insensitivity to PD-1 in pMMR CRC,

which still needs to be further explored in combination with other drugs. Although there is no cancer vaccine approved for clinical use, a large number of clinical trials are ongoing and are expected to further improve the therapeutic effect on CRC.

Tumor-Derived Exosomes Therapy

Tumor-derived exosomes have a certain potential antigenicity and can induce a strong antitumor immune response (289). Therefore, in addition to being a potential diagnostic marker, some studies have found that these exosomes can play a role as vaccines in CRC. A phase I clinical trial included 40 patients with HLA-A0201$^+$ CEA$^+$ advanced CRC who were randomly treated with AEX (ascites-derived exosomes) or AEX plus GM-CSF, and both methods were safe and tolerable. The patients in the AEX plus GM-CSF group showed a strong tumor-specific anti-tumor cytotoxic T lymphocyte reaction. These data suggest that immunotherapy with AEX plus GM-CSF can be used as an effective vaccine for mCRC patients (290).

CONCLUSION AND PROSPECTS

The TME is a complicated landscape that is not only closely related to the growth and development of CRC but also affects the treatment and prognosis of patients with colorectal cancer. A variety of cytokines, chemokines, matrix enzymes and immunosuppressive cells, such as Tregs and MDSCs, shape the immunosuppressive environment of CRC. Although immunotherapy has achieved good results in malignant melanoma and lung cancer, its results in CRC are still poor. Therefore, it is particularly important to deeply study the TME, reverse or prevent tumor immune resistance and find a better way to treat CRC. At present, research on anti-PD-1 antibodies, adoptive cell immunotherapy, vaccine therapeutics and oncolytic viruses is being carried out. We need to carry out more clinical experiments, find more biomarkers for CRC, and make rational use of the differences in immune typing and genotyping of CRC such that suitable patients can benefit from immunotherapy.

AUTHOR CONTRIBUTIONS

The manuscript was conceptualized by YC and CW. YC wrote the majority of the manuscript and produced the tables. XZ helped to write the manuscript. CW critically revised the manuscript. All authors contributed to the article and approved the submitted version.

FUNDING

This work was supported by grants from the National Natural Science Foundation of China (No. 31570908).

REFERENCES

1. Keum N, Giovannucci E. Global Burden of Colorectal Cancer: Emerging Trends, Risk Factors and Prevention Strategies. *Nat Rev Gastroenterol Hepatol* (2019) 16:713–32. doi: 10.1038/s41575-019-0189-8
2. De Almeida CV, De Camargo MR, Russo E, Amedei A. Role of Diet and Gut Microbiota on Colorectal Cancer Immunomodulation. *World J Gastroenterol* (2019) 25:151–62. doi: 10.3748/wjg.v25.i2.151
3. Koi M, Carethers JM. The Colorectal Cancer Immune Microenvironment and Approach to Immunotherapies. *Future Oncol* (2017) 13:1633–47. doi: 10.2217/fon-2017-0145
4. Fidelle M, Yonekura S, Picard M, Cogdill A, Hollebecque A, Roberti MP, et al. Resolving the Paradox of Colon Cancer Through the Integration of Genetics, Immunology, and the Microbiota. *Front Immunol* (2020) 11:600886. doi: 10.3389/fimmu.2020.600886
5. Hinshaw DC, Shevde LA. The Tumor Microenvironment Innately Modulates Cancer Progression. *Cancer Res* (2019) 79:4557–66. doi: 10.1158/0008-5472.CAN-18-3962
6. Cardoso-Silva D, Delbue D, Itzlinger A, Moerkens R, Withoff S, Branchi F, et al. Intestinal Barrier Function in Gluten-Related Disorders. *Nutrients* (2019) 11:2325. doi: 10.3390/nu11102325
7. Suzuki T. Regulation of the Intestinal Barrier by Nutrients: The Role of Tight Junctions. *Anim Sci J* (2020) 91:e13357. doi: 10.1111/asj.13357
8. Johansson ME, Gustafsson JK, Holmen-Larsson J, Jabbar KS, Xia L, Xu H, et al. Bacteria Penetrate the Normally Impenetrable Inner Colon Mucus Layer in Both Murine Colitis Models and Patients With Ulcerative Colitis. *Gut* (2014) 63:281–91. doi: 10.1136/gutjnl-2012-303207
9. Birchenough GM, Johansson ME, Gustafsson JK, Bergstrom JH, Hansson GC. New Developments in Goblet Cell Mucus Secretion and Function. *Mucosal Immunol* (2015) 8:712–9. doi: 10.1038/mi.2015.32
10. Knoop KA, Newberry RD. Goblet Cells: Multifaceted Players in Immunity at Mucosal Surfaces. *Mucosal Immunol* (2018) 11:1551–7. doi: 10.1038/s41385-018-0039-y
11. Mcdole JR, Wheeler LW, Mcdonald KG, Wang B, Konjufca V, Knoop KA, et al. Goblet Cells Deliver Luminal Antigen to CD103+ Dendritic Cells in the Small Intestine. *Nature* (2012) 483:345–9. doi: 10.1038/nature10863
12. Mcdonald KG, Wheeler LW, Mcdole JR, Joerger S, Gustafsson JK, Kulkarni DH, et al. CCR6 Promotes Steady-State Mononuclear Phagocyte Association With the Intestinal Epithelium, Imprinting and Immune Surveillance. *Immunology* (2017) 152:613–27. doi: 10.1111/imm.12801
13. Worthington JJ, Reimann F, Gribble FM. Enteroendocrine Cells-Sensory Sentinels of the Intestinal Environment and Orchestrators of Mucosal Immunity. *Mucosal Immunol* (2018) 11:3–20. doi: 10.1038/mi.2017.73
14. Tsukahara T, Watanabe K, Watanabe T, Yamagami H, Sogawa M, Tanigawa T, et al. Tumor Necrosis Factor Alpha Decreases Glucagon-Like Peptide-2 Expression by Up-Regulating G-Protein-Coupled Receptor 120 in Crohn Disease. *Am J Pathol* (2015) 185:185–96. doi: 10.1016/j.ajpath.2014.09.010
15. Ellingsgaard H, Hauselmann I, Schuler B, Habib AM, Baggio LL, Meier DT, et al. Interleukin-6 Enhances Insulin Secretion by Increasing Glucagon-Like Peptide-1 Secretion From L Cells and Alpha Cells. *Nat Med* (2011) 17:1481–9. doi: 10.1038/nm.2513
16. Hadjiyanni I, Siminovitch KA, Danska JS, Drucker DJ. Glucagon-Like Peptide-1 Receptor Signalling Selectively Regulates Murine Lymphocyte Proliferation and Maintenance of Peripheral Regulatory T Cells. *Diabetologia* (2010) 53:730–40. doi: 10.1007/s00125-009-1643-x
17. Kishikawa S, Sato S, Kaneto S, Uchino S, Kohsaka S, Nakamura S, et al. Allograft Inflammatory Factor 1 Is a Regulator of Transcytosis in M Cells. *Nat Commun* (2017) 8:14509. doi: 10.1038/ncomms14509
18. Mishima T, Iwabuchi K, Fujii S, Tanaka SY, Ogura H, Watano-Miyata K, et al. Allograft Inflammatory Factor-1 Augments Macrophage Phagocytotic Activity and Accelerates the Progression of Atherosclerosis in ApoE-/- Mice. *Int J Mol Med* (2008) 21:181–7. doi: 10.3892/ijmm.21.2.181
19. Olivares-Villagomez D, Van Kaer L. Intestinal Intraepithelial Lymphocytes: Sentinels of the Mucosal Barrier. *Trends Immunol* (2018) 39:264–75. doi: 10.1016/j.it.2017.11.003

20. Bilate AM, London M, Castro TBR, Mesin L, Bortolatto J, Kongthong S, et al. T Cell Receptor Is Required for Differentiation, But Not Maintenance, of Intestinal CD4(+) Intraepithelial Lymphocytes. *Immunity* (2020) 53:1001–1014 e20. doi: 10.1016/j.immuni.2020.09.003
21. Denning TL, Norris BA, Medina-Contreras O, Manicassamy S, Geem D, Madan R, et al. Functional Specializations of Intestinal Dendritic Cell and Macrophage Subsets That Control Th17 and Regulatory T Cell Responses Are Dependent on the T Cell/APC Ratio, Source of Mouse Strain, and Regional Localization. *J Immunol* (2011) 187:733–47. doi: 10.4049/jimmunol.1002701
22. Watchmaker PB, Lahl K, Lee M, Baumjohann D, Morton J, Kim SJ, et al. Comparative Transcriptional and Functional Profiling Defines Conserved Programs of Intestinal DC Differentiation in Humans and Mice. *Nat Immunol* (2014) 15:98–108. doi: 10.1038/ni.2768
23. Knoop KA, Mcdonald KG, Mccrate S, Mcdole JR, Newberry RD. Microbial Sensing by Goblet Cells Controls Immune Surveillance of Luminal Antigens in the Colon. *Mucosal Immunol* (2015) 8:198–210. doi: 10.1038/mi.2014.58
24. Brandtzaeg P, Farstad IN, Johansen FE, Morton HC, Norderhaug IN, Yamanaka T. The B-Cell System of Human Mucosae and Exocrine Glands. *Immunol Rev* (1999) 171:45–87. doi: 10.1111/j.1600-065x.1999.tb01342.x
25. Cox TR. The Matrix in Cancer. *Nat Rev Cancer* (2021) 21:217–38. doi: 10.1038/s41568-020-00329-7
26. Conti JA, Kendall TJ, Bateman A, Armstrong TA, Papa-Adams A, Xu Q, et al. The Desmoplastic Reaction Surrounding Hepatic Colorectal Adenocarcinoma Metastases Aids Tumor Growth and Survival *via* Alphav Integrin Ligation. *Clin Cancer Res* (2008) 14:6405–13. doi: 10.1158/1078-0432.CCR-08-0816
27. Schober M, Jesenofsky R, Faissner R, Weidenauer C, Hagmann W, Michl P, et al. Desmoplasia and Chemoresistance in Pancreatic Cancer. *Cancers (Basel)* (2014) 6:2137–54. doi: 10.3390/cancers6042137
28. Hanahan D, Weinberg RA. Hallmarks of Cancer: The Next Generation. *Cell* (2011) 144:646–74. doi: 10.1016/j.cell.2011.02.013
29. Wei SC, Fattet L, Tsai JH, Guo Y, Pai VH, Majeski HE, et al. Matrix Stiffness Drives Epithelial-Mesenchymal Transition and Tumour Metastasis Through a TWIST1-G3BP2 Mechanotransduction Pathway. *Nat Cell Biol* (2015) 17:678–88. doi: 10.1038/ncb3157
30. Henke E, Nandigama R, Ergun S. Extracellular Matrix in the Tumor Microenvironment and Its Impact on Cancer Therapy. *Front Mol Biosci* (2019) 6:160. doi: 10.3389/fmolb.2019.00160
31. Lu P, Weaver VM, Werb Z. The Extracellular Matrix: A Dynamic Niche in Cancer Progression. *J Cell Biol* (2012) 196:395–406. doi: 10.1083/jcb.201102147
32. Vossenaar ER, Zendman AJ, Van Venrooij WJ, Pruijn GJ. A Growing Family of Citrullinating Enzymes: Genes, Features and Involvement in Disease. *Bioessays* (2003) 25:1106–18. doi: 10.1002/bies.10357
33. Yuzhalin AE, Lim SY, Kutikhin AG, Gordon-Weeks AN. Dynamic Matrisome: ECM Remodeling Factors Licensing Cancer Progression and Metastasis. *Biochim Biophys Acta Rev Cancer* (2018) 1870:207–28. doi: 10.1016/j.bbcan.2018.09.002
34. Yuzhalin AE, Gordon-Weeks AN, Tognoli ML, Jones K, Markelc B, Konietzny R, et al. Colorectal Cancer Liver Metastatic Growth Depends on PAD4-Driven Citrullination of the Extracellular Matrix. *Nat Commun* (2018) 9:4783. doi: 10.1038/s41467-018-07306-7
35. Lowy CM, Oskarsson T. Tenascin C in Metastasis: A View From the Invasive Front. *Cell Adh Migr* (2015) 9:112–24. doi: 10.1080/19336918.2015.1008331
36. Murakami T, Kikuchi H, Ishimatsu H, Iino I, Hirotsu A, Matsumoto T, et al. Tenascin C in Colorectal Cancer Stroma Is a Predictive Marker for Liver Metastasis and Is a Potent Target of miR-198 as Identified by microRNA Analysis. *Br J Cancer* (2017) 117:1360–70. doi: 10.1038/bjc.2017.291
37. Voss H, Wurlitzer M, Smit DJ, Ewald F, Alawi M, Spohn M, et al. Differential Regulation of Extracellular Matrix Proteins in Three Recurrent Liver Metastases of a Single Patient With Colorectal Cancer. *Clin Exp Metastasis* (2020) 37:649–56. doi: 10.1007/s10585-020-10058-8
38. Lagory EL, Giaccia AJ. The Ever-Expanding Role of HIF in Tumour and Stromal Biology. *Nat Cell Biol* (2016) 18:356–65. doi: 10.1038/ncb3330
39. De Palma M, Biziato D, Petrova TV. Microenvironmental Regulation of Tumour Angiogenesis. *Nat Rev Cancer* (2017) 17:457–74. doi: 10.1038/nrc.2017.51
40. Ferrarotto R, Hoff PM. Antiangiogenic Drugs for Colorectal Cancer: Exploring New Possibilities. *Clin Colorectal Cancer* (2013) 12:1–7. doi: 10.1016/j.clcc.2012.06.002
41. Ellis LM, Takahashi Y, Liu W, Shaheen RM. Vascular Endothelial Growth Factor in Human Colon Cancer: Biology and Therapeutic Implications. *Oncologist* (2000) 5 Suppl 1:11–5. doi: 10.1634/theoncologist.5-suppl_1-11
42. Rmali KA, Puntis MC, Jiang WG. Tumour-Associated Angiogenesis in Human Colorectal Cancer. *Colorectal Dis* (2007) 9:3–14. doi: 10.1111/j.1463-1318.2006.01089.x
43. Witte D, Thomas A, Ali N, Carlson N, Younes M. Expression of the Vascular Endothelial Growth Factor Receptor-3 (VEGFR-3) and its Ligand VEGF-C in Human Colorectal Adenocarcinoma. *Anticancer Res* (2002) 22:1463–6.
44. Denton AE, Roberts EW, Fearon DT. Stromal Cells in the Tumor Microenvironment. *Adv Exp Med Biol* (2018) 1060:99–114. doi: 10.1007/978-3-319-78127-3_6
45. Jungwirth U, Van Weverwijk A, Evans RJ, Jenkins L, Vicente D, Alexander J, et al. Impairment of a Distinct Cancer-Associated Fibroblast Population Limits Tumour Growth and Metastasis. *Nat Commun* (2021) 12:3516. doi: 10.1038/s41467-021-23583-1
46. Yin C, Evason KJ, Asahina K, Stainier DY. Hepatic Stellate Cells in Liver Development, Regeneration, and Cancer. *J Clin Invest* (2013) 123:1902–10. doi: 10.1172/JCI66369
47. Kidd S, Spaeth E, Watson K, Burks J, Lu H, Klopp A, et al. Origins of the Tumor Microenvironment: Quantitative Assessment of Adipose-Derived and Bone Marrow-Derived Stroma. *PloS One* (2012) 7:e30563. doi: 10.1371/journal.pone.0030563
48. Zeisberg EM, Potenta S, Xie L, Zeisberg M, Kalluri R. Discovery of Endothelial to Mesenchymal Transition as a Source for Carcinoma-Associated Fibroblasts. *Cancer Res* (2007) 67:10123–8. doi: 10.1158/0008-5472.CAN-07-3127
49. Paauwe M, Schoonderwoerd MJA, Helderman R, Harryvan TJ, Groenewoud A, Van Pelt GW, et al. Endoglin Expression on Cancer-Associated Fibroblasts Regulates Invasion and Stimulates Colorectal Cancer Metastasis. *Clin Cancer Res* (2018) 24:6331–44. doi: 10.1158/1078-0432.CCR-18-0329
50. Hu JL, Wang W, Lan XL, Zeng ZC, Liang YS, Yan YR, et al. CAFs Secreted Exosomes Promote Metastasis and Chemotherapy Resistance by Enhancing Cell Stemness and Epithelial-Mesenchymal Transition in Colorectal Cancer. *Mol Cancer* (2019) 18:91. doi: 10.1186/s12943-019-1019-x
51. Heichler C, Scheibe K, Schmied A, Geppert CI, Schmid B, Wirtz S, et al. STAT3 Activation Through IL-6/IL-11 in Cancer-Associated Fibroblasts Promotes Colorectal Tumour Development and Correlates With Poor Prognosis. *Gut* (2020) 69:1269–82. doi: 10.1136/gutjnl-2019-319200
52. Ham IH, Lee D, Hur H. Cancer-Associated Fibroblast-Induced Resistance to Chemotherapy and Radiotherapy in Gastrointestinal Cancers. *Cancers (Basel)* (2021) 13:1172. doi: 10.3390/cancers13051172
53. Cassetta L, Pollard JW. Tumor-Associated Macrophages. *Curr Biol* (2020) 30:R246–8. doi: 10.1016/j.cub.2020.01.031
54. Chen C, He W, Huang J, Wang B, Li H, Cai Q, et al. LNMAT1 Promotes Lymphatic Metastasis of Bladder Cancer *via* CCL2 Dependent Macrophage Recruitment. *Nat Commun* (2018) 9:3826. doi: 10.1038/s41467-018-06152-x
55. Stockmann C, Doedens A, Weidemann A, Zhang N, Takeda N, Greenberg JI, et al. Deletion of Vascular Endothelial Growth Factor in Myeloid Cells Accelerates Tumorigenesis. *Nature* (2008) 456:814–8. doi: 10.1038/nature07445
56. Kessenbrock K, Plaks V, Werb Z. Matrix Metalloproteinases: Regulators of the Tumor Microenvironment. *Cell* (2010) 141:52–67. doi: 10.1016/j.cell.2010.03.015
57. Squadrito ML, De Palma M. Macrophage Regulation of Tumor Angiogenesis: Implications for Cancer Therapy. *Mol Aspects Med* (2011) 32:123–45. doi: 10.1016/j.mam.2011.04.005
58. Fu XT, Dai Z, Song K, Zhang ZJ, Zhou ZJ, Zhou SL, et al. Macrophage-Secreted IL-8 Induces Epithelial-Mesenchymal Transition in Hepatocellular Carcinoma Cells by Activating the JAK2/STAT3/Snail Pathway. *Int J Oncol* (2015) 46:587–96. doi: 10.3892/ijo.2014.2761
59. Wei C, Yang C, Wang S, Shi D, Zhang C, Lin X, et al. Crosstalk Between Cancer Cells and Tumor Associated Macrophages Is Required for Mesenchymal Circulating Tumor Cell-Mediated Colorectal Cancer Metastasis. *Mol Cancer* (2019) 18:64. doi: 10.1186/s12943-019-0976-4

60. Afik R, Zigmond E, Vugman M, Klepfish M, Shimshoni E, Pasmanik-Chor M, et al. Tumor Macrophages Are Pivotal Constructors of Tumor Collagenous Matrix. *J Exp Med* (2016) 213:2315–31. doi: 10.1084/jem.20151193
61. Marech I, Ammendola M, Sacco R, Sammarco G, Zuccala V, Zizzo N, et al. Tumour-Associated Macrophages Correlate With Microvascular Bed Extension in Colorectal Cancer Patients. *J Cell Mol Med* (2016) 20:1373–80. doi: 10.1111/jcmm.12826
62. Nakayama Y, Nagashima N, Minagawa N, Inoue Y, Katsuki T, Onitsuka K, et al. Relationships Between Tumor-Associated Macrophages and Clinicopathological Factors in Patients With Colorectal Cancer. *Anticancer Res* (2002) 22:4291–6.
63. Koelzer VH, Canonica K, Dawson H, Sokol L, Karamitopoulou-Diamantis E, Lugli A, et al. Phenotyping of Tumor-Associated Macrophages in Colorectal Cancer: Impact on Single Cell Invasion (Tumor Budding) and Clinicopathological Outcome. *Oncoimmunology* (2016) 5:e1106677. doi: 10.1080/2162402X.2015.1106677
64. Cavnar MJ, Turcotte S, Katz SC, Kuk D, Gonen M, Shia J, et al. Tumor-Associated Macrophage Infiltration in Colorectal Cancer Liver Metastases Is Associated With Better Outcome. *Ann Surg Oncol* (2017) 24:1835–42. doi: 10.1245/s10434-017-5812-8
65. Yang C, Wei C, Wang S, Shi D, Zhang C, Lin X, et al. Elevated CD163 (+)/CD68(+) Ratio at Tumor Invasive Front Is Closely Associated With Aggressive Phenotype and Poor Prognosis in Colorectal Cancer. *Int J Biol Sci* (2019) 15:984–98. doi: 10.7150/ijbs.29836
66. Veglia F, Perego M, Gabrilovich D. Myeloid-Derived Suppressor Cells Coming of Age. *Nat Immunol* (2018) 19:108–19. doi: 10.1038/s41590-017-0022-x
67. Geissmann F, Manz MG, Jung S, Sieweke MH, Merad M, Ley K. Development of Monocytes, Macrophages, and Dendritic Cells. *Science* (2010) 327:656–61. doi: 10.1126/science.1178331
68. Veglia F, Gabrilovich DI. Dendritic Cells in Cancer: The Role Revisited. *Curr Opin Immunol* (2017) 45:43–51. doi: 10.1016/j.coi.2017.01.002
69. Gabrilovich DI, Bronte V, Chen SH, Colombo MP, Ochoa A, Ostrand-Rosenberg S, et al. The Terminology Issue for Myeloid-Derived Suppressor Cells. *Cancer Res* (2007) 67:425; author reply 426. doi: 10.1158/0008-5472.CAN-06-3037
70. Dysthe M, Parihar R. Myeloid-Derived Suppressor Cells in the Tumor Microenvironment. *Adv Exp Med Biol* (2020) 1224:117–40. doi: 10.1007/978-3-030-35723-8_8
71. Shi H, Zhang J, Han X, Li H, Xie M, Sun Y, et al. Recruited Monocytic Myeloid-Derived Suppressor Cells Promote the Arrest of Tumor Cells in the Premetastatic Niche Through an IL-1beta-Mediated Increase in E-Selectin Expression. *Int J Cancer* (2017) 140:1370–83. doi: 10.1002/ijc.30538
72. Sasano T, Mabuchi S, Kozasa K, Kuroda H, Kawano M, Takahashi R, et al. The Highly Metastatic Nature of Uterine Cervical/Endometrial Cancer Displaying Tumor-Related Leukocytosis: Clinical and Preclinical Investigations. *Clin Cancer Res* (2018) 24:4018–29. doi: 10.1158/1078-0432.CCR-17-2472
73. Chun E, Lavoie S, Michaud M, Gallini CA, Kim J, Soucy G, et al. CCL2 Promotes Colorectal Carcinogenesis by Enhancing Polymorphonuclear Myeloid-Derived Suppressor Cell Population and Function. *Cell Rep* (2015) 12:244–57. doi: 10.1016/j.celrep.2015.06.024
74. Gabrilovich DI, Nagaraj S. Myeloid-Derived Suppressor Cells as Regulators of the Immune System. *Nat Rev Immunol* (2009) 9:162–74. doi: 10.1038/nri2506
75. Xu P, He H, Gu Y, Wang Y, Sun Z, Yang L, et al. Surgical Trauma Contributes to Progression of Colon Cancer by Downregulating CXCL4 and Recruiting MDSCs. *Exp Cell Res* (2018) 370:692–8. doi: 10.1016/j.yexcr.2018.07.035
76. Ouyang LY, Wu XJ, Ye SB, Zhang RX, Li ZL, Liao W, et al. Tumor-Induced Myeloid-Derived Suppressor Cells Promote Tumor Progression Through Oxidative Metabolism in Human Colorectal Cancer. *J Transl Med* (2015) 13:47. doi: 10.1186/s12967-015-0410-7
77. Leliefeld PH, Wessels CM, Leenen LP, Koenderman L, Pillay J. The Role of Neutrophils in Immune Dysfunction During Severe Inflammation. *Crit Care* (2016) 20:73. doi: 10.1186/s13054-016-1250-4
78. Irimia D, Balazsi G, Agrawal N, Toner M. Adaptive-Control Model for Neutrophil Orientation in the Direction of Chemical Gradients. *Biophys J* (2009) 96:3897–916. doi: 10.1016/j.bpj.2008.12.3967
79. Ji H, Houghton AM, Mariani TJ, Perera S, Kim CB, Padera R, et al. K-Ras Activation Generates an Inflammatory Response in Lung Tumors. *Oncogene* (2006) 25:2105–12. doi: 10.1038/sj.onc.1209237
80. Uribe-Querol E, Rosales C. Neutrophils in Cancer: Two Sides of the Same Coin. *J Immunol Res* (2015) 2015:983698. doi: 10.1155/2015/983698
81. Mizuno R, Kawada K, Itatani Y, Ogawa R, Kiyasu Y, Sakai Y. The Role of Tumor-Associated Neutrophils in Colorectal Cancer. *Int J Mol Sci* (2019) 20:529. doi: 10.3390/ijms20030529
82. Rao HL, Chen JW, Li M, Xiao YB, Fu J, Zeng YX, et al. Increased Intratumoral Neutrophil in Colorectal Carcinomas Correlates Closely With Malignant Phenotype and Predicts Patients' Adverse Prognosis. *PloS One* (2012) 7:e30806. doi: 10.1371/journal.pone.0030806
83. Galdiero MR, Bianchi P, Grizzi F, Di Caro G, Basso G, Ponzetta A, et al. Occurrence and Significance of Tumor-Associated Neutrophils in Patients With Colorectal Cancer. *Int J Cancer* (2016) 139:446–56. doi: 10.1002/ijc.30076
84. Berry RS, Xiong MJ, Greenbaum A, Mortaji P, Nofchissey RA, Schultz F, et al. High Levels of Tumor-Associated Neutrophils Are Associated With Improved Overall Survival in Patients With Stage II Colorectal Cancer. *PloS One* (2017) 12:e0188799. doi: 10.1371/journal.pone.0188799
85. Ishizuka M, Nagata H, Takagi K, Iwasaki Y, Kubota K. Combination of Platelet Count and Neutrophil to Lymphocyte Ratio Is a Useful Predictor of Postoperative Survival in Patients With Colorectal Cancer. *Br J Cancer* (2013) 109:401–7. doi: 10.1038/bjc.2013.350
86. Li Z, Zhao R, Cui Y, Zhou Y, Wu X. The Dynamic Change of Neutrophil to Lymphocyte Ratio Can Predict Clinical Outcome in Stage I-III Colon Cancer. *Sci Rep* (2018) 8:9453. doi: 10.1038/s41598-018-27896-y
87. Borazan E, Balik AA, Bozdag Z, Arik MK, Aytekin A, Yilmaz L, et al. Assessment of the Relationship Between Neutrophil Lymphocyte Ratio and Prognostic Factors in Non-Metastatic Colorectal Cancer. *Turk J Surg* (2017) 33:185–9. doi: 10.5152/turkjsurg.2017.3528
88. Halle S, Halle O, Forster R. Mechanisms and Dynamics of T Cell-Mediated Cytotoxicity *In Vivo*. *Trends Immunol* (2017) 38:432–43. doi: 10.1016/j.it.2017.04.002
89. Dominguez-Villar M, Hafler D. A Regulatory T Cells in Autoimmune Disease. *Nat Immunol* (2018) 19:665–73. doi: 10.1038/s41590-018-0120-4
90. Stockis J, Roychoudhuri R, Halim TYF. Regulation of Regulatory T Cells in Cancer. *Immunology* (2019) 157:219–31. doi: 10.1111/imm.13064
91. Shitara K, Nishikawa H. Regulatory T Cells: A Potential Target in Cancer Immunotherapy. *Ann N Y Acad Sci* (2018) 1417:104–15. doi: 10.1111/nyas.13625
92. Takeuchi Y, Nishikawa H. Roles of Regulatory T Cells in Cancer Immunity. *Int Immunol* (2016) 28:401–9. doi: 10.1093/intimm/dxw025
93. Marshall EA, Ng KW, Kung SH, Conway EM, Martinez VD, Halvorsen EC, et al. Emerging Roles of T Helper 17 and Regulatory T Cells in Lung Cancer Progression and Metastasis. *Mol Cancer* (2016) 15:67. doi: 10.1186/s12943-016-0551-1
94. Luen SJ, Salgado R, Dieci MV, Vingiani A, Curigliano G, Gould RE, et al. Prognostic Implications of Residual Disease Tumor-Infiltrating Lymphocytes and Residual Cancer Burden in Triple-Negative Breast Cancer Patients After Neoadjuvant Chemotherapy. *Ann Oncol* (2019) 30:236–42. doi: 10.1093/annonc/mdy547
95. Shen Z, Zhou S, Wang Y, Li RL, Zhong C, Liang C, et al. Higher Intratumoral Infiltrated Foxp3+ Treg Numbers and Foxp3+/CD8+ Ratio Are Associated With Adverse Prognosis in Resectable Gastric Cancer. *J Cancer Res Clin Oncol* (2010) 136:1585–95. doi: 10.1007/s00432-010-0816-9
96. Zhou SL, Zhou ZJ, Hu ZQ, Huang XW, Wang Z, Chen EB, et al. Tumor-Associated Neutrophils Recruit Macrophages and T-Regulatory Cells to Promote Progression of Hepatocellular Carcinoma and Resistance to Sorafenib. *Gastroenterology* (2016) 150:1646–1658.e17. doi: 10.1053/j.gastro.2016.02.040
97. Kouketsu A, Sato I, Oikawa M, Shimizu Y, Saito H, Tashiro K, et al. Regulatory T Cells and M2-Polarized Tumour-Associated Macrophages Are Associated With the Oncogenesis and Progression of Oral Squamous Cell Carcinoma. *Int J Oral Maxillofac Surg* (2019) 48:1279–88. doi: 10.1016/j.ijom.2019.04.004
98. Frey DM, Droeser RA, Viehl CT, Zlobec I, Lugli A, Zingg U, et al. High Frequency of Tumor-Infiltrating FOXP3(+) Regulatory T Cells Predicts

Improved Survival in Mismatch Repair-Proficient Colorectal Cancer Patients. *Int J Cancer* (2010) 126:2635–43. doi: 10.1002/ijc.24989
99. Hanke T, Melling N, Simon R, Sauter G, Bokemeyer C, Lebok P, et al. High Intratumoral FOXP3(+) T Regulatory Cell (Tregs) Density Is an Independent Good Prognosticator in Nodal Negative Colorectal Cancer. *Int J Clin Exp Pathol* (2015) 8:8227–35.
100. Vlad C, Kubelac P, Fetica B, Vlad D, Irimie A, Achimas-Cadariu P. The Prognostic Value of FOXP3+ T Regulatory Cells in Colorectal Cancer. *J BUON* (2015) 20:114–9.
101. Shang B, Liu Y, Jiang SJ, Liu Y. Prognostic Value of Tumor-Infiltrating FoxP3+ Regulatory T Cells in Cancers: A Systematic Review and Meta-Analysis. *Sci Rep* (2015) 5:15179. doi: 10.1038/srep15179
102. Deng G, Song X, Fujimoto S, Piccirillo CA, Nagai Y, Greene MI. Foxp3 Post-Translational Modifications and Treg Suppressive Activity. *Front Immunol* (2019) 10:2486. doi: 10.3389/fimmu.2019.02486
103. Tadmor T, Zhang Y, Cho HM, Podack ER, Rosenblatt JD. The Absence of B Lymphocytes Reduces the Number and Function of T-Regulatory Cells and Enhances the Anti-Tumor Response in a Murine Tumor Model. *Cancer Immunol Immunother* (2011) 60:609–19. doi: 10.1007/s00262-011-0972-z
104. Xiao X, Lao XM, Chen MM, Liu RX, Wei Y, Ouyang FZ, et al. PD-1hi Identifies a Novel Regulatory B-Cell Population in Human Hepatoma That Promotes Disease Progression. *Cancer Discov* (2016) 6:546–59. doi: 10.1158/2159-8290.CD-15-1408
105. Dilillo DJ, Yanaba K, Tedder TF. B Cells Are Required for Optimal CD4+ and CD8+ T Cell Tumor Immunity: Therapeutic B Cell Depletion Enhances B16 Melanoma Growth in Mice. *J Immunol* (2010) 184:4006–16. doi: 10.4049/jimmunol.0903009
106. Sarvaria A, Madrigal JA, Saudemont A. B Cell Regulation in Cancer and Anti-Tumor Immunity. *Cell Mol Immunol* (2017) 14:662–74. doi: 10.1038/cmi.2017.35
107. Sorrentino R, Morello S, Forte G, Montinaro A, De Vita G, Luciano A, et al. B Cells Contribute to the Antitumor Activity of CpG-Oligodeoxynucleotide in a Mouse Model of Metastatic Lung Carcinoma. *Am J Respir Crit Care Med* (2011) 183:1369–79. doi: 10.1164/rccm.201010-1738OC
108. Cabrita R, Lauss M, Sanna A, Donia M, Skaarup Larsen M, Mitra S, et al. Tertiary Lymphoid Structures Improve Immunotherapy and Survival in Melanoma. *Nature* (2020) 577:561–5. doi: 10.1038/s41586-019-1914-8
109. Zirakzadeh AA, Marits P, Sherif A, Winqvist O. Multiplex B Cell Characterization in Blood, Lymph Nodes, and Tumors From Patients With Malignancies. *J Immunol* (2013) 190:5847–55. doi: 10.4049/jimmunol.1203279
110. Shimabukuro-Vornhagen A, Schlosser HA, Gryschok L, Malcher J, Wennhold K, Garcia-Marquez M, et al. Characterization of Tumor-Associated B-Cell Subsets in Patients With Colorectal Cancer. *Oncotarget* (2014) 5:4651–64. doi: 10.18632/oncotarget.1701
111. Guo L, Wang C, Qiu X, Pu X, Chang P. Colorectal Cancer Immune Infiltrates: Significance in Patient Prognosis and Immunotherapeutic Efficacy. *Front Immunol* (2020) 11:1052. doi: 10.3389/fimmu.2020.01052
112. Berntsson J, Nodin B, Eberhard J, Micke P, Jirstrom K. Prognostic Impact of Tumour-Infiltrating B Cells and Plasma Cells in Colorectal Cancer. *Int J Cancer* (2016) 139:1129–39. doi: 10.1002/ijc.30138
113. Wang W, Zhong Y, Zhuang Z, Xie J, Lu Y, Huang C, et al. Multiregion Single-Cell Sequencing Reveals the Transcriptional Landscape of the Immune Microenvironment of Colorectal Cancer. *Clin Transl Med* (2021) 11:e253. doi: 10.1002/ctm2.253
114. Reid FSW, Egoroff N, Pockney PG, Smith SR. A Systematic Scoping Review on Natural Killer Cell Function in Colorectal Cancer. *Cancer Immunol Immunother* (2021) 70:597–606. doi: 10.1007/s00262-020-02721-6
115. Halama N, Braun M, Kahlert C, Spille A, Quack C, Rahbari N, et al. Natural Killer Cells Are Scarce in Colorectal Carcinoma Tissue Despite High Levels of Chemokines and Cytokines. *Clin Cancer Res* (2011) 17:678–89. doi: 10.1158/1078-0432.CCR-10-2173
116. Rocca YS, Roberti MP, Arriaga JM, Amat M, Bruno L, Pampena MB, et al. Altered Phenotype in Peripheral Blood and Tumor-Associated NK Cells From Colorectal Cancer Patients. *Innate Immun* (2013) 19:76–85. doi: 10.1177/1753425912453187
117. Krijgsman D, Roelands J, Andersen MN, Wieringa C, Tollenaar R, Hendrickx W, et al. Expression of NK Cell Receptor Ligands in Primary Colorectal Cancer Tissue in Relation to the Phenotype of Circulating NK- and NKT Cells, and Clinical Outcome. *Mol Immunol* (2020) 128:205–18. doi: 10.1016/j.molimm.2020.10.012
118. Veluchamy JP, Spanholtz J, Tordoir M, Thijssen VL, Heideman DA, Verheul HM, et al. Combination of NK Cells and Cetuximab to Enhance Anti-Tumor Responses in RAS Mutant Metastatic Colorectal Cancer. *PloS One* (2016) 11:e0157830. doi: 10.1371/journal.pone.0157830
119. Ishikawa T, Okayama T, Sakamoto N, Ideno M, Oka K, Enoki T, et al. Phase I Clinical Trial of Adoptive Transfer of Expanded Natural Killer Cells in Combination With IgG1 Antibody in Patients With Gastric or Colorectal Cancer. *Int J Cancer* (2018) 142:2599–609. doi: 10.1002/ijc.31285
120. Xiao L, Cen D, Gan H, Sun Y, Huang N, Xiong H, et al. Adoptive Transfer of NKG2D CAR mRNA-Engineered Natural Killer Cells in Colorectal Cancer Patients. *Mol Ther* (2019) 27:1114–25. doi: 10.1016/j.ymthe.2019.03.011
121. Marechal R, De Schutter J, Nagy N, Demetter P, Lemmers A, Deviere J, et al. Putative Contribution of CD56 Positive Cells in Cetuximab Treatment Efficacy in First-Line Metastatic Colorectal Cancer Patients. *BMC Cancer* (2010) 10:340. doi: 10.1186/1471-2407-10-340
122. Van Kaer L. NKT cells: T Lymphocytes With Innate Effector Functions. *Curr Opin Immunol.* (2007) 19:354–64. doi: 10.1016/j.coi.2007.03.001
123. Coles MC, Raulet DH. NK1.1+ T Cells in the Liver Arise in the Thymus and Are Selected by Interactions With Class I Molecules on CD4+CD8+ Cells. *J Immunol* (2000) 164:2412–8. doi: 10.4049/jimmunol.164.5.2412
124. Gerth E, Mattner J. The Role of Adaptor Proteins in the Biology of Natural Killer T (NKT) Cells. *Front Immunol* (2019) 10:1449. doi: 10.3389/fimmu.2019.01449
125. Brennan PJ, Brigl M, Brenner MB. Invariant Natural Killer T Cells: An Innate Activation Scheme Linked to Diverse Effector Functions. *Nat Rev Immunol* (2013) 13:101–17. doi: 10.1038/nri3369
126. Kinjo Y, Illarionov P, Vela JL, Pei B, Girardi E, Li X, et al. Invariant Natural Killer T Cells Recognize Glycolipids From Pathogenic Gram-Positive Bacteria. *Nat Immunol* (2011) 12:966–74. doi: 10.1038/ni.2096
127. Kumar V, Delovitch TL. Different Subsets of Natural Killer T Cells may Vary in Their Roles in Health and Disease. *Immunology* (2014) 142:321–36. doi: 10.1111/imm.12247
128. Wang Y, Bhave MS, Yagita H, Cardell SL. Natural Killer T-Cell Agonist Alpha-Galactosylceramide and PD-1 Blockade Synergize to Reduce Tumor Development in a Preclinical Model of Colon Cancer. *Front Immunol* (2020) 11:581301. doi: 10.3389/fimmu.2020.581301
129. Tachibana T, Onodera H, Tsuruyama T, Mori A, Nagayama S, Hiai H, et al. Increased Intratumor Valpha24-Positive Natural Killer T Cells: A Prognostic Factor for Primary Colorectal Carcinomas. *Clin Cancer Res* (2005) 11:7322–7. doi: 10.1158/1078-0432.CCR-05-0877
130. Xu R, Rai A, Chen M, Suwakulsiri W, Greening DW, Simpson RJ. Extracellular Vesicles in Cancer - Implications for Future Improvements in Cancer Care. *Nat Rev Clin Oncol* (2018) 15:617–38. doi: 10.1038/s41571-018-0036-9
131. Khan S, Jutzy JM, Valenzuela MM, Turay D, Aspe JR, Ashok A, et al. Plasma-Derived Exosomal Survivin, a Plausible Biomarker for Early Detection of Prostate Cancer. *PloS One* (2012) 7:e46737. doi: 10.1371/journal.pone.0046737
132. Lasser C, Alikhani VS, Ekstrom K, Eldh M, Paredes PT, Bossios A, et al. Human Saliva, Plasma and Breast Milk Exosomes Contain RNA: Uptake by Macrophages. *J Transl Med* (2011) 9:9. doi: 10.1186/1479-5876-9-9
133. Admyre C, Johansson SM, Qazi KR, Filen JJ, Lahesmaa R, Norman M, et al. Exosomes With Immune Modulatory Features Are Present in Human Breast Milk. *J Immunol* (2007) 179:1969–78. doi: 10.4049/jimmunol.179.3.1969
134. Yun B, Kim Y, Park DJ, Oh S. Comparative Analysis of Dietary Exosome-Derived microRNAs From Human, Bovine and Caprine Colostrum and Mature Milk. *J Anim Sci Technol* (2021) 63:593–602. doi: 10.5187/jast.2021.e39
135. Street JM, Barran PE, Mackay CL, Weidt S, Balmforth C, Walsh TS, et al. Identification and Proteomic Profiling of Exosomes in Human Cerebrospinal Fluid. *J Transl Med* (2012) 10:5. doi: 10.1186/1479-5876-10-5
136. Malenica M, Vukomanovic M, Kurtjak M, Masciotti V, Dal Zilio S, Greco S, et al. Perspectives of Microscopy Methods for Morphology Characterisation of Extracellular Vesicles From Human Biofluids. *Biomedicines* (2021) 9:603. doi: 10.3390/biomedicines9060603

137. Hassanzadeh A, Rahman HS, Markov A, Endjun JJ, Zekiy AO, Chartrand MS, et al. Mesenchymal Stem/Stromal Cell-Derived Exosomes in Regenerative Medicine and Cancer; Overview of Development, Challenges, and Opportunities. *Stem Cell Res Ther* (2021) 12:297. doi: 10.1186/s13287-021-02378-7
138. Pisitkun T, Shen RF, Knepper M. A Identification and Proteomic Profiling of Exosomes in Human Urine. *Proc Natl Acad Sci USA* (2004) 101:13368–73. doi: 10.1073/pnas.0403453101
139. Gonzales PA, Pisitkun T, Hoffert JD, Tchapyjnikov D, Star RA, Kleta R, et al. Large-Scale Proteomics and Phosphoproteomics of Urinary Exosomes. *J Am Soc Nephrol* (2009) 20:363–79. doi: 10.1681/ASN.2008040406
140. Sung CC, Chen MH, Lin YC, Lin YC, Lin YJ, Yang SS, et al. Urinary Extracellular Vesicles for Renal Tubular Transporters Expression in Patients With Gitelman Syndrome. *Front Med (Lausanne)* (2021) 8:679171. doi: 10.3389/fmed.2021.679171
141. Morup N, Stakaitis R, Golubickaite I, Riera M, Dalgaard MD, Schierup MH, et al. Small RNAs in Seminal Plasma as Novel Biomarkers for Germ Cell Tumors. *Cancers (Basel)* (2021) 13:2346. doi: 10.3390/cancers13102346
142. Silva J, Garcia V, Rodriguez M, Compte M, Cisneros E, Veguillas P, et al. Analysis of Exosome Release and its Prognostic Value in Human Colorectal Cancer. *Genes Chromosomes Cancer* (2012) 51:409–18. doi: 10.1002/gcc.21926
143. Que R, Ding G, Chen J, Cao L. Analysis of Serum Exosomal microRNAs and Clinicopathologic Features of Patients With Pancreatic Adenocarcinoma. *World J Surg Oncol* (2013) 11:219. doi: 10.1186/1477-7819-11-219
144. Xue X, Wang C, Xue Z, Wen J, Han J, Ma X, et al. Exosomal miRNA Profiling Before and After Surgery Revealed Potential Diagnostic and Prognostic Markers for Lung Adenocarcinoma. *Acta Biochim Biophys Sin (Shanghai)* (2020) 52:281–93. doi: 10.1093/abbs/gmz164
145. Lessi F, Aretini P, Rizzo M, Morelli M, Menicagli M, Franceschi S, et al. Analysis of Exosome-Derived microRNAs Reveals Insights of Intercellular Communication During Invasion of Breast, Prostate and Glioblastoma Cancer Cells. *Cell Adh Migr* (2021) 15:180–201. doi: 10.1080/19336918.2021.1935407
146. Fan X, Zou X, Liu C, Cheng W, Zhang S, Geng X, et al. MicroRNA Expression Profile in Serum Reveals Novel Diagnostic Biomarkers for Endometrial Cancer. *Biosci Rep* (2021) 41:BSR20210111. doi: 10.1042/BSR20210111
147. Zeng Z, Li Y, Pan Y, Lan X, Song F, Sun J, et al. Cancer-Derived Exosomal miR-25-3p Promotes Pre-Metastatic Niche Formation by Inducing Vascular Permeability and Angiogenesis. *Nat Commun* (2018) 9:5395. doi: 10.1038/s41467-018-07810-w
148. Liu H, Liu Y, Sun P, Leng K, Xu Y, Mei L, et al. Colorectal Cancer-Derived Exosomal miR-106b-3p Promotes Metastasis by Down-Regulating DLC-1 Expression. *Clin Sci (Lond)* (2020) 134:419–34. doi: 10.1042/CS20191087
149. Jiang Y, Ji X, Liu K, Shi Y, Wang C, Li Y, et al. Exosomal miR-200c-3p Negatively Regulates the Migraion and Invasion of Lipopolysaccharide (LPS)-Stimulated Colorectal Cancer (CRC). *BMC Mol Cell Biol* (2020) 21:48. doi: 10.1186/s12860-020-00291-0
150. Shang A, Gu C, Wang W, Wang X, Sun J, Zeng B, et al. Exosomal circPACRGL Promotes Progression of Colorectal Cancer *via* the miR-142-3p/miR-506-3p- TGF-Beta1 Axis. *Mol Cancer* (2020) 19:117. doi: 10.1186/s12943-020-01235-0
151. Bhome R, Goh RW, Bullock MD, Pillar N, Thirdborough SM, Mellone M, et al. Exosomal microRNAs Derived From Colorectal Cancer-Associated Fibroblasts: Role in Driving Cancer Progression. *Aging (Albany NY)* (2017) 9:2666–94. doi: 10.18632/aging.101355
152. Maminezhad H, Ghanadian S, Pakravan K, Razmara E, Rouhollah F, Mossahebi-Mohammadi M, et al. A Panel of Six-Circulating miRNA Signature in Serum and its Potential Diagnostic Value in Colorectal Cancer. *Life Sci* (2020) 258:118226. doi: 10.1016/j.lfs.2020.118226
153. Wan Z, Gao X, Dong Y, Zhao Y, Chen X, Yang G, et al. Exosome-Mediated Cell-Cell Communication in Tumor Progression. *Am J Cancer Res* (2018) 8:1661–73.
154. Fane M, Weeraratna AT. How the Ageing Microenvironment Influences Tumour Progression. *Nat Rev Cancer* (2020) 20:89–106. doi: 10.1038/s41568-019-0222-9
155. Larbi A, Fulop T. From "Truly Naive" to "Exhausted Senescent" T Cells: When Markers Predict Functionality. *Cytometry A* (2014) 85:25–35. doi: 10.1002/cyto.a.22351
156. Giunco S, Petrara MR, Bergamo F, Del Bianco P, Zanchetta M, Carmona F, et al. Immune Senescence and Immune Activation in Elderly Colorectal Cancer Patients. *Aging (Albany NY)* (2019) 11:3864–75. doi: 10.18632/aging.102022
157. Di J, Liu M, Fan Y, Gao P, Wang Z, Jiang B, et al. Phenotype Molding of T Cells in Colorectal Cancer by Single-Cell Analysis. *Int J Cancer* (2020) 146:2281–95. doi: 10.1002/ijc.32856
158. Rosen LS, Jacobs IA, Burkes RL. Bevacizumab in Colorectal Cancer: Current Role in Treatment and the Potential of Biosimilars. *Target Oncol* (2017) 12:599–610. doi: 10.1007/s11523-017-0518-1
159. Modest DP, Pant S, Sartore-Bianchi A. Treatment Sequencing in Metastatic Colorectal Cancer. *Eur J Cancer* (2019) 109:70–83. doi: 10.1016/j.ejca.2018.12.019
160. Roviello G, Bachelot T, Hudis CA, Curigliano G, Reynolds AR, Petrioli R, et al. The Role of Bevacizumab in Solid Tumours: A Literature Based Meta-Analysis of Randomised Trials. *Eur J Cancer* (2017) 75:245–58. doi: 10.1016/j.ejca.2017.01.026
161. Cremolini C, Loupakis F, Antoniotti C, Lupi C, Sensi E, Lonardi S, et al. FOLFOXIRI Plus Bevacizumab Versus FOLFIRI Plus Bevacizumab as First-Line Treatment of Patients With Metastatic Colorectal Cancer: Updated Overall Survival and Molecular Subgroup Analyses of the Open-Label, Phase 3 TRIBE Study. *Lancet Oncol* (2015) 16:1306–15. doi: 10.1016/S1470-2045(15)00122-9
162. Botrel TEA, Clark LGO, Paladini L, Clark OAC. Efficacy and Safety of Bevacizumab Plus Chemotherapy Compared to Chemotherapy Alone in Previously Untreated Advanced or Metastatic Colorectal Cancer: A Systematic Review and Meta-Analysis. *BMC Cancer* (2016) 16:677. doi: 10.1186/s12885-016-2734-y
163. Bang YH, Kim JE, Lee JS, Kim SY, Kim KP, Kim TW, et al. Bevacizumab Plus Capecitabine as Later-Line Treatment for Patients With Metastatic Colorectal Cancer Refractory to Irinotecan, Oxaliplatin, and Fluoropyrimidines. *Sci Rep* (2021) 11:7118. doi: 10.1038/s41598-021-86482-x
164. Ramjiawan RR, Griffioen AW, Duda DG. Anti-Angiogenesis for Cancer Revisited: Is There a Role for Combinations With Immunotherapy? *Angiogenesis* (2017) 20:185–204. doi: 10.1007/s10456-017-9552-y
165. Comunanza V, Bussolino F. Therapy for Cancer: Strategy of Combining Anti-Angiogenic and Target Therapies. *Front Cell Dev Biol* (2017) 5:101. doi: 10.3389/fcell.2017.00101
166. Chen DS, Hurwitz H. Combinations of Bevacizumab With Cancer Immunotherapy. *Cancer J* (2018) 24:193–204. doi: 10.1097/PPO.0000000000000327
167. Wallin JJ, Bendell JC, Funke R, Sznol M, Korski K, Jones S, et al. Atezolizumab in Combination With Bevacizumab Enhances Antigen-Specific T-Cell Migration in Metastatic Renal Cell Carcinoma. *Nat Commun* (2016) 7:12624. doi: 10.1038/ncomms12624
168. Osada T, Chong G, Tansik R, Hong T, Spector N, Kumar R, et al. The Effect of Anti-VEGF Therapy on Immature Myeloid Cell and Dendritic Cells in Cancer Patients. *Cancer Immunol Immunother* (2008) 57:1115–24. doi: 10.1007/s00262-007-0441-x
169. Limagne E, Euvrard R, Thibaudin M, Rebe C, Derangere V, Chevriaux A, et al. Accumulation of MDSC and Th17 Cells in Patients With Metastatic Colorectal Cancer Predicts the Efficacy of a FOLFOX-Bevacizumab Drug Treatment Regimen. *Cancer Res* (2016) 76:5241–52. doi: 10.1158/0008-5472.CAN-15-3164
170. Fuchs CS, Tomasek J, Yong CJ, Dumitru F, Passalacqua R, Goswami C, et al. Ramucirumab Monotherapy for Previously Treated Advanced Gastric or Gastro-Oesophageal Junction Adenocarcinoma (REGARD): An International, Randomised, Multicentre, Placebo-Controlled, Phase 3 Trial. *Lancet* (2014) 383:31–9. doi: 10.1016/S0140-6736(13)61719-5
171. Buyukkaramikli NC, Blommestein HM, Riemsma R, Armstrong N, Clay FJ, Ross J, et al. Ramucirumab for Treating Advanced Gastric Cancer or Gastro-Oesophageal Junction Adenocarcinoma Previously Treated With Chemotherapy: An Evidence Review Group Perspective of a NICE Single Technology Appraisal. *Pharmacoeconomics* (2017) 35:1211–21. doi: 10.1007/s40273-017-0528-y
172. Murahashi S, Takahari D, Wakatsuki T, Fukuda N, Ichimura T, Ogura M, et al. A Retrospective Analysis of Ramucirumab Monotherapy in Previously

Treated Japanese Patients With Advanced or Metastatic Gastric Adenocarcinoma. *Int J Clin Oncol* (2018) 23:92–7. doi: 10.1007/s10147-017-1192-0

173. Garon EB, Ciuleanu TE, Arrieta O, Prabhash K, Syrigos KN, Goksel T, et al. Ramucirumab Plus Docetaxel Versus Placebo Plus Docetaxel for Second-Line Treatment of Stage IV non-Small-Cell Lung Cancer After Disease Progression on Platinum-Based Therapy (REVEL): A Multicentre, Double-Blind, Randomised Phase 3 Trial. *Lancet* (2014) 384:665–73. doi: 10.1016/S0140-6736(14)60845-X
174. Ren S, Xiong X, You H, Shen J, Zhou P. The Combination of Immune Checkpoint Blockade and Angiogenesis Inhibitors in the Treatment of Advanced Non-Small Cell Lung Cancer. *Front Immunol* (2021) 12:689132. doi: 10.3389/fimmu.2021.689132
175. Verdaguer H, Tabernero J, Macarulla T. Ramucirumab in Metastatic Colorectal Cancer: Evidence to Date and Place in Therapy. *Ther Adv Med Oncol* (2016) 8:230–42. doi: 10.1177/1758834016635888
176. Tabernero J, Yoshino T, Cohn AL, Obermannova R, Bodoky G, Garcia-Carbonero R, et al. Ramucirumab Versus Placebo in Combination With Second-Line FOLFIRI in Patients With Metastatic Colorectal Carcinoma That Progressed During or After First-Line Therapy With Bevacizumab, Oxaliplatin, and a Fluoropyrimidine (RAISE): A Randomised, Double-Blind, Multicentre, Phase 3 Study. *Lancet Oncol* (2015) 16:499–508. doi: 10.1016/S1470-2045(15)70127-0
177. Denda T, Sakai D, Hamaguchi T, Sugimoto N, Ura T, Yamazaki K, et al. Phase II Trial of Aflibercept With FOLFIRI as a Second-Line Treatment for Japanese Patients With Metastatic Colorectal Cancer. *Cancer Sci* (2019) 110:1032–43. doi: 10.1111/cas.13943
178. Tabernero J, Van Cutsem E, Lakomy R, Prausova J, Ruff P, Van Hazel GA, et al. Aflibercept Versus Placebo in Combination With Fluorouracil, Leucovorin and Irinotecan in the Treatment of Previously Treated Metastatic Colorectal Cancer: Prespecified Subgroup Analyses From the VELOUR Trial. *Eur J Cancer* (2014) 50:320–31. doi: 10.1016/j.ejca.2013.09.013
179. Ruff P, Van Cutsem E, Lakomy R, Prausova J, Van Hazel GA, Moiseyenko VM, et al. Observed Benefit and Safety of Aflibercept in Elderly Patients With Metastatic Colorectal Cancer: An Age-Based Analysis From the Randomized Placebo-Controlled Phase III VELOUR Trial. *J Geriatr Oncol* (2018) 9:32–9. doi: 10.1016/j.jgo.2017.07.010
180. Grothey A, Van Cutsem E, Sobrero A, Siena S, Falcone A, Ychou M, et al. Regorafenib Monotherapy for Previously Treated Metastatic Colorectal Cancer (CORRECT): An International, Multicentre, Randomised, Placebo-Controlled, Phase 3 Trial. *Lancet* (2013) 381:303–12. doi: 10.1016/S0140-6736(12)61900-X
181. Wang C, Chevalier D, Saluja J, Sandhu J, Lau C, Fakih M. Regorafenib and Nivolumab or Pembrolizumab Combination and Circulating Tumor DNA Response Assessment in Refractory Microsatellite Stable Colorectal Cancer. *Oncologist* (2020) 25:e1188–94. doi: 10.1634/theoncologist.2020-0161
182. Xie H, Lafky JM, Morlan BW, Stella PJ, Dakhil SR, Gross GG, et al. Dual VEGF Inhibition With Sorafenib and Bevacizumab as Salvage Therapy in Metastatic Colorectal Cancer: Results of the Phase II North Central Cancer Treatment Group Study N054C (Alliance). *Ther Adv Med Oncol* (2020) 12:1758835920910913. doi: 10.1177/1758835920910913
183. Escudier B, Eisen T, Stadler WM, Szczylik C, Oudard S, Staehler M, et al. Sorafenib for Treatment of Renal Cell Carcinoma: Final Efficacy and Safety Results of the Phase III Treatment Approaches in Renal Cancer Global Evaluation Trial. *J Clin Oncol* (2009) 27:3312–8. doi: 10.1200/JCO.2008.19.5511
184. Llovet JM, Ricci S, Mazzaferro V, Hilgard P, Gane E, Blanc JF, et al. Sorafenib in Advanced Hepatocellular Carcinoma. *N Engl J Med* (2008) 359:378–90. doi: 10.1056/NEJMoa0708857
185. Bruix J, Takayama T, Mazzaferro V, Chau GY, Yang J, Kudo M, et al. Adjuvant Sorafenib for Hepatocellular Carcinoma After Resection or Ablation (STORM): A Phase 3, Randomised, Double-Blind, Placebo-Controlled Trial. *Lancet Oncol* (2015) 16:1344–54. doi: 10.1016/S1470-2045(15)00198-9
186. Brose MS, Nutting CM, Sherman SI, Shong YK, Smit JW, Reike G, et al. Rationale and Design of Decision: A Double-Blind, Randomized, Placebo-Controlled Phase III Trial Evaluating the Efficacy and Safety of Sorafenib in Patients With Locally Advanced or Metastatic Radioactive Iodine (RAI)-Refractory, Differentiated Thyroid Cancer. *BMC Cancer* (2011) 11:349. doi: 10.1186/1471-2407-11-349
187. Tabernero J, Garcia-Carbonero R, Cassidy J, Sobrero A, Van Cutsem E, Kohne CH, et al. Sorafenib in Combination With Oxaliplatin, Leucovorin, and Fluorouracil (Modified FOLFOX6) as First-Line Treatment of Metastatic Colorectal Cancer: The RESPECT Trial. *Clin Cancer Res* (2013) 19:2541–50. doi: 10.1158/1078-0432.CCR-13-0107
188. Samalin E, Fouchardiere C, Thezenas S, Boige V, Senellart H, Guimbaud R, et al. Sorafenib Plus Irinotecan Combination in Patients With RAS-Mutated Metastatic Colorectal Cancer Refractory To Standard Combined Chemotherapies: A Multicenter, Randomized Phase 2 Trial (NEXIRI-2/PRODIGE 27). *Clin Colorectal Cancer* (2020) 19:301–310 e1. doi: 10.1016/j.clcc.2020.04.008
189. Tsuji Y, Satoh T, Tsuji A, Muro K, Yoshida M, Nishina T, et al. First-Line Sunitinib Plus FOLFIRI in Japanese Patients With Unresectable/Metastatic Colorectal Cancer: A Phase II Study. *Cancer Sci* (2012) 103:1502–7. doi: 10.1111/j.1349-7006.2012.02320.x
190. Carrato A, Swieboda-Sadlej A, Staszewska-Skurczynska M, Lim R, Roman L, Shparyk Y, et al. Fluorouracil, Leucovorin, and Irinotecan Plus Either Sunitinib or Placebo in Metastatic Colorectal Cancer: A Randomized, Phase III Trial. *J Clin Oncol* (2013) 31:1341–7. doi: 10.1200/JCO.2012.45.1930
191. Li J, Qin S, Xu RH, Shen L, Xu J, Bai Y, et al. Effect of Fruquintinib vs Placebo on Overall Survival in Patients With Previously Treated Metastatic Colorectal Cancer: The FRESCO Randomized Clinical Trial. *JAMA* (2018) 319:2486–96. doi: 10.1001/jama.2018.7855
192. Becouarn Y, Cany L, Pulido M, Beyssac R, Texereau P, Le Morvan V, et al. FOLFIRI(R) and Bevacizumab in First-Line Treatment for Colorectal Cancer Patients: Safety, Efficacy and Genetic Polymorphisms. *BMC Res Notes* (2014) 7:260. doi: 10.1186/1756-0500-7-260
193. Hurwitz H, Mitchell EP, Cartwright T, Kwok A, Hu S, Mckenna E, et al. A Randomized, Phase II Trial of Standard Triweekly Compared With Dose-Dense Biweekly Capecitabine Plus Oxaliplatin Plus Bevacizumab as First-Line Treatment for Metastatic Colorectal Cancer: XELOX-A-DVS (Dense Versus Standard). *Oncologist* (2012) 17:937–46. doi: 10.1634/theoncologist.2012-0071
194. Cremolini C, Antoniotti C, Stein A, Bendell J, Gruenberger T, Rossini D, et al. Individual Patient Data Meta-Analysis of FOLFOXIRI Plus Bevacizumab Versus Doublets Plus Bevacizumab as Initial Therapy of Unresectable Metastatic Colorectal Cancer. *J Clin Oncol* (2020) 38:3314–24. doi: 10.1200/JCO.20.01225
195. Stein A, Glockzin G, Wienke A, Arnold D, Edelmann T, Hildebrandt B, et al. Treatment With Bevacizumab and FOLFOXIRI in Patients With Advanced Colorectal Cancer: Presentation of Two Novel Trials (CHARTA and PERIMAX) and Review of the Literature. *BMC Cancer* (2012) 12:356. doi: 10.1186/1471-2407-12-356
196. Cunningham D, Lang I, Marcuello E, Lorusso V, Ocvirk J, Shin DB, et al. Bevacizumab Plus Capecitabine Versus Capecitabine Alone in Elderly Patients With Previously Untreated Metastatic Colorectal Cancer (AVEX): An Open-Label, Randomised Phase 3 Trial. *Lancet Oncol* (2013) 14:1077–85. doi: 10.1016/S1470-2045(13)70154-2
197. Venook AP, Niedzwiecki D, Lenz HJ, Innocenti F, Fruth B, Meyerhardt JA, et al. Effect of First-Line Chemotherapy Combined With Cetuximab or Bevacizumab on Overall Survival in Patients With KRAS Wild-Type Advanced or Metastatic Colorectal Cancer: A Randomized Clinical Trial. *JAMA* (2017) 317:2392–401. doi: 10.1001/jama.2017.7105
198. Robertson JD, Botwood NA, Rothenberg ML, Schmoll HJ. Phase III Trial of FOLFOX Plus Bevacizumab or Cediranib (AZD2171) as First-Line Treatment of Patients With Metastatic Colorectal Cancer: HORIZON III. *Clin Colorectal Cancer* (2009) 8:59–60. doi: 10.3816/CCC.2009.n.010
199. De Gramont A, Van Cutsem E, Schmoll HJ, Tabernero J, Clarke S, Moore MJ, et al. Bevacizumab Plus Oxaliplatin-Based Chemotherapy as Adjuvant Treatment for Colon Cancer (AVANT): A Phase 3 Randomised Controlled Trial. *Lancet Oncol* (2012) 13:1225–33. doi: 10.1016/S1470-2045(12)70509-0
200. Antonuzzo L, Giommoni E, Pastorelli D, Latiano T, Pavese I, Azzarello D, et al. Bevacizumab Plus XELOX as First-Line Treatment of Metastatic Colorectal Cancer: The OBELIX Study. *World J Gastroenterol* (2015) 21:7281–8. doi: 10.3748/wjg.v21.i23.7281

201. Li J, Xu R, Qin S, Liu T, Pan H, Xu J, et al. Aflibercept Plus FOLFIRI in Asian Patients With Pretreated Metastatic Colorectal Cancer: A Randomized Phase III Study. *Future Oncol* (2018) 14:2031–44. doi: 10.2217/fon-2017-0669
202. Van Cutsem E, Tabernero J, Lakomy R, Prenen H, Prausova J, Macarulla T, et al. Addition of Aflibercept to Fluorouracil, Leucovorin, and Irinotecan Improves Survival in a Phase III Randomized Trial in Patients With Metastatic Colorectal Cancer Previously Treated With an Oxaliplatin-Based Regimen. *J Clin Oncol* (2012) 30:3499–506. doi: 10.1200/JCO.2012.42.8201
203. Dane F, Ozgurdal K, Yalcin S, Benekli M, Aykan NF, Yucel I, et al. Safety and Efficacy of Regorafenib in Patients With Treatment-Refractory Metastatic Colorectal Cancer in Turkey: The Single-Arm, Open-Label REGARD Study. *BMJ Open* (2020) 10:e027665. doi: 10.1136/bmjopen-2018-027665
204. Li J, Qin S, Xu R, Yau TC, Ma B, Pan H, et al. Regorafenib Plus Best Supportive Care Versus Placebo Plus Best Supportive Care in Asian Patients With Previously Treated Metastatic Colorectal Cancer (CONCUR): A Randomised, Double-Blind, Placebo-Controlled, Phase 3 Trial. *Lancet Oncol* (2015) 16:619–29. doi: 10.1016/S1470-2045(15)70156-7
205. Qin S, Xu RH, Shen L, Xu J, Bai Y, Yang L, et al. Subgroup Analysis by Liver Metastasis in the FRESCO Trial Comparing Fruquintinib Versus Placebo Plus Best Supportive Care in Chinese Patients With Metastatic Colorectal Cancer. *Onco Targets Ther* (2021) 14:4439–50. doi: 10.2147/OTT.S307273
206. Yarden Y. The EGFR Family and its Ligands in Human Cancer. Signalling Mechanisms and Therapeutic Opportunities. *Eur J Cancer* (2001) 37 (Suppl 4):S3–8. doi: 10.1016/s0959-8049(01)00230-1
207. Yamaoka T, Ohba M, Ohmori T. Molecular-Targeted Therapies for Epidermal Growth Factor Receptor and Its Resistance Mechanisms. *Int J Mol Sci* (2017) 18:2420. doi: 10.3390/ijms18112420
208. Chan DLH, Segelov E, Wong RS, Smith A, Herbertson RA, Li BT, et al. Epidermal Growth Factor Receptor (EGFR) Inhibitors for Metastatic Colorectal Cancer. *Cochrane Database Syst Rev* (2017) 6:CD007047. doi: 10.1002/14651858.CD007047.pub2
209. Fornasier G, Francescon S, Baldo P. An Update of Efficacy and Safety of Cetuximab in Metastatic Colorectal Cancer: A Narrative Review. *Adv Ther* (2018) 35:1497–509. doi: 10.1007/s12325-018-0791-0
210. Herbst RS, Hong WK. IMC-C225, an Anti-Epidermal Growth Factor Receptor Monoclonal Antibody for Treatment of Head and Neck Cancer. *Semin Oncol* (2002) 29:18–30. doi: 10.1053/sonc.2002.35644
211. Personeni N, Hendlisz A, Gallez J, Galdon MG, Larsimont D, Van Laethem JL, et al. Correlation Between the Response to Cetuximab Alone or in Combination With Irinotecan and the Activated/Phosphorylated Epidermal Growth Factor Receptor in Metastatic Colorectal Cancer. *Semin Oncol* (2005) 32:S59–62. doi: 10.1053/j.seminoncol.2005.04.029
212. Saltz LB, Meropol NJ, Loehrer PJSr., Needle MN, Kopit J, Mayer RJ. Phase II Trial of Cetuximab in Patients With Refractory Colorectal Cancer That Expresses the Epidermal Growth Factor Receptor. *J Clin Oncol* (2004) 22:1201–8. doi: 10.1200/JCO.2004.10.182
213. Van Cutsem E, Kohne CH, Hitre E, Zaluski J, Chang Chien CR, Makhson A, et al. Cetuximab and Chemotherapy as Initial Treatment for Metastatic Colorectal Cancer. *N Engl J Med* (2009) 360:1408–17. doi: 10.1056/NEJMoa0805019
214. Yarla NS, Madka V, Pathuri G, Rao CV. Molecular Targets in Precision Chemoprevention of Colorectal Cancer: An Update From Pre-Clinical to Clinical Trials. *Int J Mol Sci* (2020) 21:9609. doi: 10.3390/ijms21249609
215. Vangala D, Ladigan S, Liffers ST, Noseir S, Maghnouj A, Gotze TM, et al. Secondary Resistance to Anti-EGFR Therapy by Transcriptional Reprogramming in Patient-Derived Colorectal Cancer Models. *Genome Med* (2021) 13:116. doi: 10.1186/s13073-021-00926-7
216. Kasper S, Meiler J, Knipp H, Hohler T, Reimer P, Steinmetz T, et al. Biweekly Cetuximab Plus FOLFOX6 as First-Line Therapy in Patients With RAS Wild-Type Metastatic Colorectal Cancer: The CEBIFOX Trial. *Clin Colorectal Cancer* (2020) 19:236–247 e6. doi: 10.1016/j.clcc.2020.03.003
217. Van Cutsem E, Peeters M, Siena S, Humblet Y, Hendlisz A, Neyns B, et al. Open-Label Phase III Trial of Panitumumab Plus Best Supportive Care Compared With Best Supportive Care Alone in Patients With Chemotherapy-Refractory Metastatic Colorectal Cancer. *J Clin Oncol* (2007) 25:1658–64. doi: 10.1200/JCO.2006.08.1620
218. Douillard JY, Siena S, Cassidy J, Tabernero J, Burkes R, Barugel M, et al. Randomized, Phase III Trial of Panitumumab With Infusional Fluorouracil, Leucovorin, and Oxaliplatin (FOLFOX4) Versus FOLFOX4 Alone as First-Line Treatment in Patients With Previously Untreated Metastatic Colorectal Cancer: The PRIME Study. *J Clin Oncol* (2010) 28:4697–705. doi: 10.1200/JCO.2009.27.4860
219. Modest DP, Martens UM, Riera-Knorrenschild J, Greeve J, Florschutz A, Wessendorf S, et al. FOLFOXIRI Plus Panitumumab As First-Line Treatment of RAS Wild-Type Metastatic Colorectal Cancer: The Randomized, Open-Label, Phase II VOLFI Study (AIO Krk0109). *J Clin Oncol* (2019) 37:3401–11. doi: 10.1200/JCO.19.01340
220. De Felice F, D'ambrosio G, Iafrate F, Gelibter A, Magliocca FM, Musio D, et al. Intensified Total Neoadjuvant Therapy in Patients With Locally Advanced Rectal Cancer: A Phase II Trial. *Clin Oncol (R Coll Radiol)* (2021) 33:788–94. doi: 10.1016/j.clon.2021.06.006
221. Tol J, Koopman M, Cats A, Rodenburg CJ, Creemers GJ, Schrama JG, et al. Chemotherapy, Bevacizumab, and Cetuximab in Metastatic Colorectal Cancer. *N Engl J Med* (2009) 360:563–72. doi: 10.1056/NEJMoa0808268
222. Ljunggren HG, Jonsson R, Hoglund P. Seminal Immunologic Discoveries With Direct Clinical Implications: The 2018 Nobel Prize in Physiology or Medicine Honours Discoveries in Cancer Immunotherapy. *Scand J Immunol* (2018) 88:e12731. doi: 10.1111/sji.12731
223. Makkouk A, Weiner GJ. Cancer Immunotherapy and Breaking Immune Tolerance: New Approaches to an Old Challenge. *Cancer Res* (2015) 75:5–10. doi: 10.1158/0008-5472.CAN-14-2538
224. Vinay DS, Ryan EP, Pawelec G, Talib WH, Stagg J, Elkord E, et al. Immune Evasion in Cancer: Mechanistic Basis and Therapeutic Strategies. *Semin Cancer Biol* (2015) 35 Suppl:S185–98. doi: 10.1016/j.semcancer.2015.03.004
225. Gu L, Khadaroo PA, Su H, Kong L, Chen L, Wang X, et al. The Safety and Tolerability of Combined Immune Checkpoint Inhibitors (Anti-PD-1/PD-L1 Plus Anti-CTLA-4): A Systematic Review and Meta-Analysis. *BMC Cancer* (2019) 19:559. doi: 10.1186/s12885-019-5785-z
226. Seidel JA, Otsuka A, Kabashima K. Anti-PD-1 and Anti-CTLA-4 Therapies in Cancer: Mechanisms of Action, Efficacy, and Limitations. *Front Oncol* (2018) 8:86. doi: 10.3389/fonc.2018.00086
227. Li X, Shao C, Shi Y, Han W. Lessons Learned From the Blockade of Immune Checkpoints in Cancer Immunotherapy. *J Hematol Oncol* (2018) 11:31. doi: 10.1186/s13045-018-0578-4
228. Ouyang T, Cao Y, Kan X, Chen L, Ren Y, Sun T, et al. Treatment-Related Serious Adverse Events of Immune Checkpoint Inhibitors in Clinical Trials: A Systematic Review. *Front Oncol* (2021) 11:621639. doi: 10.3389/fonc.2021.621639
229. Anderson AC, Joller N, Kuchroo VK. Lag-3, Tim-3, and TIGIT: Co-Inhibitory Receptors With Specialized Functions in Immune Regulation. *Immunity* (2016) 44:989–1004. doi: 10.1016/j.immuni.2016.05.001
230. Dougall WC, Kurtulus S, Smyth MJ, Anderson AC. TIGIT and CD96: New Checkpoint Receptor Targets for Cancer Immunotherapy. *Immunol Rev* (2017) 276:112–20. doi: 10.1111/imr.12518
231. Maruhashi T, Sugiura D, Okazaki IM, Okazaki T. LAG-3: From Molecular Functions to Clinical Applications. *J Immunother Cancer* (2020) 8:e001014. doi: 10.1136/jitc-2020-001014
232. Das M, Zhu C, Kuchroo VK. Tim-3 and its Role in Regulating Anti-Tumor Immunity. *Immunol Rev* (2017) 276:97–111. doi: 10.1111/imr.12520
233. De Mingo Pulido A, Gardner A, Hiebler S, Soliman H, Rugo HS, Krummel MF, et al. TIM-3 Regulates CD103(+) Dendritic Cell Function and Response to Chemotherapy in Breast Cancer. *Cancer Cell* (2018) 33:60–74 e6. doi: 10.1016/j.ccell.2017.11.019
234. Brunet JF, Denizot F, Luciani MF, Roux-Dosseto M, Suzan M, Mattei MG, et al. A New Member of the Immunoglobulin Superfamily–CTLA-4. *Nature* (1987) 328:267–70. doi: 10.1038/328267a0
235. Corse E, Allison JP. Cutting Edge: CTLA-4 on Effector T Cells Inhibits in Trans. *J Immunol* (2012) 189:1123–7. doi: 10.4049/jimmunol.1200695
236. De Sousa Linhares A, Leitner J, Grabmeier-Pfistershammer K, Steinberger P. Not All Immune Checkpoints Are Created Equal. *Front Immunol* (2018) 9:1909. doi: 10.3389/fimmu.2018.01909
237. Hodi FS, O'day SJ, Mcdermott DF, Weber RW, Sosman JA, Haanen JB, et al. Improved Survival With Ipilimumab in Patients With Metastatic Melanoma. *N Engl J Med* (2010) 363:711–23. doi: 10.1056/NEJMoa1003466
238. Zoroquiain P, Esposito E, Logan P, Aldrees S, Dias AB, Mansure JJ, et al. Programmed Cell Death Ligand-1 Expression in Tumor and

Immune Cells Is Associated With Better Patient Outcome and Decreased Tumor-Infiltrating Lymphocytes in Uveal Melanoma. *Mod Pathol* (2018) 31:1201–10. doi: 10.1038/s41379-018-0043-5

239. Ahmadzadeh M, Johnson LA, Heemskerk B, Wunderlich JR, Dudley ME, White DE, et al. Tumor Antigen-Specific CD8 T Cells Infiltrating the Tumor Express High Levels of PD-1 and Are Functionally Impaired. *Blood* (2009) 114:1537–44. doi: 10.1182/blood-2008-12-195792
240. Salmaninejad A, Khoramshahi V, Azani A, Soltaninejad E, Aslani S, Zamani MR, et al. PD-1 and Cancer: Molecular Mechanisms and Polymorphisms. *Immunogenetics* (2018) 70:73–86. doi: 10.1007/s00251-017-1015-5
241. Zamani MR, Aslani S, Salmaninejad A, Javan MR, Rezaei N. PD-1/PD-L and Autoimmunity: A Growing Relationship. *Cell Immunol* (2016) 310:27–41. doi: 10.1016/j.cellimm.2016.09.009
242. Ren M, Dai B, Kong YY, Lv JJ, Cai X. PD-L1 Expression in Tumour-Infiltrating Lymphocytes Is a Poor Prognostic Factor for Primary Acral Melanoma Patients. *Histopathology* (2018) 73:386–96. doi: 10.1111/his.13527
243. Andre T, Shiu KK, Kim TW, Jensen BV, Jensen LH, Punt C, et al. Pembrolizumab in Microsatellite-Instability-High Advanced Colorectal Cancer. *N Engl J Med* (2020) 383:2207–18. doi: 10.1056/NEJMoa2017699
244. Le DT, Kim TW, Van Cutsem E, Geva R, Jager D, Hara H, et al. Phase II Open-Label Study of Pembrolizumab in Treatment-Refractory, Microsatellite Instability-High/Mismatch Repair-Deficient Metastatic Colorectal Cancer: KEYNOTE-164. *J Clin Oncol* (2020) 38:11–9. doi: 10.1200/JCO.19.02107
245. Le DT, Uram JN, Wang H, Bartlett BR, Kemberling H, Eyring AD, et al. PD-1 Blockade in Tumors With Mismatch-Repair Deficiency. *N Engl J Med* (2015) 372:2509–20. doi: 10.1056/NEJMoa1500596
246. Weber JS, D'angelo SP, Minor D, Hodi FS, Gutzmer R, Neyns B, et al. Nivolumab Versus Chemotherapy in Patients With Advanced Melanoma Who Progressed After Anti-CTLA-4 Treatment (CheckMate 037): A Randomised, Controlled, Open-Label, Phase 3 Trial. *Lancet Oncol* (2015) 16:375–84. doi: 10.1016/S1470-2045(15)70076-8
247. Robert C, Long GV, Brady B, Dutriaux C, Maio M, Mortier L, et al. Nivolumab in Previously Untreated Melanoma Without BRAF Mutation. *N Engl J Med* (2015) 372:320–30. doi: 10.1056/NEJMoa1412082
248. Overman MJ, Mcdermott R, Leach JL, Lonardi S, Lenz HJ, Morse MA, et al. Nivolumab in Patients With Metastatic DNA Mismatch Repair-Deficient or Microsatellite Instability-High Colorectal Cancer (CheckMate 142): An Open-Label, Multicentre, Phase 2 Study. *Lancet Oncol* (2017) 18:1182–91. doi: 10.1016/S1470-2045(17)30422-9
249. Overman MJ, Lonardi S, Wong KYM, Lenz HJ, Gelsomino F, Aglietta M, et al. Durable Clinical Benefit With Nivolumab Plus Ipilimumab in DNA Mismatch Repair-Deficient/Microsatellite Instability-High Metastatic Colorectal Cancer. *J Clin Oncol* (2018) 36:773–9. doi: 10.1200/JCO.2017.76.9901
250. Morse MA, Overman MJ, Hartman L, Khoukaz T, Brutcher E, Lenz HJ, et al. Safety of Nivolumab Plus Low-Dose Ipilimumab in Previously Treated Microsatellite Instability-High/Mismatch Repair-Deficient Metastatic Colorectal Cancer. *Oncologist* (2019) 24:1453–61. doi: 10.1634/theoncologist.2019-0129
251. Lenz HJ, Van Cutsem E, Luisa Limon M, Wong KYM, Hendlisz A, Aglietta M, et al. First-Line Nivolumab Plus Low-Dose Ipilimumab for Microsatellite Instability-High/Mismatch Repair-Deficient Metastatic Colorectal Cancer: The Phase II CheckMate 142 Study. *J Clin Oncol* (2021), JCO2101015. doi: 10.1200/JCO.21.01015
252. Barone A, Hazarika M, Theoret MR, Mishra-Kalyani P, Chen H, He K, et al. FDA Approval Summary: Pembrolizumab for the Treatment of Patients With Unresectable or Metastatic Melanoma. *Clin Cancer Res* (2017) 23:5661–5. doi: 10.1158/1078-0432.CCR-16-0664
253. Leighl NB, Hellmann MD, Hui R, Carcereny E, Felip E, Ahn MJ, et al. Pembrolizumab in Patients With Advanced Non-Small-Cell Lung Cancer (KEYNOTE-001): 3-Year Results From an Open-Label, Phase 1 Study. *Lancet Respir Med* (2019) 7:347–57. doi: 10.1016/S2213-2600(18)30500-9
254. Herbst RS, Baas P, Kim DW, Felip E, Perez-Gracia JL, Han JY, et al. Pembrolizumab Versus Docetaxel for Previously Treated, PD-L1-Positive, Advanced non-Small-Cell Lung Cancer (KEYNOTE-010): A Randomised Controlled Trial. *Lancet* (2016) 387:1540–50. doi: 10.1016/S0140-6736(15)01281-7
255. Chen R, Zinzani PL, Fanale MA, Armand P, Johnson NA, Brice P, et al. Phase II Study of the Efficacy and Safety of Pembrolizumab for Relapsed/Refractory Classic Hodgkin Lymphoma. *J Clin Oncol* (2017) 35:2125–32. doi: 10.1200/JCO.2016.72.1316
256. Kuruvilla J, Ramchandren R, Santoro A, Paszkiewicz-Kozik E, Gasiorowski R, Johnson NA, et al. Pembrolizumab Versus Brentuximab Vedotin in Relapsed or Refractory Classical Hodgkin Lymphoma (KEYNOTE-204): An Interim Analysis of a Multicentre, Randomised, Open-Label, Phase 3 Study. *Lancet Oncol* (2021) 22:512–24. doi: 10.1016/S1470-2045(21)00005-X
257. Bauml J, Seiwert TY, Pfister DG, Worden F, Liu SV, Gilbert J, et al. Pembrolizumab for Platinum- and Cetuximab-Refractory Head and Neck Cancer: Results From a Single-Arm, Phase II Study. *J Clin Oncol* (2017) 35:1542–9. doi: 10.1200/JCO.2016.70.1524
258. Bellmunt J, De Wit R, Vaughn DJ, Fradet Y, Lee JL, Fong L, et al. Pembrolizumab as Second-Line Therapy for Advanced Urothelial Carcinoma. *N Engl J Med* (2017) 376:1015–26. doi: 10.1056/NEJMoa1613683
259. Balar AV, Castellano D, O'donnell PH, Grivas P, Vuky J, Powles T, et al. First-Line Pembrolizumab in Cisplatin-Ineligible Patients With Locally Advanced and Unresectable or Metastatic Urothelial Cancer (KEYNOTE-052): A Multicentre, Single-Arm, Phase 2 Study. *Lancet Oncol* (2017) 18:1483–92. doi: 10.1016/S1470-2045(17)30616-2
260. Janjigian YY, Maron SB, Chatila WK, Millang B, Chavan SS, Alterman C, et al. First-Line Pembrolizumab and Trastuzumab in HER2-Positive Oesophageal, Gastric, or Gastro-Oesophageal Junction Cancer: An Open-Label, Single-Arm, Phase 2 Trial. *Lancet Oncol* (2020) 21:821–31. doi: 10.1016/S1470-2045(20)30169-8
261. Marcus L, Lemery SJ, Keegan P, Pazdur R. FDA Approval Summary: Pembrolizumab for the Treatment of Microsatellite Instability-High Solid Tumors. *Clin Cancer Res* (2019) 25:3753–8. doi: 10.1158/1078-0432.CCR-18-4070
262. Gardini A, Ercolani G, Riccobon A, Ravaioli M, Ridolfi L, Flamini E, et al. Adjuvant, Adoptive Immunotherapy With Tumor Infiltrating Lymphocytes Plus Interleukin-2 After Radical Hepatic Resection for Colorectal Liver Metastases: 5-Year Analysis. *J Surg Oncol* (2004) 87:46–52. doi: 10.1002/jso.20066
263. Karlsson M, Marits P, Dahl K, Dagoo T, Enerback S, Thorn M, et al. Pilot Study of Sentinel-Node-Based Adoptive Immunotherapy in Advanced Colorectal Cancer. *Ann Surg Oncol* (2010) 17:1747–57. doi: 10.1245/s10434-010-0920-8
264. Zhen YH, Liu XH, Yang Y, Li B, Tang JL, Zeng QX, et al. Phase I/II Study of Adjuvant Immunotherapy With Sentinel Lymph Node T Lymphocytes in Patients With Colorectal Cancer. *Cancer Immunol Immunother* (2015) 64:1083–93. doi: 10.1007/s00262-015-1715-3
265. Parkhurst MR, Yang JC, Langan RC, Dudley ME, Nathan DA, Feldman SA, et al. T Cells Targeting Carcinoembryonic Antigen can Mediate Regression of Metastatic Colorectal Cancer But Induce Severe Transient Colitis. *Mol Ther* (2011) 19:620–6. doi: 10.1038/mt.2010.272
266. Porter DL, Levine BL, Kalos M, Bagg A, June CH. Chimeric Antigen Receptor-Modified T Cells in Chronic Lymphoid Leukemia. *N Engl J Med* (2011) 365:725–33. doi: 10.1056/NEJMoa1103849
267. Maude SL, Teachey DT, Porter DL, Grupp SA. CD19-Targeted Chimeric Antigen Receptor T-Cell Therapy for Acute Lymphoblastic Leukemia. *Blood* (2015) 125:4017–23. doi: 10.1182/blood-2014-12-580068
268. Zhang C, Wang Z, Yang Z, Wang M, Li S, Li Y, et al. Phase I Escalating-Dose Trial of CAR-T Therapy Targeting CEA(+) Metastatic Colorectal Cancers. *Mol Ther* (2017) 25:1248–58. doi: 10.1016/j.ymthe.2017.03.010
269. Hege KM, Bergsland EK, Fisher GA, Nemunaitis JJ, Warren RS, Mcarthur JG, et al. Safety, Tumor Trafficking and Immunogenicity of Chimeric Antigen Receptor (CAR)-T Cells Specific for TAG-72 in Colorectal Cancer. *J Immunother Cancer* (2017) 5:22. doi: 10.1186/s40425-017-0222-9
270. Zhao H, Wang Y, Yu J, Wei F, Cao S, Zhang X, et al. Autologous Cytokine-Induced Killer Cells Improves Overall Survival of Metastatic Colorectal Cancer Patients: Results From a Phase II Clinical Trial. *Clin Colorectal Cancer* (2016) 15:228–35. doi: 10.1016/j.clcc.2016.02.005
271. Zhang J, Zhu L, Zhang Q, He X, Yin Y, Gu Y, et al. Effects of Cytokine-Induced Killer Cell Treatment in Colorectal Cancer Patients: A Retrospective Study. *BioMed Pharmacother* (2014) 68:715–20. doi: 10.1016/j.biopha.2014.07.010
272. Lin T, Song C, Chuo DY, Zhang H, Zhao J. Clinical Effects of Autologous Dendritic Cells Combined With Cytokine-Induced Killer Cells Followed by Chemotherapy in Treating Patients With Advanced Colorectal Cancer: A

Prospective Study. *Tumour Biol* (2016) 37:4367–72. doi: 10.1007/s13277-015-3957-2

273. Xie Y, Huang L, Chen L, Lin X, Chen L, Zheng Q. Effect of Dendritic Cell-Cytokine-Induced Killer Cells in Patients With Advanced Colorectal Cancer Combined With First-Line Treatment. *World J Surg Oncol* (2017) 15:209. doi: 10.1186/s12957-017-1278-1
274. Morse MA, Chaudhry A, Gabitzsch ES, Hobeika AC, Osada T, Clay TM, et al. Novel Adenoviral Vector Induces T-Cell Responses Despite Anti-Adenoviral Neutralizing Antibodies in Colorectal Cancer Patients. *Cancer Immunol Immunother* (2013) 62:1293–301. doi: 10.1007/s00262-013-1400-3
275. Morse MA, Niedzwiecki D, Marshall JL, Garrett C, Chang DZ, Aklilu M, et al. A Randomized Phase II Study of Immunization With Dendritic Cells Modified With Poxvectors Encoding CEA and MUC1 Compared With the Same Poxvectors Plus GM-CSF for Resected Metastatic Colorectal Cancer. *Ann Surg* (2013) 258:879–86. doi: 10.1097/SLA.0b013e318292919e
276. Scurr M, Pembroke T, Bloom A, Roberts D, Thomson A, Smart K, et al. Effect of Modified Vaccinia Ankara-5T4 and Low-Dose Cyclophosphamide on Antitumor Immunity in Metastatic Colorectal Cancer: A Randomized Clinical Trial. *JAMA Oncol* (2017) 3:e172579. doi: 10.1001/jamaoncol.2017.2579
277. Heery CR, Palena C, Mcmahon S, Donahue RN, Lepone LM, Grenga I, et al. Phase I Study of a Poxviral TRICOM-Based Vaccine Directed Against the Transcription Factor Brachyury. *Clin Cancer Res* (2017) 23:6833–45. doi: 10.1158/1078-0432.CCR-17-1087
278. Gatti-Mays ME, Strauss J, Donahue RN, Palena C, Del Rivero J, Redman JM, et al. A Phase I Dose-Escalation Trial of BN-CV301, a Recombinant Poxviral Vaccine Targeting MUC1 and CEA With Costimulatory Molecules. *Clin Cancer Res* (2019) 25:4933–44. doi: 10.1158/1078-0432.CCR-19-0183
279. Hoover HC Jr., Brandhorst JS, Peters LC, Surdyke MG, Takeshita Y, Madariaga J, et al. Adjuvant Active Specific Immunotherapy for Human Colorectal Cancer: 6.5-Year Median Follow-Up of a Phase III Prospectively Randomized Trial. *J Clin Oncol* (1993) 11:390–9. doi: 10.1200/JCO.1993.11.3.390
280. Harris JE, Ryan L, Hoover HC Jr., Stuart RK, Oken MM, Benson AB3rd, et al. Adjuvant Active Specific Immunotherapy for Stage II and III Colon Cancer With an Autologous Tumor Cell Vaccine: Eastern Cooperative Oncology Group Study E5283. *J Clin Oncol* (2000) 18:148–57. doi: 10.1200/JCO.2000.18.1.148
281. Vermorken JB, Claessen AM, Van Tinteren H, Gall HE, Ezinga R, Meijer S, et al. Active Specific Immunotherapy for Stage II and Stage III Human Colon Cancer: A Randomised Trial. *Lancet* (1999) 353:345–50. doi: 10.1016/S0140-6736(98)07186-4
282. Barth RJJr., Fisher DA, Wallace PK, Channon JY, Noelle RJ, Gui J, et al. A Randomized Trial of *Ex Vivo* CD40L Activation of a Dendritic Cell Vaccine in Colorectal Cancer Patients: Tumor-Specific Immune Responses Are Associated With Improved Survival. *Clin Cancer Res* (2010) 16:5548–56. doi: 10.1158/1078-0432.CCR-10-2138
283. Rodriguez J, Castanon E, Perez-Gracia JL, Rodriguez I, Viudez A, Alfaro C, et al. A Randomized Phase II Clinical Trial of Dendritic Cell Vaccination Following Complete Resection of Colon Cancer Liver Metastasis. *J Immunother Cancer* (2018) 6:96. doi: 10.1186/s40425-018-0405-z
284. Frick GS, Pitari GM, Weinberg DS, Hyslop T, Schulz S, Waldman SA. Guanylyl Cyclase C: A Molecular Marker for Staging and Postoperative Surveillance of Patients With Colorectal Cancer. *Expert Rev Mol Diagn* (2005) 5:701–13. doi: 10.1586/14737159.5.5.701
285. Snook AE, Baybutt TR, Xiang B, Abraham TS, Flickinger JC Jr., Hyslop T, et al. Split Tolerance Permits Safe Ad5-GUCY2C-PADRE Vaccine-Induced T-Cell Responses in Colon Cancer Patients. *J Immunother Cancer* (2019) 7:104. doi: 10.1186/s40425-019-0576-2
286. Balint JP, Gabitzsch ES, Rice A, Latchman Y, Xu Y, Messerschmidt GL, et al. Extended Evaluation of a Phase 1/2 Trial on Dosing, Safety, Immunogenicity, and Overall Survival After Immunizations With an Advanced-Generation Ad5 [E1-, E2b-]-CEA(6D) Vaccine in Late-Stage Colorectal Cancer. *Cancer Immunol Immunother* (2015) 64:977–87. doi: 10.1007/s00262-015-1706-4
287. Crosby EJ, Hobeika AC, Niedzwiecki D, Rushing C, Hsu D, Berglund P, et al. Long-Term Survival of Patients With Stage III Colon Cancer Treated With VRP-CEA(6D), an Alphavirus Vector That Increases the CD8+ Effector Memory T Cell to Treg Ratio. *J Immunother Cancer* (2020) 8:e001662. doi: 10.1136/jitc-2020-001662
288. Yarchoan M, Huang CY, Zhu Q, Ferguson AK, Durham JN, Anders RA, et al. A Phase 2 Study of GVAX Colon Vaccine With Cyclophosphamide and Pembrolizumab in Patients With Mismatch Repair Proficient Advanced Colorectal Cancer. *Cancer Med* (2020) 9:1485–94. doi: 10.1002/cam4.2763
289. Santos P, Almeida F. Exosome-Based Vaccines: History, Current State, and Clinical Trials. *Front Immunol* (2021) 12:711565. doi: 10.3389/fimmu.2021.711565
290. Dai S, Wei D, Wu Z, Zhou X, Wei X, Huang H, et al. Phase I Clinical Trial of Autologous Ascites-Derived Exosomes Combined With GM-CSF for Colorectal Cancer. *Mol Ther* (2008) 16:782–90. doi: 10.1038/mt.2008.1

Conflict of Interest: The authors declare that the research was conducted in the absence of any commercial or financial relationships that could be construed as a potential conflict of interest.

Publisher's Note: All claims expressed in this article are solely those of the authors and do not necessarily represent those of their affiliated organizations, or those of the publisher, the editors and the reviewers. Any product that may be evaluated in this article, or claim that may be made by its manufacturer, is not guaranteed or endorsed by the publisher.

Copyright © 2021 Chen, Zheng and Wu. This is an open-access article distributed under the terms of the Creative Commons Attribution License (CC BY). The use, distribution or reproduction in other forums is permitted, provided the original author(s) and the copyright owner(s) are credited and that the original publication in this journal is cited, in accordance with accepted academic practice. No use, distribution or reproduction is permitted which does not comply with these terms.

frontiers in Immunology

ORIGINAL RESEARCH
published: 14 January 2022
doi: 10.3389/fimmu.2021.805883

Establishing a Prognostic Signature Based on Epithelial–Mesenchymal Transition-Related Genes for Endometrial Cancer Patients

Jinhui Liu[1†], Guoliang Cui[2†], Shuning Shen[1†], Feng Gao[3†], Hongjun Zhu[4] and Yinghua Xu[5*]*

[1] Department of Gynecology, The First Affiliated Hospital of Nanjing Medical University, Nanjing, China, [2] Department of Gastroenterology, The Second Affiliated Hospital of Nanjing University of Chinese Medicine, Nanjing, China, [3] Department of Orthopedic Surgery, The First Affiliated Hospital of Nanjing Medical University, Nanjing, China, [4] Department of Oncology, Nantong Third People's Hospital Affiliated to Nantong University, Nantong, China, [5] Department of Radiation Oncology, Nantong Third People's Hospital Affiliated to Nantong University, Nantong, China

OPEN ACCESS

Edited by:
Elena Ciaglia, University of Salerno, Italy

Reviewed by:
Giorgio Giurato, University of Salerno, Italy
Francesco Montella, University of Salerno, Italy

***Correspondence:**
Yinghua Xu
hsmily@126.com
Hongjun Zhu
zhj28254282@163.com

[†]These authors have contributed equally to this work

Specialty section:
This article was submitted to Cancer Immunity and Immunotherapy, a section of the journal Frontiers in Immunology

Received: *31 October 2021*
Accepted: *21 December 2021*
Published: *14 January 2022*

Citation:
Liu J, Cui G, Shen S, Gao F, Zhu H and Xu Y (2022) Establishing a Prognostic Signature Based on Epithelial–Mesenchymal Transition-Related Genes for Endometrial Cancer Patients. Front. Immunol. 12:805883. doi: 10.3389/fimmu.2021.805883

Backgrounds: Epithelial–mesenchymal transition (EMT) is a sequential process where tumor cells develop from the epithelial state to the mesenchymal state. EMT contributes to various tumor functions including initiation, propagating potential, and resistance to therapy, thus affecting the survival time of patients. The aim of this research is to set up an EMT-related prognostic signature for endometrial cancer (EC).

Methods: EMT-related gene (ERG) expression and clinical data were acquired from The Cancer Genome Atlas (TCGA). The entire set was randomly divided into two sets, one for contributing the risk model (risk score) and the other for validating. Univariate and multivariate Cox proportional hazards regression analyses were applied to the training set to select the prognostic ERGs. The expression of 10 ERGs was confirmed by qRT-PCR in clinical samples. Then, we developed a nomogram predicting 1-/3-/5-year survival possibility combining the risk score and clinical factors. The entire set was stratified into the high- and low-risk groups, which was used to analyze the immune infiltrating, tumorigenesis pathways, and response to drugs.

Results: A total of 220 genes were screened out from 1,316 ERGs for their differential expression in tumor versus normal. Next, 10 genes were found to be associated with overall survival (OS) in EC, and the expression was validated by qRT-PCR using clinical samples, so we constructed a 10-ERG-based risk score to distinguish high-/low-risk patients and a nomogram to predict survival rate. The calibration plots proved the predictive value of our model. Gene Set Enrichment Analysis (GSEA) discovered that in the low-risk group, immune-related pathways were enriched; in the high-risk group, tumorigenesis pathways were enriched. The low-risk group showed more immune activities, higher tumor mutational burden (TMB), and higher CTAL4/PD1 expression, which was in line with a better response to immune checkpoint inhibitors. Nevertheless, response to chemotherapeutic drugs turned out better in the high-risk group. The high-

risk group had higher N^6-methyladenosine (m^6A) RNA expression, microsatellite instability level, and stemness indices.

Conclusion: We constructed the ERG-related signature model to predict the prognosis of EC patients. What is more, it might offer a reference for predicting individualized response to immune checkpoint inhibitors and chemotherapeutic drugs.

Keywords: epithelial–mesenchymal transition, endometrial cancer, The Cancer Genome Atlas, prognosis, immunity

INTRODUCTION

Endometrial cancer (EC) is one of the most common gynecologic cancer, with rising incidence and associated mortality (1). According to the American Cancer Society, the 5-year relative survival (2010–2016) of uterine corpus cancer was 81%; the probability of dying from cancer of uterine corpus was 0.6% (2015–2017). Although the prognosis of EC is better than that of cervical and ovarian cancers, it is meaningful to screen out the high-risk part of EC patients who would have a higher possibility of advanced cancer and early death.

Epithelial–mesenchymal transition (EMT) is a biological process (BP) where epithelial cells gain mesenchymal features. During this process, cells in hybrid EMT state express both epithelial and mesenchymal biomarkers, such as E-cadherin, vimentin, keratin 5, keratin 14, and Cdh2. Through EMT-related pathways, cells gain stem-like features, reduced cell polarity, weakened cell–cell adherence, and the ability to migrate. In cancers, these cells present high metastatic potential (2). Some studies have revealed the role of EMT in EC. EMT status, represented by both reduced E-cadherin and nuclear expression of Snail, was found to be significantly related to clinical features including myometrial invasion, positive cytology, and overall survival (OS) (3), suggesting that EMT signature could be a prognostic factor of EC. As to the molecular mechanism behind, estrogen-related receptor alpha (ERRα) was reported to participate in the TGF-β-induced EMT through cancer–stromal interactions in EC cells (4). Ubiquitin-conjugating enzyme E2C (UBE2C), which is regulated by estrogen, promotes EMT *via* p53 in EC (5). What is more, PD-L1 was found to be modulating EMT and cancer stem cell (CSC)-like phenotype through several signaling pathways (6), which inspired us to investigate the association between EMT status and response to immune checkpoint inhibitor therapy in EC. Tumors are infiltrated by immune cells, such as T cells, NK cells, macrophages, and dendritic cells (DCs), composing the microenvironment around cancer cells. Some inflammatory cells like macrophages shift their ground to support cancer cells during long-term crosstalk with them, which might contribute to resistance to drug therapy. Tumors escape from regular immune recognition by regulating immune checkpoints. The current risk stratification models used in EC mostly stick to clinical features (stage, histological type, and grade), but genomic factors have not been applied to standard clinical use (7). Therefore, we tried to establish an EMT-related gene (ERG)-related risk model for EC in prognosis and might offer a reference for individual treatment in the future.

MATERIALS AND METHODS

Public Data Sources

ERGs were attained from a previous study of EMT-related signatures for CRC (8). ERG expression data and clinical features of 522 EC patients and 23 normal samples were downloaded from The Cancer Genome Atlas (TCGA), and the transcriptome data files were "FPKM". The clinical and pathological characteristics of the tumor samples are shown in **Table S1** ($p > 0.05$, chi-squared test).

Identification of Overall Survival-Related Epithelial–Mesenchymal Transition-Related Genes

We analyzed 1,316 ERGs between EC and normal tissues with the "limma" package in R software with a cutoff threshold (the adjusted false discovery rate < 0.05 and absolute $|\log_2 FC| > 2$). The different expression levels of ERGs were visualized by heatmap and volcano plot.

Construction and Validation of the Epithelial–Mesenchymal Transition-Related Gene Signature Model

We randomly divided the entire set (511 samples) into two sets using the R package "caret." The training set was used for the construction of the risk model, while the testing set and the entire set were used for validation. Univariate Cox regression analysis was performed in the R package "survival", and multivariate Cox regression analysis in the "survminer" package to pick out the prognostic ERGs. Then we established the risk score with the following formula: risk score = Σ_i multi-Cox-coefficient (ERGi) * expression (ERGi). Survival analysis was used to investigate the relationship between ERG-related risk score and OS. The Kaplan–Meier (K-M) analysis was performed with the "survival" package. Principal component analysis (PCA) was used for dimensionality reduction (9). Time-dependent receiver operating characteristic (ROC) was performed with the "survivalROC" package.

Construction of the Nomogram

Univariate and multivariate Cox regression analyses were used to investigate whether risk score was an independent prognostic factor in the training, testing, and entire cohorts. We further verified the prognostic value of the risk score stratified by clinicopathological parameters. We constructed the nomogram

predicting 1-/3-/5-year survival possibility using the "rms" package. The calibration plots were used to validate the prognostic value of the nomogram.

Gene Set Enrichment Analysis

Gene Set Enrichment Analysis (GSEA) was used to determine the significantly enriched Kyoto Encyclopedia of Genes and Genomes (KEGG) pathways of ERG mRNA.

GSEA (http://software.broadinstitute.org/gsea/index.jsp) was used to identify BPs that are enriched in the gene rank. Based on a model of the risk score, EC samples in the entire set were divided into high-risk and low-risk groups. Comparing the enrichment of BPs, the underlying biological functions of two groups were identified. The collection of annotated gene sets in the Molecular Signatures Database (MSigDB, http://software.broadinstitute.org/gsea/msigdb/index.jsp) was chosen as the reference gene set in GSEA software. The Nom. $p < 0.05$ was chosen as the cutoff criterion (10). The c2.cp.kegg.v7.4.symbols.gmt was chosen as the reference file.

Evaluation of Tumor Microenvironment

CIBERSORT tool was used to quantify 22 types of immunocyte fractions based on TCGA RNA-sequencing data (11). ESTIMATE algorithm was used to calculate the immune score, stromal score, ESTIMATE score, and tumor purity based on the expression of immune and stromal cells in the tumor microenvironment (12). Infiltration of immune cells was estimated in several ways including TIMER, CIBERSORT, CIBERSORT-ABS, QUANTISEQ, MCPCOUNTER, XCELL, and EPIC. The activity of immune-related pathways was estimated with single-sample GSEA (ssGSEA) (13).

Immune Prognostic Signature Analysis

Immune prognostic signature (IPS) can be obtained in an unbiased manner using machine learning method based on four major gene categories (PD1, PD-L1, PD-L2, and CTLA4) that determine immunogenicity. The IPS was calculated using z-scores of representative genes associated with immunogenicity. The IPSs of patients with uterine corpus endometrial carcinoma (UCEC) were extracted from The Cancer Immunome Atlas (TCIA) (https://tcia.at/home) (14).

Somatic Mutation, Tumor Stemness, and Drug Sensitivity Analysis

The mutation data of endometrial carcinoma patients were obtained from TCGA (Data Category = copy number variation; "maf" file). The top 10 mutation genes were visualized by fall plots using the "maftools" packages in R software (15). In addition, the correlation between tumor mutational burden (TMB) and risk score was also assessed. As previously reported, one-class logistic regression (OCLR) was used to calculate the stemlike indices for each endometrial carcinoma sample (16). The response to chemotherapy and small-molecule drugs in UCEC patients was determined using a public database called Genomics of Drug Sensitivity in Cancer (GDSC; https://www.cancerrxgene.org). The half-maximal inhibitory concentration (IC50) was estimated, which represented the drug response (17). The NCI-60 database is currently the most widely used for cancer drug testing, which was accessed through the CellMiner interface (https://discover.nci.nih.gov/cellminer) (18). Pearson's correlation analysis was performed to explore the underlying drug sensitivity difference between the high- and low-risk groups.

Consensus Clustering Analysis

TCGA UCEC cohort was clustered into different groups according to the consensus expression of 10 ERGs with "Consensus Cluster Plus" in R (19). Then we used the K-M method and log-rank test to obtain the OS data between different clusters. A chi-square test was carried out to compare the distribution of age, histologic type, tumor status, stage, and grade between two clusters.

Quantitative Real-Time PCR

TRIzol reagent (Thermo Fisher Scientific, USA) was used to extract total RNA from 16 EC tissues and 16 normal tissues, and cDNA was reverse-transcribed by Revert Aid First Strand cDNA Synthesis kit (Thermo Fisher Scientific, USA). The qRT-PCR was conducted by SYBR-Green PCR kit (Takara, Tokyo, Japan), and the cycle threshold (CT) of 10 ERGs was recorded. The relative expression of the target gene was estimated using the $2^{-\Delta\Delta CT}$ method. The primer sequences are listed in **Table S2**.

Statistical Analysis

All the analyses were performed in the R software (version 4.1.0). Wilcoxon test was used to compare the continuous variables that were not normally distributed. A p-value of less than 0.05 was considered statistically significant.

RESULTS

Searching for Epithelial–Mesenchymal Transition-Related Genes in Endometrial Cancer

To screen out differently expressed ERGs in EC, we compared the mRNA expression profiles of 552 tumor samples and 23 normal samples from TCGA database. Out of 1,316 ERGs, 220 showed a significant difference, in which 122 were upregulated ($\log_2$(fold change) > 2), while 98 were downregulated ($\log_2$(fold change) < −2). The ERGs were displayed with the clustering heatmap and volcano plot (**Supplementary Figures 1A, B**). Gene Ontology (GO) function analysis was divided into three groups: BP group, cellular compartment (CC) group, and molecular function (MF) group. In the BP group, ERGs were mainly involved in the extracellular matrix organization, extracellular structure organization, and external encapsulating structure organization. ERGs in the CC group were mainly enriched in the collagen-containing extracellular matrix, external side of the plasma membrane, and secretory granule lumen. ERGs in the MF group were mainly involved in receptor-ligand activity, signaling receptor activator activity, and cytokine activity (**Supplementary Figure 1C**). The results of KEGG

pathway enrichment revealed that the ERGs were mainly concentrated in cytokine–cytokine receptor interaction, microRNAs in cancer, and transcriptional misregulation in cancer (**Supplementary Figure 1D**).

Identification of Hub Epithelial–Mesenchymal Transition-Related Genes and Development of a Prognostic Index

To investigate the prognostic value of 200 candidate genes associated with EMT, we randomly split the entire set (511 tumor samples) into the training set (n = 153) and the testing set (n = 358). There were no significant differences in clinical factors including age, histological type, grade, and stage between the training set and the testing set by chi-square test and Wilcoxon rank-sum test (**Table S1**). After univariate Cox regression was used to combine clinical information with transcriptional profiles, a total of 31 ERGs associated with survival were identified in the training set (**Table 1**). To generate a prognostic ERG signature model (risk score), multivariate Cox proportional hazards regression analysis was applied to evaluate the connection between ERGs and OS in the training set, and 10 ERGs were identified as the prognostic ERGs (**Table S3**). At last, the ERGs FBN1, HIC1, SFRP4, COL11A1, ONECUT2, HOXB9, DLX4, MSX1, TNF, and SIX1 were included in our prognosis model with the formula of "Risk score = 0.1019 * FBN1 − 0.2529 * HIC1 − 0.0076 * SFRP4 + 0.0544 * COL11A1 + 0.1850 * ONECUT2 + 0.0057 * HOXB9 + 0.1853 * DLX4 − 0.0009 * MSX1 + 0.0265 * TNF + 0.0392 * SIX1 in the training set. In the training set, the median risk score of the training set was the cutoff to divide samples into the high-risk group and low-risk group. To reflect the association between the risk score and prognosis of EC, we dotted the samples of different risk scores according to their survival time. The heatmap showed an expression level of 10 ERGs in the high-risk and low-risk groups (**Figure 1A**). More red dots in the high-risk group indicated that more patients died in less than 5 years, and the K-M analysis suggested that the survival outcome of the low-risk group was significantly better (**Figure 1D**). The ROC curve revealed that our predictive model exhibited good sensitivity and specificity in predicting EC patient OS (5 years, area under the curve (AUC) = 0.816; 3 years, AUC = 0.753; 1 year, AUC = 0.75) (**Figure 1G**). The PCA showed that the samples in the two groups were distributed in different directions (**Figure 1J**).

Validating the Epithelial–Mesenchymal Transition-Related Gene Signature Model in the Testing Set and the Entire Set

To validate the predictive value of the risk score, we performed a similar analysis in the testing set and entire set. In the testing set and entire set, EC samples were stratified into the high-risk and low-risk groups according to the median risk score of the training set. The heatmap showed ERG expression between the high-risk and low-risk groups in the testing set and entire set (**Figures 1B, C**). Survival time plot showed a higher possibility of early death in patients with a higher risk score, and the K-M plot proved that a high-risk score is associated with worse OS (**Figures 1E, F**). Besides, the AUC of the testing set was 0.723 at 1-year survival, 0.742 at 3-year survival, and 0.644 at 5-year survival; the AUC of the entire set was 0.742 at 1-year survival, 0.752 at 3-year survival, and 0.768 at 5-year survival (**Figures 1H, I**). PCA displayed discrete directions of distribution in subgroups (**Figures 1K, L**). All of the above studies demonstrated good performance of our risk score model in the prognosis of EC.

As to the expression and predictive value of each ERG in the risk score formula, we first analyzed the gene expression level in tumor and in normal samples. FBN1, HIC1, and SFRP4 were lower in the tumor than normal tissues; the expressions of other ERGs were the opposite (**Supplementary Figure 2A**). The K-M analysis according to the optimal cutoff expression value of each ERG and the results concluded that 8 ERGs were related to survival possibility (**Supplementary Figure 2B**). Spearman's correlation analysis showed an interaction among 10 ERGs, and the connection between HIC1 and SFRP4 stood out (**Supplementary Figure 2C**). We further validated the expression level of 10 ERGs using qRT-PCR in clinical sample tissues (**Supplementary Figure 2D**). The results revealed that the mRNA expression levels of DLX4, FBN1, HIC1, HOXB9, ONECUT2, and SIX1 were significantly different between tumor samples and normal tissues, which were consistent with the results from TCGA. However, there was no difference in COL11A1 and TNF expression in clinical sample tissues. In addition, the expression of NSX was significantly lower in EC tissues, which was contrary to the prediction.

Constructing an Epithelial–Mesenchymal Transition-Related Gene-Featured Predictive Nomogram for Endometrial Cancer

Furthermore, we evaluated the prognostic impact of the risk signature in EC patients with different clinicopathological features in the entire set. Clinical factors including age, histological type, grade, and stage are related to the survival outcome of patients. As shown in **Figure 2A**, risk scores increase with age and disease progression (grade, histological type, and stage). In addition, the risk score reached satisfactory prognostic discrimination in patients with age (**Figure 2B**), grade (**Figure 2C**), histological type (**Figure 2D**), and stage (**Figure 2E**). In aggregate, the above results reveal that the risk model is a promising prognostic classifier for EC patients.

Univariate and multivariate Cox regression analyses were employed to evaluate whether the ERG signature was an independent prognostic indicator for EC patients. The univariate Cox regression analysis proved that risk score, stage, and histological type were independent factors affecting OS in three sets. However, the multivariate Cox regression analysis of the three sets demonstrated only that the signature-based risk score was remarkably correlated with OS (**Table 2**).

Based on the ERG-featured risk score and clinical factors, we constructed a nomogram, taking risk score, stage, and histological type into account, to predict the outcome of EC patients (**Figure 3A**). According to the point of three factors, we could calculate the total points so as to predict the 1-/3-/5-year

TABLE 1 | Univariate Cox regression analysis of 31 EMT-related genes in EC in the training set.

Genes	HR	Low 95% CI	Up 95% CI	*p*-Value
CTHRC1	1.006	1.001	1.011	0.010
FBN1	1.092	1.022	1.167	0.009
HIC1	0.700	0.511	0.960	0.027
GRIN1	0.519	0.274	0.984	0.045
SFRP4	0.987	0.977	0.998	0.022
COL11A1	1.084	1.043	1.127	<0.001
SOX17	0.995	0.991	0.998	0.005
SZH2	1.071	1.014	1.131	0.013
AURKA	1.053	1.014	1.093	0.007
POSTN	1.017	1.001	1.033	0.042
SPDEF	0.993	0.989	0.998	0.002
IL6	1.016	1.005	1.028	0.006
FOXA2	0.981	0.963	0.999	0.039
ONECUT2	1.253	1.049	1.497	0.013
HOXB9	1.008	1.002	1.013	0.005
APLP1	1.013	1.002	1.025	0.027
DLX4	1.239	1.134	1.354	<0.001
BIRC5	1.022	1.005	1.039	0.012
NTRK3	3.122	1.002	9.732	0.050
FBN2	1.013	1.001	1.026	0.028
CPEB1	1.806	1.066	3.059	0.028
HMGB3	1.018	1.004	1.033	0.012
MSX1	0.998	0.997	0.999	0.002
TIMP2	1.013	1.005	1.021	0.001
PCSK1	1.054	1.023	1.085	<0.001
MMP1	1.016	1.007	1.091	<0.001
TNF	1.033	1.013	1.054	0.001
DLX2	1.048	1.007	1.091	0.023
VCAM1	1.085	1.006	1.171	0.034
TPM1	1.029	1.002	1.058	0.036
SIX1	1.060	1.024	1.098	<0.001

EMT, epithelial–mesenchymal transition; EC, endometrial cancer.

survival possibility of a certain patient. Higher total points mean poorer outcomes. The multi-ROC curves proved that synthesizing clinical factors and risk scores would be better than a single factor (**Figure 3B**). The correlation of ERG expression and risk score with clinical factors are exhibited in **Table S4**. The calibration plots demonstrate the concordance of our nomogram result with the actual circumstances (**Figure 3C**). In order to further prove the predictive performance of the ROC curve for ERGs in this model, we compare three recently published articles on the signatures of the prognostic model in EC (20–22). Based on the same TCGA patient cohort, we found that in this model, the AUC of OS for our signatures is 0.742, which is significantly higher than that of other existing EMT-related signatures (**Figure 3D**).

Exploring Biological Functions of Epithelial–Mesenchymal Transition-Related Genes

To further investigate the molecular mechanism of these ERGs, we analyzed the expression profile of transcription factors (TFs) between EC and normal endometrium and screened out 27 differentially expressed TFs (**Table S5**), which are shown with the clustering heatmap and the volcano plot (**Supplementary Figures 3A, B**). A regulatory network was also constructed by ERGs with relevant TFs (**Supplementary Figure 3C**). Second, we used GSEA to discover significant pathways of ERGs. The top 5 KEGG pathways enriched in the high-risk group (cell cycle, DNA replication, homologous recombination, EC, and pathways in cancer) were associated with tumorigenesis; those of the low-risk group (asthma, autoimmune thyroid disease, cytokine–cytokine receptor interaction, graft-versus-host disease, and intestinal immune network for IgA production) were immune-related (**Supplementary Figure 3D**). The results indicated that low-risk scores were associated with immune signaling pathways.

Evaluating Immune Status in Groups Stratified by Risk

Tumor immune-related cells were compared in different risk groups, and ssGSEA showed more immune activities in the low-risk group. The results exhibited that the abundances of activated DCs (aDCs) were significantly decreased in the low-risk group, while in the high-risk group, B cells, CD8+ T cells, DCs, interdigitating DCs (iDCs), mast cells, neutrophils, natural killer (NK) cells, plasmacytoid DCs (pDCs), T helper cells, Tfh, Th1 cells, TIL, and regulatory T cells (Tregs) were markedly decreased (**Figure 4A**). Comparisons of 13 immune-related functions in the high-risk and low-risk groups confirmed the difference of antigen-presenting cell (APC) co-inhibition, CC chemokine receptor (CCR), checkpoint, cytolytic activity, human leukocyte antigen (HLA), inflammation promoting, T-cell co-

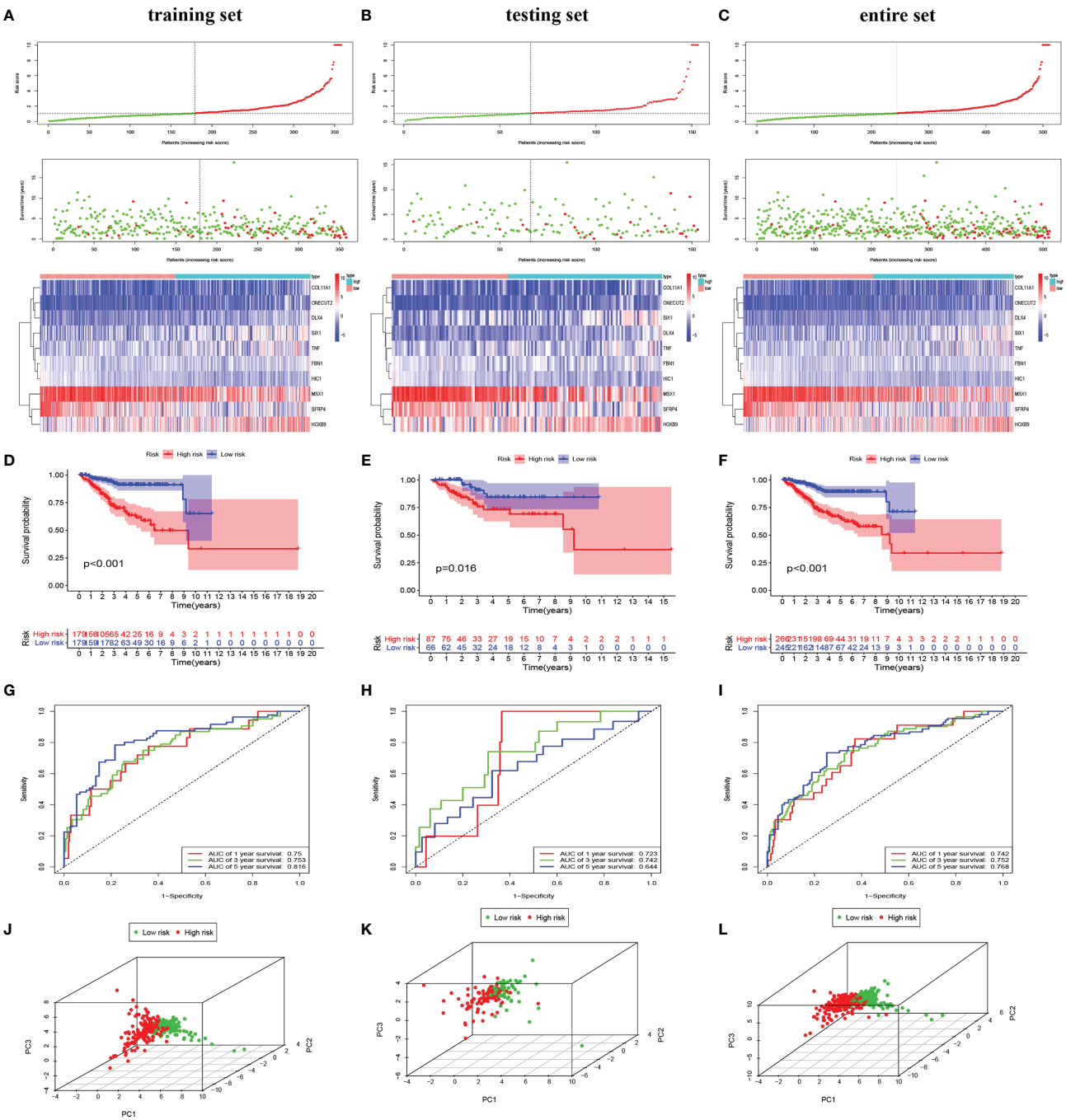


FIGURE 1 | Identification and validation of the EMT-related genes signature in the training, testing, and entire sets. The risk curve and scatter plot of each sample reordered by risk score and the heatmap showed the expression profiles of 10 ERGs in the low-risk group and high-risk group in the training set **(A)**, testing set **(B)**, and entire set **(C)**. Each square represents a clinical sample, and its color is associated with the gene expression. The higher the gene expression, the darker the color (red represents upregulated genes, and blue represents downregulated genes). Kaplan–Meier survival curves and area under the curve (AUC) value of the prognostic factors of 10 ERGs in the training set **(D, G)**, testing set **(E, H)**, and entire set **(F, I)**. **(G)** PCA reveals the difference between the high-risk and low-risk groups in the training set **(J)**, testing set **(K)**, and entire set **(L)**. EMT, epithelial–mesenchymal transition; ERG, EMT-related gene; PCA, principal component analysis.

inhibition, T-cell co-stimulation, type I IFN response, and type II IFN response (**Figure 4B**). We further investigated the expression of key immunity genes, HLA genes, which were mostly higher in the low-risk group (**Figure 4C**). In addition, we calculated ESTIMATE SCORE and found that the low-risk group had a higher ESTIMATE score, immune score, and stromal score (**Figure 4D**). The correlation analysis revealed that risk score was significantly negatively associated with

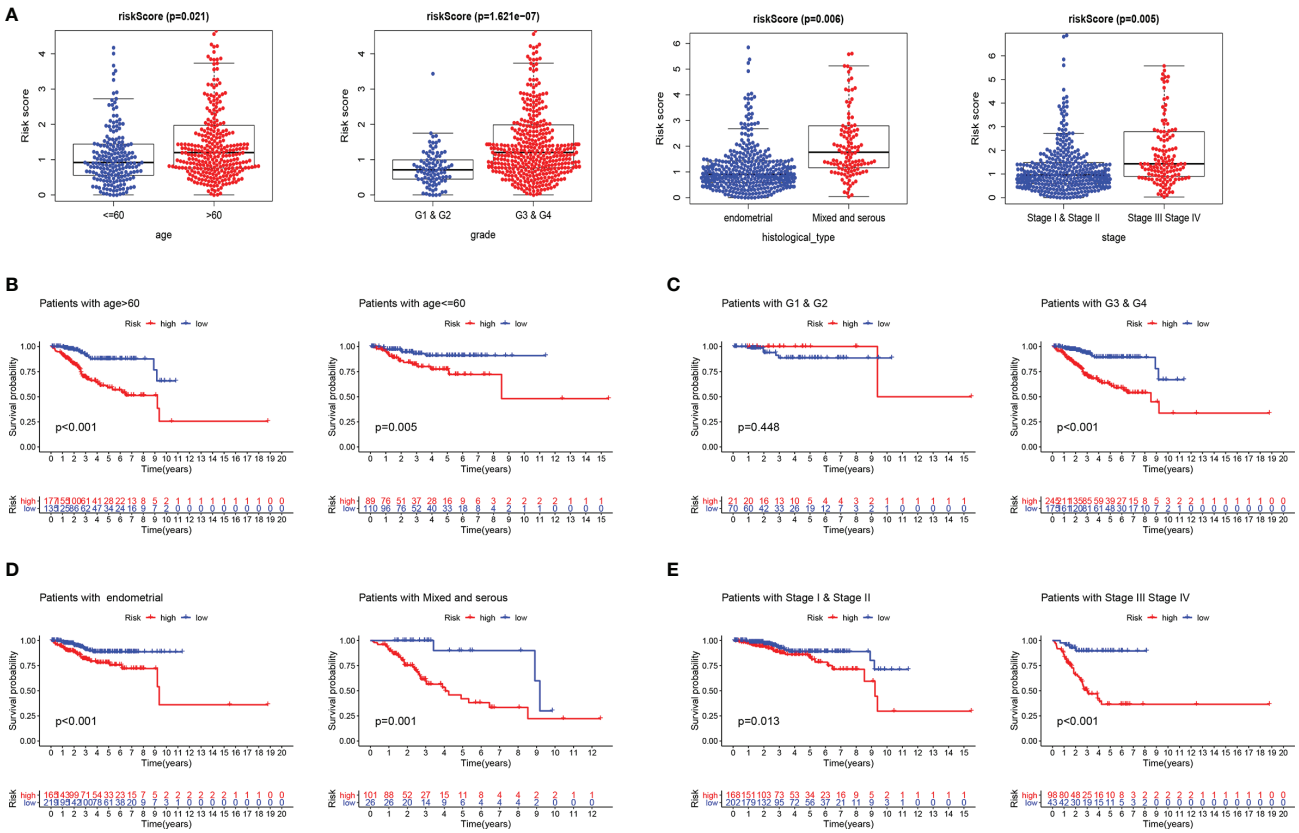


FIGURE 2 | Subgroup analysis of the prognostic value of risk score in EC patients. **(A)** Boxplots of the risk score in EC stratified by age, grade, histological_type, and stage. Prognostic value of risk score in patients with different ages **(B)**, different grades **(C)**, different histological_types **(D)**, and different stages **(E)**. EC, endometrial cancer.

ESTIMATE score, immune score, and stromal score. RNA stemness score (RNAss) and DNA stemness score (DNAss) were performed to measure tumor stemness based on mRNA expression and DNA methylation pattern, respectively. The results indicated that the risk score was not significantly associated with DNAss, but significantly positively correlated with RNAss (**Figure 4E**). We further investigated the association between the expression of 10 ERGs and the tumor-infiltrating immune cells (TIICs) in EC using the TIMER database (**Figure 4F**). To explore the relationship between risk score and immune component, we identified the correlation between risk score and immune infiltration. There are six different types of immune infiltrates in human tumors, corresponding to tumor promotion and tumor suppression, namely, C1(wound healing), C2 (INF-g dominant), C3 (inflammatory), and C4 (lymphocyte depleted) (23). The results showed that a higher risk score was significantly associated with C1, while a lower risk score was significantly associated with C4 (**Figure 4G**).

TIICs contribute to building the microenvironment of tumors. We used TIMER, CIBERSORT, CIBERSORT-ABS, QUANTISEQ, MCPCOUNTER, XCELL, and EPIC to estimate infiltration of 21 types of immune cells in the high-risk and low-risk groups (**Figure 5A**). CD8 T cells, Tregs, and plasma cells have a bigger fraction in the low-risk group; M0/M1/M2 macrophages and T follicular helper cells have a larger proportion in the high-risk group (**Figures 5B, C**). The correlation of risk score and TIICs is shown in **Figure 5D**, which demonstrated that aDCs, macrophages M0, macrophages M1, macrophages M2, mast cells activated, NK cells resting, and T cells follicular helper were positively correlated with a risk score, while risk score was negatively associated with mast cell resting, monocytes, plasma cells, T cells CD4 memory resting, T cells CD8, and Tregs.

The Prognostic Value of Immune Checkpoint Modulators and Response to Immune Checkpoint Inhibitor

Immune checkpoint modulators play a critical role in immune cells' battle with cancer cells. We analyzed the distribution of 17 pivotal modulators in the high- and low-risk groups in the entire set. As a result, 9 of them (CD27, CTLA4, PD-L2, B7-H3, B7-H4, PD-1, CD40, PD-L1, and CD270) have a statistically significant difference in two different risk groups (**Figure 6A**). We focused on CTLA4 and PD1, and the box plot and correlation plot of the two molecules with risk scores demonstrated that patients with low risk have higher CTLA4 and PD1 expression

TABLE 2 | Univariate and multivariable Cox regression analysis of the EMT-related genes and overall survival in different patient sets.

Variable	Univariable model			Multivariable model		
	HR	95% CI	*p*-Value	HR	95% CI	*p*-Value
Training set (n = 153)						
Age	2.024	1.115–3.675	0.021	1.698	0.901–3.199	0.101
histological_type	2.888	1.754–4.755	3.05E–05	1.625	0.929–2.841	0.089
Grade	2.939	1.176–7.342	0.021	1.248	0.461–3.381	0.663
Stage	4.446	2.680–7.374	7.53E–09	3.361	1.914–5.902	2.43E–05
riskScore	1.105	1.075–1.136	1.53E–12	1.084	1.054–1.116	3.34E–08
Testing set (n = 358)						
Age	1.397	0.633–3.086	0.408			
histological_type	3.501	1.609–7.618	0.002	2.903	1.264–6.670	0.012
Grade	5.407	0.732–39.947	0.098			
Stage	3.413	1.575–7.398	0.002	2.251	0.974–5.202	0.058
riskScore	1.036	1.012–1.061	0.003	1.033	1.006–1.061	0.016
Entire set (n = 511)						
Age	1.778	1.112–2.843	0.016	1.498	0.915–2.454	0.108
histological_type	3.044	2.003–4.624	1.84E–07	1.940	1.219–3.087	0.005
Grade	3.363	1.467–7.710	0.004	1.479	0.609–3.592	0.387
Stage	4.116	2.700–6.275	4.82E–11	3.014	1.892–4.799	3.38E–06
riskScore	1.048	1.033–1.062	6.81E–11	1.038	1.021–1.054	5.15E–06

EMT, epithelial–mesenchymal transition.

(**Figures 6B, C**). These two molecules might be protective factors in EC.

Then we used Immunophenoscore to estimate the response to immune checkpoint inhibitors (CTLA4-blocker, CTLA4-PD1-PDL1-PDL2-blocker, and PD1-PDL1-PDL2-blocker) in subgroups stratified by risk score. As is shown in **Figure 6D**, the low-risk group had higher IPS, indicating higher immunogenicity of tumors.

Tumorigenesis Biological Processes and Epithelial–Mesenchymal Transition-Related Gene-Based Risk Score

Tumorigenesis pathways were enriched in the high-risk group. Therefore, we looked into TMB, N^6-methyladenosine (m^6A) RNA modification, microsatellite instability (MSI), and CSC characteristics. Gene mutations lead to the generation and development of tumors. TMB corresponds with the objective response rate for anti-PD-1 therapy across multiple cancer types (24). The oncoplot displays that in the high-risk group, genes of the top 3 mutation rate were tp53, PTEN, and PIK3CA; in the low-risk group, the top 3 mutated genes were PTEN, ARID1A, and PIK3CA. What is more, the mutation frequency of PTEN and PIK3CA was higher in the low-risk group than in the high-risk group (**Figures 7A, B**). The K-M plot shows the relationship of higher TMB and better OS (**Figure 7C**), which was consistent with a better response to immune checkpoint inhibitors in the low-risk group mentioned above. Using both TMB and ERG risk scores could better predict the survival time of EC patients (**Figure 7D**). The was no significant correlation between risk score and TMB (**Figure 7E**).

m^6A RNA modification regulates the generation and maintenance of CSCs, which drives the progression of cancer (25). We studied the expression level of the main genes of m6A writers, erasers, and readers in the EC cohort. The expression of HNRNPC, YTHDF1, YTHDF2, RBM15, and WTAP was significantly higher in the high-risk group (**Figure 7F**). Approximately 30% of primary ECs are MSI-high/hypermutated (MSI-H), and 13% to 30% of recurrent ECs are MSI-H or mismatch repair deficient (dMMR) (26). MLH1, MSH2, MSH6, and PMS2 were lost more frequently in the high-risk group (**Figure 7G**). Two stemness indices, mRNAsi and EREG-mRNAsi, were utilized to investigate the expression of stem cell-related genes in EC. In the high-risk group, both indices were higher. Oncogenic dedifferentiation marked by CSC characteristics might be another predictive marker of EC (**Figure 7H**).

Response to Chemotherapeutic Drugs and Epithelial–Mesenchymal Transition-Related Gene-Based Risk Score

The sensitivity of four kinds of chemotherapeutic drugs including cisplatin, doxorubicin, etoposide, and paclitaxel was analyzed (**Figure 8A**). The low-risk group had a higher IC50 of etoposide, cisplatin, and doxorubicin than the high-risk group, which demonstrated that patients with higher risk scores were more sensitive to those chemotherapeutic drugs. In addition, the expression of 10 ERGs in NCI-60 cell lines was investigated, and the relationship between their expression levels and drug sensitivity was revealed at the same time. The results showed that 6 ERGs were correlative to some chemotherapy drug sensitivity ($p < 0.01$, **Figure 8B**).

Consensus Clustering Analysis of Epithelial–Mesenchymal Transition-Related Genes

By consensus unsupervised clustering of 511 samples from EC patients, we found that 2 clusters had lower values of ambiguously clustered pairs (PAC), which reflected the near-perfect stability of the samples under the correct K value distribution (**Supplementary Figures 4A, B**). We classified the

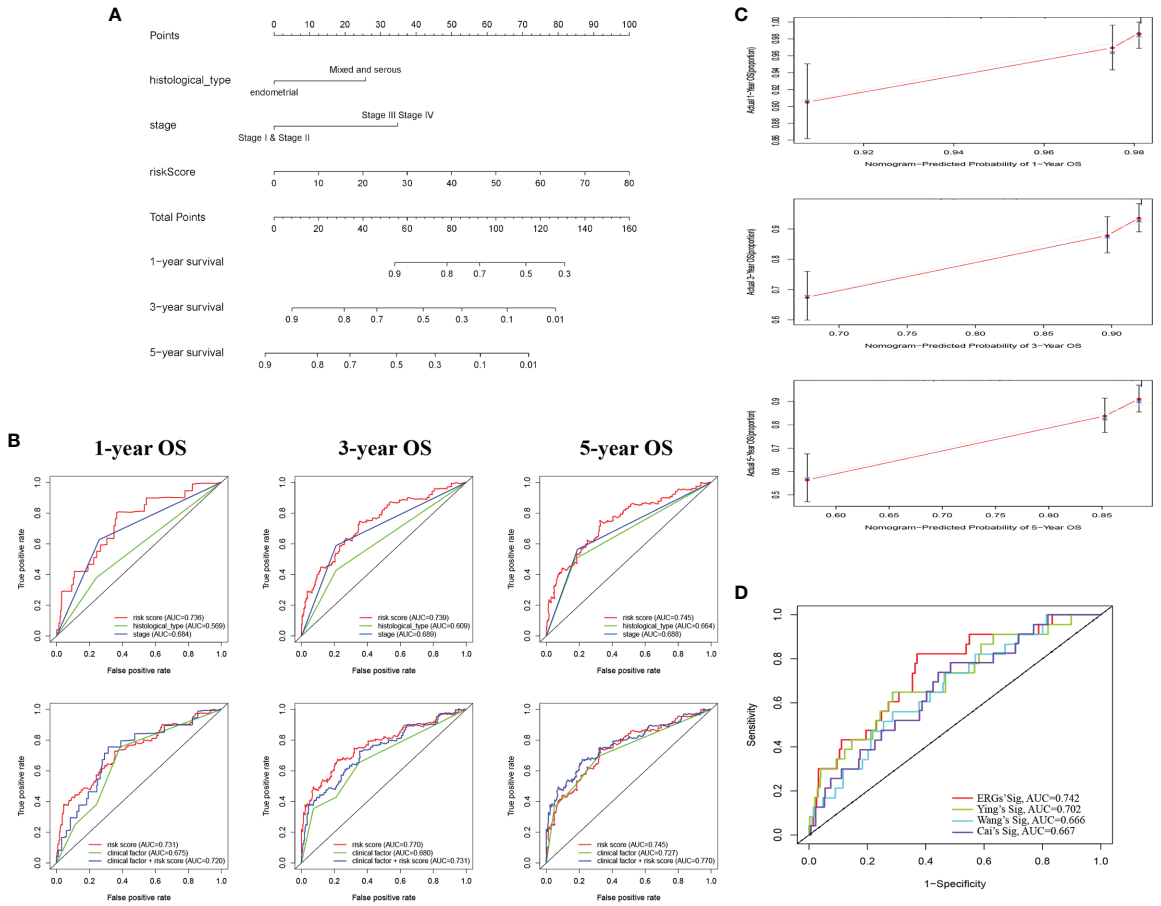


FIGURE 3 | Construction of a nomogram for survival prediction of EC patients. **(A)** The nomogram combining signature with clinicopathological features (histological_type, clinical stage, and risk score). **(B)** ROC curves of 1-, 3-, and 5-year overall survival (OS), indicating that the ERG-based signatures had better predictive ability than other clinical factors. Furthermore, when combined risk score with clinical factors for analysis, the AUC values of 5-year OS increased further, which suggested that the nomograms had superior predictive capacity for the long-term prognosis of EC. **(C)** Calibration plot showing that nomogram-predicted survival probabilities corresponded closely to the actually observed proportions. **(D)** The AUC for ERGs and the existing EMT-related signatures. EC, endometrial cancer; ROC, receiver operating characteristic; EMT, epithelial–mesenchymal transition; ERG, EMT-related gene; AUC, area under the curve.

samples into two clusters (k = 2) based on ERG expression (**Supplementary Figures 4C, D**). The clinical characters distributed in two clusters are shown in **Supplementary Figures 4E–H**. The heatmap demonstrates the distinction of ERG expression between two clusters (**Supplementary Figure 4I**). Cluster2 had obviously more MSX1 expression and longer OS (**Supplementary Figure 4J**). The analysis also implied that the genes involved in the signature could have great possibilities to become biomarkers for EC and proved that the signature might have a vital role in the clinical contributions.

DISCUSSION

As the incidence rate of EC increases and the type of cases becomes complicated, TCGA reported a classification for EC—POLE-mutated, MSI-H, copy number-low, and copy number-high (27)—inspiring us that genomic characters can be a guide for prognoses and treatments. However, some patients still cannot benefit from therapy according to the current classification. Better surveillance and therapeutic regimens are an urgent need. Therefore, we developed an ERG-related signature model as a novel classification tool for EC patients.

EMT has been noticed as a characteristic of tumor cells acquiring both epithelial and mesenchymal features, which is associated with progress and metastasis. In this study, we collected clinical data and expression files of ERGs from TCGA database. From 1,316 ERGs, we found 220 genes expressed differently between tumor and normal samples and finally identified 10 genes (FBN1, HIC1, SFRP4, COL11A1, ONECUT2, HOXB9, DLX4, MSX1, TNF, and SIX1) associated with the prognosis of EC to establish a predicting model. The AUC value based on the training set and the entire set was all above 0.7. Next, taking traditional clinical categories into consideration, we generated an ERG-based predictive nomogram. The nomogram can offer a total score for a specific

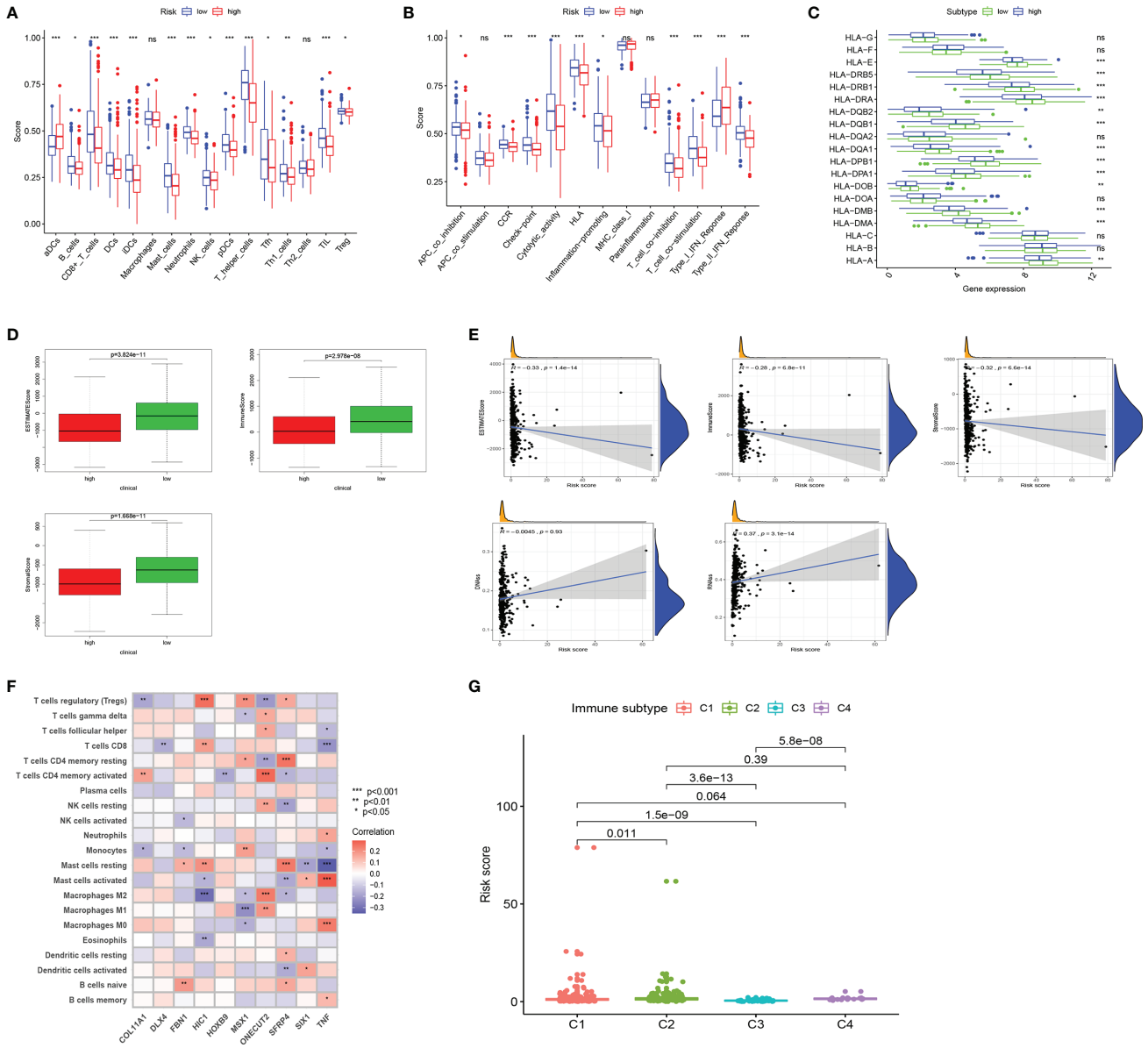


FIGURE 4 | Landscape of immune cell infiltration. **(A)** Comparison of 16 tumor immune-related cells in the high-risk and low-risk groups. **(B)** Comparison of 13 immune-related functions in the high-risk and low-risk groups. **(C)** The distribution of HLA-related genes of the high-risk and low-risk groups. **(D)** Comparison of ESTIMATES score, Immune score, and Stromal score in high-risk and low-risk groups. **(E)** The relationship between risk score and ESTIMATES score, Immune score, Stromal score, RNAss, and DNAss. **(F)** The correlation between 10 ERGs and immune cells infiltration. **(G)** Comparison of the risk score in different immune infiltration subtypes. EC, endometrial cancer; ROC, receiver operating characteristic; EMT, epithelial–mesenchymal transition; ERG, EMT-related gene; AUC, area under the curve; HLA, human leukocyte antigen. Adjusted p-values were shown as ns, not significant; *p < 0.05; **p < 0.01; ***p < 0.001.

patient, and the score can identify the predicting 1-/3-/5-year survival possibility.

Among the critical 10 genes, FBN1 encodes fibrillin-1, composed of microfibrils in the extracellular matrix. The mutation in FBN1 was responsible for Marfan's syndrome and other disorders of connective tissues (28). In EC, FBN1 was identified as a substrate for FBXO2-mediated ubiquitin-dependent degradation. FBOX2 promotes EC proliferation by regulating the cell cycle and the autophagy signaling pathway, whose function would be blocked by the absence of FBN1 (29). HIC1 (Hypermethylated in Cancer1) is a tumor suppressor gene inactivated by epigenetic silence (30). HIC1 is found in a CpG island of chromosome 17p13.3 region, frequently hypermethylated in various types of tumors, and is associated with poorer survival (31). Its methylation density increases from normal tissues to precancerous lesions to cancer. Few papers mentioned the role of HIC1 in EC, except one that found that HIC1 expression significantly reduced in RT-PCR analysis in rat EC cells

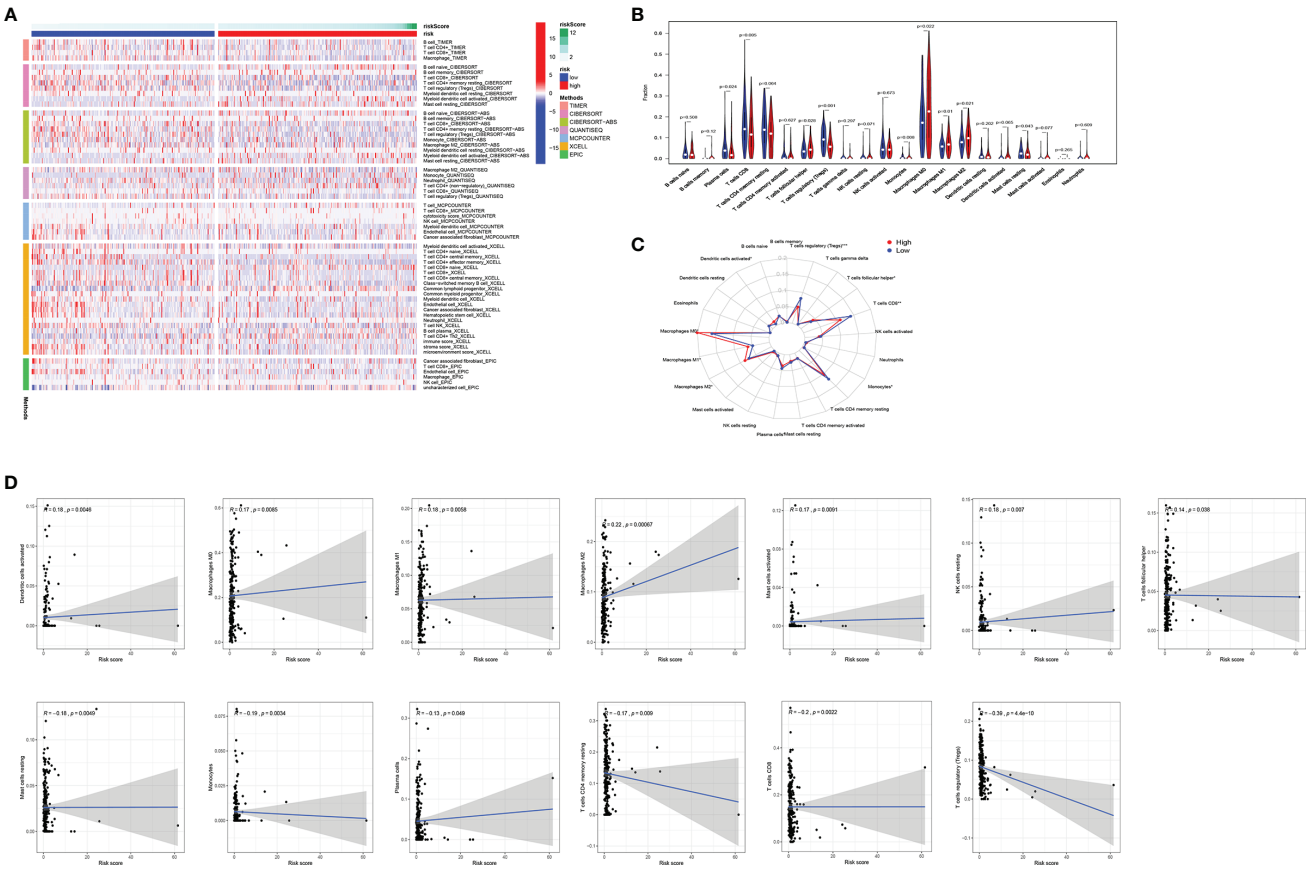


FIGURE 5 | Comparison of immune signature between the high-risk and low-risk groups of EC patients. **(A)** The infiltration of 21 types of immune cells in high-risk and low-risk groups was estimated by TIMER, CIBERSORT, CIBERSORT-ABS, QUANTISEQ, MCPCOUNTER, XCELL, and EPIC database. **(B, C)** Comparison of tumor-infiltrating immune cells between different risk groups. **(D)** The correlation of risk score and tumor-infiltrating immune cells. EC, endometrial cancer.

compared with non-malignant samples, but could not see the same decrease in protein level (32). Our study discovered the association of HIC1 expression level with the prognosis of EC. SFRP4 (secreted frizzled related protein 4) is an extracellular antagonist of the Wnt/β-catenin pathway. Its loss was noticed in aggressive ovarian cancer types and recombinant SFRP4 (rSFRP4) treatment of serous ovarian cancer cells that result in the inactivation of the Wnt/β-catenin pathway, mesenchymal-to-epithelial transition, and decreasing ability to migrate (33). SFRP4 is more frequently downregulated in MSI type of EC compared with microsatellite stable ones (MSS) (34). COL11A1 encodes one of the two alpha chains of type XI collagen. In ovarian cancer, COL11A1 is expressed in the intra/peri-tumoral stromal cells and rare foci of tumor epithelial cells, indicating COL11A1 as a marker of carcinoma-associated fibroblasts and possibly cancer cells undergoing EMT (35). ONECUT2 encodes a member of the one cut family of TFs. It is involved in EMT, resulting in cell growth and invasion in gastric (36) and colorectal and ovarian cancers (37, 38). HOXB9, a TF induces angiogenesis, increased cell motility, and acquisition of mesenchymal characters, thus contributing to lung metastasis of breast cancer (39). HOXB9 induces EMT through TGF-β1-Smad signaling in HCC, promoting migration and invasion of HCC cells (40). DLX4, widely expressed in different types of cancer but absent in most normal adult tissues, induces EMT through directly binding to regulatory regions of TWIST gene (41). What is more, DLX4-mediated EMT in trophoblasts may be a possible pathophysiological mechanism for preeclampsia (42). MSX1 is significantly upregulated in EC, which plays a crucial role in progestin resistance. Knockdown of MSX1 inhibited EMT and improved the therapeutic effect of progesterone (43). TNF-α, a pro-inflammatory cytokine, enhances TGF-β-induced EMT by activating the Smad2/3 signal (44). A similar mechanism is found for SIX1 in papillary thyroid carcinoma (45). Further, SIX1 increases CSC recruit macrophages and stimulate angiogenesis, contributing to the progression of cancer. All the above elucidate the function of these 10 genes in EMT. Our study propels knowledge of the relationship of these genes with the prognosis of EC.

Then, through GSEA, we investigated biological functions of the 10 ERG and we found that our signature was significantly associated with the immuno-microenvironment of the EC. According to the results that immune-related pathways were enriched in the low-risk group, we analyzed immune cell infiltration in two groups. In addition, CD8+ T cells, Tregs, and plasma cells were distributed more in the low-risk group,

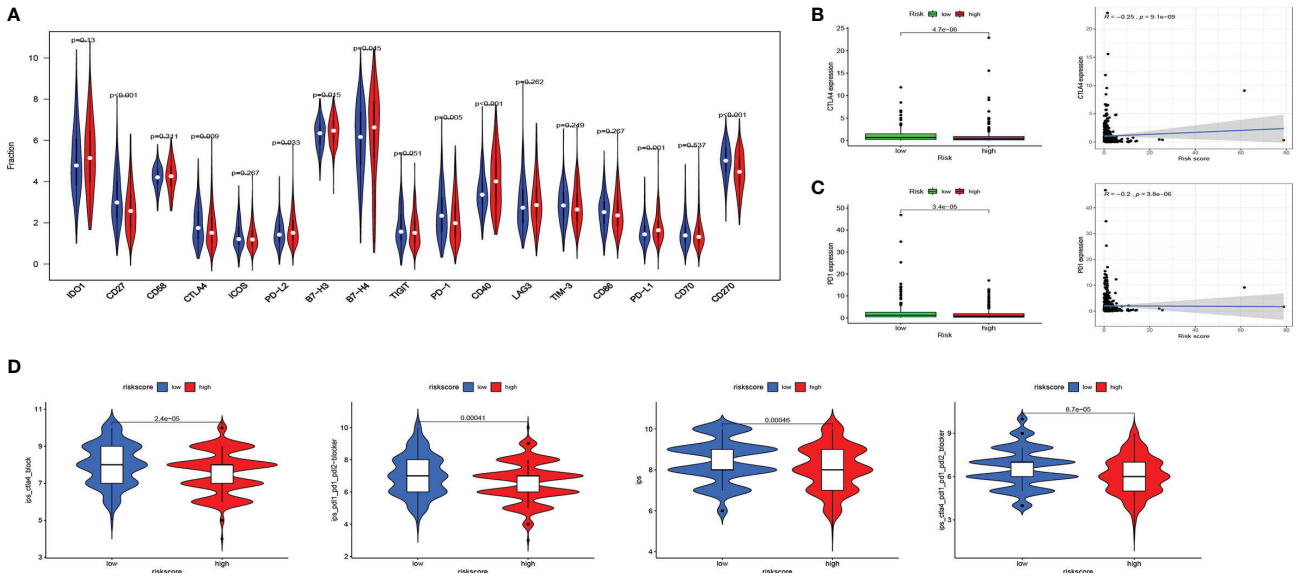


FIGURE 6 | Associations of immune cell infiltration, immune checkpoints expression, and IPS and the EMT-related risk signature. **(A)** The distribution of immunomodulators in high-risk and low-risk groups. **(B, C)** The expression of 2 immune checkpoint molecules (CTLA4 and PD1) in high-risk and low-risk groups and Pearson's correlation coefficient calculated between risk score and 2 immune checkpoint molecules. **(D)** The association between IPS and the risk score in EC patients. IPS, immune prognostic signature; EMT, epithelial–mesenchymal transition; EC, endometrial cancer.

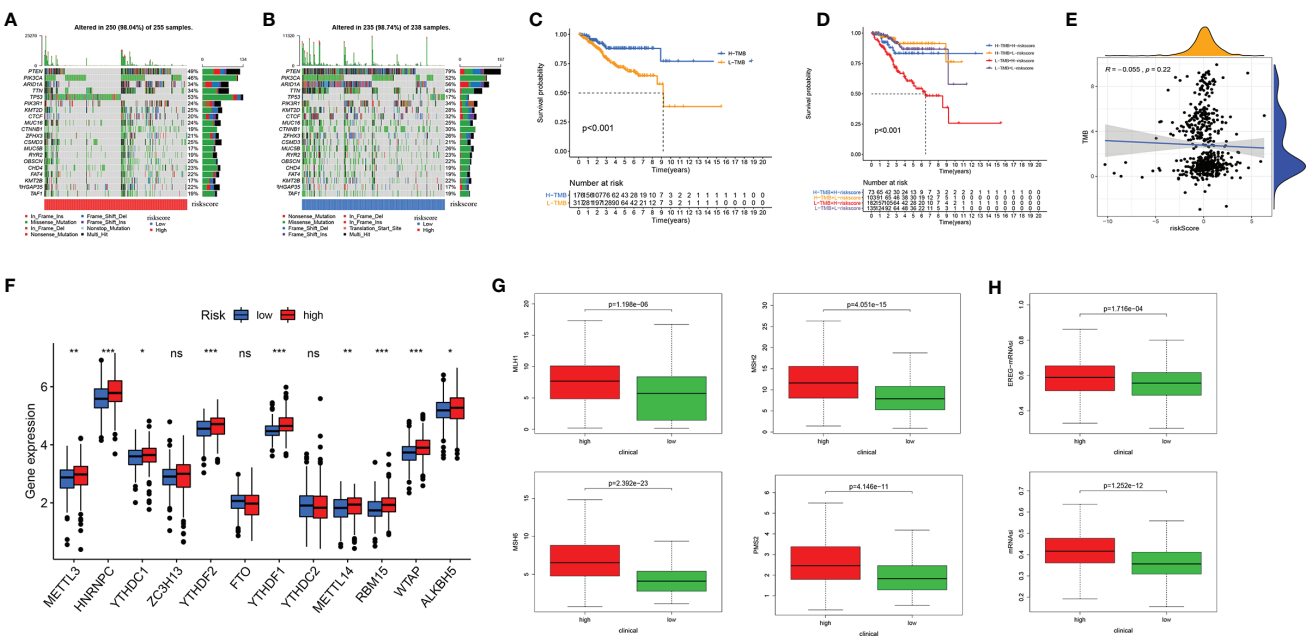


FIGURE 7 | Tumor mutational burden (TMB), somatic mutation, N^6-methyladenosine, and microsatellite instability (MSI) analysis. Oncoplot displaying the somatic landscape of EC with high-risk group **(A)** and low-risk group **(B)**; the genes are sorted according to their mutation frequency. **(C)** Survival analysis between high-TMB and low-TMB EC patients. **(D)** Two-factor survival analyses of risk score and TMB level. **(E)** Relationship between TMB and EMT-related risk score. **(F)** The expression level of main genes of m^6A writers, erasers, and readers (HNRNPC, YTHDF1, YTHDF2, RBM15, and WTAP) in high-risk and low-risk groups. **(G)** The expression of MLH1, MSH2, MSH6, and PMS2 in high-risk and low-risk groups. **(H)** mRNA stemness indices between high-risk and low-risk groups. EC, endometrial cancer. Adjusted p-values were shown as ns, not significant; *p < 0.05; **p < 0.01; ***p < 0.001.

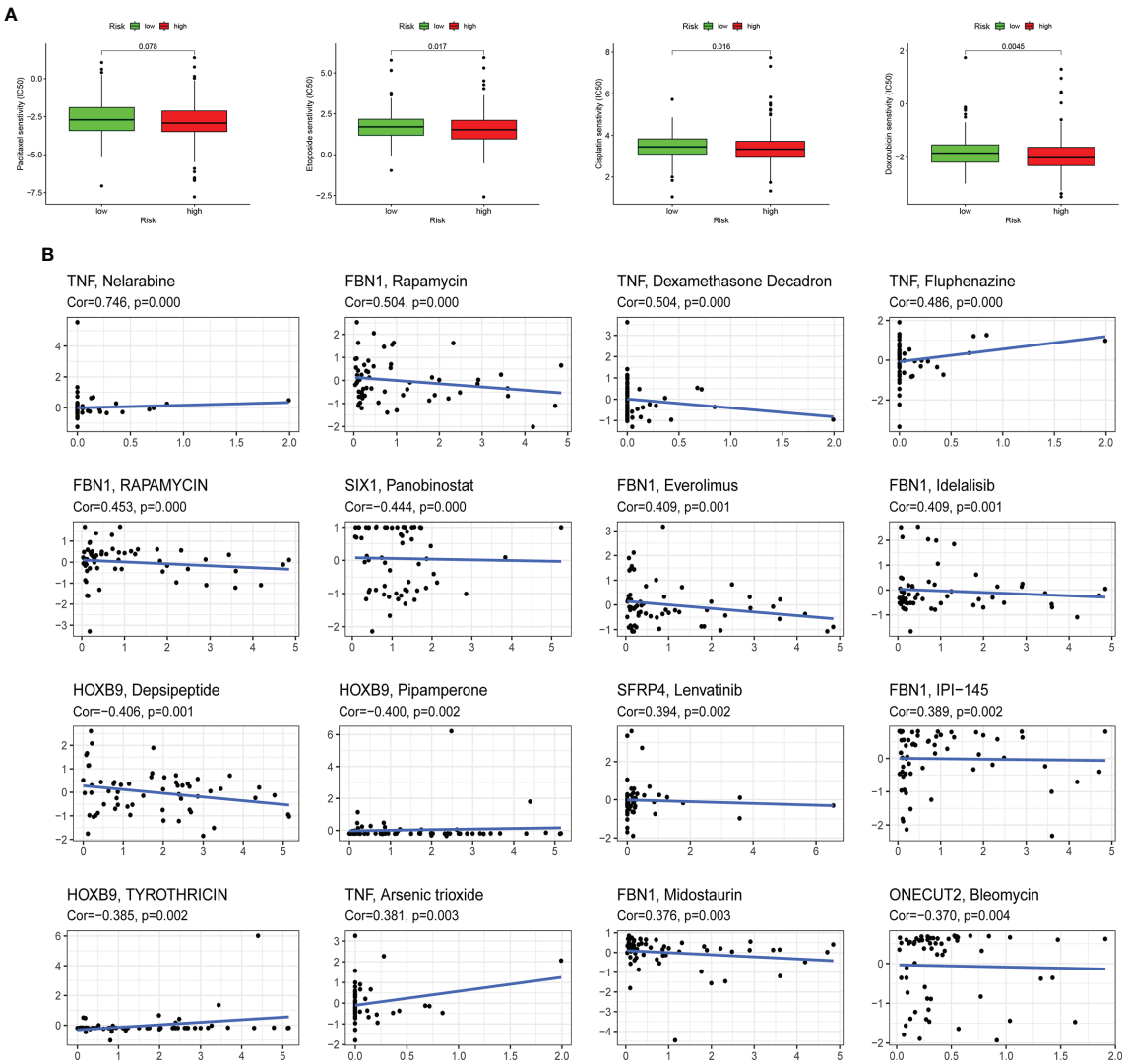


FIGURE 8 | Association between the risk score, ERGs, and chemosensitivity in EC. **(A)** The box plots of the estimated IC50 for paclitaxel, etoposide, cisplatin, and doxorubicin in high-risk and low-risk groups. **(B)** Scatter plot of the relationship between the expression of ERGs and drug sensitivity. EMT, epithelial–mesenchymal transition; ERG, EMT-related gene; EC, endometrial cancer.

while macrophages and T follicular helper cells were distributed more in the high-risk group. Previous studies demonstrated that CD8+ count could be an independent prognostic factor of EC (46, 47). In our signature, we found that CD8+ T cells were lower in the high-risk group, leading to a poor prognosis. dMMR was observed to be related to positive PD-L1 expression and high CD8+ cell count (48, 49), in which the subgroup might benefit from immunotherapy. From our study, we found higher CTLA4 and PD1 expressed in the low-risk group and higher IPS, indicating better response to immune checkpoint inhibitors. dMMR was observed more frequently in the high-risk group. Apart from immunotherapy, we also evaluated the effect of chemotherapeutic drugs, including cisplatin, doxorubicin, etoposide, and paclitaxel. Similarly, patients in the low-risk group were more sensitive to chemotherapy. In recent years, in-depth studies have been conducted on ERGs for different immune states of tumors, and a large number of diagnostic and prognostic assessment methods have been identified (20–22, 50). Compared with existing prognostic features, our new prognostic model has greater clinical application potential. Therefore, the signature we established may be helpful to classify patients into different risk groups and offer different recommendations about treatments.

Nowadays, complex predicting models consisting of more cancer-related genes and clinical characters may be a trend for comprehensive individualized diagnosis and treatment. We generated a nomogram taking 10 ERG and clinical features together to identify the 1-/3-/5-year survival possibility of EC patients. However, there are still some restrictions in our study. First, data were based on TCGA database, and validation was

performed inside the entire cohort. Second, the mechanism of how these ten genes regulated EMT in EC needs further study. Third, more clinical information about the accuracy of our signature in predicting drug response needs to be collected worldwide.

CONCLUSIONS

In summary, we developed a signature model based on 10 ERG for EC patients and verified its independent prognostic value. What is more, it might offer a reference for predicting individualized response to immune checkpoint inhibitors and chemotherapeutic drugs.

DATA AVAILABILITY STATEMENT

The datasets presented in this study can be found in online repositories. The names of the repository/repositories and accession number(s) can be found in the article/**Supplementary Material**.

ETHICS STATEMENT

The studies involving human participants were reviewed and approved by The Third People's Hospital of Nantong. The patients/participants provided their written informed consent to participate in this study.

AUTHOR CONTRIBUTIONS

HZ and YX conceived the study and participated in the study design, performance, and manuscript writing. JL, GC, FG, and SS conducted the bioinformatics analysis. All authors read and approved the final manuscript.

ACKNOWLEDGMENTS

We would like to thank the researchers and study participants for their contributions.

SUPPLEMENTARY MATERIAL

The Supplementary Material for this article can be found online at: https://www.frontiersin.org/articles/10.3389/fimmu.2021.805883/full#supplementary-material

Supplementary Figure 1 | Identification of EMT-related genes (ERGs) from endometrial cancer samples. Heatmap **(A)** and volcano plot **(B)** of ERGs between EC and normal endometrium. Each square represents a clinical sample, and its color is associated with the gene expression. The higher the gene expression, the darker the color. Red dots represent up-regulated ERGs, green dots represent down-regulated ERGs and black dots represented no ERGs. Results of Gene ontology analysis **(C)**, Kyoto Encyclopedia of Genes and Genomes pathways pathway enrichment analysis **(D)**.

Supplementary Figure 2 | The expression levels and prognostic value of ERGs. **(A)** Compared with the normal tissues, the expression levels of 10 ERGs in EC. **(B)** Kaplan-Meier survival curves of the high and low expression of ERGs in EC were compared based on the optimal cut-off expression value of each ERG. **(C)** The interaction between 10 ERGs was analyzed by the Spearman's correlation analysis. **(D)** Expression level of COL11A1, DLX4, PBN1, HIC1, HOXB9, MSX1, ONECUT2, SFRP4, SIX1 and TNF in clinical samples.

Supplementary Figure 3 | Identification of survival associated EMT-related genes (ERGs) and relevant transcription factors (TFs). **(A)** Heatmap and **(B)** volcano plot of differentially expressed TFs between EC and normal endometrium. Red dots represented up-regulated TFs, green dots represented down-regulated TFs and black dots represented no TFs. **(C)** Differentially expressed ERGs and regulatory network with relevant TFs. **(D)** Five representative KEGG pathways for the high-risk and low-risk group.

Supplementary Figure 4 | Consensus clustering analysis of ERGs. **(A)** cumulative distribution function (CDF) curve of K = 2–10. **(B)** The relative change in area under the CDF curve of K = 2–10. **(C)** Sample clustering heatmap. **(D)** Tracking plot of k in the consensus cluster of EMT-related genes. **(E–H)** The proportion of clinical characters (age, grade, histological type and stage) in two clusters. **(I)** The heatmap of ERG expression in two clusters. **(J)** Prognostic prediction in two clusters by Kaplan-Meier.

REFERENCES

1. Lu KH, Broaddus RR. Endometrial Cancer. *N Engl J Med* (2020) 383 (21):2053–64. doi: 10.1056/NEJMra1514010
2. Pastushenko I, Blanpain C. EMT Transition States During Tumor Progression and Metastasis. *Trends Cell Biol* (2019) 29(3):212–26. doi: 10.1016/j.tcb.2018.12.001
3. Tanaka Y, Terai Y, Kawaguchi H, Fujiwara S, Yoo S, Tsunetoh S, et al. Prognostic Impact of EMT (Epithelial-Mesenchymal-Transition)-Related Protein Expression in Endometrial Cancer. *Cancer Biol Ther* (2013) 14 (1):13–9. doi: 10.4161/cbt.22625
4. Yoriki K, Mori T, Kokabu T, Matsushima H, Umemura S, Tarumi Y, et al. Estrogen-Related Receptor Alpha Induces Epithelial-Mesenchymal Transition Through Cancer-Stromal Interactions in Endometrial Cancer. *Sci Rep* (2019) 9(1):6697. doi: 10.1038/s41598-019-43261-z
5. Liu Y, Zhao R, Chi S, Zhang W, Xiao C, Zhou X, et al. UBE2C Is Upregulated by Estrogen and Promotes Epithelial-Mesenchymal Transition *via* P53 in Endometrial Cancer. *Mol Cancer Res* (2020) 18(2):204–15. doi: 10.1158/1541-7786.MCR-19-0561
6. Dong P, Xiong Y, Yue J, Hanley SJB, Watari H. Tumor-Intrinsic PD-L1 Signaling in Cancer Initiation, Development and Treatment: Beyond Immune Evasion. *Front Oncol* (2018) 8:386. doi: 10.3389/fonc.2018.00386
7. Brooks RA, Fleming GF, Lastra RR, Lee NK, Moroney JW, Son CH, et al. Current Recommendations and Recent Progress in Endometrial Cancer. *CA Cancer J Clin* (2019) 69(4):258–79. doi: 10.3322/caac.21561
8. Zhang Z, Zheng S, Lin Y, Sun J, Ding N, Chen J, et al. Genomics and Prognosis Analysis of Epithelial-Mesenchymal Transition in Colorectal Cancer Patients. *BMC Cancer* (2020) 20(1):1135. doi: 10.1186/s12885-020-07615-5
9. Liu J, Zhou S, Li S, Jiang Y, Wan Y, Ma X, et al. Eleven Genes Associated With Progression and Prognosis of Endometrial Cancer (EC) Identified by Comprehensive Bioinformatics Analysis. *Cancer Cell Int* (2019) 19:136. doi: 10.1186/s12935-019-0859-1
10. Song P, Jiang B, Liu Z, Ding J, Liu S, Guan W. A Three-lncRNA Expression Signature Associated With the Prognosis of Gastric Cancer Patients. *Cancer Med* (2017) 6(6):1154–64. doi: 10.1002/cam4.1047
11. Wang Y, Ji C, Liu J, Wang Y, Song N, Cao P. A Model Based on Tumor-Infiltrating Immune Cells for Predicting the Relapse Rates of Patients With Testicular Germ Cell Tumors. *Int Immunopharmacol* (2020) 86:106710. doi: 10.1016/j.intimp.2020.106710
12. Yoshihara K, Shahmoradgoli M, Martínez E, Vegesna R, Kim H, Torres-Garcia W, et al. Inferring Tumour Purity and Stromal and Immune Cell Admixture From Expression Data. *Nat Commun* (2013) 4:2612. doi: 10.1038/ncomms3612

13. Mei J, Xing Y, Lv J, Gu D, Pan J, Zhang Y, et al. Construction of an Immune-Related Gene Signature for Prediction of Prognosis in Patients With Cervical Cancer. *Int Immunopharmacol* (2020) 88:106882. doi: 10.1016/j.intimp.2020.106882
14. Liu J, Ji C, Wang Y, Zhang C, Zhu H. Identification of Methylation-Driven Genes Prognosis Signature and Immune Microenvironment in Uterus Corpus Endometrial Cancer. *Cancer Cell Int* (2021) 21(1):365. doi: 10.1186/s12935-021-02038-z
15. Mayakonda A, Lin DC, Assenov Y, Plass C, Koeffler HP. Maftools: Efficient and Comprehensive Analysis of Somatic Variants in Cancer. *Genome Res* (2018) 28(11):1747–56. doi: 10.1101/gr.239244.118
16. Yi L, Huang P, Zou X, Guo L, Gu Y, Wen C, et al. Integrative Stemness Characteristics Associated With Prognosis and the Immune Microenvironment in Esophageal Cancer. *Pharmacol Res* (2020) 161:105144. doi: 10.1016/j.phrs.2020.105144
17. Liu J, Wang Y, Meng H, Yin Y, Zhu H, Ni T. Identification of the Prognostic Signature Associated With Tumor Immune Microenvironment of Uterine Corpus Endometrial Carcinoma Based on Ferroptosis-Related Genes. *Front Cell Dev Biol* (2021) 9:735013. doi: 10.3389/fcell.2021.735013
18. Shankavaram UT, Varma S, Kane D, Sunshine M, Chary KK, Reinhold WC, et al. CellMiner: A Relational Database and Query Tool for the NCI-60 Cancer Cell Lines. *BMC Genomics* (2009) 10:277. doi: 10.1186/1471-2164-10-277
19. Zhou Q, Yan X, Liu W, Yin W, Xu H, Cheng D, et al. Three Immune-Associated Subtypes of Diffuse Glioma Differ in Immune Infiltration, Immune Checkpoint Molecules, and Prognosis. *Front Oncol* (2020) 10:586019. doi: 10.3389/fonc.2020.586019
20. Ying J, Wang Q, Xu T, Lyu J. Establishment of a Nine-Gene Prognostic Model for Predicting Overall Survival of Patients With Endometrial Carcinoma. *Cancer Med* (2018) 7(6):2601–11. doi: 10.1002/cam4.1498
21. Wang ZH, Zhang YZ, Wang YS, Ma XX. Identification of Novel Cell Glycolysis Related Gene Signature Predicting Survival in Patients With Endometrial Cancer. *Cancer Cell Int* (2019) 19:296. doi: 10.1186/s12935-019-1001-0
22. Cai L, Hu C, Yu S, Liu L, Zhao J, Zhao Y, et al. Identification of EMT-Related Gene Signatures to Predict the Prognosis of Patients With Endometrial Cancer. *Front Genet* (2020) 11:582274. doi: 10.3389/fgene.2020.582274
23. Tamborero D, Rubio-Perez C, Muiños F, Sabarinathan R, Piulats JM, Muntasell A, et al. A Pan-Cancer Landscape of Interactions Between Solid Tumors and Infiltrating Immune Cell Populations. *Clin Cancer Res* (2018) 24(15):3717–28. doi: 10.1158/1078-0432.CCR-17-3509
24. Yarchoan M, Hopkins A, Jaffee EM. Tumor Mutational Burden and Response Rate to PD-1 Inhibition. *N Engl J Med* (2017) 377(25):2500–1. doi: 10.1056/NEJMc1713444
25. Ma Z, Ji J. N6-Methyladenosine (M6a) RNA Modification in Cancer Stem Cells. *Stem Cells (Dayton Ohio)* (2020) 28(12):1511–9. doi: 10.1002/stem.3279.36
26. Green AK, Feinberg J, Makker V. A Review of Immune Checkpoint Blockade Therapy in Endometrial Cancer. *Am Soc Clin Oncol Educ Book* (2020) 40:1–7. doi: 10.1200/EDBK_280503
27. Kandoth C, Schultz N, Cherniack AD, Akbani R, Liu Y, Shen H, et al. Integrated Genomic Characterization of Endometrial Carcinoma. *Nature* (2013) 497(7447):67–73. doi: 10.1038/nature12113
28. Sakai LY, Keene DR, Renard M, De Backer J. FBN1: The Disease-Causing Gene for Marfan Syndrome and Other Genetic Disorders. *Gene* (2016) 591(1):279–91. doi: 10.1016/j.gene.2016.07.033
29. Che X, Jian F, Wang Y, Zhang J, Shen J, Cheng Q, et al. FBXO2 Promotes Proliferation of Endometrial Cancer by Ubiquitin-Mediated Degradation of FBN1 in the Regulation of the Cell Cycle and the Autophagy Pathway. *Front Cell Dev Biol* (2020) 8:843. doi: 10.3389/fcell.2020.00843
30. Rood BR, Leprince D. Deciphering HIC1 Control Pathways to Reveal New Avenues in Cancer Therapeutics. *Expert Opin Ther Targets* (2013) 17(7):811–27. doi: 10.1517/14728222.2013.788152
31. Li P, Liu X, Dong ZM, Ling ZQ. Epigenetic Silencing of HIC1 Promotes Epithelial-Mesenchymal Transition and Drives Progression in Esophageal Squamous Cell Carcinoma. *Oncotarget* (2015) 6(35):38151–65. doi: 10.18632/oncotarget.5832
32. Hedberg Oldfors C, Dios DG, Linder A, Visuttijai K, Samuelson E, Karlsson S, et al. Analysis of an Independent Tumor Suppressor Locus Telomeric to Tp53 Suggested Inpp5k and Myo1c as Novel Tumor Suppressor Gene Candidates in This Region. *BMC Genet* (2015) 16:80. doi: 10.1186/s12863-015-0238-4
33. Ford CE, Jary E, Ma SS, Nixdorf S, Heinzelmann-Schwarz VA, Ward RL. The Wnt Gatekeeper SFRP4 Modulates EMT, Cell Migration and Downstream Wnt Signalling in Serous Ovarian Cancer Cells. *PloS One* (2013) 8(1):e54362. doi: 10.1371/journal.pone.0054362
34. Risinger JI, Maxwell GL, Chandramouli GV, Aprelikova O, Litzi T, Umar A, et al. Gene Expression Profiling of Microsatellite Unstable and Microsatellite Stable Endometrial Cancers Indicates Distinct Pathways of Aberrant Signaling. *Cancer Res* (2005) 65(12):5031–7. doi: 10.1158/0008-5472.CAN-04-0850
35. Cheon DJ, Tong Y, Sim MS, Dering J, Berel D, Cui X, et al. A Collagen-Remodeling Gene Signature Regulated by TGF-β Signaling is Associated With Metastasis and Poor Survival in Serous Ovarian Cancer. *Clin Cancer Res* (2014) 20(3):711–23. doi: 10.1158/1078-0432.CCR-13-1256
36. Wang GH, Zhou YM, Yu Z, Deng JP, Liu SF, Wei CZ, et al. Up-Regulated ONECUT2 and Down-Regulated SST Promote Gastric Cell Migration, Invasion, Epithelial-Mesenchymal Transition and Tumor Growth in Gastric Cancer. *Eur Rev Med Pharmacol Sci* (2020) 24(18):9378–90. doi: 10.26355/eurrev_202009_23021
37. Sun Y, Shen S, Liu X, Tang H, Wang Z, Yu Z, et al. MiR-429 Inhibits Cells Growth and Invasion and Regulates EMT-Related Marker Genes by Targeting Onecut2 in Colorectal Carcinoma. *Mol Cell Biochem* (2014) 390(1-2):19–30. doi: 10.1007/s11010-013-1950-x
38. Lu T, Wu B, Yu Y, Zhu W, Zhang S, Zhang Y, et al. Blockade of ONECUT2 Expression in Ovarian Cancer Inhibited Tumor Cell Proliferation, Migration, Invasion and Angiogenesis. *Cancer Sci* (2018) 109(7):2221–34. doi: 10.1111/cas.13633
39. Hayashida T, Takahashi F, Chiba N, Brachtel E, Takahashi M, Godin-Heymann N, et al. HOXB9, a Gene Overexpressed in Breast Cancer, Promotes Tumorigenicity and Lung Metastasis. *Proc Natl Acad Sci USA* (2010) 107(3):1100–5. doi: 10.1073/pnas.0912710107
40. Sha L, Dong L, Lv L, Bai L, Ji X. HOXB9 Promotes Epithelial-to-Mesenchymal Transition *via* Transforming Growth Factor-β1 Pathway in Hepatocellular Carcinoma Cells. *Clin Exp Med* (2015) 15(1):55–64. doi: 10.1007/s10238-014-0276-7
41. Zhang L, Yang M, Gan L, He T, Xiao X, Stewart MD, et al. DLX4 Upregulates TWIST and Enhances Tumor Migration, Invasion and Metastasis. *Int J Biol Sci* (2012) 8(8):1178–87. doi: 10.7150/ijbs.4458
42. Sun Y, Lu M, Xi X, Qiao Q, Chen L, Xu X, et al. Regulation of Epithelial-Mesenchymal Transition by Homeobox Gene DLX4 in JEG-3 Trophoblast Cells: A Role in Preeclampsia. *Reprod Sci* (2011) 18(11):1138–45. doi: 10.1177/1933719111408112
43. Yang L, Cui Y, Huang T, Sun X, Wang Y. Identification and Validation of MSX1 as a Key Candidate for Progestin Resistance in Endometrial Cancer. *Onco Targets Ther* (2020) 13:11669–88. doi: 10.2147/OTT.S271494
44. Yoshimatsu Y, Wakabayashi I, Kimuro S, Takahashi N, Takahashi K, Kobayashi M, et al. TNF-α Enhances TGF-β-Induced Endothelial-to-Mesenchymal Transition *via* TGF-β Signal Augmentation. *Cancer Sci* (2020) 111(7):2385–99. doi: 10.1111/cas.14455
45. Min WP, Wei XF. Silencing SIX1 Inhibits Epithelial Mesenchymal Transition Through Regulating TGF-β/Smad2/3 Signaling Pathway in Papillary Thyroid Carcinoma. *Auris Nasus Larynx* (2021) 48(3):487–95. doi: 10.1016/j.anl.2020.10.002
46. Vagios S, Yiannou P, Giannikaki E, Doulgeraki T, Papadimitriou C, Rodolakis A, et al. The Impact of Programmed Cell Death-Ligand 1 (PD-L1) and CD8 Expression in Grade 3 Endometrial Carcinomas. *Int J Clin Oncol* (2019) 24(11):1419–28. doi: 10.1007/s10147-019-01484-0
47. Antomarchi J, Ambrosetti D, Cohen C, Delotte J, Chevallier A, Karimdjee-Soilihi B, et al. Immunosuppressive Tumor Microenvironment Status and Histological Grading of Endometrial Carcinoma. *Cancer Microenviron* (2019) 12(2-3):169–79. doi: 10.1007/s12307-019-00225-1
48. Vagios S, Doulgeraki T, Giannikaki E, Kavoura E, Papadimitriou C, Gakiopoulou H, et al. Could Mismatch Repair Status Serve as a Biomarker for Immunotherapy in Endometrial Carcinoma? *Anticancer Res* (2020) 40(3):1669–76. doi: 10.21873/anticanres.14118
49. Cui G, Wang C, Lin Z, Feng X, Wei M, Miao Z, et al. Prognostic and Immunological Role of Ras-Related Protein Rap1b in Pan-Cancer. *Bioengineered* (2021) 12(1):4828–40. doi: 10.1080/21655979.2021.1955559

50. Li Q, Jiang S, Feng T, Zhu T, Qian B. Identification of the EMT-Related Genes Signature for Predicting Occurrence and Progression in Thyroid Cancer. *Onco Targets Ther* (2021) 14:3119–31. doi: 10.2147/OTT.S301127

Conflict of Interest: The authors declare that the research was conducted in the absence of any commercial or financial relationships that could be construed as a potential conflict of interest.

Publisher's Note: All claims expressed in this article are solely those of the authors and do not necessarily represent those of their affiliated organizations, or those of the publisher, the editors and the reviewers. Any product that may be evaluated in this article, or claim that may be made by its manufacturer, is not guaranteed or endorsed by the publisher.

Copyright © 2022 Liu, Cui, Shen, Gao, Zhu and Xu. This is an open-access article distributed under the terms of the Creative Commons Attribution License (CC BY). The use, distribution or reproduction in other forums is permitted, provided the original author(s) and the copyright owner(s) are credited and that the original publication in this journal is cited, in accordance with accepted academic practice. No use, distribution or reproduction is permitted which does not comply with these terms.

frontiers in Immunology

ORIGINAL RESEARCH
published: 27 January 2022
doi: 10.3389/fimmu.2022.803355

Identifying a Novel Defined Pyroptosis-Associated Long Noncoding RNA Signature Contributes to Predicting Prognosis and Tumor Microenvironment of Bladder Cancer

Hongcheng Lu[1†], *Jiajin Wu*[1†], *Linghui Liang*[1†], *Xinwei Wang*[2*] and *Hongzhou Cai*[3*]

[1] Department of Urology, The First Affiliated Hospital of Nanjing Medical University, Nanjing, China, [2] Department of Oncology, Jiangsu Cancer Hospital and Jiangsu Institute of Cancer Research and The Affiliated Cancer Hospital of Nanjing Medical University, Nanjing, China, [3] Department of Urology, Jiangsu Cancer Hospital and Jiangsu Institute of Cancer Research and The Affiliated Cancer Hospital of Nanjing Medical University, Nanjing, China

OPEN ACCESS

Edited by:
Elena Ciaglia,
University of Salerno, Italy

Reviewed by:
Guangzheng Zhong,
Sun Yat-sen University, China
Valentina Giudice,
University of Salerno, Italy

***Correspondence:**
Hongzhou Cai
caihongzhou@njmu.edu.cn
Xinwei Wang
wxwswy@163.com

[†]These authors have contributed equally to this work

Specialty section:
This article was submitted to Cancer Immunity and Immunotherapy, a section of the journal Frontiers in Immunology

Received: 27 October 2021
Accepted: 04 January 2022
Published: 27 January 2022

Citation:
Lu H, Wu J, Liang L, Wang X and Cai H (2022) Identifying a Novel Defined Pyroptosis-Associated Long Noncoding RNA Signature Contributes to Predicting Prognosis and Tumor Microenvironment of Bladder Cancer. Front. Immunol. 13:803355. doi: 10.3389/fimmu.2022.803355

Background: Bladder cancer (BLCA) is a common malignant tumor of the urinary tract, which is the sixth most common cancer among men. Numerous studies suggested that pyroptosis and long noncoding RNAs (lncRNAs) played an essential role in the development of cancers. However, the role of pyroptosis-related lncRNAs in BLCA and their prognostic value are still unclear.

Methods: In this study, we constructed a signature model through least absolute shrinkage and selection operator (LASSO) Cox regression analysis and Cox univariate analysis based on The Cancer Genome Atlas (TCGA) database. The expression of 12 pyroptosis-related lncRNAs was also confirmed by qRT-PCR in BLCA cell lines. TIMER, XCELL, QUANTISEQ, MCPCOUNTER, EPIC, and CIBERSORT R script were applied to quantify the relative proportions of infiltrating immune cells. Correlation coefficients were computed by Spearman analyses. The Kaplan–Meier method, Cox regression model, and log-rank tests were used to evaluate the prognostic value. The R package of pRRophetic was used to predict IC50 of common chemotherapeutic agents.

Results: A total of 12 pyroptosis-related lncRNAs with great prognosis value were identified. The expression was investigated by qRT-PCR in four BLCA cell lines. Then, 126 cases were identified as high-risk group, and 277 cases were identified as low-risk group based on the cutoff point. Patients in the low-risk group showed a significant survival advantage. Furthermore, we found that clinical features were significantly related to the risk score. As well, based on the C-index values, a nomogram was constructed. The gene set enrichment analysis (GSEA) results showed that mitogen-activated protein kinase (MAPK) signaling, transforming growth factor (TGF)-β signaling, and WNT signaling were

with important significance in the high-risk group. Moreover, we found that riskscore was positively correlated with M0 macrophages and M2 macrophages.

Conclusions: In conclusion, our study indicated that pyroptosis is closely connected to BLCA. The riskscore generated from the expression of 12 pyroptosis-related lncRNAs was evaluated by various clinical features including survival status, tumor microenvironment, clinicopathological characteristic, and chemotherapy. It may offer a significant basis for future studies.

Keywords: bladder cancer, lncRNAs, pyroptosis, tumor microenvironment, nomogram

INTRODUCTION

Bladder cancer (BLCA) is the sixth most common cancer in men that is characterized by high risks of recurrence and mortality (1). As a common malignant tumor of the urinary tract, the 5-year overall survival rate of BLCA ranges from 23% to 48% (2, 3). Cisplatin-based chemotherapy, immunotherapy, and surgery are the most effective approaches and standard of care for BLCA (4). Novel therapeutic targets are necessary to ameliorate survival time of patients due to the limitations of BLCA treatments. Therefore, there is an urgent need for reliable new prognostic models to make targeted therapy more feasible. However, well-accepted prognostic biomarkers for BLCA are still lacking. As a result, urologists have difficulty in distinguishing the risk of BLCA patients and determine accurate treatment decisions (5).

The phenomenon of pyroptosis was first observed in the 1990s (6–9). Pyroptosis is one of the programmed cell necroses triggered and activated by some inflammasomes, which played an important role in the development of cancers. It was reported that pyroptotic death signaling was inhibited in human papillomavirus (HPV)-infected cervical cancer cells, which was correlated with poor clinical outcomes in cervical cancer (10). On the other hand, some chemotherapy drugs such as cisplatin could kill cancer cells by inducing pyroptosis (11). Pyroptosis was also found to be associated with tumor immune microenvironment. Recently, a study showed that pyroptotic cancer death could activate tumor-associated T-cell and dendritic cell (DC) infiltrations (12). It was reported that Gasdermin-D (GSDMD) was essential for effector CD8+ T cell to respond to lung cancer as well (13). These results suggested that pyroptosis was associated with the oncogenesis, immune microenvironment, and prognosis of cancer.

Long noncoding RNAs (lncRNAs) are a type of RNA more than 200 nucleotides long, which do not code for proteins (14). LncRNAs contribute to regulating the mechanisms associated with epigenetic modifications, transcriptional and posttranscriptional processes, and immune microenvironment in many diseases (15–19). Accumulated evidence has illustrated that lncRNAs are intimately related to cancer (20). For instance, lncRNA UCA1 could improve the survival of BLCA cells and reshape the tumor microenvironment (21). In addition, lncRNA ADAMTS9-AS2 enhanced cisplatin sensitivity in gastric cancer and suppressed tumor growth by mediating pyroptotic cell death (22). Moreover, lncRNA-XIST promoted non-small cell lung cancer progression by mediating pyroptotic cell death (23). Therefore, we believed that pyroptosis-related lncRNAs might participate in tumor cell proliferation and migration in cancer. However, the exact mechanism of pyroptosis-related lncRNAs in BLCA remains to be elucidated clearly.

In this study, we combined two kinds of biomarkers to construct a diagnostic model for cancers that was superior to simple genes. Few studies have confirmed the role of lncRNAs in this situation. We applied a novel modeling algorithm, paring, and iteration to construct a pyroptosis-related lncRNA signature. As well, we estimated its predictive value, diagnostic effectiveness, chemotherapeutic efficacy, immunotherapy efficacy, and tumor immune infiltration for patients with BLCA.

MATERIALS AND METHODS

Microarray Datasets

The RNA sequencing (RNA-seq) of BLCA patients with clinical features was obtained from The Cancer Genome Atlas (TCGA) (https://portal.gdc.cancer.gov/repository). Thirty-seven pyroptosis-related genes (GPX4, NLRP7, NLRP2, CASP3, CASP6, TNF, IL1B, IL18, CASP8, NLRP6, IL6, GSDMA, GSDMC, PYCARD, CASP5, AIM2, NOD2, NLRC4, NLRP3, CASP4, CASP1, PRKACA, ELANE, TIRAP, SCAF11, PJVK, CASP9, NOD1, PLCG1, NLRP1, GSDME, GSDMD, GSDMB, P2RX7, NAIP, CLPS, and TLR4) were selected for further analysis. Co-expression pyroptosis-related lncRNAs were identified with the cutoff criteria of Pearson $|R|>0.3$ and P value <0.001.

Identifying Differentially Expressed Genes and Functional Enrichment

R "limma" package was used to identify differently expressed genes (DEGs). The cutoff criterion was set as log fold change (FC) >1.5 along with false discovery rate (FDR) <0.05. Gene Ontology (GO) analysis and Kyoto Encyclopedia of Genes and Genomes (KEGG) pathway analysis were conducted by "clusterProfiler" package. As well, FDR <0.05 was considered statistically significant.

Establishment of a Risk Model to Evaluate the Risk Score

The least absolute shrinkage and selection operator (LASSO), a machine-learning algorithm, was performed by "glmnet"

package. Afterward, Cox proportional hazards regression analysis was conducted for the model. The area under the curve (AUC) value was also calculated. The highest point indicated the maximum AUC value. The procedure of calculation was terminated while the model was chosen as the optimal candidate. The 1-, 2-, 3-, 4-, and 5-year receiver operating characteristic (ROC) curves were plotted. Then, we applied a formula to define risk score:

$$\text{RiskScore} = \Sigma\beta i Si$$

We distinguished high or low risk of Risk Scores by the AUC values of the 5-year ROC curve.

Calculation of Tumor Microenvironment Cell Infiltration

TIMER, XCELL, QUANTISEQ, MCPCOUNTER, EPIC, and CIBERSORT R script were applied to quantify the relative proportions of infiltrating immune cells (24). We used Spearman's rank correlation analysis when exploring the relationship between the risk score values and the immune infiltrated cells.

Prediction of Response to Chemotherapy

The R package of pRRophetic was used to predict IC50 of common chemotherapeutic agents (25). IC50 indicates the effectiveness of a substance in inhibiting specific biological or biochemical functions. The difference between groups was tested by Wilcoxon signed-rank test.

Statistical Analysis

Correlation coefficients were computed by Spearman analyses. The Kaplan–Meier method, Cox regression model, and log-rank tests were used to evaluate the prognostic value. All statistical analyses were two-sided, and $P < 0.05$ was regarded as statistically significant. All statistical analyses were performed by R (version 4.0.3).

RNA Extraction and qRT-PCR

TRIzol reagent (Invitrogen, USA) was used to isolate total RNA from tissues. HiScript II (Vazyme, China) was used to synthesize cDNA. Primers for qRT-PCR were provided by TSINGKE Biological Technology. Beta-actin was chosen as the internal reference. Expression levels of lncRNAs were calculated with $2^{-\Delta\Delta CT}$. The primers used for PCR were exhibited in **Table S1**.

Patients and Tissue Samples

The study was approved by the ethical committee of Jiangsu Cancer Hospital. Thirty-one patients with multiple BLCA who accepted partial and radical cystectomy at Jiangsu Cancer Hospital from December 2018 to August 2020 were recruited. All patients were diagnosed with urothelial carcinoma. Thirty-one tumor samples and normal bladder tissues were achieved for the experiment. Detailed clinical data were collected from the electronic medical records retrospectively. Sequencing was conducted using the Illumina PE150 platform at Novogene Bioinformatics Technology Co., Ltd.

RESULTS

Identification of Co-Expressed Pyroptosis-Related Long Noncoding RNAs

The flowchart of this study was shown in **Figure S1**. Firstly, we obtained 37 pyroptosis-related genes from literature review. GO and KEGG analysis were carried out to investigate the function of these pyroptosis-related genes. The top 10 enriched GO and KEGG terms were shown in **Figures 1A, B**. The GO results indicated that pyroptosis-related genes were enriched in he regulation of cytokine, especially interleukin-1 (IL-1). The KEGG results indicated that pyroptosis-related genes were enriched in Peroxisome proliferator-activated receptor (PPAR) signaling pathway, calcium signaling pathway, phosphatidylinositol-3-kinase(PI3K) protein kinase B(AKT) (PI3K–AKT) signaling pathway, and so on. Then, we detected the relationship between pyroptosis-related mRNAs and pyroptosis-related lncRNAs to identify co-expressed lncRNAs. Next, the LASSO regression was conducted to identify OS-related pyroptosis lncRNAs. Twelve lncRNAs were selected for further analysis (**Figures 1C, D**). The detailed information of lncRNAs for constructing the pyroptosis-related prognostic signature was shown in **Table 1**. Univariate Cox regression analysis was conducted to analyze the prognostic values of pyroptosis-related lncRNAs in meta-data cohort and validation cohort (**Figures 1E, F**). The expressions of these 12 lncRNAs were shown in **Figure 1G** as well.

Expression Level of Long Noncoding RNAs in Bladder Cancer Cell Lines

We further validated the expression of 12 pyroptosis-related lncRNAs in BLCA cells T24, BIU87, J82, and UMUC3 by qRT-PCR. As shown in **Figure 2**, we could observe that AL049840.5, AL136084.3, MAFG-DT, and LINC00942 were significantly upregulated in BLCA cell lines compared to those in SV-HUC cells. Meanwhile, the expressions of SNHG18, OCIAD1-AS1, AC008035.1, LINC02195, AC116366.1, and OCIAD1-AS1 were significantly lower in BLCA cell lines. However, no clear trend was noticed in the expression level of AL024508.1 and AC005261.1 in BLCA cell lines.

Construction of the Risk Assessment Model

The relationship between pyroptosis-related mRNAs and 12 pyroptosis-related lncRNAs was exhibited in **Figure 3A**. The alluvial diagram was used to visualize the attribute changes of pyroptosis-related mRNAs (**Figure 3B**). In the meta-data cohort, we found that the highest point of the AUC for each ROC curve was 0.776 (**Figure 3C**). Next, we observed that AUC values of 1-, 2-, 3-, 4-, and 5-year curves were all over 0.75 (**Figure 3D**). We collected data of 403 patients with BLCA from TCGA and calculated the risk scores for all of them. Several clinical characteristics including risk score curves were also conducted (**Figure 3E**). Then, 126 cases were identified as high-risk group, and 277 cases were identified as low-risk group based on the cutoff point confirmed previously. Risk scores and survival status

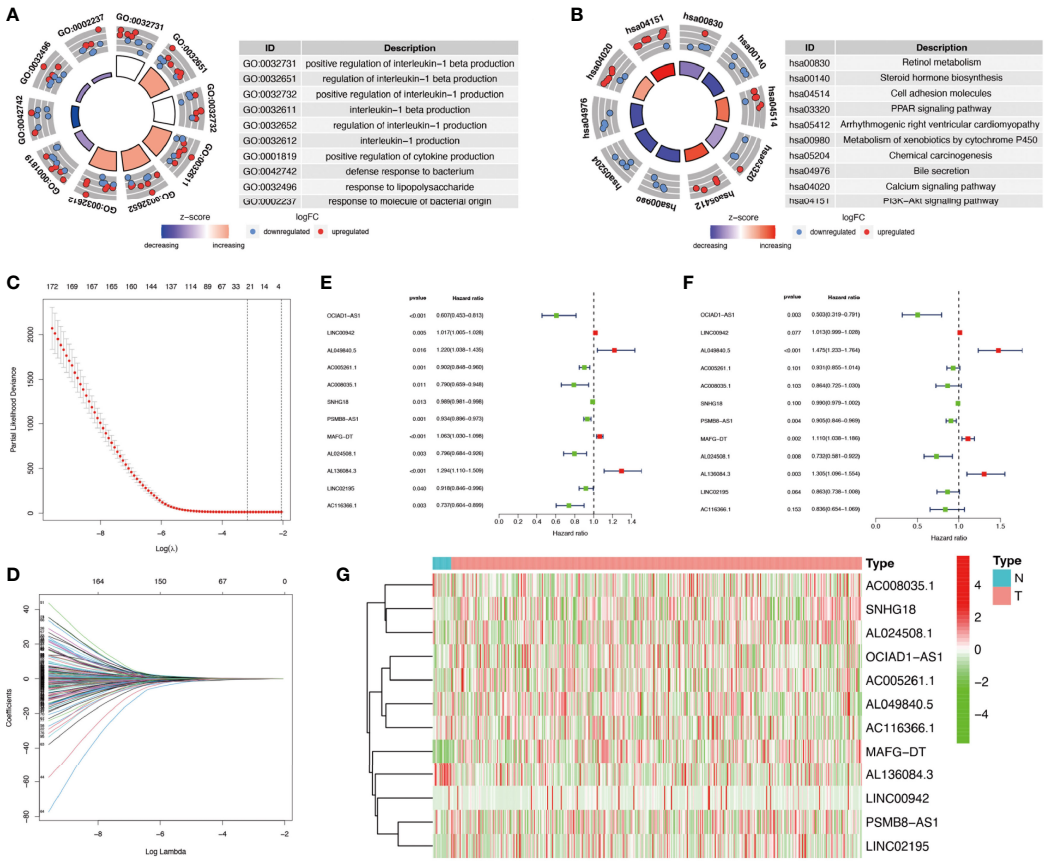


FIGURE 1 | Identification of co-expressed pyroptosis-related lncRNAs. **(A, B)** Circle plots of Gene Ontology (GO) terms and Kyoto Encyclopedia of Genes and Genomes (KEGG) pathway analysis for pyroptosis-related genes. The outer circle of circle plots showed a scatter plot for each term of the logFC of the assigned genes. Red circles represented upregulation, and blue ones represented downregulation. **(C, D)** Identification of overall survival (OS)-related pyroptosis lncRNAs using the least absolute shrinkage and selection operator (LASSO) regression algorithm. **(E, F)** A forest map showed 12 pyroptosis-related lncRNAs identified by Cox proportional hazards regression in the meta-data cohort and validation cohort. **(G)** The heatmap of pyroptosis-related lncRNAs based on their expression levels.

of each patient were depicted in **Figure 3F**. Obviously, we could observe that patients in the low-risk group showed a significant survival advantage that was consistent with the result of Kaplan–Meier analysis (**Figures 3G, H**). Similar results were obtained in the validation cohort and the whole cohort (**Figure S2**).

Relationship Between Clinical Characteristics and Risk Score

Clinical characteristics of the two groups were also exhibited in **Figure S3**. Clinicopathological characteristics of patients in TCGA-BLCA cohort were displayed in **Table 2**. We observed

TABLE 1 | The detailed information of lncRNAs for constructing the pyroptosis-related prognostic signature.

Gene	Ensemble ID	Location	β (Cox)	HR	P
OCIAD1-AS1	ENSG00000248256.1	chr4:48,852,008-48,860,203	-0.6881175	0.60692147	0.00082398
LINC00942	ENSG00000249628.3	chr12:1,500,525-1,504,424	0.01300705	1.01658149	0.00452522
AL049840.5	ENSG00000269958.1	chr14:103,696,353-103,697,163	0.38852869	1.22031272	0.01611728
AC005261.1	ENSG00000268205.1	chr19:57,304,305-57,308,562	-0.0715262	0.90203259	0.00115463
AC008035.1	ENSG00000272369.1	chr12:46,537,502-46,652,550	-0.1459938	0.79041647	0.01132062
SNHG18	ENSG00000250786.2	chr5:9,546,200-9,550,609	-0.0098145	0.98915525	0.01298739
PSMB8-AS1	ENSG00000204261.9	chr6:32,844,108-32,846,484	-0.0994647	0.93392805	0.00108726
MAFG-DT	ENSG00000265688.2	chr17:81,927,829-81,930,753	0.1041579	1.06325755	0.0001518
AL024508.1	ENSG00000272189.1	chr6:136,550,661-136,552,554	-0.3126264	0.79582983	0.00313973
AL136084.3	ENSG00000267026.5	chr9:98,847,231-98,872,403	0.26628244	1.29445181	0.0009828
LINC02195	ENSG00000236481.1	chr16:26,584,755-26,594,813	-0.1477065	0.91785548	0.03986348
AC116366.1	ENSG00000234290.2	chr5:132,468,890-132,473,043	-0.1792917	0.73672008	0.00259579

HR, hazard ratio; lncRNA, long noncoding RNA.

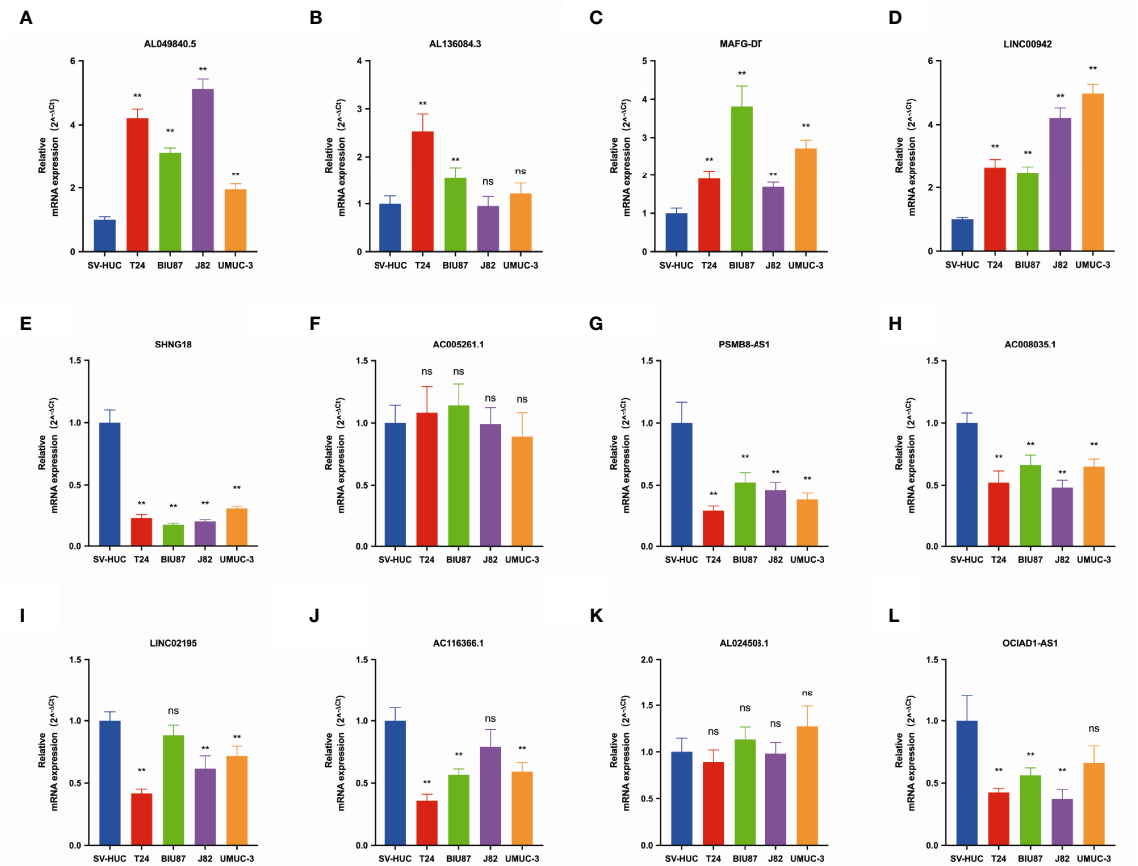


FIGURE 2 | The qRT-PCR results of 12 lncRNAs in four bladder cancer cell lines. Notes: **(A)** qRT-PCR result of AL049840.5; **(B)** qRT-PCR result of AL136084.3; **(C)** qRT-PCR result of MAFG-DT; **(D)** qRT-PCR result of LINC00942; **(E)** qRT-PCR result of SNHG18; **(F)** qRT-PCR result of AC005261.1; **(G)** qRT-PCR result of PSMB8-AS1. **(H)** qRT-PCR result of AC008035.1. **(I)** qRT-PCR result of LINC02195. **(J)** qRT-PCR result of AC116366.1. **(K)** qRT-PCR result of AL024508.1. **(L)** qRT-PCR result of OCIAD1-AS1. **P < 0.01. ns, not statistically significant.

that most clinical features were significantly related to the risk score. As well, we found that age [P < 0.001, hazard ratio (HR) = 1.038, 95% CI 1.019–1.056], clinical stage (P < 0.001, HR = 1.941, 95% CI 1.543–2.441), T stage (P < 0.001, HR = 1.744, 95% CI 1.365–2.227), and risk score (P < 0.001, HR = 1.941, 95% CI 1.682–2.240) showed statistical differences by univariate Cox regression analysis in the meta-data cohort and validation cohort (**Figures S4A, B**). Therefore, based on the C-index values, a nomogram integrating the risk score, age, gender, clinical stage, tumor differentiation, and TNM stage was constructed (**Figure S4C**). The nomogram-predicted results were consistent with the survival status of the patients (**Figures S4D–F**). The result of decision curve analysis (DCA) further elucidated that the risk score served as the most exact prognostic indicator among clinical variables in clinical decision-making (**Figure S4G**).

DEGs between high- and low-risk groups were identified and exhibited in **Figure 4A**. The GO results showed that DEGs were enriched in many metabolic processes, such as steroid and hormone (**Figure 4B**). The gene set enrichment analysis (GSEA) results showed that mitogen-activated protein kinase (MAPK) signaling, transforming growth factor (TGF)-β signaling, and WNT signaling were with important significance in the high-risk group (**Figure 4C**).

Estimation of Tumor Microenvironment and Chemotherapeutics

The correlation between immune cells and riskScore was calculated as well (**Figure 5A**). The immune infiltration results of the two groups were shown in **Figure 5B**. The proportions of M0 macrophages and M2 macrophages in the high-riskscore group were significantly higher than those in the low-riskscore group. However, the proportion of CD8+ T cells was significantly lower in the high-riskscore group (**Figures 5C–E**).

Based on the pRRophetic algorithm, we explored the relationship between riskscore and chemoresistance by calculating the half-maximal inhibitory concentration (IC50) of 3 common chemotherapeutic agents (cisplatin, docetaxel, and paclitaxel) for BLCA. We observed that patients in the high-riskscore group were more sensitive to these three chemotherapeutic agents (**Figures 5F–H**).

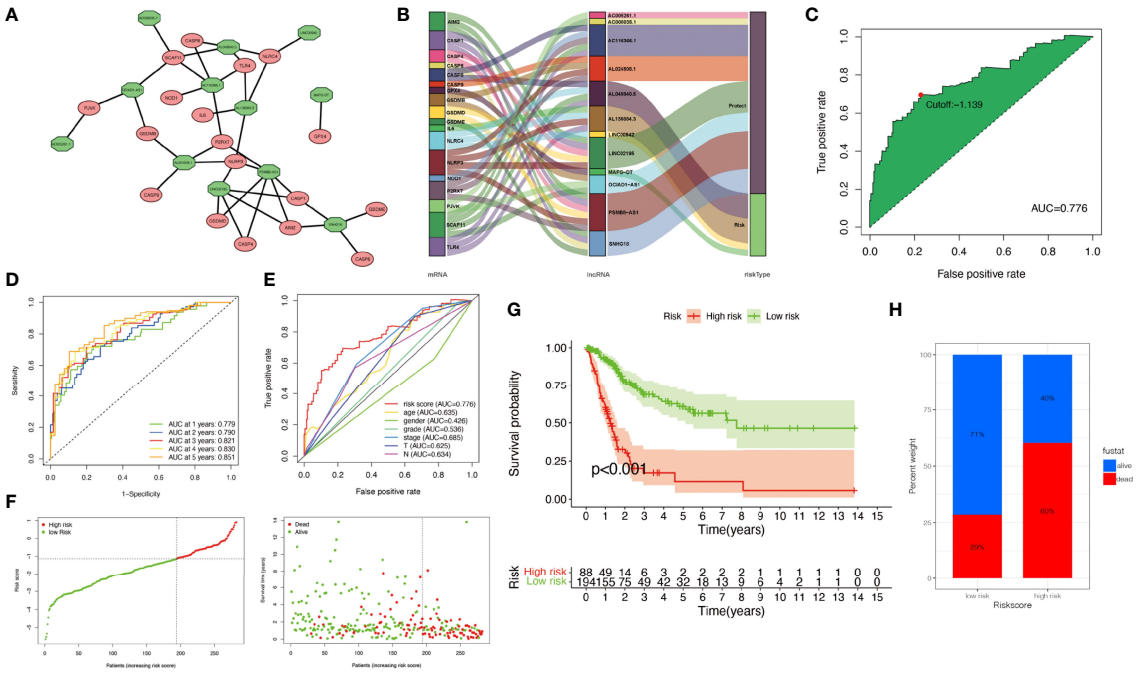


FIGURE 3 | Construction of risk signature in the meta-data cohort. **(A)** The relationship between pyroptosis-related genes (red circle) and lncRNAs (green circle). **(B)** The alluvial diagram was used to visualize the attribute changes of pyroptosis-related mRNAs. **(C)** Receiver operating characteristic (ROC) curves were plotted for examining the most predictive efficacy of the signature. **(D)** Area under the curve (AUC) of time-dependent ROC curves verified the prognostic performance of the risk score. **(E)** A comparison of 5-year ROC curves with other common clinical characteristics showed the superiority of the riskScore. **(F)** Distribution of patients in The Cancer Genome Atlas (TCGA) cohort based on the median risk score and survival status for each case. **(G)** Kaplan–Meier curves of the overall survival (OS) between low- and high-risk groups. **(H)** Rate of clinical outcome in the low- and high-risk groups.

Immunotherapy Analysis

Considering the clinical application and benefits of immune checkpoint inhibitors, we identified 68 immune checkpoint genes from a review of the literature (26, 27). We found that the expression of many immune checkpoints showed significant differences between the two groups (**Figure 5I**). As well, riskscore was observed to be negatively correlated with BTN2A2, BTN3A1, CD276, PDCD1LG2, CTLA4, CD160, TNFRSF14, CD40, CD40LG, LGALS9, CD96, BTN2A1, KIR2DL3, KIR2DL4, HLA-A, HLA-B, HLA-C, HLA-DMA, HLA-E, and HLA-F and positively correlated with TNFSF4 and PVR (**Figure 6A**). As described in **Figure 6B**, the scores of IPS, IPS–PD1 blocker, IPS–CTLA4 blocker, and IPS –PD1 –CTLA4 blocker were lower in the high-risk group. All these results suggested that risk score may be related to immunotherapy.

Validation of Long Noncoding RNAs and Riskscore in the Original Cohort

We used 31 primary BLCA samples and 31 normal bladder tissues for microarray analysis. The clinical characteristics were described in **Table 3**. The results showed that the expressions of MAFG-DT, SNHG18, and AL024508.1 were higher in tumor tissues, while the expressions of LINC00942, PSMB8-AS1, and AC116366.1 were higher in normal tissues (**Figure 6C**). Riskscores were also calculated by the same formula. Clinical characteristics of the two groups were also exhibited in **Figure S5**.

DISCUSSION

As far as we are aware, our research is the first comprehensive and detailed analysis of pyroptosis-related lncRNAs in BLCA that could contribute to offering a significant basis for future studies.

To begin with, we retrieved raw data of lncRNAs and transcripts from TCGA. The functional analyses indicated that the pyroptosis-related genes were associated with the regulation of cytokine, especially IL-1. Caspase-1, which could initiate pyroptosis, could mediate the maturation and secretion of IL-1 as well (28). The activation of pyroptosis led to the release of the inflammatory mediator IL-1, which promoted the occurrence of cancer in many ways (29). As well, the functional analyses indicated that many pathways such as PPAR signaling pathway, calcium signaling pathway, and PI3K–AKT signaling pathway contributed to the process. It was confirmed that Cyclin A2 and cyclin-dependent kinase dysregulated GSDMD through the inhibition of PI3K–AKT pathway in gastric cancer (30).

Then, we compared the mRNA expression levels of 37 well-accepted pyroptosis-related genes between BLCA and normal tissues. Interestingly, we found that most of these genes were

TABLE 2 | Clinicopathological characteristics of patients in TCGA-BLCA cohort.

Characteristic	TCGA-BLCA cohort (n = 407)	
	Number	%
Age (years)		
≤65	161	39.6
>65	246	60.4
Gender		
Male	301	74.0
Female	106	26.0
Histological grade		
Low stage	20	5.0
High stage	384	94.3
Unknow	3	0.7
Pathological stage		
Stage I	2	0.5
Stage II	129	31.7
Stage III	141	34.6
Stage IV	133	32.7
Unknown	2	0.5
T stage		
T1	4	1.0
T2	118	29.0
T3	194	47.7
T4	58	14.3
Unknown	33	8.0
N stage		
N0	237	58.2
N1	45	11.1
N2	76	18.6
N3	7	1.7
NX	42	10.4
M stage		
M0	195	47.9
M1	11	2.7
MX	201	49.4
Outcome		
Alive	250	61.4
Dead	157	38.6

BLCA, bladder cancer; TCGA, The Cancer Genome Atlas.

expressed aberrantly, which suggested that pyroptosis contributed to the development of BLCA. Considering the role of lncRNAs, we identified 172 co-expressed pyroptosis-related lncRNAs.

Afterward, we constructed a 12-lncRNA risk signature to explore the relationship between BLCA and pyroptosis-related lncRNAs. Among these selected lncRNAs, updates confirm that some of them may play different functional roles in the progress of cancer. For instance, lncRNAs OCIAD1-AS1, LINC02195, MAFG-DT, AL136084.3, and PSMB8-AS1 were with great prognostic value for BLCA (31–34). As discovered by Sun et al. (35), lncRNA LINC00942 exerted its functions as an oncogene in promoting METTL14-mediated m6A methylation and regulating the expression and stability of its target genes CXCR4 and CYP1B1 in BRCA initiation and progression. Fan et al. (36) found that lncRNA SNHG18 facilitated non-small cell lung cancer growth and metastasis by modulating the miR-211-5p/BRD4 and may be a potential therapeutic target for the treatment.

Not only did we count each AUC value of ROC to get the most accurate model, but also getting the optimal cutoff point distinguished the high- or low-risk group among patients with BLCA. Obviously, patients in the high-risk group showed a significant survival disadvantage by using Kaplan–Meier analysis. Surprisingly, we found that riskscore was related to gender and age. Moreover, patients with high-grade BLCA had significantly higher riskscores than those with low-grade BLCA. The riskscore of patients with different T, N, M, and clinical stage also showed a significant difference that was consistent with prognosis. Therefore, a nomogram integrating these characteristics was constructed that could predict clinical outcomes well.

After identifying differently expressed genes between high- and low-risk groups, GSEA results also showed that the pathways of adherens junction, cell cycle, DNA replication, extracellular matrix (ECM) receptor signaling, epidermal growth factor receptor (ERBB) signaling, focal adhesion, MAPK signaling, TGF-β signaling, and WNT signaling were enriched in the high-risk group. This suggests that pyroptosis-related lncRNAs in BLCA may be related to pathways such as MAPK signaling, TGF-β signaling, and WNT signaling. For example, miR-186-5p suppressed BLCA cell proliferation, migration, invasion, and epithelial-mesenchymal transition (EMT) process by targeting RAB27A/B to inactivate the MAPK signaling (37). Moreover, grape seed proanthocyanidins effectively inhibited the migration and invasion of bladder cancer (BC) cells by reversing EMT through suppression of the TGF-β signaling pathway (38). As Gao and Ji (39) suggested, LINC00707 contributed to the proliferation and metastasis of BLCA by activating Wnt/β-catenin signaling. Pathways such as ECM receptor signaling, ERBB signaling, and focal adhesion were associated with the tumor microenvironment.

The results of immune infiltration analysis indicated that the risk score exhibited a positive correlation with the infiltration of B cells naive, CD4+ T cells, DCs, macrophages M0, and macrophages M2. In a previous study, CD4+ T cells were proven to be more recruited by BLCA cells, which promoted the BLCA metastasis (40). Both DCs and CD4+ T cells were proven related to Bacillus Calmette Guerin (BCG)-induced immune response, which indicated the importance of tumor-infiltrating immune cells in BLCA progression and therapy (41).

Response to immune checkpoint inhibitors [such as cytotoxic T lymphocyte-associated antigen-4 (CTLA4)] is the key to satisfying treatment. However, not every patient could benefit from immunotherapy (42). In our study, we surprisingly observed that the expressions of many immune checkpoint genes, including CTLA4, showed significant differences between the two groups. The riskscore model was negatively correlated with most immune checkpoint genes. As well, the scores of IPS, IPS–PD1 blocker, IPS –CTLA4 blocker, and IPS–PD1–CTLA4 blocker were lower in the high-risk group. It has been reported that IPS was a superior predictor of response to CTLA-4 and anti-PD-1 (43). All results above suggested that our model may be a potential index for evaluating the response to immunotherapy in patients with BLCA. Besides, we also detected the response to chemotherapy sensitivity

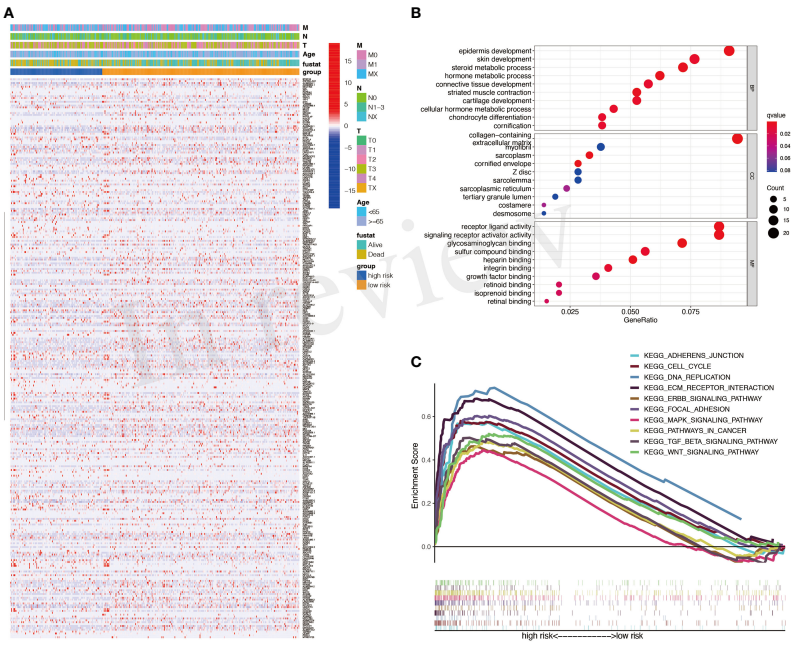


FIGURE 4 | Differentially expressed genes (DEGs) between high- and low-risk groups. **(A)** A heatmap for DEGs between high- and low-risk groups. **(B)** Gene Ontology (GO) analysis for DEGs. **(C)** Activated pathways analyzed by gene set enrichment analysis (GSEA).

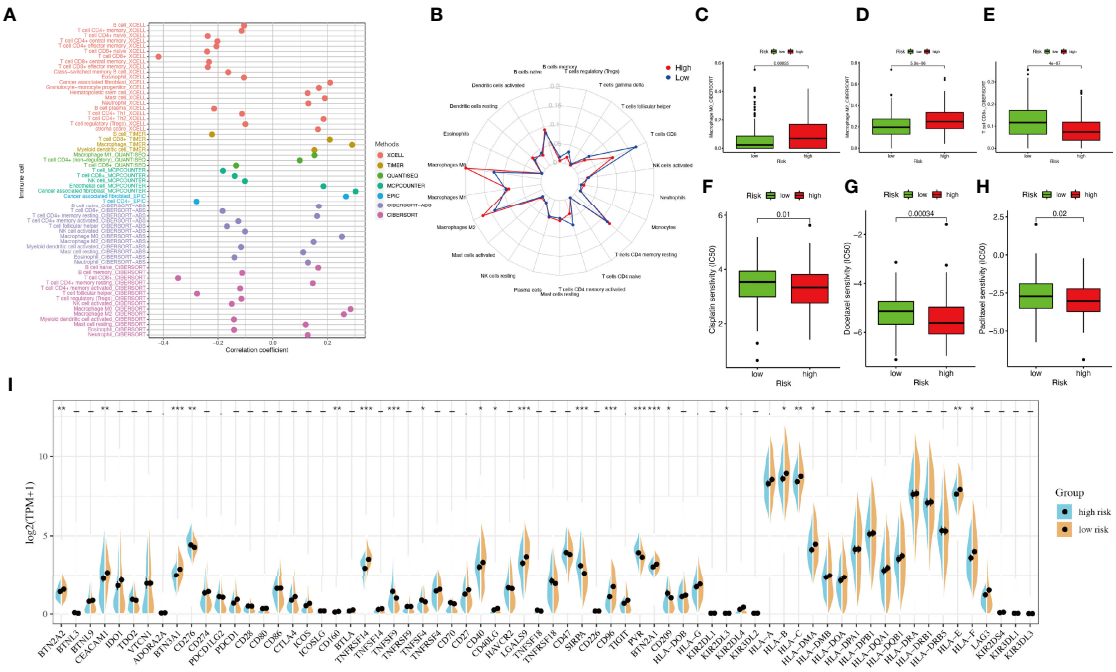


FIGURE 5 | Tumor-infiltrating immune cells and chemotherapeutics. **(A)** The relationship between immune cells and riskScore. Each color represented a distinct algorithm. **(B)** The proportions of immune cells in the high- and low-risk groups. **(C–E)** The proportions of macrophages M0, macrophages M2, and CD8+ T cell in the high- and low-risk groups. **(F–H)** The half-maximal inhibitory concentration (IC50) of 3 common chemotherapeutic agents (cisplatin, docetaxel, and paclitaxel). **(I)** The expression of 68 immune checkpoint genes in the high- and low-risk groups. *P < 0.05, **P < 0.01, ***P < 0.001.

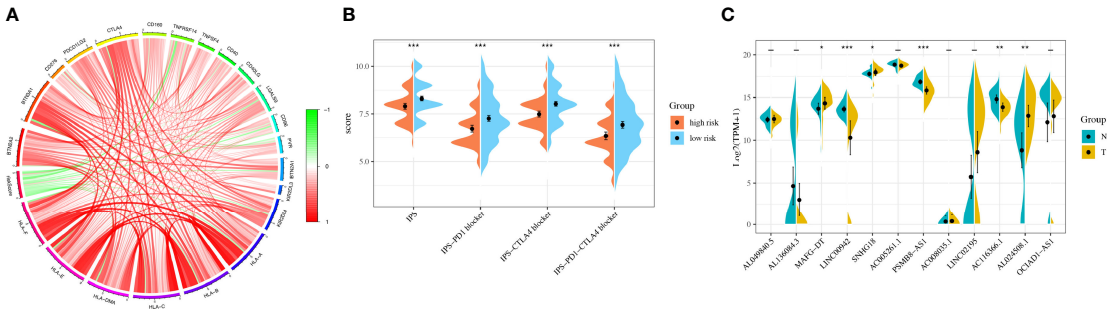


FIGURE 6 | Immunotherapy analysis and validation in the original cohort. **(A)** The correlation between immune checkpoint genes and riskscore. **(B)** The IPS, IPS-PD1 blocker, IPS–CTLA4 blocker, and IPS–PD1–CTLA4 blocker values in the high- and low-risk groups. **(C)** The RNA sequencing (RNA-Seq) results of 12 lncRNAs in bladder cancer tissues and normal tissues. *P < 0.05, **P < 0.01, ***P < 0.001.

of patients by calculating IC50 value and screen out candidate small-molecule compounds. Collectively, these discoveries may offer suitable treatment alternatives for BLCA patients.

Overall, our research indicated that pyroptosis is closely connected to BLCA. Moreover, the score based on risk signature generated from 12 pyroptosis-related lncRNAs evaluated this original model *via* various clinical settings such as TNM stage, clinicopathological characteristics, tumor microenvironment, and chemotherapy. It may offer a significant basis for future studies.

TABLE 3 | Clinicopathological characteristics of patients in the original cohort.

Characteristics	Case	riskscore		P value
		Low	High	
All cases	31	15	16	
Age				1
< 65	13	6	7	
≥ 65	18	9	9	
Gender				1
Male	24	12	12	
Female	7	3	4	
T stage				0.034
Ta	4	4	0	
T1	9	2	7	
T2	9	5	4	
T3	6	4	2	
T4	3	0	3	
N stage				0.484
N0	27	13	14	
N1	0	0	0	
N2	2	0	2	
N3	1	1	0	
Nx	1	1	0	
M stage				0.461
M0	26	12	14	
M1	4	3	1	
Mx	1	0	1	
Grade				0.654
Low	6	2	4	
High	25	13	12	
Smoke				0.473
Yes	12	7	5	
No	19	8	11	
Recurrence				
Yes	10	5	5	1
No	21	10	11	

DATA AVAILABILITY STATEMENT

Publicly available datasets were analyzed in this study. These data can be found here: https://portal.gdc.cancer.gov/repository.

ETHICS STATEMENT

The studies involving human participants were reviewed and approved by the ethical committee of Jiangsu Cancer Hospital. The patients/participants provided their written informed consent to participate in this study.

AUTHOR CONTRIBUTIONS

HL designed the article and wrote the article. JW and LL conducted the experiments and revised the article. XW obtained the samples and clinical information. HC contributed to the concept and revised the article. All authors contributed to the article and approved the submitted version.

ACKNOWLEDGMENTS

We acknowledge TCGA database for providing its platforms.

SUPPLEMENTARY MATERIAL

The Supplementary Material for this article can be found online at: https://www.frontiersin.org/articles/10.3389/fimmu.2022.803355/full#supplementary-material

REFERENCES

1. Sung H, Ferlay J, Siegel RL, Laversanne M, Soerjomataram I, Jemal A, et al. Global Cancer Statistics 2020: GLOBOCAN Estimates of Incidence and Mortality Worldwide for 36 Cancers in 185 Countries. *CA Cancer J Clin* (2021) 71:209–49. doi: 10.3322/caac.21660
2. Kuroki L, Guntupalli SR. Treatment of Epithelial Ovarian Cancer. *BMJ* (2020) 371:m3773. doi: 10.1136/bmj.m3773
3. Lee JY, Kim S, Kim YT, Lim MC, Lee B, Jung KW, et al. Changes in Ovarian Cancer Survival During the 20 Years Before the Era of Targeted Therapy. *BMC Cancer* (2018) 18:601. doi: 10.1186/s12885-018-4498-z
4. Seiler R, Ashab HAD, Erho N, van Rhijn BWG, Winters B, Douglas J, et al. Impact of Molecular Subtypes in Muscle-Invasive Bladder Cancer on Predicting Response and Survival After Neoadjuvant Chemotherapy. *Eur Urol* (2017) 72:544–54. doi: 10.1016/j.eururo.2017.03.030
5. Witjes JA, Bruins HM, Cathomas R, Compérat EM, Cowan NC, Gakis G, et al. European Association of Urology Guidelines on Muscle-Invasive and Metastatic Bladder Cancer: Summary of the 2020 Guidelines. *Eur Urol* (2021) 79:82–104. doi: 10.1016/j.eururo.2020.03.055
6. Monack DM, Raupach B, Hromockyj AE, Falkow S. Salmonella Typhimurium Invasion Induces Apoptosis in Infected Macrophages. *Proc Natl Acad Sci U S A* (1996) 93(18):9833–8. doi: 10.1073/pnas.93.18.9833
7. Zychlinsky A, Prevost MC, Sansonetti PJ. Shigella Flexneri Induces Apoptosis in Infected Macrophages. *Nature* (1992) 358:167–9. doi: 10.1038/358167a0
8. Hilbi H, Chen Y, Thirumalai K, Zychlinsky A. The Interleukin 1beta-Converting Enzyme, Caspase 1, is Activated During Shigella Flexneri-Induced Apoptosis in Human Monocyte-Derived Macrophages. *Infect Immun* (1997) 65:5165–70. doi: 10.1128/iai.65.12.5165-5170.1997
9. Hersh D, Monack DM, Smith MR, Ghori N, Falkow S, Zychlinsky A. The Salmonella Invasin SipB Induces Macrophage Apoptosis by Binding to Caspase-1. *Proc Natl Acad Sci U S A* (1999) 96(5):2396–401. doi: 10.1073/pnas.96.5.2396
10. So D, Shin HW, Kim J, Lee M, Myeong J, Chun YS, et al. Cervical Cancer Is Addicted to SIRT1 Disarming the AIM2 Antiviral Defense. *Oncogene* (2018) 37:5191–204. doi: 10.1038/s41388-018-0339-4
11. Zhang CC, Li CG, Wang YF, Xu LH, He XH, Zeng QZ, et al. Chemotherapeutic Paclitaxel and Cisplatin Differentially Induce Pyroptosis in A549 Lung Cancer Cells *via* Caspase-3/GSDME Activation. *Apoptosis* (2019) 24:312–25. doi: 10.1007/s10495-019-01515-1
12. Erkes DA, Cai W, Sanchez IM, Purwin TJ, Rogers C, Field CO, et al. Mutant BRAF and MEK Inhibitors Regulate the Tumor Immune Microenvironment *via* Pyroptosis. *Cancer Discov* (2020) 10:254–69. doi: 10.1158/2159-8290.CD-19-0672
13. Xi G, Gao J, Wan B, Zhan P, Xu W, Lv T, et al. GSDMD Is Required for Effector CD8(+) T Cell Responses to Lung Cancer Cells. *Int Immunopharmacol* (2019) 74:105713. doi: 10.1016/j.intimp.2019.105713
14. Nobili L, Lionetti M, Neri A. Long Non-Coding RNAs in Normal and Malignant Hematopoiesis. *Oncotarget* (2016) 7:50666–81. doi: 10.18632/oncotarget.9308
15. Yang Y, Junjie P, Sanjun C, Ma Y. Long Non-Coding RNAs in Colorectal Cancer: Progression and Future Directions. *J Cancer* (2017) 8:3212–25. doi: 10.7150/jca.19794
16. He D, Zheng J, Hu J, Chen J, Wei X. Long Non-Coding RNAs and Pyroptosis. *Clin Chim Acta* (2020) 504:201–8. doi: 10.1016/j.cca.2019.11.035
17. Atianand MK, Caffrey DR, Fitzgerald KA. Immunobiology of Long Noncoding RNAs. *Annu Rev Immunol* (2017) 35:177–98. doi: 10.1146/annurev-immunol-041015-055459
18. Chen YG, Satpathy AT, Chang HY. Gene Regulation in the Immune System by Long Noncoding RNAs. *Nat Immunol* (2017) 18:962–72. doi: 10.1038/ni.3771
19. Wu Z, Gao S, Zhao X, Chen J, Keyvanfar K, Feng X, et al. Long Noncoding RNAs of Single Hematopoietic Stem and Progenitor Cells in Healthy and Dysplastic Human Bone Marrow. *Haematologica* (2019) 104:894–906. doi: 10.3324/haematol.2018.208926
20. Qian Y, Shi L, Luo Z. Long Non-Coding RNAs in Cancer: Implications for Diagnosis, Prognosis, and Therapy. *Front Med (Lausanne)* (2020) 7:612393. doi: 10.3389/fmed.2020.612393
21. Zhen S, Lu J, Chen W, Zhao L, Li X. Synergistic Antitumor Effect on Bladder Cancer by Rational Combination of Programmed Cell Death 1 Blockade and CRISPR-Cas9-Mediated Long Non-Coding RNA Urothelial Carcinoma Associated 1 Knockout. *Hum Gene Ther* (2018) 29:1352–63. doi: 10.1089/hum.2018.048
22. Ren N, Jiang T, Wang C, Xie S, Xing Y, Piao D, et al. LncRNA ADAMTS9-AS2 Inhibits Gastric Cancer (GC) Development and Sensitizes Chemoresistant GC Cells to Cisplatin by Regulating miR-223-3p/NLRP3 Axis. *Aging (Albany NY)* (2020) 12:11025–41. doi: 10.18632/aging.103314
23. Liu J, Yao L, Zhang M, Jiang J, Yang M, Wang Y. Downregulation of LncRNA-XIST Inhibited Development of Non-Small Cell Lung Cancer by Activating miR-335/SOD2/ROS Signal Pathway Mediated Pyroptotic Cell Death. *Aging (Albany NY)* (2019) 11:7830–46. doi: 10.18632/aging.102291
24. Newman AM, Liu CL, Green MR, Gentles AJ, Feng W, Xu Y, et al. Robust Enumeration of Cell Subsets From Tissue Expression Profiles. *Nat Methods* (2015) 12:453–7. doi: 10.1038/nmeth.3337
25. Geeleher P, Cox N, Huang RS. Prrophetic: An R Package for Prediction of Clinical Chemotherapeutic Response From Tumor Gene Expression Levels. *PLoS One* (2014) 9:e107468. doi: 10.1371/journal.pone.0107468
26. Pardoll DM. The Blockade of Immune Checkpoints in Cancer Immunotherapy. *Nat Rev Cancer* (2012) 12:252–64. doi: 10.1038/nrc3239
27. Afrache H, Gouret P, Ainouche S, Pontarotti P, Olive D. The Butyrophilin (BTN) Gene Family: From Milk Fat to the Regulation of the Immune Response. *Immunogenetics* (2012) 64:781–94. doi: 10.1007/s00251-012-0619-z
28. Jorgensen I, Miao EA. Pyroptotic Cell Death Defends Against Intracellular Pathogens. *Immunol Rev* (2015) 265:130–42. doi: 10.1111/imr.12287
29. Xia X, Wang X, Cheng Z, Qin W, Lei L, Jiang J, et al. The Role of Pyroptosis in Cancer: Pro-Cancer or Pro-"Host"? *Cell Death Dis* (2019) 10:650. doi: 10.1038/s41419-019-1883-8
30. Wang WJ, Chen D, Jiang MZ, Xu B, Li XW, Chu Y, et al. Downregulation of Gasdermin D Promotes Gastric Cancer Proliferation by Regulating Cell Cycle-Related Proteins. *J Dig Dis* (2018) 19:74–83. doi: 10.1111/1751-2980.12576
31. Wang J, Shen C, Dong D, Zhong X, Wang Y, Yang X. Identification and Verification of an Immune-Related lncRNA Signature for Predicting the Prognosis of Patients With Bladder Cancer. *Int Immunopharmacol* (2021) 90:107146. doi: 10.1016/j.intimp.2020.107146
32. Tong H, Li T, Gao S, Yin H, Cao H, He W. An Epithelial-Mesenchymal Transition-Related Long Noncoding RNA Signature Correlates With the Prognosis and Progression in Patients With Bladder Cancer. *Biosci Rep* (2021) 41(1). doi: 10.1042/BSR20203944
33. Cui Y, Zhou Z, Chai Y, Che X, Zhang Y. Identification of a Nomogram From Ferroptosis-Related Long Noncoding RNAs Signature to Analyze Overall Survival in Patients With Bladder Cancer. *J Oncol* (2021) 2021:8533464. doi: 10.1155/2021/8533464
34. Gao X, Zhang S, Chen Y, Wen X, Chen M, Wang S, et al. Development of a Novel Six-Long Noncoding RNA Signature Predicting Survival of Patients With Bladder Urothelial Carcinoma. *J Cell Biochem* (2019) 120:19796–809. doi: 10.1002/jcb.29285
35. Sun T, Wu Z, Wang X, Wang Y, Hu X, Qin W, et al. LNC942 Promoting METTL14-Mediated M(6)A Methylation in Breast Cancer Cell Proliferation and Progression. *Oncogene* (2020) 39:5358–72. doi: 10.1038/s41388-020-1338-9
36. Fan H, Yuan J, Li Y, Jia Y, Li J, Wang X, et al. MKL1-Induced lncRNA SNHG18 Drives the Growth and Metastasis of Non-Small Cell Lung Cancer *via* the miR-211-5p/BRD4 Axis. *Cell Death Dis* (2021) 12:128. doi: 10.1038/s41419-021-03399-z
37. Zhang Q, Hao L, Shen Z, Wang F, Han C. MiR-186-5p Suppresses Cell Migration, Invasion, and Epithelial Mesenchymal Transition in Bladder Cancer by Targeting RAB27A/B. *Environ Toxicol* (2021) 36:2174–85. doi: 10.1002/tox.23331
38. Yang N, Gao J, Hou R, Xu X, Yang N, Huang S. Grape Seed Proanthocyanidins Inhibit Migration and Invasion of Bladder Cancer Cells by Reversing EMT Through Suppression of TGF-β Signaling Pathway. *Oxid Med Cell Longev* (2021) 2021:5564312. doi: 10.1155/2021/5564312

39. Gao T, Ji Y. Long Noncoding RNA LINC00707 Accelerates Tumorigenesis and Progression of Bladder Cancer *via* Targeting miR-145/CDCA3 Regulatory Loop. *Urol Int* (2021) 105:891–905. doi: 10.1159/000514388
40. Tao L, Qiu J, Slavin S, Ou Z, Liu Z, Ge J, et al. Recruited T Cells Promote the Bladder Cancer Metastasis *via* Up-Regulation of the Estrogen Receptor β/IL-1/C-MET Signals. *Cancer Lett* (2018) 430:215–23. doi: 10.1016/j.canlet.2018.03.045
41. Redelman-Sidi G, Glickman MS, Bochner BH. The Mechanism of Action of BCG Therapy for Bladder Cancer–a Current Perspective. *Nat Rev Urol* (2014) 11:153–62. doi: 10.1038/nrurol.2014.15
42. Havel JJ, Chowell D, Chan TA. The Evolving Landscape of Biomarkers for Checkpoint Inhibitor Immunotherapy. *Nat Rev Cancer* (2019) 19:133–50. doi: 10.1038/s41568-019-0116-x
43. Charoentong P, Finotello F, Angelova M, Mayer C, Efremova M, Rieder D, et al. Pan-Cancer Immunogenomic Analyses Reveal Genotype-Immunophenotype Relationships and Predictors of Response to Checkpoint Blockade. *Cell Rep* (2017) 18:248–62. doi: 10.1016/j.celrep.2016.12.019

Conflict of Interest: The authors declare that the research was conducted in the absence of any commercial or financial relationships that could be construed as a potential conflict of interest.

Publisher's Note: All claims expressed in this article are solely those of the authors and do not necessarily represent those of their affiliated organizations, or those of the publisher, the editors and the reviewers. Any product that may be evaluated in this article, or claim that may be made by its manufacturer, is not guaranteed or endorsed by the publisher.

Copyright © 2022 Lu, Wu, Liang, Wang and Cai. This is an open-access article distributed under the terms of the Creative Commons Attribution License (CC BY). The use, distribution or reproduction in other forums is permitted, provided the original author(s) and the copyright owner(s) are credited and that the original publication in this journal is cited, in accordance with accepted academic practice. No use, distribution or reproduction is permitted which does not comply with these terms.

frontiers in Immunology

ORIGINAL RESEARCH
published: 24 March 2022
doi: 10.3389/fimmu.2022.805967

A Novel m1A-Score Model Correlated With the Immune Microenvironment Predicts Prognosis in Hepatocellular Carcinoma

Mingxing Zhao[1], *Shen Shen*[2,3]* *and Chen Xue*[2,3]*

[1] Department of Traditional Chinese Medicine, The First Affiliated Hospital of Zhengzhou University, Zhengzhou, China, [2] Gene Hospital of Henan Province, Precision Medicine Center, The First Affiliated Hospital of Zhengzhou University, Zhengzhou, China, [3] Department of Infectious Diseases, The First Affiliated Hospital of Zhengzhou University, Zhengzhou, China

OPEN ACCESS

Edited by:
Katy Rezvani,
University of Texas MD Anderson Cancer Center, United States

Reviewed by:
Shatovisha Dey,
Christiana Care Health System, United States
Wenzhi Guo,
First Affiliated Hospital of Zhengzhou University, China
Giulia Accardi,
University of Palermo, Italy

***Correspondence:**
Shen Shen
fccshenk@zzu.edu.cn
Chen Xue
zzuxuechen001@163.com

Specialty section:
This article was submitted to Cancer Immunity and Immunotherapy, a section of the journal Frontiers in Immunology

Received: 31 October 2021
Accepted: 03 March 2022
Published: 24 March 2022

Citation:
Zhao M, Shen S and Xue C (2022) A Novel m1A-Score Model Correlated With the Immune Microenvironment Predicts Prognosis in Hepatocellular Carcinoma. Front. Immunol. 13:805967. doi: 10.3389/fimmu.2022.805967

RNA methylation plays crucial roles in gene expression and has been indicated to be involved in tumorigenesis, while it is still unclear whether m1A modifications have potential roles in the prognosis of hepatocellular carcinoma (HCC). In this study, we comprehensively analyzed RNA sequencing (RNA-seq) data and clinical information using The Cancer Genome Atlas (TCGA) and Gene Expression Omnibus (GEO) databases. We collected 10 m1A regulators and performed consensus clustering to determine m1A modification patterns in HCC. The CIBERSORT method was utilized to evaluate the level of immune cell infiltration. Principal component analysis was used to construct the m1A-score model. In the TCGA-LIHC cohort, the expression of all 10 m1A regulators was higher in tumor tissues than in normal control tissues, and 8 of 10 genes were closely related to the prognosis of HCC patients. Two distinct m1A methylation modification patterns (Clusters C1 and C2) were identified by the 10 regulators and were associated with different overall survival, TNM stage and tumor microenvironment (TME) characteristics. Based on the differentially expressed genes (DEGs) between C1 and C2, we identified three gene clusters (Clusters A, B and C). C1 with a better prognosis was mainly distributed in Cluster C, while Cluster A contained the fewest samples of C1. An m1A-score model was constructed using five m1A regulators related to prognosis. Patients with higher m1A scores showed a poorer prognosis than those with lower scores in the TCGA-LIHC and GSE14520 datasets. In conclusions, our study showed the vital role of m1A modification in the TME and progression of HCC. Quantitative evaluation of the m1A modification patterns of individual patients facilitates the development of more effective biomarkers for predicting the prognosis of patients with HCC.

Keywords: HCC, m1A modification, tumor microenvironment, prognosis, biomarker

INTRODUCTION

Specific chemical modifications, such as modifications of DNA and proteins, are classical ways of regulating molecular function. Various regulators responsible for regulating protein and DNA modifications are potential targets of cancer treatment (1). Compared with protein and DNA modifications, RNA modification is a new frontier of this area (1). Recently, with the advancement of next-generation sequencing technologies, RNA modifications have gained much attention because they participate in several physiological and pathological processes. To date, more than 150 RNA modifications have been identified (2, 3). Among them, RNA methylation is the most extensively studied type. Many studies have indicated that RNA methylation plays an essential role in diverse physiological processes in human cancers (4). RNA methylation plays crucial roles in gene expression and has been proven to be involved in tumorigenesis by regulating cancer cell proliferation, invasion, metastasis, and drug resistance.

N^1-methyladenosine (m1A) is an important posttranscriptional RNA modification that was first discovered in tRNA in 1966 (5). Decades later, m1A was found in tRNA (5), rRNA (6, 7), mitochondrial RNA (8, 9) and mRNA (10). Under the action of a methyltransferase, m1A can be formed by adding a methyl group at the N1 position of adenosine, which blocks Watson-Crick base pairing, affecting transcription and protein-RNA interactions (11). m1A is a dynamic and reversible RNA modification that is mediated by RNA-modifying proteins called "writers" (methyltransferases) catalysing the formation of methylation, "readers" (modified RNA-binding proteins) reading the information of methylation modification, and "erasers" (demethylases) detecting the methylation modification of RNA. Emerging data suggest that m1A regulators play important roles in tumorigenesis and progression. Silencing TRMT10C has been found to inhibit the malignant characteristics of ovarian cancer and cervical cancer tumor cells (12). The writer TRMT6 was reported to be significantly upregulated in hepatocellular carcinoma (HCC) tissues compared to adjacent tissues, and higher expression of TRMT6 was correlated with poor prognosis in HCC patients (13). The eraser ALKBH3 contributes to lung cancer development and correlates with recurrence-free survival in adenocarcinoma (14). However, previous studies have mainly focused on only one m1A regulator in cancer. Therefore, comprehensive analysis of the genetic variations in these m1A regulators and their relationships with the tumor microenvironment (TME) and clinical characteristics will enhance our understanding of the molecular mechanisms of m1A in cancer.

Here, we integrated the gene expression information and clinical data of HCC patients to comprehensively evaluate the genetic variations in 10 m1A regulators, m1A modification patterns, and the association between m1A modification patterns and TME characteristics. Additionally, we generated an m1A model based on m1A regulators and related genes that can quantify the m1A modification pattern in individual patients. The m1A score is closely associated with tumor immune microenvironment (TIME) characterization and displays potential in predicting the prognosis of patients with HCC.

METHODS

Data Source and Preprocessing

RNA sequencing (RNA-seq) data and clinical information were downloaded from the Gene Expression Omnibus (GEO) and The Cancer Genome Atlas (TCGA) databases. mRNA, single nucleotide variation (SNV), copy number variation (CNV) and clinical data were obtained from the TCGA database (https://portal.gdc.cancer.gov/). The GSE14520 cohort from GEO (https://www.earthobservations.org) was included for further analysis. Patients without complete survival data were excluded from further analysis.

CIBERSORT

CIBERSORT is a machine learning approach for characterizing the cell composition of a tumor biopsy from gene expression data (http://cibersort.stanford.edu) and is a useful method for the high-throughput characterization of various cell types, such as tumor-infiltrating leukocytes (15). Usually, a feature matrix containing 22 functionally defined human immune subgroups (LM22) is used for verification. Here, we used the CIBERSORT method to calculate the proportions of 22 immune cells in the two m1A clusters.

Construction and Validation of a Prognostic Risk Model

First, we identified the differentially expressed genes (DEGs) between distinct m1A clusters. The survival data and DEGs were analyzed by univariate Cox regression analysis. Second, least absolute shrinkage and selection operator (LASSO) Cox regression analysis was utilized to further narrow down the DEGs associated with prognosis. Finally, we performed multivariate Cox regression analysis to establish the prognostic model. The risk score was calculated by summing the risk coefficient of each gene.

Generation of the m1A-Score Model

To quantify the m1A modification patterns of individual patients with HCC, we generated a scoring system named the m1A-score model. The procedures for establishing the m1A-score model were as follows. First, we performed principal component analysis to construct the m1A-score model. Principal components 1 and 2 were used as signature scores for each sample. The calculation formula was as follows: m1A-score = $\Sigma PC1i + PC2i$ where i is the expression of the 5 genes (PON1, CFHR3, CAD, NT5DC2 and CDC20) that were screened from the prognostic risk model and related to the m1A clusters.

Single-Sample Gene Set Enrichment Analysis (ssGSEA)

The ssGSEA method is used to calculate an enrichment score that represents the degree of absolute enrichment of a gene set

(16). In this study, we performed gene set variation analysis (GSVA) using the GSVA (17) R package and the c2.cp.kegg.v7.0.symbols.gmt gene set. In addition, we used the limma package to perform differential analysis on the results of GSVA. The Pheatmap package was used to draw a heatmap.

Cell Culture

The normal human liver cell line L02 and human liver cancer cell line HepG2 were obtained from the Chinese Academy of Sciences (Shanghai, China). The cell lines were maintained in Dulbecco's modified Eagle's medium (DMEM, Gibco USA) supplemented with 10% foetal bovine serum and 1% penicillin. All the cells were cultured at 37°C in a humidified incubator with a 5% CO2 atmosphere.

Quantitative Reverse-Transcription PCR (qRT-PCR)

Total RNA was isolated from the L02 and HepG2 cell lines using TRIzol reagent (Invitrogen) and then reverse transcription was performed using the PrimeScript RT-PCR Kit (Takara, Japan) according to the manufacturer's instructions. Relative mRNA levels were detected by an ABI7500fast PCR instrument. GAPDH was used as the internal control. The relative expression levels of the m1A-related regulator genes were normalized to the expression of GAPDH, which was calculated using the $2^{-\Delta\Delta Ct}$ method.

Statistical Analysis

The statistical analyses in this study were carried out with SPSS 25 (IBM Corporation, Armonk NY) and R software (version 3.5.1). Student's t-test was utilized to estimate the differences between two groups. For comparisons of more than two groups, one-way analysis of variance was used. Kaplan–Meier survival analysis and the log-rank test were used to establish survival curves and compare the differences. All P values were two-sided, and $P < 0.05$ was considered statistically significant.

RESULTS

Features of Genetic Variations in m1A Regulators in HCC

A total of 10 m1A RNA modification regulators (including TRMT10C, TRMT61B, TRMT6/61A, YTHDF1, YTHDF2, YTHDF3, YTHDC1, ALKBH1, and ALKBH3) were included in the current study based on the findings of previously published studies (9, 18, 19). To describe the landscape of genetic alterations in m1A regulators in HCC, we assessed the degree of CNVs of individual m1A regulators. According to the degree of CNVs, CNVs were divided into three types: amplification, diploid and deletion. The proportions of the 10 genes with amplifications and deletions are shown in **Table 1**. According to the types of CNVs of individual regulators, we further explored the correlation between the expression of each regulator and CNVs, and the results are shown in **Figure S1A**. Additionally, in the 364 TCGA-liver hepatocellular carcinoma (LIHC) samples, most SNV mutations occurred in the TRMT10C, YTHDF1 and YTHDC1 genes (**Figure S1B**). All these results suggested that the genetic variations in m1A regulators might lead to expression and functional changes in those regulators that play a critical role in the occurrence, progression and prognosis of HCC.

Changes in m1A Regulators Were Correlated With the Prognosis of HCC Patients

Among the 10 m1A regulators, there were 4 modification writers, 4 readers and 2 erasers. We explored the expression of the 10 m1A regulators in tumor tissues compared with normal control tissues from the TCGA-LIHC cohort. We discovered that all regulators were more highly expressed in tumor tissues than in normal tissues (**Figure 1A**). Consistent with the expression in the TCGA-LIHC cohort, a total of 9 genes (Trmt61B, TRMT6, TRMT61A, YTHDF1, YTHDF2, YTHDF3, YTHDC1, ALKBH1, and ALKBH3) were highly expressed in the HepG2 cell line compared with the normal liver cell line L02. The expression level of TRMT10C was not significantly different between the HepG2 and L02 cell lines (**Figure 1B**). Furthermore, we performed univariate Cox analysis on the 10 genes by extracting clinical information from TCGA-LIHC, and the results showed that 8 of the 10 genes were closely related to the prognosis of HCC patients (**Figure 1C**). To comprehensively explain the associations among the 10 m1A regulators, we constructed a regulatory network by unsupervised cluster analysis to describe the interactions of m1A regulators and their influence on the prognosis of LIHC patients. These regulator genes were classified into 4 distinct clusters, as illustrated in **Figure 1D**.

TABLE 1 | The proportion of 10 genes related to m1a modification that have undergone amplification and deletion.

		diploid	deletion	CNV-sum	amplification %	Deletion%
writer	TRMT10C	719	14	768	4.557291667	1.822916667
	TRMT61B	717	9	767	5.345501956	1.173402868
	TRMT6	657	25	773	11.77231565	3.234152652
	TRMT61A	645	108	768	1.953125	14.0625
reader	YTHDF1	665	100	768	0.390625	13.02083333
	YTHDF2	644	115	769	1.300390117	14.95448635
	YTHDF3	563	22	769	23.92717815	2.860858257
	YTHDC1	640	117	768	1.432291667	15.234375
eraser	ALKBH1	653	101	770	2.077922078	13.11688312
	ALKBH3	721	31	777	3.217503218	3.98970399

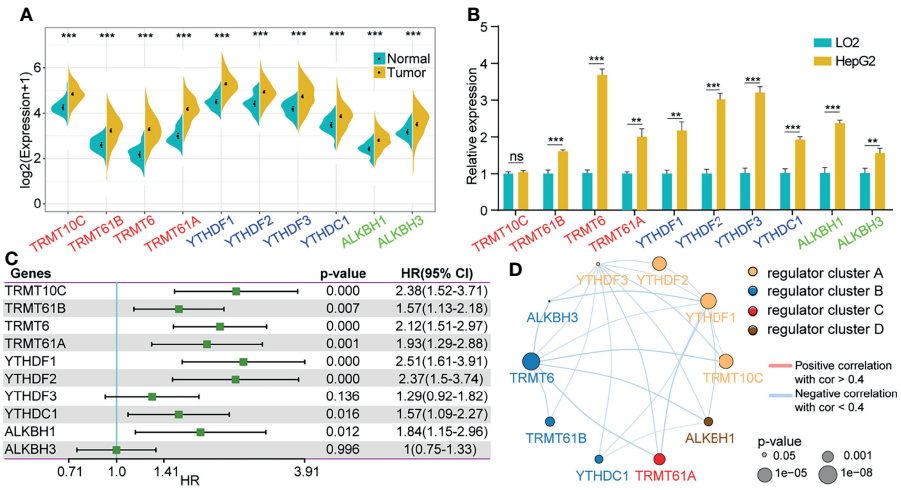


FIGURE 1 | Changes in m1A regulators were correlated with the prognosis of HCC patients. **(A)** Expression of 10 m1A-related genes in tumor tissues compared to normal liver tissues from the TCGA-LIHC cohort. **(B)** Expression of 10 m1A-related genes in the HepG2 cell line compared with the normal cell line L02. **(C)** Univariate cox analysis of the 10 regulators. **(D)** Construction of the m1A regulatory network. **P < 0.01, ***P < 0.001; ns, nonsense.

m1A Modification Patterns Mediated by 10 Regulators

We classified patients with different m1A modification patterns based on the expression of the 10 m1A regulators using the ConsensusClusterPlus R package. We set the parameters clusterAlg = "pam" and distance = "euclidean" to determine the optimal number of clusters according to the cumulative distribution function (CDF) and observe the CDF delta from the area curve. When the cluster number was 2, there was a relatively stable clustering result (**Figure 2A**); thus, we choose k=2 to obtain two distinct m1A clusters (C1 and C2) (**Figure 2B**). Further analysis of the prognostic characteristics of these two subtypes showed that there were prognostic differences between them, and C1 tended to have a prominent survival advantage (**Figure 2C**).

To further explore the biological behaviours of the m1A modification phenotypes, we focused on the TME cell infiltration characteristics of different m1A modification patterns. We used the CIBERSORT method to calculate the proportions of 22 immune cells for the two subtypes (**Figure 2D**). We also compared the score differences of 10 pathways related to tumor abnormalities in the different subtypes. The results showed that C2 patients with a poor prognosis had a higher enrichment score in the 8 pathways of the cell cycle, HIPPO, NOTCH, NRF1, TGF-beta, RAS, TP53 and WNT than C1 patients (**Figure 2E**). Additionally, we calculated the enrichment scores of 187 pathways for each sample by ssGSEA. The results showed that C1 was enriched in pathways mainly related to metabolism, and C2 was enriched in 18 pathways mainly related to the cell cycle and tumors (**Figure S2**).

Association of m1A Modification Patterns With Clinical Characteristics of HCC Patients

To reveal the role of m1A modification patterns in the progression of HCC, we compared the various clinical characteristics of distinct patterns. We found that there was no difference in the survival status of patients with modified m1A patterns (**Figure 3A**, P>0.05). In terms of sex, T stage and stage, there were significant differences in the m1A-modified subtypes (**Figures 3B–D**, all P<0.05). There was no difference in the grade, N stage, M stage, or age of the m1A-modified subtypes (**Figures 3E–H**, all P>0.05). This finding suggests that m1A modification patterns might be markedly related to the prognosis and progression of HCC.

Identification of Gene Clusters Related to m1A Modification Patterns

To determine which genes were associated with the m1A modification patterns, we used the limma package to identify the DEGs between m1A clusters C1 and C2. The volcano map of the DEGs is shown in **Figure 4A**. Then, we identified three gene clusters (clusters A, B and C) related to the DEGs through unsupervised cluster analysis (**Figure 4B**). We also found that C1 with a better prognosis was mainly distributed in Cluster C, while Cluster A contained the fewest samples of C1 (**Figure 4B**). Furthermore, we explored the expression of these 10 genes in the m1A clusters and m1A-related gene clusters (**Figures 4C, D**). Survival analysis showed that patients in Cluster A tended to have the worst prognosis, and those in Cluster C had the best prognosis (**Figure 4E**). Then, we performed GSVA on these three gene clusters by calculating the average enrichment score of the pathways in each gene cluster. The top 20 pathways with the largest differences were selected for visualization. The results showed that Cluster A was mainly enriched in nonhomologous end-joining and ribosomes, while Cluster B was mainly enriched in lysine degradation, limonene and pinene degradation, circadian rhythm mammals, and endometrial cancer. Cluster C was enriched in autoimmune thyroid disease, oxidative phosphorylation, Parkinson's disease, Alzheimer's disease,

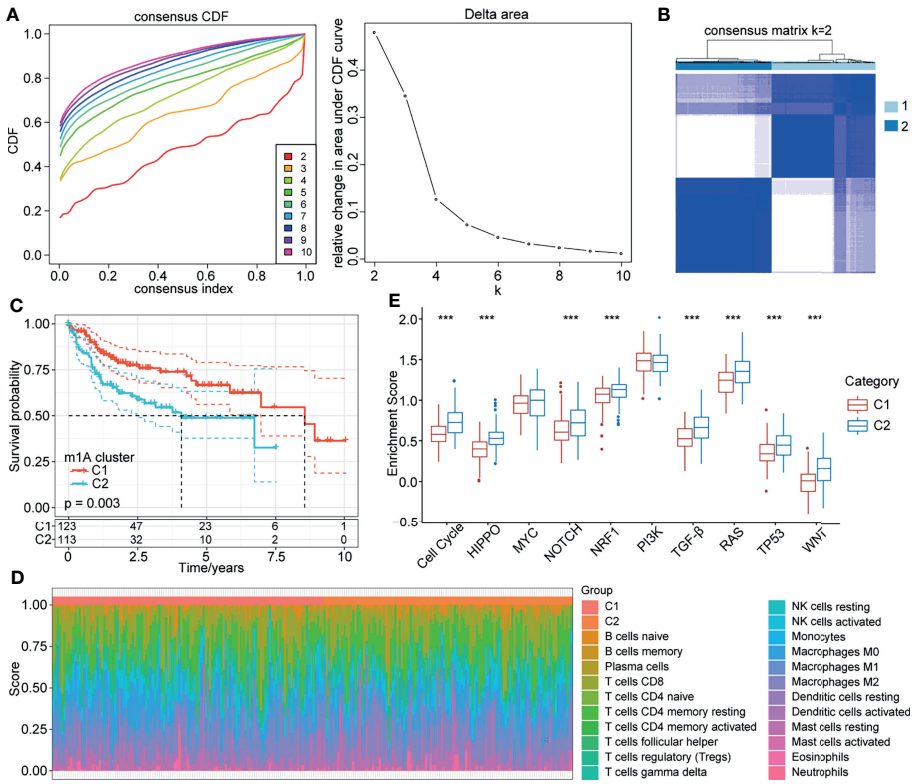


FIGURE 2 | m1A modification patterns mediated by 10 regulators. **(A)** CDF curve and CDF delta area curve in TCGA-LIHC cohort. **(B)** Clustering heatmap when consensus k=2. **(C)** Kaplan-Meier curve of the prognostic relationship between the two clusters in the TCGA-LIHC cohort. **(D)** Proportions of 22 immune cell components in samples in C1 and C2. **(E)** Differences in the scores of 10 pathways related to tumor abnormalities in C1 and C2. ***P < 0.001.

Huntington's disease, RNA polymerase, proteasome, and cardiac muscle contraction (**Figure 4F**).

Construction of a Prognostic Model Based on the DEGs Between m1A-Related Gene Clusters

To identify potential prognostic biomarkers among the m1A-related genes, we constructed a prognostic risk model. First, we randomly divided 232 samples from the TCGA-LIHC dataset into a training set (n=162) and a validation set (n=70). The sample information is shown in **Table 2**. In the training set, 853 DEGs and survival data were analyzed, and 292 genes associated with HCC prognosis were identified by univariate Cox regression analysis. Then, LASSO Cox regression analysis was used to further narrow down the 292 DEGs. The change trajectory of each independent variable is shown in **Figure 5A**. With the gradual increase in lambda, the number of independent variable coefficients that tended to 0 increased (**Figure 5B**). The model reached the optimum when lambda = 0.1187. For this reason, we chose lambda = 0.1187, and finally, 5 genes were screened for further analysis. Then, we performed multivariate Cox regression analysis to establish the prognostic model. The risk score was calculated by summing the risk coefficient of each gene. The final risk score formula was as follows:

$$\text{Risk score} = -0.048 * \text{PON1} - 0.105 * \text{CFH}R3 + 0.290 * \text{CAD} + 0.053 * \text{NT5DC2} + 0.156 * \text{CDC20}$$

Next, we evaluated the sensitivity and specificity of the five-gene model using the area under the curve (AUC) of a time-dependent receiver operating characteristic (ROC) curve (**Figure 5C**). The prognoses of the high- and low-risk groups were significantly different (P < 0.0001; **Figure 5D**). Additionally, to validate the stability of the five-gene-based model in predicting the overall survival of patients with HCC, we assessed the risk model in the TCGA-LIHC validation set and the whole TCGA-LIHC dataset. In TCGA-LIHC validation dataset, the AUCs at 1, 3, and 5 years were 0.71, 0.69, and 0.74, respectively (**Figure 5E**), and the high-risk group presented a significantly poorer prognosis than the low-risk group (**Figure 5F**). Similarly, the five-gene model also showed excellent predictive efficiency, and the prognosis was poorer for high-risk patients than for low-risk patients in the whole TCGA-LIHC dataset (**Figures 5G, H**).

Generation of the m1A-Score Model

The above results suggested the impact of m1A-related genes on the prognosis of patients with HCC. To systematically analyse this impact on individuals, we established a scoring system

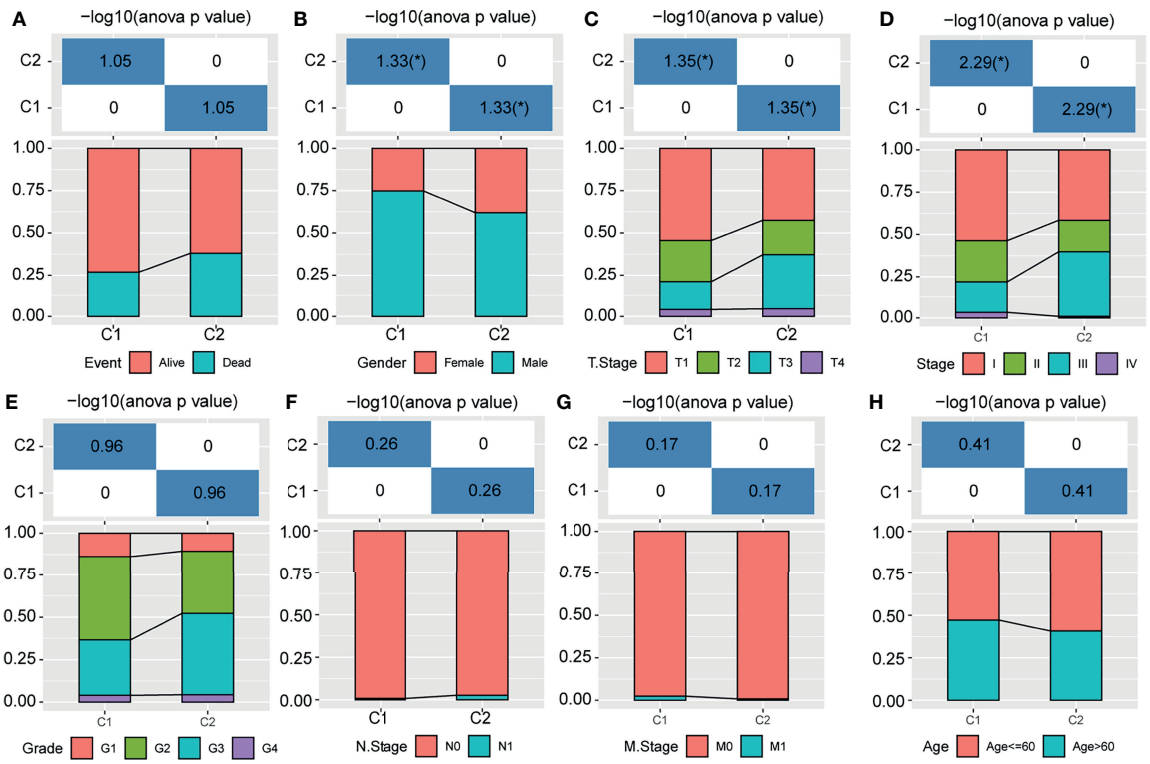


FIGURE 3 | Distribution of m1A-related subtypes in clinical features. **(A–H)** The survival status, sex, T stage, stage, grade, N stage, M stage, and age of the m1A-modified subtypes. *P < 0.05.

named the m1A-score model. First, we performed principal component analysis to construct the m1A-score model. Principal components 1 and 2 were used to calculate the signature scores for each sample. The calculation formula was as follows: m1A score = $\Sigma PC1i + PC2i$ where i represents the expression of 5 genes (PON1, CFHR3, CAD, NT5DC2 and CDC20). We assessed the m1A-score value of each sample based on the expression levels of these 5 genes in the sample. Then, we performed ROC analysis for the prognostic classification of the m1A score model (**Figure 6A**). The results of survival analysis showed that the prognosis of patients in the high- and low-risk groups was different (**Figure 6A**). To further determine the robustness of this model, the TCGA training dataset and GSE14520 dataset were analyzed. Consistent with the results of the TCGA-LIHC training dataset, patients with high m1A scores tended to have poorer survival than patients with low m1A scores, and the AUC values were all above 0.6 for the entire TCGA-LIHC dataset (**Figure 6B**) and the GSE14520 dataset (**Figure 6C**). The evidence collectively suggested that the m1A-score model may be a stable scoring tool for predicting the survival of HCC patients.

Correlation Analysis of Immune Regulation and the m1A Score

To further investigate the association between the m1A score value and the TME of HCC, we evaluated the levels of immune cell infiltration and the expression of immune checkpoint genes in distinct m1A score groups. We found that approximately 31.82% of the 22 immune cells were significantly different between the two groups using the CIBERSORT method (**Figure 7A**). Then, the expression of 37 immune checkpoints published in a previous study (20) was assessed in the two groups (**Figure 7B**). The results showed that approximately 56.76% (21) of the 37 immune checkpoints had significant differences. For example, the high-m1A score group showed higher expression levels of CD200, NRP1, LAIR1, TNFSF4, ICOS CTLA4, HAVCR2, CD276, PDCD1, LGALS9, IDO1, CD70, TNFSF9, TNFRSF9, TNFSF18, TNFSF15, CD86, and CD44 (**Figure 7B**), whereas the lowm1A score group was more correlated with high expression of IDO2. The results above indicate that the patients in the high-m1A score group may respond poorly to immune checkpoint drugs, which needs to be further researched.

Predictive Performance of the m1A-Score Model in Clinical Application

After confirming the correlation of the m1A score and TME cell infiltration characteristics, it was subsequently investigated whether the scoring model could be applied to predict the prognosis of patients with different clinical features. We found that the m1A score was markedly correlated with prognosis in patients older than or younger than 60 years of age, of different sexes, and with different TNM stages, grades and stage statuses (**Figure S3**, all P<0.01).

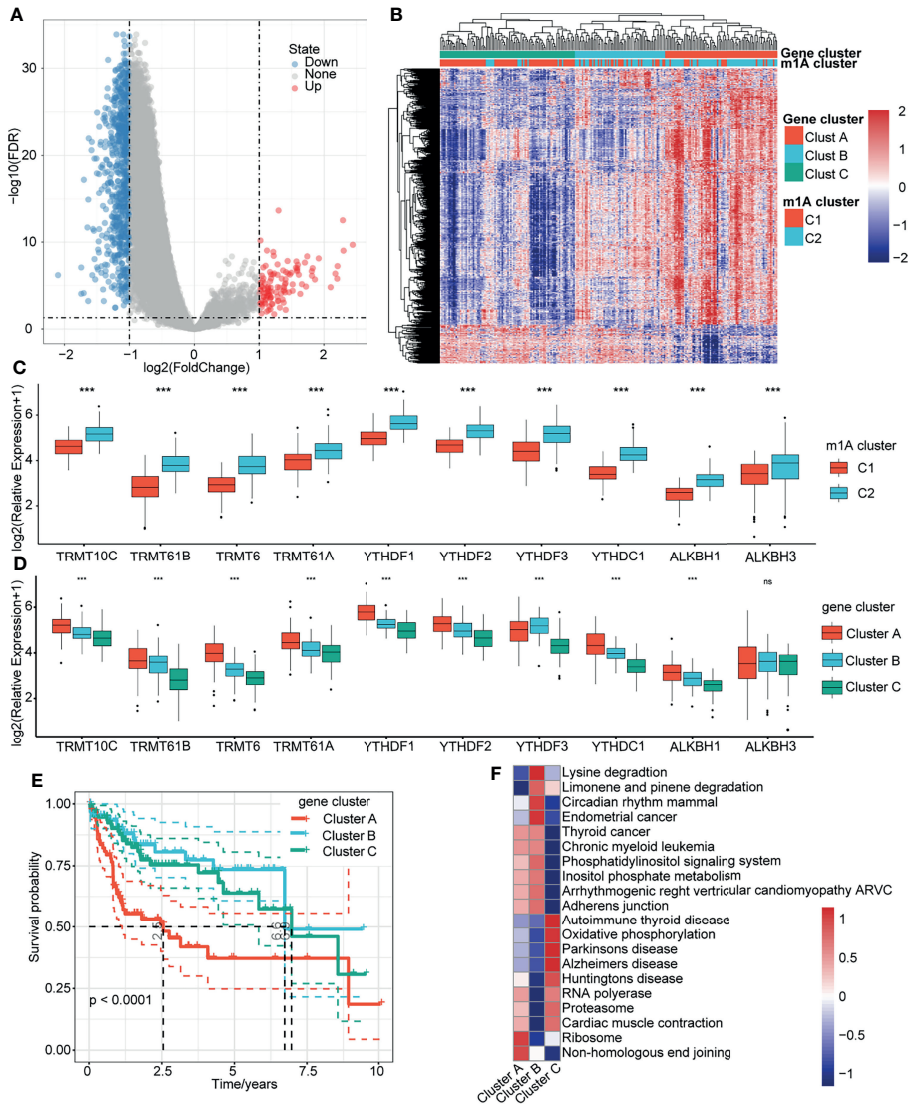


FIGURE 4 | Gene clusters related to m1A modification patterns. **(A)** Volcano map of the DEGs in m1A Clusters C1 and C2. **(B)** Heatmap of m1A-related DEG unsupervised clustering. **(C)** Distribution of 10 m1A regulator genes in C1 and C2. **(D)** Distribution of 10 m1A regulator genes in gene clusters A, B, and C. **(E)** Overall survival differences among the three gene clusters. **(F)** Enrichment pathways of the three gene clusters. ***P < 0.001; ns, nonsense.

The m1A-Score Model Might Serve as an Independent Prognostic Biomarker in Clinical Application

To identify whether the m1A-score model could serve as an independent biomarker for prognosis, we performed univariate and multivariate Cox regression analyses of clinical data to assess the relevant hazard ratios (HRs) and 95% confidence intervals (CIs) in the entire TCGA-LIHC dataset. The results of univariate regression analysis revealed that the m1A score was significantly related to survival (**Figure 8A**). Multivariate Cox regression analysis showed that the m1A score was an independent risk factor for prognosis (**Figure 8B**). The above findings showed that the m1A-score model has good predictive performance for the prognosis of patients in clinical application.

Association Between the m1A Score and KEGG Pathways

To explore the correlation between biological behaviours and different m1A scores, we performed functional annotations of TCGA-LIHC samples using ssGSEA *via* the GSVA R package. After we obtained the ssGSEA score for different functions in each sample, we further explored the correlation between these functions and the m1A score (correlation coefficient >=0.4). Finally, a total of 36 KEGG pathways were negatively correlated with the sample m1A scores (for example, peroxisome), and 2 pathways (including cell cycle and spliceosome) were positively correlated with the sample m1A scores (**Figure 8C**). Cluster analysis based on the 36 KEGG pathways was performed according to their enrichment scores.

TABLE 2 | The sample information in training set and validation set.

Clinical Features	TCGA-train	TCGA-test	P
OS			
0	115	41	0.08966
1	47	29	
T stage			
T1	83	32	0.4374
T2	38	13	
T3	35	21	
T4	6	4	
Stage			
I	82	31	0.3966
II	37	13	
III	41	24	
IV	2	2	
Grade			
G1	20	9	0.5613
G2	69	32	
G3	64	28	
G4	9	1	
Gender			
Female	22	50	1
Male	48	112	
Age			
>60	39	89	1
<=60	31	73	

We found that the pathways of the cell cycle and spliceosome increased with increasing m1A scores (**Figure 8D**).

DISCUSSION

m1A regulators govern m1A RNA methylation functions. Some research groups have reported that m1A regulators play important roles in the progression of tumorigenesis. In this study, we described the genetic variations in m1A regulators in HCC and found that the changes in m1A regulators were correlated with the prognosis of HCC patients. Similarly, Shi et al. (18) observed a high mutation frequency in the 10 m1A regulators using TCGA-LIHC dataset and identified four regulators that were significantly correlated with prognosis. In ovarian cancer, Liu et al. (21) found that three different m1A modification patterns which could predict patient survival, stage and grade. In pancreatic cancer, m1A regulator genetic variations are related to clinical stage, and CNVs are closely associated with the expression of m1A regulators. Notably, the expression level of ALKBH1 is closely associated with the prognosis of patients with pancreatic cancer (22). Li et al. (23) systematically analyzed the association of the molecular alterations of m1A regulators and the clinical data of 33 cancer types from the TCGA. This group found that m1A regulatory protein expression was correlated with various carcinogenic pathways and patient overall survival, indicating that m1A regulators have the potential for prognostic prediction in many types of cancer and may now provide new treatment strategies (23).

Increasing evidence has revealed that RNA methylation modifications influence the formation of the TME and the immune cell-infiltrating characteristics of the tumor; thus, the association between the RNA modification represented by m6A and the TME has aroused extensive interest from researchers (24). Zhang et al. (25) identified three m6A modification patterns and found that the immune cell-infiltrating features under these three patterns were highly consistent with the well-known immune phenotypes, namely, the immune-inflamed, immune-desert and immune-excluded phenotypes. In colon cancer, Chong et al. (26) also identified three m6A modification

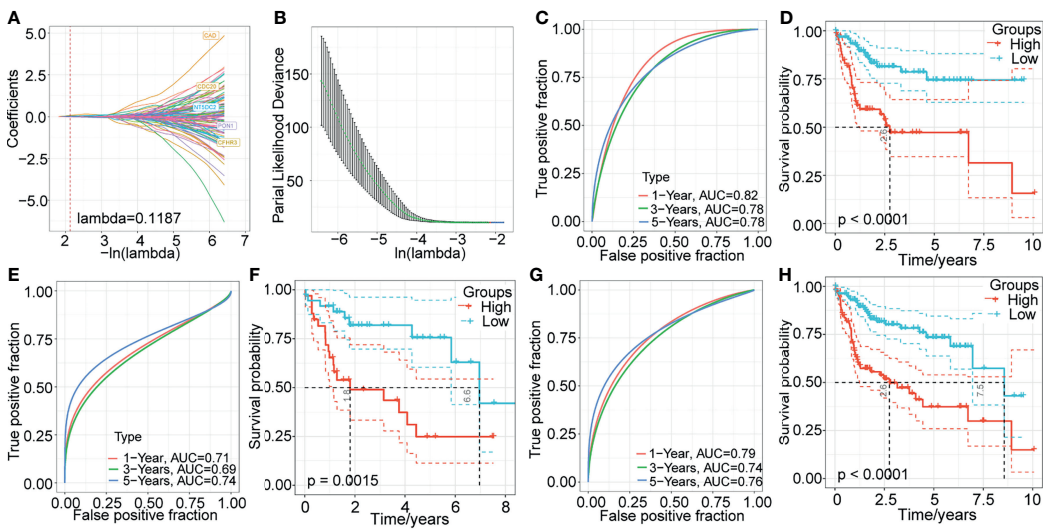


FIGURE 5 | Construction and validation of a prognostic model based on the DEGs between m1A-related gene clusters. **(A)** The change trajectory of each independent variable. **(B)** The confidence interval under each lambda. **(C–H)** Time-dependent ROC curve measuring the predictive value of the five-gene model in the TCGA training set, TCGA-LIHC validation dataset, and whole TCGA-LIHC dataset. Kaplan-Meier curves for overall survival by the 5-gene model in the TCGA training set, TCGA-LIHC validation dataset, and whole TCGA-LIHC dataset.

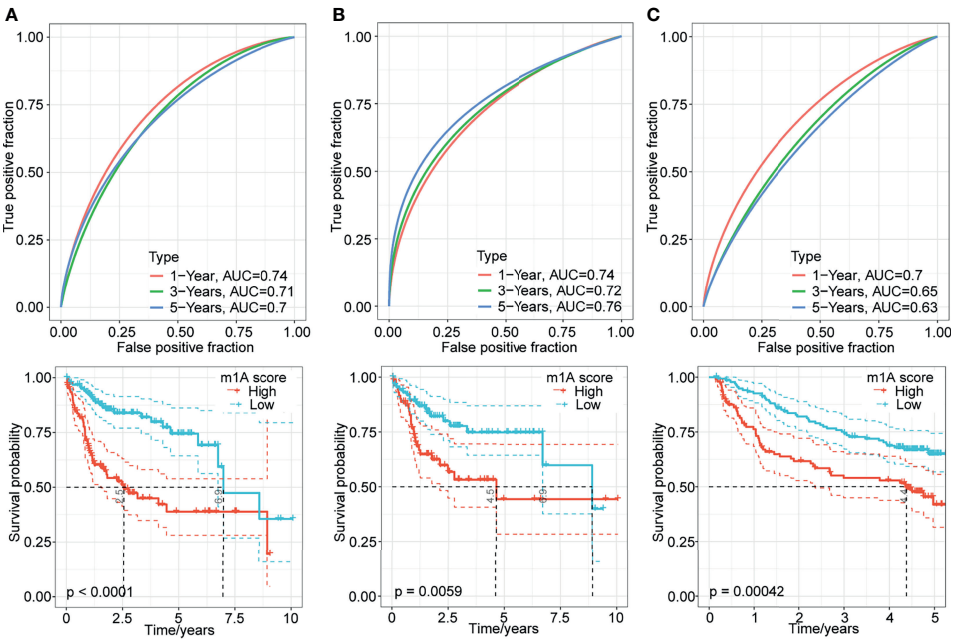


FIGURE 6 | Generation of the m1A-score model. **(A–C)** Time-dependent ROC analysis and Kaplan-Meier analysis of the five-gene model in the TCGA-LIHC training dataset, entire TCGA-LIHC dataset, and GSE14520 dataset.

patterns, and those patterns were highly consistent with the three immune phenotypes, suggesting that m6A was correlated with the diversity and complexity of the TME. Yi et al. (27) reported that m6A regulators were significantly correlated with PD-L1 expression and distinct immune cell infiltration in head and neck squamous cell carcinomas. The association between m6A modification patterns and the TME was also assessed in lung adenocarcinoma and gliomas (28, 29). Nevertheless, the role of m1A in the TME is still unclear. Here, we identified 2 distinct m1A modification patterns (Clusters 1 and 2) based on the

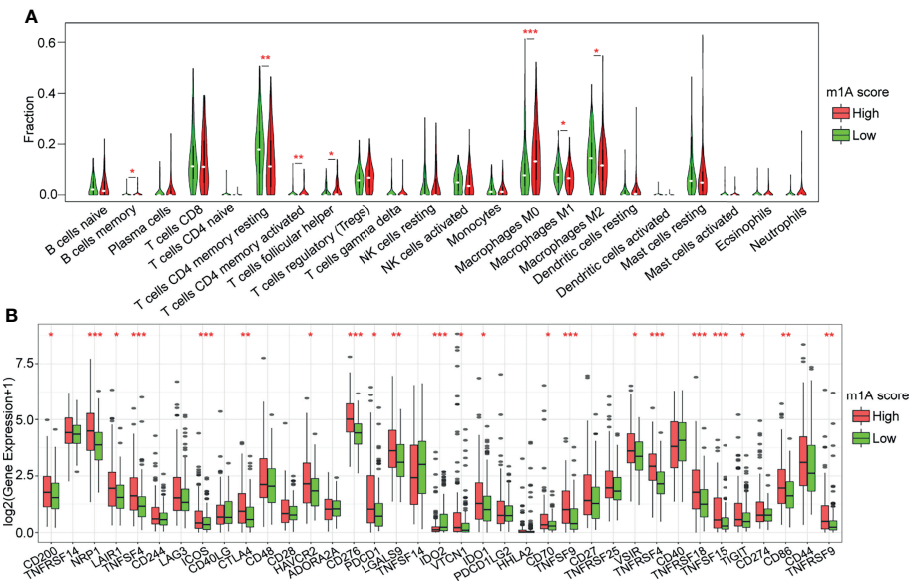


FIGURE 7 | Correlation analysis of immune regulation and the m1A score. **(A)** Distribution of 22 types of immune cells in the high- and low-m1A score groups. **(B)** Expression of 37 immune checkpoints in the high- and low-m1A score groups. *P < 0.05, **P < 0.01, ***P < 0.001.

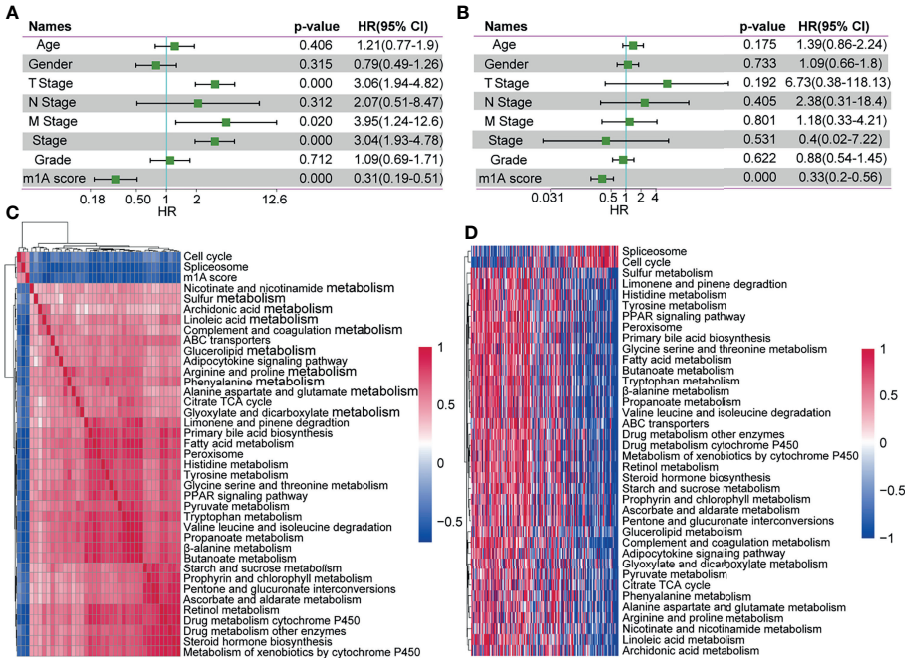


FIGURE 8 | The m1A-score model might serve as an independent prognostic biomarker in clinical application. **(A, B)** Univariate regression analysis and multivariate regression analysis of the m1A score in the whole TCGA-LIHC cohort. **(C)** Clustering of correlation coefficients between KEGG pathways with a risk score correlation greater than 0.4. **(D)** KEGG pathway analysis with a risk score correlation greater than 0.4. As the m1A score increases, the ssGSEA in each sample changes in score.

expression of 10 m1A regulators. We extracted clinical information from TCGA-LIHC and found that patients in Cluster 1 had longer overall survival times than those in Cluster 2. We also compared the immune cell infiltration characteristics of different m1A modification patterns using the CIBERSORT method. After construction of the m1A-score model, we evaluated the immune cell infiltration levels and expression of immune checkpoint genes in distinct m1A score groups. We found that several of the 22 immune cells were significantly different between the two groups. In addition, the expression of 37 immune checkpoints was significantly different between the two groups. These results might enhance our understanding of the function of m1A modification in the formation of a complex TME in HCC.

Here, we not only identified the m1A modification patterns of HCC samples from the TCGA and GEO databases but also constructed the m1A-score model and systematically analyzed its impacts on individuals. The results of ROC and survival analyses indicated that the m1A-score model could serve as a stable scoring tool for predicting the survival of HCC patients. Additionally, analysis of the clinical information of the entire TCGA-LIHC dataset to determine the HR showed that the m1A-score model was an independent biomarker for prognosis in clinical application. Conclusively, evaluating the m1A modification patterns of individual patients with HCC will enhance our understanding of the characteristics of TME infiltration and provide novel ideas for prognostic biomarkers and therapeutic strategies.

CONCLUSION

We identified two distinct m1A modification patterns which were associated with different overall survival and TME characteristics of patients with HCC. In addition, we constructed an m1A-score model to quantitatively evaluate the m1A modification patterns of individual patients which might be served as effective biomarkers for predicting the prognosis of patients with HCC.

DATA AVAILABILITY STATEMENT

The original contributions presented in the study are included in the article/**Supplementary Material**. Further inquiries can be directed to the corresponding authors.

AUTHOR CONTRIBUTIONS

CX conceived and planned the study design. SS and MZ performed formal analysis and data interpretation. MZ wrote the original draft. SS provided critical revisions and contributed to the editing of the paper. All authors read and approved the final manuscript.

FUNDING

This work was supported by grants from the Science and Technology Research Project of Henan Province (202102310115), and Henan Medical Science and Technology Joint Building Program (LHGJ20200387).

ACKNOWLEDGMENTS

We greatly thank the patients and investigators who participated in TCGA and GEO for providing data.

SUPPLEMENTARY MATERIAL

The Supplementary Material for this article can be found online at: https://www.frontiersin.org/articles/10.3389/fimmu.2022.805967/full#supplementary-material

Supplementary Figure 1 | Features of genetic variations in m1A regulators in HCC. **(A)** Correlation between the expression of each regulator and CNVs. **(B)** SNV mutation of m1A regulators.

Supplementary Figure 2 | GSVA of m1A-related patterns.

Supplementary Figure 3 | The m1A-score model was applied to predict the prognosis of HCC patients with different clinical characteristics.

REFERENCES

1. Barbieri I, Kouzarides T. Role of RNA Modifications in Cancer. *Nat Rev Cancer* (2020) 20:303–22. doi: 10.1038/s41568-020-0253-2
2. Boccaletto P, Machnicka MA, Purta E, Piatkowski P, Baginski B, Wirecki TK, et al. MODOMICS: A Database of RNA Modification Pathways. 2017 Update. *Nucleic Acids Res* (2018) 46:D303–7. doi: 10.1093/nar/gkx1030
3. Roundtree IA, Evans ME, Pan T, He C. Dynamic RNA Modifications in Gene Expression Regulation. *Cell* (2017) 169:1187–200. doi: 10.1016/j.cell.2017.05.045
4. Xie S, Chen W, Chen K, Chang Y, Yang F, Lin A, et al. Emerging Roles of RNA Methylation in Gastrointestinal Cancers. *Cancer Cell Int* (2020) 20:585. doi: 10.1186/s12935-020-01679-w
5. RajBhandary UL, Stuart A, Faulkner RD, Chang SH, Khorana HG. Nucleotide Sequence Studies on Yeast Phenylalanine Srna. *Cold Spring Harb Symp Quant Biol* (1966) 31:425–34. doi: 10.1101/SQB.1966.031.01.055
6. Sharma S, Watzinger P, Kötter P, Entian KD. Identification of a Novel Methyltransferase, Bmt2, Responsible for the N-1-Methyl-Adenosine Base Modification of 25S Rrna in Saccharomyces Cerevisiae. *Nucleic Acids Res* (2013) 41:5428–43. doi: 10.1093/nar/gkt195
7. Peifer C, Sharma S, Watzinger P, Lamberth S, Kötter P, Entian KD. Yeast Rrp8p, a Novel Methyltransferase Responsible for M1a 645 Base Modification of 25S Rrna. *Nucleic Acids Res* (2013) 41:1151–63. doi: 10.1093/nar/gks1102
8. Li X, Xiong X, Zhang M, Wang K, Chen Y, Zhou J, et al. Base-Resolution Mapping Reveals Distinct M(1)a Methylome in Nuclear- and Mitochondrial-Encoded Transcripts. *Mol Cell* (2017) 68:993–1005.e9. doi: 10.1016/j.molcel.2017.10.019
9. Safra M, Sas-Chen A, Nir R, Winkler R, Nachshon A, Bar-Yaacov D, et al. The M1a Landscape on Cytosolic and Mitochondrial Mrna at Single-Base Resolution. *Nature* (2017) 551:251–5. doi: 10.1038/nature24456
10. Zhang C, Jia G. Reversible RNA Modification N(1)-Methyladenosine (M(1)a) in Mrna and Trna. *Genomics Proteomics Bioinf* (2018) 16:155–61. doi: 10.1016/j.gpb.2018.03.003
11. Dominissini D, Nachtergaele S, Moshitch-Moshkovitz S, Peer E, Kol N, Ben-Haim MS, et al. The Dynamic N(1)-Methyladenosine Methylome in Eukaryotic Messenger RNA. *Nature* (2016) 530:441–6. doi: 10.1038/nature16998
12. Wang Q, Zhang Q, Huang Y, Zhang J. M(1)a Regulator TRMT10C Predicts Poorer Survival and Contributes to Malignant Behavior in Gynecological Cancers. *DNA Cell Biol* (2020) 39:1767–78. doi: 10.1089/dna.2020.5624
13. Wang Y, Huang Q, Deng T, Li BH, Ren XQ. Clinical Significance of TRMT6 in Hepatocellular Carcinoma: A Bioinformatics-Based Study. *Med Sci Monit* (2019) 25:3894–901. doi: 10.12659/MSM.913556
14. Tasaki M, Shimada K, Kimura H, Tsujikawa K, Konishi N. ALKBH3, a Human Alkb Homologue, Contributes to Cell Survival in Human Non-Small-Cell Lung Cancer. *Br J Cancer* (2011) 104:700–6. doi: 10.1038/sj.bjc.6606012
15. Chen B, Khodadoust MS, Liu CL, Newman AM, Alizadeh AA. Profiling Tumor Infiltrating Immune Cells With CIBERSORT. *Methods Mol Biol* (2018) 1711:243–59. doi: 10.1007/978-1-4939-7493-1_12
16. Barbie DA, Tamayo P, Boehm JS, Kim SY, Moody SE, Dunn IF, et al. Systematic RNA Interference Reveals That Oncogenic KRAS-Driven Cancers Require TBK1. *Nature* (2009) 462:108–12. doi: 10.1038/nature08460
17. Subramanian A, Tamayo P, Mootha VK, Mukherjee S, Ebert BL, Gillette MA, et al. Gene Set Enrichment Analysis: A Knowledge-Based Approach for Interpreting Genome-Wide Expression Profiles. *Proc Natl Acad Sci USA* (2005) 102:15545–50. doi: 10.1073/pnas.0506580102
18. Shi Q, Xue C, Yuan X, He Y, Yu Z. Gene Signatures and Prognostic Values of M1a-Related Regulatory Genes in Hepatocellular Carcinoma. *Sci Rep* (2020) 10:15083. doi: 10.1038/s41598-020-72178-1
19. Dai X, Wang T, Gonzalez G, Wang Y. Identification of YTH Domain-Containing Proteins as the Readers for N1-Methyladenosine in RNA. *Anal Chem* (2018) 90:6380–4. doi: 10.1021/acs.analchem.8b01703
20. Charoentong P, Finotello F, Angelova M, Mayer C, Efremova M, Rieder D, et al. Pan-Cancer Immunogenomic Analyses Reveal Genotype-Immunophenotype Relationships and Predictors of Response to Checkpoint Blockade. *Cell Rep* (2017) 18:248–62. doi: 10.1016/j.celrep.2016.12.019
21. Liu J, Chen C, Wang Y, Qian C, Wei J, Xing Y, et al. Comprehensive of N1-Methyladenosine Modifications Patterns and Immunological Characteristics in Ovarian Cancer. *Front Immunol* (2021) 12:746647. doi: 10.3389/fimmu.2021.746647
22. Zheng Q, Yu X, Zhang Q, He Y, Guo W. Genetic Characteristics and Prognostic Implications of M1a Regulators in Pancreatic Cancer. *Biosci Rep* (2021) 41:BSR20210337. doi: 10.1042/BSR20210337
23. Li J, Zhang C, Yuan X, Cao Y. Molecular Characteristics of N1-Methyladenosine Regulators and Their Correlation With Overall Cancer Survival. *DNA Cell Biol* (2021) 40:513–22. doi: 10.1089/dna.2020.6214
24. Zhou Y, Kong Y, Fan W, Tao T, Xiao Q, Li N, et al. Principles of RNA Methylation and Their Implications for Biology and Medicine. *BioMed Pharmacother* (2020) 131:110731. doi: 10.1016/j.biopha.2020.110731
25. Zhang B, Wu Q, Li B, Wang D, Wang L, Zhou YL. M(6)a Regulator-Mediated Methylation Modification Patterns and Tumor Microenvironment Infiltration Characterization in Gastric Cancer. *Mol Cancer* (2020) 19:53. doi: 10.1186/s12943-020-01170-0
26. Chong W, Shang L, Liu J, Fang Z, Du F, Wu H, et al. M(6)a Regulator-Based Methylation Modification Patterns Characterized by Distinct Tumor Microenvironment Immune Profiles in Colon Cancer. *Theranostics* (2021) 11:2201–17. doi: 10.7150/thno.52717
27. Yi L, Wu G, Guo L, Zou X, Huang P. Comprehensive Analysis of the PD-L1 and Immune Infiltrates of M(6)a RNA Methylation Regulators in Head and Neck Squamous Cell Carcinoma. *Mol Ther Nucleic Acids* (2020) 21:299–314. doi: 10.1016/j.omtn.2020.06.001
28. Li Y, Gu J, Xu F, Zhu Q, Chen Y, Ge D, et al. Molecular Characterization, Biological Function, Tumor Microenvironment Association and Clinical Significance of M6a Regulators in Lung Adenocarcinoma. *Brief Bioinform* (2021) 22:bbaa225. doi: 10.1093/bib/bbaa225

29. Xu S, Tang L, Dai G, Luo C, Liu Z. Expression of M6a Regulators Correlated With Immune Microenvironment Predicts Therapeutic Efficacy and Prognosis in Gliomas. *Front Cell Dev Biol* (2020) 8:594112. doi: 10.3389/fcell.2020.594112

Conflict of Interest: The authors declare that the research was conducted in the absence of any commercial or financial relationships that could be construed as a potential conflict of interest.

The reviewer W.G. declared a shared affiliation with the authors to the handling editor at time of review.

Publisher's Note: All claims expressed in this article are solely those of the authors and do not necessarily represent those of their affiliated organizations, or those of the publisher, the editors and the reviewers. Any product that may be evaluated in this article, or claim that may be made by its manufacturer, is not guaranteed or endorsed by the publisher.

Copyright © 2022 Zhao, Shen and Xue. This is an open-access article distributed under the terms of the Creative Commons Attribution License (CC BY). The use, distribution or reproduction in other forums is permitted, provided the original author(s) and the copyright owner(s) are credited and that the original publication in this journal is cited, in accordance with accepted academic practice. No use, distribution or reproduction is permitted which does not comply with these terms.

frontiers | Frontiers in Immunology

ORIGINAL RESEARCH
published: 31 May 2022
doi: 10.3389/fimmu.2022.828243

Characteristics of Prognostic Programmed Cell Death–Related Long Noncoding RNAs Associated With Immune Infiltration and Therapeutic Responses to Colon Cancer

Yan Chen[1†], Yue Zhang[1,2†], Jiayi Lu[1†], Zhongchen Liu[3], Shasha Zhao[1], Mengmei Zhang[1], Mingzhi Lu[1,4], Wen Xu[1,4], Fenyong Sun[1], Qi Wu[1], Qi Zhong[1*] and Zhongqi Cui[1*]*

[1] Department of Clinical Laboratory, Shanghai Tenth People's Hospital, Tongji University, Shanghai, China, [2] Department of Central Laboratory, Clinical Medicine Scientific and Technical Innovation Park, Shanghai Tenth People's Hospital, Shanghai, China, [3] Department of Gastrointestinal Surgery, Shanghai Tenth People's Hospital Affiliated to TongJi University, Shanghai, China, [4] Shanghai Clinical College, Anhui Medical University, Hefei, China

Programmed cell death (PCD) plays an important role in the onset and progression of various cancers. The molecular events surrounding the occurrence of abnormally expressed long noncoding RNAs (lncRNAs) leading to colon cancer (CC) have become a focus. We comprehensively evaluated the roles of PCD-related lncRNAs in the clinical management of CC and their immune responses. Therefore, we screened 41 prognostic PCD-related lncRNAs in The Cancer Genome Atlas database using co-expression analysis and assigned patients to groups according to the results of cluster analysis. The immune response and functions of cluster 2 were substantially suppressed, which might explain the poor prognosis in this group. A prognostic model comprising eight PCD-related lncRNAs was developed, and its effectiveness was verified using an external database. High-and low-risk groups had different epigenetic modifications and changes in immune cell infiltration. Patients in the high-risk group were resistant to immunotherapy and various chemotherapeutic drugs. Studies *in vitro* and *in vivo* further confirmed a carcinogenic role of the lncRNA U62317.4. Our findings of the prognostic value of PCD-related lncRNAs revealed their important roles in immune response disorders, thus providing valuable insights into the clinical management and molecular mechanisms of CC.

Keywords: programmed cell death, colon cancer, lncRNA, immune infiltration, TMB, therapeutic response

OPEN ACCESS

Edited by:
Giulia Accardi,
University of Palermo, Italy

Reviewed by:
Jin Hou,
Second Military Medical University, China
Yandong Miao,
Lanzhou University, China

***Correspondence:**
Zhongqi Cui
1632084@tongji.edu.cn
Qi Zhong
zhongqi0607@163.com
Qi Wu
wuqi496@163.com

†These authors have contributed equally to this work

Specialty section:
This article was submitted to Cancer Immunity and Immunotherapy, a section of the journal Frontiers in Immunology

Received: *03 December 2021*
Accepted: *26 April 2022*
Published: *31 May 2022*

Citation:
Chen Y, Zhang Y, Lu J, Liu Z, Zhao S, Zhang M, Lu M, Xu W, Sun F, Wu Q, Zhong Q and Cui Z (2022) Characteristics of Prognostic Programmed Cell Death–Related Long Noncoding RNAs Associated With Immune Infiltration and Therapeutic Responses to Colon Cancer. Front. Immunol. 13:828243. doi: 10.3389/fimmu.2022.828243

INTRODUCTION

Among gastrointestinal malignancies, colon cancer (CC) is the second most common cause of tumor-related deaths worldwide (1). An increasing incidence (2) and high mortality rates has led to CC becoming a serious threat to human health (3). Research data show that the 5-year survival rate of early colon cancer (85%-90%) is much higher than that of advanced colon cancer (<14%) (4, 5), however, the clinical management of colon cancer has not yet achieved satisfactory results. Therefore, it is urgent to develop a new biological Markers for prognostic assessment and clinical management of patients.

Cancer cells utilize the immunosuppressive network and create a tumor microenvironment (TME) that allows them to evade host immune surveillance and the potent antitumor activity of immune cells. Numerous cell death processes are initiated in the TME as a result of normal biological responses, external stimuli, or responses to treatment. Apoptosis, pyroptosis, and ferroptosis play important roles in immunogenic cell death (6, 7). Apoptosis is the traditional mode of programmed cell death (PCD) that consists primarily of a mitochondria-mediated intrinsic pathway and an extrinsic pathway involving death receptors (8). Its characteristic features are cell shrinkage, chromatin agglutination, and apoptotic body formation (9). Pyroptosis is a recently-discovered, iron-dependent, novel mode of PCD characterized by continuous cell expansion until the cell membrane ruptures, releasing cellular contents and activating an intense inflammatory response. Pyroptosis is an important part of the natural immune response that plays important roles in combating infections and malignancies (10). Ferroptosis is a novel iron-dependent mode of PCD. The main mechanism is the catalyzed lipid peroxidation of abundant unsaturated fatty acids on the cell membrane by ferrous ions or ester oxygenases, which induces cell death (11). The resulting immune response to changes in the death activities of TME components can affect tumor development and the efficiency of anticancer therapeutics (12, 13).

Long noncoding RNAs (lncRNAs) comprise > 200 nucleotides and they influence many disease processes such as tumors (14, 15) and regulate PCD. For example, the lncRNA HOTAIR-miR-20a-5p-HMGA2 axis plays an important role in the growth, migration, invasion, and apoptosis of breast cancer cells (16). The lncRNA, HOTTIP, inhibits cell pyrolysis in ovarian cancer by targeting the microRNA (miR)-148a-3p/AKT2 axis (17). Furthermore, LINC00336 inhibits ferroptosis during carcinogenesis by interacting with Embryonic Lethal, Abnormal Vision, Drosophila, Homolog-Like 1 to reduce intracellular levels of iron and lipid reactive oxygen species (18). However, only a few biological functions of lncRNAs have been conclusively verified. The clinical significance of most lncRNAs, especially those associated with PCD, remains unclear. Therefore, exploring and understanding the role(s) of PCD-related lncRNAs in CC are important to improve the diagnosis and prognosis of patients.

We analyzed the roles of PCD-related lncRNAs in the prognosis of CC patients and their correlations with clinicopathological characteristics; we then verified the accuracy of our prognostic model using external databases. We also explored the correlations between PCD-related lncRNAs and the TME, immune checkpoint genes, tumor mutation burden (TMB), immunotherapy, and chemotherapeutic drug sensitivity. Thereafter, we analyzed the biological functions of lncRNA U62317.4 in CC *in vitro* and *in vivo*. Our findings will provide the basis for new ideas regarding the prognosis and treatment of CC patients.

MATERIALS AND METHODS

Data Processing and Screening of PCD-Related Genes

Transcriptome sequencing data and clinical information on CC patients were downloaded from The Cancer Genome Atlas (TCGA) (https://www.cancer.gov/tcga/). Patients with incomplete clinical pathological information and missing survival data were excluded. We finally followed up 436 CC patients. We downloaded RNA-seq TCGA transcriptome data in a standardized fragment format per kilobase exon model per million mapped reads. **Supplementary Table S1** shows the clinical information of all patients.

Identification of PCD-Related lncRNAs

To obtain the lncRNA expression profiles, we mapped TCGA sequencing data to lncRNA annotation files in the GENCODE database (http://www.gencodegenes.org) and eliminated lncRNAs with no expression in > 20% of samples. We screened PCD-related lncRNAs in TCGA-Colon Adenocarcinoma (COAD) data using Spearman correlation analyses based on correlation coefficients > 0.3 and $P < 0.05$ (**Supplementary Table S2**). The top 10 lncRNAs for differential PCD genes were visualized using Cytoscape to explore the prognostic value of PCD-related lncRNAs, and those with prognostic value were screened using univariate Cox regression analysis. The expression of PCD-related lncRNAs in CC and normal tissues was analyzed using Wilcoxon signed-rank tests.

Analysis of CC Subtypes Defined by PCD-Related lncRNAs

We used the ConsensusClusterPlus package in R to determine the number of consistent clusters based on the expression PCD-related prognostic lncRNAs and their potential biological characteristics. Prognostic value and clinicopathological characteristics in subgroups were analyzed using Kaplan–Meier (KM) survival analysis and log-rank tests.

Biological Functions and Immune Infiltration Level Analysis Among Different Subgroups

Differential genes among subgroups were screened using the limma package in R with the following criteria: $|logFC| \geq 0.5$ and a false discovery rate (FDR) < 0.05 (**Supplementary Table S3**). Differentially expressed genes (DEGs) among subgroups were

analyzed using Gene Ontology (GO), the Kyoto Encyclopedia of Genes and Genomes (KEGG), clusterProfiler, org.Hs.eg.db, and the enrichplot package in R to determine their biological functions. Differences in tumor signal pathways between patients in clusters 1 and 2 were screened *via* Gene Set Enrichment Analysis (GSEA) using FDR < 0.05 as the criterion.

We calculated immune and stromal scores in CC to compare immune infiltration between the subgroups using the ESTIMATE algorithm. The abundance of immune cells was determined using TIMER (19), CIBERSORT (20, 21), QUANTISEQ (22), Microenvironment Cell Populations-counter (MCPCOUNTER) (23), XCELL (24), and the Estimating the Proportion of Immune and Cancer cells (EPIC) algorithm (25). Immune pathways in groups were quantified using the GSVA package in R. Differences in immune checkpoints between subgroups were evaluated using Wilcoxon tests.

Construction of PCD-Related lncRNA Risk Model of CC

We constructed a prognostic model by screening eight PCD-related lncRNAs and then optimized readability using the LASSO regression algorithm based on their expression and corresponding risk coefficients. The formula was calculated as follows:

$$Risk\ \ score = \sum regression\ \ coefficient(gene\ \ i) \times expression\ \ value(gene\ i)$$

The training and validation sets were divided into high- and low-risk groups based on the median risk score. The overall survival (OS) of patients was assessed using KM curves and log-rank tests. The effectiveness of the model was evaluated using receiver operator characteristic (ROC) curves. Whether risk scores and clinical characteristics were independent prognostic factors for patients were evaluated using univariate and multivariate Cox analyses. Differences in risk scores, immune scores, and clinicopathological characteristics were assessed using Wilcoxon tests. We used the RMS package in R to integrate clinical characteristics with risk scores and construct a nomogram and calibration curve to realize a quantitative prognostic tool. Consistency between the prognostic assessment by the nomogram and actual results was evaluated using a calculation with a guide method that included 1,000 resamples. The diagnostic power of the nomogram and individual predictors was evaluated using ROC curves. The clinical benefits conferred by prognostic evaluation of the nomogram and a single predictor were further compared using decision curve analysis (DCA).

Analysis of TMB and Gene Copy Number Variation Among Subgroups

Somatic CC mutation data were retrieved from TCGA (https://www.cancer.gov/tcga/). The TMB was calculated by dividing the total number of mutations by the size of the coding region of the target gene. Patients were classified as having high or low TMB based on the median value. We also visualized the top 20 genes with the highest mutation frequency in high- and low-risk groups using the maftools package in R. Copy number variations (CNV) between subgroups were calculated using Chi-square tests, and the positions of CNVs on the chromosome were visualized using the Rciorcos package in R.

Immunotherapy and Targeted Drug Screening

The sensitivity of subgroups of patients to immunotherapy was assessed using http://tide.dfci.harvard.edu. Based on the Genomics of Drug Sensitivity in Cancer (https://www.cancerrxgene.org), we used the pRRophetic package in R to evaluate the sensitivity of patients to chemotherapeutic agents and visualized the three-dimensional (3D) molecular structure of each agent using the cMAP database (https://clue.io/cmap).

Source of Clinical Samples

We collected CC tumor and adjacent cancerous tissue from patients who underwent CC resection between 2016 and 2021 at the Colorectal Cancer Center of Shanghai Tenth People's Hospital. After excluding patients with incomplete clinical data, 96 were included in the follow-up analysis. The study was approved by the Ethics Committee at Shanghai 10th People's Hospital.

Extraction of RNA and Real-Time Quantitative Polymerase Chain Reaction (RT-qPCR)

Total RNA from tissues or cells was extracted using TRIzol reagent (Invitrogen, Carlsbad, CA, USA) and quantified using a Nanodrop 2000 spectrophotometer (Thermo Fisher Scientific Inc., Waltham, MA, USA). Total RNA was reverse transcribed to cDNA using the PrimeScript™ RT Reagent Kit (Takara Bio Inc., Kusatsu, Japan). Amplicons were quantified using a 7500 Fast Real-time PCR system (Applied Biosystems, Piscataway, NJ, USA). The relative expression (fold change) of the target genes was determined using the 2-ΔΔCT method. Glyceraldehyde 3-phosphate dehydrogenase was the internal control. **Supplementary Table 4** shows the sequences of the RT-qPCR primers (Beijing Qingke Biotech Ltd., Beijing, China).

Cell Culture and Transfection

Human HCT-116 and SW480 CC cell lines (American Type Culture Collection, Manassas, VA, USA) were cultured in Dulbecco's modified Eagle's medium containing 10% fetal bovine serum (FBS; both from Thermo Fisher Scientific Inc., Waltham, MA, USA) with 1% streptomycin and penicillin, at 37°C under a humidified 5% CO_2 atmosphere.

Cells were transiently transfected using Lipofectamine 2000 (Invitrogen) as described by the manufacturer. Small interfering RNA (siRNA) was purchased from GenePharma (Shanghai, China) The sense and anti-sense si-U62317.4 sequences were: 5′-GAAGAGAAGGACAAGUUGACG-3′ and 5′-UCAACU UGUCCUUCUCUUCUG-3′, respectively. We created a stable knockout U62317.4 cell line using short hairpin RNA (shRNA)

targeting U62317.4 (sh-U62317.4; General Biosystems, Anhui, China) with the sense and anti-sense sequences, 5′-GATA CTTGATCCTGATAAA-3′ and 5′- TTTATCAGGATCAAG TATC-3′, respectively.

Lentiviral particles were obtained as described (16). HCT-116 cells were directly infected with Polybrene (Santa Cruz Biotechnology, Dallas, TX, USA) for 24 h and then, transfected cells were screened for 7–10 days with 2 μg/mL of puromycin (Invitrogen).

Cell Proliferation and Colony Analysis

We transfected HCT-116 or SW480 cells for 48 h and then seeded 1×10^3 cells/well in 96-well plates. After 24, 48, and 72 h, the cells were incubated with CCK-8 reagent (10 μL) in serum-free medium (100 μL) for 2 h at 37°C. The optical density at 450 nm was measured using a microplate reader. Similarly transfected CC cells were seeded in six-well plates and cultured in DMEM medium containing 10% FBS for 7 days to analyze colony formation. The cells were then fixed with paraformaldehyde and stained with 0.1% crystal violet. Colonies were counted using ImageJ software.

Cell Invasion, Migration, and Wound Healing Assay

Cell invasion and migration were measured using Transwell chambers (Corning CoStar, Tewksbury, MA, USA). Cells (4×10^4) were resuspended in serum-free medium and added to the upper part of Matrigel®-coated chambers. Medium (500 μL) containing 10% FBS was added to the lower chamber. The cells were fixed with paraformaldehyde 48 h later and stained with 0.5% crystal violet. Cells that passed through the bottom of the membrane were assessed and counted using a microscope. The cells were resuspended in serum-free medium and seeded in six-well plates until they reached 100% confluence, when they were damaged by being gently scratched with a 200-μL sterile micropipette tip for wound healing assays. Representative images of cell migration were acquired after 0, 24, and 48 h, and the cell migration rate was determined by time-lapse analysis using ImageJ software.

Cell Apoptosis Assay

We assayed apoptosis using Flow Apoptosis Kits (BD Biosciences, San Diego, CA, USA) as described by the manufacturer. Briefly, digested cells were washed twice with cooled PBS and stained using FITC Annexin V apoptosis detection kits (BD Biosciences); thereafter, cell populations were evaluated using a BD LSRFortessa™ analyzer (BD Biosciences).

Tumor Xenotransplantation

Four-week-old female BALB/C nude mice were randomly assigned to two groups (n = 5 per group) to determine tumor formation *in vivo*. CC cells stably transfected with sh-normal control (NC) or sh-U62317.4 were implanted subcutaneously into the axillae of nude mice. One week after injection, tumor volumes (cm^3) were measured every 3 days as (length × $width^2$)/2. The mice were euthanized 21 days later, and tumors were removed and weighed. The Animal Experiment Ethics Committee of Tongji University approved all the animal experiments.

Western Blotting

Proteins were collected from CC cells in RIPA lysis buffer (Invitrogen) containing phenylmethylsulfonyl fluoride (PMSF; Bio-Rad Laboratories Inc., Hercules, CA, USA). Proteins were resolved by 10% sodium dodecyl sulfate-polyacrylamide gel electrophoresis and then transferred onto polyvinylidene difluoride membranes (Invitrogen). Non-specific antigen binding was blocked by shaking the membranes in 5% skim milk for 2 h at 37°C. Thereafter, the membranes were incubated with primary antibody overnight at 4°C, followed by secondary antibody for 2 h. The blots were visualized and analyzed using the Odyssey system (LI-COR Biosciences, Lincoln, NE, USA). **Supplementary Table 5** shows details of the antibodies.

Statistical Analyses

Data were statistically analyzed, and images were generated using R and GraphPad Prism 8.03 (GraphPad Software Inc., San Diego, CA, USA). The Wilcoxon signed-rank and Kruskal-Wallis tests were used for between-group comparisons. Values with $P < 0.05$ were considered statistically significant.

RESULTS

Consensus Clustering in CC Identified Prognostically Distinct Clusters Based on PCD-Related lncRNAs

Figure 1 shows a flow chart of the study. We initially re-annotated TCGA expression matrix to distinguish between mRNAs and lncRNAs and identified 199 genes related to PCD among which, 33, 52, and 114 were associated with apoptosis (26), pyroptosis (9, 27), and ferroptosis (28). **Figures 2A–C** shows that the expressions of most PCD-related genes significantly differed between CC and normal tissues. We then screened the lncRNAs that were the most closely associated with the expression of these genes using correlation analysis. Among the 437 PCD-related lncRNAs, 85, 161, and 297 were associated with pyroptosis, apoptosis, and ferroptosis, respectively (**Figures 2D–F**). Univariate Cox analysis of the screened PCD-lncRNAs identified 41 PCD prognosis–related lncRNAs (**Figures 3A, B**). Differential analysis showed that the expression of these lncRNAs significantly differed between tumor and normal tissues (**Figure 3C**). Consensus clustering based on the expression of these lncRNAs revealed biological differences among different CC subgroups. Combining the consensus matrix cumulative distribution function curve and the delta area plot showed that interference between clusters was minimal and the classification was significant when K = 2 (**Figures 3D–F**). KM survival curves showed that the OS rate was significantly better for cluster 1 than that cluster 2 (**Figure 3G**). We then constructed a heat map to compare the clinical characteristics between these subgroups and found high scores for T stage, lymphatic metastasis, and tumor stage in cluster 1 (**Figure 3H**).

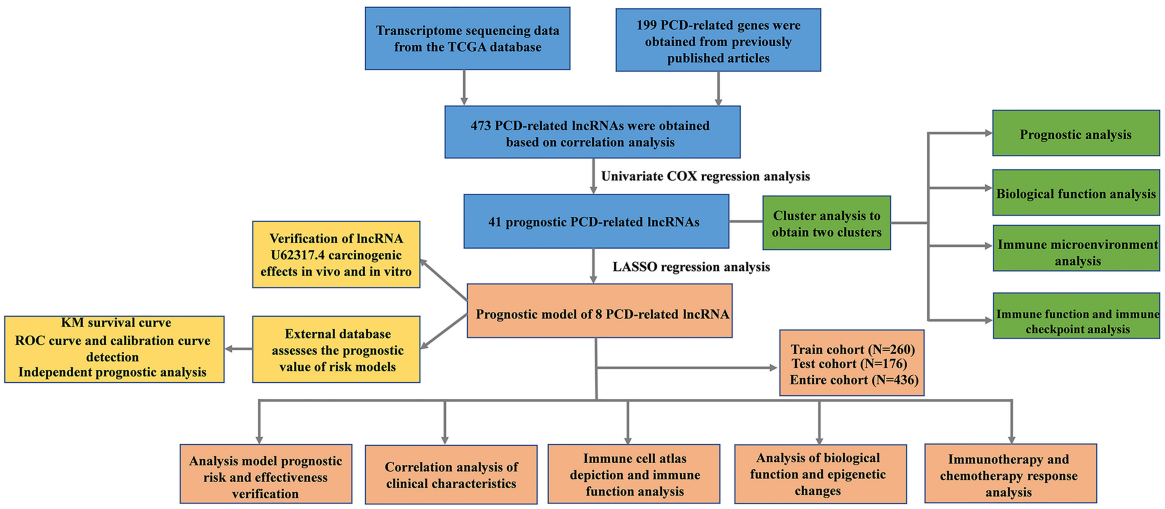


FIGURE 1 | Flow chart of the study.

Analysis of Biological Functions Between CC Subgroups

The survival results revealed evident prognostic differences between the CC subgroups. To explore the potential reason for this, we analyzed DEGs in the subgroups using GSEA, GO, and KEGG. The GSEA results showed that the immune-related B cell receptor, chemokine, JAK-STAT, T cell receptor, and Toll-like receptor signaling pathways were abnormally activated in cluster 1 (**Figure 4A**). The GO results showed that the DEGs were involved in several immune-related functions, which was consistent with the GSEA findings (**Figures 4B–D**). The KEGG analysis showed that the DEGs were primarily involved in cell growth, chemokines, cytokines, and phagosomes related to signaling pathways (**Figure 4E**).

Analysis of the Tumor Immune Microenvironment and Immune Checkpoint Genes Clusters 1 and 2

Considering that the DEGs were primarily related to immune-related functions, we examined the immune cell distribution in the immune microenvironment of CC. The amounts of immune cell infiltration differed between clusters 1 and 2 (**Figure 5A**). Cluster 1 had abundant memory CD4 T cells and eosinophils, whereas cluster 2 had more follicular helper T and resting natural killer (NK) cells (**Figures 5B–E**). We further explored differences in the distribution of immune and stromal ratios between the two clusters using the ESTIMATE algorithm. **Figures 5F–H** shows that cluster 2 had lower immune, stromal, and ESTIMATE scores than those of cluster 1. A comparative analysis revealed fully suppressed immune function in cluster 2 (**Figure 5I**). Considering the importance of immune checkpoints in immunotherapy, we analyzed the expression of immune checkpoints in the two clusters and found that all immune checkpoint genes except the TNF Receptor Superfamily Members *(TNFRSF) 25* and *14* were significantly suppressed in cluster 2 (**Figure 5J**). Thus, the lower OS rate of patients in this cluster might have been due to suppressed immune function.

Construction of a PCD-Related lncRNA Prognostic Model for CC Patients Using TCGA

LASSO Cox analysis of PCD prognosis–related lncRNAs in TCGA identified the filter genes AC004080.1, AC078923.1, AC114730.3, AC156455.1, long intergenic non-protein coding RNA 1419 (LINC01419), LINC00997, NF-kappaB interacting lncRNA (NKILA), and U62317.4 with which to construct a prognostic model. Risk scores were calculated based on the regression coefficients and expression of these eight genes (**Figures 6A–C**). The risk formula was 0.5023 * expression (U62317.4) + 0.3836 * expression (AC078923.1) + 0.0082 * expression (AC114730.3) + 0.075 * expression (LINC00997) + 0.1341 * expression (NKILA) + 0.1278 * expression (AC156455.1) + 0.0195 * expression (LINC01419) + 0.1131 * expression (AC004080.1). To improve the accuracy and effectiveness of the prognostic model, we randomly assigned the patients to training (N = 260) and test (N = 176) groups and then divided them into high-and low-risk groups according to the median risk score. The KM survival curves indicated worse OS for patients in the training group with high risk scores than those with low risk scores (**Figure 6D**). The risk curves indicated a significantly higher death rate among patients with high risk scores than those with low risk scores (**Figure 6G**). The ROC curves showed that the prognostic model accurately predicted the 1, 3, and 5-year survival rates of CC patients (**Figure 6J**). This model was further verified in the test group (**Figures 6E, H, K**) and the entire TCGA database (**Figures 6F, I, L**). These findings indicated that our prognostic model is unbiased and can be used as a reference tool for predicting the OS rate of CC.

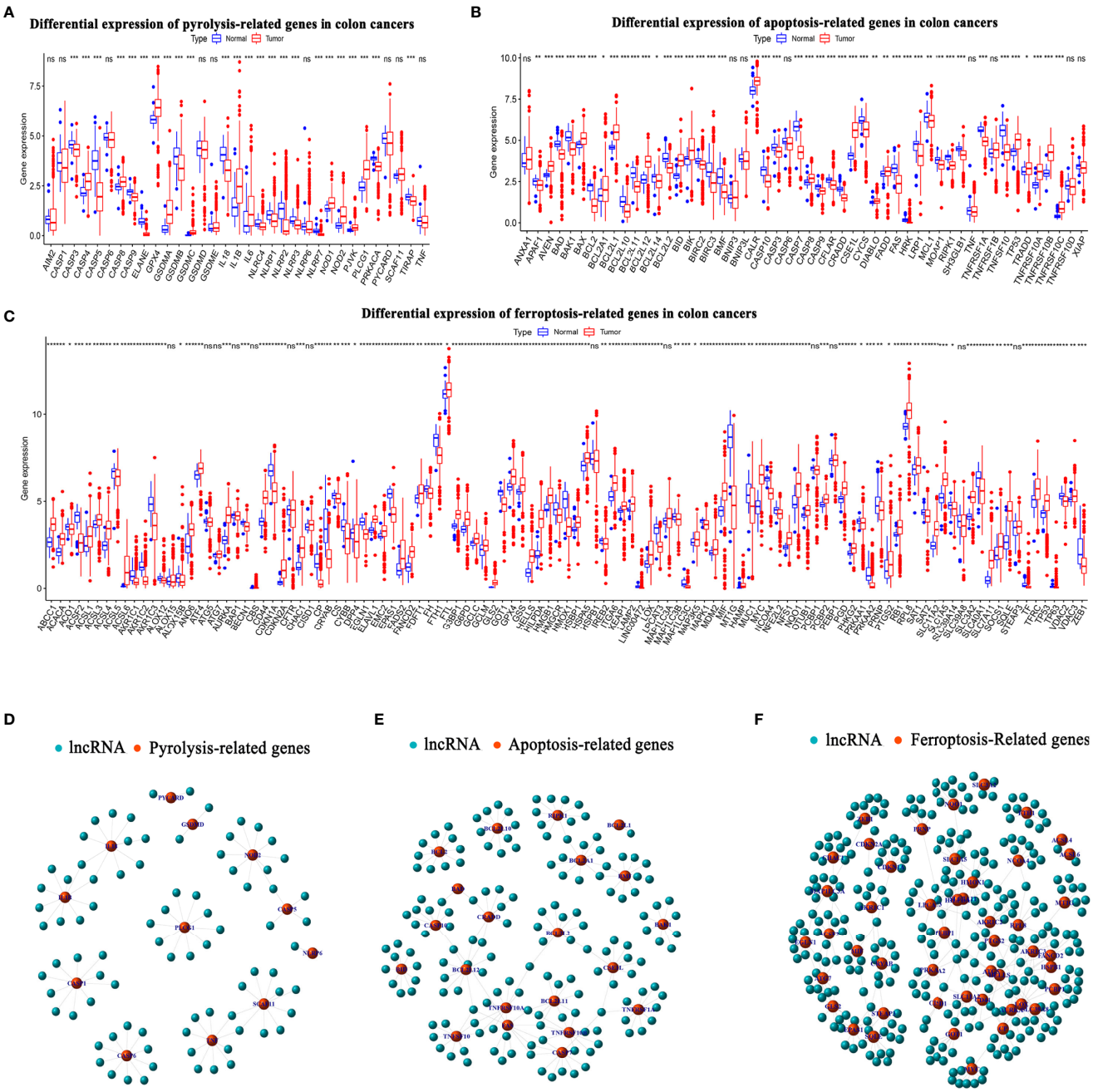


FIGURE 2 | Long noncoding RNAs (lncRNAs) associated with PCD in colon cancer. **(A–C)** Expression levels of PCD-related genes in TCGA-COAD cancer database in CC and normal groups. **(A)** Pyroptosis- **(B)** apoptosis-, and **(C)** ferroptosis-related genes. **(D–F)** Top 10 lncRNAs in TCGA-COAD database associated with differentially expressed PCD genes. **(D)** Pyroptosis-, **(E)** apoptosis-, and **(F)** ferroptosis-related lncRNAs. CC, colon cancer; COAD, colon adenocarcinoma; PCD, programmed cell death; TCGA, The Cancer Genome Atlas. *P < 0.05, **P < 0.01, ***P < 0.001, ns, non-significant.

Analysis of Independent Factors and Clinicopathological Correlations of the Prognostic Model

We further confirmed the independence of the CC prognostic model using univariate and multivariate Cox analyses. **Figures 7A, B** shows that age (hazard ratio [HR], 1.042; 95% confidence interval [CI], 1.019–1.067; P < 0.001) and risk score (HR, 1.493; 95% CI, 1.346–1.655; P < 0.001) were independent prognostic factors for CC patients. We then evaluated the relationship between the risk score and PCD prognosis–related lncRNA. A heatmap showed significantly increased expression of

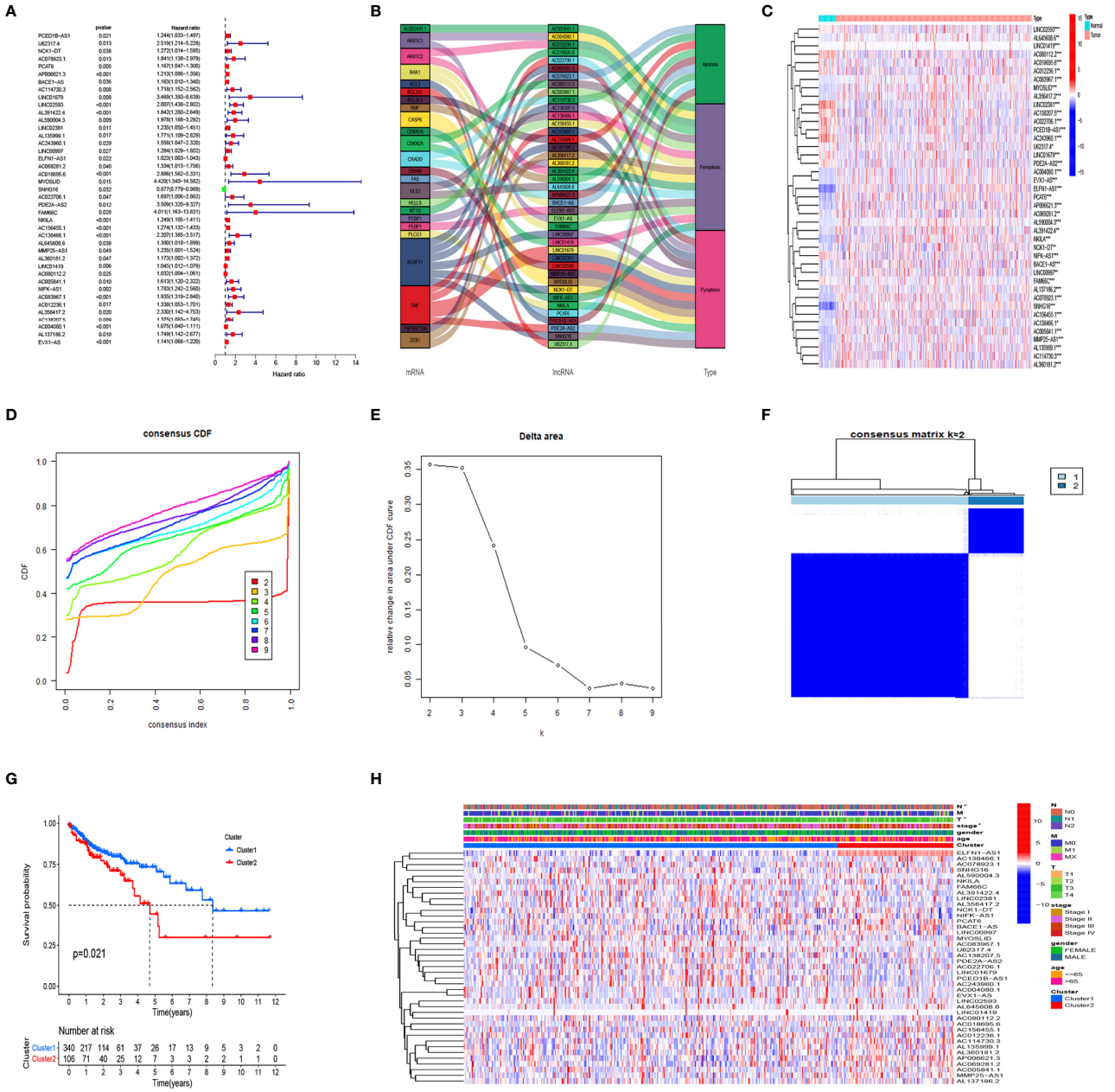
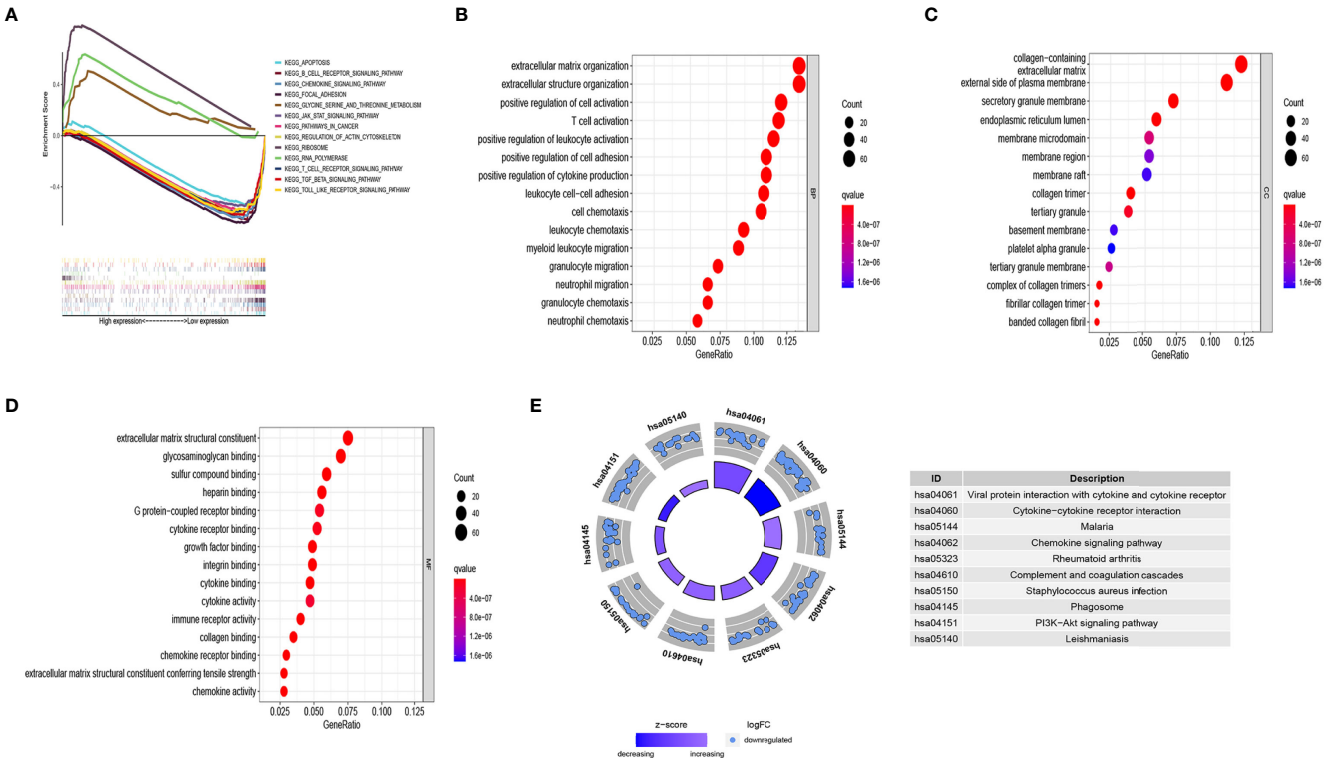


FIGURE 3 | Consensus cluster analysis of PCD-related lncRNA in colon cancer. **(A)** Prognostic value of 41 PCD-related lncRNAs. **(B)** Relationships among prognostic-related lncRNA, mRNA, and type of death. **(C)** Expression of PCD prognostic-related lncRNA in CC and normal tissues. **(D–F)** Cumulative distribution function. **(D)** change in area under the CDF curve, **(E)** for k=2-9, **(F)** Consensus clustering matrix for k = 2. **(G)** Kaplan–Meier survival analysis of patients in clusters 1 and 2. **(H)** Clinicopathological characteristics and lncRNA expression in clusters 1 and 2. CC, colon cancer, CDF, cumulative distribution function; PCD, programmed cell death. *P < 0.05, **P < 0.01, ***P < 0.001.

all eight PCD-related lncRNAs in the high-risk group (**Figure 7C**). Risk scores were statistically different in cluster stratification, tumor stage, and lymph node metastasis (**Supplementary Figure 1A**). In addition, risk scores could assess the prognosis of patients in multiple clinical subgroups, except for patients in the T1-2 group (**Supplementary 1B**). We constructed a nomogram that included patient age, sex, tumor stage, distant metastasis, lymph node metastasis, and risk score to accurately quantify survival rates (**Figure 7D**). The calibration curves showed that the actual 1-, 3-, and 5-year OS rates of patients and those estimated by the nomogram were close (**Figure 7E**). The areas under the ROC curve (AUC; **Figure 7F**) revealed that the 1, 3, and 5-year survival rates determined by the nomogram were accurate (AUC = 0.820



ID	Description
hsa04061	Viral protein interaction with cytokine and cytokine receptor
hsa04060	Cytokine−cytokine receptor interaction
hsa05144	Malaria
hsa04062	Chemokine signaling pathway
hsa05323	Rheumatoid arthritis
hsa04610	Complement and coagulation cascades
hsa05150	Staphylococcus aureus infection
hsa04145	Phagosome
hsa04151	PI3K−Akt signaling pathway
hsa05140	Leishmaniasis

FIGURE 4 | Analysis of the biological function of differentially expressed genes (DEGs) in different clusters. **(A)** KEGG enrichment of cluster 1 and cluster 2 by GSEA. Only gene sets with FDR q < 0.05 were considered significant. **(B)** Biological process (BP) analysis of DEGs. **(C)** Cellular component (CC) analysis of DEGs. **(D)** Molecular function (MF) analysis of DEGs. **(E)** KEGG pathway enrichment analysis of DEGs. Only gene sets with FDR q < 0.05 were considered significant.

0.824, and 0.838, respectively). The DCA decision curve showed that the net rate of return for the OS rates assessed by the combined model was better than other clinical characteristics (**Figures 7G–I**). The ROC curve also showed that the combined model was more sensitive than other clinical features (**Figures 7J–L**). These results showed that our nomogram can help clinicians plan accurate follow-up strategies.

Analysis of Functional Enrichment and Immune Cell Infiltration Levels in High- and Low-Risk Groups

We explored the potential biological functions of and signaling pathways enriched by the DEGs in the high- and low-risk groups (**Supplementry Table 6**). The GO results showed that DEGs were significantly enriched in the processes of epithelial-mesenchymal transition, Wnt signaling pathway regulation, and cytokine stimulation (**Supplementary Figure 2A**). The KEGG results revealed that DEGs were primarily involved in Wnt, Hippo, extracellular matrix-receptor interactions, transforming growth factor-beta, and cytokine-cytokine receptor interaction signaling pathways (**Supplementary Figure 2B**).

Figure 8A shows an immune infiltration heat map based on the TIMNER, CIBERSORT, QUANTISEQ, MCPCOUNTER, XCELL, and EPIC algorithms. Among immune functions, difference analysis showed that Apcin (APC) co-inhibition, APC co-stimulation, checkpoint, cytolytic activity, inflammation promotion, MHC class I, T cell co-inhibition, and T cell co-stimulation significantly differed between the high-and low-risk groups (**Figure 8B**). These findings showed that the eight PCD-related lncRNA prognostic characteristics of CC are somewhat related to immune cell infiltration.

Correlation of Risk Score With TMB and Gene CNVs

In view of the evident prognostic differences in the high- and low-risk patients, we analyzed the TMBs and CNVs to further uncover underlying causes. **Figure 8C** shows lower TMB levels in patients with high risk scores than those with low risk scores. Further correlation analysis showed that the risk score negatively correlated with TMB (**Figure 8D**). We then divided the patients into groups with a high or low TMB based on the median TMB. KM curves revealed a significantly worse OS rate for patients with a high TMB than those with a low TMB (**Figure 8E**). Considering that the risk score and the TMB have good prognostic value in CC patients, we evaluated the synergistic effects of these scores on the prognostic stratification of CC. We found that the TMB did not affect the assessment of the prognosis of CC patients according to risk score. Survival in risk score subtypes significantly differed between groups with a high or low TMB (**Figure 8F**). These results indicated that the

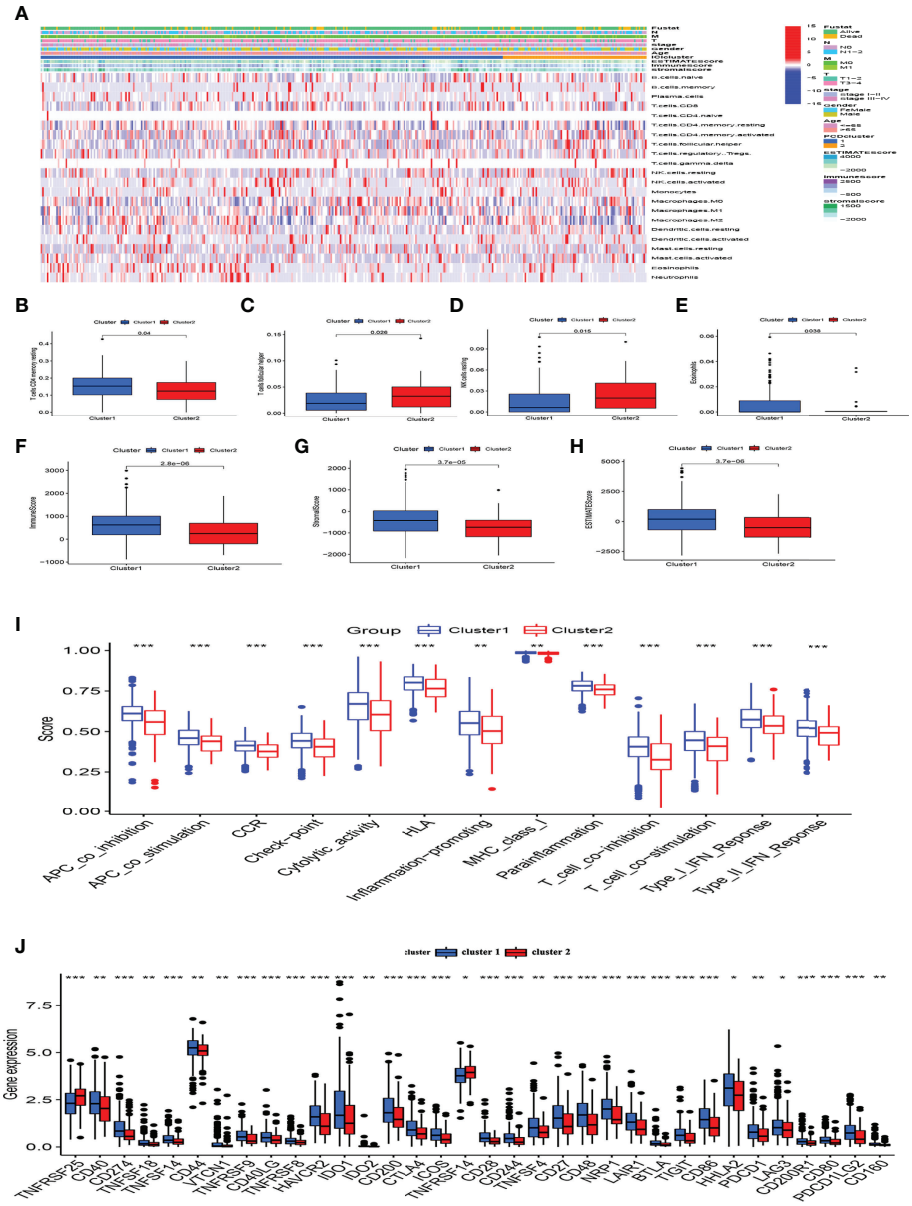


FIGURE 5 | Analysis of the immune microenvironment and immune functions in different clusters. **(A)** Panoramic view of immune microenvironment in different clusters. **(B–E)** CIBERSORT analysis of differences in immune cells among clusters, only $P < 0.05$ was considered statistically significant. **(F–H)** Immune, stromal and ESTIMATE scores among subgroups. **(I)** Immune function scores in different clusters. **(J)** Expression of immune checkpoints in clusters. *$P < 0.05$, **$P < 0.01$, ***$P < 0.001$.

risk score might be an effective indicator that can evaluate prognosis independently of the TMB. We assessed the distribution of somatic variations in CC driver genes between the high- and low-risk groups. A waterfall chart shows the top 20 genes with the highest mutation frequency (**Figures 8G, H**). Our analysis of mutation annotation files in TCGA cohort revealed that FAT4, OBSCN, PCLO, ABCA13, ZFHX4, DNAH11, RYR2, and USH2A significantly differed between the high- and low-risk groups (**Supplementary Table 7**). In addition, we performed CNV analysis of the top 40 genes with the greatest differences between the high- and low-risk groups. We found a higher frequency of CNV mutations in DEGs between the high-and low-risk groups, where CNV expansion occurred in SALL4, KRT16, PEG10, EPHB6, PRR9, GP2, FGF19, and SULT1C4, whereas CST1, H2BC8, HOXD10, HOXD10, HOXD11, CLCA4, DKK1, IGFL1, ALDOB, CALCA, and PLIN4 underwent CNV deletion (**Figure 8I**). The locations of CNV mutations in these DEGs are shown in **Figure 8J**. These results may provide new ideas for studying gene mutations in PCD-related lncRNAs in CC.

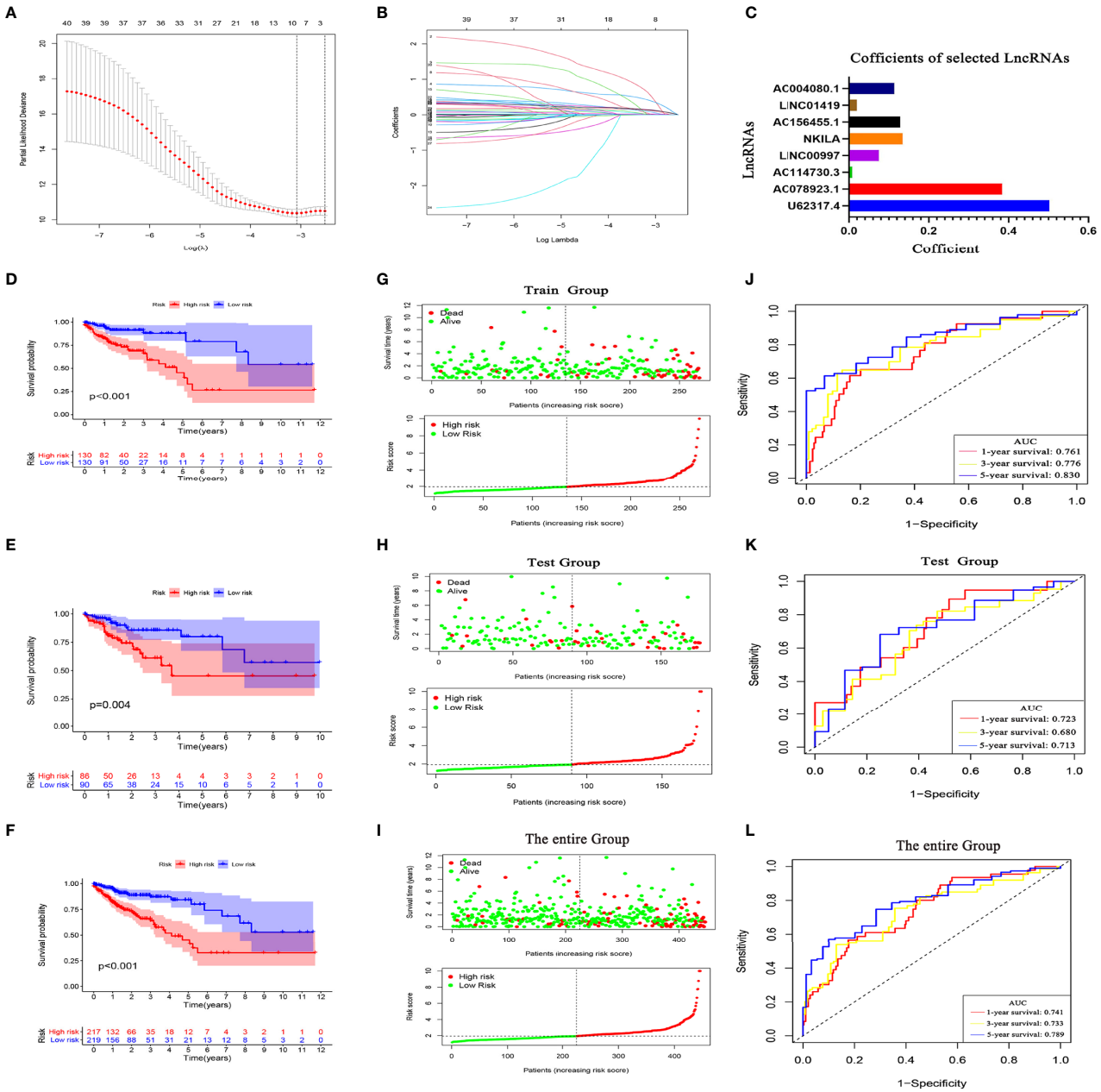


FIGURE 6 | Programmed cell death (PCD)-related lncRNA risk prognostic model. **(A)** Coefficient spectrum of PCD-related lncRNAs. **(B)** Trajectory of correlation coefficients of factors increasing with Log λ. **(C)** Coefficients of eight PCD-related lncRNAs. Kaplan–Meier survival curves in TCGA training **(D)**, test **(E)**, and entire **(F)** sets. Distribution of risk scores and survival status in training **(G)**, test **(H)**, and entire **(I)** sets. evaluation of prognostic model effectiveness in training **(J)**, test **(K)**, and entire **(L)** sets.

Benefits of Immunotherapy to High- and Low-Risk Groups

We evaluated the efficacy of immunotherapy in the high- and low-risk groups using the website http://tide.dfci.harvard.edu/. A higher tumor immune dysfunction and exclusion (TIDE) score implies a higher possibility of immune escape, indicating that the patient has a lower benefit from immunotherapy. As shown in **Figure 8K** and **Supplememtary Table 8**, the TIDE scores of patients in the high-risk group were significantly higher than those in the low-risk group, implying that the low-risk group patients would benefit from immunotherapy. Patients in the high-risk group had lower microsatellite instability (MSI) scores (**Figure 8L**), whereas patients in the low-risk group had higher T cell exclusion scores

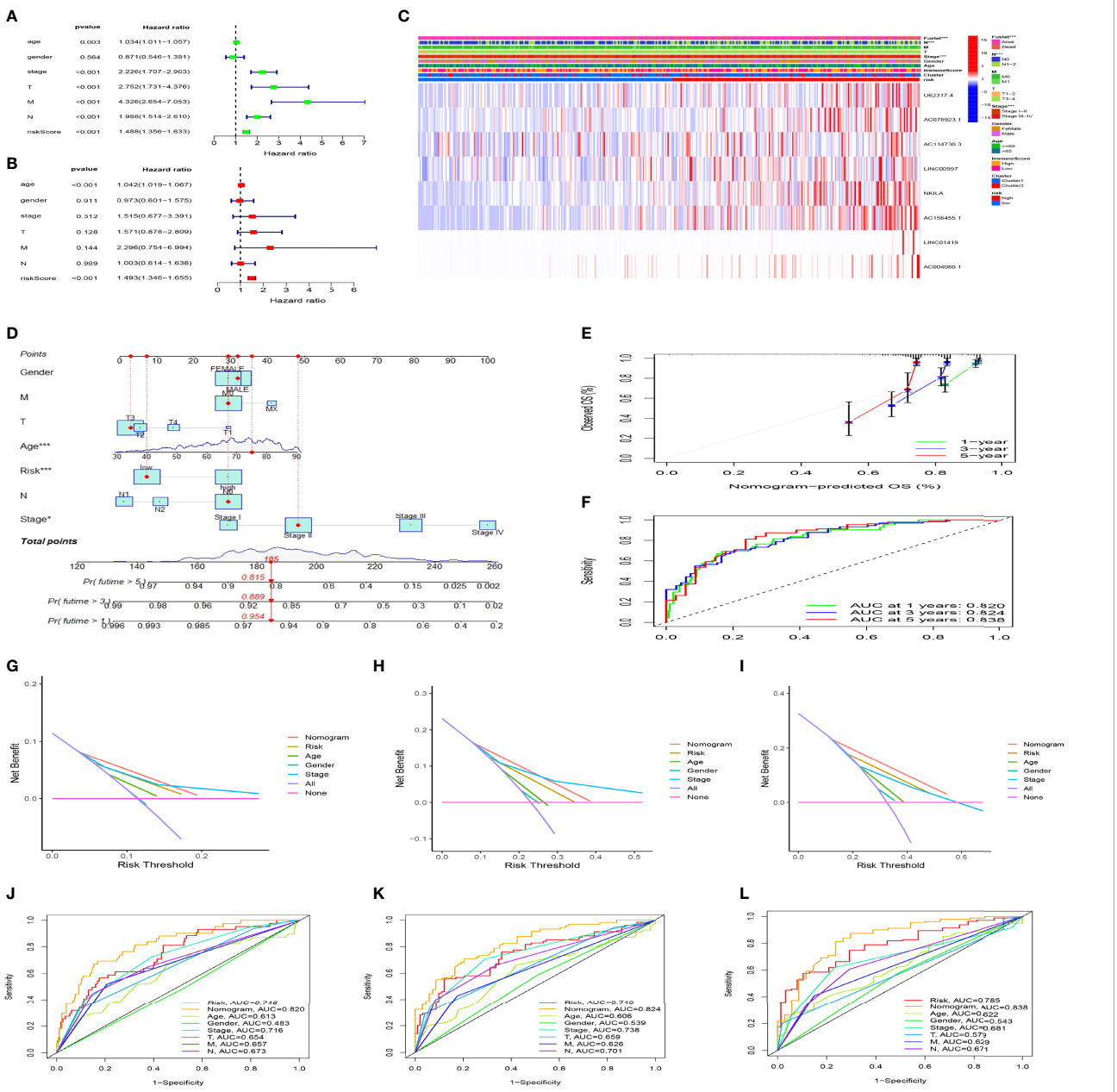


FIGURE 7 | The risk model constructed using programmed cell death (PCD)-related lncRNAs is an independent prognostic factor for colon cancer. Cox univariate **(A)** and multivariate **(B)** analyses of clinical characters and risk scores. **(C)** Heat maps of correlations among clinical characteristics, immune score clusters, and risk scores. **(D)** Nomogram for clinical prognosis assessment. **(E)** Calibration curve to evaluate nomogram accuracy. **(F)** Assessment of prognostic effect of nomogram. **(G-I)** Evaluation of clinical benefits of nomogram. **(J-L)** Comparison of prognostic efficacy of single prognostic factor and nomogram. *P < 0.05, ***P < 0.001.

(**Figure 8M**). T cell dysfunction did not significantly differ between the subgroups (**Figure 8N**). These results support a basis for novel customized immunotherapies for CC patients.

Analysis of Drug Sensitivity Potential in High- and Low-Risk Groups

Considering that chemotherapy and targeted therapies are popular strategies for treating CC, understanding the sensitivity of subgroups of patients to such drugs is important. We predicted the sensitivity of the high-and low-risk groups to agents that are commonly administered to CC patients. **Figures 9A–F** shows that the group with low-risk scores was more sensitive to PD.0325901 METFORMIN MK.2206 AZD8055 PD.0332991, and sorafenib, whereas that with high-risk scores was more sensitive to imatinib, lapatinib, PHA.665752, and MS.275 (**Figures 9G–J**). We determined the

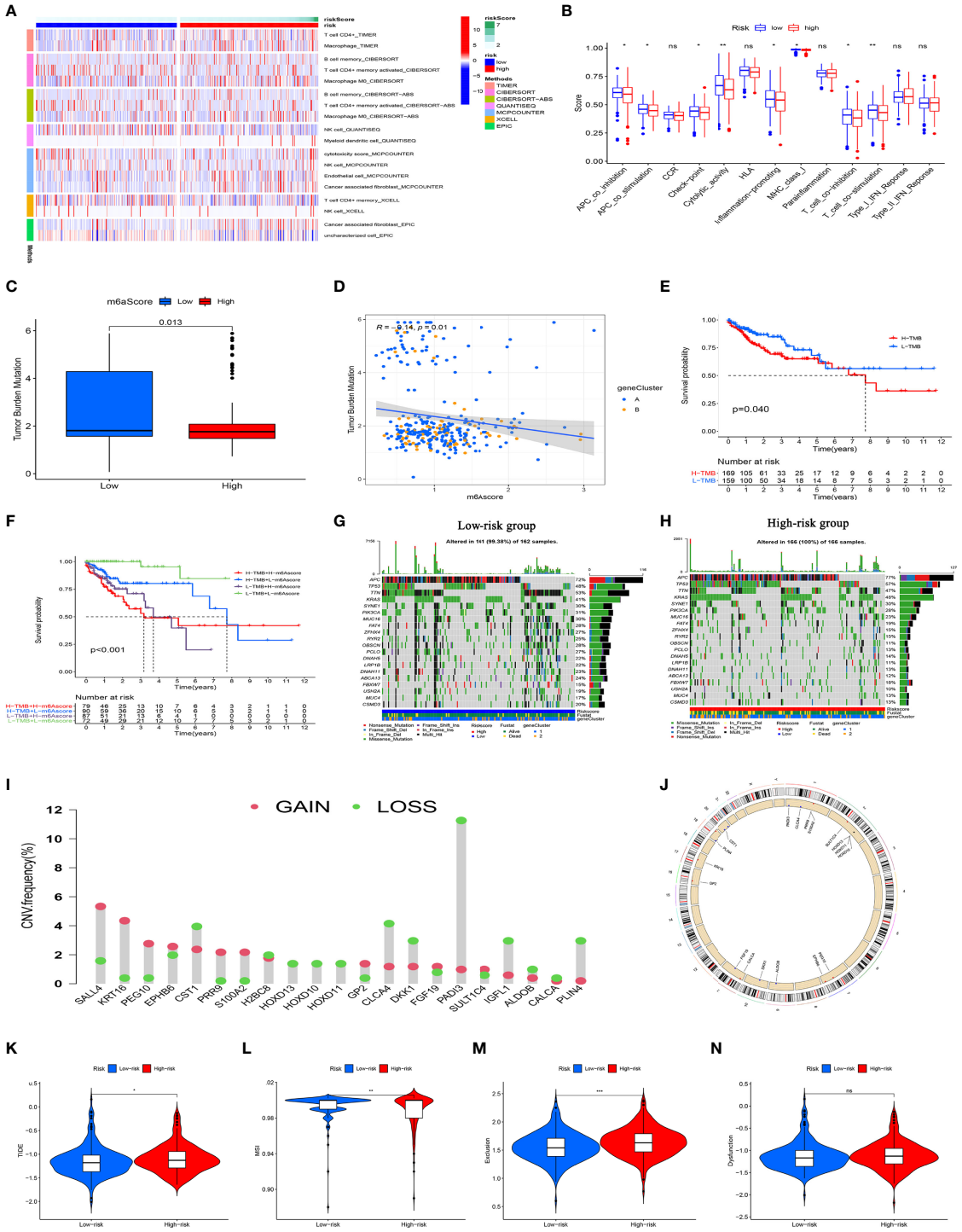


FIGURE 8 | Immune response, TMB, CNV, and immunotherapy analysis of high- and low-risk groups. **(A)** Immune cell infiltration analysis among risk groups using TIMER, CIBERSORT, QUANTISEQ, MCPCOUNTER, XCELL, and EPIC algorithms. All immune cells shown statistically differed. **(B)** Immune function scores for high- and low-risk groups. **(C)** Tumor metastasis burden differs between high- and low-risk groups. **(D)** Scatter plot of negative correlation between risk score and TMB. **(E)** Survival analysis of high-and low TMB in TCGA database. **(F)** Survival analysis of TCGA colon cancer stratified by TMB and risk score. **(G, H)** Waterfall chart shows more genes with increased mutation frequency in high- and low-risk groups. **(I)** Distribution of CNV frequency among DEGs in the high- and low-risk groups. Green and red, deletion and amplification, respectively. **(J)** Distribution of DEGs with different CNVs on chromosomes. **(K–N)** TIDE, MSI, and T cell exclusion and dysfunction scores in high- and low- risk group., *P<0.05, **P<0.01, ***P<0.001; ns, not significant. CNV, copy number variations; DEGs, differentially expressed genes; MSI, microsatellite instability; TCGA, The Cancer Genome Atlas; TIDE, tumor immune dysfunction and exclusion; TMB, tumor mutation burden.

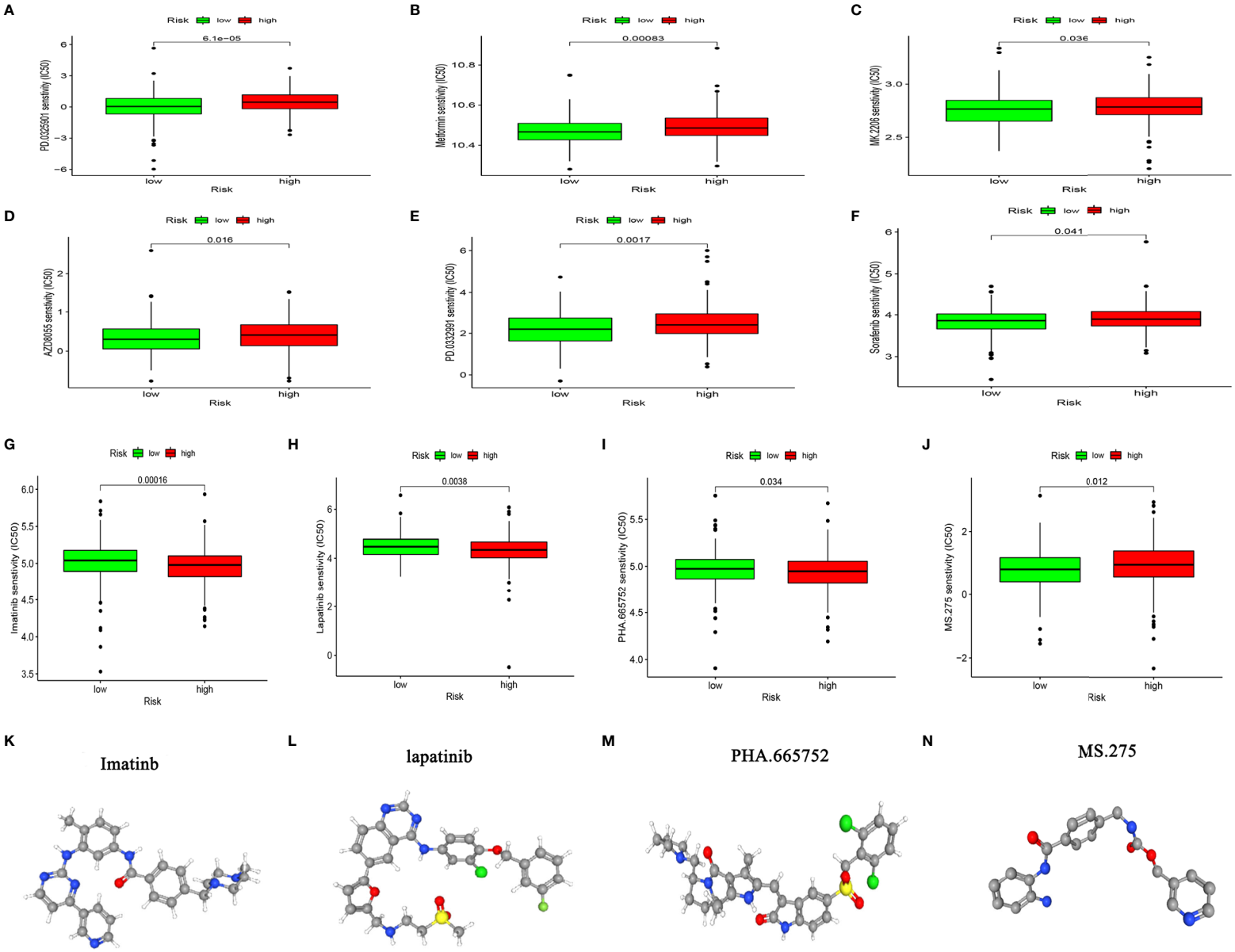


FIGURE 9 | Chemosensitivity analysis. **(A–J)** Responses of high- and low-risk groups to chemotherapy drugs. **(K–N)** Three-dimensional structure of small molecule drugs.

3D structure of four chemotherapy drugs that could be used for patients in the high-risk group using the CMAP database (**Figures 9K-N**). These results should facilitate the application of precise and or new personalized medicines for treating CC.

External Database Verified the Prognostic Value of the Risk Model Constructed With PCD-Related lncRNAs

We selected 96 CC patients from the Colorectal Cancer Center of Shanghai Tenth People's Hospital to verify the external dataset and examined the expression of the eight PCD-associated lncRNAs in CC and adjacent tissues by RT-qPCR. The expression trends were consistent with those listed in TCGA (**Figure 10A**). We calculated the risk scores of the patients and divided them into high- and low-risk groups according to the median risk score. KM curves showed that the OS was significantly worse in the high- risk group than that in the low-risk group (**Figure 10B**). The AUC showed that the risk model could predict the outcome of CC patients (**Figure 10C**). Univariate and multivariate Cox regression analyses of clinical characteristics and risk scores determined that risk scores, stage and age were independent prognostic factors (**Figures 10D, E**).

Silencing U62317.4 Inhibits the Proliferation, Invasion, and Migration of CC

The findings that the lncRNA U62317.4 had the highest risk coefficient in the prognostic model indicated that U62317.4 is closely associated with the prognosis of CC. However, its role in the occurrence and development of CC is unclear. Therefore, we explored whether U62317.4 is involved in the malignant progression of CC. We synthesized a siRNA against U62317.4 and evaluated its interference *via* RT-qPCR. The expression of U62317.4 in HCT-116 and SW480 cells was significantly reduced after transfection with si-U62317.4 (**Figures 11A, B**). Silencing U62317.4 significantly inhibited CC cell viability and clone formation (**Figures 11C–E**) and significantly increased the apoptosis of CC cells (**Figures 11F, G**). Metastasis is another important feature of malignant tumors. Thus, we explored the role of U62317.4 in CC metastasis using wound healing and Transwell assays. Knockdown of U62317.4 significantly reduced wound healing ability as well as the migratory and invasive capacity of CC cells (**Figures 11H, J**). We constructed a nude mouse subcutaneous tumor model. to evaluate the tumorigenicity of U62317.4 *in vivo*. Silencing U62317.4

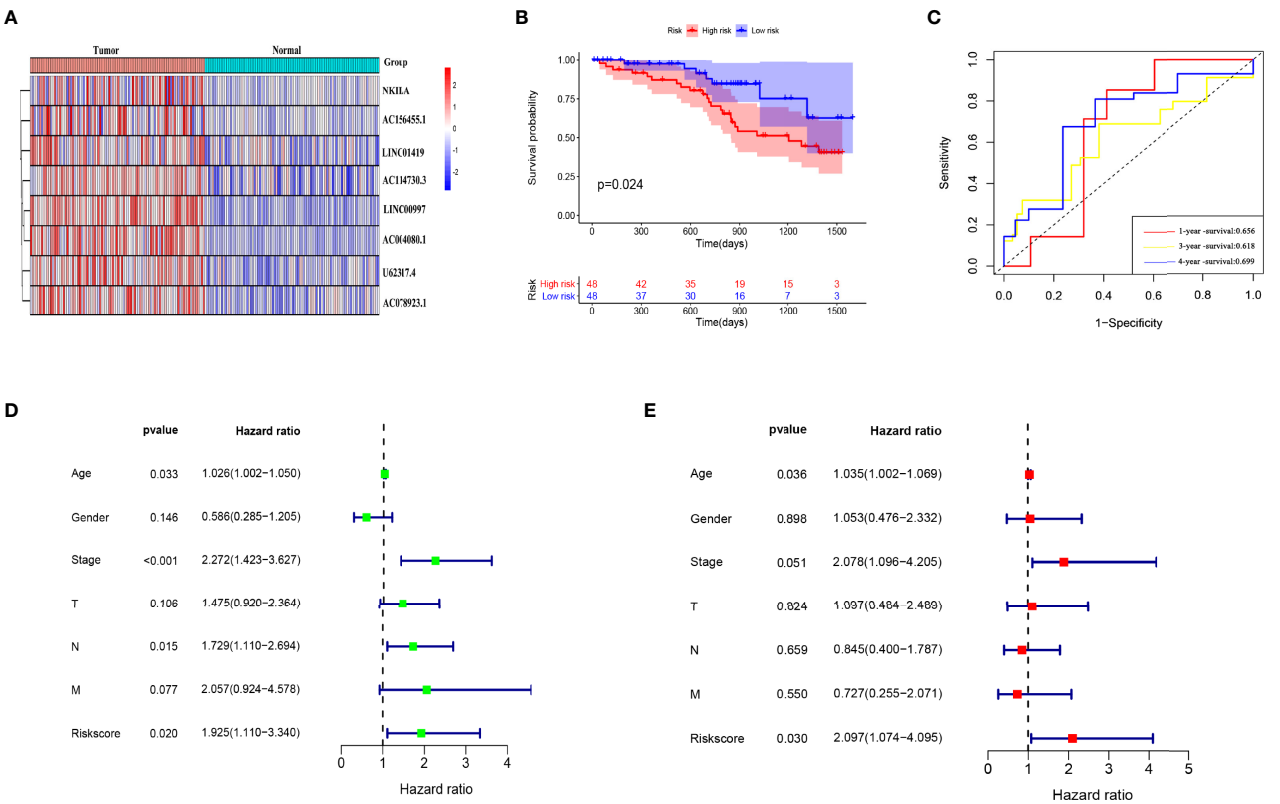


FIGURE 10 | External database verification that risk model has prognostic value. **(A)** Model lncRNA expression in 96 CC and adjacent tissues. **(B)** Kaplan-Meier Survival analysis of patients in high- and low-risk groups. **(C)** Evaluation of risk model effectiveness. **(D, E)** Univariate and multivariate regression analyses of clinical characteristics and risk scores.

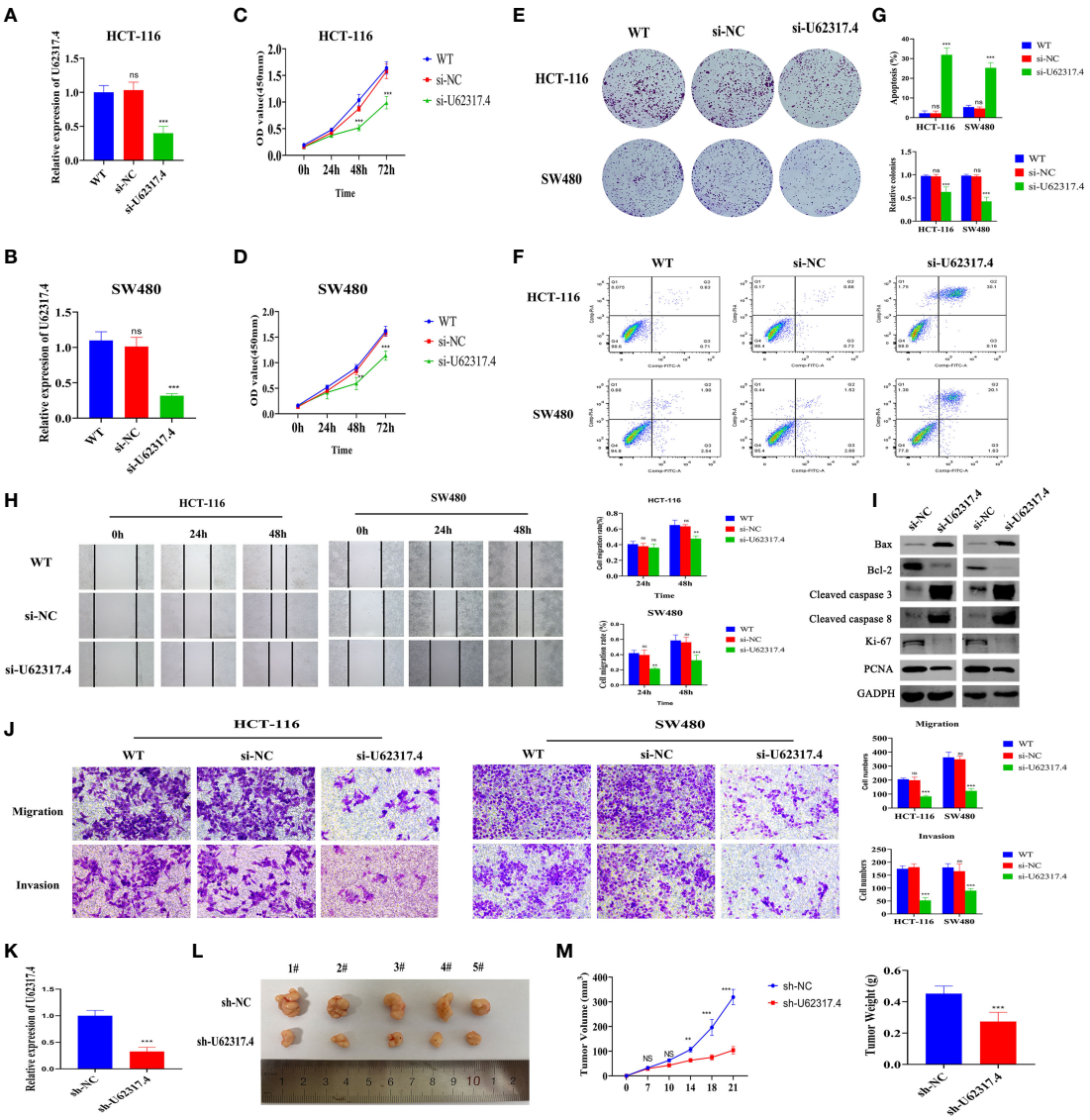


FIGURE 11 | Silencing U62317.4 suppressed the malignant CC phenotype. **(A, B)** Detection of U62317.4 expression in HCT-116 **(A)** and SW480 **(B)** cells using RT-qPCR. **(C, D)** CCK-8 analysis of HCT-116 **(C)** and SW480 **(D)** cells transfected with si-NC or si-U62317.4, and wild-type cells. **(E)** Colony formation of HCT-116 and SW480 cells transfected with si-NC, si-U62317.4, and wild-type cells. **(F)** Flow cytometry of HCT-116 and SW480 transfected si-NC or si-U62317.4, and wild-type cells. **(G)** Numbers of cell clones and apoptosis rates from three independent experiments. **(H)** Evaluation of migration abilities of HCT-116– and SW480-transfected si-NC or si-U62317.4, and wild-type cells using wound scratch assays. **(I)** Western blots of cell apoptosis and growth-related protein indicators. **(J)** Transwell assays of si-NC– or si-U62317.4–transfected HCT-116 and SW480 cell migration and invasion ability and wild-type cells **(K)** Efficiency of shRNA interference of U62317.4 confirmed *via* RT-qPCR. **(L, M)** Silencing U62317.4 significantly inhibits tumor weight and volume; n = 3. CC, colon cancer; NC, normal control. $^{**}P < 0.01$, $^{***}P < 0.001$, ns, non-significant.

significantly inhibited the growth of CC in these mice (**Figures 11K–M**). Western blotting revealed changes in the abundance of proliferation- and apoptosis-related proteins when U62317.4 was silenced. **Figures 11I** shows that the expression of ki-67, PCNA, and BCL-2 decreased, whereas that of cleaved caspases-3 (cleaved casp-3) and -8 increased when U62317.4 was silenced in CC. These results showed that silencing U62317.4 inhibits CC cell proliferation and metastasis.

DISCUSSION

Apoptosis is a classical form of PCD that is considered the most promising target for tumor therapy. Pyroptosis and ferroptosis are important types of PCD-related death that are distinct from apoptosis. Their dysfunction is critical in the development of various tumors (6, 7, 29). Biomarkers of PCD play crucial roles in tumor prognosis assessment and tumor efficacy monitoring (30,

31). However, most previous studies have focused on genes that can be programmed for proteins. Considering the key roles of lncRNAs in PCD, their roles in the clinical features and prognosis of CC should be comprehensively evaluated.

We screened TCGA data and identified 41 lncRNAs associated with PCD in CC based on their prognostic value. We classified them into two subtypes based on their expression profiles. Prognostic evaluation and clinical correlation analysis showed that OS rate, tumor stage and tumor lymphatic metastasis significantly differed between these subtypes. We constructed a prognostic model comprising eight-PCD-related lncRNAs using LASSO regression analysis. We found that patients with high-risk scores had a poorer prognosis and that the prognostic model had high diagnostic power. In view of its importance in the prognostic model, we verified the roles of U62317.4 lncRNA *in vivo* and *in vitro*. Silencing U62317.4 lncRNA inhibited tumor proliferation and invasion, and promoted tumor apoptosis, indicating that the abundant expression of this gene is closely related to the progression of CC. We judged the prognostic significance of risk scores and clinical characteristics in CC using univariate and multivariate Cox regression analyses. Age and risk score were independent prognostic factors for CC patients. The results of the external database analysis provided further evidence that our model could accurately assess the prognosis of CC. The nomogram is a quantitative tool that can predict a certain clinical outcome or the probability of a certain type of event based on the values of several variables (32). The DCA decision and ROC curves showed a better net profit rate and diagnostic ability for the nomogram than those for a single indicator in terms of assessing patient prognosis. These findings indicated that this quantitative tool is important for patient disease management.

Cell death is an integral part of the immune response and serves as a signal (second messenger) to guide the immune system and the TME to ensure tissue repair and homeostasis (10, 33). A disordered immune system is an important cause of cancer progression, treatment failure, and eventual death (34). The significantly reduced immune microenvironment and immune function scores in cluster 2, implied suppressed immune function, which could explain the lower OS rate in this cluster. Many immune checkpoints (negative regulatory receptors) are expressed on T cells only after activation (35). Immune checkpoints influence the progression and treatment of CC (34, 36, 37). We found significantly reduced immune checkpoints in cluster 2, which might have been associated with the overall suppression of immune function. In addition, significantly more macrophage M0 and cancer-associated fibroblast infiltration was found in the high-risk group, which had significantly less NK and memory CD4 T cell infiltration that might have further exacerbated the immune depletion status of patients. Liu et al. found that NK cells can inhibit the proliferation of breast cancer cells by secreting perforin/granzyme to activate the apoptotic pathway (38). Nagorsen et al. (39) and Cui et al. (40) showed that increased M0 macrophage infiltration can inhibit the tumor immune activity of the digestive system and suggested that this leads to a poor prognosis. Cancer-related fibroblasts can tame immune cells to create a microenvironment suitable for tumor survival (41, 42). The loss of memory T lymphocytes further aggravates the exhaustion of T cells, which is also an important cause of immune dysfunction in patients with tumors (34, 43). These collective findings indicated that PCD-related lncRNAs impact the dysfunction of immune cells in CC immunity, thus providing a new platform for the development of novel immunotherapies.

A comprehensive assessment of PCD-related lncRNAs would help to understand the characteristics of immune cell infiltration and predict responses to immunotherapy. The TMB is a promising indicator of responses to immune checkpoint inhibitors, that closely correlate with immunity (44). We found that the TMB and MSI scores associated with sensitivity to immunotherapy were significantly lower in the high- risk group than those in the low-risk group. This was also consistent with the immunotherapy and immune status of the two subgroups assessed by the http://tide.dfci.harvard.edu website. The results of our stratified analysis showed that the risk model constructed using PCD-associated lncRNA was not associated with the TMB in CC. This means that the PCD-related risk model and TMB represent different aspects of tumor immunobiology and that the model can predict responses to immunotherapy independently of TMB.

Chemotherapy and immunotherapy are the most important adjuvant therapies for CC, as they can improve the prognosis and quality of life of patients. Considering the low immunogenicity and immunosuppression of patients in the high-risk group, we screened a batch of small molecule chemotherapeutics using the GDSC drug susceptibility database, with the aim of improving personalized medication guidance for CC patients. Based on the IC50 prediction, the high-risk group of patients was more sensitive to imatinib, lapatinib, PHA.665752, and MS.275. Dolloff et al. indicated that lapatinib can upregulate TRAIL receptors to induce CC cell apoptosis through off-target effects activated by the c-Jun N-terminal kinase and c-Jun pathways (45). The synthetic small molecule benzamide derivative of histone deacetylase inhibitor, MS-275 is currently in phase I/II clinical trials. This agent has demonstrated significant CC inhibition *in vitro* and *in vivo* (46, 47). The antitumor activity of MS-275 is primarily reflected in the induction of endogenous and exogenous apoptotic cell death in tumor cells (48). These results improve the guidance for personalized drug use in CC.

We provided a comprehensive view of the management of CC and we established a robust prognostic model. However, the present study has some limitations. TCGA was the main source of multi-omics data and clinical information. The results of the multi-omics analysis could not be verified. For example, we covered transcriptome sequencing, TMB, and CNV analyses. However, these tests are expensive and difficult to implement in practical applications. We hope that rapid advances in biotechnologies will lead to the development of robust toolkits that will pay the way for their widespread implementation. The

TME might differ among tumor regions. However, most of the tissues that we analyzed were collected from core areas of tumors, which might have impacted our evaluation of TME characteristics and the immune functions of different tumor areas to some extent. We did not have any external data to validate the drug sensitivity results, which would undoubtedly likely be lengthy and expensive.

The present findings require further prospective validation by a multicenter study. Our study has some limitations. Nonetheless, we provided clues for elucidating the relationships between PCD-related lncRNAs and the TME as well as treatment responses. Our prognostic model has good clinical value and might lead to new ideas for improving the OS of CC patients and facilitate individualized treatment.

DATA AVAILABILITY STATEMENT

The original contributions presented in the study are included in the article/**Supplementary Material**. Further inquiries can be directed to the corresponding authors.

ETHICS STATEMENT

The studies involving human participants were reviewed and approved by Shanghai Tenth People's Hospital Ethics Committee. The patients/participants provided their written informed consent to participate in this study. The animal study was reviewed and approved by Animal Experiment Ethics Committee of Tongji University.

AUTHOR CONTRIBUTIONS

YC and ZC designed the project and analyzed the data. YZ and JL verified the results of the functional experiments. MZ, ML, WX, and ZL collected clinical samples and information. SZ and FS provided financial support. QW and ZC drafted and revised the manuscript. All authors agree with the publication of this manuscript.

FUNDING

This work was supported by the Research Fund of Shanghai Municipal Health Bureau (No. 2019cxjq03), National Natural Science Foundation of China (Nos. 81930066, 81772941, and 82102449), Shanghai Tenth People's Hospital Climbing Training Program (2021SYPDRC060), and Shanghai Municipal Health Commission (No. 20204Y0088).

SUPPLEMENTARY MATERIAL

The Supplementary Material for this article can be found online at: https://www.frontiersin.org/articles/10.3389/fimmu.2022.828243/full#supplementary-material

Supplementary Figure 1 | Significance of risk scores in clinical subgroups. **(A)** Distribution of risk scores and **(B)** prognostic evaluation of risk scores in clinical subgroups.

Supplementary Figure 2 | Biological functions of differentially expressed genes (DEGs) in high- and low-risk groups. **(A)** Gene Ontology and **(B)** Kyoto Encyclopedia of Genes and Genomes analyses of DEGs in high- and low-risk groups.

REFERENCES

1. Siegel RL, Miller KD, Fuchs HE, Jemal A. Cancer Statistics, 2021. *CA Cancer J Clin* (2021) 71(1):7–33. doi: 10.3322/caac.21654
2. Chen W, Zheng R, Baade PD, Zhang S, Zeng H, Bray F, et al. Cancer Statistics in China, 2015. *CA Cancer J Clin* (2016) 66(2):115–32. doi: 10.3322/caac.21338
3. Nie H, Wang Y, Liao Z, Zhou J, Ou C. The Function and Mechanism of Circular RNAs in Gastrointestinal Tumours. *Cell Prolif* (2020) 53(7):e12815. doi: 10.1111/cpr.12815
4. Lichtenstern CR, Ngu RK, Shalapour S, Karin M. Immunotherapy, Inflammation and Colorectal Cancer. *Cells* (2020) 9(3):618. doi: 10.3390/cells9030618
5. Li Y, Liu W, Zhou Z, Ge H, Zhao L, Liu H, et al. Development and Validation of Prognostic Nomograms for Early-Onset Locally Advanced Colon Cancer. *Aging (Albany NY)* (2021) 13(1):477–92. doi: 10.18632/aging.202157
6. Tang R, Xu J, Zhang B, Liu J, Liang C, Hua J, et al. Ferroptosis, Necroptosis, and Pyroptosis in Anticancer Immunity. *J Hematol Oncol* (2020) 13(1):110. doi: 10.1186/s13045-020-00946-7
7. Green DR. The Coming Decade of Cell Death Research: Five Riddles. *Cell* (2019) 177(5):1094–107. doi: 10.1016/j.cell.2019.04.024
8. Jan R, Chaudhry GE. Understanding Apoptosis and Apoptotic Pathways Targeted Cancer Therapeutics. *Adv Pharm Bull* (2019) 9(2):205–18. doi: 10.15171/apb.2019.024
9. Kerr JF, Wyllie AH, Currie AR. Apoptosis: A Basic Biological Phenomenon With Wide-Ranging Implications in Tissue Kinetics. *Br J Cancer* (1972) 26 (4):239–57. doi: 10.1038/bjc.1972.33
10. Shi J, Gao W, Shao F. Pyroptosis: Gasdermin-Mediated Programmed Necrotic Cell Death. *Trends Biochem Sci* (2017) 42(4):245–54. doi: 10.1016/j.tibs.2016.10.004
11. Li J, Cao F, Yin HL, Huang ZJ, Lin ZT, Mao N, et al. Ferroptosis: Past, Present and Future. *Cell Death Dis* (2020) 11(2):88. doi: 10.1038/s41419-020-2298-2
12. Havel JJ, Chowell D, Chan TA. The Evolving Landscape of Biomarkers for Checkpoint Inhibitor Immunotherapy. *Nat Rev Cancer* (2019) 19(3):133–50. doi: 10.1038/s41568-019-0116-x
13. Hui L, Chen Y. Tumor Microenvironment: Sanctuary of the Devil. *Cancer Lett* (2015) 368(1):7–13. doi: 10.1016/j.canlet.2015.07.039
14. Chan JJ, Tay Y. Noncoding RNA: RNA Regulatory Networks in Cancer. *Int J Mol Sci* (2018) 19(5):1310. doi: 10.3390/ijms19051310
15. Marchese FP, Raimondi I, Huarte M. The Multidimensional Mechanisms of Long Noncoding RNA Function. *Genome Biol* (2017) 18(1):206. doi: 10.1186/s13059-017-1348-2
16. Zhao W, Geng D, Li S, Chen Z, Sun M. LncRNA HOTAIR Influences Cell Growth, Migration, Invasion, and Apoptosis *via* the miR-20a-5p/HMGA2 Axis in Breast Cancer. *Cancer Med* (2018) 7(3):842–55. doi: 10.1002/cam4.1353
17. Tan C, Liu W, Zheng ZH, Wan XG. LncRNA HOTTIP Inhibits Cell Pyroptosis by Targeting miR-148a-3p/AKT2 Axis in Ovarian Cancer. *Cell Biol Int* (2021) 45(7):1487–97. doi: 10.1002/cbin.11588
18. Wang M, Mao C, Ouyang L, Liu Y, Lai W, Liu N, et al. Long Noncoding RNA LINC00336 Inhibits Ferroptosis in Lung Cancer by Functioning as a Competing Endogenous RNA. *Cell Death Diff* (2019) 26(11):2329–43. doi: 10.1038/s41418-019-0304-y
19. Li T, Fu J, Zeng Z, Cohen D, Li J, Chen Q, et al. TIMER2.0 for Analysis of Tumor-Infiltrating Immune Cells. *Nucleic Acids Res* (2020) 48(W1):W509–14. doi: 10.1093/nar/gkaa407
20. Chen B, Khodadoust MS, Liu CL, Newman AM, Alizadeh AA. Profiling Tumor Infiltrating Immune Cells With CIBERSORT. *Methods Mol Biol* (2018) 1711:243–59. doi: 10.1007/978-1-4939-7493-1_12

21. Newman AM, Liu CL, Green MR, Gentles AJ, Feng W, Xu Y, et al. Robust Enumeration of Cell Subsets From Tissue Expression Profiles. *Nat Methods* (2015) 12(5):453–7. doi: 10.1038/nmeth.3337
22. Finotello F, Mayer C, Plattner C, Laschober G, Rieder D, Hackl H, et al. Molecular and Pharmacological Modulators of the Tumor Immune Contexture Revealed by Deconvolution of RNA-Seq Data. *Genome Med* (2019) 11(1):34. doi: 10.1186/s13073-019-0638-6
23. Becht E, Giraldo NA, Lacroix L, Buttard B, Elarouci N, Petitprez F, et al. Estimating the Population Abundance of Tissue-Infiltrating Immune and Stromal Cell Populations Using Gene Expression. *Genome Biol* (2016) 17 (1):218. doi: 10.1186/s13059-016-1070-5
24. Aran D, Hu Z, Butte AJ. Xcell: Digitally Portraying the Tissue Cellular Heterogeneity Landscape. *Genome Biol* (2017) 18(1):220. doi: 10.1186/s13059-017-1349-1
25. Racle J, Gfeller D. EPIC: A Tool to Estimate the Proportions of Different Cell Types From Bulk Gene Expression Data. *Methods Mol Biol* (2020) 2120:233–48. doi: 10.1007/978-1-0716-0327-7_17
26. Lv W, Tan Y, Zhao C, Wang Y, Wu M, Wu Y, et al. Identification of Pyroptosis-Related lncRNAs for Constructing a Prognostic Model and Their Correlation With Immune Infiltration in Breast Cancer. *J Cell Mol Med* (2021) 25(22):10403–17. doi: 10.1111/jcmm.16969
27. Ahluwalia P, Ahluwalia M, Mondal AK, Sahajpal N, Kota V, Rojiani MV, et al. Immunogenomic Gene Signature of Cell-Death Associated Genes With Prognostic Implications in Lung Cancer. *Cancers (Basel)* (2021) 13(1):155. doi: 10.3390/cancers13010155
28. Moujalled D, Strasser A, Liddell JR. Molecular Mechanisms of Cell Death in Neurological Diseases. *Cell Death Diff* (2021) 28(7):2029–44. doi: 10.1038/s41418-021-00814-y
29. Guo F, Zhang C, Fubo W, Zhang W, Shi X, Zhu Y, et al. Deubiquitinating Enzyme USP33 Restrains Docetaxel-Induced Apoptosis *via* Stabilising the Phosphatase DUSP1 in Prostate Cancer. *Cell Death Diff* (2020) 27(6):1938–51. doi: 10.1038/s41418-019-0473-8
30. Nie J, Shan D, Li S, Zhang S, Zi X, Xing F, et al. A Novel Ferroptosis Related Gene Signature for Prognosis Prediction in Patients With Colon Cancer. *Front Oncol* (2021) 11:654076. doi: 10.3389/fonc.2021.654076
31. Ye Y, Qinjin D, Qi H. A Novel Defined Pyroptosis-Related Gene Signature for Predicting the Prognosis of Ovarian Cancer. *Cell Death Discov* (2021) 7(1):71. doi: 10.1038/s41420-021-00451-x
32. Pietrantonio F, Lonardi S, Corti F, Infante G, Elez ME, Fakih M, et al. Nomogram to Predict the Outcomes of Patients With Microsatellite Instability-High Metastatic Colorectal Cancer Receiving Immune Checkpoint Inhibitors. *J Immunother Cancer* (2021) 9(8):e003370. doi: 10.1136/jitc-2021-003370
33. Legrand AJ, Konstantinou M, Goode EF, Pascal M. The Diversification of Cell Death and Immunity: Memento Mori. *Mol Cell* (2019) 76(2):232–42. doi: 10.1016/j.molcel.2019.09.006
34. Noh KH, Kim BW, Song KH, Cho H, Lee YH, Kim JH, et al. Nanog Signaling in Cancer Promotes Stem-Like Phenotype and Immune Evasion. *J Clin Invest* (2012) 122(11):4077–93. doi: 10.1172/JCI64057
35. Saibil SD, Ohashi PS. Targeting T Cell Activation in Immuno-Oncology. *Curr Oncol* (2020) 27(Suppl 2):S98–S105. doi: 10.3747/co.27.5285
36. Jacobs J, Smits E, Lardon F, Pauwels P, Deschoolmeester V. Immune Checkpoint Modulation in Colorectal Cancer: What's New and What to Expect. *J Immunol Res* (2015), 158038. doi: 10.1155/2015/158038
37. Emambux S, Tachon G, Junca A, Tougeron D. Results and Challenges of Immune Checkpoint Inhibitors in Colorectal Cancer. *Expert Opin Biol Ther* (2018) 18(5):561–73. doi: 10.1080/14712598.2018.1445222
38. Mallmann-Gottschalk N, Sax Y, Kimmig R, Lang S, Brandau S. EGFR-Specific Tyrosine Kinase Inhibitor Modifies NK Cell-Mediated Antitumoral Activity Against Ovarian Cancer Cells. *Int J Mol Sci* (2019) 20(19):4693–709. doi: 10.3390/ijms20194693
39. Nagorsen D, Voigt S, Berg E, Stein H, Thiel E, Loddenkemper C. Tumor-Infiltrating Macrophages and Dendritic Cells in Human Colorectal Cancer: Relation to Local Regulatory T Cells, Systemic T-Cell Response Against Tumor-Associated Antigens and Survival. *J Transl Med* (2007) 5:62. doi: 10.1186/1479-5876-5-62
40. Cui Z, Sun G, Bhandari R, Lu J, Zhang M, Bhandari R, et al. Comprehensive Analysis of Glycolysis-Related Genes for Prognosis, Immune Features, and Candidate Drug Development in Colon Cancer. *Front Cell Dev Biol* (2021) 9:684322. doi: 10.3389/fcell.2021.684322
41. Orimo A, Gupta PB, Sgroi DC, Arenzana-Seisdedos F, Delaunay T, Naeem R, et al. Stromal Fibroblasts Present in Invasive Human Breast Carcinomas Promote Tumor Growth and Angiogenesis Through Elevated SDF-1/CXCL12 Secretion. *Cell* (2005) 121(3):335–48. doi: 10.1016/j.cell.2005.02.034
42. Xiang H, Ramil CP, Hai J, Zhang C, Wang H, Watkins AA, et al. Cancer-Associated Fibroblasts Promote Immunosuppression by Inducing ROS-Generating Monocytic MDSCs in Lung Squamous Cell Carcinoma. *Cancer Immunol Res* (2020) 8(4):436–50. doi: 10.1158/2326-6066.CIR-19-0507
43. Rye IH, Huse K, Josefsson SE, Kildal W, Danielsen HE, Schlichting E, et al. Breast Cancer Metastasis: Immune Profiling of Lymph Nodes Reveals Exhaustion of Effector T Cells and Immunosuppression. *Mol Oncol* (2021) 16(1):88–103. doi: 10.1002/1878-0261.13047
44. Hosseinkhani N, Derakhshani A, Kooshkaki O, Abdoli Shadbad M, Hajiasgharzadeh K, Baghbanzadeh A, et al. Immune Checkpoints and CAR-T Cells: The Pioneers in Future Cancer Therapies? *Int J Mol Sci* (2020) 21(21):8305. doi: 10.3390/ijms21218305
45. Dolloff NG, Mayes PA, Hart LS, Dicker DT, Humphreys R, El-Deiry WS. Off-Target Lapatinib Activity Sensitizes Colon Cancer Cells Through TRAIL Death Receptor Up-Regulation. *Sci Transl Med* (2011) 3(86):86ra50. doi: 10.1126/scitranslmed.3001384
46. Hess-Stumpp H, Bracker TU, Henderson D, Politz O. MS-275, a Potent Orally Available Inhibitor of Histone Deacetylases—the Development of an Anticancer Agent. *Int J Biochem Cell Biol* (2007) 39(7–8):1388–405. doi: 10.1016/j.biocel.2007.02.009
47. Zhan Y, Gong K, Chen C, Wang H, Li W. P38 MAP Kinase Functions as a Switch in MS-275-Induced Reactive Oxygen Species-Dependent Autophagy and Apoptosis in Human Colon Cancer Cells. *Free Radic Biol Med* (2012) 53 (3):532–43. doi: 10.1016/j.freeradbiomed.2012.05.018
48. Merghoub T, Gurrieri C, Piazza F, Pandolfi PP. Modeling Acute Promyelocytic Leukemia in the Mouse: New Insights in the Pathogenesis of Human Leukemias. *Blood Cells Mol Dis* (2001) 27(1):231–48. doi: 10.1006/bcmd.2001.0385

Conflict of Interest: The authors declare that the research was conducted in the absence of any commercial or financial relationships that could be construed as a potential conflict of interest.

Publisher's Note: All claims expressed in this article are solely those of the authors and do not necessarily represent those of their affiliated organizations, or those of the publisher, the editors and the reviewers. Any product that may be evaluated in this article, or claim that may be made by its manufacturer, is not guaranteed or endorsed by the publisher.

Copyright © 2022 Chen, Zhang, Lu, Liu, Zhao, Zhang, Lu, Xu, Sun, Wu, Zhong and Cui. This is an open-access article distributed under the terms of the Creative Commons Attribution License (CC BY). The use, distribution or reproduction in other forums is permitted, provided the original author(s) and the copyright owner(s) are credited and that the original publication in this journal is cited, in accordance with accepted academic practice. No use, distribution or reproduction is permitted which does not comply with these terms.

frontiers | Frontiers in Immunology

ORIGINAL RESEARCH
published: 02 June 2022
doi: 10.3389/fimmu.2022.901671

Comprehensive Analysis of Senescence Characteristics Defines a Novel Prognostic Signature to Guide Personalized Treatment for Clear Cell Renal Cell Carcinoma

Peng Zhou, Zheng Liu, Henglong Hu, Yuchao Lu, Jun Xiao, Yanan Wang, Yang Xun, Qidong Xia, Chenqian Liu, Jia Hu and Shaogang Wang**

Department of Urology, Tongji Hospital, Tongji Medical College, Huazhong University of Science and Technology, Wuhan, China

Accumulating evidence has suggested the impact of senescence on tumor progression, but no report has yet described how senescence shapes the tumor microenvironment of clear cell renal cell carcinoma (ccRCC). The objective of this study was to delineate the senescence features of ccRCC and its role in shaping the tumor microenvironment through a comprehensive analysis of multiple datasets, including 2,072 ccRCC samples. Unsupervised consensus clustering identified three senescence subtypes, and we found that the senescence-activated subtype survived the worst, even in the condition of targeted therapy and immunotherapy. The activated senescence program was correlated to increased genomic instability, unbalanced PBMR1/BAP1 mutations, elevated immune cell infiltration, and enhanced immune inhibitory factors (cancer-associated fibroblasts, immune suppression, immune exclusion, and immune exhaustion signaling). A senescence score based on nine senescence-related genes (i.e., P3H1, PROX1, HJURP, HK3, CDKN1A, AR, VENTX, MAGOHB, and MAP2K6) was identified by adaptive lasso regression and showed robust prognostic predictive power in development and external validation cohorts. Notably, we found that the senescence score was correlated to immune suppression, and the low-score subgroup was predicted to respond to anti–PD-1 therapy, whereas the high-score subgroup was predicted to respond to Sunitinib/Everolimus treatment. Collectively, senescence acted as an active cancer hallmark of ccRCC, shaped the immune microenvironment, and profoundly affected tumor prognosis and drug treatment response.

Keywords: cellular senescence, tumor microenvironment, prognostic signature, targeted therapy, immune checkpoint blockade

OPEN ACCESS

Edited by:
Elena Ciaglia,
University of Salerno, Italy

Reviewed by:
Valentina Lopardo,
University of Salerno, Italy
Nicola Alessio,
Università della Campania Luigi Vanvitelli, Italy

****Correspondence:***
Jia Hu
Jiahutjm@163.com
Shaogang Wang
sgwangtjm@163.com

Specialty section:
This article was submitted to Cancer Immunity and Immunotherapy, a section of the journal Frontiers in Immunology

Received: *22 March 2022*
Accepted: *03 May 2022*
Published: *02 June 2022*

Citation:
Zhou P, Liu Z, Hu H, Lu Y, Xiao J, Wang Y, Xun Y, Xia Q, Liu C, Hu J and Wang S (2022) Comprehensive Analysis of Senescence Characteristics Defines a Novel Prognostic Signature to Guide Personalized Treatment for Clear Cell Renal Cell Carcinoma. Front. Immunol. 13:901671. doi: 10.3389/fimmu.2022.901671

INTRODUCTION

Renal cell carcinoma (RCC) is a common malignancy of the urinary tract, and its predominant histological type is clear cell carcinoma (80%–90% of cases). Approximately one-third of patients with RCC harbor distant metastases at the first diagnosis, and the 5-year overall survival (OS) of these patients is only 10%–20% versus 70% of patients with localized tumors (1). In recent years, the description of novel cancer subtypes based on expression profiles has helped us gain deeper insight into the molecular features and oncological heterogeneity of RCC, such as the mRNA/miRNA subtypes identified by The Cancer Genome Atlas (TCGA) project (2), the four subtypes of metastatic clear cell renal cell carcinoma (ccRCC) identified to distinguish sunitinib treatment response (3), the seven subtypes to describe the clonal origin of RCC (4), and the seven molecular subtypes of high-grade ccRCC (5). However, these molecular subtypes still face great challenges in differentiating patients' prognosis and guiding personalized treatment options for ccRCC.

It is well known that RCC is chemotherapy and radiotherapy-insensitive, and targeted therapies represented by anti-angiogenic tyrosine kinase inhibitors (TKIs) and inhibitors of rapamycin protein (mTOR) are the main post-operative adjuvant treatment strategies for patients with ccRCC (6). Immune checkpoint blockade (ICB) presents a new option for ccRCC patients, with approximately 20%–35% objective response rates and a significant survival benefit over targeted therapy (7–10). The pan-cancer analysis reported a moderate tumor mutation burden (TMB) in ccRCC, whereas approximately 70% of ccRCC are immune cells infiltrated, giving ccRCC an abundance of pre-existing anti-tumor immunity (11). However, clinical trials in RCC did not report the predictive value of TMB, baseline CD8+ T infiltration, or PD-1/PD-L1 expression levels for ICB treatment response (10). In addition, several clinical trials testing the efficacy of the ICB +anti-vascular treatment strategy in patients with metastatic ccRCC have reached their endpoints. According to two meta-analyses of published reports, the combination regimen can increase CR rates by more than threefold when compared to anti-vascular monotherapy (12). Therefore, there is an urgent need to introduce novel theories to further elucidate the molecular heterogeneity of ccRCC and to guide personalized treatment selection.

Accumulating evidence has suggested the impact of senescence on tumor progression (13, 14), but no report has yet described how senescence shapes the tumor microenvironment of ccRCC. The current perspective suggests that senescence and tumorogenesis are two different manifestations resulting from the accumulation of cell damage over time. López-Otín et al. summarized and proposed nine biological features to define the senescence phenotype (15). The evolution of the senescence microenvironment is inextricably linked to a shift in fibroblast behavior (13). In the young tissue microenvironment, fibroblasts promote immune infiltration and clearance of adverse factors, whereas, in the senescent microenvironment, fibroblasts undergo a persistent senescence-associated secretory phenotype (SASP) and turn to support immunosuppressive cell infiltration such as MDSC and Treg (16–19). On the other hand, the accumulation of cellular senescence features in macrophages, dendritic cells (DCs), natural killer (NK) cells, and effector T cells also leads to a decrease in anti-tumor immunity (13). In addition, it has been demonstrated that integrity loss of extracellular matrix (ECM) in the senescent microenvironment is another leading cause of the onset and progression of malignant events (20). In other words, the development of the senescence theory may provide new ideas to further delineate the immune characteristics of ccRCC. Therefore, there is a need for understanding the senescence features of ccRCC, especially the association of senescence factors with clinical prognosis and therapeutic benefit, which may be informative for the development of interventions targeting senescence.

Here, we conducted a comprehensive delineation of senescence features in 2,072 ccRCC samples and identified three senescence subtypes with significantly different molecular and immune microenvironmental characteristics. We constructed a senescence score using the senescence-related genes, which is not only a robust prognostic indicator, but subgroup analysis revealed senescence score subgroups with different sensitivity to targeted therapies and immunotherapy.

MATERIALS AND METHODS

Raw Data Retrieval and Preparation

We retrospectively collected expression profiles of frozen tumor specimens from 13 publicly available ccRCC cohorts: RNA-seq data of the TCG-Kidney renal clear cell carcinoma (KIRC) cohort from the TCGA project; a total of nine microarray cohorts based on the GPL570 and GPL10588 platforms archived in the GEO portal (https://www.ncbi.nlm.nih.gov/geo/); and two microarray archived in the ArrayExpress database (https://www.ebi.ac.uk/arrayexpress/). Complete clinical information is available in the TCGA-KIRC, E-MTAB-1980, E-MTAB-3267, and Checkmate, with E-MTAB-3267 containing 53 advanced metastatic ccRCC treated with sunitinib and Checkmate containing 181 advanced ccRCC treated with Nivolumab and 130 patients treated with

Abbreviations: RCC, renal cell carcinoma; ccRCC, clear cell renal cell carcinoma; TCGA, The Cancer Genome Atlas; GEO, Gene Expression Omnibus; ICB, immune checkpoint blockade; MDSC, myeloid-derived suppressor cells; CNV, copy number variation; FPKM, fragments per kilobase million; TPM, transcripts per kilobase million; ssGSEA, single-sample gene set enrichment analysis; GSVA, gene set variation analysis; GO, gene ontology; KEGG Kyoto Encyclopedia of Genes and Genomes; DESG, differentially expressed senescence-related genes; TMB, tumor mutation burden; CR, complete recession; PR, partial recession; SD, stable disease; PD, progressed disease; CB, clinical benefit; ICB, intermediate clinical benefit; NCB, no clinical benefit; OS, overall survival; DFS, disease free survival; PFS, progression free survival; TKI, tyrosine kinase inhibitor; MDSC, myeloid-derived suppressor cells; NK, natural killer; DC, dendritic cell; CAF, cancer-associated fibroblast; LASSO, least absolute shrinkage and selection operator; SASP, senescence-associated secretory phenotype; SKCM, skin cutaneous melanoma; ECM, extracellular matrix; ROC, receiver operating characteristic curve; AUC, areas under curve.

Everolimus. Baseline information for datasets involved in this study was summarized in **Table S1**. FPKM values of TCGA-KIRC provided by the UCSC Xena website (https://xena.ucsc.edu/) were transformed into TPM values and log2-transformed to maintain comparability with microarray platform-produced data. Raw data of the "CEL" format generated from the Affymetrix platform was background corrected and normalized using the "affy" package. For datasets from the GEO database, six datasets based on the GPL570 platform (i.e., GSE36895, GSE53757, GSE66272, GSE73731, GSE46699, and GSE22541) and three datasets based on GPL10588 (i.e., GSE40435, GSE105261, an GSE65615) were merged as GPL570-merge and GPL10588-merge using the "sva" function of the "Combat" package.

Senescence Signatures and Cellular Senescence-Related Genes Retrieval

Fifteen senescence-related gene sets were retrieved and archived in the MSigDB database, including nine GO biological processes and six Reactome hallmarks. A total of 279 experimentally confirmed cellular senescence-related genes were archived in the CellAge database (https://genomics.senescence.info/cells/).

Differentially Expressed Senescence-Related Genes (DESG) Analysis and Functional Annotation

Differential expression analysis was performed using the "limma" package, and an adjusted p-value < 0.05 was set to identify the DESGs. Gene set enrichment analysis (GSEA) was performed using the "ReactomePA" package. GO/KEGG annotation of the DESGs was performed using the "ClusterProfiler" package.

Identification of the Senescence Subtypes in ccRCC

Gene set variation analysis (GSVA) was developed to estimate the signaling pathway activity of a single sample based on reference gene sets {Haenzelmann:2013ga}. We used the "GSVA" package to estimate the activity of the senescence-related biological processes of tumor samples. The unsupervised consensus clustering using the "km" algorithm was adopted to identify senescence subtypes in tumor samples of TCGA-KIRC based on the GSVA enrichment score. The similarity of samples was determined by the Euclidean distance. One thousand iterations were recycled in the clustering to ensure the stability of the results. The discrimination of the samples of subtypes was assessed using t-distributed stochastic neighbor embedding (t-SNE) downscaling analysis provided by the "Rtsne" package.

Cancer Hallmarks and Tumor Microenvironment Characteristics Analysis

We use the "IOBR" package to analyze the molecular and immune microenvironment characteristics of ccRCC (21). The cancer hallmarks, GO/KEGG biological process, metabolic, and tumor microenvironment signatures, as well as eight immune cell estimation methods (i.e., Cibersort, MCP, xCell, EPIC, Estimate, quantiseq, IPS, and TIMER) were integrated into the "IOBR" package. We estimated the biological process activity of tumor samples using the calculate_sig_score function. The percentage of immune cells was deconvoluted using the deconvo_tme function. In addition, the relative infiltration abundance of 28 immune cells (16 adaptive immune cells and 12 intrinsic immune cells) was estimated using the ssGSEA algorithm provided by the "GSVA" package (22).

Construction and Verification of the Senescence Score and Nomogram for Clinical Application

The TCGA-KIRC (n = 514) was used as the development cohort and the E-MTAB-1980 (n = 100) as the test cohort to validate the prognostic model, and the baseline clinic parameters were summarized in **Table S2**. The predictive value of the senescence score for targeted therapy and immunotherapy responsiveness was verified in the E-MTAB-3267 and Checkmate cohorts. To ensure the robustness of the prognostic model, we excluded samples with survival times shorter than 1 month from the TCGA-KIRC and E-MTAB1980 cohorts. Firstly, the Pearson's correlation of all differentially expressed senescence-related genes with PD-1/PD-L1/CTLA4 expression levels was calculated, and genes with a Bonferroni corrected p-value < 0.05 were retained. Secondly, univariate cox analysis identified prognostic senescence-related genes with p<0.05. Subsequently, the best combination of senescence genes to construct a multivariate cox model was determined by performing adaptive lasso regression using the "glmnet" package. Adaptive lasso regression eliminates the overfitting bias by introducing weights to the traditional lasso model and obtains a more succinct model without compromising model performance (23). A multivariate Cox model was constructed using the senescence genes identified by lasso Cox regression, the coefficient value of each gene was derived, and the senescence score was generated by multiplying the gene expression by the non-zero coefficient of each gene:

$$\text{Senescence score} = \sum \text{Gi} * \text{Bi}$$

where Gi is the expression level and Bi is the coefficient. A nomogram was built up using the "rms" package and assessed by the calibration curves.

Prediction of Patients' Sensitivity to Targeted Therapy and Immunotherapy

We used the "pRRophetic" package to infer the sensitivity of tumor samples to targeted therapeutic agents. Specifically, the cancer cell gene expression profiles and corresponding IC50 values under drug agent treatment retrieved from the GDSC database were used as references. pRRophetic runs a 10-fold cross-validation ridge regression to estimate the IC50 values of the ccRCC samples based on their gene expression profiles. The similarity of gene expression profiles between the ccRCC samples and 47 skin melanoma patients treated with anti-CTLA4/PD-1

was inferred using the Subclass Mapping module provided by the GenePattern portal (24, 25).

Statistical Analysis

All statistical analysis was performed and all results were visualized in Rstudio 4.0.1. The Wilcoxon or Kruskal–Wallis tests evaluated the difference between two or more groups of continuously distributed variables. Fisher's exact test evaluated the distribution difference of categorical variables. Survival status was visualized by the Kaplan–Meier method, and the OS difference was assessed using the log-rank test. The ROC curves were adopted to assess the predictive capacity of the prognostic indicators. The Bonferroni correction for multiple tests was adopted to reduce the probability of Class I error, and the statistical difference was considered significant when the p-value of bilateral tests < 0.05.

RESULTS

Senescence Signatures Are Generally Activated in ccRCC

To delineate the senescence characteristics of ccRCC, we conducted a comparison of tumor and para-cancerous tissues in three independent datasets. GSEA analysis of TCGA-KIRC showed that cellular senescence, oncogene-induced senescence, and SASP were significantly activated in tumor samples (**Figure 1A**). Similar results were obtained in the GPL570-merge and GPL10588-merge datasets (**Figures 1B, C**). We merged the three datasets into metadata, and the heatmap showed that the senescence-related GO/Reactome terms were markedly activated in tumor samples (**Figure 1D**). These results suggest that senescence is an important hallmark of ccRCC. Using DEG analysis, we identified 204 differentially expressed senescence-related genes in TCGA-KIRC, including 124 upregulated and 82 downregulated (**Table S3**). GO annotation showed the significant enrichment of cell aging, regulation of the cell cycle, and chromosomal behavior (**Figure 1E**). The KEGG annotation showed the enrichment of the cell cycle, cell senescence, and p53 signaling pathway (**Figure 1F**).

Senescence Subtypes Identification in ccRCC Based on Senescence Signatures

To better understand the senescence phenotypes in ccRCC, we performed unsupervised consensus clustering based on the activity of the senescence-related GO/Reactome terms. The clustering heatmaps and cumulative distribution function (CDF) curves suggested the existence of three senescence subtypes in ccRCC (**Figures 2A-C**). The t-SNE plots exhibited good discrimination among the three clusters (**Figure S1B**). We termed them senescence-silenced (Cluster A), senescence-suppressed (Cluster B), and senescence-activated phenotypes (Cluster C), respectively (**Figure 2A**). The heatmap of the DEG showed that senescence-related genes were generally inhibited in senescence suppressed phenotype while highly expressed in senescence activated phenotype (**Figure S1A**). The OS and disease-free survival (DFS) rates of the senescence-activated phenotype were significantly lower than the senescence-suppressed and senescence-silenced phenotypes (**Figure 2D**). We then generated three senescence subtypes in the E-MTAB-1980 and Checkmate cohorts for further analysis (**Figures S1C–F**). Similarly, patients of the senescence-activated phenotype in E-MTAB-1980 survived the worst (**Figure 2E**). Interestingly, the senescence-activated subtype had the worst progression-free survival (PFS) and OS rates in both the Nivolumab- and Everolimus-treated arms (**Figure 2F**). Whereas no significant differences in objective response or clinical benefit were found among the subtypes (**Figure 2G**). The correlation of previously published VEGF pathway- and inflammation-related gene signatures with senescence subtypes was also investigated. The results showed an increase in immunoinflammatory-related gene signature activity (Javelin_Immuno, Merck18, IMmotion150_Myeloid, IMmotion150_Teff), and a decrease in VEGF-related gene signature activity (IMmotio150_Angio) as the senescence program was activated (**Figure 2H**).

Molecular and Immune Microenvironment Characteristics of the Senescence Subtypes

We then depicted the cancer hallmarks of senescence subtypes. The results showed that the majority of cancer hallmarks were significantly differentially distributed among the subtypes (**Figure 3A**). The activity of cell cycle regulation-related biological processes such as DNA repair, MYC targets, and G2M checkpoints was highest in the senescence-activated subtype. The senescence-suppressed subtype was associated with metabolic pathways such as adipogenesis, bile acid metabolism, and fatty acid metabolism.

In terms of genomic heterogeneity, we focused on the differentially distributed mutations and copy number variants (CNV). The upper panel of the heatmap (**Figure 3B**) displayed the mutation spectrum of genes with frequencies >5%. We identified six differentially distributed mutated genes (PBRM1, MUC16, BAP1, XIRP2, DNAH3, TSHZ3, and SSH2). The senescence-activated subtype carried fewer PBRM1 mutations and more BAP1 mutations. The bottom panel of the heatmap (**Figure 3B**) displayed the differentially distributed chromosomal fragment copy number alterations, with an overall decreased copy number amplification and increased deletion events in the senescence-activated subtype. More specifically, CNV in the senescent subtype is characterized by decreased 5q fragment amplification and increased 3p fragment deletion.

Subsequently, we deconvoluted the tumor microenvironment of the senescence subtypes. Overall, the abundance of immune cell infiltration, except for NK cells, eosinophils, and neutrophils, within the tumor tended to increase with senescence program activation (**Figure 3C**), which was consistent with the increased immunoinflammatory-related gene signature activity in the Checkmate cohort in **Figure 2H**. Meanwhile, we checked the signaling activity of cancer-associated fibroblasts (CAFs), immune suppression, immune exclusion, and immune exhaustion (**Figures 3D–G**). Dramatically, we found these features were also significantly upregulated along with senescence activation.

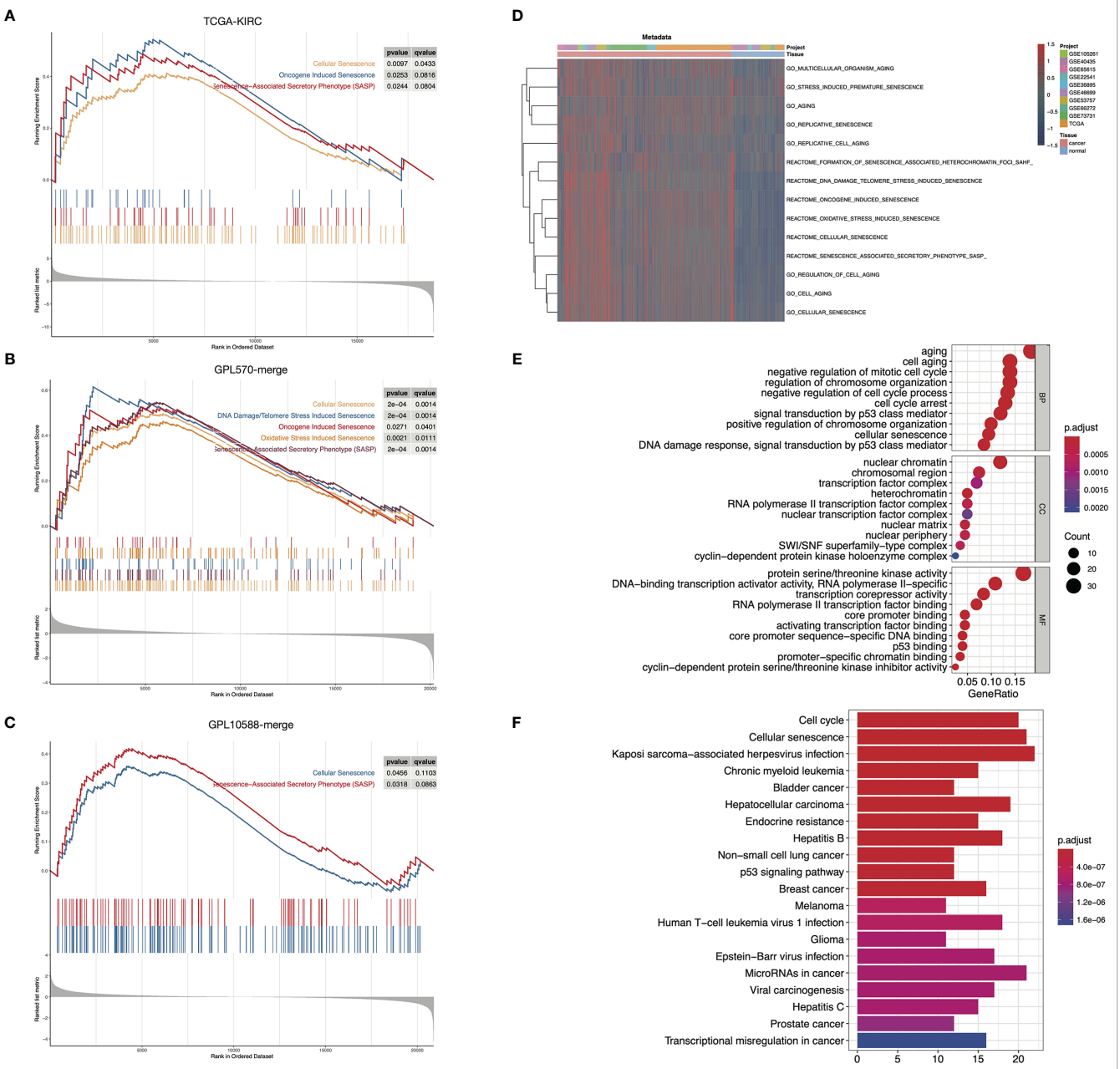


FIGURE 1 | Senescence-related biological processes were highly activated in ccRCC. **(A–C)** GSEA results showed that senescence-related biological processes were activated in ccRCC tumor samples in TCGA-KIRC **(A)**, GPL570-merge **(B)**, and GPL10588-merge **(C)** datasets. **(D)** Senescence-related biological processes were generally activated in ccRCC tumor samples in the metadata set. The biological process activity was assessed using the "GSVA" package. **(E, F)** Functional annotation of the 204 DESGs in the GO **(E)** and KEGG **(F)** database.

Signatures from different gene expression profiles suggest that the senescence program is closely correlated with CAFs of the tumor stroma and self-limited antitumor immunity.

Development of Senescence Score to Predict Patients' Prognosis

The senescence subtypes profoundly influence tumor progression and the immune landscape, leading to distinctive clinical outcomes. Here, we developed a multivariate model containing nine senescence-related genes (i.e., P3H1, PROX1, HJURP, HK3, CDKN1A, AR, VENTX, MAGOHB, and MAP2K6; **Table S4**) by performing adaptive lasso regression to predict patients' outcomes (**Figures 4A, B**). The senescence score was generated by multiplying the gene expression by the corresponding non-zero coefficient (**Table S4**). Patients were stratified into two groups using the median senescence score, and

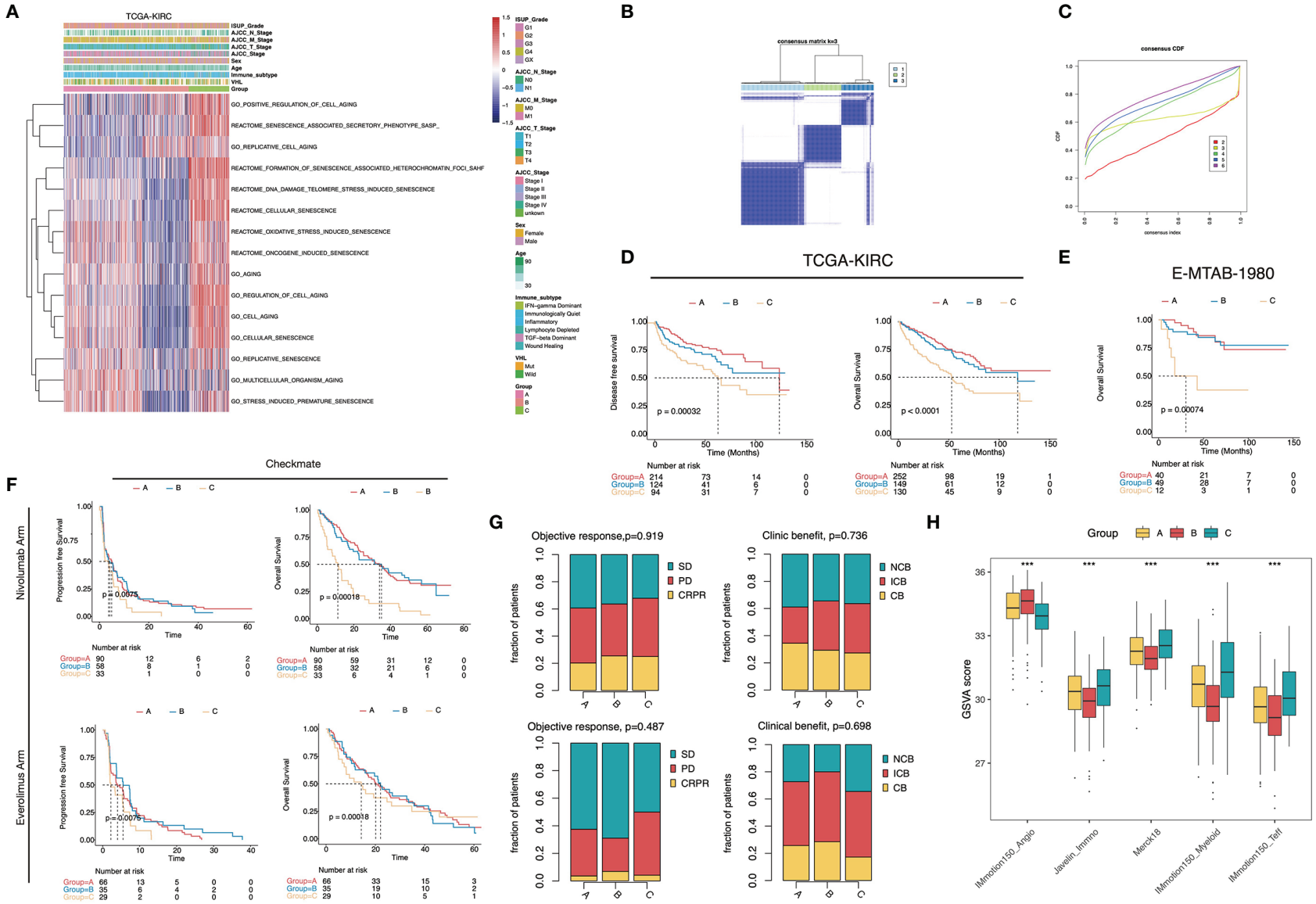


FIGURE 2 | Senescence subtype was correlated with stratified patients' prognosis and treatment benefits. **(A)** Heatmap of the 15 senescence-related biological processes of the senescence subtypes in TCGA-KIRC. **(B)** The heatmap of the k-means consensus clustering result. **(C)** CDF curves of the consensus clustering. **(D–F)** Kaplan–Meier curves showed the survival difference among the senescence subtypes in TCGA-KIRC **(D)**, E-MTAB-1980 **(E)**, and Checkmate **(F)**. Log-rank test. **(G)** Bar plots displayed the proportion of objective response and clinical benefit rates among the senescence subtypes in Checkmate. **(H)** Boxplot showed the difference of the VEGF- and inflammatory-related signature scores in Checkmate. ***, p<0.001.

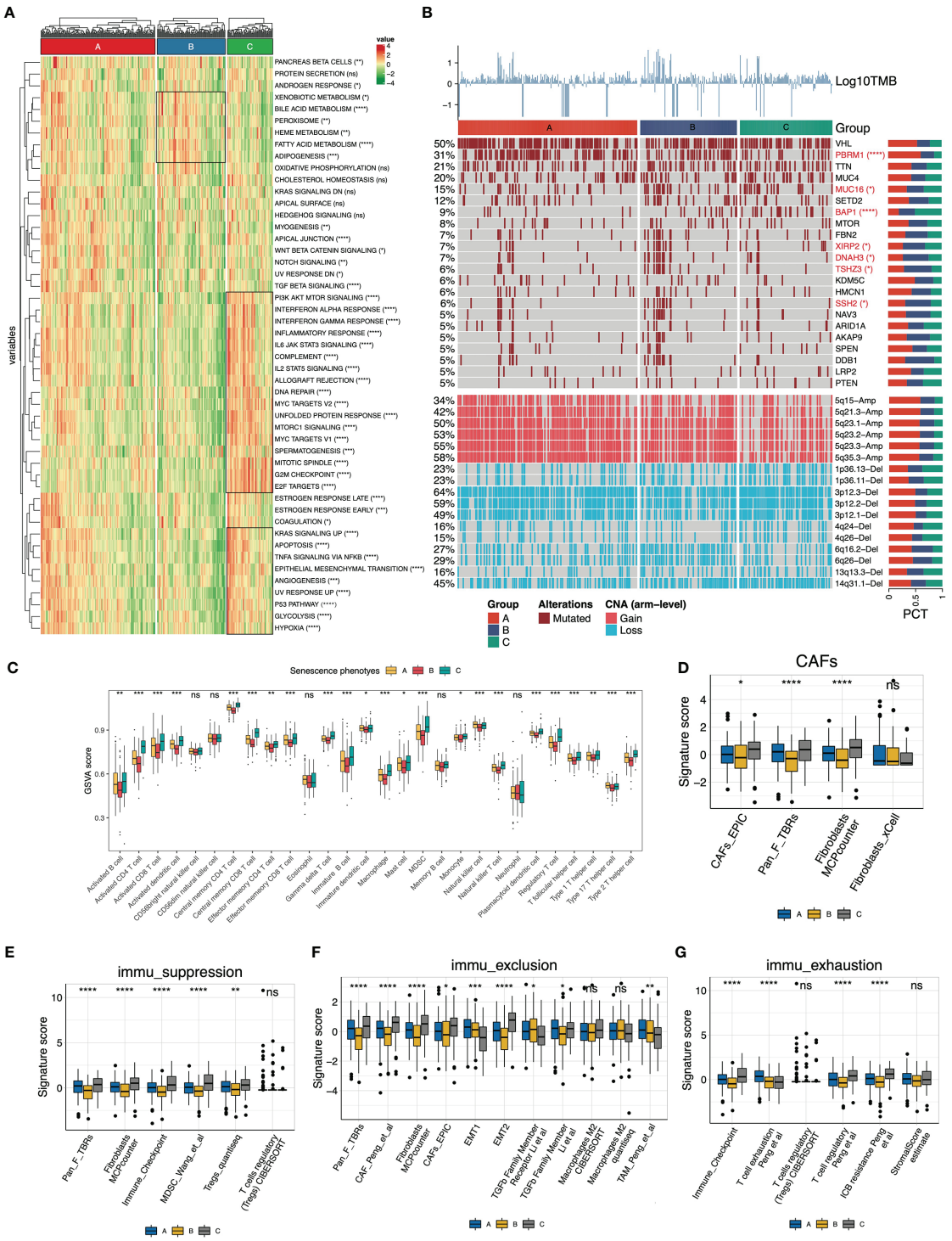


FIGURE 3 | Molecular and immune features of the senescence subtypes of TCGA-KIRC. **(A)** Heatmap of the cancer hallmarks estimated by the ssGSEA algorithm. **(B)** Genomic heterogeneity of the senescence subtypes. The heatmap displayed log10TMB, gene mutation profile (frequency >5%), and differentially distributed arm-level copy number variants (CNV) from top to bottom, respectively. The distribution difference was determined by Fisher's exact test. **(C)** The 28 immune cells (16 adaptive and 12 intrinsic immune cells) were differentially distributed in the senescence subtypes. The infiltration abundance was estimated by the ssGSEA algorithm. **(D–G)** Signature panels calculated using the "IOBR" package, **(D)** Cancer-associated fibroblasts (CAFs), **(E)** immune suppression, **(F)** immune exclusion, and **(G)** immune exhaustion signatures. The level of statistical difference was labeled with ns, *, **, ***, and ****, which represents no statistical difference, $p < 0.05$, $p < 0.01$, $p < 0.001$, and $p < 0.0001$, respectively.

significantly poorer survival rates were observed in the high-senescence score group (**Figures 4C, D**). The predictive accuracy of senescence scores at 1, 3, and 5 years for OS was 0.753, 0.748, and 0.785, respectively, whereas it was 0.690, 0.708, and 0.695 for DFS, respectively (**Figures 4E, F**). The senescence score remained an independent unfavorable factor for patients' prognosis after adjusting clinicopathological parameters (**Figure 4G**). To facilitate clinical application, we integrated the senescence score with patients' age, American Joint Committee on Cancer (AJCC) stage, metastatic status, and international summer university program (ISUP) grade to establish a nomogram (**Figure 4H**). The calibration curves for the nomogram were plotted, and the results showed that the actually observed status was very close to the predicted survival

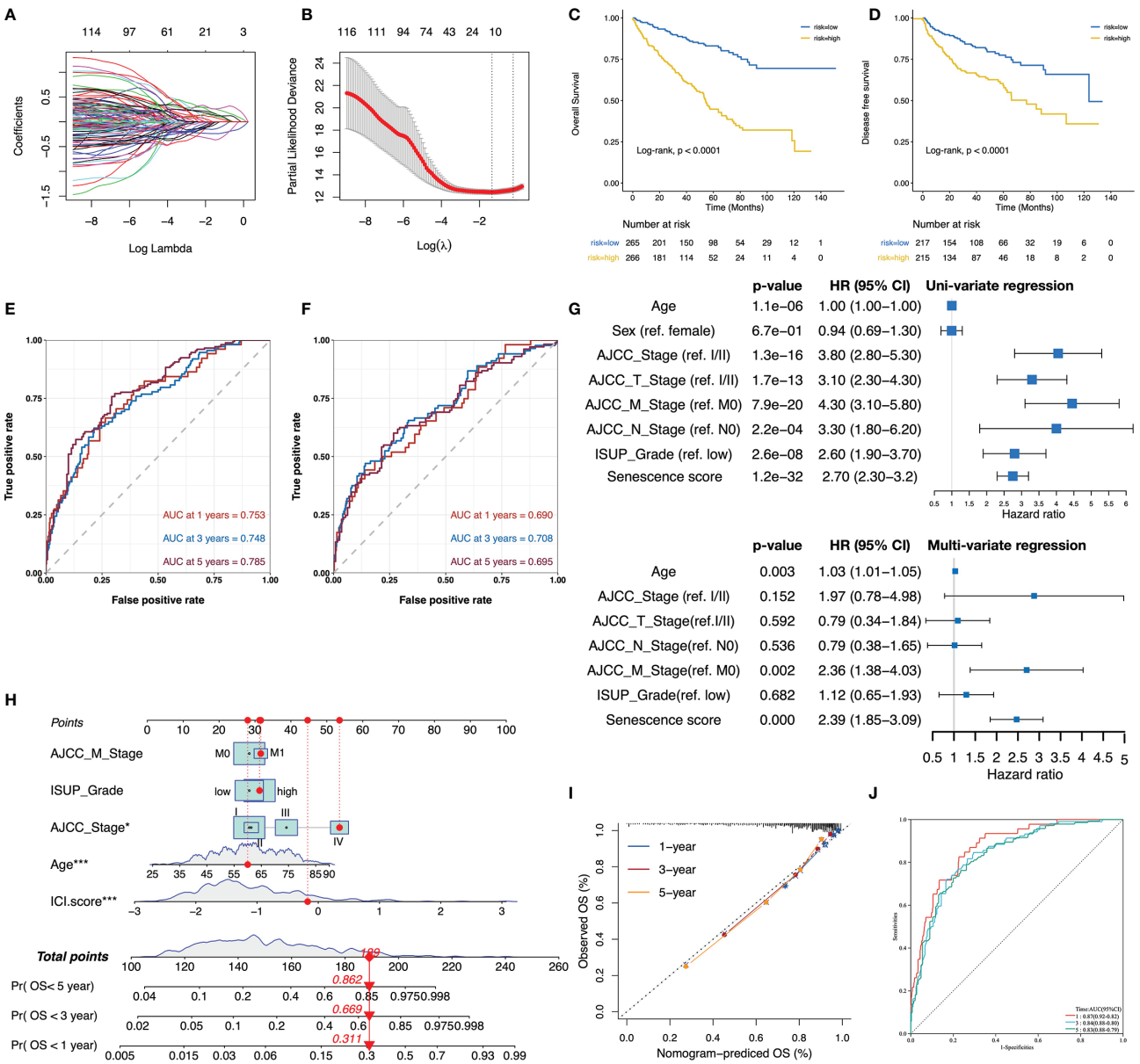


FIGURE 4 | The senescence score was a prognostic indicator for patients' prognosis in TCGA-KIRC. **(A, B)** The adaptive lasso regression selected the best combination of senescence genes to construct a multivariate Cox model. **(C, D)** Survival analysis showed a different survival portion between the high- and low-senescence score subgroups in TCGA-KIRC for OS **(C)** and DFS **(D)**. **(E, F)** The predictive power of the senescence score for 1-, 3-, and 5-year OS **(E)** and DFS **(F)** was assessed by ROC curves. **(G)** Forest plots of the uni- and multivariate Cox models in TCGA. **(H)** Nomogram to predict patients' overall survival. The model incorporated the AJCC_Stage, ISUP_Grade, metastatic status, patients' age, and the senescence score. **(I)** The calibration curves show that the survival status of patients predicted by nomogram at 1, 3, and 5 years remains highly consistent with that actually observed. **(J)** ROC curves to evaluate the predictive efficacy of the nomogram for overall survival at 1, 3, and 5 years. *,p<0.05, ***, p<0.001.

status at the observation time points, indicating a robust predictive capacity of the nomogram (**Figure 4I**). ROC curves assessed the predictive power of the senescence score for patient's prognosis at 1, 3, and 5 years, and the areas under curves (AUC) reached 0.87, 0.84, and 0.83, respectively (**Figure 4J**).

Given the SASP phenotype mediates the transition in cancer-inhibiting to cancer-promoting roles of the senescence process, we next assessed the relationship between the senescence score and SASP activity. The senescence score was positively correlated to the SASP score in each subtype, and the highest Pearson's coefficient was detected in the senescence-activation group (**Figure 5A**). In terms of immunophenotypes, wound healing and TGF-dominant phenotypes had the highest senescence scores, whereas inflammatory and immunologically quiet phenotypes had the lowest (**Figure 5B**). Subsequently, we found that the senescence score was negatively correlated to the immune cell infiltration levels by performing correlation analysis (**Figure 5C**). Furthermore, the senescence score was negatively correlated with CAFs and antigen-presenting cells (DCs and macrophages) as quantified by several deconvolution tools (**Figure 5D**). These results suggest that high senescence scores suppress the anti-tumor immune potential.

Verification of the Senescence Score and Nomogram in Predicting Patients' Prognosis

The predictive value of the senescence score for the patients' prognosis was further tested in E-MTAB-1980. Similar to TCGA-KIRC, a comparison of subgroups based on cohort-specific median senescence scores demonstrated significantly decreased OS rates in the high-score group (**Figure 5E**). The senescence score achieved a predictive efficacy of 0.861, 0.844, and 0.795 for 1-, 3-, and 5-year survival, respectively (**Figure 5F**). Even after adjusting for patients' age, clinical stage, T/M stage, and tumor grade, the senescence score remained an independent risk factor for patients' prognosis (**Figure 5G**). When applying the nomogram established in TCGA-KIRC to E-MTAB1980, the calibration curve exhibited consistency between the nomogram-predicted and actually observed survival status (**Figure 5H**). Furthermore, the nomogram's predictive efficacy for the patients' prognosis at 1, 3, and 5 years reached an impressive 0.9, 0.91, and 0.89, respectively (**Figure 5I**).

Correlation of the High Senescence Score Group With Targeted Therapy Benefit

Patients in E-METAB-3267 were all treated with sunitinib (n = 53). Validation of E-METAB-3267 showed an extended PFS in the high-senescence score subgroup (**Figure 6A**). The senescence score achieved a predictive efficacy of 0.74, 0.751, and 0.680 for 1-, 2-, and 3-year PFS, respectively (**Figure 6B**). When comparing the Sunitinib-response and no-response groups, we found significantly higher scores in the Sunitinib-response group (**Figure 6C**), with a predictive efficiency of 0.623 for Sunitinib treatment response (**Figure 6D**). Everolimus is an mTOR-targeted inhibitor for patients who have failed Sunitinib or Sorafenib therapy. Testing in the Checkmate-Everolimus treatment arm found no PFS benefit ($p = 0.19$) but an OS benefit ($p = 0.036$) in the high-score group (**Figures 6E, F**). In addition, we stratified TCGA-KIRC, E-MTAB-1980, GPL570-merge, and GPL10588-merge by cohort-specific median senescence score and inferred the drug sensitivity to Sunitinib (VEGF-targeted) and Temsirolimus (mTOR-targeted). In the high-senescence score subgroup (**Figure 6G**), we found significantly lower predicted IC50 values for Sunitinib and Temsirolimus. Collectively, these results indicated anti-VEGF/mTOR-based targeted treatment benefits in the high-senescence score subgroup.

Correlation of the Low Senescence Score Group With ICB Benefit

We next investigated the association of the senescence score with immunotherapy benefit in the Checkmate cohort. We classified patients by median senescence score and found a significant OS benefit of Nivolumab treatment over Everolimus treatment in the low-senescence score subgroup (**Figures S2A, B**). In contrast, no significant PFS/OS survival difference between the treatment arms was observed in the high-senescence score group (**Figures S2C, D**). For Nivolumab treatment, patients in the high-senescence score group determined by the surv_cutpoint function had significantly shorter PFS and OS time (**Figures 7A, B**). Recently, 9p21.3 deletion was reported as an unfavorable factor for immunotherapy responsive in CD8+ T infiltrated ccRCC, whereas PBRM1 mutation was a favorable factor in non-infiltrated ccRCC (10). We observed significantly higher senescence scores in the 9p21.3 loss group and lower scores in the PBRM1 mutation group in both the Checkmate and TCGA-KIRC cohorts (**Figures 7C, D**). In the context of senescence score suppressing immune infiltration, these findings further explain the strong association of the high senescence score group with ICB treatment resistance. Finally, we performed submap mapping inference to further validate the association of the senescence score with ICB benefit in four independent cohorts. As a result, the four cohorts consistently showed a high concordance of the gene expression profiles between low-score group patients and anti–PD-1 SKCM responders (**Figure 7E**), demonstrating the low senescence score group would benefit from anti–PD-1 treatment.

DISCUSSION

In this study, our exploration of multiple independent ccRCC datasets revealed that activation of senescence-related biological processes is a hallmark of ccRCC. Through delineating the three senescence subtypes, we found that the senescence-activated subtypes possess the worst oncological outcomes, even in the condition of targeted therapy/immunotherapy. Cellular senescence is defined as permanent cell cycle arrest, in which p53/CDKN1A and CDKN2A/pRB signaling play a leading role (14). We found that cell cycle–related signals, including G2M checkpoint, p53 signaling, MYC target, and accumulation of cellular damage events, such as DNA repair and apoptosis, are enriched in the senescence-activated subtype in ccRCC. In addition, senescence program activation was also correlated to

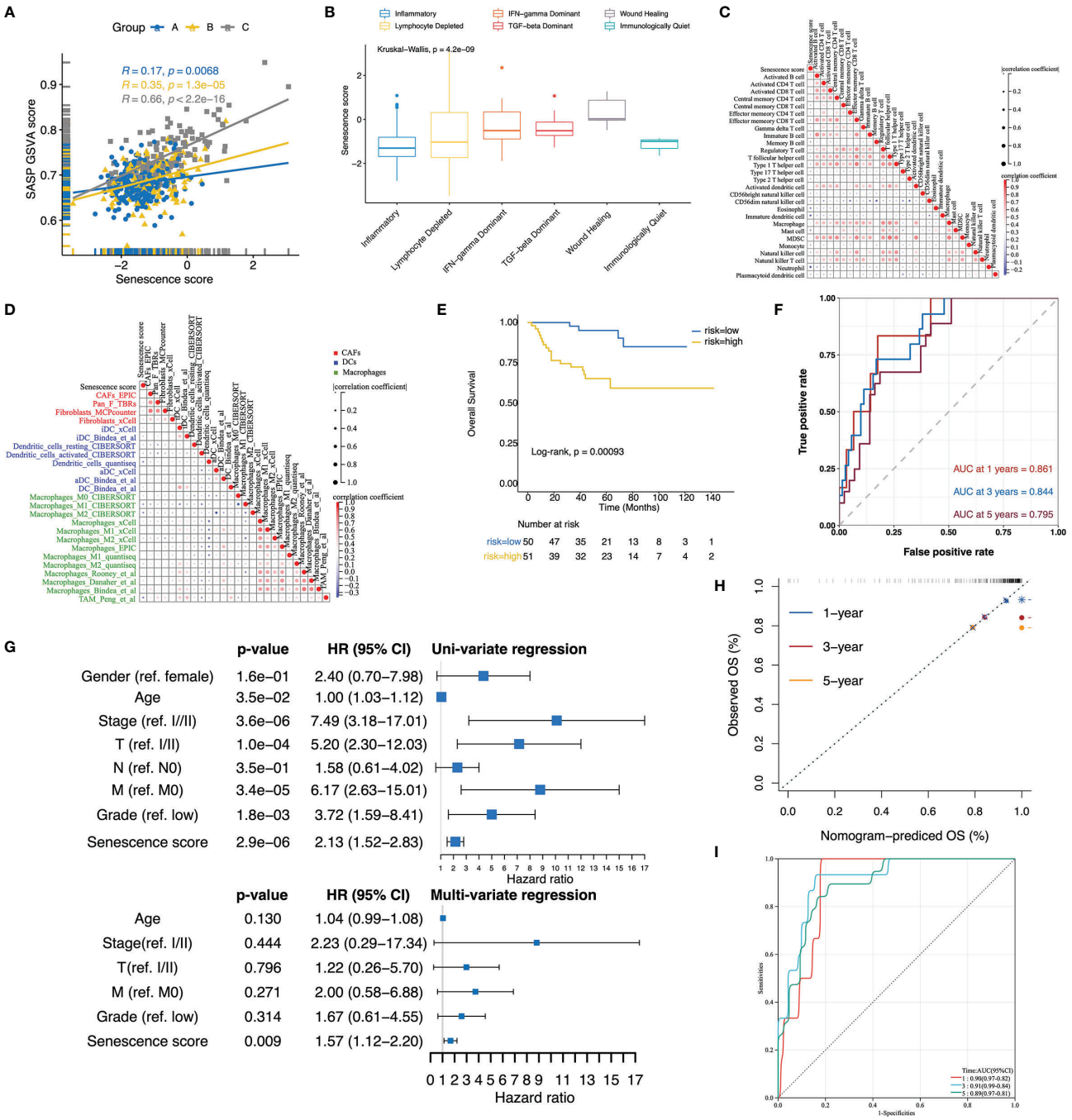


FIGURE 5 | Validation of the senescence score and nomogram to predict patients' overall survival in E-MTAB-1980. **(A)** Scatterplot with regression lines for senescence score with SASP activity stratified by senescence subtypes. **(B)** The boxplot displayed that the senescence score was differentially distributed among immune subtypes. **(C, D)** Correlation plots displayed a negative correlation of the senescence score with infiltrated immune cells **(C)**, CAFs, DCs, and macrophage signatures **(D)**. The correlation was evaluated using Pearson's correlation coefficients. **(E)** In E-MTAB-1980, the Kaplan–Meier curves revealed a different survival portion between the high- and low-senescence score subgroups. **(F)** ROC curve assessed the predictive power of the senescence score for 1-, 3-, and 5- year overall survival in E-MTAB-1980. **(G)** Forest plots of the uni- and multivariate Cox models in E-MTAB-1980. **(H)** The calibration curves showed that the survival status of patients predicted by the nomogram applied to E-MTAB1980 at 1, 3, and 5 years remains highly consistent with that actually observed. **(I)** ROC curves to evaluate the predictive efficacy of the nomogram for overall patient survival at 1, 3, and 5 years in E-MTAB-1980.

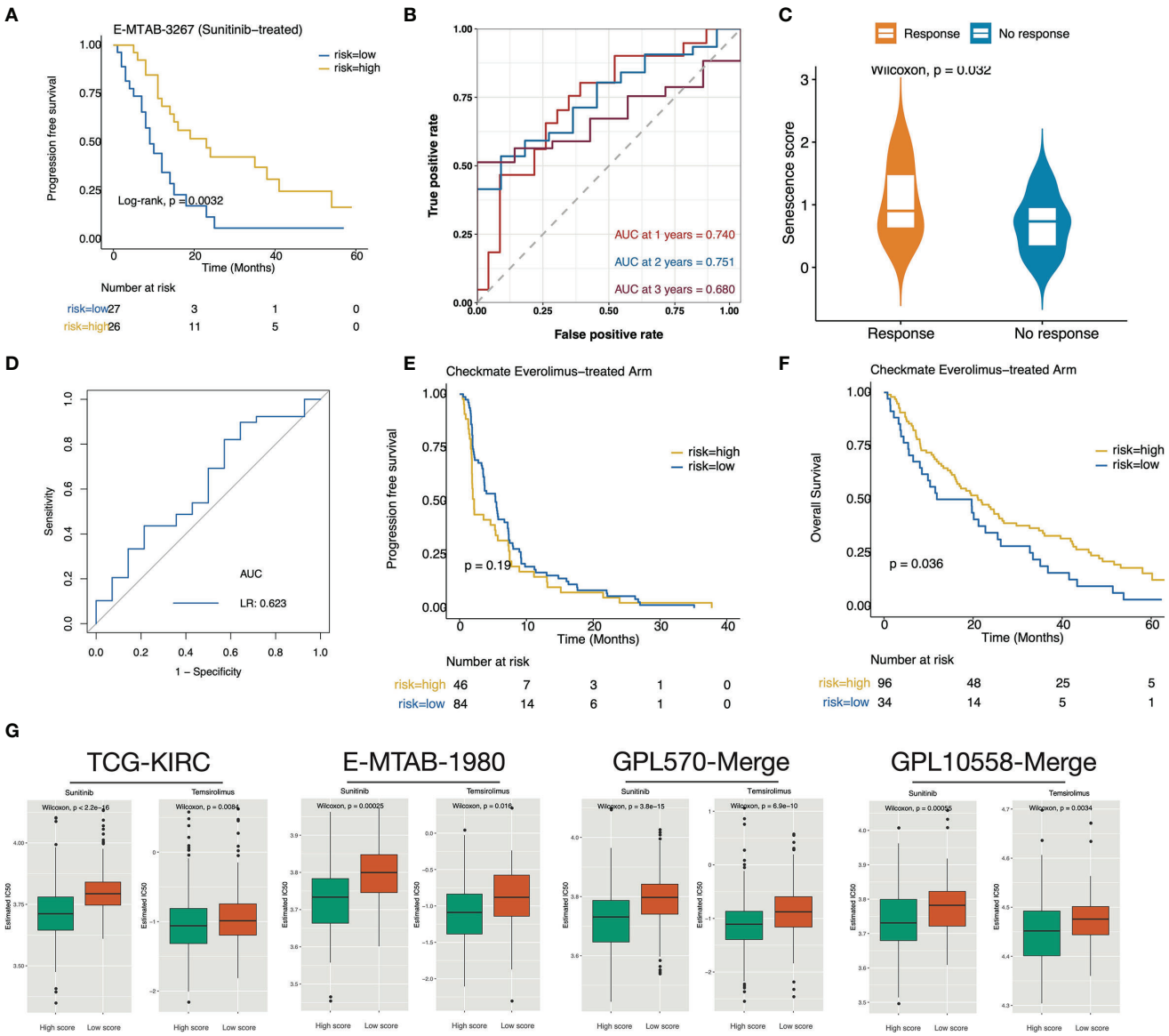


FIGURE 6 | The high senescence score subgroup was correlated with targeted therapy benefit. **(A)** Kaplan–Meier curve exhibited extended PFS time in patients of the high-senescence score groups. **(B)** The predictive value of the senescence score for PFS after sunitinib treatment. **(C)** Boxplot showed that the Sunitinib-response group possesses significantly higher senescence scores. **(D)** Predictive power of the senescence score for sunitinib response. **(E, F)** Survival curves showed that the high-score group determined by the surv_cutponit function gained OS benefit **(F)** in Everolimus treatment rather than PFS benefit **(E)**. **(G)** The predicted IC50 values for Sunitinib and Temsirolimus in the TCGA-KIRC, E-MTAB-1980, GPL570-merge, and GPL10588-merge datasets. A lower IC50 value represents more sensitivity to the drug treatment.

the activation of tumor malignant events such as hypoxia, angiogenesis, and EMT signaling.

ccRCC is characterized by widespread loss of 3p and amplification of 5q fragments, and genes encoded by 3p fragments (e.g., PBRM1, BAP1, and SETD2) are frequently mutated and closely correlated to altered prognosis (26). Both BAP1 and PBRM1 are encoded in the 3p21.1 location and are involved in chromatin remodeling to maintain genomic stability. We observed that the senescence subtypes are closely associated with 3p loss/5q amplification and differentially distributed PBMR1/BAP1 mutations, indicating a non-negligible role in ccRCC progression that the senescence process plays. The PBRM1 mutation has been linked to activated angiogenesis and improved sunitinib treatment outcomes when compared to Atezolizumab+Bevacizumab combination treatment (5). In addition, the PBRM1 mutant subgroup also conferred a significant benefit compared with the wild-type subgroup in the Sunitinib treatment arm (27). Clinical trials also reported the correlation of PBRM1 mutation with improved Everolimus treatment outcomes (28), which was demonstrated to be a result of mTOR signaling activation (26). Interestingly, the most recent

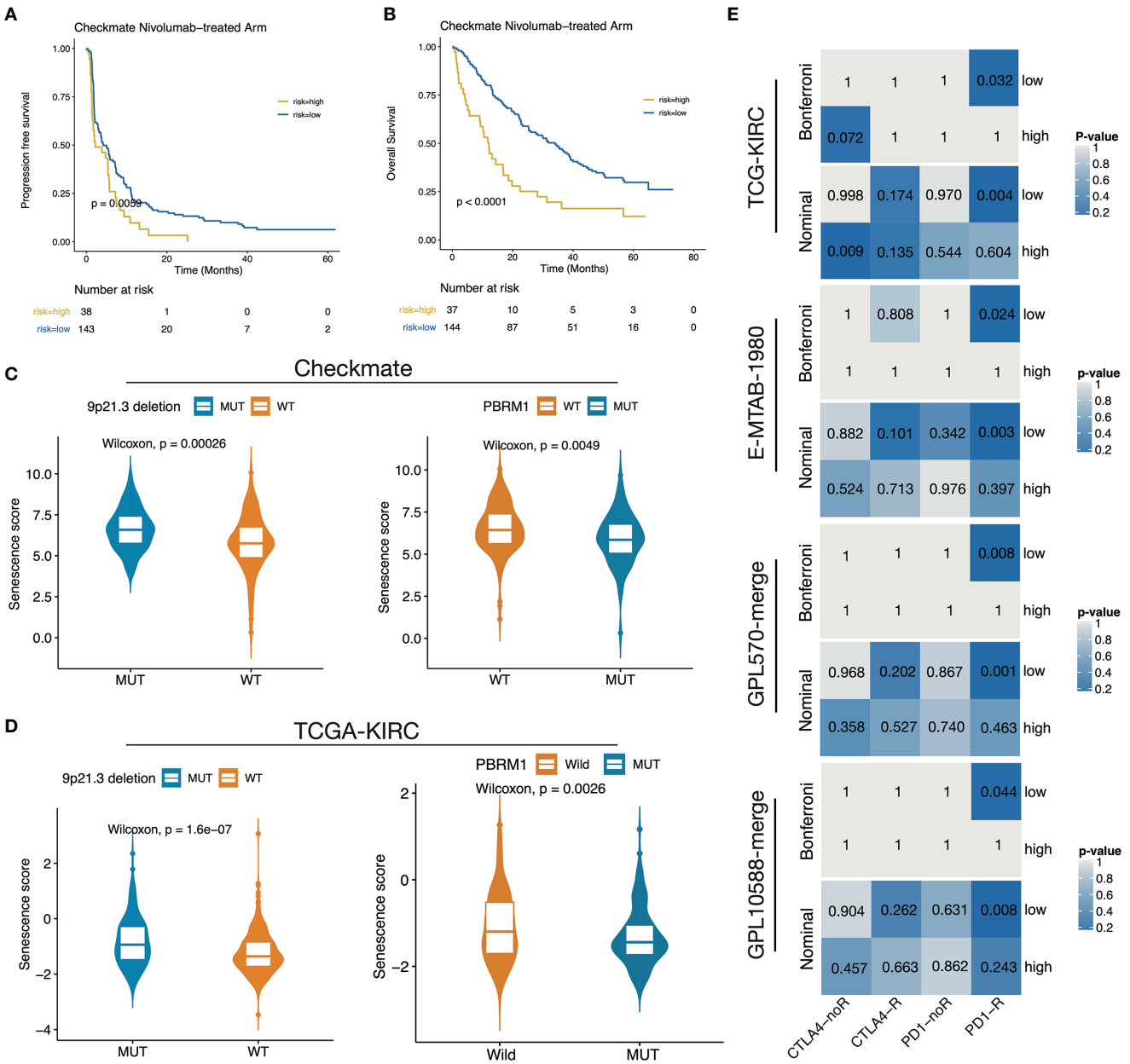


FIGURE 7 | The low senescence score subgroup was predicted to respond to anti–PD-1 treatment. **(A, B)** Survival curves showed that the high-score group determined by the surv_cutponit function gained PFS **(A)** and OS **(B)** benefits. **(C, D)** The boxplot showed that 9p21.3 loss groups possess higher senescence scores while PRBM1 mutant groups possess lower senescence scores in Checkmate **(C)** and TCGA-KIRC **(D)**. **(E)** Subclass mapping results in TCGA-KIRC, E-MTAB-1980, GPL570-merge, and GPL10588-merge datasets using a melanoma dataset treated with anti-CTLA4/PD-1 as a reference.

clinical trial reported the correlation of PBRM1 mutation with anti–PD-1 treatment response in CD8+ T no-infiltrated ccRCC (10). The BAP1 mutation is not only an independent risk factor for ccRCC prognosis (29) but is also linked to poorer Sunitinib/Everolimus treatment outcomes (28). The unbalanced distribution of PBRM1/BAP1 mutations provided a genomic-level explanation for the association of the senescence-activated subtype with poor targeted/immunotherapy treatment outcomes.

Literature also demonstrated that targeted therapeutic agents were able to induce the senescent phenotype of kidney cancer cells. Zhu et al. reported that Sunitinib-treated RCC cell lines manifested distinct senescence features such as the SASP phenotype and cell cycle arrest with DNA damage. This work suggests that the benefit of sunitinib treatment may be attributed to p53/Dec1 signaling activation and drug-induced cellular senescence (30). Another study showed that Axitinib induced

DNA damage response in a ROS-dependent manner and eventually led to G2M cell cycle arrest and a senescent phenotype in RCC cell lines (31). Similarly, Mongiardi et al. reported that Axitinib could trigger cellular senescence through oxidative stress-dependent activation of the ATM kinase (32). In summary, these facts provide a theoretical basis for our finding that the high senescence score subgroup would benefit from targeted therapy. Moreover, given that TKI treatment can induce cancer cellular senescence, combining TKI with senescent cell scavengers might be an option for the development of novel treatment strategies for ccRCC. The proposal has already shown promising preliminary results in some preclinical studies, such as the combination of MDM2 inhibitors with AURKA inhibitors (senescence inducers), which not only induced melanoma cell death but also promoted the expression of numerous immune factors, thereby enhancing the anti-tumor immune response (33). However, currently known senescence scavengers, such as MDM2 inhibitors and BCL-2 family inhibitors, are not cell specific, and, therefore, the removal of senescent anti-tumor immune cells will lead to unpredictable toxic side effects (34, 35).

This study also represented the first report to deconstruct the intrinsic association between ccRCC senescence and the immune microenvironment features. Overall, the senescence process not only enhanced immune infiltration but, more importantly, promoted multiple immunosuppressive factors, such as CAFs, immune exclusion, and immune exhaustion signaling at the same time, leading to poorer oncologic outcomes. Using the adaptive lasso regression, we established a senescence score and demonstrated it was negatively correlated with immune infiltration. This behavioral shift might be attributed to the duplex impact of the SASP phenotype on the remodeling of the immune microenvironment. Identified SASP factors include soluble signaling molecules (e.g., interleukins, chemokines, inflammatory factors, and growth factors), proteases, and ECM components (17). Actually, it has long been noted that the stromal fibroblasts manipulate the pro-tumoral/anti-tumoral role of senescence through the SASP phenotype-associated secretion profiles (17, 36, 37). For example, MMP-2 and MMP-9, which are mainly secreted by CAFs, have been shown to be associated with RCC progression (38). However, different studies have reported a pro- or anti-tumorigenic ability of CAFs through the secretion of several factors, which is still debated and may be dependent on tumor type, tumor stage, CAF–tumor interaction, and senescence (39, 40). In addition, evidence demonstrated that the senescent secretome could be modified when there is an interaction between the tumor cells and fibroblasts (41). Collectively, it is currently believed that transient SASP is beneficial, whereas chronic SASP leads to negative outcomes. Many members of the SASP factors can promote tumor invasion or be involved in helping tumor cells evade immune clearance (13, 17). The combination of ICB with key SASP factor-targeted therapies, such as NOTCH and TGF-a inhibitors, holds the potential to block or reverse SASP-induced immunosuppression, thereby enhancing anti-tumor response (42). On the other hand, it is unclear how immune cell senescence affects their functional status, specifically M1 macrophages, DC cells, and CD8+ T cells, and whether interventions on key inducers of cellular senescence can rescue exhausted cytotoxic lymphocytes. Nonetheless, we demonstrated that the remodeling effect of senescence on the immune microenvironment leads to different immunotherapeutic outcomes in patients, and the senescence score was able to distinguish anti–PD-1 responders in ccRCC.

Last, as a preliminary exploration, this study can be further improved in some aspects. First, characterization of senescence features in key immune cell populations, such as CAFs, macrophages, and CD8+ T cells, based on single-cell sequencing data would help us better define stable and specific cellular senescence markers. Second, limited by the available open-access data, this study failed to further evaluate the role of senescence-related genes and senescence score in the clinical benefit of ICB plus anti-VEGF therapy. Given that the combination treatment strategy revolutionized the management of metastatic ccRCC, further investigation into this topic is necessary and desirable.

CONCLUSION

In summary, this study elucidated that the senescence process is closely correlated to genomic instability and unbalanced PBMR1/BAP1 mutations in ccRCC. The senescence microenvironment, which switches from immune activation to immune suppression, has a significant impact on anti-tumor immunity. We successfully constructed a senescence score, which is not only a robust prognostic indicator for patients' prognosis but also provides a new reference basis for personalized treatment selection.

DATA AVAILABILITY STATEMENT

The original contributions presented in the study are included in the article/**Supplementary Material**. Further inquiries can be directed to the corresponding authors.

ETHICS STATEMENT

The data source involved in this present study was open access; therefore, ethics approval was not applicable.

AUTHOR CONTRIBUTIONS

SW, JH, and ZL proposed and designed the framework of this study; QX and CL completed the collation and pre-processing of the raw data required for subsequent analysis; PZ, HH, and YL performed a detailed analysis the raw data; JX and YW visualized the analytical results; PZ interpretated the results and drafted this manuscript; YX, ZL, JH, and SW reviewed and critically revised the manuscript. All authors contributed to the article and approved the submitted version.

FUNDING

This presented study was supported by the National Natural Science Foundation of China, Youth Science Fund Project (Grant Number: 81772729), Natural Science Foundation of Hubei Province (No. ZRMS2020002466), and the Chen Xiao-ping Foundation for The Development of Science and Technology

of Hubei Province (No.202094). The funders have no role in designing and completing this study.

ACKNOWLEDGEMENTS

The corresponding author declared full access to data involved in this study and final responsibility for the decision to submit for peer review. Moreover, we would like to thank Dr. Xiaofan Lu (State Key Laboratory of Natural Medicines, Research Center of Biostatistics and Computational Pharmacy, China Pharmaceutical University) for the methdology support of this study.

SUPPLEMENTARY MATERIAL

The Supplementary Material for this article can be found online at: https://www.frontiersin.org/articles/10.3389/fimmu.2022.901671/full#supplementary-material

Supplementary Figure 1 | Regeneration of the senescence subtypes in external cohorts. **(A)** Heatmap displayed the expression level of the DESGs across the senescence subtypes in TCGA-KIRC. **(B, D, F)** the t-SNE down-dimension plots showed good discrimination of tumor samples among the senescence subtypes in TCGA-KIRC **(B)**, E-MTAB-1980 **(D)**, and Checkmate **(F)**. **(C, E)** Heatmaps of the 15 senescence-related biological processes in E-MTAB-1980 **(C)** and Checkmate **(E)**.

Supplementary Figure 2 | Subgroup analysis of ICB treatment benefit versus targeted therapy in Checkmate. **(A, B)** In patients of the low-senescence score group, the use of Nivolumab resulted in an OS, but not a PFS benefit over Everolimus. **(C, D)** In the high-senescence score group, there was no PFS or OS difference between the Nivolumab- and Everolimus-treatment arms.

Supplementary Table 1 | Information of datasets involved in our study.

Supplementary Table 2 | Clinic information for the development and validation datasets of the prognostic model.

Supplementary Table 3 | Differentially expressed senescence-related genes in TCGA-KIRC ($p < 0.05$).

Supplementary Table 4 | Features and corresponding coefficients for the generation of the senescence score.

REFERENCES

1. Znaor A, Lortet–Tieulent J, Laversanne M, Jemal A, Bray F. International Variations and Trends in Renal Cell Carcinoma Incidence and Mortality. *Eur Urol* (2015) 67:519–30. doi: 10.1016/j.eururo.2014.10.002
2. Cancer Genome Atlas Research Network. Comprehensive Molecular Characterization of Clear Cell Renal Cell Carcinoma. *Nature* (2013) 499:43–9. doi: 10.1038/nature12222
3. Beuselinck B, Job S, Becht E, Karadimou A, Verkarre V, Couchy G, et al. Molecular Subtypes of Clear Cell Renal Cell Carcinoma Are Associated With Sunitinib Response in the Metastatic Setting. *Clin Cancer Res* (2015) 21:1329–39. doi: 10.1158/1078-0432.CCR-14-1128
4. Turajlic S, Xu H, Litchfield K, Rowan A, Horswell S, Chambers T, et al. Deterministic Evolutionary Trajectories Influence Primary Tumor Growth: TRACERx Renal. *Cell* (2018) 173:595–610.e11. doi: 10.1016/j.cell.2018.03.043
5. Motzer RJ, Banchereau R, Hamidi H, Powles T, McDermott D, Michael B, et al. Molecular Subsets in Renal Cancer Determine Outcome to Checkpoint and Angiogenesis Blockade. *Cancer Cell* (2020) 38:803. doi: 10.1016/j.ccell.2020.10.011
6. Benamran D, Albiges L, Bex A, Giannarini G, Capitanio U, Rouprêt M, et al. Treatment Options for De Novo Metastatic Clear–Cell Renal Cell Carcinoma: Current Recommendations and Future Insights. *Eur Urol Oncol* (2022) 5:125–33. doi: 10.1016/j.euo.2021.08.003
7. Motzer RJ, Tannir NM, McDermott DF, Arén Frontera O, Melichar B, Choueiri TK, et al. Nivolumab Plus Ipilimumab Versus Sunitinib in Advanced Renal–Cell Carcinoma. *N Engl J Med* (2018) 378:1277–90. doi: 10.1056/NEJMoa1712126
8. Motzer RJ, Penkov K, Haanen J, Rini B, Albiges L, Campbell MT, et al. Avelumab Plus Axitinib Versus Sunitinib for Advanced Renal–Cell Carcinoma. *N Engl J Med* (2019) 380:1103–15. doi: 10.1056/NEJMoa1816047
9. Motzer RJ, Penkov K, Haanen J, Rini B, Albiges L, Campbell MT, et al. Avelumab Plus Axitinib Versus Sunitinib in Advanced Renal Cell Carcinoma: Biomarker Analysis of the Phase 3 JAVELIN Renal 101 Trial. *Nat Med* (2020) 26:1733–41. doi: 10.1038/s41591-020-1044-8
10. Braun DA, Hou Y, Bakouny Z, Ficial M, Sant' Angelo M, Forman J, et al. Interplay of Somatic Alterations and Immune Infiltration Modulates Response to PD–1 Blockade in Advanced Clear Cell Renal Cell Carcinoma. *Nat Med* (2020) 26:909–18. doi: 10.1038/s41591-020-0839-y
11. Rooney MS, Shukla SA, Wu CJ, Getz G, Hacohen N. Molecular and Genetic Properties of Tumors Associated With Local Immune Cytolytic Activity. *Cell* (2015) 160:48–61. doi: 10.1016/j.cell.2014.12.033
12. Massari F, Rizzo A, Mollica V, Rosellini M, Marchetti A, Ardizzoni A, et al. Immune–based Combinations for the Treatment of Metastatic Renal Cell Carcinoma: A Meta–Analysis of Randomised Clinical Trials. *Eur J Cancer* (2021) 154:120–7. doi: 10.1016/j.ejca.2021.06.015
13. Fane M, Weeraratna AT. How the Ageing Microenvironment Influences Tumour Progression. *Nat Rev Cancer* (2020) 20:89–106. doi: 10.1038/s41568-019-0222-9
14. Xu P, Wang M, Song W–M, Wang Q, Yuan G–C, Sudmant PH, et al. The Landscape of Human Tissue and Cell Type Specific Expression and Co–Regulation of Senescence Genes. *Mol Neurodegener* (2022) 17:5–20. doi: 10.1186/s13024-021-00507-7
15. López–Otín C, Blasco MA, Partridge L, Serrano M, Kroemer G. The Hallmarks of Aging. *Cell* (2013) 153:1194–217. doi: 10.1016/j.cell.2013.05.039
16. Rosenkranz D, Weyer S, Tolosa E, Gaenslen A, Berg D, Leyhe T, et al. Higher Frequency of Regulatory T Cells in the Elderly and Increased Suppressive Activity in Neurodegeneration. *J Neuroimmunol* (2007) 188:117–27. doi: 10.1016/j.jneuroim.2007.05.011
17. Coppé J–P, Desprez P–Y, Krtolica A, Campisi J. The Senescence–Associated Secretory Phenotype: The Dark Side of Tumor Suppression. *Annu Rev Pathol* (2010) 5:99–118. doi: 10.1146/annurev-pathol-121808-102144
18. Enioutina EY, Bareyan D, Daynes RA. A Role for Immature Myeloid Cells in Immune Senescence. *J Immunol* (2011) 186:697–707. doi: 10.4049/jimmunol.1002987
19. He S, Sharpless NE. Senescence in Health and Disease. *Cell* (2017) 169:1000–11. doi: 10.1016/j.cell.2017.05.015
20. Levi N, Papismadov N, Solomonov I, Sagi I, Krizhanovsky V. The ECM Path of Senescence in Aging: Components and Modifiers. *FEBS J* (2020) 287:2636–46. doi: 10.1111/febs.15282
21. Zeng D, Ye Z, Shen R, Yu G, Wu J, Xiong Y, et al. IOBR: Multi–Omics Immuno–Oncology Biological Research to Decode Tumor Microenvironment and Signatures. *Front Immunol* (2021) 12:687975. doi: 10.3389/fimmu.2021.687975
22. Charoentong P, Finotello F, Angelova M, Mayer C, Efremova M, Rieder D, et al. Pan–Cancer Immunogenomic Analyses Reveal Genotype–Immunophenotype Relationships and Predictors of Response to Checkpoint Blockade. *Cell Rep* (2017) 18:248–62. doi: 10.1016/j.celrep.2016.12.019
23. Lu X, Meng J, Zhu J, Zhou Y, Jiang L, Wang Y, et al. Prognosis Stratification and Personalized Treatment in Bladder Cancer Through a Robust Immune Gene Pair–Based Signature. *Clin Transl Med* (2021) 11(6): e453. doi: 10.1002/ctm2.453

24. Hoshida Y, Brunet J–P, Tamayo P, Golub TR, Mesirov JP. Subclass Mapping: Identifying Common Subtypes in Independent Disease Data Sets. *PloS One* (2007) 2:e1195. doi: 10.1371/journal.pone.0001195
25. Roh W, Chen P-L, Reuben A, Spencer CN, Prieto PA, Miller JP, et al. Integrated Molecular Analysis of Tumor Biopsies on Sequential CTLA–4 and PD–1 Blockade Reveals Markers of Response and Resistance. *Sci Transl Med* (2017) 9:eaah3560. doi: 10.1126/scitranslmed.aah3560
26. Jonasch E, Walker CL, Rathmell WK. Clear Cell Renal Cell Carcinoma Ontogeny and Mechanisms of Lethality. *Nat Rev Nephrol* (2021) 17:245–61. doi: 10.1038/s41581-020-00359-2
27. McDermott DF, Huseni MA, Atkins MB, Motzer RJ, Rini BI, Escudier B, et al. Clinical Activity and Molecular Correlates of Response to Atezolizumab Alone or in Combination With Bevacizumab Versus Sunitinib in Renal Cell Carcinoma. *Nat Med* (2018) 24:749–57. doi: 10.1038/s41591-018-0053-3
28. Hsieh JJ, Chen D, Wang PI, Marker M, Redzematovic A, Chen Y-B, et al. Genomic Biomarkers of a Randomized Trial Comparing First–Line Everolimus and Sunitinib in Patients With Metastatic Renal Cell Carcinoma. *Eur Urol* (2017) 71:405–14. doi: 10.1016/j.eururo.2017.01.013
29. Joseph RW, Kapur P, Serie DJ, Eckel-Passow JE, Parasramka M, Ho T, et al. Loss of BAP1 Protein Expression Is an Independent Marker of Poor Prognosis in Patients With Low–Risk Clear Cell Renal Cell Carcinoma. *Cancer* (2014) 120:1059–67. doi: 10.1002/cncr.28521
30. Zhu Y, Xu L, Zhang J, Hu X, Liu Y, Yin H, et al. Sunitinib Induces Cellular Senescence *via* P53/Dec1 Activation in Renal Cell Carcinoma Cells. *Cancer Sci* (2013) 104:1052–61. doi: 10.1111/cas.12176
31. Morelli MB, Amantini C, Santoni M, Soriani A, Nabissi M, Cardinali C, et al. Axitinib Induces DNA Damage Response Leading to Senescence, Mitotic Catastrophe, and Increased NK Cell Recognition in Human Renal Carcinoma Cells. *Oncotarget* (2015) 6:36245–59. doi: 10.18632/oncotarget.5768
32. Mongiardi MP, Radice G, Piras M, Stagni V, Pacioni S, Re A, et al. Axitinib Exposure Triggers Endothelial Cells Senescence Through ROS Accumulation and ATM Activation. *Oncogene* (2019) 38:5413–24. doi: 10.1038/s41388-019-0798-2
33. Vilgelm AE, Pawlikowski JS, Liu Y, Hawkins OE, Davis TA, Smith J, et al. Mdm2 and Aurora Kinase A Inhibitors Synergize to Block Melanoma Growth by Driving Apoptosis and Immune Clearance of Tumor Cells. *Cancer Res* (2015) 75:181–93. doi: 10.1158/0008-5472.CAN-14-2405
34. Kaefer A, Yang J, Noertersheuser P, Mensing S, Humerickhouse R, Awni W, et al. Mechanism–based Pharmacokinetic/Pharmacodynamic Meta–Analysis of Navitoclax (ABT–263) Induced Thrombocytopenia. *Cancer Chemother Pharmacol* (2014) 74:593–602. doi: 10.1007/s00280-014-2530-9
35. Pi L, Rooprai J, Allan DS, Atkins H, Bredeson C, Fulcher AJ, et al. Evaluating Dose–Limiting Toxicities of MDM2 Inhibitors in Patients With Solid Organ and Hematologic Malignancies: A Systematic Review of the Literature. *Leuk Res* (2019) 86:106222. doi: 10.1016/j.leukres.2019.106222
36. Kumari R, Jat P. Mechanisms of Cellular Senescence: Cell Cycle Arrest and Senescence Associated Secretory Phenotype. *Front Cell Dev Biol* (2021) 9:645593. doi: 10.3389/fcell.2021.645593
37. Rentschler M, Braumüller H, Briquez PS, Wieder T. Cytokine–Induced Senescence in the Tumor Microenvironment and Its Effects on Anti–Tumor Immune Responses. *Cancers (Basel)* (2022) 14:1364. doi: 10.3390/cancers14061364
38. Errarte P, Larrinaga G, Lopez JI. The Role of Cancer–Associated Fibroblasts in Renal Cell Carcinoma. An Example of Tumor Modulation Through Tumor/Non–Tumor Cell Interactions. *J Adv Res* (2020) 21:103–8. doi: 10.1016/j.jare.2019.09.004
39. Gabasa M, Radisky ES, Ikemori R, Bertolini G, Arshakyan M, Hockla A, et al. MMP1 Drives Tumor Progression in Large Cell Carcinoma of the Lung Through Fibroblast Senescence. *Cancer Lett* (2021) 507:1–12. doi: 10.1016/j.canlet.2021.01.028
40. Kaasinen M, Hagström J, Mustonen H, Sorsa T, Sund M, Haglund C, et al. Matrix Metalloproteinase 8 Expression in a Tumour Predicts a Favourable Prognosis in Pancreatic Ductal Adenocarcinoma. *Int J Mol Sci* (2022) 23:3314. doi: 10.3390/ijms23063314
41. Özcan S, Alessio N, Acar MB, Mert E, Omerli F, Peluso G, et al. Unbiased Analysis of Senescence Associated Secretory Phenotype (SASP) to Identify Common Components Following Different Genotoxic Stresses. *Aging (Albany NY)* (2016) 8:1316–29. doi: 10.18632/aging.100971
42. Chibaya L, Snyder J, Ruscetti M. Senescence and the Tumor–Immune Landscape: Implications for Cancer Immunotherapy. *Semin Cancer Biol* (2022) S1044-579X(22)00026-8. doi: 10.1016/j.semcancer.2022.02.005

Conflict of Interest: The authors declare that the research was conducted in the absence of any commercial or financial relationships that could be construed as a potential conflict of interest.

Publisher's Note: All claims expressed in this article are solely those of the authors and do not necessarily represent those of their affiliated organizations, or those of the publisher, the editors and the reviewers. Any product that may be evaluated in this article, or claim that may be made by its manufacturer, is not guaranteed or endorsed by the publisher.

Copyright © 2022 Zhou, Liu, Hu, Lu, Xiao, Wang, Xun, Xia, Liu, Hu and Wang. This is an open-access article distributed under the terms of the Creative Commons Attribution License (CC BY). The use, distribution or reproduction in other forums is permitted, provided the original author(s) and the copyright owner(s) are credited and that the original publication in this journal is cited, in accordance with accepted academic practice. No use, distribution or reproduction is permitted which does not comply with these terms.

frontiers | Frontiers in Immunology

REVIEW
published: 09 June 2022
doi: 10.3389/fimmu.2022.917998

Endogenous Retroviruses (ERVs): Does RLR (RIG-I-Like Receptors)-MAVS Pathway Directly Control Senescence and Aging as a Consequence of ERV De-Repression?

Eros Di Giorgio * *and Luigi E. Xodo* *

Laboratory of Biochemistry, Department of Medicine, University of Udine, Udine, Italy

OPEN ACCESS

Edited by:
Pei-Hui Wang,
Shandong University, China

Reviewed by:
Tomoko Takahashi,
Saitama University, Japan
Cao-Qi Lei,
Wuhan University, China
Hironori Yoshino,
Hirosaki University, Japan

***Correspondence:**
Eros Di Giorgio
eros.digiorgio@uniud.it
Luigi E. Xodo
luigi.xodo@uniud.it

Specialty section:
This article was submitted to Viral Immunology, a section of the journal Frontiers in Immunology

Received: *12 April 2022*
Accepted: *18 May 2022*
Published: *09 June 2022*

Citation:
Di Giorgio E and Xodo LE (2022) Endogenous Retroviruses (ERVs): Does RLR (RIG-I-Like Receptors)-MAVS Pathway Directly Control Senescence and Aging as a Consequence of ERV De-Repression? Front. Immunol. 13:917998. doi: 10.3389/fimmu.2022.917998

Bi-directional transcription of Human Endogenous Retroviruses (hERVs) is a common feature of autoimmunity, neurodegeneration and cancer. Higher rates of cancer incidence, neurodegeneration and autoimmunity but a lower prevalence of autoimmune diseases characterize elderly people. Although the re-expression of hERVs is commonly observed in different cellular models of senescence as a result of the loss of their epigenetic transcriptional silencing, the hERVs modulation during aging is more complex, with a peak of activation in the sixties and a decline in the nineties. What is clearly accepted, instead, is the impact of the re-activation of dormant hERV on the maintenance of stemness and tissue self-renewing properties. An innate cellular immunity system, based on the RLR-MAVS circuit, controls the degradation of dsRNAs arising from the transcription of hERV elements, similarly to what happens for the accumulation of cytoplasmic DNA leading to the activation of cGAS/STING pathway. While agonists and inhibitors of the cGAS–STING pathway are considered promising immunomodulatory molecules, the effect of the RLR-MAVS pathway on innate immunity is still largely based on correlations and not on causality. Here we review the most recent evidence regarding the activation of MDA5-RIG1-MAVS pathway as a result of hERV de-repression during aging, immunosenescence, cancer and autoimmunity. We will also deal with the epigenetic mechanisms controlling hERV repression and with the strategies that can be adopted to modulate hERV expression in a therapeutic perspective. Finally, we will discuss if the RLR-MAVS signalling pathway actively modulates physiological and pathological conditions or if it is passively activated by them.

Keywords: endogenous retrovirus, dsRNA, MAVS, RLR, senescence

INTRODUCTION: COMPLEXITIES AND PECULIARITIES OF HERVS

Transposable elements (TE) make up about 46% of the human genome (1). They consist in repetitive sequences which are capable to or potentially capable to actively or passively insert copies of themselves elsewhere in the genome (1). TE are classified in Class I TEs, if they are RNA retrotransposons that require reverse transcriptase activity for transposition, and Class II TEs, or DNA transposons, that require transposase enzyme for their mobilization. LINE (long interspersed nuclear elements) and SINE (short interspersed nuclear elements) are the most studied and abundant class I TEs, representing respectively 17 and 11% of human genome (2). LINE and SINE will not be discussed in this manuscript, as there are in the literature a good number of excellent reviews on the subject.

The third family of Class I TEs consists of long terminal repeat (LTR) retroelements, known as HERVs (human endogenous retroviruses) (3). HERV are residues of viral infections from the past that have remained in the human genome and occupy about 8% of it. Complete HERV elements (**Figure 1**) have a length of 1-10Kb and contains the ORF of four viral-like genes: *gag, pol, env, pro* encoding respectively the viral capsid protein, the reverse transcriptase, the envelope-associated glycoprotein and the viral protease (4). 5' and 3' LTR control the bidirectional transcription by RNAP2 of HERV elements (5), their polyadenylation (6) and chromatin folding (7). HERV are often not complete consisting only of short LTRs. However, solitary LTR can control and impact the transcription of neighbor genes or other adjacent genomic elements (3). A non-coding sequence present between the 5′ LTR and the *gag* gene contains a tRNA-specific primer-binding site (PBS) and prime reverse transcription (8); a polypurine tract (PPT) present between env and 3'LTR prime the (+) strand DNA synthesis (9). PBS specificity has been used in the past to classify HERVs into subfamilies. However, due to some degree of promiscuity in the use of PBS, this classification method fell apart.

New methods have been applied to overcome the historical classification of hERVs into three families, based on sequence homology with the original viral strains (10). Nowadays, 504 groups of HERVs and more than 700 thousands of HERV members have been described (11).

The accumulation of mutations from generation to generation has reduced or nearly halted the transcription, translation, and retrotranscription rates of these genomic elements, with some important exceptions (12). However, these genomic elements exert active functions in modulating genomic plasticity by actively affecting: a) genome stability, as they can affect the mobility of transposable elements or influence intra- and interchromosomal rearrangements (13, 14); b) the transcription rate of the neighbor genes, as the LTR elements can redirect RNAP2 activities (15), or their translation (16); c) the interference process, by acting as miRNA sponges (12, 17).

REGULATION OF ERV EXPRESSION AT TRANSCRIPTIONAL AND POST-TRANSCRIPTIONAL LEVELS

HERV are normally kept silenced by a strong epigenetic mechanism that acts at DNA (CpG methylation) and chromatin (histone methylation and heterochromatinization) levels (3) (**Figure 2**). Starting from the first, it has been proposed that the primary function of cytosine methylation might be the genome defense against transposons and retroviruses (18). Cytosine DNA methylation is a highly conserved form of epigenetic regulation among all eukaryotes. When the methylome of primary fibroblasts from seven vertebrates (human, mouse, rabbit, dog, cattle, pig, and chicken) was compared, chicken were found to have lower levels of methylation compared with mammals (19). However, the treatment with the DNA demethylating agent, 5-azacytidine (5-aza) leads to a strong de-repression of ERVs in all the examined species, including the hypomethylated chicken fibroblasts, thus confirming that DNA methylation is a conserved mechanism for repressing ERVs in vertebrates (19). The de-repression of ERVs achieved after 5-aza treatment was observed in many different physiological and pathological contexts (20–26). As a matter of fact, female mice deficient for the DNA demethylase Tet1 experience premature infertility consistent with premature ovarian failure that correlates with Line 1 and ERV activation (27).

Evolutionarily, the controlled demethylation of ERV loci has been used to regulate functional physiological processes, such as placenta formation (28). Indeed, the fusion between trophoblast cells into cytotrophoblast and then into syncytiotrophoblast during placenta formation requires a functional Syncitin-1 gene expression (29). Syncytin-1 is the envelope gene of the human Endogenous Retrovirus ERVW-1 (29). Interestingly, aberrant methylation of ERVW-1 and perturbed expression of Syncytin-1 were observed in many pregnancy diseases associated to placental morphology alterations (30). This process

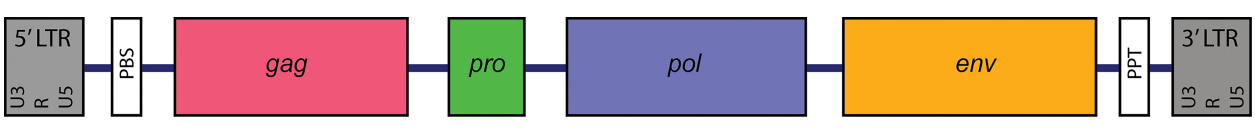


FIGURE 1 | Simplified schematic structure of the organization of a complete ERV. LTR, long terminal repeat control ERV transcription and polyadenylation; *gag*, viral capsid; *pol,* reverse transcriptase, *env,* glycoprotein of the envelope; *pro,* viral protease; PBS, tRNA-specific primer-binding site; PPT, polypurine tract.

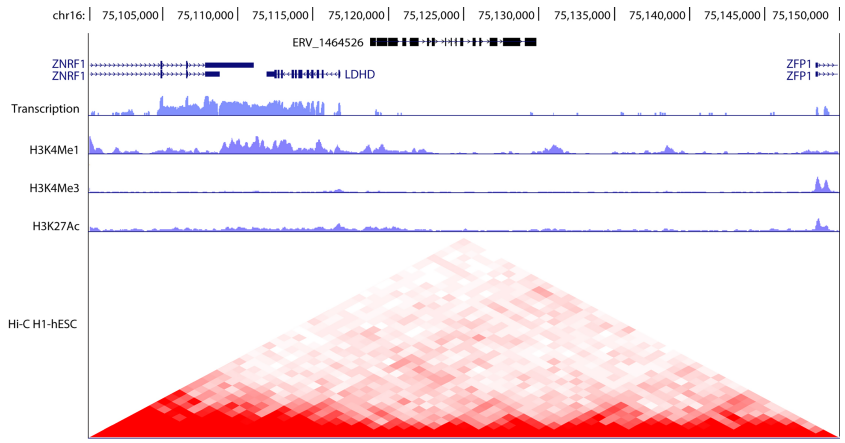


FIGURE 2 | Genomic organization of hERV 1464526 in chromosome 16. Typically, as in this case, ERV elements are discontinuous and interspersed with other genomic elements. hERV_1464526 is interposed between three coding genes (ZNRF1, LDHD, ZFP1). The transcript levels as well as H3K4me1, H3K4me3, H3K27ac and Hi-C data were obtained from UCSC genome browser (https://genome.ucsc.edu/) and refer to human embryonic stem cells (hESC). A drop in the transcriptional activity is observed in correspondence to hERV_1464526 locus, in respect to neighbor coding genes. However, the heterochromatinization of ERV locus is not complete, as observed by H3K4me1 levels. Hi-C data evidence the involvement of ERV locus in chromatin looping dynamics and plasticity.

demonstrates that the primary methylation response after retroviral elements integration in mammalian genome during evolution underwent a process of controlled demethylation to mediate the acquisition of a new biological function (31).

Elsewhere in mammalian genome, the silencing response induced by DNA methylation of ERV elements is reinforced by the KAP1/SETDB1/DNMT1 dependent H3K9 tri-methylation (32, 33). In murine embryonic stem cells the H3K9me3 induced heterochromatinization seem to require the ATRX and DAXX-dependent deposition of histone H3.3, as H3.3 deletion decreases the H3K9me3 levels especially in correspondence to class I and class II ERVs (21, 34). The incorporation of H3.3 by the histone chaperone Daxx requires a functional Morc3-ATPase cycle and Morc3-SUMOylation, as Morc3 knock-out leads to reduced H3.3 and H3K9me3 deposition and to the de-repression of ERVs (35).

Histone citrullination (H3R8cit) has been shown to attenuate HP1α binding to H3K9me3, leading to HERV de-repression in peripheral blood mononuclear cells (PBMCs) obtained from patients with multiple sclerosis (MS) (36). Importantly, inhibition of peptidylarginine deiminase 4 (PADI4), the major enzyme responsible for the conversion of arginine to citrulline, reversed ERVs de-repression and blocked the release of inflammatory cytokines (36). However, it must be kept in mind that direct protein citrullination, and in particular citrullination of myelin basic protein, plays a controversial role in the pathogenesis of MS (37, 38).

Histone acetylation of ERVs loci should theoretically de-repress their transcription. However, conflicting data have been reported in this regard by using Histone Deacetylase (HDAC) inhibitors (39, 40). DNA methylation and histone deacetylation may act as integrated mechanisms to ensure a concerted repression of latent retroviral elements. This is supported by the finding that combined treatments of different cancer cell lines with DNMT and HDAC inhibitors strongly stimulate HERVs transcription and show synergistic effects compared with single treatments (41, 42).

In B and T cells of C57BL/6 J, DNA methylation levels in TEs of retroviral origin correlate inversely with CTCF binding. This indicates that there is a close relationship between DNA methylation and the regulation of chromatin status and loop formation (43) (**Figure 2**).

At post-transcriptional level, literature reports scattered information about a possible role of RNA interference as a mechanism to impair the stability of ERV RNAs. 19 miRNAs were found to be significantly homologous to HERV-W family members (44). Intriguingly, it has been reported that the Xist-mediated silencing of the second female X chromosome could be evolved by pretending a viral infection, as Xist sequence is recognized by the RNA binding protein Spen that has the capability to bind also retroviral RNAs (45). If confirmed, this fascinating hypothesis would explain the origin of the RNA interference mechanism as a putative ancient antiviral mechanism.

Post-transcriptional editing of ERVs RNAs has been observed in many cellular models. By performing a CRISPR screen for IAP suppressors in murine ES cells, Chelmicki and colleagues identified m6A RNA methylation as a predominant way to decrease ERV RNA stability in conditions in which their expression is re-activated (46). The methyltransferase-like METTL3 and METTL14 are two key components of the enzymatic complex that provides methylation at the LTR and 5'UTR of IAP-related ERVK elements, while the YTH-domain containing proteins act as m6A readers and triggers methylated RNA decay, which occurs probably in P-bodies (46). It was proposed that m6A-dependent ERVs regulation could decrease their immunogenic potential and the activation of inflammatory processes (46).

Adenosine-to-inosine (A-to-I) editing by ADAR (adenosine deaminase acting on RNA) of dsRNAs of retroviral origin

induces mismatches in their transcripts in this way preventing their recognition by MDA5 and the activation of the inflammatory pathway (47–49). Interestingly, *Adar1*$^{-/-}$ tumors are sensitized to anti-tumor immunity and IFNβ and γ treatment (48); moreover, *Adar1* depletion allows to overcome different mechanisms of acquired resistance to immunotherapy with a significant increase in immune cells infiltration, including non-MHC I-restricted cytotoxic cells (48).

Finally, the acquisition of a Z-RNA structure by dsRNA ERV elements was proposed but only indirectly demonstrated recently (50). In particular, it was observed that murine dsRNAs of retroviral origin are recognized by the Zα-domain of Z-DNA-binding protein 1 (ZBP1) and contribute to trigger a RIPK3-dependent necroptotic process that leads to inflammation and eventually to the development of chronic inflammatory conditions as observed in RIPK1 mutated mice (50).

By analyzing the chromatin accessibility and the transcription rate of murine HSCs exposed to 5-FU treatment *in vivo*, it was observed that some transposable elements mainly belonging to the LINE1, ERV1 and ERVK families were derepressed and activate the RNA sensor MDA5 (51). This leads to the phosphorylation and activation of IRF3 and to the subsequent activation of interferon and inflammation. As a consequence of the activation of a pro-inflammatory state, these HSCs exposed to chemotherapy became more active and allowed the rapid reconstitution of murine blood system; on the opposite *Mda5* -/- HSC failed to detect ERVs and maintained a prolonged quiescence state that allows for better long-term bone marrow performance but worse rapid response to stressful conditions such as serial 5-FU treatment (51). Similarly, ionizing radiations trigger monocyte to macrophage differentiation as a result of the establishment of a pro-inflammatory environment which is due to the significant de-repression of ERVs and their asymmetric and anti-sense privileged transcription and the subsequent activation of the MDA5/MAVS (52). This leads to the polarization of the macrophages toward a pro-inflammatory phenotype that allows their high resistance to radiation, but also the acquisition of oncogenic features (52). Despite the multiple evidence for an effect of genotoxic agents (51, 52) and radiotherapy (53) in activating the transcription of ERVs, the epigenetic mechanism underlying this phenomenon remains to be elucidated. However, the involvement of ATM kinase is highly plausible (53). Indeed, ATM has been shown to phosphorylate KRAB-associated protein-1 (KAP-1) at Ser 824 in the presence of double-strand breaks, thereby abolishing its repressive properties (54).

DSRNA DETECTION: SPECIFIC RECOGNITION AND SIGNAL TRANSDUCTION

The major sources of intracellular dsRNAs are: the mitochondrial transcripts, repetitive nuclear sequences, ERVs and natural antisense transcripts (55). Mitochondrial DNA is bidirectionally transcribed and encodes 13 genes. The heavy strand encodes 12 of them, whereas the light chain encodes the thirteenth (55). dsRNAs resulting from bidirectional transcription are minimized by the action of polynucleotide phosphorylase (PNPase) and helicase HSuv3, which form a 330-kDa heteropentamer complex involved in light chain degradation (56). Defects in the mitochondrial RNA turnover pathway lead to the accumulation of dsRNAs (57) and eventually to an altered immune response as a consequence of the release of mitochondrial contents following membrane permeabilization (58). Importantly, mitochondrial dsRNAs are not substrates of ADAR (59) and if released in the cytoplasm they are preferentially recognized by PKR (55).

Nearly 70% of cellular dsRNA is the result of the transcription of repetitive elements, mainly LINEs (3%) and SINEs (67%). Although they undergo extensive adenosine deamination (60) and degradation by RNAseIII (61), untargeted dsRNAs lead to the engagement and activation of MDA5 (melanoma differentiation-associated gene 5), in the case of LINEs, and PKR (protein kinase R) for SINEs, ultimately leading to a Type I Interferon response (62).

dsRNAs also arise from antisense transcripts that pair with sense targets in the cytoplasm (55). However, the high processing rate during the interference process makes quantification and detection of sense:antisense dsRNA challenging (63).

ERVs transcripts fold into dsRNA by bidirectional transcription from LTRs or by self-paring between duplicated ERVs (41). They are frequently deaminated and detected by RLRs (55).

Regardless of their origin, cytoplasmic dsRNAs are recognized by dsRNA-binding proteins, including RIG-I-like receptors (RLRs), PKR, ADAR and oligo adenylate synthetase (OAS) (**Table 1**). Despite a certain degree of heterogeneity, dsRNA-binding proteins share a dsRNA-binding domain (dsRBD) that adopts an α–β–β–β–α topology structure close to the RNA-recognition motif (RRM) (64).

RLRs are described in detail in the following paragraph. PKR is interferon-inducible, recognizes dsRNA comprised between 33 and 85-100 base pairs (bp) in length and once activated homodimerizes and phosphorylates eukaryotic translation initiation factor 2A (EIF2A) leading to translational inhibition (65) and eventually to apoptosis (66).

ADAR enzymes (ADAR1, ADAR2, ADAR3) perform adenosine-to-inosine (A-to-I) RNA editing of dsRNAs, resulting in A:U->I:C mismatching (59). Mitochondrial dsRNAs and dsRNA derived from sense:antisense pairing are not bound by ADAR enzymes and therefore are not actively deaminated (55). dsRNA ADAR are potent dsRNA binders that

TABLE 1 | Indication of the major endogenous sources of dsRNA, their privileged dsRNA-binding proteins, and their propensity to be deaminated.

Endogenous dsRNA source	*dsRNA binding proteins engaged*	*ADAR sub-strates*
Mitochondrial dsRNA	PKR	No
LINE dsRNA	MDA5	Yes
SINE dsRNA	PKR	Yes
ERV dsRNA	MDA5 > RIG-I	Yes
ncRNA dsRNA	Drosha, Dicer, miRISC	No

sequester dsRNA and prevent their recognition by RLRs (67); at the same time, deamination has destabilizing effects on dsRNA, resulting in decreased activation of the interferon signaling pathway (68). Interestingly, Adar1 mutant mice are embryonically lethal and show and enhanced IFN signature, but concomitant deletion of the RLR MDA5 rescues the phenotype (67), whereas deletion of MAVS delays lethality (69) and RIG-I has no relevant effects (69). For completeness, we report here that it has recently been shown that transcription of ERVs can also be repressed by their genomic deamination by the cytidine deaminase APOBEC3 (70).

In humans, the OAS family consists of four genes (OAS1, OAS2, OAS3, OASL). With the exception of OASL, which is catalytically inactive, OAS enzymes bind short dsRNAs (<20 bp) and catalyze the non-processive synthesis of 2′-5′-linked oligoadenylate (2–5A) molecules which lead to the activation of endoribonuclease L (RNase L) and the subsequent degradation of the modified RNAs (71, 72).

OAS proteins, particularly OAS1, and the editing enzymes ADAR and APOBEC were found upregulated in Systemic Lupus Erythematosus (SLE) (73, 74). Conversely, mutations in *ADAR*, the gene encoding ADAR1, are associated with immune diseases, like Aicardi-Goutières syndrome (AGS), as a consequence of Type I Interferon hyperactivation (75). Similarly, the risk allele rs10774671 affecting the splicing of OAS1 is associated to the autoimmune disease Sjögren's syndrome (76). A possible explanation for these divergent findings comes from the observation that the excessive RNA editing observed in SLE facilitates the generation of autoantigens in peripheral tissues, leading to T cells hyper-reactivity (74).

These data indicate that the balance between the decoding of dsRNA and their degradation or modification allows fine activation of the interferon pathway and maintenance of optimal levels of innate cellular immunity (55). This condition is required for the maintenance of cellular and tissue fitness.

ERVS INTRACELLULAR SENSING AND SIGNALING

Toll-like receptors (TLRs), in particular TLR3, are localized in the endosomal membrane and are involved in recognizing extracellular dsRNA (77). For the detection of intracellular foreign nucleic acids, cells have evolved other classes of cytoplasmic pattern recognition receptors (PRR). The cytosolic DNA sensor cyclic GMP–AMP synthase (cGAS) allows the detection of cytoplasmic DNA, while RLRs are cytoplasmic sensors of dsRNAs of retroviral origin (78). However, recent evidence prove that these two responses can be integrated. In particular, cytosolic DNA scars arising from combined radiotherapy and ATR inhibition (79) can be transcribed by RNA polIII and fold as dsRNA (80) that are recognized by RIG-I, leading to STAT1 activation and reinforcing the cGAS/STING dependent inflammatory response (79). On the opposite, reverse transcription of RNA viral genome can result in the host in the generation of dsDNA that lead to cGAS/STING activation, as reviewed in (81). An intriguing hypothesis emerging from recent literature is that activation of cGAS/STING in the presence of dsRNA is required to regulate cap-dependent mRNA translation (82) by acting at the level of PKR-like ER kinase (PERK) upstream of TBK1 to redirect ribosomes toward encoding pro-inflammatory factors (83).

RLRs family includes three members: RIG-I (retinoic acid-inducible gene 1, also known as DDX58), MDA5 (melanoma differentiation- associated protein 5, also known as IFIH1), LGP2 (laboratory of genetics and physiology 2) (78). LGP2 is structurally different from MDA5 and RIG-I and it is considered as an adaptor protein involved in the regulation of RIG-I and MDA5 functions. In particular LGP2 promotes the nucleation and the following activation of MDA5 (84), while it seems to block directly the activation of RIG-I by inhibiting its ubiquitylation (85), or indirectly through the competitive binding to dsRNAs (86) or MAVS (87). However, conventional dendritic cells (cDCs) obtained from *Lgp2-/-* or with a point mutation in the LGP2 helicase domain (K30A) were reported to be unable to release IFNβ in response to infection with RNA viruses (picornaviridae, EMCV, and mengovirus), with the exception of influenza virus, while they efficiently responded to synthetic poly I:C (88). Therefore, further studies seem necessary to clarify the role of the CARD-less LGP2 in regulating MDA5 and RIG-I signaling.

RLRs have a central SF2 helicase domain with ATPase activity and a carboxy-terminal domain (CTD) that bears an RNA binding domain. While in RIG-I the binding to RNA leads to the unlock of its closed conformation and to the formation of short RIG-I oligomers, in MDA5 it triggers the polymerization of long MDA5 filaments (89). This difference reflects their binding preference as RIG-I binds 5'-triphosphate ssRNA (90) and small dsRNAs (70-2000 bp long, like the ones generated by negative strand paramyxoviruses, influenza virus and Japanese encephalitis virus), whereas MDA5 recognizes long dsRNA molecules, as the positive strand picornaviruses (> 2kb long) (91, 92). In fact, *Rig1-/-* mice are embryonic lethal, while *Mda5 -/-* mice are healthy up to 6 months of age, but in both the cases the knock-out mice are highly sensitive to viral infections with the respectively recognized viral strains (91). RIG-I and MDA5, but not LGP2, contain two caspase activation and recruitment domains (CARDs) at their amino terminus. Once activated, as a consequence of a conformational change, MDA5 and RIG-I expose the CARD domains. This allows homotypic CARD–CARD interactions with MAVS. MAVS (93–95) is a mitochondrial protein that once activated by RLRs gives rise to the formation of fibrils with a prion-like structure (96) in response to a TRIM31-dependent K63-linked MAVS polyubiquitination; once aggregated, MAVS activates TBK1 and IKKε kinases, which in turn activate the transcription factors IRF3/IRF7 and NF-κB, ultimately leading to type I interferon pathway activation (97). The deletion of the CARD domain at the N-terminus of MAVS prevents its RLR-activated aggregation (98) and displays a dominant-negative effect on endogenous MAVS aggregation and signaling (94). Similarly, IFNAR depletion or IFN signaling blockage blunts RLR/MAVS

pathway and limits the effects of cytolysis observable after an RNA virus infection (99, 100).

The activities of RLRs are deeply regulated at post-transcriptional levels (78). RIG-I is activated by the TRIM25 mediated K63 poly-ubiquitylation of its CARD domain that triggers RIG-I oligomerization (101). Conversely, the K48 poly-ubiquitylation of RIG-I triggers its proteasomal degradation (102), that is blocked by its TRIM38 dependent SUMOylation (103). The phosphorylation of RLRs is linked to their inactivation: the PKC and CKII mediated phosphorylation of RIG-I (S8, T170, T770, S854, S855) and the RIOK3 mediated phosphorylation of MDA5 (S88, S828) are both reversed by the activating dephosphorylation exerted by PP1 (78). The acetylation of RIG-I in its CTD blocks its ability to bind dsRNA, while its HDAC6-mediated deacetylation switches on its activity (104). Curiously, another class II HDAC, HDAC4, was identified for its ability to block the antiviral response by inhibiting IRF3, TBK1 and IKKε downstream to PRR (105), or by regulating the acetylation status of well-defined inflammatory -related super-enhancers (106). Finally, many partners regulate the oligomerization of RIG-I and MDA5 or act as co-receptors of dsRNAs (ZCCHC3, DDX60, DHX15, PACT, reviewed in (78)), while 14-3-3 proteins mediate the cytosol-to-mitochondria translocation of RLRs, thus allowing their interaction with MAVS (107).

IMPACT OF RLRS ON CELLULAR SENESCENCE AND AGING

RLR signaling was reported to impact on cellular processes likewise cellular senescence, proliferation and survival, and on physiological and pathological processes such as aging and autoimmune diseases (108–110).

Aged senescence-accelerated mouse prone-8 (SAMP8) mice are characterized by the activation of RIG-I/NF-κB pathway and the accumulation of proinflammatory cytokines (IL-6, NO) in the absence of exogenous viral stimulation (111). Moreover, RIG-I was found to be up-regulated both at RNA and protein levels in models of replicative senescence and murine aging, in an ATM-dependent manner (112). In senescent cells, RLRs activation promotes TBK1-dependent phosphorylation of IRF3 and IRF7 (primary response), their subsequent nuclear translocation and the transcription of IFN and IFN-regulated transcription factors (secondary response) that further reinforce IFN-signaling (113). In parallel, RLRs trough MAVS engagement trigger the NF-κB dependent induction of IL-6 and IL-8, while Klotho suppresses RIG-I-mediated senescence-associated inflammation by directly interacting with it and blocking its multimerization (112). On the contrary, *Rig-I*$^{-/-}$ mice display marks of premature aging like hair loss and moderate lethargy and *Rig-I*$^{-/-}$ MEFs fibroblasts undergo a premature replicative senescence characterized by amplified integrin β3/p38 MAPK signaling (114). These two reported functions of RIG-I are difficult to reconcile unless we hypothesize that the existence of compensatory circuits, such as the one involving MDA5, may affect the phenotype observed in *Rig-I*$^{-/-}$ mice.

Indirect evidences link MAVS to the induction of cellular senescence. In SLE, Bone marrow-derived mesenchymal stem cells (BM-MSCs) undergo premature senescence that correlates with the increased mRNA and protein levels of MAVS and IFNβ (115). The knock-down of MAVS partially rescues the phenotype by decreasing the levels of p16 and p53 and attenuating the release of pro-inflammatory cytokines (115).

The unclear role of RLRs in affecting senescence onset is traced by the reciprocal influences of the oncogene HRAS on RLR signaling. In fact, while oncogenic HRAS (*HRAS*^{G12V}) strongly inhibits Sendai virus-induced type I interferon signaling, ectopic expression of HRAS or the catalytically inactive HRAS^{N17} in 293 cells impairs the formation of MAVS-TNF receptor-associated factor 3 signaling complexes (116).

In consideration of these data, it is even more urgent to determine the impact of RLRs modulation in models of Oncogene-Induced senescence.

Patients with mutations in RIG-I and MDA5 suffer for autoimmune diseases. RIG-I mutations lead to atypical Singleton-Merten Syndrome, while MDA5 mutations are associated to classical Singleton-Merten Syndrome, Aicardi-Goutières syndrome, Systemic Lupus Erythematosus, Type 1 Diabetes and Graves disease (117). The RLR missense mutations observed in these diseases are gain-of-function and lead to exaggerated Type I Interferon response activation (118), probably reinforced by autoantigens generation (74).

How much RLRs over-activation depends on de-repression of ERVs is still unknown. However, it is not incorrect to hypothesize that a prolonged basal RLR activation following a prolonged exposure to RNA viruses or to ERVs de-repression could lead to the establishment of chronic inflammatory states.

ERVS IN CELLULAR SENESCENCE, NEURODEGENERATION AND AGING

A deep epigenetic resetting (119) and the activation of certain super-enhancers (106) characterize replicative senescence and aging. On the opposite, heterochromatinization has been considered for decades a typical feature of senescent cells (120), even though by the time its specificity and relevance as senescent marker has been a matter of debate (121, 122). In general, a perturbation of the epigenetic environment has been reported to trigger or allow the escape of cellular senescence, demonstrating in this way the centrality of the epigenetic control of this process (119). The alteration of heterochromatin/euchromatin compartments lead to the activation of TE and ERVs expression in different models of cellular senescence (123) (**Figure 3**). ERV expression is expected to sustain the establishment of a senescence-associated secretory phenotype (SASP) (123), which in turn should reinforce the senescence response (119, 124). Accordingly to this evidence, the PRC2-dependent heterochromatinization induced by re-expressing the

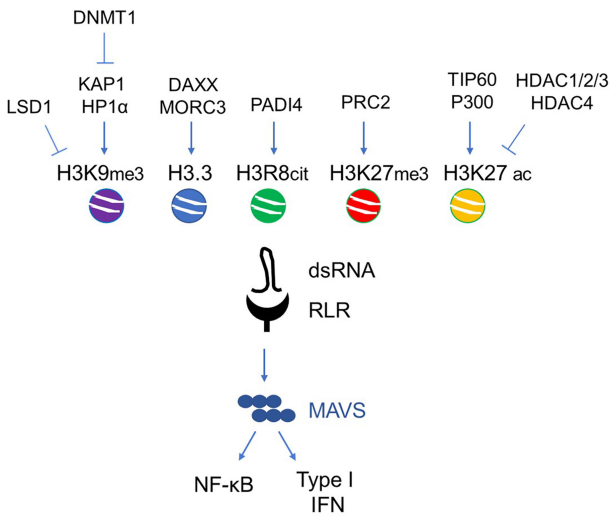


FIGURE 3 | Main histone epigenetic regulators involved in ERV de-repression during senescence and aging. Exemplary scheme of the agonistic/antagonistic epigenetic regulators acting on the chromatin remodeling of ERV loci.

methyltransferase DNMT3L in pre-senescent MEFs allows the repression of ERVs and a marked delay in the onset of senescence (125).

Methyl-binding domain sequencing and RNA sequencing of murine skeletal muscles evidenced a global down-regulation coupled to increased DNA methylation of ERVs in the early phase of aging, that is followed by their de-repression and demethylation in the late phase (>20 months) of aging (126). Curiously this methylation rewiring was not observed in T cells (126).

By comparing the expression of HERV-K and HERV-W proviruses in red blood cells obtained from young and nonagerians individuals, Nevalainen and colleagues observed a statistically significant differential expression among the two groups of 3 out of 33 and 1 out of 45 detectable HERV-K and HERV-W members (127). Despite the slightest differences, the global expression of the HERV-K and HERV-W members allows the two groups to be perfectly segregated (127). On the contrary, by analyzing by means of qPCR the transcriptional activity of HERV-H, HERV-K, HERV-W, and HERV-E in PBMCs from 261 subjects, Balestrieri and colleagues identified increased levels of HERV-K and HERV-W in oldest subjects (128). Similarly, in another study, the DNA methylation status of HERV-K loci in 177 samples of peripheral blood mononuclear cells obtained from volunteers between 20 and 88 years of age evidenced two waves of demethylation that occur during ages 40-63 and again during ages 64-83 (129). To explain at least in part the ambiguities and contradictions associated with the expression of ERVs during aging, it has been demonstrated that the percentage of circulating senescent human hematopoietic stem and progenitor cells (HSPC) does not increase with age, as they are actively cleared by the organism as a consequence of the release of eat-me signals (130). This evidence is questioned by the concept of immunosenescence, that will be explored later on in the manuscript. Furthermore, due to technical difficulties, it is currently not possible to clarify how many of the transcripts resulting from ERV de-repression are actively deaminated and inactivated (22).

On the opposite, transposable elements (TE), and ERV in particular, were de-repressed in HSPC cells brought to senescence *in vitro* (130). This de-repression is coupled to DNA demethylation that occurs in senescent HSPC cells (131). In particular, hypomethylated regions in senescent HSPC cells obtained from three healthy donors and sorted out on the basis of senescence-associated beta-galactosidase (SA-βgal) activity (C12FDG staining) are focal rather than global (131) and mainly fall in correspondence to repetitive elements and active enhancers characterized by CEBP binding (131). Curiously, expression of repetitive elements (Alu, ERV1, ERVL, ERVK, and LTR retrotransposons) and inflammatory cytokines is attenuated in leukemic stem cells (LSCs) in acute myeloid leukemia (AML), suggesting that escape from senescence and immune surveillance may be the origin of AML (132).

Tauopathies are neurodegenerative diseases characterized by the accumulation of pathological deposits of Tau protein in the brain (133). In Alzheimer's disease (AD), the accumulation of misfolded amyloid-β peptide or of Tau aggregates leads to heterochromatin relaxation and de-repression of silenced loci that ultimately leads to DNA damage and activation of cellular inflammation (134). De-repression of retroviral and transposable elements have been proposed to play a role in neurodegeneration and AD (3, 135). Retrospective analysis of 636 deceased AD-affected-subjects identified significant de-repression of HERV-Fc1 transcripts (136). In a *Drosophila* model of AD achieved by expressing a mutant isoform of Tau protein (tau^{R406W}) and analyzing the data obtained from head samples at day 10 of adulthood, an age at which neuronal deficits become evident, the same authors identified a significant de-repression of retroviral elements, similarly to what observed in human samples (136). RNA-seq analysis performed in tau^{R406W} and WT heads identified 50 and 60 transposable elements that are respectively significantly increased and decreased in tau transgenic model (137). Most of them are Class I long terminal repeat (LTR) retrotransposons (137). Moreover, the forced mobilization of transposable element achieved in tau^{R406W} flies by silencing the flamenco locus increased neurotoxicity and locomotor deficits. In tauopathy, the mobilization and transcription of transposable elements is the result of the decreased expression of piwi and piRNAs (137) and heterochromatin decondensation (137), probably as a result of impaired H3.3 turnover (138).

Curiously, the de-repression of ERVs was observed also in cancer models and in cancer patients (139). In tumors, TERT promotes the Sp1-dependent de-repression of hERVs that fold in dsRNA and trigger the RIG-I/MDA5-MAVS signaling thus inducing inflammation and creating an immunosuppressive environment (140). The de-repression of retroviral elements was observed also in melanoma patients and was the result of CpG demethylation (141). Decreased DNA methylation levels allow the segregation between nevi and malignant melanocytic

lesions and successful predict a worse prognosis (141). It has been reported that the activation of p53 leads to the repression of the H3K4 Histone demethylase KDM1A (LSD1) and the DNA demethylase DNMT1 and to the subsequent de-repression of hERV transcription. The concomitant repression of RISC components DICER, AGO2, and TRBP2 and the induction of dsRNA sensors RIG-I and MDA5 lead to the activation of Type I and III Interferon responses and could be exploited to overcome cancer resistance to immune checkpoint blockage (142). In multiple myeloma (MM), the dual inhibition of H3K27 and H3K9 methyltransferases EZH2 and G9a leads to the de-repression of ERVs genes, the activation of IFN signaling, the suppression of IRF4-MYC axis and the impairment of xenograft formation by MM cells in mice (143). Finally, radiation resistant head and neck squamous cell carcinoma clones are characterized by the acquisition of a senescence-associated secretory phenotype (SASP) and the de-repression of ERVs (ERV3-1) (144).

To sum up, ERVs were found to be reactivated and actively transcribed in patients with autoimmune diseases, neurodegeneration, cancer (139, 145, 146) and during physiological aging (123, 127, 131, 147). Common characteristics of these states are the accumulation of DNA damage, ER-stress and higher systemic inflammation (148). Different cellular responses are mediated by the activation of interferon in these states: survival, cell death, cytokines release. More work is required to clarify whether these differential responses depend on the intensity and magnitude of the signaling pathways activated or on the differential signal transducers activated in the different contexts. Moreover, the integration of the RLR and cGAS/STING pathways (79, 80) makes the analysis of the contribution of the different signaling molecules even more complex but reiterates the importance of nucleic acid sensors in regulating not only cellular innate immunity but also cellular fitness (83).

ERVS AND RLRS IN IMMUNOSENESCENCE

Immunosenescence is characterized by increased proportions of CD14+ monocytes, decreased CD19+ B lymphocytes and increased proportions of CD4+CD28- and CD8+CD28- T lymphocytes, resulting in a deep immunosuppression concomitant with an high inflammation (149). The aging-associated decline of the immune system was observed to predispose individuals to fatal infections or increase the risk of cancer (150). By comparing the expression levels of *HERV-K(HML-2)* in the peripheral blood mononuclear cells between nonagenarians (n=61) and young controls (n=37), Marttila and colleagues identified lower levels of *HERV-K(HML-2)* in nonagerians and *HERV-K(HML-2)* levels did not correlate with any marker of immunosenescence (151). Moreover, the release in the blood of pro-inflammatory cytokines (TNF-α, IL-1β, IL-6, and IL-8) after stimulation with RLR ligands (5'ppp-dsDNA and poly(I:C)) was comparable between young (20-39 years) and elderly (60-84 years) healthy participants (152). On the contrary, an indirect evidence of a driving role of HERV de-repression in inflammaging comes from the analysis of HERV-K (HML-2) provirus levels in the peripheral blood mononuclear cells (PBMC). In PBMC obtained from older individuals, HERV-K transcript levels correlate with deregulated activities of neutrophils (147).

Psoriasis is a Th17 cytokine-mediated chronic inflammatory disease; CD8+ T cells obtained from psoriasis patients display features of immunosenescence as they are for the most part senescent or terminally differentiated. Curiously, psoriasis patients have increased proportions of Tregs but with a decreased regulatory potential (153). Interestingly, MDA5 levels are increased in psoriatic lesions. Whether this represents a consequence of the inflammatory state or its source is still unknown (153).

Monocytes obtained from older (age 65-89) adult donors in respect to younger (age 21-30) donors were found to be impaired in IFN induction after exposure to RIG-I–specific 5'-ppp 14-bp dsRNA ligand (113), correlating to the increased vulnerability of elderly people to Influenza A virus (IAV) infection (154). The impairment in RIG-I signaling in aged monocytes is related to the increased basal proteasomal degradation of the adaptor protein tumor necrosis factor receptor–associated factor 3 (TRAF3) and to the defective induction of IRF8, as the re-expression of TRAF3 and IRF7 rescues IFN-signaling (113). Defective IFN signaling was detected also in Plasmacytoid Dendritic Cells (pDCs) from elderly people after the engagement of TLR (155) and in memory T cells after TCR engagement (156).

Further studies are needed to determine whether ERV de-repression may directly lead to immunosenescence or is merely a contributory cause that combines with the signaling decoding defects observed in aged immune cells. A better understanding of the multiple defects in innate antiviral signaling that occur with aging will help identify new potential targets for precise therapeutic interventions.

DISCUSSION: DOES THE ERV DEPENDENT ACTIVATION OF RLR (RIG-I-LIKE RECEPTORS)-MAVS PATHWAY DIRECTLY CONTROL SENESCENCE AND AGING?

The de-repression of ERVs and the activation of RIG-I/MDA5/MAVS pathway were observed during neurodegeneration, cancer, aging and autoimmune diseases (108, 109). Whether loss-of-function experiments have clarified the direct role of RLRs in sustaining the inflammatory states and the interferon signaling observed in this physiological and pathological states, the studies regarding the roles played by ERV in sustaining this signaling pathways are mainly correlative. The high number of repetitions and their inhomogeneous distribution in the genome make the modulation of ERV expression biotechnologically demanding. New approaches based on CRISPR/Cas9 technology are demonstrating that the expression of ERVs and the subsequent activation of RLRs can impact on cellular fitness; however, the intra-cellular and extra-cellular effects resulting in ERVs de-repression appear to be only complementary to a primary stressful event, such as DNA damage (157) or the activation of a basal inflammatory state (158).

Nevertheless, RLRs inhibition holds promise for the treatment of autoimmune diseases and interferonopathies, while RLR agonists may have a future in cancer therapy, to induce a pre-senescence state or to increase sensitivity to apoptotic agents. In this regard, agonistic activation of RIG -I by IVT4 was found to increase tumor shrinkage by CD8+ and NK cells in immunocompetent EGFR-driven *in vivo* tumor models treated with EGFR inhibitors (159).

AUTHOR CONTRIBUTIONS

EG: conceptualization, writing, editing. LX: writing, editing. All authors contributed to the article and approved the submitted version.

FUNDING

This work was supported by the grants from AIRC - Associazione Italiana per la Ricerca sul Cancro to EDG (MFAG2020 ID 25000) and LX.

ACKNOWLEDGMENTS

Authors acknowledge prof. Claudio Brancolini and Liliana Ranzino for helpful discussion. We apologize in advance to all the authors that we have not been able to mention in the references despite their important contribution to research on related topics.

REFERENCES

1. Lanciano S, Cristofari G. Measuring and Interpreting Transposable Element Expression. *Nat Rev Genet* (2020) 21:721–36. doi: 10.1038/s41576-020-0251-y
2. Chuong EB, Elde NC, Feschotte C. Regulatory Activities of Transposable Elements: From Conflicts to Benefits. *Nat Rev Genet* (2017) 18:71–86. doi: 10.1038/nrg.2016.139
3. Cardelli M. The Epigenetic Alterations of Endogenous Retroelements in Aging. *Mech Ageing Dev* (2018) 174:30–46. doi: 10.1016/j.mad.2018.02.002
4. Durnaoglu S, Lee S-K, Ahnn J. Human Endogenous Retroviruses as Gene Expression Regulators: Insights From Animal Models Into Human Diseases. *Mol Cells* (2021) 44:861–78. doi: 10.14348/molcells.2021.5016
5. Buzdin A, Kovalskaya-Alexandrova E, Gogvadze E, Sverdlov E. At Least 50% of Human-Specific HERV-K (HML-2) Long Terminal Repeats Serve *In Vivo* as Active Promoters for Host Nonrepetitive DNA Transcription. *J Virol* (2006) 80:10752–62. doi: 10.1128/JVI.00871-06
6. Suntsova M, Gogvadze EV, Salozhin S, Gaifullin N, Eroshkin F, Dmitriev SE, et al. Human-Specific Endogenous Retroviral Insert Serves as an Enhancer for the Schizophrenia-Linked Gene PRODH. *Proc Natl Acad Sci* (2013) 110:19472–7. doi: 10.1073/pnas.1318172110
7. Schumann GG, Gogvadze EV, Osanai-Futahashi M, Kuroki A, Münk C, Fujiwara H, et al. Unique Functions of Repetitive Transcriptomes. *Int Rev Cell Mol Biol* (2010) 285:115–88. doi: 10.1016/B978-0-12-381047-2.00003-7
8. Gifford RJ, Blomberg J, Coffin JM, Fan H, Heidmann T, Mayer J, et al. Nomenclature for Endogenous Retrovirus (ERV) Loci. *Retrovirology* (2018) 15:59. doi: 10.1186/s12977-018-0442-1
9. Grandi N, Tramontano E. HERV Envelope Proteins: Physiological Role and Pathogenic Potential in Cancer and Autoimmunity. *Front Microbiol* (2018) 9:2018.00462. doi: 10.3389/fmicb.2018.00462
10. Vargiu L, Rodriguez-Tomé P, Sperber GO, Cadeddu M, Grandi N, Blikstad V, et al. Classification and Characterization of Human Endogenous Retroviruses; Mosaic Forms Are Common. *Retrovirology* (2016) 13:7. doi: 10.1186/s12977-015-0232-y
11. Buzdin AA, Prassolov V, Garazha AV. Friends-Enemies: Endogenous Retroviruses Are Major Transcriptional Regulators of Human DNA. *Front Chem* (2017) 5:2017.00035. doi: 10.3389/fchem.2017.00035
12. Grandi N, Tramontano E. Human Endogenous Retroviruses Are Ancient Acquired Elements Still Shaping Innate Immune Responses. *Front Immunol* (2018) 9:2018.02039. doi: 10.3389/fimmu.2018.02039
13. Kamp C, Hirschmann P, Voss H, Huellen K, Vogt PH. Two Long Homologous Retroviral Sequence Blocks in Proximal Yq11 Cause AZFa Microdeletions as a Result of Intrachromosomal Recombination Events. *Hum Mol Genet* (2000) 9:2563–72. doi: 10.1093/hmg/9.17.2563
14. Cakmak Guner B, Karlik E, Marakli S, Gozukirmizi N. Detection of HERV-K6 and HERV-K11 Transpositions in the Human Genome. *Biomed Rep* (2018) 9:53–9. doi: 10.3892/br.2018.1096
15. Lu X, Sachs F, Ramsay L, Jacques P.-É., Göke J, Bourque G, et al. The Retrovirus HERVH is a Long Noncoding RNA Required for Human Embryonic Stem Cell Identity. *Nat Struct Mol Biol* (2014) 21:423–5. doi: 10.1038/nsmb.2799
16. Kowalski PE, Mager DL. A Human Endogenous Retrovirus Suppresses Translation of an Associated Fusion Transcript, PLA2L. *J Virol* (1998) 72:6164–8. doi: 10.1128/JVI.72.7.6164-6168.1998
17. Lee H-E, Jo A, Im J, Cha H-J, Kim W-J, Kim HH, et al. Characterization of the Long Terminal Repeat of the Endogenous Retrovirus-Derived microRNAs in the Olive Flounder. *Sci Rep* (2019) 9:14007. doi: 10.1038/s41598-019-50492-7
18. Walsh CP, Bestor TH. Cytosine Methylation and Mammalian Development. *Genes Dev* (1999) 13:26–34. doi: 10.1101/gad.13.1.26
19. Al Adhami H, Bardet AF, Dumas M, Cleroux E, Guibert S, Fauque P, et al. A Comparative Methylome Analysis Reveals Conservation and Divergence of DNA Methylation Patterns and Functions in Vertebrates. *BMC Biol* (2022) 20:70. doi: 10.1186/s12915-022-01270-x
20. Bensberg M, Rundquist O, Selimović A, Lagerwall C, Benson M, Gustafsson M, et al. TET2 as a Tumor Suppressor and Therapeutic Target in T-Cell Acute Lymphoblastic Leukemia. *Proc Natl Acad Sci U S A* (2021) 118(34). doi: 10.1073/pnas.2110758118
21. Ku Y, Park J-H, Cho R, Lee Y, Park H-M, Kim M, et al. Noncanonical Immune Response to the Inhibition of DNA Methylation by Staufen1 *via* Stabilization of Endogenous Retrovirus RNAs. *Proc Natl Acad Sci U S A* (2021) 118:e2016289118. doi: 10.1073/pnas.2016289118
22. Sun S, Frontini F, Qi W, Hariharan A, Ronner M, Wipplinger M, et al. Endogenous Retrovirus Expression Activates Type-I Interferon Signaling in an Experimental Mouse Model of Mesothelioma Development. *Cancer Lett* (2021) 507:26–38. doi: 10.1016/j.canlet.2021.03.004
23. Liu M, Ohtani H, Zhou W, Ørskov AD, Charlet J, Zhang YW, et al. Vitamin C Increases Viral Mimicry Induced by 5-Aza-2'-Deoxycytidine. *Proc Natl Acad Sci U S A* (2016) 113:10238–44. doi: 10.1073/pnas.1612262113
24. Liu M, Thomas SL, DeWitt AK, Zhou W, Madaj ZB, Ohtani H, et al. Dual Inhibition of DNA and Histone Methyltransferases Increases Viral Mimicry in Ovarian Cancer Cells. *Cancer Res* (2018) 78:5754–66. doi: 10.1158/0008-5472.CAN-17-3953
25. Wu Z, Mei X, Zhao D, Sun Y, Song J, Pan W, et al. DNA Methylation Modulates HERV-E Expression in CD4+ T Cells From Systemic Lupus Erythematosus Patients. *J Dermatol Sci* (2015) 77:110–6. doi: 10.1016/j.jdermsci.2014.12.004
26. Groudine M, Eisenman R, Weintraub H. Chromatin Structure of Endogenous Retroviral Genes and Activation by an Inhibitor of DNA Methylation. *Nature* (1981) 292:311–7. doi: 10.1038/292311a0
27. Liu L, Wang H, Xu GL, Liu L. Tet1 Deficiency Leads to Premature Ovarian Failure. *Front Cell Dev Biol* (2021) 9:2021.644135. doi: 10.3389/fcell.2021.644135
28. Kloc M, Uosef A, Kubiak JZ, Ghobrial RM. Exaptation of Retroviral Syncytin for Development of Syncytialized Placenta, Its Limited Homology to the SARS-CoV-2 Spike Protein and Arguments Against Disturbing Narrative in the Context of COVID-19 Vaccination. *Biol (Basel)* (2021) 10:238. doi: 10.3390/biology10030238

29. Mi S, Lee X, Li X, Veldman GM, Finnerty H, Racie L, et al. Syncytin is a Captive Retroviral Envelope Protein Involved in Human Placental Morphogenesis. *Nature* (2000) 403:785–9. doi: 10.1038/35001608
30. Ruebner M, Strissel PL, Ekici AB, Stiegler E, Dammer U, Goecke TW, et al. Reduced Syncytin-1 Expression Levels in Placental Syndromes Correlates With Epigenetic Hypermethylation of the ERVW-1 Promoter Region. *PloS One* (2013) 8:e56145. doi: 10.1371/journal.pone.0056145
31. Milano-Foster J, Ray S, Home P, Ganguly A, Bhattacharya B, Bajpai S, et al. Regulation of Human Trophoblast Syncytialization by Histone Demethylase LSD1. *J Biol Chem* (2019) 294:17301–13. doi: 10.1074/jbc.RA119.010518
32. Groh S, Schotta G. Silencing of Endogenous Retroviruses by Heterochromatin. *Cell Mol Life Sci* (2017) 74:2055–65. doi: 10.1007/s00018-017-2454-8
33. Rowe HM, Jakobsson J, Mesnard D, Rougemont J, Reynard S, Aktas T, et al. KAP1 Controls Endogenous Retroviruses in Embryonic Stem Cells. *Nature* (2010) 463:237–40. doi: 10.1038/nature08674
34. Elsässer SJ, Noh K-M, Diaz N, Allis CD, Banaszynski LA. Histone H3.3 is Required for Endogenous Retroviral Element Silencing in Embryonic Stem Cells. *Nature* (2015) 522:240–4. doi: 10.1038/nature14345
35. Groh S, Milton AV, Marinelli LK, Sickinger CV, Russo A, Bollig H, et al. Morc3 Silences Endogenous Retroviruses by Enabling Daxx-Mediated Histone H3.3 Incorporation. *Nat Commun* (2021) 12:5996. doi: 10.1038/s41467-021-26288-7
36. Sharma P, Azebi S, England P, Christensen T, Møller-Larsen A, Petersen T, et al. Citrullination of Histone H3 Interferes With HP1-Mediated Transcriptional Repression. *PloS Genet* (2012) 8:e1002934. doi: 10.1371/journal.pgen.1002934
37. Faigle W, Cruciani C, Wolski W, Roschitzki B, Puthenparampil M, Tomas-Ojer P, et al. Brain Citrullination Patterns and T Cell Reactivity of Cerebrospinal Fluid-Derived CD4+ T Cells in Multiple Sclerosis. *Front Immunol* (2019) 10:2019.00540. doi: 10.3389/fimmu.2019.00540
38. Wood DD, Ackerley CA, Brand, den Bv, Zhang L, Raijmakers R, et al. Myelin Localization of Peptidylarginine Deiminases 2 and 4: Comparison of PAD2 and PAD4 Activities.0. *Lab Investig* (2008) 88:354–64. doi: 10.1038/labinvest.3700748
39. Hurst T, Pace M, Katzourakis A, Phillips R, Klenerman P, Frater J, et al. Human Endogenous Retrovirus (HERV) Expression is Not Induced by Treatment With the Histone Deacetylase (HDAC) Inhibitors in Cellular Models of HIV-1 Latency. *Retrovirology* (2016) 13:10. doi: 10.1186/s12977-016-0242-4
40. Curty G, Iñiguez LP, Nixon DF, Soares MA, de Mulder Rougvie M. Hallmarks of Retroelement Expression in T-Cells Treated With HDAC Inhibitors. *Front Virol* (2021) 1:2021.756635. doi: 10.3389/fviro.2021.756635
41. Chiappinelli KB, Strissel PL, Desrichard A, Li H, Henke C, Akman B, et al. Inhibiting DNA Methylation Causes an Interferon Response in Cancer *via* dsRNA Including Endogenous Retroviruses. *Cell* (2015) 162:974–86. doi: 10.1016/j.cell.2015.07.011
42. Daskalakis M, Brocks D, Sheng Y-H, Islam MS, Ressnerova A, Assenov Y, et al. Reactivation of Endogenous Retroviral Elements *via* Treatment With DNMT- and HDAC-Inhibitors. *Cell Cycle* (2018) 17:811–22. doi: 10.1080/15384101.2018.1442623
43. Elmer JL, Hay AD, Kessler NJ, Bertozzi TM, Ainscough EAC, Ferguson-Smith AC. Genomic Properties of Variably Methylated Retrotransposons in Mouse. *Mob DNA* (2021) 12:6. doi: 10.1186/s13100-021-00235-1
44. Hakim ST, Alsayari M, McLean DC, Saleem S, Addanki KC, Aggarwal M, et al. A Large Number of the Human microRNAs Target Lentiviruses, Retroviruses, and Endogenous Retroviruses. *Biochem Biophys Res Commun* (2008) 369:357–62. doi: 10.1016/j.bbrc.2008.02.025
45. Carter AC, Xu J, Nakamoto MY, Wei Y, Zarnegar BJ, Shi Q, et al. Spen Links RNA-Mediated Endogenous Retrovirus Silencing and X Chromosome Inactivation. *Elife* (2020) 9:e54508. doi: 10.7554/eLife.54508
46. Chelmicki T, Roger E, Teissandier A, Dura M, Bonneville L, Rucli S, et al. M6a RNA Methylation Regulates the Fate of Endogenous Retroviruses. *Nature* (2021) 591:312–6. doi: 10.1038/s41586-020-03135-1
47. Herzner A-M, Khan Z, Van Nostrand EL, Chan S, Cuellar T, Chen R, et al. ADAR and hnRNPC Deficiency Synergize in Activating Endogenous dsRNA-Induced Type I IFN Responses. *J Exp Med* (2021) 218:e20201833. doi: 10.1084/jem.20201833
48. Ishizuka JJ, Manguso RT, Cheruiyot CK, Bi K, Panda A, Iracheta-Vellve A, et al. Loss of ADAR1 in Tumours Overcomes Resistance to Immune Checkpoint Blockade. *Nature* (2019) 565:43–8. doi: 10.1038/s41586-018-0768-9
49. Fischer SEJ, Ruvkun G. Caenorhabditis Elegans ADAR Editing and the ERI-6/7/MOV10 RNAi Pathway Silence Endogenous Viral Elements and LTR Retrotransposons. *Proc Natl Acad Sci U S A* (2020) 117:5987–96. doi: 10.1073/pnas.1919028117
50. Jiao H, Wachsmuth L, Kumari S, Schwarzer R, Lin J, Eren RO, et al. Z-Nucleic-Acid Sensing Triggers ZBP1-Dependent Necroptosis and Inflammation. *Nature* (2020) 580:391–5. doi: 10.1038/s41586-020-2129-8
51. Clapes T, Polyzou A, Prater P, Sagar, Morales-Hernández A, Ferrarini MG, et al. Chemotherapy-Induced Transposable Elements Activate MDA5 to Enhance Haematopoietic Regeneration. *Nat Cell Biol* (2021) 23:704–17. doi: 10.1038/s41556-021-00707-9
52. Mikhalkevich N, O'Carroll IP, Tkavc R, Lund K, Sukumar G, Dalgard CL, et al. Response of Human Macrophages to Gamma Radiation is Mediated *via* Expression of Endogenous Retroviruses. *PloS Pathog* (2021) 17:e1009305. doi: 10.1371/journal.ppat.1009305
53. Lee AK, Pan D, Bao X, Hu M, Li F, Li C-Y. Endogenous Retrovirus Activation as a Key Mechanism of Anti-Tumor Immune Response in Radiotherapy. *Radiat Res* (2020) 193:305. doi: 10.1667/RADE-20-00013
54. Ziv Y, Bielopolski D, Galanty Y, Lukas C, Taya Y, Schultz DC, et al. Chromatin Relaxation in Response to DNA Double-Strand Breaks is Modulated by a Novel ATM- and KAP-1 Dependent Pathway. *Nat Cell Biol* (2006) 8:870–6. doi: 10.1038/ncb1446
55. Sadeq S, Al-Hashimi S, Cusack CM, Werner A. Endogenous Double-Stranded RNA. *Non-coding RNA* (2021) 7:15. doi: 10.3390/ncrna7010015
56. Wang DD-H, Shu Z, Lieser SA, Chen P-L, Lee W-H. Human Mitochondrial SUV3 and Polynucleotide Phosphorylase Form a 330-kDa Heteropentamer to Cooperatively Degrade Double-Stranded RNA With a 3'-to-5' Directionality. *J Biol Chem* (2009) 284:20812–21. doi: 10.1074/jbc.M109.009605
57. Pajak A, Laine I, Clemente P, El-Fissi N, Schober FA, Maffezzini C, et al. Defects of Mitochondrial RNA Turnover Lead to the Accumulation of Double-Stranded RNA *In Vivo*. *PloS Genet* (2019) 15:e1008240. doi: 10.1371/journal.pgen.1008240
58. Arnaiz E, Miar A, Dias Junior AG, Prasad N, Schulze U, Waithe D, et al. Hypoxia Regulates Endogenous Double-Stranded RNA Production *via* Reduced Mitochondrial DNA Transcription. *Front Oncol* (2021) 11:2021.779739. doi: 10.3389/fonc.2021.779739
59. Wulff B-E, Nishikura K. Substitutional A-To-I RNA Editing. *Wiley Interdiscip Rev RNA* (2010) 1:90–101. doi: 10.1002/wrna.10
60. Porath HT, Knisbacher BA, Eisenberg E, Levanon EY. Massive A-To-I RNA Editing is Common Across the Metazoa and Correlates With dsRNA Abundance. *Genome Biol* (2017) 18:185. doi: 10.1186/s13059-017-1315-y
61. Svobodova E, Kubikova J, Svoboda P. Production of Small RNAs by Mammalian Dicer. *Pflugers Arch* (2016) 468:1089–102. doi: 10.1007/s00424-016-1817-6
62. Kim Y, Park J, Kim S, Kim M, Kang M-G, Kwak C, et al. PKR Senses Nuclear and Mitochondrial Signals by Interacting With Endogenous Double-Stranded RNAs. *Mol Cell* (2018) 71:1051–63.e6. doi: 10.1016/j.molcel.2018.07.029
63. Balbin OA, Malik R, Dhanasekaran SM, Prensner JR, Cao X, Wu Y-M, et al. The Landscape of Antisense Gene Expression in Human Cancers. *Genome Res* (2015) 25:1068–79. doi: 10.1101/gr.180596.114
64. Tian B, Bevilacqua PC, Diegelman-Parente A, Mathews MB. The Double-Stranded-RNA-Binding Motif: Interference and Much More. *Nat Rev Mol Cell Biol* (2004) 5:1013–23. doi: 10.1038/nrm1528
65. Sadler AJ, Williams BRG. Interferon-Inducible Antiviral Effectors. *Nat Rev Immunol* (2008) 8:559–68. doi: 10.1038/nri2314
66. von Roretz C, Gallouzi I-E. Protein Kinase RNA/FADD/Caspase-8 Pathway Mediates the Proapoptotic Activity of the RNA-Binding Protein Human Antigen R (HuR). *J Biol Chem* (2010) 285:16806–13. doi: 10.1074/jbc.M109.087320
67. Liddicoat BJ, Piskol R, Chalk AM, Ramaswami G, Higuchi M, Hartner JC, et al. RNA Editing by ADAR1 Prevents MDA5 Sensing of Endogenous

dsRNA as Nonself. *Science* (2015) 349:1115–20. doi: 10.1126/science.aac7049
68. Patterson JB, Samuel CE. Expression and Regulation by Interferon of a Double-Stranded-RNA-Specific Adenosine Deaminase From Human Cells: Evidence for Two Forms of the Deaminase. *Mol Cell Biol* (1995) 15:5376–88. doi: 10.1128/MCB.15.10.5376
69. Pestal K, Funk CC, Snyder JM, Price ND, Treuting PM, Stetson DB. Isoforms of RNA-Editing Enzyme ADAR1 Independently Control Nucleic Acid Sensor MDA5-Driven Autoimmunity and Multi-Organ Development. *Immunity* (2015) 43:933–44. doi: 10.1016/j.immuni.2015.11.001
70. Treger RS, Tokuyama M, Dong H, Salas-Briceno K, Ross SR, Kong Y, et al. Human APOBEC3G Prevents Emergence of Infectious Endogenous Retrovirus in Mice. *J Virol* (2019) 93:e00728–19. doi: 10.1128/JVI.00728-19
71. Dong B, Xu L, Zhou A, Hassel BA, Lee X, Torrence PF, et al. Intrinsic Molecular Activities of the Interferon-Induced 2-5A-Dependent RNase. *J Biol Chem* (1994) 269:14153–8. doi: 10.1016/S0021-9258(17)36767-4
72. Huang H, Zeqiraj E, Dong B, Jha BK, Duffy NM, Orlicky S, et al. Dimeric Structure of Pseudokinase RNase L Bound to 2-5A Reveals a Basis for Interferon-Induced Antiviral Activity. *Mol Cell* (2014) 53:221–34. doi: 10.1016/j.molcel.2013.12.025
73. Choi UY, Kang J-S, Hwang YS, Kim Y-J. Oligoadenylate Synthase-Like (OASL) Proteins: Dual Functions and Associations With Diseases. *Exp Mol Med* (2015) 47:e144. doi: 10.1038/emm.2014.110
74. Roth SH, Danan-Gotthold M, Ben-Izhak M, Rechavi G, Cohen CJ, Louzoun Y, et al. Increased RNA Editing May Provide a Source for Autoantigens in Systemic Lupus Erythematosus. *Cell Rep* (2018) 23:50–7. doi: 10.1016/j.celrep.2018.03.036
75. Maurano M, Snyder JM, Connelly C, Henao-Mejia J, Sidrauski C, Stetson DB. Protein Kinase R and the Integrated Stress Response Drive Immunopathology Caused by Mutations in the RNA Deaminase ADAR1. *Immunity* (2021) 54:1948–1960.e5. doi: 10.1016/j.immuni.2021.07.001
76. Li H, Reksten TR, Ice JA, Kelly JA, Adrianto I, Rasmussen A, et al. Identification of a Sjögren's Syndrome Susceptibility Locus at OAS1 That Influences Isoform Switching, Protein Expression, and Responsiveness to Type I Interferons. *PloS Genet* (2017) 13:e1006820. doi: 10.1371/journal.pgen.1006820
77. Weiss R, Sachet M, Zinngrebe J, Aschacher T, Krainer M, Hegedus B, et al. IL-24 Sensitizes Tumor Cells to TLR3-Mediated Apoptosis. *Cell Death Differ* (2013) 123:93–104. doi: 10.1038/cdd.2013.15
78. Rehwinkel J, Gack MU. RIG-I-Like Receptors: Their Regulation and Roles in RNA Sensing. *Nat Rev Immunol* (2020) 20:537–51. doi: 10.1038/s41577-020-0288-3
79. Feng X, Tubbs A, Zhang C, Tang M, Sridharan S, Wang C, et al. ATR Inhibition Potentiates Ionizing Radiation-Induced Interferon Response *via* Cytosolic Nucleic Acid-Sensing Pathways. *EMBO J* (2020) 39:e104036. doi: 10.15252/embj.2019104036
80. Chiu Y-H, MacMillan JB, Chen ZJ. RNA Polymerase III Detects Cytosolic DNA and Induces Type I Interferons Through the RIG-I Pathway. *Cell* (2009) 138:576–91. doi: 10.1016/j.cell.2009.06.015
81. Zevini A, Olagnier D, Hiscott J. Crosstalk Between Cytoplasmic RIG-I and STING Sensing Pathways. *Trends Immunol* (2017) 38:194–205. doi: 10.1016/j.it.2016.12.004
82. Franz KM, Neidermyer WJ, Tan Y-J, Whelan SPJ, Kagan JC. STING-Dependent Translation Inhibition Restricts RNA Virus Replication. *Proc Natl Acad Sci* (2018) 115:e2058–67. doi: 10.1073/pnas.1716937115
83. Zhang D, Liu Y, Zhu Y, Zhang Q, Guan H, Liu S, et al. A Non-Canonical cGAS–STING–PERK Pathway Facilitates the Translational Program Critical for Senescence and Organ Fibrosis. *Nat Cell Biol* (2022) 24:766–82. doi: 10.1038/s41556-022-00894-z
84. Bruns AM, Leser GP, Lamb RA, Horvath CM. The Innate Immune Sensor LGP2 Activates Antiviral Signaling by Regulating MDA5-RNA Interaction and Filament Assembly. *Mol Cell* (2014) 55:771–81. doi: 10.1016/j.molcel.2014.07.003
85. Quicke KM, Kim KY, Horvath CM, Suthar MS. RNA Helicase LGP2 Negatively Regulates RIG-I Signaling by Preventing TRIM25-Mediated Caspase Activation and Recruitment Domain Ubiquitination. *J Interferon Cytokine Res* (2019) 39:669–83. doi: 10.1089/jir.2019.0059
86. Rothenfusser S, Goutagny N, DiPerna G, Gong M, Monks BG, Schoenemeyer A, et al. The RNA Helicase Lgp2 Inhibits TLR-Independent Sensing of Viral Replication by Retinoic Acid-Inducible Gene-I. *J Immunol* (2005) 175:5260–8. doi: 10.4049/jimmunol.175.8.5260
87. Komuro A, Horvath CM. RNA- and Virus-Independent Inhibition of Antiviral Signaling by RNA Helicase LGP2. *J Virol* (2006) 80:12332–42. doi: 10.1128/JVI.01325-06
88. Satoh T, Kato H, Kumagai Y, Yoneyama M, Sato S, Matsushita K, et al. LGP2 is a Positive Regulator of RIG-I- and MDA5-Mediated Antiviral Responses. *Proc Natl Acad Sci U S A* (2010) 107:1512–7. doi: 10.1073/pnas.0912986107
89. Peisley A, Wu B, Yao H, Walz T, Hur S. RIG-I Forms Signaling-Competent Filaments in an ATP-Dependent, Ubiquitin-Independent Manner. *Mol Cell* (2013) 51:573–83. doi: 10.1016/j.molcel.2013.07.024
90. Hornung V, Ellegast J, Kim S, Brzoízka K, Jung A, Kato H, et al. 5'-Triphosphate RNA Is the Ligand for RIG-I. *Science* (2006) 314:994–7. doi: 10.1126/science.1132505
91. Kato H, Takeuchi O, Sato S, Yoneyama M, Yamamoto M, Matsui K, et al. Differential Roles of MDA5 and RIG-I Helicases in the Recognition of RNA Viruses. *Nature* (2006) 441:101–5. doi: 10.1038/nature04734
92. Kato H, Takeuchi O, Mikamo-Satoh E, Hirai R, Kawai T, Matsushita K, et al. Length-Dependent Recognition of Double-Stranded Ribonucleic Acids by Retinoic Acid–Inducible Gene-I and Melanoma Differentiation–Associated Gene 5. *J Exp Med* (2008) 205:1601–10. doi: 10.1084/jem.20080091
93. Xu L-G, Wang Y-Y, Han K-J, Li L-Y, Zhai Z, Shu H-B. VISA Is an Adapter Protein Required for Virus-Triggered IFN-β Signaling. *Mol Cell* (2005) 19:727–40. doi: 10.1016/j.molcel.2005.08.014
94. Seth RB, Sun L, Ea C-K, Chen ZJ. Identification and Characterization of MAVS, a Mitochondrial Antiviral Signaling Protein That Activates NF-kappaB and IRF 3. *Cell* (2005) 122:669–82. doi: 10.1016/j.cell.2005.08.012
95. Meylan E, Curran J, Hofmann K, Moradpour D, Binder M, Bartenschlager R, et al. Cardif is an Adaptor Protein in the RIG-I Antiviral Pathway and is Targeted by Hepatitis C Virus. *Nature* (2005) 437:1167–72. doi: 10.1038/nature04193
96. Hou F, Sun L, Zheng H, Skaug B, Jiang Q-X, Chen ZJ. MAVS Forms Functional Prion-Like Aggregates to Activate and Propagate Antiviral Innate Immune Response. *Cell* (2011) 146:448–61. doi: 10.1016/j.cell.2011.06.041
97. McWhirter SM, TenOever BR, Maniatis T. Connecting Mitochondria and Innate Immunity. *Cell* (2005) 122:645–7. doi: 10.1016/j.cell.2005.08.026
98. Qi N, Shi Y, Zhang R, Zhu W, Yuan B, Li X, et al. Multiple Truncated Isoforms of MAVS Prevent its Spontaneous Aggregation in Antiviral Innate Immune Signalling. *Nat Commun* (2017) 8:15676. doi: 10.1038/ncomms15676
99. Lei X, Dong X, Ma R, Wang W, Xiao X, Tian Z, et al. Activation and Evasion of Type I Interferon Responses by SARS-CoV-2. *Nat Commun* (2020) 11:3810. doi: 10.1038/s41467-020-17665-9
100. Pinto AK, Ramos HJ, Wu X, Aggarwal S, Shrestha B, Gorman M, et al. Deficient IFN Signaling by Myeloid Cells Leads to MAVS-Dependent Virus-Induced Sepsis. *PloS Pathog* (2014) 10:e1004086. doi: 10.1371/journal.ppat
101. Zeng W, Sun L, Jiang X, Chen X, Hou F, Adhikari A, et al. Reconstitution of the RIG-I Pathway Reveals a Signaling Role of Unanchored Polyubiquitin Chains in Innate Immunity. *Cell* (2010) 141:315–30. doi: 10.1016/j.cell.2010.03.029
102. Inn K-S, Gack MU, Tokunaga F, Shi M, Wong L-Y, Iwai K, et al. Linear Ubiquitin Assembly Complex Negatively Regulates RIG-I- and TRIM25-Mediated Type I Interferon Induction. *Mol Cell* (2011) 41:354–65. doi: 10.1016/j.molcel.2010.12.029
103. Hu M-M, Liao C-Y, Yang Q, Xie X-Q, Shu H-B. Innate Immunity to RNA Virus is Regulated by Temporal and Reversible Sumoylation of RIG-I and MDA5. *J Exp Med* (2017) 214:973–89. doi: 10.1084/jem.20161015
104. Choi SJ, Lee H-C, Kim J-H, Park SY, Kim T-H, Lee W-K, et al. HDAC6 Regulates Cellular Viral RNA Sensing by Deacetylation of RIG-I. *EMBO J* (2016) 35:429–42. doi: 10.15252/embj.201592586
105. Yang Q, Tang J, Pei R, Gao X, Guo J, Xu C, et al. Host HDAC4 Regulates the Antiviral Response by Inhibiting the Phosphorylation of IRF3. *J Mol Cell Biol* (2019) 11:158–69. doi: 10.1093/jmcb/mjy035
106. Di Giorgio E, Paluvai H, Dalla E, Ranzino L, Renzini A, Moresi V, et al. HDAC4 Degradation During Senescence Unleashes an Epigenetic Program

Driven by AP-1/P300 at Selected Enhancers and Super-Enhancers. *Genome Biol* (2021) 22:129. doi: 10.1186/s13059-021-02340-z
107. Lin J-P, Fan Y-K, Liu HM. The 14-3-3η Chaperone Protein Promotes Antiviral Innate Immunity *via* Facilitating MDA5 Oligomerization and Intracellular Redistribution. *PloS Pathog* (2019) 15:e1007582. doi: 10.1371/journal.ppat.1007582
108. Mao J, Zhang Q, Cong Y-S. Human Endogenous Retroviruses in Development and Disease. *Comput Struct Biotechnol J* (2021) 19:5978–86. doi: 10.1016/j.csbj.2021.10.037
109. Ireton RC, Gale JM. RIG-I Like Receptors in Antiviral Immunity and Therapeutic Applications. *Viruses* (2011) 3:906–19. doi: 10.3390/v3060906
110. Li D, Wu M. Pattern Recognition Receptors in Health and Diseases. *Signal Transduction Targeting Ther* (2021) 6:291. doi: 10.1038/s41392-021-00687-0
111. Zeng Y, Wang P-H, Zhang M, Du J-R. Aging-Related Renal Injury and Inflammation Are Associated With Downregulation of Klotho and Induction of RIG-I/NF-κb Signaling Pathway in Senescence-Accelerated Mice. *Aging Clin Exp Res* (2016) 28:69–76. doi: 10.1007/s40520-015-0371-y
112. Liu F, Wu S, Ren H, Gu J. Klotho Suppresses RIG-I-Mediated Senescence-Associated Inflammation. *Nat Cell Biol* (2011) 13:254–62. doi: 10.1038/ncb2167
113. Molony RD, Nguyen JT, Kong Y, Montgomery RR, Shaw AC, Iwasaki A. Aging Impairs Both Primary and Secondary RIG-I Signaling for Interferon Induction in Human Monocytes. *Sci Signal* (2017) 10:eaan2392. doi: 10.1126/scisignal.aan2392
114. Zhao J, Jiang X, Yan L, Lin J, Guo H, Yu S, et al. Retinoic Acid Inducible Gene-I Slows Down Cellular Senescence Through Negatively Regulating the Integrin β3/P38 MAPK Pathway. *Cell Cycle* (2019) 18:3378–92. doi: 10.1080/15384101.2019.1677074
115. Gao L, Bird AK, Meednu N, Dauenhauer K, Liesveld J, Anolik J, et al. Bone Marrow-Derived Mesenchymal Stem Cells From Patients With Systemic Lupus Erythematosus Have a Senescence-Associated Secretory Phenotype Mediated by a Mitochondrial Antiviral Signaling Protein-Interferon-β Feedback Loop. *Arthritis Rheumatol* (2017) 69:1623–35. doi: 10.1002/art.40142
116. Chen G-A, Lin Y-R, Chung H-T, Hwang L-H. H-Ras Exerts Opposing Effects on Type I Interferon Responses Depending on Its Activation Status. *Front Immunol* (2017) 8:2017.00972. doi: 10.3389/fimmu.2017.00972
117. Brisse M, Ly H. Comparative Structure and Function Analysis of the RIG-I-Like Receptors: RIG-I and MDA5. *Front Immunol* (2019) 10:2019.01586. doi: 10.3389/fimmu.2019.01586
118. Rutsch F, MacDougall M, Lu C, Buers I, Mamaeva O, Nitschke Y, et al. A Specific IFIH1 Gain-of-Function Mutation Causes Singleton-Merten Syndrome. *Am J Hum Genet* (2015) 96:275–82. doi: 10.1016/j.ajhg.2014.12.014
119. Paluvai H, Di Giorgio E, Brancolini C. The Histone Code of Senescence. *Cells* (2020) 9:466. doi: 10.3390/cells9020466
120. Narita M, Nuñez S, Heard E, Narita M, Lin AW, Hearn SA, et al. Rb-Mediated Heterochromatin Formation and Silencing of E2F Target Genes During Cellular Senescence. *Cell* (2003) 113:703–16. doi: 10.1016/S0092-8674(03)00401-X
121. Kennedy AL, McBryan T, Enders GH, Johnson FB, Zhang R, Adams PD. Senescent Mouse Cells Fail to Overtly Regulate the HIRA Histone Chaperone and do Not Form Robust Senescence Associated Heterochromatin Foci. *Cell Div* (2010) 5:16. doi: 10.1186/1747-1028-5-16
122. Di Micco R, Sulli G, Dobreva M, Liontos M, Botrugno OA, Gargiulo G, et al. Interplay Between Oncogene-Induced DNA Damage Response and Heterochromatin in Senescence and Cancer. *Nat Cell Biol* (2011) 13:292–302. doi: 10.1038/ncb2170
123. Colombo AR, Elias HK, Ramsingh G. Senescence Induction Universally Activates Transposable Element Expression. *Cell Cycle* (2018) 17:1846–57. doi: 10.1080/15384101.2018.1502576
124. Guan Y, Zhang C, Lyu G, Huang X, Zhang X, Zhuang T, et al. Senescence-Activated Enhancer Landscape Orchestrates the Senescence-Associated Secretory Phenotype in Murine Fibroblasts. *Nucleic Acids Res* (2020) 48:10909–23. doi: 10.1093/nar/gkaa858
125. Yu YC-Y, Hui TZ, Kao T-H, Liao H-F, Yang C-Y, Hou C-C, et al. Transient DNMT3L Expression Reinforces Chromatin Surveillance to Halt Senescence Progression in Mouse Embryonic Fibroblast. *Front Cell Dev Biol* (2020) 8:2020.00103. doi: 10.3389/fcell.2020.00103
126. Min B, Jeon K, Park JS, Kang Y-K. Demethylation and Derepression of Genomic Retroelements in the Skeletal Muscles of Aged Mice. *Aging Cell* (2019) 18:e13042. doi: 10.1111/acel.13042
127. Nevalainen T, Autio A, Mishra BH, Marttila S, Jylhä M, Hurme M. Aging-Associated Patterns in the Expression of Human Endogenous Retroviruses. *PloS One* (2018) 13:e0207407. doi: 10.1371/journal.pone.0207407
128. Balestrieri E, Pica F, Matteucci C, Zenobi R, Sorrentino R, Argaw-Denboba A, et al. Transcriptional Activity of Human Endogenous Retroviruses in Human Peripheral Blood Mononuclear Cells. *BioMed Res Int* (2015) 164529:1–9. doi: 10.1155/2015/164529
129. Jintaridth P, Mutirangura A. Distinctive Patterns of Age-Dependent Hypomethylation in Interspersed Repetitive Sequences. *Physiol Genomics* (2010) 41:194–200. doi: 10.1152/physiolgenomics.00146.2009
130. Capone S, Connor KM, Colombo A, Li X, Triche TJ, Ramsingh G. Senescent Human Hematopoietic Progenitors Show Elevated Expression of Transposable Elements and Inflammatory Genes. *Exp Hematol* (2018) 62:33–8.e6. doi: 10.1016/j.exphem.2018.03.003
131. Capone S, Colombo AR, Johnson BK, Triche TJ, Ramsingh G. Methylome of Human Senescent Hematopoietic Progenitors. *Exp Hematol Oncol* (2018) 7:32. doi: 10.1186/s40164-018-0123-8
132. Colombo AR, Zubair A, Thiagarajan D, Nuzhdin S, Triche TJ, Ramsingh G. Suppression of Transposable Elements in Leukemic Stem Cells. *Sci Rep* (2017) 7:7029. doi: 10.1038/s41598-017-07356-9
133. Frost B, Hemberg M, Lewis J, Feany MB. Tau Promotes Neurodegeneration Through Global Chromatin Relaxation. *Nat Neurosci* (2014) 17:357–66. doi: 10.1038/nn.3639
134. Khurana V, Merlo P, DuBoff B, Fulga TA, Sharp KA, Campbell SD, et al. A Neuroprotective Role for the DNA Damage Checkpoint in Tauopathy. *Aging Cell* (2012) 11:360–2. doi: 10.1111/j.1474-9726.2011.00778.x
135. Licastro F, Porcellini E. Activation of Endogenous Retrovirus, Brain Infections and Environmental Insults in Neurodegeneration and Alzheimer's Disease. *Int J Mol Sci* (2021) 22:7263. doi: 10.3390/ijms22147263
136. Guo C, Jeong H-H, Hsieh Y-C, Klein H-U, Bennett DA, De Jager PL, et al. Tau Activates Transposable Elements in Alzheimer's Disease. *Cell Rep* (2018) 23:2874–80. doi: 10.1016/j.celrep.2018.05.004
137. Sun W, Samimi H, Gamez M, Zare H, Frost B. Pathogenic Tau-Induced piRNA Depletion Promotes Neuronal Death Through Transposable Element Dysregulation in Neurodegenerative Tauopathies. *Nat Neurosci* (2018) 21:1038–48. doi: 10.1038/s41593-018-0194-1
138. Wenderski W, Maze I. Histone Turnover and Chromatin Accessibility: Critical Mediators of Neurological Development, Plasticity, and Disease. *Bioessays* (2016) 38:410–9. doi: 10.1002/bies.201500171
139. Kassiotis G. Endogenous Retroviruses and the Development of Cancer. *J Immunol* (2014) 192:1343–9. doi: 10.4049/jimmunol.1302972
140. Mao J, Zhang Q, Wang Y, Zhuang Y, Xu L, Ma X, et al. TERT Activates Endogenous Retroviruses to Promote an Immunosuppressive Tumour Microenvironment. *EMBO Rep* (2022) 23:e52984. doi: 10.15252/embr.202152984
141. Cardelli M, Doorn Rv, Larcher L, Donato M, Piacenza F, Pierpaoli E, et al. Association of HERV-K and LINE-1 Hypomethylation With Reduced Disease-Free Survival in Melanoma Patients. *Epigenomics* (2020) 12:1689–706. doi: 10.2217/epi-2020-0127
142. Zhou X, Singh M, Sanz Santos G, Guerlavais V, Carvajal LA, Aivado M, et al. Pharmacologic Activation of P53 Triggers Viral Mimicry Response Thereby Abolishing Tumor Immune Evasion and Promoting Antitumor Immunity. *Cancer Discov* (2021) 11:3090–105. doi: 10.1158/2159-8290.CD-20-1741
143. Ishiguro K, Kitajima H, Niinuma T, Maruyama R, Nishiyama N, Ohtani H, et al. Dual EZH2 and G9a Inhibition Suppresses Multiple Myeloma Cell Proliferation by Regulating the Interferon Signal and IRF4-MYC Axis. *Cell Death Discov* (2021) 7:7. doi: 10.1038/s41420-020-00400-0
144. Michna A, Schötz U, Selmansberger M, Zitzelsberger H, Lauber K, Unger, et al. Transcriptomic Analyses of the Radiation Response in Head and Neck Squamous Cell Carcinoma Subclones With Different Radiation Sensitivity: Time-Course Gene Expression Profiles and Gene Association Networks. *Radiat Oncol* (2016) 11:94. doi: 10.1186/s13014-016-0672-0

145. Hohn O, Hanke K, Bannert N. HERV-K(HML-2), the Best Preserved Family of HERVs: Endogenization, Expression, and Implications in Health and Disease. *Front Oncol* (2013) 3:2013.00246. doi: 10.3389/fonc.2013.00246
146. Dembny P, Newman AG, Singh M, Hinz M, Szczepek M, Krüger C, et al. Human Endogenous Retrovirus HERV-K(HML-2) RNA Causes Neurodegeneration Through Toll-Like Receptors. *JCI Insight* (2020) 5: e131093. doi: 10.1172/jci.insight.131093
147. Autio A, Nevalainen T, Mishra BH, Jylhä M, Flinck H, Hurme M. Effect of Aging on the Transcriptomic Changes Associated With the Expression of the HERV-K (HML-2) Provirus at 1q22. *Immun Ageing* (2020) 17:11. doi: 10.1186/s12979-020-00182-0
148. Zhu X, Chen Z, Shen W, Huang G, Sedivy JM, Wang H, et al. Inflammation, Epigenetics, and Metabolism Converge to Cell Senescence and Ageing: The Regulation and Intervention. *Signal Transduction Targeting Ther* (2021) 6:245. doi: 10.1038/s41392-021-00646-9
149. Aiello A, Farzaneh F, Candore G, Caruso C, Davinelli S, Gambino CM, et al. Immunosenescence and Its Hallmarks: How to Oppose Aging Strategically? A Review of Potential Options for Therapeutic Intervention. *Front Immunol* (2019) 10:2019.02247. doi: 10.3389/fimmu.2019.02247
150. Weyand CM, Goronzy JJ. Aging of the Immune System. Mechanisms and Therapeutic Targets. *Ann Am Thorac Soc* (2016) 13 Suppl;5:S422–8. doi: 10.1513/AnnalsATS.201602-095AW
151. Marttila S, Nevalainen T, Jylhävä J, Kananen L, Jylhä M, Hervonen A, et al. Human Endogenous Retrovirus HERV-K(HML-2) Env Expression is Not Associated With Markers of Immunosenescence. *Exp Gerontol* (2017) 97:60–3. doi: 10.1016/j.exger.2017.07.019
152. Wang Q, Westra J, van der Geest KSM, Moser J, Bijzet J, Kuiper T, et al. Reduced Levels of Cytosolic DNA Sensor AIM2 Are Associated With Impaired Cytokine Responses in Healthy Elderly. *Exp Gerontol* (2016) 78:39–46. doi: 10.1016/j.exger.2016.02.016
153. Šahmatova L, Sügis E, Šunina M, Hermann H, Prans E, Pihlap M, et al. Signs of Innate Immune Activation and Premature Immunosenescence in Psoriasis Patients. *Sci Rep* (2017) 7:7553. doi: 10.1038/s41598-017-07975-2
154. Pillai PS, Molony RD, Martinod K, Dong H, Pang IK, Tal MC, et al. Mx1 Reveals Innate Pathways to Antiviral Resistance and Lethal Influenza Disease. *Science* (2016) 352:463–6. doi: 10.1126/science.aaf3926
155. Sridharan A, Esposo M, Kaushal K, Tay J, Osann K, Agrawal S, et al. Age-Associated Impaired Plasmacytoid Dendritic Cell Functions Lead to Decreased CD4 and CD8 T Cell Immunity. *Age* (2011) 33:363–76. doi: 10.1007/s11357-010-9191-3
156. Montoya-Ortiz G. Immunosenescence, Aging, and Systemic Lupus Erythematous. *Autoimmune Dis* (2013) 267078:1–15. doi: 10.1155/2013/267078
157. Bray S, Turnbull M, Hebert S, Douville RN. Insight Into the ERVK Integrase – Propensity for DNA Damage. *Front Microbiol* (2016) 7:2016.01941. doi: 10.3389/fmicb.2016.01941
158. Faucard R, Madeira A, Gehin N, Authier F-J, Panaite P-A, Lesage C, et al. Human Endogenous Retrovirus and Neuroinflammation in Chronic Inflammatory Demyelinating Polyradiculoneuropathy. *EBioMedicine* (2016) 6:190–8. doi: 10.1016/j.ebiom.2016.03.001
159. Brägelmann J, Lorenz C, Borchmann S, Nishii K, Wegner J, Meder L, et al. MAPK-Pathway Inhibition Mediates Inflammatory Reprogramming and Sensitizes Tumors to Targeted Activation of Innate Immunity Sensor RIG-I. *Nat Commun* (2021) 12:5505. doi: 10.1038/s41467-021-25728-8

Conflict of Interest: The authors declare that the research was conducted in the absence of any commercial or financial relationships that could be construed as a potential conflict of interest.

Publisher's Note: All claims expressed in this article are solely those of the authors and do not necessarily represent those of their affiliated organizations, or those of the publisher, the editors and the reviewers. Any product that may be evaluated in this article, or claim that may be made by its manufacturer, is not guaranteed or endorsed by the publisher.

Copyright © 2022 Di Giorgio and Xodo. This is an open-access article distributed under the terms of the Creative Commons Attribution License (CC BY). The use, distribution or reproduction in other forums is permitted, provided the original author(s) and the copyright owner(s) are credited and that the original publication in this journal is cited, in accordance with accepted academic practice. No use, distribution or reproduction is permitted which does not comply with these terms.

frontiers | Frontiers in Immunology

ORIGINAL RESEARCH
published: 30 June 2022
doi: 10.3389/fimmu.2022.908449

Senescent Tumor Cells in the Peritoneal Carcinomatosis Drive Immunosenescence in the Tumor Microenvironment

Heidi Braumüller[1], Bernhard Mauerer[1], Christopher Berlin[1,2,3], Dorothea Plundrich[1], Patrick Marbach[1], Pierre Cauchy[1,2,3], Claudia Laessle[1], Esther Biesel[1], Philipp Anton Holzner[1] and Rebecca Kesselring[1,2,3]*

[1] Department of General and Visceral Surgery, Medical Center – University of Freiburg, Faculty of Medicine, University of Freiburg, Freiburg, Germany, [2] German Cancer Consortium (DKTK) Partner Site Freiburg, Heidelberg, Germany, [3] German Cancer Research Center (DKFZ), Heidelberg, Germany

More than half of all patients with colorectal cancer (CRC) develop distant metastasis and, depending on the local stage of the primary tumor, up to 48% of patients present peritoneal carcinomatosis (PC). PC is often considered as a widespread metastatic disease, which is almost resistant to current systemic therapies like chemotherapeutic and immunotherapeutic regimens. Here we could show that tumor cells of PC besides being senescent also exhibit stem cell features. To investigate these surprising findings in more detail, we established a murine model based on tumor organoids that resembles the clinical setting. In this murine orthotopic transplantation model for peritoneal carcinomatosis, we could show that the metastatic site in the peritoneum is responsible for senescence and stemness induction in tumor cells and that induction of senescence is not due to oncogene activation or therapy. In both mouse and human PC, senescence is associated with a senescence-associated secretory phenotype (SASP) influencing the tumor microenvironment (TME) of PC. SASP factors are able to induce a senescence phenotype in neighbouring cells. Here we could show that SASP leads to enhanced immunosenescence in the TME of PC. Our results provide a new immunoescape mechanism in PC explaining the resistance of PC to known chemo- and immunotherapeutic approaches. Therefore, senolytic approaches may represent a novel roadmap to target this terminal stage of CRC.

Keywords: Colorectal cancer, peritoneal carcinomatosis, tumor cell senescence, T cell senescence, stem cell phenotype

OPEN ACCESS

Edited by:
Elena Ciaglia, University of Salerno, Italy

Reviewed by:
Valentina Lopardo, University of Salerno, Italy
Sven E. Niklander, Universidad Andres Bello, Chile

****Correspondence:***
Heidi Braumüller
Heidi.Braumueller@uniklinik-freiburg.de

Specialty section:
This article was submitted to Cancer Immunity and Immunotherapy, a section of the journal Frontiers in Immunology

Received: *30 March 2022*
Accepted: *03 June 2022*
Published: *30 June 2022*

Citation:
Braumüller H, Mauerer B, Berlin C, Plundrich D, Marbach P, Cauchy P, Laessle C, Biesel E, Holzner PA and Kesselring R (2022) Senescent Tumor Cells in the Peritoneal Carcinomatosis Drive Immunosenescence in the Tumor Microenvironment. Front. Immunol. 13:908449. doi: 10.3389/fimmu.2022.908449

INTRODUCTION

Colorectal cancer (CRC) is the second leading cause of cancer-related deaths in the Western world (1). Although there are increasing efforts for better clinical and mechanistic insights, CRC patients displaying metastasis at the time of diagnosis show a poor five-year survival rate of only 14% (1). In this context, patients with PC show worst prognosis (2) and do not benefit from systemic

chemotherapy. The only successful therapy so far is the removal of all visible metastases (3). One possible reason for the resistance of PC patients to chemotherapy is the low penetration of systemically applied chemotherapeutics in the peritoneal cavity (4). To overcome this resistance, Sugarbaker introduced a heated intraperitoneal chemotherapy (HIPEC) nearly 30 years ago (5). However, the advantage of HIPEC together with cytoreductive surgery is not clear as a (clinical) phase III trial showed no superior overall survival in the cytoreductive surgery (CRS) plus HIPEC group as compared with cytoreductive surgery alone (6). Senescence, a permanent cell cycle arrest, has long been viewed as a mechanism against malignant transformation (7). In a mouse model recapitulating pancreatic cancer development, the prevention of senescence leads to excessive tumor growth, highlighting the need for senescence induction in cancer containment (8, 9). In general, stressed cells halt their cell cycle machinery and become either apoptotic or become senescent. We previously showed that PC is characterized by tumor cells showing features of senescence (10). These results argue against the long held view that senescence amounts to permanent cell-cycle arrest that prevents cancer formation and progression in mammals. In line with human PC samples, several studies could show that senescent cells can escape from senescence and give rise to aggressive tumors in human cell lines and in murine cancer models (11–13).

Although senescent cells are arrested in the G1 or G2/M phase of the cell cycle (14, 15), they heavily upregulate proinflammatory molecules encompassed by SASP *via* active metabolic reprogramming (16). Secretion of proinflammatory molecules mediate many of the physiopathological effects of senescent cells.Although senescent PC cancer cells should attract immune cells and get eliminated through the immune surveillance (17, 18), most PC cancer cells upregulate senescence markers and accumulate within the tumor. Senescent cancer cells that escape from growth arrest and resume proliferation appear to express stem cell markers, linking senescence-associated stemness with treatment failure and subsequent relapse (19). Senescent cells are able to induce a senescent phenotype in adjacent cells, including immune cells (20). Yet, to date, the role of senescence in the tumor microenvironment (TME) remains poorly characterized.

In vivo mouse models of CRC develop a tumor burden that causes death of the animals before solid tumors can even progress to a metastatic stage (21–23). Fumagalli et al. developed an orthotopic transplantation model of 3D epithelial organoid cultures, which not only progress to a primary solid tumor but also form distant metastases in the liver and the lung (24, 25). These organoids thus mimic primary tumors and are therefore suitable to recapitulate the clinical situation precisely (26). Therefore, we adapted this model for PC to analyze the cancer cells and the TME in (more) detail, and to compare PC with both primary tumor and liver metastasis samples.

We previously described a senescence phenotype within tumor cells of peritoneal carcinomatosis using human patient data. In the present study, we show, in patient specimens and in a mouse model, that senescent tumor cells are associated with increased stemness as seen by the upregulation of stem cell markers. Using our murine transplantation model, we demonstrate that PC samples similarly upregulate senescence and stem cell markers as found in human PC. In comparison to primary tumors, murine liver metastases showed no upregulation of these markers, indicating that the site of metastasis by itself, rather than oncogene expression or therapy, is critical for senescence. Both human and murine senescent PC cells showed unique SASP features, with factors that are known to induce senescence in neighboring cells. Our results show that tumor-infiltrating lymphocytes (TILs), derived from human and murine PC, carry features of dysfunctionality such as PD-1 and senescence such as IFN-γ or Tim-3 and conversely downregulate co-stimulatory molecules such as CD27 or CD28. Induction of immunosenescence by senescent tumor cells is not limited to PC but could be a broader escape mechanism of aggressive tumors that are resistant to checkpoint inhibitor blockade. within the most aggressive malignant primary brain tumor, the Glioblastoma multiforme (GBM), several studies could show that patients with GBM have significantly more senescent cancer cells and more senescent T cells not only in the TME but also systemically in the peripheral blood compared with healthy age matched controls (27–29). Our results provide insights into a unique metastatic tumor site and shed new light on the mechanistics of senescence and immunosenescence within PC. Senescent PC cells harboring stem cell characteristics and senescent TILs could thus account for resistance to chemotherapy and immunotherapy, repectively.

MATERIAL AND METHODS

Human Samples

Patients suffering from PC or liver metastasis caused by cancer of the appendix, colon, rectosigmoid or rectum as primary tumor sites were included. For immunohistochemistry, FFPE samples of patients (n = 50) who had tumor surgery on PC of colorectal origin between 2004 and 2019 were analyzed. The mean peritoneal cancer index (PCI), measuring PC extent (total score 1–39) of all patients was 16. The clinicopathological characteristics are summarized in the **Supplementary Table 2**. The extraction of samples was conducted by experienced surgeons. Tumor tissue for FACS analysis was excised during routine pathological examination. FACS analysis was performed with samples of patients (primary colorectal cancer CRC n=5, liver metastases n=5, PC n=5) treated with tumor surgery in 2021. PC patients' records in the computer database were analyzed with regard to pathological diagnosis, TNM staging and to obtain patient survival. All patients gave written consent. This study was conducted according to the Declaration of Helsinki and was approved by the ethics committee of the University of Regensburg and University of Freiburg.

Mice

C57BL/6J mice were provided by Charles River (Sulzfeld, Germany). Animal experiments were in accordance with

animal welfare regulations and had been approved by the local authorities (Regierungspräsidium Freiburg).

Organoids and Organoid Culture

APTAK organoids are tumor organoids that are devoid of Apc, Tp53, Tgfbr2 and express constitutively active Kras ($Kras^{G12D}$) and an activated/myristoilated isoform of Akt1. The organoids are a gift from F. Greten, (Georg-Speyer-Haus, Frankfurt).

The APTAK organoids were isolated from a colon of a $p53^{flox/flox}$::$Tgfbr2^{flox/flox}$ mouse. The established organoids harbor loxP sites flanking exon4 of the TGFBR2 gene and Intron 1 and 10 of the TP53 gene. The APC knock out was introduced using CRISPR/Cas9 transgenesis and confirmed by Western Blotting. The organoids were transfected with Cre-IRES-puroR plasmid (Addgene #30205) that encode Cre recombinase to ablate Tgfbr2 and p53. Kras gain of function was obtained by overexpressing the constitutive active version of the murine KRAS gene $KRAS^{G12D}$ (cloned in Addgene plasmid #111164) by retroviral transduction. Myristoilated Akt1 was obtained by overexpression the active form of Akt1 (cloned in Addgene plasmid #) by retroviral transduction. APTAK organoids were cultured in basal medium (Advanced DMEM-F12 supplemented with penicillin/streptomycin, HEPES (10mmol/L, Invitrogen), Glutamax 1x (Invitrogen), N2 1x (Gibco), B27 1x (Gibco), and N-Acetylcysteine (1mmol/L, Sigma-Aldrich). Hygromycin (200 µg/mL) and puromycin (2 µg/mL) was added to maintain that the genes are mutated. The organoids were subcultured in Cultrex Reduced Growth Factor Basement Membrane Extract, Type 2 (R&D Systems, Bio-Techne, USA) and passaged every 5-7 days.

Surgical Transplantation of Organoids Under the Subserosa of the Cecum

In Cultrex Reduced Growth Factor Basement Membrane Extract grown APTAK organoids were dissociated into a single-cell suspension by mechanical disruption followed by enzymatic digestion for 20 minutes at 37°C using TrypLE (Gibco) and were washed once in ice-cold PBS. Single cells were then resuspended in an ice-cold Type I collagen/5x Collagen neutralization Buffer (4:1 v/v) ratio) with a concentration of 125.000 cells/10 µL. The 5x collagen neutralization buffer is composed of 2.5 g alpha MEM powder (5x) and 2% (w/v) NAHCO3 in 45 mL Aqua dest. and 5 mL of 1M HEPES and set to pH 7.5. 10 µL domes of collagen were plated in 6-well multiwell plates. The domes polymerized for 45 minutes at 37°C. Afterwards basal medium was added. The collagen domes were cultured overnight until transplantation. For orthotopic transplantation, the mice were shaved and anesthetized with 2.5% (v/v) isoflurane. Analgesia was guaranteed by intraperitoneal injection with buprenorphine. The mouse was placed on its back on a heating pad and legs were fixed with leukoplast. Isoflurane was lowered to 1.8% (v/v). A 10 – 15 mm incision was made along the linea alba to open the abdomen. The cecum was placed on a wet sterile gauze. A 3 – 4 mm incision through the cecal serosa was made at the end of the cecum in an area without vessels. The serosa was separated from the submucosal layer and a deep pocket was formed. The pocket was enlarged to the size that the collagen dome could be deeply embedded in it. The collagen dome was placed under the serosa in the pocket and the serosa was tightly closed above the collagen dome securing the collagen dome to be tightly embedded in its pocket. The incision was covered with Seprafilm (Baxter, USA). The cecum was carefully placed back in the abdomen. The peritoneum and abdominal wall were separately closed by a continuous suture. The mice were placed on drinking water supplemented with metamizole (5 mg/mL) for 3 days.

RT-PCR

RNA was extracted by RNeasy Mini Kit (Qiagen) and was reverse-transcribed to cDNA with oligo(dT)16 primer (Qiagen, QuantiTect Reverse Transcription Kit) according to the manufacturer´s protocol. The cDNA served as template for amplification of target genes, as well as the housekeeping genes by real-time PCR. Intron-spanning primer sets were used throughout all experiments and were designed with Primer 3 Input (https://primer3.ut.ee/). Quantitative RT-PCR was performed with the primer described in the **Supplementary Table 1** using the Qiagen SybrGreen RT PCR Kit (Qiagen) and the LightCycler480 (Roche, Switzerland) according to the manufacturer´s protocol. The LightCycler480 software was used to obtain second derivative crossing point values and relative expression of target genes was calculated by comparative method after normalization to housekeeping gene expression.

RNAseq

Mouse APTAK tumor tissue (primary tumors n=3, PC n=3) was minced with a rotor-stator-homogenizer (IKA, fisher scientific, USA). RNA was extracted with RNeasy Mini kit (Qiagen). RNAseq was performed by Genewiz, Leipzig, Germany. Hereby cDNA sequencing libraries were prepared using poly (A) mRNA. The libraries were sequenced as 2x150 bp paired end using the Illumina NovaSeq instrument (Illumina, USA).

For bioinformatics analysis of RNAseq data, reads were aligned to the mm39 genome with STAR v2.7.3a (30) using -outSAMtype BAM SortedByCoordinate –outSAMunmapped Within –outSAMattributes Standard –readFilesCommand gunzip as parameters. Counts were obtained using featureCounts v2.0.0 (31) using -p -B -C -Q 10 –primary -T 8 -s 0 as parameters. Differential expression analysis was performed using DESeq2 v1.32.0 (32) using variance stabilization transform normalization.

Gene Set Ontology Analysis

Gene Set Ontology Analysis (GSEA) was carried out using GSEA v 3.0 (33), using weighted statistic, difference of classes (from pseudo-$\log_2$+1 tranformed data), gene set permutation and median-division normalization.

Data Availability

All RNA-Seq data used in this study were deposited at the Gene Expression Omnibus (34) under accession GSE202454.

Isolation of Tumor Cells and Leucocytes From Mouse and Human Tissue

Mice were killed and primary tumors (n=27), liver metastases (n=15) and PC (n=16) were retrieved in ice-cold PBS. Tumors were minced with scissors and dissociated enzymatically with the tumour dissociation kit mouse, (Miltenyi) and mechanically with the gentleMACS tissue dissociator (Miltenyi, Germany) according to the manufacturer's instructions. The resulting single cell suspension was filtered through a 100 µm cell strainer (Greiner Bio-One) and erythrocytes were lysed with ACK lysis buffer (Gibco). Cells were counted and either used for organoid culture or FACS staining.

Human samples for FACS analysis were excised during routine pathological examination from patients with tumor surgery in 2021. Primary CRC samples (n=5), liver metastases (n=5) and PC (n=5) were cut in small pieces and enzymatically and mechanically dissociated with the tumor dissociation kit human (Miltenyi) and the gentleMACS tissue dissociator (Miltenyi) according to the manufacturer´s protocol. After dissociation, the resulting single cell suspension was filtered through a 70 µm cell strainer and erythrocytes were lysed with ACK lysis buffer (Gibco).

Flow Cytometry

Isolated human and mouse single cell suspension were either stimulated for cytokine analysis or directly proceeded with antibody staining. For stimulation, cells were stimulated with Cell Activation cocktail (Biolegend) for 3 hours and Brefeldin A was added for another 2 hours. Cells were first stained with live/dead staining with Zombie NIR Fixable Viability kit (Biolegend) and Fc receptors were blocked with Fc block TruStain FcX™ (anti-mouse CD16/32) antibody (Biolegend). Cells were then incubated with fluorescence-labelled antibodies (**Supplementary Table 1**) for surface staining in FACS buffer (PBS, 2% BSA) for 20 minutes at 4°C. For intracellular staining, cells were fixed in fixation buffer (Foxp3 staining buffer, Invitrogen) for 1 hour and washed two times in permeabilization buffer. Cells were stained with intracellular antibodies (**Supplementary Table 1**) for 20 minutes at 4°C in permeabilization buffer, washed once in permeabilization buffer, and analyzed on a BD LSRFortessa™ flow cytometer (BD Biosciences, USA).

Immunohistochemistry

Human primary tumour tissue (n=5) and PC tissue (n=50) and mouse tissue from the orthotopic organoid mouse CRC model (primary tumor n=4, liver metastases n=4 and PC n=4) were harvested, fixed in 4% paraformaldehyde for 24 hours and embedded into paraffin.

Briefly, slides were deparaffinized with Rotihistol (Carl Roth), rehydrated in a descending alcohol series, and finally washed with PBS and water. Antigen retrieval was performed by cooking the slides in 20mM Citrate Buffer (pH 6.0) or Tris-EDTA (pH 9.0). To reduce endogenous peroxidase activity the slides were incubated with 3% H_2O_2 for 30 minutes. Background staining was reduced by incubating the slides in goat serum (Sigma-Aldrich) followed by incubation with the primary anti-mouse or anti-human antibody at 4°C overnight (**Supplementary Table 1**). Next day slides were washed and primary antibodies were detected using goat anti-rabbit or goat-anti-mouse biotinylated secondary antibody (abcam) according to the manufacturer's instructions. Streptavidin hrp (abcam) and DAB plus (Zytomed Systems) was added, the slides were washed with H_2O, counterstained with haematoxylin and mounted with Rotihistokit (Carl Roth). Tumor slides were visualized by Axio Scan.Z1 (Carl Zeiss, Germany) with 20x magnification scan. Positive-stained cells were quantified based on five high-power fields each representing characteristics of the whole tumor slide. Cells were counted by two independent examiners with ImageJ (Wayne Rasband, National Institutes of Health, USA = Rasband, W.S., ImageJ, U. S. National Institutes of Health, Bethesda, Maryland, USA, https://imagej.nih.gov/ij/, 1997-2018.).

Immunofluorescence

Organoids were stained as previously described (35). APTAK organoids were seeded in 40 µL Cultrex Reduced Growth Factor Basement Membrane Extract, Type 2 (R&D Systems, Bio-Techne) in 8-well Millicell® EZ SLIDES (Merck) and incubated for at least two days in organoid culture medium. Proliferation was analyzed by EdU incorporation (Invitrogen) 6 h prior to fixation. Organoids were fixed in 4% Paraformaldehyde in PBS at room temperature for 20 minutes. Fixative was removed and organoids were washed once in IF buffer (PBS, 0.2% Triton X-100, 0.05% Tween). Then 300 µL of permeabilization solution (PBS, 0.5% Triton X-100) was added for 30 minutes at room temperature. After permebilization, the organoids were blocked in blocking solution (IF buffer, 1% BSA) for 30 minutes at room temperature. EdU visualization *via* Click-iT cocktail was performed prior to primary antibody staining following the Invitro click-iT staining protocol (Invitrogen). Primary antibodies (**Supplementary Table 1**) were incubated overnight in a humidified chamber at 4°C. After overnight incubation, chamberslides were washed three times with IF buffer and the appropriate secondary antibody was added for 1 hour at room temperature. After incubation, secondary antibody solution was removed and organoids were stained for DNA with DAPI (1 µg/mL) in IF buffer for 5 minutes. Chambers were then washed three times with IF buffer, chambers were detached and slides were covered in fluorescence mounting medium (DAKO) and analyzed with a Zeiss LSM880 microscope (Carl Zeiss, Germany).

RNA *In-Situ* Hybridization

In-situ Hybridization (ISH) was conducted using RNAscope® (Advanced Cell Diagnostics by Bio-Techne) for Lgr5. Staining was performed using RNAscope® 2.5 HD Detection Reagent BROWN and RNAscope® FastBrown (DAB) Kit. Supplied Hs-UBC and dapB served as negative and positive control respectively. Experiments were performed according to the supplied manual. Epitope recovery was performed as described above. Nuclear staining was performed with Mayer's hematoxylin (Sigma-Aldrich) diluted 1:5 in Aqua dest.

instead of haemalum according to Gill I. Tumor slides were visualized by Axio Scan.Z1 (Carl Zeiss, Germany) with 20x magnification scan. Positive-stained cells were quantified based on five HPF with Zen Blue (Carl Zeiss, Germany). Cells were counted by two independent examiners with ImageJ (Wayne Rasband, National Institutes of Health, USA = Rasband, W.S., ImageJ, U. S. National Institutes of Health, Bethesda, Maryland, USA, https://imagej.nih.gov/ij/, 1997-2018.).

SA-β-Gal Activity Assay in Cryosections

SA-β-gal activity was measured with the senescence β-galactosidase staining kit (Cell Signaling Technology) as recommended by the manufacturer. Briefly, 20 µm serial cryosections from human liver metastases (n=3), human PC (n=3), mouse primary APTAK tumors (n=5), APTAK liver metastases (n=5) and APTAK PC (n=5) were washed with PBS and fixed in fixation solution for 10-15 minutes at room temperature. Then the slides were washed twice in PBS and β-galactosidase staining solution was added. The pH of the β-galactosidase staining solution was adjusted to pH 4.0 (positive control), pH 5.5 (SA-β-gal activity) and pH 7.0 (negative control). Slides were incubated overnight at 37°C in a dry incubator. The stained slides were rinsed in PBS and analyzed using a Zeiss Axio Scan.Z1 (Carl Zeiss, Germany) All images were analyzed using Zen Blue software (Carl Zeiss, Germany).

FACS-Based SA-β-Gal Measurement

Measurement of SA-β-gal activity by FACS analysis was done as described elsewhere (36). In brief, $1x10^6$ single cells isolated from primary tumors, liver metastases and PC were seeded into one well of a 24-well-plate and incubated with 100 nM bafilomycin A1 (Sigma-Aldrich) in serum-free medium at 37°C. Bafilomycin increases the pH in lysosomes to nearly neutral pH. After 1 hour the substrate 5-dodecanoylaminofluorescein-di-b-galactopyranoside (C_{12}-FDG, Fisher Scientific) was added at a final concentration of 50 µM. After 2 hours incubation at 37°C senescent cells have converted the non-fluorescent C_{12}-FDG to a fluorescent substrate. Finally, cells were washed in PBS and stained for viability with Zombie NIR (Bioloegend) and T cell markers as described in flow cytometry.

Statistical Analysis

Normal distributed data were evaluated by standard two-tailed Student's t-tests. Kruskal-Wallis tests or one-way ANOVA were used for data not showing a normal distribution. Statistics were evaluated with GraphPad Prism 9.2.0. GraphPad Prism was used to calculate mean and standard deviation (SD).

RESULTS

Human PC Cancer Cells Show Characteristics of Senescence, SASP and Stemness

Senescence is a highly heterogeneous state that lacks specific markers (37). We thus first analyzed proliferation and senescence-associated markers in FFPE sections from 50 patients with PC by immunohistochemistry. Senescence is characterized by stable cell-cycle arrest, regulated by the cyclin-dependent kinase (CDK) inhibitors $p16^{INK4a}$ (CDKN2A) and $p21^{CIP1}$ (CDKN1A). High $p16^{INK4a}$ and/or $p21^{CIP1}$ levels, together with a low proliferation index, constitute indicators of senescence. Human PC patient specimens showed a low rate of proliferation marker Ki67 (20% ± 16%, **Figure 1A** and **Supplementary Figure 1A**). Senescence is maintained by epigenetic alterations, notably by trimethylation of histone 3 lysine 9 (H3K9me3). The transcriptionally repressive senescence-associated mark H3K9me3 was detectable in 52% (± 29%) of the tumor cells in PC sections. 63% (± 21%) of cancer cells expressed the CDK2/4 inhibitor $p16^{INK4a}$. 26% (± 16%) of all tumor cells in PC samples expressed the cell cycle regulator $p21^{CIP1}$ (**Figure 1A** and **Supplementary Figure 1A**). These results indicate that PC is characterized by tumor cells that are predominantly senescent, and that senescence is mainly associated with $p16^{INK4a}$.

Senescent cells can acquire stem cell-like features and resume proliferation. These "previously" senescent cells show pronounced tumor-initiating potential (13). As PC is the most lethal form of CRC, we hypothesized that PC displays stem cell-like characteristics. To test this hypothesis, we stained PC tumor specimen against three different stem cell markers. First, performed staining against the stem cell marker CD44,.a transmembrane glycoprotein that is overexpressed in several cancers (38). In PC sections, 46% (± 15%) of cancer cells were CD44-positive (**Figure 1B** and **Supplementary Figure 1B**), indicating that nearly half of all PC tumor cells expressed this stem cell marker. Next, we analyzed CD133, which is also a transmembrane glycoprotein that is overexpressed in several cancers (39). In human PC sections, 5% (± 9%) of tumor cells were CD133-positive (**Figure 1B** and **Supplementary Figure 1B**). As third stem cell marker, we used the leucine-rich repeat-containing G-protein coupled receptor 5 (Lgr5). Lgr5 is a target of Wnt and a well-established marker of stem cells in various tissues (40). We detected Lgr5-positive tumor cells in 9% (± 19%) of all PC cancer cells (**Figure 1B** and **Supplementary Figure 1B**). To analyze the correlation between senescence-associated markers and stem cell markers, we applied Spearman correlation analysis. H3K9me3 showed a strong correlation with Lgr5 ($r = 0.60$, $p = 0.000007$), moderate correlation ($r = 0.39$, $p = 0.007$) with CD133, and poor correlation ($r = 0.29$, $p = 0.046$) with CD44. $P16^{INK4a}$ showed moderate correlation with Lgr5 ($r = 0.38$, $p = 0.009$) and CD44 ($r = 0.3$, $p = 0.037$) and no correlation ($r = -0.15$, $p = 0.311$) with CD133. $p21^{CIP1}$ showed moderate correlation ($r = 0.33$, $p = 0.021$) with CD44 (**Supplementary Figure 2**). From the correlation data, we conclude that senescent cancer cells in the peritoneum show features of stemness. To confirm that PC cancer cells, but not liver metastases are senescent, even though originating from the same primary tumor, we measured the activity of the senescence-associated β-galactosidase (SA-β-gal) at pH 6.5. Liver metastases showed no or only faint SA-β–gal activity compared to PC cancer cells, indicating that upregulated expression of senescence-associated markers e.g., $p16^{INK4a}$ is due

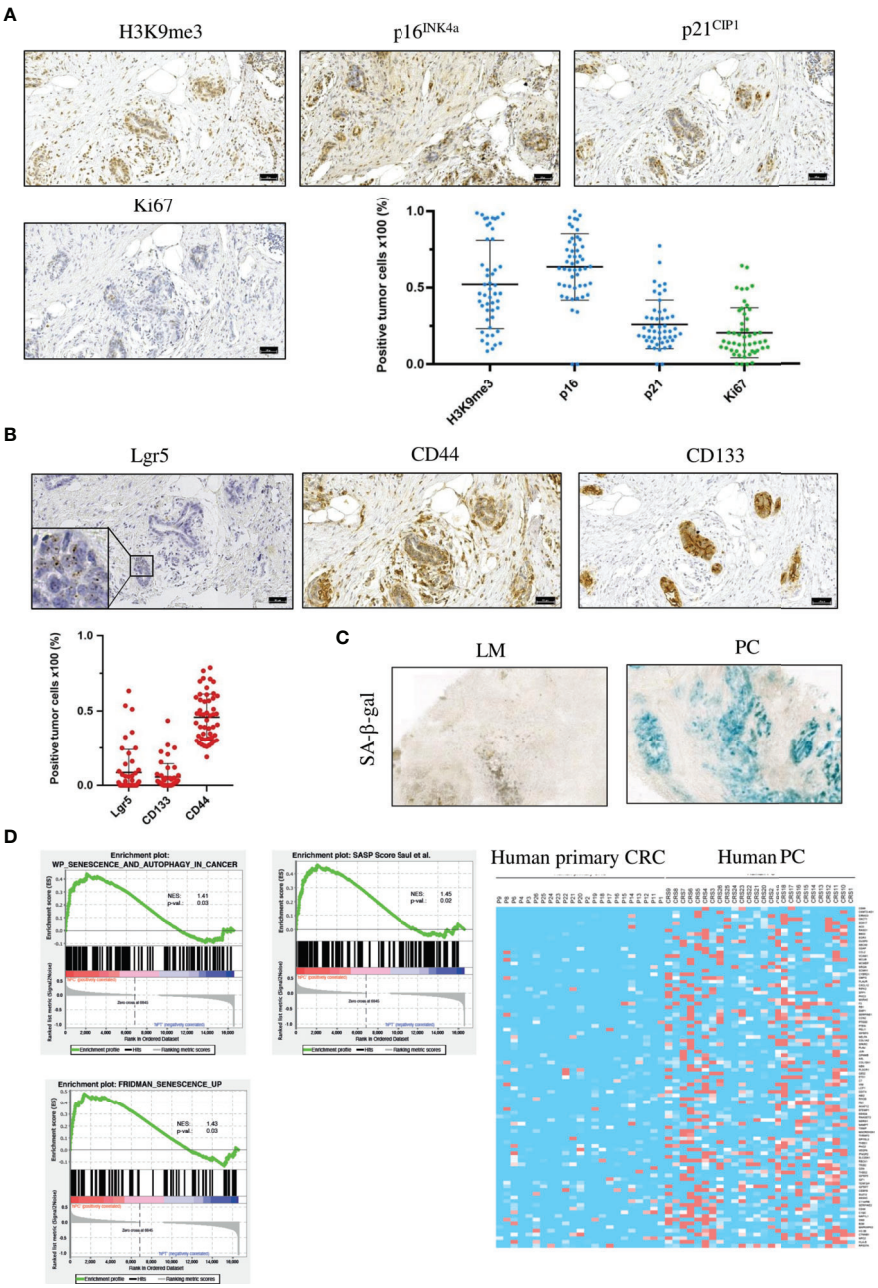


FIGURE 1 | Human PC cancer cells are senescent, have a SASP and show signs of a stem cell-like phenotype. **(A)** Representative images of IHC staining for the senescence-associated markers H3K9me3, p16^{INK4a} and p21^{CIP1} and the proliferation marker Ki67 and quantification of the different markers from one patient. Scale bar: 50 µm, error bars represent the mean ± SD. **(B)** Representative images of IHC staining for the stem cell markers CD44 and CD133 and RNA *in situ* hybridization for Lgr5 from the same patient as in **(A)** Inset represents 125x magnification. Scale bars: 50 µm, error bars represent the mean ± SD. **(C)** Representative images of SA-β-gal in a liver metastasis (left) and PC (right), n = 3 per group. **(D)** Gene set enrichment analysis profiles of senescence and autophagy genes, SASP genes and senescence-associated genes from primary tumors (n = 23) and PC samples (n = 26) from the TCGA PanCancer collection. Heat map of SASP genes from the same patient collective as in the gene set enrichment analysis.

to senescence induction in the peritoneal cavity (**Figure 1C**). The composition of SASP greatly varies dependent on the cell type and on the inducer of the senescence (41, 42). To investigate SASP in PC and to compare the expression of SASP genes with CRC samples, we performed bioinformatic analysis with publicly available RNA-seq data of 23 primary CRC and 26 PC patients using the TCGA PanCancer collection. Gene Set Enrichment Analysis (GSEA) showed that senescence-associated genes and SASP genes are upregulated in PC data sets compared with primary tumor samples, and that PC samples have a distinct

SASP (**Figure 1D**). Several SASP genes were preferentially upregulated only in human PC samples, e.g. VEGF, IFN-γ receptor or CXCL12 compared with primary tumors (**Figure 1D**), showing that senescent PC with stem cell-like features express a unique SASP.

Peritoneal Metastases Show the Same Senescent Phenotype Both for Human und Murine Tumor Tissue

Due to genetic alterations, APTAK organoids are cancer cells with a high metastatic potential To obtain a mouse model of PC, we transplanted APTAK organoids under the serosa of the cecum of C57Bl/6J mice (25) (**Figure 2A**). Transplantation of 125,000 APTAK cells leads to liver and peritoneal metastasis after about 42 days. This long latency *in vivo* gives the opportunity to study metastases of liver and peritoneal cavity in depth. **Figure 2A** shows the protocol of orthotopic transplantation. After about 42 days, we sacrificed the animals and isolated primary tumors, liver metastases and peritoneal metastases. 98% of animals had primary tumors (n=27), 54% liver metastases (n=15) and 57% peritoneal metastases (n=16), or both (**Figure 2B**).

To confirm that the mouse model resembles human peritoneal carcinomatosis, we analyzed the induction of senescence. We first performed immunohistochemistry for the proliferation markers Cyclin D1 and Ki67 in FFPE sections from

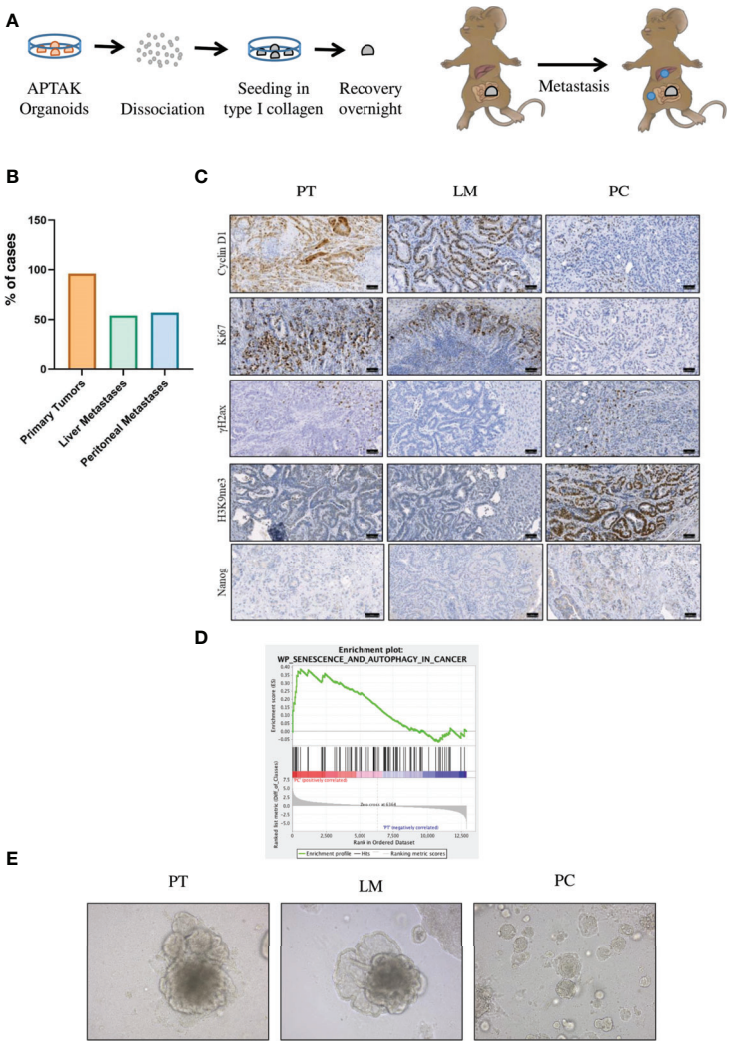


FIGURE 2 | The orthotopic transplantation of APTAK organoids leads to both liver metastases and PC but only cancer cells in the peritoneal cavity show induction of senescence. **(A)** Schematic protocol of the orthotopic transplantation of APTAK organoids under the serosa of the cecum. **(B)** Quantification of primary tumors (98%, n = 27), liver metastases (54%, n = 15) and PC (57%, n = 16) about 42 days after orthotopic transplantation of APTAK organoids. **(C)** Representative images of IHC staining for the proliferation markers Cyclin D1 and Ki67, the DDR marker γ-H2AX, the senescence marker H3K9me3 and the stem cell marker Nanog in primary tumors (PT), liver metastases (LM) and PC. Scale bar: 50 µm **(D)** Gene set enrichment analysis (GSEA) of senescence and autophagy markers in PC versus primary tumor samples (n = 3 per group). **(E)** Representative images of tumor organoids cultured as 3D culture at d5 derived from tumors (primary tumor (PT), liver metastasis (LM) and peritoneal carcinomatosis (PC)) of the same mouse in the orthothopic organoid transplantation model. Magnification 20X.

primary tumors, liver metastases and PC. Cancer cells in primary tumors and liver metastases were highly proliferative as shown by positive staining with Ki67 and Cyclin D1 antibodies in contrast to PC sections (**Figure 2C** and **Supplementary Figures 3A, B**). Senescent cells show nuclear alterations as a result from activation of DNA damage response (DDR) pathways, leading to phosphorylation of histone H2AX. Sections from PC showed γ-H2AX-positive staining, however liver metastases and primary tumor sections were also positive for this marker, although to a lesser extent (**Figure 2C** and **Supplementary Figure 4**). To confirm that the peritoneal cavity is a metastatic niche where senescence is induced, we went on to stain against the senescence-associated marker H3K9me3. This analysis revealed that the repressive epigenetic mark H3K9me3 was exclusively expressed in PC sections, whereas primary tumors and liver metastases showed no staining (**Figure 2C** and **Supplementary Figure 5**). As human PC sections showed marked upregulation of stem cell markers, we analyzed the expression of another stem cell marker Nanog. PC sections showed upregulated Nanog expression, while primary tumors and liver metastases showed no expression (**Figure 2C** and **Supplementary Figure 6**). To confirm the immunochemistry results, we performed GSEA analysis. Consistent with findings in human PC genes, senescence and autophagy genes were markedly upregulated in PC samples from our mouse model (**Figure 2D**). Since we could not exclude that in TME but not cancer cells were senescent in PC, we isolated cancer cells from primary tumors, liver metastases and peritoneal metastases and cultured them as 3D tumor organoids. In culture, organoids derived from PC showed reduced proliferation compared with organoids from liver metastases or primary tumors (**Figure 2E**), indicating that the metastatic niche transforms tumor cells. After one passage, we performed immunofluorescence staining (**Figure 3A**). PC tumor cells showed significantly lower proliferation (as seen by the EdU staining) compared with primary tumors ($p<0.0001$) and liver metastases ($p<0.0001$). We also observed significantly higher expression of the senescence-associated marker H3K9me3 compared with primary tumors ($p = 0.0002$) and liver metastases ($p<0.0001$). $p16^{INK4a}$ (CDKN2a) was significantly more expressed in PC organoids than in primary tumors ($p<0.0001$) and liver metastases ($p<0.0001$). Only the heterochromatin protein 1 gamma (HP1γ) was not significantly upregulated in PC compared with primary tumors ($p = 0.1435$) (**Figure 3B**). In most cases, senescence is induced by $p16^{INK4a}$ or by the transcription factor p53 and its downstream target p21. However, p21 can induce senescence independently of p53, although to a much lesser extent. As APTAK tumor cells harbor a mutation in the p53 protein, we expected very little to no expression of p21 in the nuclei of senescent cells. To avoid having three different stainings (DAPI in blue, EdU in red and p21 in green) in one nucleus, we swapped EdU staining with the cell membrane-bound E-Cadherin. The senescence marker $p21^{CIP1}$ was significantly higher in liver metastases compared with primary tumors ($p = 0.0101$) and PC ($p = 0.0206$) but not significantly upregulated in PC compared with primary tumors ($p = 0.9999$). (**Figures 3A, B**). By evaluating enzyme activity in cryosections of PC tumors, liver metastases and primary tumors, we were able to demonstrate that primary tumors and liver metastases showed only faint X-Gal staining compared with PC (**Figure 3C**). Our results show that in the case of senescence, orthotopic transplantation of APTAK organoids resembles the clinical situation in human PC. In conclusion, the peritoneal cavity represents a metastatic niche that induces senescence, whereas the same tumor cells show no signs of senescence induction within the metastatic environment of the liver.

Peritoneal Metastases After Orthotopic Transplantation Show Stem Cell and SASP-Like Phenotypes

Regarding the analyzed patient samples, more than half of tumor cells acquired stem cell-like features with markers such as CD44, CD133, and Lgr5 (**Figure 1B**). To validate that our CRC metastasis model also resembles the clinical situation in terms of stem cell-like characteristics, we stained primary tumor cells, liver metastases and PC with antibodies against the stem cell markers CD44, CD133, and c-Myc (**Figure 4A**). As expected, PC tumor cells showed enhanced expression of CD44 ($p = 0.0007$) and CD133 ($p = 0.0224$) together with significantly reduced proliferation rate ($p<0.0001$) as compared to primary tumor cells, whereas the upregulation ofc-Myc was not significant ($p = 0.2826$) (**Figure 4B**). Thus, our mouse model truly recapitulates the situation of CRC patients with disseminated disease. SASP varies between cell types and according to the inducer of senescence (42).. To analyze the SASP phenotype in murine PC, we performed qPCRs for several genes that are typically expressed in senescent epithelial cells. Some of these genes such as Vascular Endothelial Growth Factor (VEGF), Vascular Endothelial Growth Factor Receptor 1 (VEGFR1), Spondin 1 (Spon1), Transforming Growth Factor beta (TGFβ) or Metalloproteinase 9 (MMP9) were exclusively upregulated in cancer cells from the peritoneal cavity (**Figure 4C**). These results show that although cancer cells acquire a stem cell-like phenotype in PC, they still express SASP.

Peritoneal Carcinomatosis Harbors a Tumor Microenvironment With Senescence-like T Cells

Previously, we could show that T-cell infiltration of human peritoneal metastases is significantly lower than in corresponding primary colorectal cancer samples (10). To verify whether our PC mouse model clinically mimics tumor-infiltrating lymphocytes (TILs), we analyzed PC-, liver metastasis- and primary tumor-derived TILs by FACS. Primary tumor, liver metastasis and PC samples showed similar infiltration of CD45-positive leukocytes and CD3-positive T-cells. There were minor differences in the amount of CD4-positive T-helper cells, but a significant reduction in the amount of CD8-positive T cells in PC compared with primary tumors ($p = 0.0287$) (**Figure 5A**). In a previous study, immunohistochemistry of surgical PC specimens from patients showed significant upregulation of interferon-gamma (IFN-γ)-

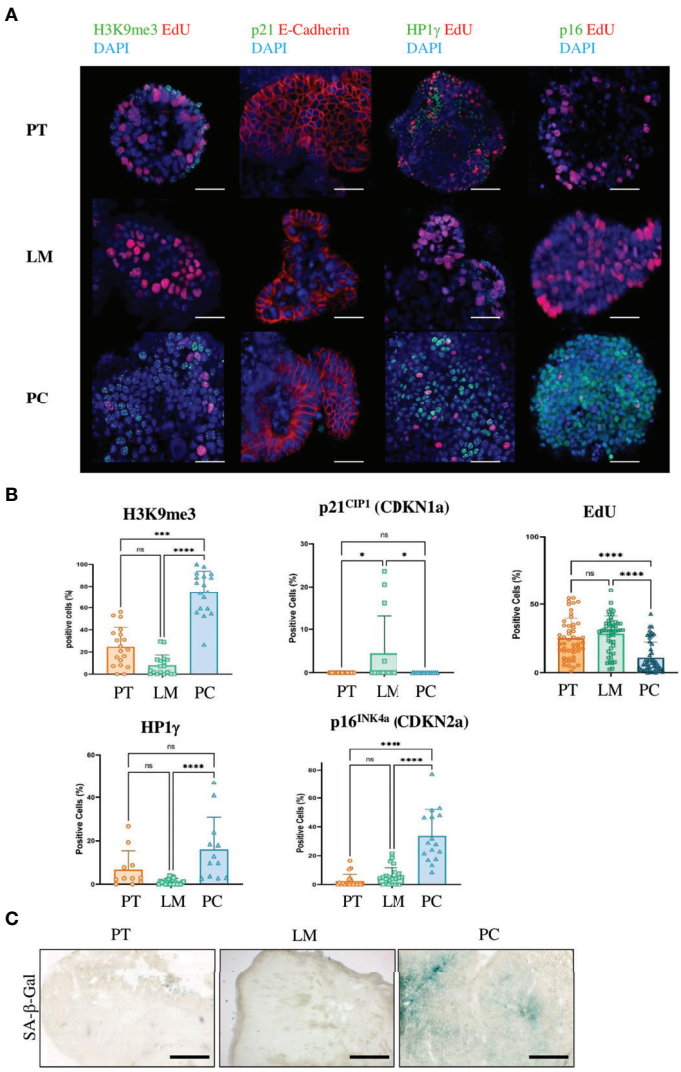


FIGURE 3 | Only cancer cells from metastases in the peritoneal cavity of the APTAK mouse model show a senescent phenotype. **(A)** Representative immunofluorescence (IF) images of the senescence-associated markers H3K9me3, $p21^{CIP1}$, HP1γ and $p16^{INK4a}$ (all green) from organoids derived from primary tumors (PT), liver metastases (LM) and PC from the orthotopic organoid transplantation CRC mouse model. The proliferation marker EdU was stained in red and nuclei were stained in blue. p21 was combined with the cell membrane-bound E-Cadherin (red) and not with EdU. Scale bars represent 50 µm. **(B)** Quantification of IF markers per group derived from primary tumors (n = 5 mice), liver metastases (n = 3 mice) and PC (n = 3 mice) from the orthotopic organoid transplantation CRC mouse model. 3-5 HPF per mouse and marker with at least 1000 APTAK cancer cells were analyzed. Error bars represent the mean ± SD. Kruskal-Wallis test **(B)** ****p < 0.0001, ***p < 0.0002, *p<0.05, n.s. = not significant. **(C)** Representative images of SA-β-gal from primary tumors (PT), liver metastasis (LM) and peritoneal carcinomatosis (PC) from a mouse of the orthotopic organoid mouse CRC model. n = 5 mice per group. Scale bars represent 1000 µm.

positive $CD4^+$ T-helper cells (Th1 cells) compared with primary tumors (10). FACS staining with IFN-γ and CD4 similarly revealed significant upregulation of Th1 TILs in our mouse PC samples compared with primary tumors (p = 0.0007) and liver metastases (p = 0.0003) (**Figure 5B**).

SASP factors can induce senescence in neighboring cells, referred as paracrine senescence. This "bystander" senescence is in part mediated by TGFβ and VEGF (43). Since we obtained marked upregulation of TGFβ and VEGF only in PC cells and not primary tumor or liver metastasis cells (**Figure 4C**), we wondered whether senescent PC cells could induce senescence in TILs. Senescent and exhausted T-cells share several overlapping characteristics. Both express checkpoint inhibitor molecules, including programmed cell death protein 1 (PD-1), cytotoxic T-lymphocyte-associated protein 4 (CTLA-4), T-cell immunoglobulin and mucin-domain containing-3 (Tim3) and V-domain Ig suppressor of T-cell activation (VISTA) (44). In our mouse model, CD4-positive T-cells as well as CD8-positive T-cells expressed high levels of VISTA, Tim3, Lag3 and PD-1, independent of the compartment (**Figures 5C, D**). However, unlike exhausted T-cells that downregulate metabolic function, senescent T-cells still produce high amounts of inflammatory cytokines such as Interleukin 2 (IL-2), Interleukin 6 (IL-6), Tumor Necrosis Factor

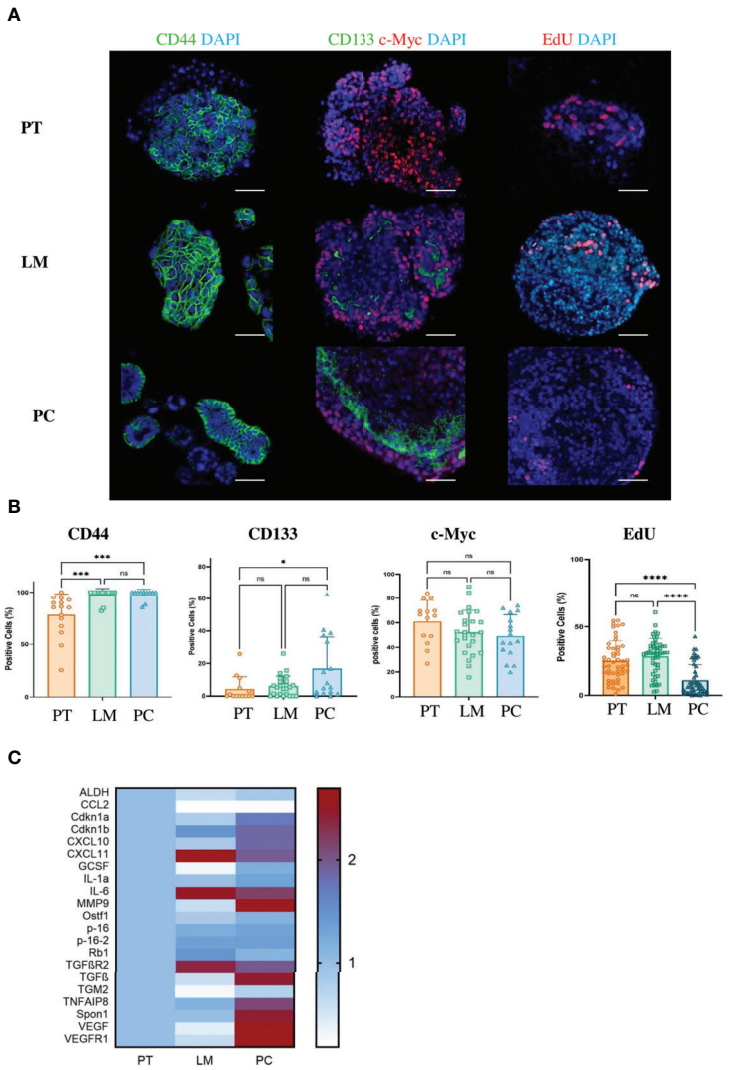


FIGURE 4 | Cancer cells from metastases in the peritoneal cavity of the APTAK mouse model show enhanced stem cell-like phenotype and a SASP. **(A)** Representative immunofluorescence (IF) images of the stem cell markers CD44, CD133 (green) and c-Myc (red) of tumor organoids derived from primary tumors (PT), liver metastases (LM) and PC from the orthotopic organoid transplantation CRC mouse model. The proliferation marker EdU stained in red and nuclei in blue. Scale bars represent 50 µm. **(B)** Quantification of IF markers from **(A)**. 5 HPF with at least 1000 cells from primary tumors (n = 5), liver metastases (n = 3) and PC (n = 3) were counted. Error bars represent the mean ± SD. Kruskal-Wallis test **(B)** ****p < 0.0001, ***p < 0.0002, *p < 0.05, n.s. = not significant. **(C)** Heatmap of characteristic SASP genes from tumor organoids derived from primary tumors (PT), liver metastases (LM) and PC (n = 3 mice per group) from the orthotopic organoid transplantation CRC mouse model. Tumors were isolated, dissociated and cultured for one passage as 3D organoids. Then mRNA was isolated and qPCR was performed.

(TNF) and IFN-γ. $CD4^+$ and $CD8^+$ PC T-cells expressed significantly higher levels of IFN-γ compared with primary tumor T-cells (p = 0.039 and p = 0.0235) (**Figure 5E**). Together with increases in inflammatory cytokines, the upregulation of checkpoint inhibitor molecules indicates that not only tumor cells but also infiltrating T-cells become senescent in PC. We next performed SA-β-gal analysis to verify that T-cells are not merely exhausted but actually senescent. We saw no significant upregulation of SA-β-gal activity in either $CD4^+$ T cells (p = 0.999) or $CD8^+$ T cells (p = 0.0746) (**Figure 5F**). In humans, T-cells downregulate or lose the co-stimulatory molecules CD27 and CD28 independently of the type of senescence (45). In contrast, senescent murine T-cells often maintain expression of CD28 and CD27 (44) and express the tumor necrosis factor ligand superfamily member 8 molecule (CD153). In our CRC metastasis mouse model, significantly increased numbers of tumor-infiltrating CD4-positive T-cells isolated from PC metastasis were CD153-positive as compared to those from originating from liver metastasis (p = 0.031) or primary tumors (p = 0.0454)(**Figure 6A**). In $CD8^+$ T-cells from PC samples, there was also a significant upregulation of $CD153^+$ compared with primary tumors (p = 0.03) and liver metastasis (p = 0.038) (**Figure 6B**). We also found significantly reduced CD28 expression in $CD4^+$ T-cells from PC as

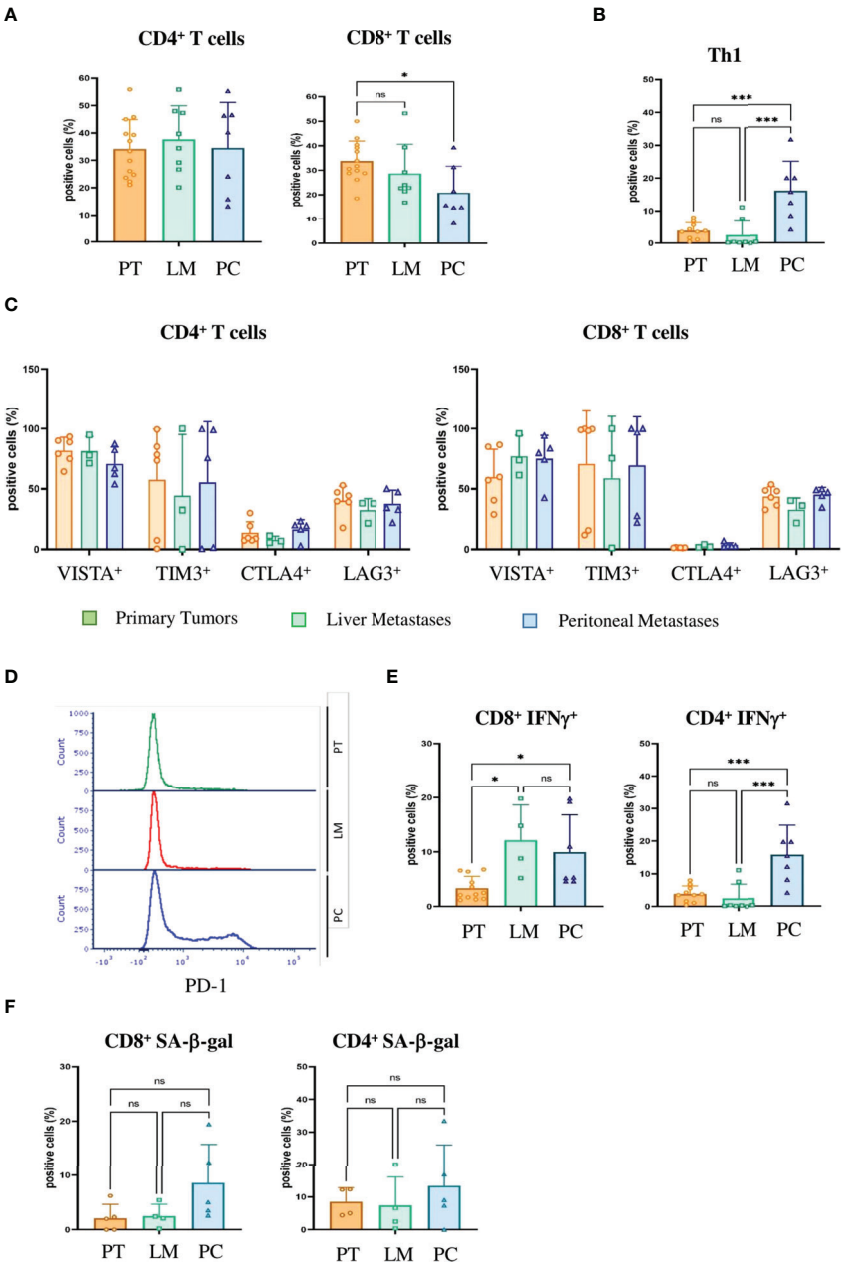


FIGURE 5 | Tumor-infiltrating T cells in PC express checkpoint inhibitor molecules, IFN-γ and markers of senescence and thus are immunosenescent **(A)** Flow cytometric analysis of the tumor infiltrating lymphocytes of primary tumors (PT), liver metastases (LM) and PC of the orthotopic organoid transplantation CRC mouse model for $CD4^+$ and $CD8^+$ T cells. Dotplots show the percentage of $CD4^+$ and $CD8^+$ T cells gated on $CD3^+$ T cells (n = 13 for PT, n = 8 for LM, n = 7 for PC). **(B)** The number of IFN-γ secreting T helper 1 (Th1) cells evaluated by FACS in the tumor microenvironment of primary tumors (PT), liver metastases (LM) and PC of the orthotopic organoid transplantation CRC mouse model. Dotplots show the percentage of IFN-γ secreting $CD4^+$ T cells gated on live $CD45^+$ $CD3^+$ T cells (n = 13 for PT, n = 8 for LM, n = 7 for PC). **(C)** Flow cytometric analysis of $CD4^+$ (left panel) and $CD8^+$ (right panel) T cells for checkpoint molecules VISTA, Tim3, CTLA4 and Lag3 in tumor infiltrating lymphocytes of primary tumors (PT), liver metastases (LM) and PC of the orthotopic organoid transplantation CRC mouse model. Dotplots show the percentage of the $CD4^+$ and $CD8^+$ T cells expressing the respective immune checkpoint molecule (n = 8 for PT, n = 3 for LM, n = 4 for PC). **(D)** Flow cytometric analysis of the expression of PD1 on tumor-infiltrating $CD8^+$ T cells from primary tumors (PT), liver metastases (LM) and PC of the orthotopic organoid transplantation CRC mouse model. **(E)** Flow cytometric analysis from tumor-infiltrating $CD8^+$ and $CD4^+$ T cells for IFN-γ secretion of primary tumors (PT), liver metastases (LM) and PC of the orthotopic organoid transplantation CRC mouse model. Dotplots show the percentage of IFN-γ positive $CD4^+$ and $CD8^+$ T cells (n = 12 for PT, n = 4 for LM, n = 7 for PC). **(F)** Flow cytometric analysis of SA-β-gal positive tumor-infiltrating $CD8^+$ and $CD4^+$ T cells in the tumor microenvironment of primary tumors (PT), liver metastases (LM) and PC of the orthotopic organoid transplantation CRC mouse model. Dotplots show the percentage of SA-β-gal $CD4^+$ and $CD8^+$ T cells (n = 5 for PT, n = 4 for LM, n = 5 for PC). Error bars represent the mean ± SD. One-way ANOVA **(A–C, E, F)** ***$p < 0.0002$, *$p<0.05$, n.s. = not significant. In all analysis Zombie NIR staining was used to discriminate dead from live cells and only live Zombie-negative cells were quantified.

compared with primary tumors (p = 0.0325) and liver metastasis (p = 0.0219). PC-derived CD8$^+$ T-cells showed significant downregulation of CD28 compared with primary tumors (p = 0,0607) and liver metastasis (p = 0.0255) (**Figure 6B**). Finally, we isolated infiltrating leukocytes from human primary CRC (n = 5), liver metastasis (n = 5) and PC (n = 5) samples and measured SA-β-gal activity by FACS analysis. Only PC-derived tumor-infiltrating cells showed features of senescence whereas primary tumor and liver metastasis showed no SA-β-gal activity (**Figure 6C**).

Altogether, these results indicate that senescent PC cells induce senescence in tumor-infiltrating leukocytes in both patients and PC mouse model.

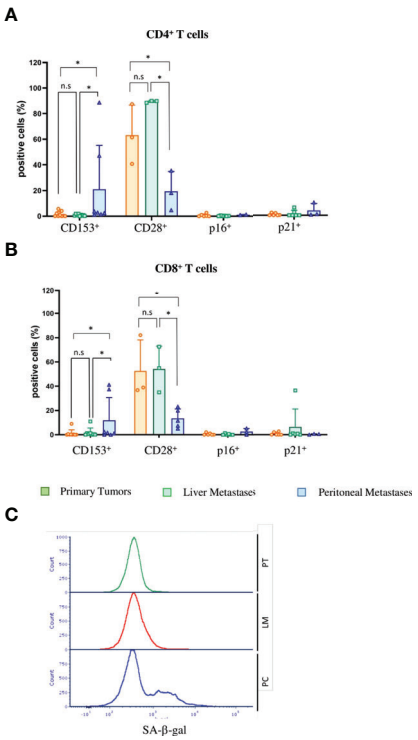


FIGURE 6 | Tumor-infiltrating lymphocytes in PC show signs of immunosenescence in mice and men **(A)** Flow cytometric analysis of immunosenescence associated markers on tumor-infiltrating CD4$^+$ T cells of primary tumors (PT), liver metastases (LM) and PC of the orthotopic organoid transplantation CRC mouse model. Dotplots show the percentage of CD4$^+$ T cells expressing CD153 (n = 10 for PT, n = 7 for LM, n = 8 for PC), CD28 (n = 3 for PT, n = 3 for LM, n = 3 for PC), p16 and p21 (n = 10 for PT, n = 7 for LM, n = 8 for PC). **(B)** Flow cytometric analysis of immunosenescence associated markers on tumor-infiltrating CD8$^+$ T cells of primary tumors (PT), liver metastases (LM) and PC of the orthotopic organoid transplantation CRC mouse model. Dotplots show the percentage of CD8$^+$ T cells expressing CD153 (n = 10 for PT, n = 7 for LM, n = 8 for PC), CD28 (n= 3 for PT, n=3 for LM, n=3 for PC), p16 and p21 (n= 10 for PT, n = 7 for LM, n = 8 for PC). **(C)** Flow cytometric analysis of SA-β-gal in tumor-infiltrating lymphocytes from human patients with primary CRC (PT), liver metastasis and PC. The histogram shows the results of 5 patients each. Error bars represent the mean ± SD. One-way ANOVA **(A, B)** *p < 0.05, n.s. = not significant.

DISCUSSION

Cellular senescence was first described in fibroblasts, where sustained cell duplication shortens telomere length and induces permanent cell cycle arrest, known as replicative senescence. Cells that are no longer able to divide cannot become highly proliferative cancer cells, showing the potential of senescent cells as a barrier against malignant transformation. Therefore senescence, a state of permanent cell cycle arrest, has been considered an intrinsic mechanism of cancer suppression (8, 46–49). Mice that lack the pro-apoptotic protein Bak have no phenotype and do not develop tumors as compared with wildtype animals (50). In contrast, inactivation of the tumor suppressor gene Cdkn2a (encoding p16^{Ink4a}) in mice leads to early formation of tumors that is not observed in wildtype littermates (51), respectively. These studies could show that senescence induction is, at least in these mouse models, a more important form of tumor control than apoptosis. Here, we show that in human patients, the peritoneal niche induces senescence in disseminated CRC cells, which instead of arresting further tumor progression leads to contradictory tumor growth. Irreversible growth arrest was long considered a hallmark of senescence that distinguishes senescence from quiescence, a transient form of growth arrest (52). However, some studies demonstrated that in therapy-induced senescence, senescent cells can escape from cell cycle arrest and give rise to even more aggressive cancer. Achutan et al. showed that treatment of multiple breast cancer cell lines with doxorubicin leads to escape from senescence by a small population of cancer cells. These senescence escapers exhibit stem cell characteristics and express increased levels of the stem cell marker CD133 (53). CD133 upregulates the WNT signaling pathway *via* PI3K/AKT pathway, increasing stem cell properties (39). A recent study by the group of Clemens Schmitt showed that the chemotherapeutic Adriamycin (Doxorubicin) induced senescence in mouse lymphoma cells and that these senescent lymphoma cells expressed stem cell markers such as CD133 or CD44. CD44 binds hyaluronate, the main component of the extracellular matrix, linking CD44 expression to cellular adhesion and communication. Cells that escaped senescence and acquired stem cell phenotypes were more aggressive *in vitro* and after implantation *in vivo* (13). Adriamycin-treated colorectal cancer cell lines become senescent and upregulate expression of CD133 and CD44. We could show that in our patient cohort, a substantial amount (46% ± 15%) of PC cancer cells expressed the stem cell marker CD44 and 5% (± 9%) the stem cell marker CD133. Achutan et al. found a such pronounced stem cell phenotype only after *in vitro* treatment with doxorubicin.

To study PC cancer cells in more detail and to compare PC with liver metastasis and primary tumor samples we aimed to introduce a mouse model that clinically mimics human PC. To date, *in vivo* animal studies of CRC rapidly show high tumor burden and mice have had to be sacrificed before metastasis occurred (21–23). To overcome this problem, we adopted an orthotopic transplantation model (25) and adapted this model with APTAK tumor organoids for metastasis in the peritoneal cavity. APTAK organoids recapitulate the transcriptome-based

consensus molecular subtype (CMS) 4 of the CMS classification of colorectal cancer (54). We found marked upregulation of senescent cancer cells in both mouse and human PC samples. One hallmark of senescence, independent of the inducer of senescence, is that senescent cells secrete multiple factors including pro-inflammatory cytokines, chemokines, growth factors and proteases (55). Some of these factors are known to induce "bystander" senescence in neighboring cells (56). In mouse PC samples, we found the same upregulation of senescence-associated markers accompanied by downregulation of proliferation as in human samples. Furthermore, we detected the same upregulation of senescent cancer cells with a stem cell phenotype in human and in mouse PC samples. Previously, we could show that infiltration of $CD4^+$ T-cells in human PC specimens is significantly reduced compared with primary tumor samples (10). The group Ohira group also showed that infiltration of $CD8^+$ T cells in peritoneal metastasis is also reduced compared with liver and lung metastasis (57). In our mouse model, the degree of $CD8^+$ T-cell infiltration was significantly reduced compared with primary tumor and liver metastasis samples, showing that our new mouse model truly recapitulates the clinical setting of human peritoneal carcinomatosis.

In our study, we observed that although about 25% of PC cancer cells from our PC mouse model had a stem cell phenotype. These cells still uniquely expressed SASP factors. *Via* qPCR we measured the expression of SASP factors that can induce bystander senescence in neighboring cells, e.g. VEGF and TGFβ (20). Induction of paracrine senescence by SASP factors is not limited to cancer cells. Many solid tumors progress rapidly, although large numbers of T-cells can still infiltrate. One reason for this discrepancy is T-cell senescence, and another might be T-cell exhaustion (58). In both states, checkpoint inhibitor molecules such as PD-1 or Tim3 are upregulated but unlike senescent T cells, exhausted T cells do not produce pro-inflammatory cytokines such as TNF or IFN-γ (58). In the mouse model, PC TILs showed expression of checkpoint inhibitor molecules and production of TNF and IFN-γ, indicating that T-cells are dysfunctional and show signs of senescence. A hallmark of senescent T-Cells in human samples is the dramatic reduction of the co-stimulatory molecules CD27 and CD28 (45). However, in mice this reduction is not always observed. Instead, upregulation of CD153 is a marker of T cell senescence in mice (44). Unexpectedly, in the peritoneal metastasis TME, we observed both. I.e, (i) a significant downregulation of CD28 and (ii) upregulation of CD153 compared with liver metastases and primary tumors. As our mouse model indicated that senescent cancer cells in the peritoneal cavity spread senescence not only to other non-senescent cancer cells *via* SASP, but induced a senescence-like phenotype in tumor-infiltrating lymphocytes, we analyzed tumor-infiltrating leukocytes in human samples. Only leukocytes isolated from human PC samples showed upregulation of SA-β-gal activity, indicating that in human PC, senescent cancer cells induce senescence in TILs. Senescent tumor cells that induce senescence in immune TME cells *via* secretion of SASP factors seem represent a more widespread phenomenon in aggressive tumors that are resistant to immune checkpoint blockade. In the most aggressive brain cancer, the Glioblastoma multiforme (GBM), patients displayed not only senescent tumor cells but also senescent immune cells in the tumor microenvironment and systemically in peripheral blood (27–29). In this context, a recent study by Puca et al. could show that treatment of senescent glioblastoma U87-MG cells and senescent T-cells derived from peripheral blood of GBM patients with the senolytic drug longevity-associated variant (LAV) of the bactericidal/permeability-increasing fold-containing family B member 4 (LAV-BPIFB4) reduced the senescent phenotype in both U87-MG cells and patient-derived PBMCs (29). In our PC model, treatment of mice with a senolytic drug may represent a successful approach to reduce senescence in PC cells and in immune TME cells and prevent the development of cancer cells with stem cell characteristics. Depleting senescent cancer stem cells could thus restore the beneficial effects of chemotherapeutics. Reducing senescence in immune cells could at least decrease resistance to immunotherapies with checkpoint inhibitors. One important limitation to successfully translate therapies such immunotherapies or senotherapeutics to the clinic is the lack of animal models that fully recapitulate the human situation. We think that our PC mouse model clinically mimics human PC. This gives us the opportunity to study the effects and results of e.g., the novel one-two punch cancer therapy approach. In this novel cancer therapy, the first punch, e.g. chemotherapy, kills cancer cells. Nevertheless, this treatment induces senescence in cancer cells. The first punch is then followed by the removal of senescent cells by senotherapeutics, the second punch. This new therapeutic approach is still experimental and there are many open questions to be answered (59).

The inducer of cancer cell senescence in the peritoneal cavity is unknown. Given that liver metastasis and PC APTAK organoids express the same oncogene, $Kras^{G12D}$, but that liver cancer cells display no senescence hallmarks, we can probably rule out oncogene-induced senescence (OIS) in the orthotopic mouse model. Unlike in PC patients, in the PC model, animals were not treated with chemotherapeutics, indicating that neither therapy-induced senescence (TIS) nor OIS are the sole inducer. Given that in PC, the level of IFN-γ is upregulated and the peritoneal cavity harbors peritoneal macrophages that secrete high levels of TNF, we suspect cytokine-induced senescence as the inducer (8, 9, 60).

About one third of all CRC patients acquire peritoneal metastasis after the initial diagnosis (61). The prognosis for CRC patients with PC is poor, and most patients do not benefit from systemic chemotherapy (3). To date, the only successful treatment option is cytoreductive surgery, as a clinical phase III study showed that combination with hyperthermic intraperitoneal chemotherapy was not superior to surgery alone (6). Several cytotoxic drugs show increased activity with higher temperature and thus better penetrate in mild

hyperthermia (4). This was the rationale for HIPEC therapy. Most chemotherapeutics rely on proliferating cells, as most chemotherapeutic drugs target cells at different phases of the cell cycle. In our study, we could show that most human PC cancer cells became senescent with strongly reduced proliferation rates. This could account for resistance of PC against chemotherapy. In addition, although senescent cells usually do not divide anymore, they are still viable and resistant to apoptosis. Local treatment of senescent PC cells with HIPEC might force even more cells into a stem cell-like phenotype, rendering PC metastasis even more aggressive and resistant to any other anti-cancer treatment except surgery.

Altogether, in our study, we could show that the peritoneal cavity is a unique metastatic niche that induces senescence in cancer cells in both patients and mice. Up to 40% of these senescent cancer cells acquired a stem cell-like phenotype. This can have serious therapeutic consequences, as cancer stem cells are resistant to most forms of chemotherapy (13). In addition, senescent cells secrete a multitude of SASP factors that can induce senescence in neighboring TME cells. In our mouse model, we could show that infiltrating T-cells upregulate checkpoint inhibitor molecules as well as senescence-associated molecules, indicating that T-cells were not exhausted but senescent. In human PC samples, we could show that tumor-infiltrating immune cells show signs of senescence as measured by upregulated SA-β-gal activity, whereas immune cells isolated from the primary tumors and liver metastases show no senescence induction. This might represent another important therapeutic problem, as senescent immune cells are unaffected by checkpoint inhibitor therapy.

DATA AVAILABILITY STATEMENT

The datasets presented in this study can be found in online repositories. The names of the repository/repositories and accession number(s) can be found below: NCBI GEO, accession no: GSE202454.

ETHICS STATEMENT

The studies involving human participants were reviewed and approved by Ethics committee Regensburg No. 14-101-0014 Ethics committee Freiburg No. 21-1162. The patients/participants provided their written informed consent to participate in this study. The animal study was reviewed and approved by Regierungspräsidium Freiburg G19/041.

AUTHOR CONTRIBUTIONS

HB and RK conceived and conducted the project. HB wrote the manuscript, PC and CB performed bioinformatics, HB and DP performed experiments, CL helped in establishment of the mouse model, CB, EB, and PH helped in clinical evaluation of PC patients. All authors reviewed the manuscript. All authors contributed to the article and approved the submitted version.

FUNDING

Deutsche Forschungsgemeinschaft (FOR2438, KE2164/1-1) for RK supported the work.

ACKNOWLEDGMENTS

We would like to acknowledge the Lighthouse Core Facility, Freiburg for their assistance with confocal microscopy and flow cytometry. We would like to thank Celine Denise Enderle, Julia Riedlinger and Natalie Frank for technical assistance.

SUPPLEMENTARY MATERIAL

The Supplementary Material for this article can be found online at: https://www.frontiersin.org/articles/10.3389/fimmu.2022.908449/full#supplementary-material

Supplementary Figure 1 | (A) Representative images of immunohistochemical (IHC) staining for the senescence-associated markers H3K9me3, $p16^{INK4a}$ and $p21^{CIP}$ and the proliferation marker Ki67 from 5 different PC patients. Scale bar: 50 µm **(B)** Representative images of immunohistochemical (IHC) staining for the stem cell markers CD44, CD133 and Lgr5 from 5 different PC patients. Scale bar: 50 µm, 20 µm (Lgr5).

Supplementary Figure 2 | Pearson coefficients correlation for the senescence-associated markers H3K9me3, $p16^{INK4a}$, $p21^{CIP1}$ and the stem cell marker Lgr5, CD133 and CD44 from 50 different PC patients.

Supplementary Figure 3 | (A) Representative images of immunohistochemical (IHC) staining for the proliferation marker Ki67 from primary tumors (PT), liver metastasis (LM) and peritoneal carcinomatosis (PC) from 4 different mice of the orthotopic organoid mouse CRC model. Scale bar: 50 µm. **(B)** Representative images of immunohistochemical (IHC) staining for the proliferation marker Cyclin D1 from primary tumors (PT), liver metastasis (LM) and peritoneal carcinomatosis (PC) from 4 different mice of the orthotopic organoid mouse CRC model. Scale bar: 50 µm.

Supplementary Figure 4 | Representative images of immunohistochemical (IHC) staining for senescence-associated marker γH2ax from primary tumors (PT), liver metastasis (LM) and peritoneal carcinomatosis (PC) from 4 different mice of the orthotopic organoid mouse CRC model. Scale bar: 50 µm.

Supplementary Figure 5 | Representative images of immunohistochemical (IHC) staining for senescence-associated marker H3K9me3 from primary tumors (PT), liver metastasis (LM) and peritoneal carcinomatosis (PC) from 4 different mice of the orthotopic organoid mouse CRC model. Scale bar: 50 µm.

Supplementary Figure 6 | Representative images of immunohistochemical (IHC) staining for stem cell marker Nanog from primary tumors (PT), liver metastasis (LM) and peritoneal carcinomatosis (PC) from 3 different mice of the orthotopic organoid mouse CRC model. Scale bar: 50 µm.

REFERENCES

1. Siegel RL, Miller KD, Jemal A. Cancer Statistics, 2020. *CA Cancer J Clin* (2020) 70(1):7–30. doi: 10.3322/caac.21590
2. Franko J, Shi Q, Meyers JP, Maughan TS, Adams RA, Seymour MT, et al. Prognosis of Patients With Peritoneal Metastatic Colorectal Cancer Given Systemic Therapy: An Analysis of Individual Patient Data From Prospective Randomised Trials From the Analysis and Research in Cancers of the Digestive System (ARCAD) Database. *Lancet Oncol* (2016) 17(12):1709–19. doi: 10.1016/S1470-2045(16)30500-9
3. Franko J. Therapeutic Efficacy of Systemic Therapy for Colorectal Peritoneal Carcinomatosis: Surgeon's Perspective. *Pleura Peritoneum* (2018) 3 (1):20180102. doi: 10.1515/pp-2018-0102
4. Gonzalez-Moreno S, Gonzalez-Bayon LA, Ortega-Perez G. Hyperthermic Intraperitoneal Chemotherapy: Rationale and Technique. *World J Gastrointest Oncol* (2010) 2(2):68–75. doi: 10.4251/wjgo.v2.i2.68
5. Sugarbaker PH, Zhu BW, Sese GB, Shmookler B. Peritoneal Carcinomatosis From Appendiceal Cancer - Results in 69 Patients Treated by Cytoreductive Surgery and Intraperitoneal Chemotherapy. *Dis Colon Rectum* (1993) 36 (4):323–9. doi: 10.1007/Bf02053933
6. Quenet F, Elias D, Roca L, Goere D, Ghouti L, Pocard M, et al. Cytoreductive Surgery Plus Hyperthermic Intraperitoneal Chemotherapy Versus Cytoreductive Surgery Alone for Colorectal Peritoneal Metastases (PRODIGE 7): A Multicentre, Randomised, Open-Label, Phase 3 Trial. *Lancet Oncol* (2021) 22(2):256–66. doi: 10.1016/S1470-2045(20)30599-4
7. Hanahan D. Hallmarks of Cancer: New Dimensions. *Cancer Discovery* (2022) 12(1):31–46. doi: 10.1158/2159-8290.CD-21-1059
8. Braumuller H, Wieder T, Brenner E, Assmann S, Hahn M, Alkhaled M, et al. T-Helper-1-Cell Cytokines Drive Cancer Into Senescence. *Nature* (2013) 494 (7437):361–5. doi: 10.1038/nature11824
9. Brenner E, Schorg BF, Ahmetlic F, Wieder T, Hilke FJ, Simon N, et al. Cancer Immune Control Needs Senescence Induction by Interferon-Dependent Cell Cycle Regulator Pathways in Tumours. *Nat Commun* (2020) 11(1):1335. doi: 10.1038/s41467-020-14987-6
10. Seebauer CT, Brunner S, Glockzin G, Piso P, Ruemmele P, Schlitt HJ, et al. Peritoneal Carcinomatosis of Colorectal Cancer Is Characterized by Structural and Functional Reorganization of the Tumor Microenvironment Inducing Senescence and Proliferation Arrest in Cancer Cells. *Oncoimmunology* (2016) 5(12):e1242543. doi: 10.1080/2162402X.2016.1242543
11. Beausejour CM, Krtolica A, Galimi F, Narita M, Lowe SW, Yaswen P, et al. Reversal of Human Cellular Senescence: Roles of the P53 and P16 Pathways. *EMBO J* (2003) 22(16):4212–22. doi: 10.1093/emboj/cdg417
12. Sage J, Miller AL, Perez-Mancera PA, Wysocki JM, Jacks T. Acute Mutation of Retinoblastoma Gene Function Is Sufficient for Cell Cycle Re-Entry. *Nature* (2003) 424(6945):223–8. doi: 10.1038/nature01764
13. Milanovic M, Fan DNY, Belenki D, Dabritz JHM, Zhao Z, Yu Y, et al. Senescence-Associated Reprogramming Promotes Cancer Stemness. *Nature* (2018) 553(7686):96–100. doi: 10.1038/nature25167
14. Lossaint G, Horvat A, Gire V, Bacevic K, Mrouj K, Charrier-Savournin F, et al. Reciprocal Regulation of P21 and Chk1 Controls the Cyclin D1-RB Pathway to Mediate Senescence Onset After G2 Arrest. *J Cell Sci* (2022) 135(8):1–15. doi: 10.1242/jcs.259114
15. Wang L, Lankhorst L, Bernards R. Exploiting Senescence for the Treatment of Cancer. *Nat Rev Cancer* (2022) 22(6):340–55. doi: 10.1038/s41568-022-00450-9
16. Wang B, Kohli J, Demaria M. Senescent Cells in Cancer Therapy: Friends or Foes? *Trends Cancer* (2020) 6(10):838–57. doi: 10.1016/j.trecan.2020.05.004
17. Hoenicke L, Zender L. Immune Surveillance of Senescent Cells–Biological Significance in Cancer- and non-Cancer Pathologies. *Carcinogenesis* (2012) 33 (6):1123–6. doi: 10.1093/carcin/bgs124
18. Lujambio A. To Clear, or Not to Clear (Senescent Cells)? That Is the Question. *Bioessays* (2016) 38 Suppl 1:S56–64. doi: 10.1002/bies.201670910
19. Milanovic M, Yu Y, Schmitt CA. The Senescence-Stemness Alliance - A Cancer-Hijacked Regeneration Principle. *Trends Cell Biol* (2018) 28 (12):1049–61. doi: 10.1016/j.tcb.2018.09.001
20. Acosta JC, Banito A, Wuestefeld T, Georgilis A, Janich P, Morton JP, et al. A Complex Secretory Program Orchestrated by the Inflammasome Controls Paracrine Senescence. *Nat Cell Biol* (2013) 15(8):978–90. doi: 10.1038/ncb2784
21. Moser AR, Pitot HC, Dove WF. A Dominant Mutation That Predisposes to Multiple Intestinal Neoplasia in the Mouse. *Science* (1990) 247(4940):322–4. doi: 10.1126/science.2296722
22. Deming DA, Leystra AA, Nettekoven L, Sievers C, Miller D, Middlebrooks M, et al. PIK3CA and APC Mutations Are Synergistic in the Development of Intestinal Cancers. *Oncogene* (2014) 33(17):2245–54. doi: 10.1038/onc.2013.167
23. Hinoi T, Akyol A, Theisen BK, Ferguson DO, Greenson JK, Williams BO, et al. Mouse Model of Colonic Adenoma-Carcinoma Progression Based on Somatic Apc Inactivation. *Cancer Res* (2007) 67(20):9721–30. doi: 10.1158/0008-5472.CAN-07-2735
24. Fumagalli A, Drost J, Suijkerbuijk SJ, van Boxtel R, de Ligt J, Offerhaus GJ, et al. Genetic Dissection of Colorectal Cancer Progression by Orthotopic Transplantation of Engineered Cancer Organoids. *Proc Natl Acad Sci U S A* (2017) 114(12):E2357–64. doi: 10.1073/pnas.1701219114
25. Fumagalli A, Suijkerbuijk SJE, Begthel H, Beerling E, Oost KC, Snippert HJ, et al. A Surgical Orthotopic Organoid Transplantation Approach in Mice to Visualize and Study Colorectal Cancer Progression. *Nat Protoc* (2018) 13 (2):235–47. doi: 10.1038/nprot.2017.137
26. Sato T, Stange DE, Ferrante M, Vries RG, Van Es JH, Van den Brink S, et al. Long-Term Expansion of Epithelial Organoids From Human Colon, Adenoma, Adenocarcinoma, and Barrett's Epithelium. *Gastroenterology* (2011) 141(5):1762–72. doi: 10.1053/j.gastro.2011.07.050
27. Huff WX, Bam M, Shireman JM, Kwon JH, Song L, Newman S, et al. Aging- and Tumor-Mediated Increase in CD8(+)CD28(-) T Cells Might Impose a Strong Barrier to Success of Immunotherapy in Glioblastoma. *Immunohorizons* (2021) 5(6):395–409. doi: 10.4049/immunohorizons.2100008
28. Huff WX, Kwon JH, Henriquez M, Fetcko K, Dey M. The Evolving Role of CD8(+)CD28(-) Immunosenescent T Cells in Cancer Immunology. *Int J Mol Sci* (2019) 20(11):1–22. doi: 10.3390/ijms20112810
29. Puca AA, Lopardo V, Montella F, Di Pietro P, Cesselli D, Rolle IG, et al. The Longevity-Associated Variant of BPIFB4 Reduces Senescence in Glioma Cells and in Patients' Lymphocytes Favoring Chemotherapy Efficacy. *Cells* (2022) 11(2):2–15. doi: 10.3390/cells11020294
30. Dobin A, Davis CA, Schlesinger F, Drenkow J, Zaleski C, Jha S, et al. STAR: Ultrafast Universal RNA-Seq Aligner. *Bioinformatics* (2013) 29(1):15–21. doi: 10.1093/bioinformatics/bts635
31. Liao Y, Smyth GK, Shi W. Featurecounts: An Efficient General Purpose Program for Assigning Sequence Reads to Genomic Features. *Bioinformatics* (2014) 30(7):923–30. doi: 10.1093/bioinformatics/btt656
32. Love MI, Huber W, Anders S. Moderated Estimation of Fold Change and Dispersion for RNA-Seq Data With Deseq2. *Genome Biol* (2014) 15(12):550. doi: 10.1186/s13059-014-0550-8
33. Subramanian A, Tamayo P, Mootha VK, Mukherjee S, Ebert BL, Gillette MA, et al. Gene Set Enrichment Analysis: A Knowledge-Based Approach for Interpreting Genome-Wide Expression Profiles. *Proc Natl Acad Sci USA* (2005) 102(43):15545–50. doi: 10.1073/pnas.0506580102
34. Edgar R, Domrachev M, Lash AE. Gene Expression Omnibus: NCBI Gene Expression and Hybridization Array Data Repository. *Nucleic Acids Res* (2002) 30(1):207–10. doi: 10.1093/nar/30.1.207
35. O'Rourke KP, Dow LE, Lowe SW. Immunofluorescent Staining of Mouse Intestinal Stem Cells. *Bio Protoc* (2016) 6(4):1–9. doi: 10.21769/bioprotoc.1732
36. Debacq-Chainiaux F, Erusalimsky JD, Campisi J, Toussaint O. Protocols to Detect Senescence-Associated Beta-Galactosidase (SA-Betagal) Activity, a Biomarker of Senescent Cells in Culture and *In Vivo*. *Nat Protoc* (2009) 4 (12):1798–806. doi: 10.1038/nprot.2009.191
37. Gorgoulis V, Adams PD, Alimonti A, Bennett DC, Bischof O, Bishop C, et al. Cellular Senescence: Defining a Path Forward. *Cell* (2019) 179(4):813–27. doi: 10.1016/j.cell.2019.10.005
38. Hassn Mesrati M, Syafruddin SE, Mohtar MA, Syahir A. CD44: A Multifunctional Mediator of Cancer Progression. *Biomolecules* (2021) 11 (12):1850–82. doi: 10.3390/biom11121850
39. Mohan A, Raj Rajan R, Mohan G, Kollenchery Puthenveettil P, Maliekal TT. Markers and Reporters to Reveal the Hierarchy in Heterogeneous Cancer

Stem Cells. *Front Cell Dev Biol* (2021) 9:668851. doi: 10.3389/fcell.2021.668851
40. Morgan RG, Mortensson E, Williams AC. Targeting LGR5 in Colorectal Cancer: Therapeutic Gold or Too Plastic? *Br J Cancer* (2018) 118(11):1410–8. doi: 10.1038/s41416-018-0118-6
41. Takasugi M, Yoshida Y, Hara E, Ohtani N. The Role of Cellular Senescence and SASP in Tumour Microenvironment. *FEBS J* (2022). doi: 10.1111/febs.16381
42. Sturmlechner I, Zhang C, Sine CC, van Deursen EJ, Jeganathan KB, Hamada N, et al. P21 Produces a Bioactive Secretome That Places Stressed Cells Under Immunosurveillance. *Science* (2021) 374(6567):577–+. doi: 10.1126/science.abb3420
43. Acosta JC, Snijders AP, Gil J. Unbiased Characterization of the Senescence-Associated Secretome Using SILAC-Based Quantitative Proteomics. *Methods Mol Biol* (2013) 965:175–84. doi: 10.1007/978-1-62703-239-1_11
44. Yi HS, Kim SY, Kim JT, Lee YS, Moon JS, Kim M, et al. T-Cell Senescence Contributes to Abnormal Glucose Homeostasis in Humans and Mice. *Cell Death Dis* (2019) 10(3):249. doi: 10.1038/s41419-019-1494-4
45. Rodriguez IJ, Ruiz NL, Leon ML, Enriquez LM, Velasquez MDM, Aguirre JPO, et al. Immunosenescence Study of T Cells: A Systematic Review. *Front Immunol* (2021) 11:604591. doi: 10.3389/fimmu.2020.604591
46. Childs BG, Durik M, Baker DJ, van Deursen JM. Cellular Senescence in Aging and Age-Related Disease: From Mechanisms to Therapy. *Nat Med* (2015) 21(12):1424–35. doi: 10.1038/nm.4000
47. Munoz-Espin D, Serrano M. Cellular Senescence: From Physiology to Pathology. *Nat Rev Mol Cell Biol* (2014) 15(7):482–96. doi: 10.1038/nrm3823
48. Perez-Mancera PA, Young AR, Narita M. Inside and Out: The Activities of Senescence in Cancer. *Nat Rev Cancer* (2014) 14(8):547–58. doi: 10.1038/nrc3773
49. Sherr CJ. Principles of Tumor Suppression. *Cell* (2004) 116(2):235–46. doi: 10.1016/s0092-8674(03)01075-4
50. Lindsten T, Ross AJ, King A, Zong WX, Rathmell JC, Shiels HA, et al. The Combined Functions of Proapoptotic Bcl-2 Family Members Bak and Bax Are Essential for Normal Development of Multiple Tissues. *Mol Cell* (2000) 6(6):1389–99. doi: 10.1016/s1097-2765(00)00136-2
51. Sharpless NE, Ramsey MR, Balasubramanian P, Castrillon DH, DePinho RA. The Differential Impact of P16(INK4a) or P19(ARF) Deficiency on Cell Growth and Tumorigenesis. *Oncogene* (2004) 23(2):379–85. doi: 10.1038/sj.onc.1207074
52. Saleh T, Bloukh S, Carpenter VJ, Alwohoush E, Bakeer J, Darwish S, et al. Therapy-Induced Senescence: An "Old" Friend Becomes the Enemy. *Cancers (Basel)* (2020) 12(4):2504–19. doi: 10.3390/cancers12040822
53. Achuthan S, Santhoshkumar TR, Prabhakar J, Nair SA, Pillai MR. Drug-Induced Senescence Generates Chemoresistant Stemlike Cells With Low Reactive Oxygen Species. *J Biol Chem* (2011) 286(43):37813–29. doi: 10.1074/jbc.M110.200675
54. Varga J, Nicolas A, Petrocelli V, Pesic M, Mahmoud A, Michels BE, et al. AKT-Dependent NOTCH3 Activation Drives Tumor Progression in a Model of Mesenchymal Colorectal Cancer. *J Exp Med* (2020) 217(10):1–19. doi: 10.1084/jem.20191515
55. Coppé JP, Desprez PY, Krtolica A, Campisi J. The Senescence-Associated Secretory Phenotype: The Dark Side of Tumor Suppression. *Annu Rev Pathol* (2010) 5:99–118. doi: 10.1146/annurev-pathol-121808-102144
56. Sapega O, Mikyskova R, Bieblova J, Mrazkova B, Hodny Z, Reinis M. Distinct Phenotypes and "Bystander" Effects of Senescent Tumour Cells Induced by Docetaxel or Immunomodulatory Cytokines. *Int J Oncol* (2018) 53(5):1997–2009. doi: 10.3892/ijo.2018.4553
57. Wang E, Shibutani M, Nagahara H, Fukuoka T, Iseki Y, Okazaki Y, et al. Abundant Intratumoral Fibrosis Prevents Lymphocyte Infiltration Into Peritoneal Metastases of Colorectal Cancer. *PLos One* (2021) 16(7):e0255049. doi: 10.1371/journal.pone.0255049
58. Zhao Y, Shao Q, Peng G. Exhaustion and Senescence: Two Crucial Dysfunctional States of T Cells in the Tumor Microenvironment. *Cell Mol Immunol* (2020) 17(1):27–35. doi: 10.1038/s41423-019-0344-8
59. Prasanna PG, Citrin DE, Hildesheim J, Ahmed MM, Venkatachalam S, Riscuta G, et al. Therapy-Induced Senescence: Opportunities to Improve Anticancer Therapy. *J Natl Cancer Inst* (2021) 113(10):1285–98. doi: 10.1093/jnci/djab064
60. Rentschler M, Braumüller H, Briquez PS, Wieder T. Cytokine-Induced Senescence in the Tumor Microenvironment and Its Effects on Anti-Tumor Immune Responses. *Cancers* (2022) 14(6):1364. doi: 10.3390/cancers14061364
61. Parikh MS, Johnson P, Romanes JP, Freitag HE, Spring ME, Garcia-Henriquez N, et al. Cytoreductive Surgery and Hyperthermic Intraperitoneal Chemotherapy for Colorectal Peritoneal Metastases: A Systematic Review. *Dis Colon Rectum* (2022) 65(1):16–26. doi: 10.1097/dcr.0000000000002315

Conflict of Interest: The authors declare that the research was conducted in the absence of any commercial or financial relationships that could be construed as a potential conflict of interest.

Publisher's Note: All claims expressed in this article are solely those of the authors and do not necessarily represent those of their affiliated organizations, or those of the publisher, the editors and the reviewers. Any product that may be evaluated in this article, or claim that may be made by its manufacturer, is not guaranteed or endorsed by the publisher.

Copyright © 2022 Braumüller, Mauerer, Berlin, Plundrich, Marbach, Cauchy, Laessle, Biesel, Holzner and Kesselring. This is an open-access article distributed under the terms of the Creative Commons Attribution License (CC BY). The use, distribution or reproduction in other forums is permitted, provided the original author(s) and the copyright owner(s) are credited and that the original publication in this journal is cited, in accordance with accepted academic practice. No use, distribution or reproduction is permitted which does not comply with these terms.

frontiers | Frontiers in Immunology

ORIGINAL RESEARCH
published: 11 July 2022
doi: 10.3389/fimmu.2022.908068

A Four-Cell-Senescence-Regulator-Gene Prognostic Index Verified by Genome-Wide CRISPR Can Depict the Tumor Microenvironment and Guide Clinical Treatment of Bladder Cancer

Jian-Xuan Sun†, Chen-Qian Liu†, Jin-Zhou Xu, Ye An, Meng-Yao Xu, Xing-Yu Zhong, Na Zeng, Si-Yang Ma, Hao-Dong He, Zong-Biao Zhang‡, Shao-Gang Wang*‡ and Qi-Dong Xia*‡*

Department and Institute of Urology, Tongji Hospital, Tongji Medical College, Huazhong University of Science and Technology, Wuhan, China

OPEN ACCESS

Edited by:
Giulia Accardi,
University of Palermo, Italy

Reviewed by:
Xu Chen,
Sun Yat-sen Memorial Hospital, China
Emanuele Giurisato,
University of Siena, Italy
Guangzhen Wu,
Dalian Medical University, China

***Correspondence:**
Zong-Biao Zhang
zzb070@126.com
Shao-Gang Wang
sgwangtjm@163.com
Qi-Dong Xia
qidongxia_md@163.com

†*These authors have contributed equally to this work and share first authorship*

‡*These authors have contributed equally to this work*

Specialty section:
This article was submitted to Cancer Immunity and Immunotherapy, a section of the journal Frontiers in Immunology

Received: *30 March 2022*
Accepted: *08 June 2022*
Published: *11 July 2022*

Citation:
Sun J-X, Liu C-Q, Xu J-Z, An Y, Xu M-Y, Zhong X-Y, Zeng N, Ma S-Y, He H-D, Zhang Z-B, Wang S-G and Xia Q-D (2022) A Four-Cell-Senescence-Regulator-Gene Prognostic Index Verified by Genome-Wide CRISPR Can Depict the Tumor Microenvironment and Guide Clinical Treatment of Bladder Cancer. Front. Immunol. 13:908068. doi: 10.3389/fimmu.2022.908068

Bladder cancer (BCa) is the 10th most commonly diagnosed cancer worldwide, and cellular senescence is defined as a state of permanent cell cycle arrest and considered to play important roles in the development and progression of tumor. However, the comprehensive effect of senescence in BCa has not ever been systematically evaluated. Using the genome-wide CRISPR screening data acquired from DepMap (Cancer Dependency Map), senescence genes from the CellAge database, and gene expression data from The Cancer Genome Atlas (TCGA), we screened out 12 senescence genes which might play critical roles in BCa. A four-cell-senescence-regulator-gene prognostic index was constructed using the least absolute shrinkage and selection operator (LASSO) and multivariate COX regression model. The transcriptomic data and clinical information of BCa patients were downloaded from TCGA and Gene Expression Omnibus (GEO). We randomly divided the patients in TCGA cohort into training and testing cohorts and calculated the risk score according to the expression of the four senescence genes. The validity of this risk score was validated in the testing cohort (TCGA) and validation cohort (GSE13507). The Kaplan–Meier curves revealed a significant difference in the survival outcome between the high- and low-risk score groups. A nomogram including the risk score and other clinical factors (age, gender, stage, and grade) was established with better predictive capacity of OS in 1, 3, and 5 years. Besides, we found that patients in the high-risk group had higher tumor mutation burden (TMB); lower immune, stroma, and ESTIMATE scores; higher tumor purity; aberrant immune functions; and lower expression of immune checkpoints. We also performed gene set variation analysis (GSVA) and gene set enrichment analysis (GSEA) to investigate the interaction between risk score and hallmark pathways and found that a high risk score was connected with activation of senescence-related pathways. Furthermore, we found

that a high risk score was related to better response to immunotherapy and chemotherapy. In conclusion, we identified a four-cell-senescence-regulator-gene prognostic index in BCa and investigated its relationship with TMB, the immune landscape of tumor microenvironment (TME), and response to immunotherapy and chemotherapy, and we also established a nomogram to predict the prognosis of patients with BCa.

Keywords: senescence, tumor microenvironment, tumor mutation burden, bladder cancer, immunotherapy, chemotherapy

INTRODUCTION

Bladder cancer (BCa) is the 7th most commonly diagnosed cancer in men and has the 10th highest incidence in the whole population around the world, with approximately 550,000 new cases annually worldwide (1) and 85,694 in China in 2020 (2). It has the 13th highest yearly mortality among all cancers and caused more than 165,000 in 2012, and the number is still rising despite tremendous treatment efforts (3). Tobacco smoking and occupational exposure to carcinogens are the major risk factors for BCa, while genetic factors seem to have little impact (3, 4). Urothelial carcinoma accounts for more than 90% of all cases, and BCa could be divided into non-muscle-invasive bladder cancer (NMIBC) and muscle-invasive bladder cancer (MIBC) according to whether the tumor tissue invades the muscle layer of the bladder. Approximately 75% of BCa is confined to the mucosa (stage Ta, CIS) or submucosa (stage T1) and defined as NMIBC; the remaining 25% is attributed to MIBC (4, 5). The primary treatment for NMIBC is transurethral resection of the bladder (TURB) accompanied by intravesical chemotherapy or intravesical bacillus Calmette-Guérin (BCG) immunotherapy after TURB to prevent recurrence and progression (4). As for MIBC, radical cystectomy (RC) and pelvic lymph node dissection (PLND) are the main treatments, and cisplatin-based chemotherapy has become the standard procedure for disease management (6). The traditional methotrexate, vinblastine, doxorubicin, and cisplatin (MVAC) chemotherapy plan has gradually been substituted by gemcitabine plus cisplatin (GC) for its similar efficacy and improved tolerability. Immunotherapy using immune checkpoint inhibitors (ICBs) and pre- and postoperative radiotherapy are also possible alternatives for platinum-ineligible patients (5–7). Other new small-molecule drugs such as OICR-9429 have also been proved to be effective in the treatment of bladder cancer, which can enhance the antitumor effect of cisplatin or immunotherapy in BCa (8). Discovering new therapeutic strategies, choosing appropriate candidates for immunotherapy using ICDs, and predicting the therapeutic efficacy for immunotherapy and chemotherapy are the major concerns in bladder cancer treatment.

Discovered by Hayflick and Moorhead in 1961 (9), cellular senescence is defined as a state of permanent cell cycle arrest induced by various *in vitro* or *in vivo* stimuli and characterized by aberrant cellular structure and morphology, as well as the activation of several hallmark signaling pathways such as DNA damage response (DDR), apoptosis resistance, cyclin-dependent kinase (CDK) inhibition, endoplasmic reticulum (ER) stress, and increased secretion of proinflammatory and tissue-remodeling factors (10, 11). According to the different stimuli, cellular senescence can be divided into several subtypes including replicative senescence, DNA damage-induced senescence, oncogene-induced senescence (OIS), and chemotherapy-induced senescence. Cellular senescence is a double-edged sword for human health. On the one hand, senescence can promote tissue remodeling and repair and function as a powerful safeguard to prevent abnormal proliferation and tumorigenesis. On the other hand, as an important part of aging, the aberrant and excessive accumulation of senescent cells is also connected with age-related disorders like degenerative diseases and cancer (11, 12).

Cellular senescence plays a dual role in the initiation, growth, and progression of tumor. The activation of oncogenes or loss of tumor suppressors will induce OIS and tumor-suppressor gene (TSG) loss–induced senescence, respectively, which can arrest the cell cycle and prevent tumorigenesis (13). Senescent tumor cells can also modulate the tumor microenvironment (TME) through the non-cell autonomous regulation of senescence called senescence-associated secretory phenotype (SASP). Through SASP, senescent cells can induce paracrine senescence and transform surrounding non-senescent cells into senescent cells by secreting pro-inflammatory cytokines, chemokines, growth factors, and proteases like IL-6, IL-8, and TGF-β, recruiting and activating immune cells in TME, which can result in both antitumor- and tumor-promoting effects. On the one hand, the innate and adaptive immune cells like M1 macrophages and natural killer (NK) cells can clear the tumor cells and promote their senescence by secreting IFN-γ and TNF-α, thus limiting tumor growth. On the other hand, senescent tumor cells can also attract and activate myeloid-derived suppressor cells (MDSCs) and M2 macrophages *via* SASP, thus affecting the clearance of senescent tumor cells and promoting tumor progression and vascularization, which is called maladaptive senescence (11, 13, 14). Since cellular senescence has a role in limiting tumor growth and development, it has been considered as a potential therapeutic target for tumor treatment. Multiple commonly used chemotherapy drugs such as bleomycin or doxorubicin can induce senescence to exert an antitumor effect. Moreover, several other pro-senescence therapy strategies such as telomerase inhibition, immunotherapy, and SASP reprogramming have also been put forward (13). Therefore, it

is important for us to figure out the comprehensive role of senescence in tumorigenesis and TME shaping to benefit as much as possible from interventions without incurring toxicities.

In recent years, several studies have focused on the role of senescence in BCa. Xia et al. have found that berberine can induce BCa cell senescence *via* inhibiting Janus kinase 1 (JAK1)-STAT3 signaling and upregulating miR-17-5p (15). Chen et al. found a novel cellular senescence gene called SENEX, which could promote regulatory T cell (Treg) accumulation in aged urinary BCa (16). Moreover, Wang and colleagues also found that regulator of cullins-1 (ROC1) could promote NMIBC progression through anti-senescence and was linked with poor prognosis (17). However, the previous studies were limited, and all focused on few senescence genes. The role of senescence in BCa has never been systematically evaluated, and the relationship between senescence and the prognosis of BCa remains obscure.

Therefore, here, using the genome-wide CRISPR screening data acquired from DepMap (Cancer Dependency Map), senescence genes from the CellAge database, and gene expression data from The Cancer Genome Atlas (TCGA), we screened out 12 senescence genes which might play key roles in BCa. Then, we successfully constructed a four-cell-senescence-regulator-gene prognostic index using the least absolute shrinkage and selection operator (LASSO) and multivariate COX regression model and investigated its relationship with tumor mutation burden (TMB) and TME immune cell infiltration. Its correlations with the prognosis of BCa and the efficacy of immunotherapy and chemotherapy were also investigated. We also established a nomogram using the senescence risk score and other clinical characteristics to predict the prognosis of patients with BCa.

METHODS

Obtaining BLCA Patient Bulk-Seq Data and Identifying Essential Cell Senescence Regulator Genes in BLCA

The RNA bulk-seq data and corresponding clinical information were retrieved and downloaded from the GDC_Data Portal (https://portal.gdc.cancer.gov/), and the external validation set GSE13507 was obtained from the Gene Expression Omnibus (https://www.ncbi.nlm.nih.gov/geo/). More importantly, the genome-wide CRISPR screening results of bladder cancer cell lines were acquired from the DepMap Database (https://depmap.org/portal/download/), and the importance for each candidate gene was weighted by the algorithm of CERES score. Notably, the genes with CERES score <-1 across of 75% of BLCA cell lines were screened as candidate genes (18, 19). Following this, the differentially expressed genes (DEG) analysis of these candidate genes was carried out between paired tumor sample and normal sample in TCGA_BLCA cohort. FDR <0.05 and $\log_2$FC >0 were set as the filter threshold to identify the essential BLCA genes. Also, 279 cell senescence regulator genes were obtained from the CellAge database (https://genomics.senescence.info/cells/) (20). Finally, we took an intersection of the essential BLCA genes and cell senescence regulator genes and got a total of 12 essential cell senescence regulator genes (ECSRGs) in BLCA for further analysis.

Comprehensive Analysis of the Essential Cell Senescence Regulator Genes in BLCA

Having got 12 ECSRGs in BLCA, we firstly conducted a comprehensive analysis to investigate the role of these ECSRGs. Both the expression profile and copy number variation (CNV) profiles were used for further analysis. Then, the differentially expressed analysis and expression correlation analysis of these 12 ECSRGs between tumor tissues and normal tissues (or normal adjuvant tumor tissues) were carried out to check the expression patterns of these ECSRGs in TCGA_BLCA cohort and GSE13507 cohort. Also, the copy number variation of these ECSRGs was further investigated. Finally, the 12 ECSRGs were uploaded to the STRING database (https://string-db.org/cgi/input.pl) to explore the protein–protein interaction network, and Cytoscape (version 3.8.2) was used to visualize the PPI network of these 12 ECSRGs.

Elimination of the Batch Effects, Sample Random Grouping, Construction, and Verification of the Prognostic Cell Senescence Index

We merged the expression matrix of TCGA_BLCA cohort and GSE13507 cohort, and the batch effects were eliminated by the combat algorithm using the "sva" package in R program (21). Notably, only 11 ECSRGs were covered in both TCGA_BLCA cohort and GSE13507 cohort, and they were CDK1, PSMD14, CHEK1, PSMB5, MAD2L1, RUVBL2, GAPDH, PRPF19, TPR, RAD21, and SUPT5H. Then we randomly split the samples with a ratio of 1:1 in TCGA_BLCA cohort into train group and validation group. The least absolute shrinkage and selection operator (LASSO) method was conducted in the training group to screen the appropriate variables of the above 11 ECSRGs. Following this, the multivariate cox regression of the left variables was performed in the training group to establish a prognostic cell senescence index (PCSI). Meanwhile, each sample in TCGA_validation cohort and GSE13507 cohort acquired a PCSI according to the following formula:

$$PCSI = \sum_{i=1}^{n} coef(i) \cdot expr(i) .$$

Among them, coef(i) is the coefficient of the ith ECSRGs in PCSI, and expr(i) is the normalized expression values of the ith ECSRGs. The medium value of the PCSI in TCGA_training cohort was set as the threshold, the higher PCSI was defined as high risk, and the lower PCSI was low risk; each patient in both TCGA cohort and GSE13507 cohort obtained a risk stratification level according to their PCSI.

The log-rank test-based survival analysis and Kaplan–Meier method-based survival curves were used to investigate the survival differences between high-PCSI patients and low-PCSI patients in TCGA_training cohort, TCGA_test cohort, and GSE13507 validation cohort. Both receiver operating

characteristic curve (ROC) and univariate-cox regression were carried out to further explore the prognostic capability of the PCSI. Following this, considering that these three cohorts were independent between each other, we performed heterogeneity test and meta-analysis of the hazard ratio (HR) in these three cohorts to objectively check the summary prognostic role of the PCSI. In addition, we would like to improve the prognostic accuracy of the PCSI. Thus, we combined the PCSI with other commonly used clinicopathological characteristics including age, gender, grade, and stage to assemble a nomogram; the 1-, 3-, and 5-year calibration curves and 5-year ROC curves were plotted to examine the efficacy of the nomogram.

Mutation Atlas, Immune Infiltrations, Immune Checkpoints, and Immune-Related Functions Between High- and Low-PCSI Patients

Having verified the efficacy of the PCSI and PCSI-based nomogram, we were interested in the potential mechanisms behind the differential PCSI groups. Considering that the expression matrix of TCGA was more complete, the further function analysis was all based on TCGA cohort. The mutation profiles of TCGA_BLCA cohort were retrieved and downloaded from GDC_Data_Portal (https://portal.gdc.cancer.gov/), then the TMB of each patient is calculated and the mutation profiles were sorted according to the PCSI levels. A differential mutation atlas between high-/low-PCSI groups was visualized as waterfall plots, and the χ^2 test was carried out to check the significantly differentially mutated genes between high-/low-PCSI groups. Following this, we combined the PCSI with TMB to stratify the patients and check the prognostic effects of these two indicators.

Considering that there existed a total of seven algorithms to quantify the immune infiltration according to the expression matrix, we downloaded the immune infiltration calculated by TIMER, CIBERSORT, CIBERSORT-ABS, QUANTISEQ, MCPCOUNTER, XCELL, and EPIC methods from the TIMER 2.0 database (http://timer.cistrome.org/) (22). Then both correlation tests and differential immune infiltration analysis were performed to investigate the immune infiltration between differential PCSI groups. Besides, the immune-related scores and immune-related functions were also investigated by the ESTIMATE algorithm (23) and single-sample gene set enrichment analysis (ssGSEA) algorithm (24, 25). The immune checkpoint expression matrix was extracted and used for further DEG analysis and correlation tests.

GSEA, GSVA, Drug Response, External Validation in Immunotherapy Cohort IMvigor-210, and the Histological Verification in Protein Levels

Gene set enrichment analysis (GSEA) was conducted by the "clusterProfiler" package in R program (26, 27), and HALLMARK gene sets were set as the enrichment gene sets. Also, gene set variation analysis (GSVA) was conducted by the "GSVA" package in R program (28). The HALLMARK gene sets, KEGG_signaling pathways, programmed cell death-related gene sets, and cell senescence-related gene sets were separately used for GSVA, and the correlation between the PCSI levels and the activated levels of these gene functions or pathways was examined by the Spearman test. Notably, all the gene sets were searched and downloaded from MSigDb (https://www.gsea-msigdb.org/gsea/msigdb/).

The drug response to chemotherapy or targeted therapy was predicted by the ProPhetic algorithm, and then the drug sensitivity to chemotherapy or targeted therapy (summarized by the IC50) was compared between high-PCSI and low-PCSI patients. Moreover, the drug response to immunotherapy was summarized by the Tumor Immune Dysfunction and Exclusion (TIDE) scores in the TIDE database (http://tide.dfci.harvard.edu/) (29), then the differential immune escape potentials (TIDE scores) between high-/low-PCSI groups were investigated by the Wilcoxon test. More importantly, we added an external bladder cancer anti-PD-L1 immunotherapy cohort IMvigor 210 (30, 31). Each patient's PCSI in IMvigor210 was calculated by the same method, and the differential PCSI distribution between differential response to the anti-PDL1 immunotherapy groups (CR/PR or PD/SD) was compared by the Wilcoxon test. Finally, we further searched the Human Protein Atlas (https://www.proteinatlas.org/) (32) for the histological verification in protein levels of the ECSRGs enrolled in the PCSI model between bladder tumor tissues and normal bladder tissues.

RESULTS

Identification of 12 Vital Differentially Expressed Senescence Genes in Bladder Cancer

A complete flowchart of the analysis process is shown in **Figure 1**. From the beginning, we extracted the genes, which was vital to the viability of bladder cancer cell lines verified by genome-wide CRISPR knockout in the DepMap database and screened out differentially expressed genes (DEGs) in normal tissues and bladder cancer tissues using the gene expression data from TCGA database (**Figure 2A**; **Supplementary Table 1**). Then we obtained the senescence genes in the CellAge database (**Supplementary Table 2**) and intersected these genes with the DEGs, and 12 essential cell senescence regulator genes (ECSRGs) were finally sorted out (**Figure 2B**). Among the 12 ECSRGs, two (SRSF1 and CHEK1) were senescence promotors and the others were senescence inhibitors. Then we analyzed the interaction among these 12 ECSRGs and found that they were tightly interacted with each other (**Figure 2C**). Later we found that the expression of these 12 ECSRGs increased gradually in normal tissues, normal adjacent tumor tissues, and tumor tissues (**Figures 2D, E**). The location of these 12 ECSRGs on the chromosome is shown in **Figure 2G**. Moreover, we also performed copy number variation (CVN) analysis of these genes and found that most alterations were loss in copy number (**Figure 2F**). Besides, the correlation among the 12 genes was illustrated after analyzing data retrieved from TCGA

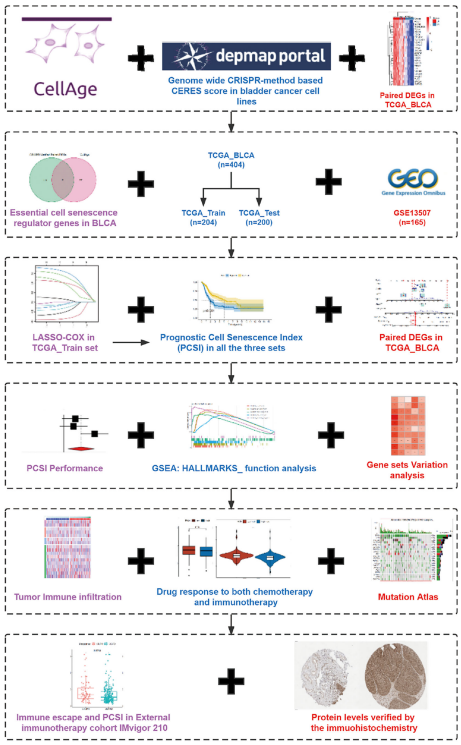


FIGURE 1 | The flowchart and graphic abstract of this study.

(**Figure 2H**) and GEO (**Figure 2I**) databases. Above all, we successfully found 12 vital ECSRGs for further analysis.

Construction and Verification of the Prognostic Cell Senescence Index

In order to construct a prognostic index, we obtained 404 samples of BCa from TCGA database and divided them into two groups as training cohort (N = 204) and testing cohort (N = 200). The basic characteristics of the patients included are shown in **Table 1**. Then we used the LASSO regression and screened out five genes for further analysis (**Figures 3A, B**) and then sifted four genes from them through multivariate Cox regression using the gene expression data in the training cohort (**Figure 3C**). These four genes were PSMD14 (HR = 0.58, 95% CI = 0.37–0.91, P = 0.018), PSMB5 (HR = 2.05, 95% CI = 1.24–3.40, P = 0.005), PRPF19 (HR = 1.69, 95% CI = 1.08–2.65, P = 0.023), and TPR (HR = 1.77, 95% CI = 1.15–2.72, P = 0.009), and their interactions are shown in **Supplementary Figure 1**. The detailed information of these four genes is exhibited in **Table 2**. To evaluate the effectiveness of this prognostic index, we also obtained 165 samples from the GEO database (GSE13507) as validation cohort. We calculated the risk score according to the expression of the four senescence genes and divided the patients in these three cohorts into high- and low-risk score groups according to the median risk score as the cut-off value acquired from the training cohort (**Figures 3E–G**). The distribution of clinical characteristics of patients in the high- and low-risk score groups is shown in **Figure 3D**. Moreover, we also evaluated the survival status of each patient in three cohorts (**Figures 3H–J**). All these results revealed that patients in the high-risk score group seemed to have the worse clinical outcome than those in the low-risk group. Subsequently, we conducted Kaplan–Meier survival analyses and plotted survival curves (**Figures 3K–M**), which indicated that patients in the high-risk score group had worse survival outcome than those in the low-risk score group. The area under the curve (AUC) was used to check the effectiveness of the prognostic index (**Supplementary Figure 2**). Besides, the result of meta-analysis based on the three cohorts illustrated that the risk score was in good validity (HR = 1.33, 95% CI = 1.07–1.66, P = 0.06) (**Figure 3N**). At last, we established a nomogram using the senescence risk score and other clinical characteristics (age, gender, stage, and grade) to predict the survival probability of patients with BCa in 1, 3, and 5 years, respectively. Moreover, we randomly selected a patient and calculated that his survival probability in 5, 3, and 1 year were 57.1%, 63.5%, and 87.4%, respectively (**Figure 4A**). The AUC of this nomogram was 0.720 and the largest among all the models, indicating that the nomogram had better accuracy in predicting the overall survival (OS) compared with other independent factors (**Figure 4B**). Calibration plots of 1-, 3-, and 5-year OS also exhibited a good predicted accuracy (**Figure 4C**). Above, all these results suggested that the four-gene prognostic index could accurately and stably predict the survival outcome of BCa patients.

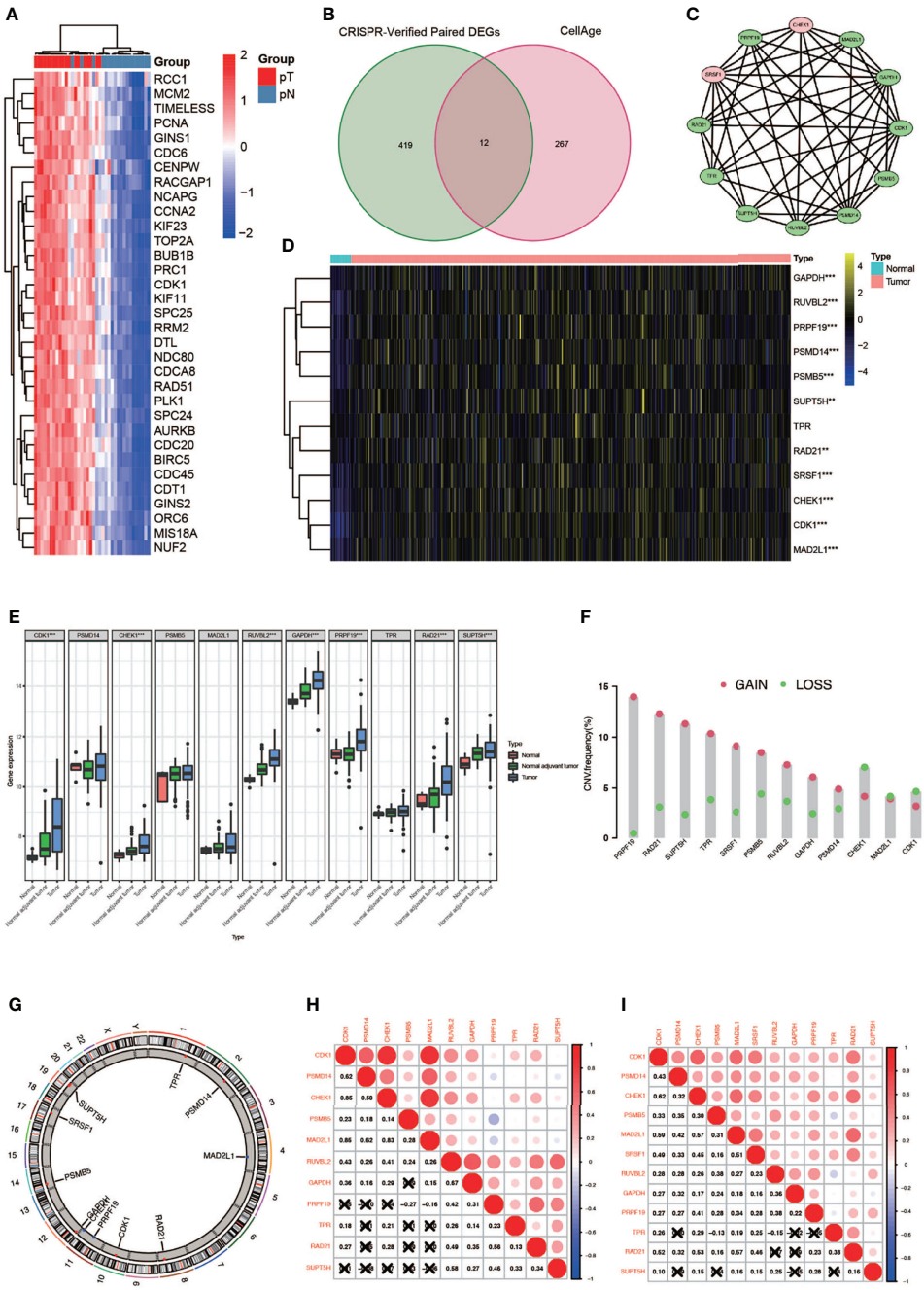


FIGURE 2 | Identification of 12 vital differentially expressed senescence genes in bladder cancer. **(A)** Genome-wide CRISPR verified paired differentially expressed gene (DEGS) in TCGA database. **(B)** Venn diagram of DEGs and senescence genes in the CellAge database. **(C)** Relationship among the 12 genes. **(D)** Twelve genes were differentially expressed in normal and tumor tissues (* $P < 0.05$; ** $P < 0.01$; *** $P < 0.001$). **(E)** Differentially expressed 12 genes in normal, normal adjuvant tumor, and tumor tissues (** $P < 0.01$; *** $P < 0.001$). **(F)** CVN diagram of 12 genes. **(G)** The location of these 12 genes on the chromosome. **(H, I)** Correlation between 12 genes in TCGA (left) and GEO (right) databases.

Exploring the Relationship Between Tumor Mutation Burden and Risk Score

Here we mapped the mutation spectrum of patients with high risk score (**Figure 5A**) and low risk score (**Figure 5B**) in TCGA and obtained six significantly differentially mutant genes including RB1, DCC, TP53, LAMA3, VPS13D, and APOB by the chi-squared test (**Supplementary Table 3**). Subsequently, we compared the TMB in high- and low-risk score patients, indicating that the TMB of patients in the high-risk score group was higher (**Figure 5C**). Survival curves also suggested

TABLE 1 | The basic characteristics of included patients.

	Overall	GSE13507	TCGA_Test	TCGA_Train	P
n	569	165	200	204	
Age [mean (SD)]	67.25 (11.10)	65.18 (11.97)	69.10 (9.91)	67.12 (11.21)	0.003
Gender = female/male (%)	135/434 (23.7/76.3)	30/135 (18.2/81.8)	47/153 (23.5/76.5)	58/146 (28.4/71.6)	0.071
Grade (%)					<0.001
High grade	440 (77.3)	60 (36.4)	185 (92.5)	195 (95.6)	
Low grade	126 (22.1)	105 (63.6)	13 (6.5)	8 (3.9)	
Unknown	3 (0.5)	0 (0.0)	2 (1.0)	1 (0.5)	
T (%)					<0.001
T1	83 (14.6)	80 (48.5)	2 (1.0)	1 (0.5)	
T2	150 (26.4)	31 (18.8)	63 (31.5)	56 (27.5)	
T3	210 (36.9)	19 (11.5)	87 (43.5)	104 (51.0)	
T4	69 (12.1)	11 (6.7)	33 (16.5)	25 (12.3)	
Ta	24 (4.2)	24 (14.5)	0 (0.0)	0 (0.0)	
Unknown	33 (5.8)	0 (0.0)	15 (7.5)	18 (8.8)	
M (%)					<0.001
M0	352 (61.9)	158 (95.8)	95 (47.5)	99 (48.5)	
M1	18 (3.2)	7 (4.2)	6 (3.0)	5 (2.5)	
MX	197 (34.6)	0 (0.0)	97 (48.5)	100 (49.0)	
Unknown	2 (0.4)	0 (0.0)	2 (1.0)	0 (0.0)	
N (%)					<0.001
N0	386 (67.8)	151 (91.5)	115 (57.5)	120 (58.8)	
N1	54 (9.5)	8 (4.8)	22 (11.0)	24 (11.8)	
N2	79 (13.9)	4 (2.4)	37 (18.5)	38 (18.6)	
N3	8 (1.4)	1 (0.6)	4 (2.0)	3 (1.5)	
NX	37 (6.5)	1 (0.6)	19 (9.5)	17 (8.3)	
Unknown	5 (0.9)	0 (0.0)	3 (1.5)	2 (1.0)	
Status = dead (%)	245 (43.1)	69 (41.8)	90 (45.0)	86 (42.2)	0.787
PCSI (median [IQR])	0.95 [0.72, 1.33]	1.00 [0.69, 1.34]	0.92 [0.70, 1.26]	0.96 [0.75, 1.33]	0.658
Risk = high/low (%)	283/286 (49.7/50.3)	90/75 (54.5/45.5)	91/109 (45.5/54.5)	102/102 (50.0/50.0)	0.227

Prognostic cell senescence index (PCSI).

TABLE 2 | The detailed information and corresponding coefficient of the four cell senescence regulator genes.

Symbol	Names	Coef
PSMD14	Proteasome 26S subunit, non-ATPase 14	-0.542818539222188
PSMB5	Proteasome 20S subunit beta 5	0.720137573972114
PRPF19	Pre-MRNA processing factor 19	0.5248045764904
TPR	Translocated promoter region, nuclear basket protein	0.5699966968373

that the clinical prognosis of patients with high TMB was better (**Figure 5D**), while patients with a low risk score and high TMB had the best prognosis (**Figure 5E**).

Correlation Between Prognostic Index and Tumor Microenvironment in Bladder Cancer

In this part, we used the ESTIMATE algorithm to assess the TME immune cell infiltration in patients with BCa. As shown in **Figure 6A**, patients with a high risk score had a lower TME score (stromal score, immune score, and ESTIMATE score) than those in the low-risk group, which illustrated a lower proportion of immune and stromal cell infiltration and higher tumor purity. Then we evaluated the correlation between risk score and the expression of immune checkpoints (ICBs), indicating that most immune checkpoints were significantly low expressed in the high-risk score group (**Figure 6B**) and were negatively correlated with the risk score (**Figure 6C**). The results of immune-related function also revealed that the high-risk group was negatively associated with expression of the chemokine receptor (CCR) and HLA, secreting inflammation-promoting factors and response to IFN-γ (**Figure 6D**). Then, we used five methods to assess the composition of immune infiltration cells. Specifically, natural killer T-cell (NK T cell) infiltration was negatively correlated with the risk score under xCell analysis (**Figures 7A, C**) and was significantly reduced in the high-risk score group (**Figure 7B**).

Gene Set Enrichment Analysis and Gene Set Variation Analysis

To verify the relationship between risk score and hallmark pathways and cell death mode, we performed GSEA and GSVA using HALLMARK gene sets, Kyoto Encyclopedia of Genes and Genomes (KEGG)_signaling pathways, programmed cell death related gene sets, and cell senescence-related gene sets. As shown in **Figure 8A**, the risk score was positively associated with totally 20 hallmark pathways including PI3K/AKT/mTOR signaling pathway, G2M checkpoint, and

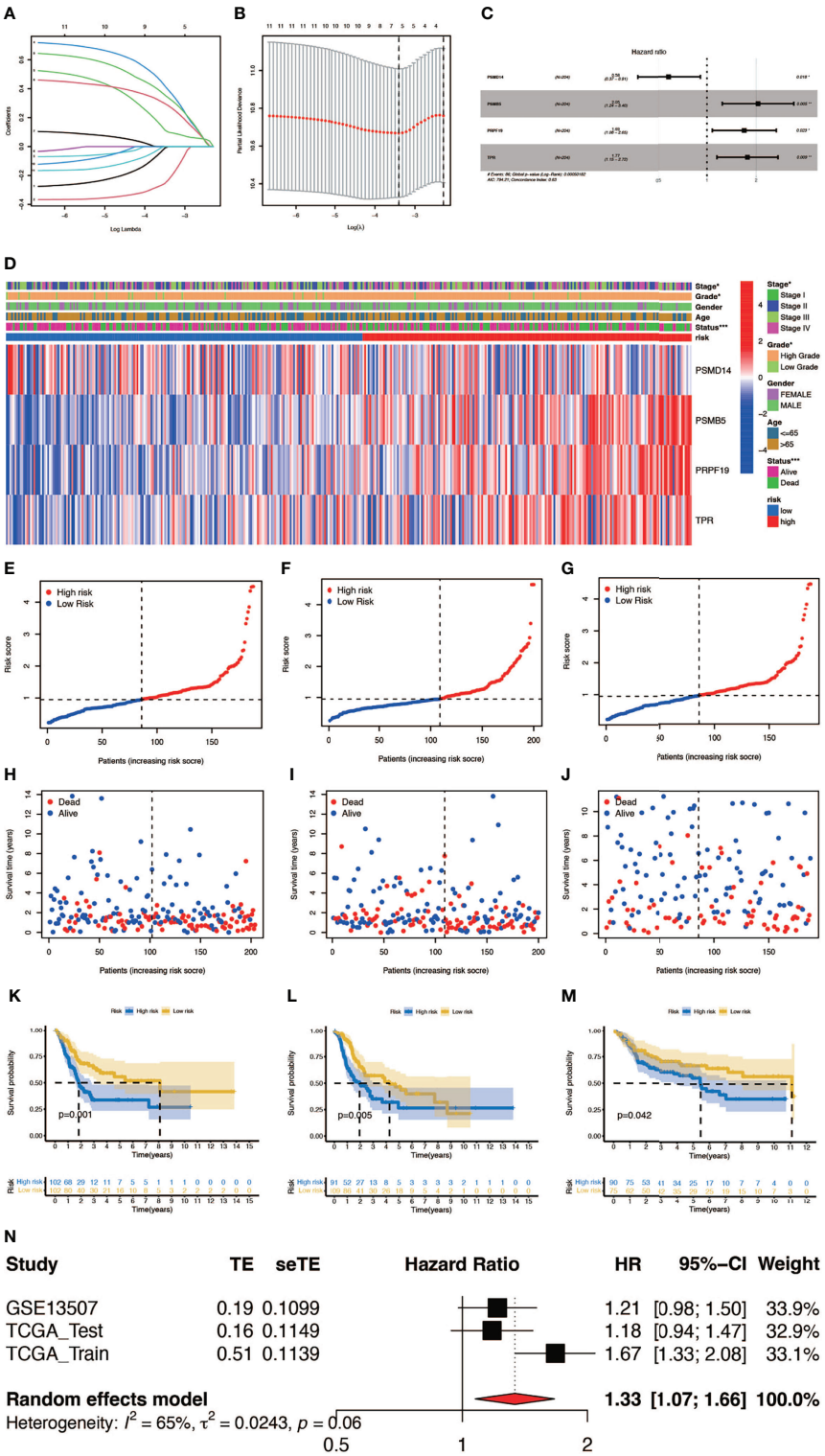


FIGURE 3 | Construction and verification of the prognostic index. **(A, B)** Result of LASSO regression analysis. **(C)** Hazard ratio of each gene after multivariate Cox regression analysis. **(D)** The distribution of clinical characteristics of patients in the high- and low-risk score groups. **(E–G)** Risk scores of each patient in the training cohort, testing cohort, and verification cohort. **(H–J)** Survival status of each patient in the training cohort, testing cohort, and verification cohort. **(K–M)** Kaplan–Meier survival analyses of each patient in the training cohort (P = 0.001, log-rank test), testing cohort (P = 0.005, log-rank test), and verification cohort (P = 0.042, log-rank test). (n) Meta-analysis of the training cohort, testing cohort, and verification cohort (*P < 0.05; **P < 0.01; ***P < 0.001).

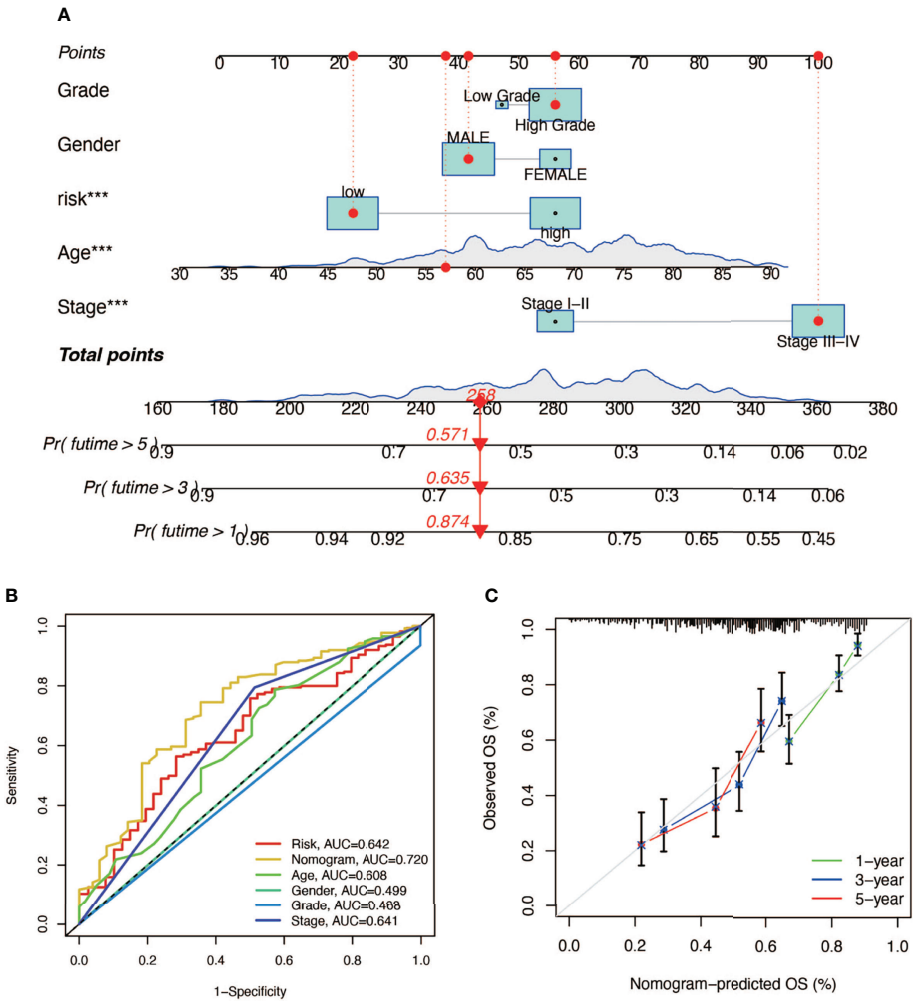


FIGURE 4 | The establishment of a nomogram predicting the prognosis of patients with BCa. **(A)** Nomogram of a randomly selected patient (*** P < 0.001). **(B)** AUC curve of the nomogram. **(C)** Calibration plot of 1-, 3-, and 5-year overall survival.

fatty-acid metabolism. Then we performed GSVA in different risk score groups (**Figures 8B, C**). Besides, we also performed KEGG analysis and discovered that the risk score was positively correlated with P53, NOTCH, and mTOR signaling pathway (**Figure 8D**). Also, we verified that the risk score was related to some pathways in cell death and cell aging. As shown in **Figures 8E, F**, the risk score was positively correlated with autophagy, apoptosis, and all cell aging-related pathways.

The Interaction Between Risk Score and Response to Chemotherapy and Immunotherapy

We analyzed the response to commonly used chemotherapy drugs in different risk score groups in order to guide clinical medication. As shown in **Figures 9A–F**, the smaller the IC50, the more sensitive patients were to drugs, so patients in the high-risk score were more sensitive to chemotherapy drugs, including cisplatin, doxorubicin, gemcitabine, mitomycin C, and vinblastine. Besides, we also analyzed many other alternative drugs when the above chemotherapy drugs did not work (**Supplementary Figure 3**). Anti-PD-L1 immunotherapy has also been proven effective for patients with metastatic urothelial carcinoma in a multicenter, single-arm phase 2 trial using atezolizumab (IMvigor 210, NCT02108652) (33). Therefore, we applied the IMvigor 210 cohort to verify the response to immunotherapy. The tumor immune dysfunction and ejection (TIDE) score was used to evaluate tumor immunotherapy response, where a smaller TIDE score meant better response to immunotherapy. In **Figure 9G**, patients with a low risk score had a larger TIDE score, indicating less sensitivity to immunotherapy, and in **Figure 9H**, patients in the CR/PR (complete response/partial response) group got a higher risk score than those in the SD/PD (stable disease/progressive disease) group. Overall, patients with a high risk score were more sensitive to immunotherapy.

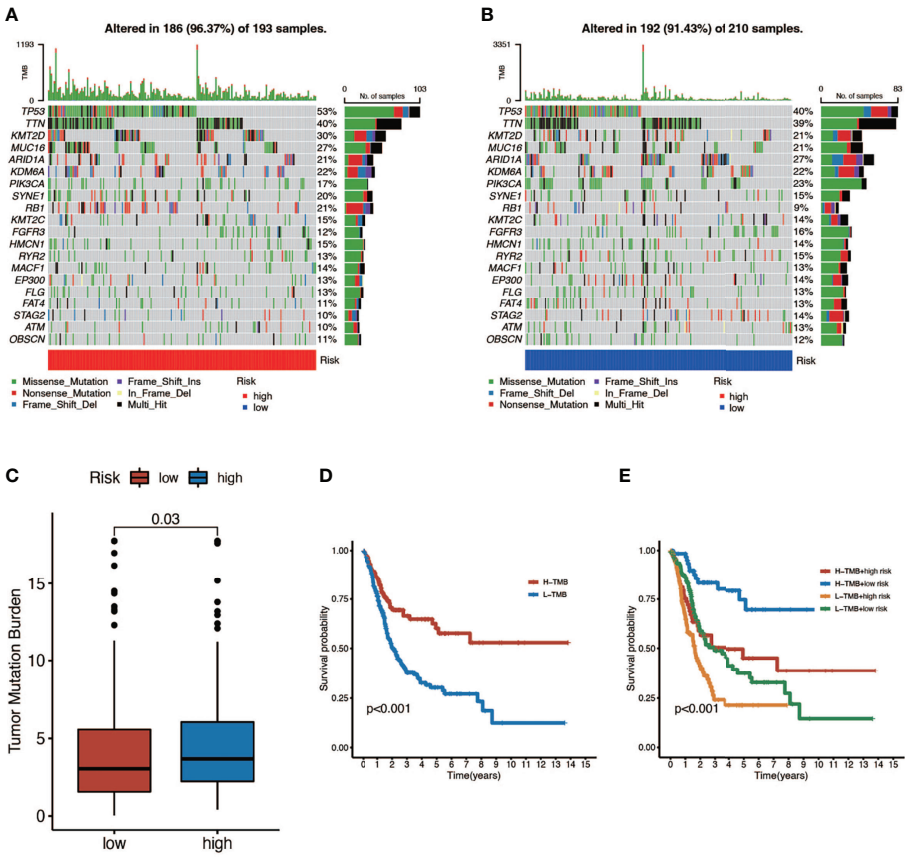


FIGURE 5 | The relationship between tumor mutation burden (TMB) and risk score. **(A, B)** Mutation spectrum of high-risk (left) and low-risk (right) patients. **(C)** Comparison of TMB between patients in the high- and low-risk score groups. **(D)** Survival analyses for low- and high-TMB patient groups in TCGA-BLCA cohort using Kaplan–Meier curves (P < 0.001, log-rank test). **(E)** Survival analyses for four groups grouped according to TMB and risk score in TCGA-BLCA cohort using Kaplan–Meier curves. The high-TMB and low-risk score groups showed significantly better overall survival than the other three groups (P < 0.001, log-rank test).

Immunohistochemical Analyses of PSMD14, PRPF19, PSMB5, and TPR

We obtained the results of immunohistochemical staining of PSMD14, PRPF19, PSMB5, and TPR in normal tissues and bladder cancer tissues (**Figures 10A–D**) and demonstrated that these four genes were highly expressed in tumor tissues and lowly expressed in normal tissues.

DISCUSSION

Senescence is a stable state characterized by permanent withdrawal from the cell cycle under endogenous and exogenous stimuli and specific changes in cell morphology and physiology. As a complementary mechanism to programmed cell death, senescence functions like a safeguard to remove dysfunctional or diseased cells and stabilize the body's internal environment. Senescence has long been considered as a protective mechanism against tumorigenesis since cancerous cells can be induced by senescence and prevented from proliferation and progression (34). However, there is growing evidence that senescence can also contribute to tumor development and progression in certain circumstances and has been regarded as a new hallmark of cancer (35). Studies thought that senescence could promote tumor phenotypes mainly *via* SASP, a phenotype characterized by enhanced secretion of pro-inflammatory cytokines, growth factors, and matrix metalloproteinases (MMPs) in an autocrine or paracrine fashion. These signaling molecules can influence the tumor and other cells in TME and lead to tumor immunity suppression, angiogenesis, tumor proliferation, invasion, and metastasis (36). Studies also found that some tumor cells were in transitory, reversible senescent states and could escape from senescence and reenter the cell cycle, resulting in recurrence and more aggressive tumors (37). Therefore, it is intriguing to deeply explore the exact role of senescence in specific tumor development and prognosis of cancer patients. Nevertheless, limited studies have investigated the effect of senescence in BCa and previous studies only focused on few senescence genes while ignoring their interactions and comprehensive function. Considering the importance of SASP in shaping TME and the development of tumor, we believed it was also valuable

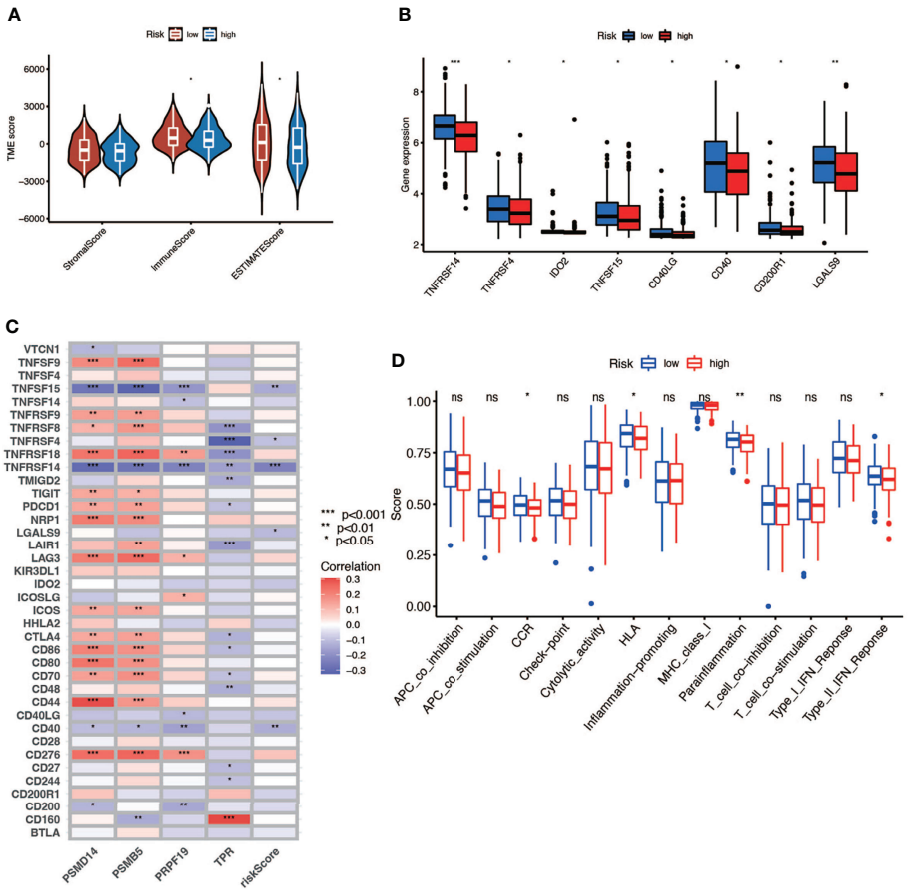


FIGURE 6 | The relationship between risk score and TME. **(A)** TME scores of high- and low-risk patients (* P < 0.05; ** P < 0.01; *** P < 0.001). **(B)** Immune checkpoints expression in high- and low-risk-score patients (* P < 0.05; ** P < 0.01; *** P < 0.001). **(C)** Correlation between immune checkpoints and four genes (* P < 0.05; ** P < 0.01; *** P < 0.001). **(D)** Comparison of immune-related function of high- and low-risk-score patients (ns, no significance; * P < 0.05; ** P < 0.01; *** P < 0.001).

and feasible to explore the interaction between TME immune cell infiltration and senescence.

Hence, in this study, using the genome-wide CRISPR screening data acquired from DepMap, we calculated the dependence score *via* the CERES algorithm and screened genes, which was essential to proliferation and survival in BCa cell lines (18). Genome-wide CRISPR has high gene editing specificity and low off-target effect. Therefore, CRISPR is more effective in screening genes. Then we sifted differently expressed genes (DEGs) between paired BCa and normal tissues from these genes using the gene expression data downloaded from TCGA. Afterward, we took the intersection between CRISPR-verified paired DEGs and genes in the CellAge database and finally identified 12 vital senescence genes in BCa, four of which were selected to construct a cell-senescence-regulator-gene prognostic index after applying LASSO and the multivariate COX regression model. To investigate the relationship between senescence index and the prognosis of patients with BCa, we randomly divided the patients in TCGA cohort into training and testing cohorts and calculated the risk score according to the expression of the four senescence genes. No matter for the training cohort and testing cohort (TCGA) or validation cohort (GSE13507), the prognostic senescence index exhibited robust capacity in predicting survival outcomes of patients with BCa. Combining the risk score with other clinical factors (age, gender, stage, and grade), a nomogram was established with better predictive capacity of OS in 1, 3, and 5 years. We further uncovered the interaction between risk score and TMB and their combined effect in predicting the patients' prognosis. Moreover, we also evaluated the differential TME immune cell infiltration landscape between the two risk subgroups from different perspectives including immune and stromal scores, the purity of tumor, the abundance of immune cells, the expression of immune checkpoints, and the functions of immune cells. We also performed GSVA and GSEA to investigate the interaction between risk score and hallmark pathways. Finally, the role of risk score in heralding the efficacy of immunotherapy and chemotherapy was also investigated.

The four genes which were finally included in the cell-senescence-regulator-gene prognostic index include PSMD14,

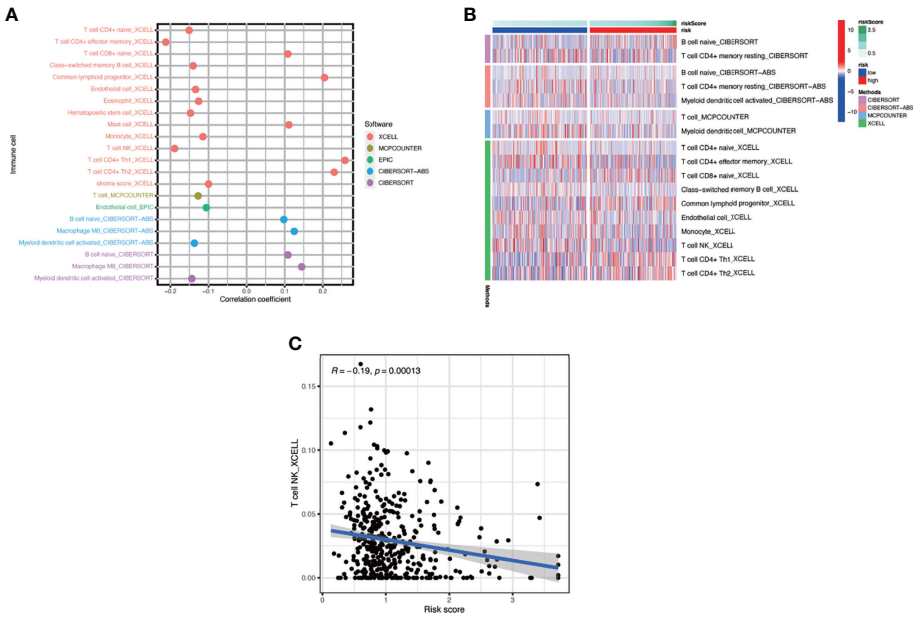


FIGURE 7 | The interaction of risk score and immune-related infiltration cells. **(A)** Correlation of immune cells infiltration and risk scores using five different methods. **(B)** Differential infiltration of immune cells between high- and low-risk-score patients. **(C)** Correlation between risk scores and NKT cells infiltration.

PSMB5, TPR, and PRPF19, and all belong to senescence inhibitors. PSMD14 is a kind of deubiquitinating enzymes (DUBs) and was reported to be connected with tumor progression and poor prognosis in many types of cancer including neck squamous cell carcinoma (38), non-small cell lung cancer (39), ovarian cancer (40), and hepatocellular carcinoma (41). Gong considered that a high expression of PSMD14 in tumor cells may lead to aging or failure of CD8+ T cells, which may explain the positive correlation between high expression of CD8+ T cells and PSMD14 and poor prognosis in osteosarcoma (42). PSMB5 is a member of the PSMB family and ubiquitin-proteasome system, which was demonstrated to play important roles in tumor progression and immune cell infiltration, especially in breast cancer. PSMB5 was downregulated in M1-polarized THP-1 macrophages. Knockout of PSMB5 with shRNA could promote THP-1 to differentiate into M1 macrophages. It can also inhibit the proliferation and migration of breast cancer cells (43, 44). TPR is essential to a variety of nuclear functions such as the transport of mRNAs and proteins through nuclear pore, chromatin organization, and mitosis, whose mutations were detected in many kinds of cancers and contributed to cancer development and aging (45, 46). PRPF19 participated in DNA damage response and pre-mRNA processing and was reported to be linked with cancer growth in tongue cancer (47) and hepatocellular carcinoma (48) and could regulate cellular senescence in a p53-dependent manner (49). In hepatocellular carcinoma, TP53 mutation may have a positive effect on PRPF19 expression by reducing the promoter methylation of PRPF19 (48). In this article, for the first time, we reported the roles of these genes in the prognosis of BCa. Consistent with other cancers, PSMB5, TPR, and PRPF19 were independent prognostic risk factors in BCa, while PSMD14 seemed to be a protective factor, which was different from other types of cancers. The result needs further verification and the mechanisms need to be explored in the future.

TMB was regarded as a potential biomarker to predict the response to immunotherapy with ICBs. High TMB could predict high ICB efficacy and better overall survival in BCa (6, 50, 51). We found that the high-risk score group had higher TMB compared to the low-risk score group and patients with high TMB had better overall survival, which was consistent with previous studies. We also found that there existed significant distribution differences of TMB in some mutated genes such as TP53 and RB1, both of which were vital TSGs and had higher mutation frequency in the high-risk score group. Previous studies have demonstrated that overexpression of oncogenes could induce cellular senescence and work as a barrier to block tumor growth in the existence of TSGs. However, the mutation of TSGs could lead to senescence escape and was a critical step in tumor progression (13). Therefore, the poor prognosis in the high-risk score group might partially attribute to the loss or inactivation of TSGs.

TME includes not only cancer cells but also immune and stromal cells and plays a vital role in the development of tumor (52). The immune cells consist of tumor-associated macrophages (TAMs), tumor-associated neutrophils (TANs), tumor-infiltrating lymphocytes (TILs), and myeloid-derived suppressor cells (MDSCs). The stromal cells include endothelial cells, cancer-associated fibroblasts (CAFs), and other cells (53). As mentioned above, SASP was characterized by increased secretion of multiple pro-inflammatory and pro-

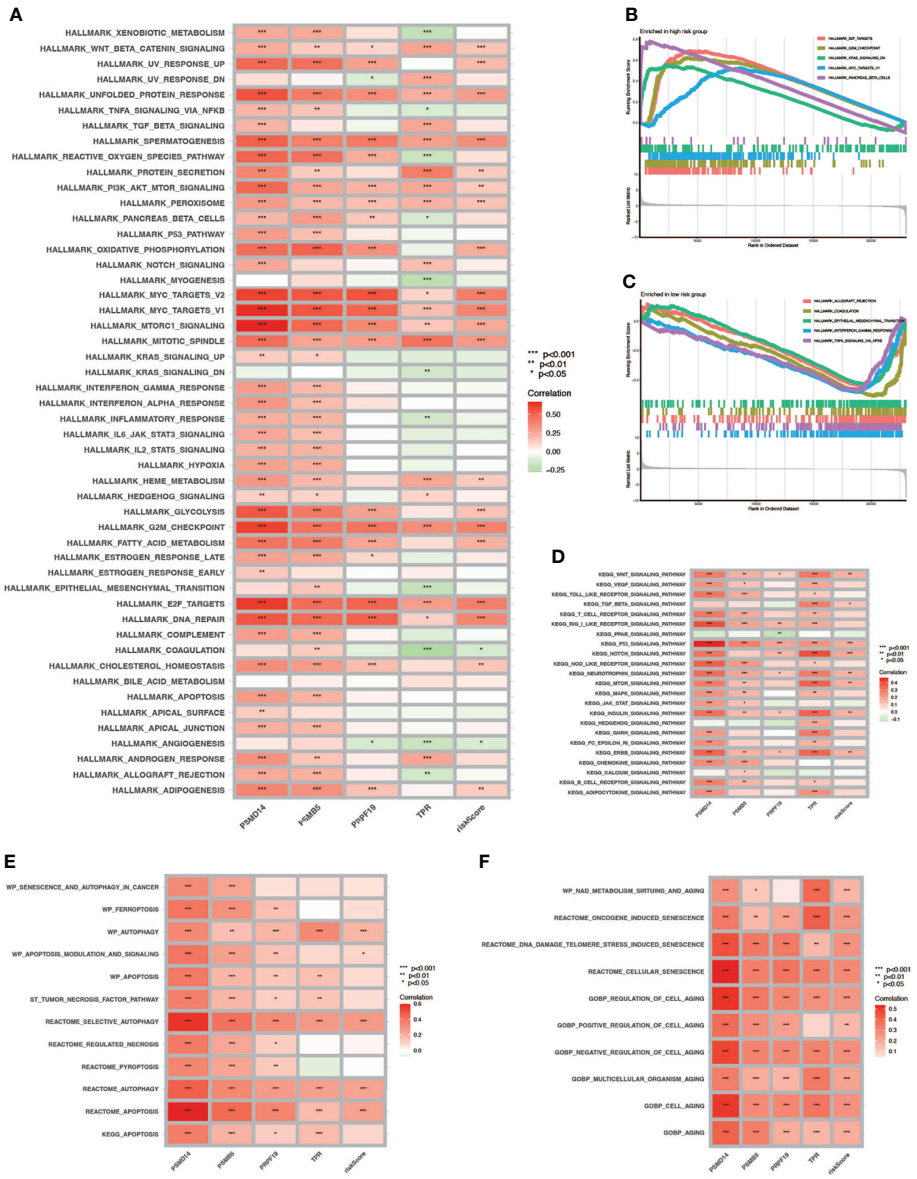


FIGURE 8 | GSVA and GSEA. **(A)** GSVA in Hallmark gene sets. **(B, C)** GSEA in high- and low-risk-score patients. **(D)** GSVA in the KEGG database. **(E)** Correlation between cell death mode and risk score. **(F)** Correlation between cell aging related pathways and risk score (* P < 0.05; ** P < 0.01; *** P < 0.001).

regenerative factors, which could attract and activate immune cells in the TME to clear the senescent cells and maintain the tissue homeostasis or lead to senescence escape and tumor progression, which depends on the kinds of immune cells and factors in the TME. Stromal cells also have the ability of promoting tumor *via* SASP. For example, senescent CAFs were demonstrated to promote tumors through conveying hallmark capabilities to cancer cells in the TME, and senescent fibroblasts in normal tissues could remodel the tissue microenvironments and contribute to tumor invasion and metastasis *via* SASP (35, 36). In our study, we found that a high risk score was connected with a low proportion of immune cells and high purity of tumor cells in the TME of BCa, which means that senescence could interfere with the enrichment of immune cells in TME and lead to the accumulation of tumor cells. We also noticed that the expressions of some immune checkpoints were negatively connected with the risk score with statistical significance, but for those commonly used for immunotherapy target such as PD-1, CTLA-4, and LAG-3, there existed no statistical difference between the high- and low-risk score subgroups. Moreover, we also found that the functions of immune cells in the high-risk score subgroup were partially aberrant compared to the low-risk score subgroup, such as expression of chemokine receptor (CCR) and HLA, secreting inflammation-promoting factors and

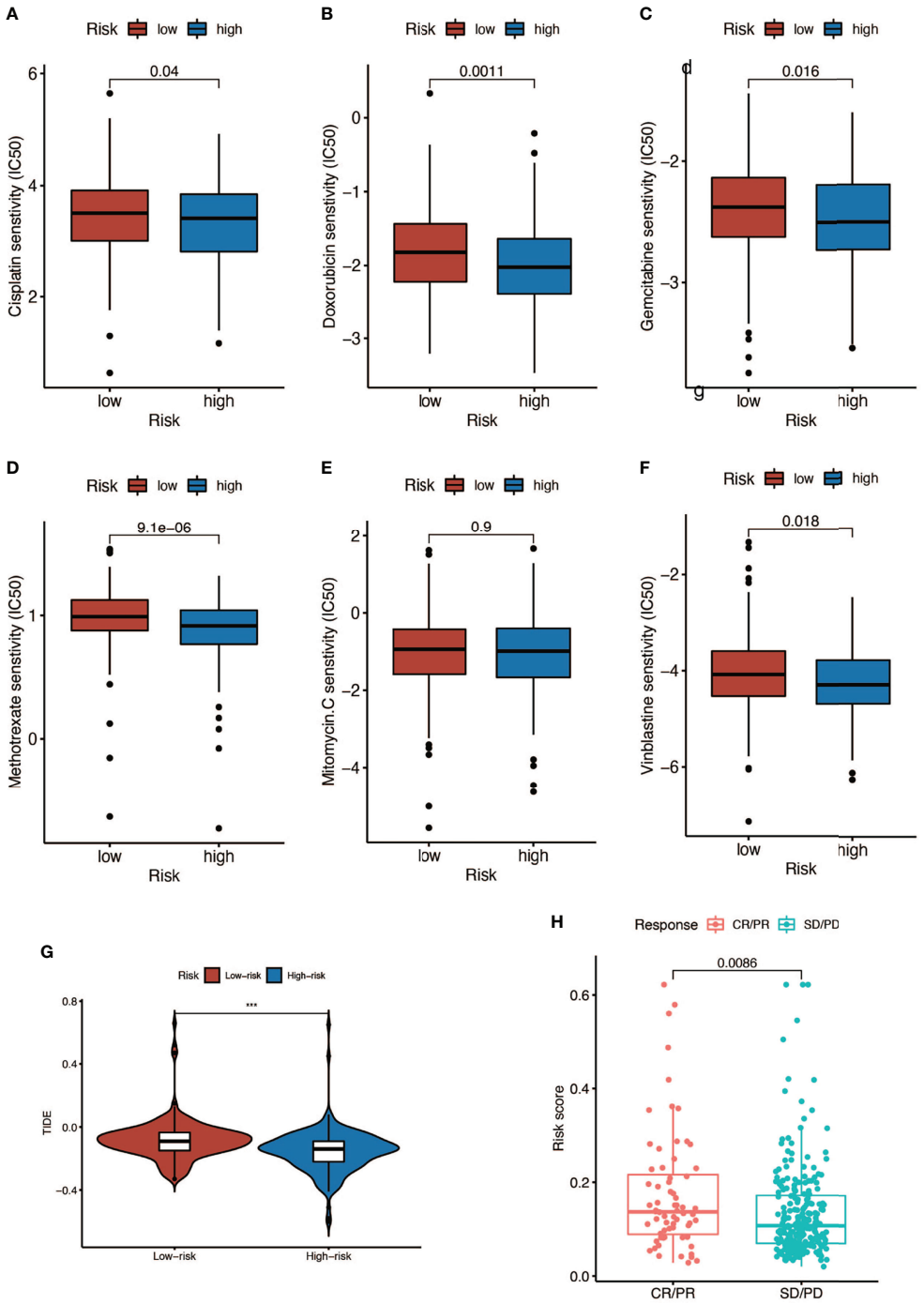


FIGURE 9 | Response to chemotherapy and immunotherapy of patients in the high- and low-risk-score groups. **(A–F)** Comparison of chemotherapy drugs sensitivity in high- and low-risk-score patients including cisplatin, doxorubicin, gemcitabine, mitomycin C, and vinblastine. **(G)** TIDE scores of high- and low-risk-score patients (*** $P < 0.001$). **(H)** Risk scores of CR (complete response)/PR (partial response) patients and SD (stable disease)/PD (progressive disease) patients after PD-L1 immunotherapy.

response to IFN-γ. CCR was important for TAMs to accumulate in the TME, and HLA, also called MHC, was essential to the activation of adaptive antitumor immunity and recognition of tumor cells by NK cells and CD8+ T cells (53). Moreover, IFN-γ could induce Th0 cells and M0 macrophages to differentiate into Th1 and M1 phenotype and exert anti-tumorigenic functions, and it could also induce senescence (53). Besides, we discovered that the NK T cells, which were crucial to the antitumor

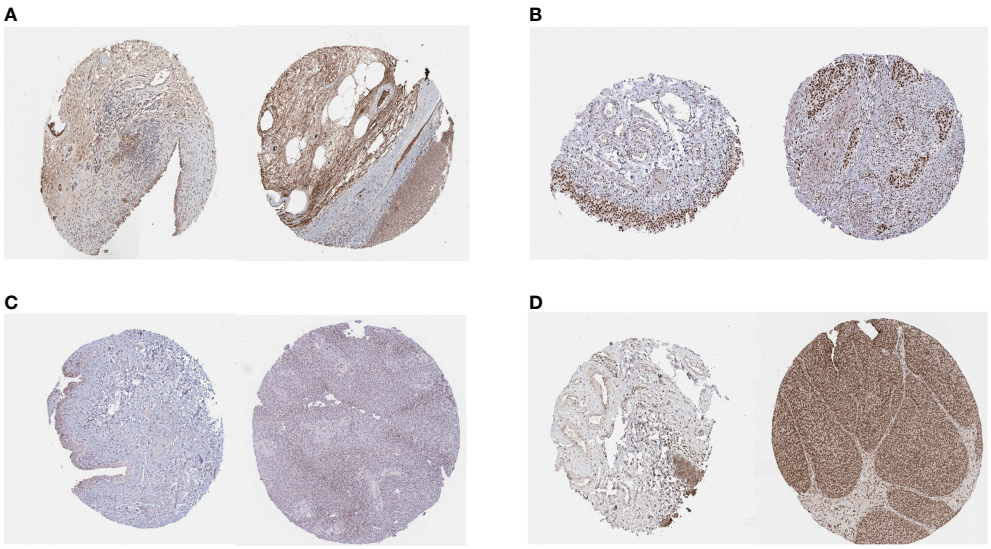


FIGURE 10 | IHC staining of **(A)** PSMD14, **(B)** PRPF19, **(C)** PSMB5, and **(D)** TPR in normal tissues (left) and bladder cancer tissues (right).

immunity (54), were negatively connected with the risk score. As a result, the patients in the high-risk score group had a poor survival outcome compared with those in the low-risk score group.

T cells are important for the establishment and maintenance of immune responses. With the process of immunosenescence, T cells could become either anergic, exhausted, or senescent, which would break the immune homeostasis. Exhausted T cells were characterized with high expression of immune checkpoints and decreased production of effector cytokines, while senescent T cells were featured by short telomeres, low expression of co-stimulatory molecules CD28 and CD27, and increased expression of senescence-associated-ß-galactosidase (SA-ß-Gal). CD8+ T cells were more easily influenced by immunosenescence than CD4+ T cells reflected by a remarkably lower number of circulating naïve CD8+ T cells (55). In this article, we found that the risk score was positively correlated with the number of naïve CD8+ T cells in the TME, which means more remarkable immunosenescence in the low-risk score group. Combining the fact that many immune checkpoints were highly expressed in the low-risk group, we thought most T cells were exhausted, which accounts for the high TIDE score and poor immunotherapy outcome using ICBs in this group. Immunotherapy using ICBs has shown promising outcomes in clinical trials among patients with BCa (33, 56). Despite powerful efficacy in some patients, only approximately one-third of the patients see pronounced clinical response to immunotherapeutic intervention (57). It was also reported that immune-mediated cancer control and senescence induction could be achieved and reinforced by the use of ICBs (58). ICBs could enhance the antitumor effect of T cells and NK cells and increase the ability of antigen presentation of dendritic cells to restore senescence barrier. Here, we have demonstrated that risk score could serve as a latent biomarker to predict the response of immunotherapy and screen out the appropriate patients, which was important for precise medicine. Besides, our study found that the high-risk group was positively correlated with a variety of cell death pathways including autophagy. Autophagy is a cellular degradation pathway, which plays a variety of roles in maintaining cell homeostasis. In addition, autophagy also has an impact on cancer initiation, progression, immune infiltration, and metabolism (59). As early as 2009, Narita et al. proposed a new mechanism of autophagy in cell aging: autophagy is activated during aging, which is the same as the result of our study, and its activation is related to the negative feedback of PI3K—mammalian target of rapamycin (mTOR) pathway (60).

Furthermore, we also explored the relationship between risk score and response to chemotherapy. Low doses of chemotherapy itself could induce senescence in cancer cells, which was called chemotherapy-induced senescence. Platinum-based compounds, such as cisplatin, could induce senescence through extensive DNA damage. Moreover, methotrexate and gemcitabine could both induce genotoxic stress by blocking DNA synthesis, thereby inducing cellular senescence (61). Methotrexate, gemcitabine, vinblastine, doxorubicin, and cisplatin were commonly used drugs for MIBC. We found that IC50 for all these drugs were significantly lower in the high-risk score group, which indicated a better response to chemotherapy in this group.

However, some limitations and shortcomings must be addressed in this study. First, the senescence genes were acquired from the CellAge database; as many new senescence genes have been put forward recently, the genes we used for analysis might not be comprehensive enough and this would bring some bias into our studies. Second, the current omics data only provide the level of mRNA and lack protein expression data, which will bring in some inaccuracies. Third, the number of clinical samples is limited and our study lacks external

verification from other clinical data sets apart from the public data. Therefore, we are prepared to collect some clinical samples to further verify our conclusions. Finally, the molecular mechanism has not been characterized and further experiments are needed.

In conclusion, our study provided a comprehensive insight into the interaction between cellular senescence, TMB, TME immune cell infiltration, and response to chemotherapy and immunotherapy and interpreted the complicated regulation mechanisms of senescence in BCa. Better understanding and evaluating senescence could be beneficial in selecting appropriate patients, guiding precise therapy, and improving the prognosis of patients with BCa.

DATA AVAILABILITY STATEMENT

The datasets presented in this study can be found in online repositories. The names of the repository/repositories and accession number(s) can be found in the article/**Supplementary Material**.

AUTHOR CONTRIBUTIONS

J-XS and C-QL analyzed the data, wrote the manuscript, and drew the figures; Z-BZ, S-GW, and Q-DX designed the study; J-ZX, YA, M-YX, X-YZ, NZ, S-YM, and H-DH contributed to the critical revision of the manuscript. J-XS, C-QL, Z-BZ, S-GW, and Q-DX contributed equally to this work. All authors contributed to the article and approved the submitted version.

FUNDING

This work was supported by the Natural Science Foundation of China (81772729).

ACKNOWLEDGMENTS

We thank all the R programming package developers.

SUPPLEMENTARY MATERIAL

The Supplementary Material for this article can be found online at: https://www.frontiersin.org/articles/10.3389/fimmu.2022.908068/full#supplementary-material

Supplementary Figure 1 | The interaction of 4 genes.

Supplementary Figure 2 | The AUC curves of this model in 1, 3, and 5 years.

Supplementary Figure 3 | Response to chemotherapy using other drugs in different risk score group.

REFERENCES

1. Richters A, Aben KKH, Kiemeney L. The Global Burden of Urinary Bladder Cancer: An Update. *World J Urol* (2020) 38(8):1895–904. doi: 10.1007/s00345-019-02984-4
2. Li HZ, Zheng RS, Du LB, Zhang SW, Zhu C, Wei WW, et al. [Bladder Cancer Incidence, Mortality and Temporal Trends in China]. *Zhonghua Zhong Liu Za Zhi* (2021) 43(3):293–8. doi: 10.3760/cma.j.cn112152-20200421-00362
3. Cumberbatch MGK, Jubber I, Black PC, Esperto F, Figueroa JD, Kamat AM, et al. Epidemiology of Bladder Cancer: A Systematic Review and Contemporary Update of Risk Factors in 2018. *Eur Urol* (2018) 74(6):784–95. doi: 10.1016/j.eururo.2018.09.001
4. Babjuk M, Burger M, Compérat EM, Gontero P, Mostafid AH, Palou J, et al. European Association of Urology Guidelines on Non-Muscle-Invasive Bladder Cancer (TaT1 and Carcinoma *In Situ*) - 2019 Update. *Eur Urol* (2019) 76(5):639–57. doi: 10.1016/j.eururo.2019.08.016
5. Witjes JA, Bruins HM, Cathomas R, Compérat EM, Cowan NC, Gakis G, et al. European Association of Urology Guidelines on Muscle-Invasive and Metastatic Bladder Cancer: Summary of the 2020 Guidelines. *Eur Urol* (2021) 79(1):82–104. doi: 10.1016/j.eururo.2020.03.055
6. Patel VG, Oh WK, Galsky MD. Treatment of Muscle-Invasive and Advanced Bladder Cancer in 2020. *CA Cancer J Clin* (2020) 70(5):404–23. doi: 10.3322/caac.21631
7. Ghandour R, Singla N, Lotan Y. Treatment Options and Outcomes in Nonmetastatic Muscle Invasive Bladder Cancer. *Trends Cancer* (2019) 5 (7):426–39. doi: 10.1016/j.trecan.2019.05.011
8. Zhang J, Zhou Q, Xie K, Cheng L, Peng S, Xie R, et al. Targeting WD Repeat Domain 5 Enhances Chemosensitivity and Inhibits Proliferation and Programmed Death-Ligand 1 Expression in Bladder Cancer. *J Exp Clin Cancer Res* (2021) 40(1):203. doi: 10.1186/s13046-021-01989-5
9. Hayflick L, Moorhead PS. The Serial Cultivation of Human Diploid Cell Strains. *Exp Cell Res* (1961) 25:585–621. doi: 10.1016/0014-4827(61)90192-6
10. Muñoz-Espín D, Serrano M. Cellular Senescence: From Physiology to Pathology. *Nat Rev Mol Cell Biol* (2014) 15(7):482–96. doi: 10.1038/nrm3823
11. Hernandez-Segura A, Nehme J, Demaria M. Hallmarks of Cellular Senescence. *Trends Cell Biol* (2018) 28(6):436–53. doi: 10.1016/j.tcb.2018.02.001
12. Sharpless NE, Sherr CJ. Forging a Signature of *In Vivo* Senescence. *Nat Rev Cancer* (2015) 15(7):397–408. doi: 10.1038/nrc3960
13. Calcinotto A, Kohli J, Zagato E, Pellegrini L, Demaria M, Alimonti A. Cellular Senescence: Aging, Cancer, and Injury. *Physiol Rev* (2019) 99(2):1047–78. doi: 10.1152/physrev.00020.2018
14. Campisi J. Aging, Cellular Senescence, and Cancer. *Annu Rev Physiol* (2013) 75:685–705. doi: 10.1146/annurev-physiol-030212-183653
15. Xia Y, Chen S, Cui J, Wang Y, Liu X, Shen Y, et al. Berberine Suppresses Bladder Cancer Cell Proliferation by Inhibiting JAK1-STAT3 Signaling via Upregulation of miR-17-5p. *Biochem Pharmacol* (2021) 188:114575. doi: 10.1016/j.bcp.2021.114575
16. Chen T, Wang H, Zhang Z, Li Q, Yan K, Tao Q, et al. A Novel Cellular Senescence Gene, SENEX, Is Involved in Peripheral Regulatory T Cells Accumulation in Aged Urinary Bladder Cancer. *PloS One* (2014) 9(2): e87774. doi: 10.1371/journal.pone.0087774
17. Wang W, Liu Z, Qu P, Zhou Z, Zeng Y, Fan J, et al. Knockdown of Regulator of Cullins-1 (ROC1) Expression Induces Bladder Cancer Cell Cycle Arrest at the G2 Phase and Senescence. *PloS One* (2013) 8(5):e62734. doi: 10.1371/journal.pone.0062734
18. Meyers RM, Bryan JG, McFarland JM, Weir BA, Sizemore AE, Xu H, et al. Computational Correction of Copy Number Effect Improves Specificity of CRISPR-Cas9 Essentiality Screens in Cancer Cells. *Nat Genet* (2017) 49 (12):1779–84. doi: 10.1038/ng.3984
19. Ho KH, Huang TW, Liu AJ, Shih CM, Chen KC. Cancer Essential Genes Stratified Lung Adenocarcinoma Patients With Distinct Survival Outcomes and Identified a Subgroup From the Terminal Respiratory Unit Type With Different Proliferative Signatures in Multiple Cohorts. *Cancers (Basel)* (2021) 13(9):2128. doi: 10.3390/cancers13092128

20. Avelar RA, Ortega JG, Tacutu R, Tyler EJ, Bennett D, Binetti P, et al. A Multidimensional Systems Biology Analysis of Cellular Senescence in Aging and Disease. *Genome Biol* (2020) 21(1):91. doi: 10.1186/s13059-020-01990-9
21. Leek JT, Johnson WE, Parker HS, Jaffe AE, Storey JD. The Sva Package for Removing Batch Effects and Other Unwanted Variation in High-Throughput Experiments. *Bioinformatics* (2012) 28(6):882–3. doi: 10.1093/bioinformatics/bts034
22. Li T, Fu J, Zeng Z, Cohen D, Li J, Chen Q, et al. TIMER2.0 for Analysis of Tumor-Infiltrating Immune Cells. *Nucleic Acids Res* (2020) 48(W1):W509–w514. doi: 10.1093/nar/gkaa407
23. Yoshihara K, Shahmoradgoli M, Martínez E, Vegesna R, Kim H, Torres-Garcia W, et al. Inferring Tumour Purity and Stromal and Immune Cell Admixture From Expression Data. *Nat Commun* (2013) 4:2612. doi: 10.1038/ncomms3612
24. Xiao B, Liu L, Li A, Xiang C, Wang P, Li H, et al. Identification and Verification of Immune-Related Gene Prognostic Signature Based on ssGSEA for Osteosarcoma. *Front Oncol* (2020) 10:607622. doi: 10.3389/fonc.2020.607622
25. Shen Y, Peng X, Shen C. Identification and Validation of Immune-Related lncRNA Prognostic Signature for Breast Cancer. *Genomics* (2020) 112 (3):2640–6. doi: 10.1016/j.ygeno.2020.02.015
26. Yu G, Wang LG, Han Y, He QY. Clusterprofiler: An R Package for Comparing Biological Themes Among Gene Clusters. *Omics* (2012) 16(5):284–7. doi: 10.1089/omi.2011.0118
27. Wu T, Hu E, Xu S, Chen M, Guo P, Dai Z, et al. Clusterprofiler 4.0: A Universal Enrichment Tool for Interpreting Omics Data. *Innovation (N Y)* (2021) 2(3):100141. doi: 10.1016/j.xinn.2021.100141
28. Hänzelmann S, Castelo R, Guinney J. GSVA: Gene Set Variation Analysis for Microarray and RNA-Seq Data. *BMC Bioinf* (2013) 14:7. doi: 10.1186/1471-2105-14-7
29. Jiang P, Gu S, Pan D, Fu J, Sahu A, Hu X, et al. Signatures of T Cell Dysfunction and Exclusion Predict Cancer Immunotherapy Response. *Nat Med* (2018) 24(10):1550–8. doi: 10.1038/s41591-018-0136-1
30. Necchi A, Joseph RW, Loriot Y, Hoffman-Censits J, Perez-Gracia JL, Petrylak DP, et al. Atezolizumab in Platinum-Treated Locally Advanced or Metastatic Urothelial Carcinoma: Post-Progression Outcomes From the Phase II IMvigor210 Study. *Ann Oncol* (2017) 28(12):3044–50. doi: 10.1093/annonc/mdx518
31. Balar AV, Galsky MD, Rosenberg JE, Powles T, Petrylak DP, Bellmunt J, et al. Atezolizumab as First-Line Treatment in Cisplatin-Ineligible Patients With Locally Advanced and Metastatic Urothelial Carcinoma: A Single-Arm, Multicentre, Phase 2 Trial. *Lancet* (2017) 389(10064):67–76. doi: 10.1016/S0140-6736(16)32455-2
32. Uhlén M, Fagerberg L, Hallström BM, Lindskog C, Oksvold P, Mardinoglu A, et al. Proteomics. Tissue-Based Map of the Human Proteome. *Science* (2015) 347(6220):1260419. doi: 10.1126/science.1260419
33. Rosenberg JE, Hoffman-Censits J, Powles T, van der Heijden MS, Balar AV, Necchi A, et al. Atezolizumab in Patients With Locally Advanced and Metastatic Urothelial Carcinoma Who Have Progressed Following Treatment With Platinum-Based Chemotherapy: A Single-Arm, Multicentre, Phase 2 Trial. *Lancet* (2016) 387(10031):1909–20. doi: 10.1016/S0140-6736(16)00561-4
34. Lee S, Schmitt CA. The Dynamic Nature of Senescence in Cancer. *Nat Cell Biol* (2019) 21(1):94–101. doi: 10.1038/s41556-018-0249-2
35. Hanahan D. Hallmarks of Cancer: New Dimensions. *Cancer Discov* (2022) 12 (1):31–46. doi: 10.1158/2159-8290.CD-21-1059
36. Faget DV, Ren Q, Stewart SA. Unmasking Senescence: Context-Dependent Effects of SASP in Cancer. *Nat Rev Cancer* (2019) 19(8):439–53. doi: 10.1038/s41568-019-0156-2
37. De Blander H, Morel AP, Senaratne AP, Ouzounova M, Puisieux A. Cellular Plasticity: A Route to Senescence Exit and Tumorigenesis. *Cancers (Basel)* (2021) 13(18):4561. doi: 10.3390/cancers13184561
38. Jing C, Duan Y, Zhou M, Yue K, Zhuo S, Li X, et al. Blockade of Deubiquitinating Enzyme PSMD14 Overcomes Chemoresistance in Head and Neck Squamous Cell Carcinoma by Antagonizing E2F1/Akt/SOX2-Mediated Stemness. *Theranostics* (2021) 11(6):2655–69. doi: 10.7150/thno.48375
39. Lei J, Liu X, Liu W, Zhang Y, Liu Z. The Prognostic Value of USP14 and PSMD14 Expression in Non-Small Cell Lung Cancer. *Ann Transl Med* (2021) 9(12):1019. doi: 10.21037/atm-21-2748
40. Sun T, Liu Z, Bi F, Yang Q. Deubiquitinase PSMD14 Promotes Ovarian Cancer Progression by Decreasing Enzymatic Activity of PKM2. *Mol Oncol* (2021) 15(12):3639–58. doi: 10.1002/1878-0261.13076
41. Lv J, Zhang S, Wu H, Lu J, Lu Y, Wang F, et al. Deubiquitinase PSMD14 Enhances Hepatocellular Carcinoma Growth and Metastasis by Stabilizing GRB2. *Cancer Lett* (2020) 469:22–34. doi: 10.1016/j.canlet.2019.10.025
42. Gong Y, Wei ZR. Identification of PSMD14 as a Potential Novel Prognosis Biomarker and Therapeutic Target for Osteosarcoma. *Cancer Rep (Hoboken)* (2021) p:e1522. doi: 10.1002/cnr2.1522
43. Wang CY, Li CY, Hsu HP, Cho CY, Yen MC, Weng TY, et al. PSMB5 Plays a Dual Role in Cancer Development and Immunosuppression. *Am J Cancer Res* (2017) 7(11):2103–20.
44. Liu L, Fu Y, Zheng Y, Ma M, Wang C. Curcumin Inhibits Proteasome Activity in Triple-Negative Breast Cancer Cells Through Regulating P300/miR-142-3p/PSMB5 Axis. *Phytomedicine* (2020) 78:153312. doi: 10.1016/j.phymed.2020.153312
45. Moon SW, Mo HY, Choi EJ, Yoo NJ, Lee SH. Cancer-Related SRCAP and TPR Mutations in Colon Cancers. *Pathol Res Pract* (2021) 217:153292. doi: 10.1016/j.prp.2020.153292
46. Snow CJ, Paschal BM. Roles of the Nucleoporin Tpr in Cancer and Aging. *Adv Exp Med Biol* (2014) 773:309–22. doi: 10.1007/978-1-4899-8032-8_14
47. He Y, Huang C, Cai K, Liu P, Chen X, Xu YI, et al. PRPF19 Promotes Tongue Cancer Growth and Chemoradiotherapy Resistance. *Acta Biochim Biophys Sin (Shanghai)* (2021) 53(7):893–902. doi: 10.1093/abbs/gmab059
48. Yang M, Qiu Y, Yang Y, Wang W. An Integrated Analysis of the Identified PRPF19 as an Onco-Immunological Biomarker Encompassing the Tumor Microenvironment, Disease Progression, and Prognoses in Hepatocellular Carcinoma. *Front Cell Dev Biol* (2022) 10:840010. doi: 10.3389/fcell.2022.840010
49. Yano K, Takahashi RU, Shiotani B, Abe J, Shidooka T, Sudo Y, et al. PRPF19 Regulates P53-Dependent Cellular Senescence by Modulating Alternative Splicing of MDM4 mRNA. *J Biol Chem* (2021) 297(1):100882. doi: 10.1016/j.jbc.2021.100882
50. Chan TA, Yarchoan M, Jaffee E, Swanton C, Quezada SA, Stenzinger A, et al. Development of Tumor Mutation Burden as an Immunotherapy Biomarker: Utility for the Oncology Clinic. *Ann Oncol* (2019) 30(1):44–56. doi: 10.1093/annonc/mdy495
51. Samstein RM, Lee CH, Shoushtari AN, Hellmann MD, Shen R, Janjigian YY, et al. Tumor Mutational Load Predicts Survival After Immunotherapy Across Multiple Cancer Types. *Nat Genet* (2019) 51(2):202–6. doi: 10.1038/s41588-018-0312-8
52. Pickup MW, Mouw JK, Weaver VM. The Extracellular Matrix Modulates the Hallmarks of Cancer. *EMBO Rep* (2014) 15(12):1243–53. doi: 10.15252/embr.201439246
53. Rentschler M, Braumüller H, Briquez PS, Wieder T. Cytokine-Induced Senescence in the Tumor Microenvironment and Its Effects on Anti-Tumor Immune Responses. *Cancers (Basel)* (2022) 14(6):1364:7016. doi: 10.3390/cancers14061364
54. Liu X, Li L, Si F, Huang L, Zhao Y, Zhang C, et al. NK and NKT Cells Have Distinct Properties and Functions in Cancer. *Oncogene* (2021) 40(27):4521–37. doi: 10.1038/s41388-021-01880-9
55. Kaiser M, Semeraro MD, Herrmann M, Absenger G, Gerger A, Renner W. Immune Aging and Immunotherapy in Cancer. *Int J Mol Sci* (2021) 22(13). doi: 10.3390/ijms22137016
56. Balar AV, Kamat AM, Kulkarni GS, Uchio EM, Boormans JL, Roumiguié M, et al. Pembrolizumab Monotherapy for the Treatment of High-Risk Non-Muscle-Invasive Bladder Cancer Unresponsive to BCG (KEYNOTE-057): An Open-Label, Single-Arm, Multicentre, Phase 2 Study. *Lancet Oncol* (2021) 22 (7):919–30. doi: 10.1016/S1470-2045(21)00147-9
57. Binnewies M, Roberts EW, Kersten K, Chan V, Fearon DF, Merad M, et al. Understanding the Tumor Immune Microenvironment (TIME) for Effective Therapy. *Nat Med* (2018) 24(5):541–50. doi: 10.1038/s41591-018-0014-x
58. Brenner E, Schörg BF, Ahmetlić F, Wieder T, Hilke FJ, Simon N, et al. Cancer Immune Control Needs Senescence Induction by Interferon-Dependent Cell

Cycle Regulator Pathways in Tumours. *Nat Commun* (2020) 11(1):1335. doi: 10.1038/s41467-020-14987-6
59. Russell RC, Guan KL. The Multifaceted Role of Autophagy in Cancer. *EMBO J* (2022) p:e110031. doi: 10.15252/embj.2021110031
60. Young AR, Narita M, Ferreira M, Kirschner K, Sadaie M, Darot JF, et al. Autophagy Mediates the Mitotic Senescence Transition. *Genes Dev* (2009) 23 (7):798–803. doi: 10.1101/gad.519709
61. Wang L, Lankhorst L, Bernards R. Exploiting Senescence for the Treatment of Cancer. *Nat Rev Cancer* (2022) 22(6):340–355. doi: 10.1038/s41568-022-00450-9

Conflict of Interest: The authors declare that the research was conducted in the absence of any commercial or financial relationships that could be construed as a potential conflict of interest.

Publisher's Note: All claims expressed in this article are solely those of the authors and do not necessarily represent those of their affiliated organizations, or those of the publisher, the editors and the reviewers. Any product that may be evaluated in this article, or claim that may be made by its manufacturer, is not guaranteed or endorsed by the publisher.

Copyright © 2022 Sun, Liu, Xu, An, Xu, Zhong, Zeng, Ma, He, Zhang, Wang and Xia. This is an open-access article distributed under the terms of the Creative Commons Attribution License (CC BY). The use, distribution or reproduction in other forums is permitted, provided the original author(s) and the copyright owner(s) are credited and that the original publication in this journal is cited, in accordance with accepted academic practice. No use, distribution or reproduction is permitted which does not comply with these terms.

frontiers | Frontiers in Immunology

TYPE Original Research
PUBLISHED 09 August 2022
DOI 10.3389/fimmu.2022.865020

Check for updates

OPEN ACCESS

EDITED BY
Tamas Fulop,
Université de Sherbrooke,
Canada

REVIEWED BY
Irina V. Larionova,
Tomsk National Research Medical Center of the Russian Academy of Sciences, Russia
Natalia Ochocka,
Nencki Institute of Experimental Biology (PAS), Poland

*CORRESPONDENCE
Daofeng Tian
tiandaofeng@163.com
Chunlong Zhong
drchunlongzhong@tongji.edu.cn
Wei Zhou
drzhouwei@yeah.net

†These authors have contributed equally to this work

SPECIALTY SECTION
This article was submitted to Cancer Immunity and Immunotherapy, a section of the journal Frontiers in Immunology

RECEIVED 29 January 2022
ACCEPTED 04 July 2022
PUBLISHED 09 August 2022

CITATION
Zhang C, Liu H, Tan Y, Xu Y, Li Y, Tong S, Qiu S, Chen Q, Su Z, Tian D, Zhou W and Zhong C (2022) MS4A6A is a new prognostic biomarker produced by macrophages in glioma patients.
Front. Immunol. 13:865020.
doi: 10.3389/fimmu.2022.865020

COPYRIGHT
© 2022 Zhang, Liu, Tan, Xu, Li, Tong, Qiu, Chen, Su, Tian, Zhou and Zhong. This is an open-access article distributed under the terms of the Creative Commons Attribution License (CC BY). The use, distribution or reproduction in other forums is permitted, provided the original author (s) and the copyright owner(s) are credited and that the original publication in this journal is cited, in accordance with accepted academic practice. No use, distribution or reproduction is permitted which does not comply with these terms.

MS4A6A is a new prognostic biomarker produced by macrophages in glioma patients

Chunyu Zhang[1,2†], Haitao Liu[3†], Yinqiu Tan[4], Yang Xu[5], Yuntao Li[5], Shiao Tong[5], Sheng Qiu[2], Qianxue Chen[5], Zhongzhou Su[2], Daofeng Tian[5*], Wei Zhou[6*] and Chunlong Zhong[1*]

[1]Department of Neurosurgery, Shanghai East Hospital, School of Medicine, Tongji University, Shanghai, China, [2]Department of Neurosurgery, Huzhou Central Hospital, Affiliated Central Hospital Huzhou Normal University, Huzhou, China, [3]Department of Cardiothoracic Surgery, Jiaxing University, The First Affiliated Hospital, Jiaxing, China, [4]Department of Neurosurgery, Union Hospital, Tongji Medical College, Huazhong University of Science and Technology, Wuhan, China, [5]Department of Neurosurgery, Wuhan University, Renmin Hospital, Wuhan, China, [6]Department of Anesthesia, Huzhou Central Hospital, Affiliated Central Hospital Huzhou Normal University, Huzhou, China

MS4A6A has been recognized as being associated with aging and the onset of neurodegenerative disease. However, the mechanisms of MS4A6A in glioma biology and prognosis are ill-defined. Here, we show that MS4A6A is upregulated in glioma tissues, resulting in unfavorable clinical outcomes and poor responses to adjuvant chemotherapy. Multivariate Cox regression analysis suggested that MS4A6A expression can act as a strong and independent predictor for glioma outcomes (CGGA1: HR: 1.765, $p < 0.001$; CGGA2: HR: 2.626, $p < 0.001$; TCGA: HR: 1.415, $p < 0.001$; Rembrandt: HR: 1.809, $p < 0.001$; Gravendeel: HR: 1.613, $p < 0.001$). A protein–protein interaction (PPI) network revealed that MS4A6A might be coexpressed with CD68, CD163, and macrophage-specific signatures. Enrichment analysis showed the innate immune response and inflammatory response to be markedly enriched in the high MS4A6A expression group. Additionally, single-cell RNA sequencing (scRNA-seq) analysis revealed distinctive expression features for MS4A6A in macrophages in the glioma immune microenvironment (GIME). Immunofluorescence staining confirmed colocalization of CD68/MS4A6A and CD163/MS4A6A in macrophages. Correlation analysis revealed that MS4A6A expression is positively related to the tumor mutation burden (TMB) of glioma, displaying the high potential of applying MS4A6A to evaluate responsiveness to immunotherapy. Altogether, our research indicates that MS4A6A upregulation may be used as a promising and effective indicator for adjuvant therapy and prognosis assessment.

KEYWORDS

glioma, immune microenvironment, prognosis, immunotherapy, indicator

Introduction

Glioma is the most common category of cancer in the central nervous system (CNS), with great aggressiveness and neurological destructiveness (1). According to the latest 2021 glioma classification, glioma malignancy is categorized as WHO II–IV based on histological and molecular features (2). Despite the advanced combination of therapeutic regimens and strategies, including surgical resection, radiation treatment, and temozolomide application, outcomes for glioma are still disappointing, especially for glioblastoma (GBM), for which the overall median survival time (MST) is no more than 20 months (3). Therefore, the main objective of the present study was to explore new possible and effective targets for personalized therapeutic management and treatment of glioma.

Publicly accessible data from TCGA, CCGA, and GEO allow for researching clinicopathological features using large-scale tumor samples, which greatly contributes to the detection and identification of effective tumor-associated candidates (4–6). In addition, the widespread application of single-cell RNA sequencing (scRNA-seq) technology has led to the development and establishment of accurate tools with high sensitivity and invasiveness for use in early disease recognition, diagnosis, and treatment. For example, based on scRNA-seq analysis, PDIA5 (Protein Disulfide Isomerase Family A Member 5) has been identified as associated with worse glioma outcomes and induction of macrophage infiltration (7). Recent studies have demonstrated a potential relationship between MS4A6A alterations and aging-related diseases, such as the SNP rs610932, which is located in the 3' untranslated region of MS4A6A and correlates with cortical and hippocampal atrophy (8). Furthermore, elevated MS4A6A expression in late-onset Alzheimer's disease (AD) tissues has been identified as correlating with an elevated Braak Tangle Score, a neuropathological measure for AD development and progression (9–11). Recent research has also revealed that MS4A6A dysregulation is involved in the acute phase of Kawasaki disease (KD) *via* macrophage infiltration induction (12). Tumor-associated macrophages (TAMs) are the most representative cell population of tumor-infiltrating leukocytes (TILs) in the glioma immune microenvironment (GIME). TAMs are heterogeneous populations that include brain-resident microglia, border-associated macrophages (BAMs), and bone marrow-derived macrophages (BMDMs), which correlate negatively with infiltration of T cells, neutrophils, and plasmacytoid dendritic cells (pDCs), leading to the immunosuppressive nature of the GIME (13–15). Moreover, intratumoral TAM accumulation is increased along with higher pathological grade in glioma, indicating the critical role of TAMs in tumor development (16, 17). In previous research, *t*-test analysis of 33 subjects showed that dysregulated methylation of MS4A6A may contribute to poor prognosis in GBM; however, the study failed to illustrate the association of methylation and expression of the potential marker (18). Another study on 154 samples proposed that MS4A6A overexpression has no significant correlation with GBM outcomes ($p = 0.83$) (19). As comprehensive large-scale analysis of the biological role of the potential marker MS4A6A in glioma tumorigenesis and prognosis has not been fully performed, there is a lack of in-depth insight.

Here, we report that MS4A6A is hypomethylated and overexpressed in glioma tissue at both transcriptional and protein levels, which is related to a significant decrease in overall survival (OS). We also identified that MS4A6A may promote the level of macrophage infiltration in the GIME.

Materials and methods

MS4A6A expression and methylation analysis

TCGA-LGG and TCGA-GBM datasets were obtained, including mRNA expression data, somatic mutation data, and follow-up information from the database TCGA (https://portal.gdc.cancer.gov/). Both sets were merged into a TCGA glioma set for further analysis. Additionally, MS4A6A expression data in the CGGA1 and CGGA2 datasets were acquired from CGGA. The RNA-seq data of TCGA and CGGA glioma datasets were log2(fragments per kilobase of exon model per million fragments mapped (FPKM)+ 1) transformed. MS4A6A microarray expression data in the Gravendeel and Rembrandt datasets were acquired from GlioVis. Clinical data such as age, sex, isocitrate dehydrogenase (IDH) status, 1p19q status, WHO grade, and O^6-methylguanine-DNA methyltransferase promoter (MGMTp) status were obtained from TCGA and CGGA; information such as age, sex, and WHO grade in Gravendeel and WHO grade in Rembrandt were also obtained. Samples with no survival data were excluded. Finally, a total of 2,089 cases, including 601 samples from TCGA, 965 from CGGA (CGGA1 cohort, $N = 656$; CGGA2 cohort, $N = 305$), 335 from Rembrandt, and 192 from Gravendeel, were included in our research (Table S1). Human Protein Atlas (HPA) was utilized to confirm MS4A6A expression levels in glioma tissues at the protein level. To detect the mechanisms of MS4A6A dysregulation, exploration of the mutation status of MS4A6A was conducted using the cBioPortal database. Three subsequent databases were selected for MS4A6A methylation analysis. First, DiseaseMeth version 2.0 (20) was chosen to evaluate MS4A6A methylation differences between glioma samples and nontumor brain tissues. Moreover, we investigated the correlation between the expression and DNA methylation status of MS4A6A based on the MEXPRESS database (21). Expression differences in DNA methyltransferases such as DNMT1 (DNA methyltransferase 1), DNMT3A (DNA methyltransferase 3 alpha), and DNMT3B (DNA methyltransferase 3 beta) between subgroups divided by

MS4A6A expression were analyzed using the CGGA database. The workflow of this study is depicted in Figure S1.

Functional annotation of differentially expressed genes related to MS4A6A expression

Patients in the CGGA1 set were divided into two subgroups according to the optimal cutoff obtained by the Survminer package based on MS4A6A expression files. First, DEGs between the subgroups ($|log2FC| > 1$ and $FDR < 0.05$) were detected using the R package edgeR and then visualized by volcano plots. Then, DEGs were selected for further analysis using the R package clusterProfiler (22) for Gene Ontology (GO), Kyoto Encyclopedia of Genes and Genomes (KEGG), and Gene Set Enrichment Analysis (GSEA). A PPI network related to MS4A6A was constructed by the STRING database (23).

Inference of immune infiltrates in the GIME

Infiltrating immune cells constitute a high percentage of nontumor cells in the tumor microenvironment and exert significant effects on cancer biology. For quantification of immune infiltrates in tumor samples, the CIBERSORT algorithm (24) was used with RNA-seq data for the CGGA1 cohort, with 1,000 permutations preset. The TIMER database (25) was selected to calculate the correlation between MS4A6A expression and six types of infiltrating immune cells in the GIME. The ESTIMATE database (26) provides calculated immune scores of TCGA data as representative of infiltrative fractions of immune cells in tumor samples. Immune scores of LGG and GBM patients in TCGA cohorts were divided into two groups, separately, in accordance with the optimal cutoffs of MS4A6A expression.

Human samples

Human tissues were obtained from the Department of Neurosurgery in Renmin Hospital of Wuhan University from July 2017 to July 2020. Frozen (at −80°C) samples, including 9 normal brain samples and 23 glioma samples, were used for real −time quantitative PCR (RT−qPCR) analysis. A total of 124 paraffin-embedded glioma tissues were selected for immunohistochemical staining (IHC) and immunofluorescence staining. Additionally, nine normal paraffin-embedded brain samples were chosen for IHC. Details of the included samples are shown in Table S2. The enrolled patients received no treatment before biopsy. Each subject signed written informed consent before enrollment, and our study received approval from the Institutional Ethical Boards of Wuhan University Renmin Hospital.

Real−time quantitative PCR analysis

RNA extraction was conducted using the PrimeScriptTM RT Reagent Kit with gDNA Eraser (Takara Bio Inc, Japan) in accordance with the manufacturer's protocols and transcribed into cDNA for further analysis. RT-qPCR was conducted with SYBR Premix Ex Taq (Takara Bio Inc., Japan). The primer sets are provided in Table S3. β-Actin was used for normalization.

Immunohistochemistry

Sections were deparaffinized, hydrated, and subjected to antigen retrieval in 10 mM sodium citrate (pH 6.0). Endogenous peroxidase was blocked with 3% H_2O_2 for 30 min. The sections were blocked with 10% normal goat serum and incubated with primary antibodies (Abcam, America) overnight, followed by incubation with a secondary antibody (Servicebio, China). Signals were evaluated by DAB staining (Servicebio, China). We obtained IHC images using an Olympus BX51 microscope (Olympus). Two independent pathologists scored the slides for the percentage of positive cells per mm^2 using ImageJ software. IHC scores were evaluated as follows: 0 was considered background staining; 1, 2, and 3 were treated as faint, moderate, and strong staining, respectively. IHC expression was scored as 0–1 for low expression and 2–3 for high expression.

Immunofluorescence staining

Sections were deparaffinized and hydrated, and antigen was retrieved in 10 mM sodium citrate (pH 6.0); the slides were then washed three times with PBS. Diluted primary antibodies against CD68 (BOSTER, China, dilution ratio: 1:400), CD163 (Abcam, America, dilution ratio: 1:500), and MS4A6A (Abcam, America, dilution ratio: 1:200) were incubated at 4°C overnight, followed by a horseradish peroxidase (HRP)-labeled secondary antibody (SeraCare, China, dilution ratio: 1:200) at 37°C for 1 h under dark conditions. DAPI (ANT046, Antgene) was added in the dark for 5 min, and we obtained IF staining images using a fluorescence microscope (Olympus BX51, Japan).

Single-cell RNA sequencing analysis

We first detected MS4A6A expression features based on the TISCH database (http://tisch.comp-genomics.org). scRNA-seq data acquisition (GSE138794) was carried out using the GEO

database, and 10 samples, including both five LGGs and five GBMs, were subjected to in-depth analysis. Samples were combined using the merge function in the Seurat package. Cells with poor quality (<200 genes/cell, <3 cells/gene, >20% mitochondrial genes, and <10% ribosomal genes) were excluded. Hemoglobin genes were removed due to their low expression levels. Finally, 16,158 genes and 19,667 cells in 10 samples were included in downstream analysis. The top 10 components of principal component analysis (PCA) on the normalized data were subjected to UMAP for dimension reduction, and the scRNA-seq data were processed with the R package Seurat. Specific cell markers were obtained for cell category annotation from the CellMarker database (27) and previous findings (13, 14, 28–34).

Statistical analysis

Examination of data normality was conducted based on the Shapiro–Wilk test. The Wilcoxon test for nonparametric data and *t*-test for parametric data were used for comparisons between two groups. The optimal cutoff was assessed and acquired using the surv_cutpoint function in the R package Survminer to separate objects into two subgroups in the corresponding independent cohort based on MS4A6A expression. Kaplan–Meier (K-M) curves were plotted. The log-rank test was chosen, and *p*-values were evaluated. The independent predictive potential of MSA4A6 expression was assessed based on multivariate Cox regression analysis. The prediction accuracy of MS4S6A expression for 1-, 3-, and 5-year OS was determined using ROC (receiver operating characteristic) curves. Mutation files of TCGA glioma sets were visualized based on the R package maftools. All statistical analyses were performed using R (v4.1.0). All tests were two-sided, and $p < 0.05$ was considered significant.

Results

MS4A6A is overexpressed and hypomethylated in glioma

Expression of MS4A6A in TCGA, Rembrandt, and Gravendeel was analyzed and visualized using data from GEPIA and GlioVis. The results showed significant overexpression of MS4A6A in glioma compared with nontumor brain samples; additionally, the elevated level of MS4A6A incrementally correlated positively with glioma WHO grade (Figures 1A–C). Furthermore, using the HPA database, we verified that MS4A6A was overexpressed in glioma at the protein level (Figures S2A–C). However, we found no significant differences among normal brain, low-grade glioma (LGG), and high-grade glioma (HGG) tissues, which might be due to the small size of the samples included in HPA (Figure S2D). RT-qPCR and IHC staining using tissues from healthy controls and LGG and GBM patients validated that MS4A6A is overexpressed in glioma (Figures 1D–H).

Hypomethylation of MS4A6A negatively modulates MS4A6A expression in glioma

To further elucidate the aberrant epigenetic and epigenomic mechanisms involved in MS4A6A dysregulation, we first conducted correlation analysis of methylation and expression. Expression levels of DNMT1, DNMT3A, and DNMT3B in the $MS4A6A^{high}$ subgroup were significantly elevated in comparison with those in the $MS4A6A^{low}$ subgroup (Figure 1I). Data from the DiseaseMeth database revealed that the degree of MS4A6A methylation was markedly higher in normal brain samples than in gliomas and correlated negatively with pathological grade (Figure 1J). In addition, the methylation data for MS4A6A were strongly related to its expression level (Figure 1K), which was validated by the Spearman correlation test ($\rho = -0.42$, $p < 2.2e{-}16$, Figure 1L). Using the MEXPRESS database, we detected six CpG sites (cg20284999, cg24026212, cg06881914, cg04353769, cg00673646, and cg03055440) in the DNA promoter regions of MS4A6A correlating negatively with MS4A6A expression in LGG tissues and that promoter methylation of cg03055440 had a negative effect on MS4A6A expression in GBM tissues (Figures 2A, B). Finally, we examined copy number changes in MS4A6A. cBioPortal analysis demonstrated no alterations in MS4A6A (Figure S2E). In summary, these findings indicate that MS4A6A is overexpressed in glioma and that hypomethylation is the major epigenetic mechanism leading to overexpression of MS4A6A in glioma.

Evaluation of prognostic significance and prediction accuracy of MS4A6A

To evaluate the prognosis-predicting potential of MS4A6A overexpression, data from TCGA, GlioVis, and CGGA were selected for analysis. According to the optimal cutoff of the expression values of MS4A6A in each dataset, the visualized K-M survival curves and log-rank test confirmed tremendous survival differences between the groups. Figures 3A–C and Figures S3A, B demonstrate that patients in the low MS4A6A expression group had better outcomes than their counterparts with high MS4A6A expression (log-rank test, $p < 0.001$). Based on AUCs, MS4A6A expression strongly and accurately predicts glioma OS at 1 year (CGGA1: 0.63; GGGA2: 0.68; TCGA: 0.77; Rembrandt: 0.60; Gravendeel: 0.62), at 3 years (CGGA1: 0.69; GGGA2: 0.75; TCGA: 0.74; Rembrandt: 0.65; Gravendeel: 0.69), and at 5 years (CGGA1: 0.69; GGGA2: 0.77; TCGA: 0.69; Rembrandt: 0.68; Gravendeel: 0.68) (Figures 3D–F

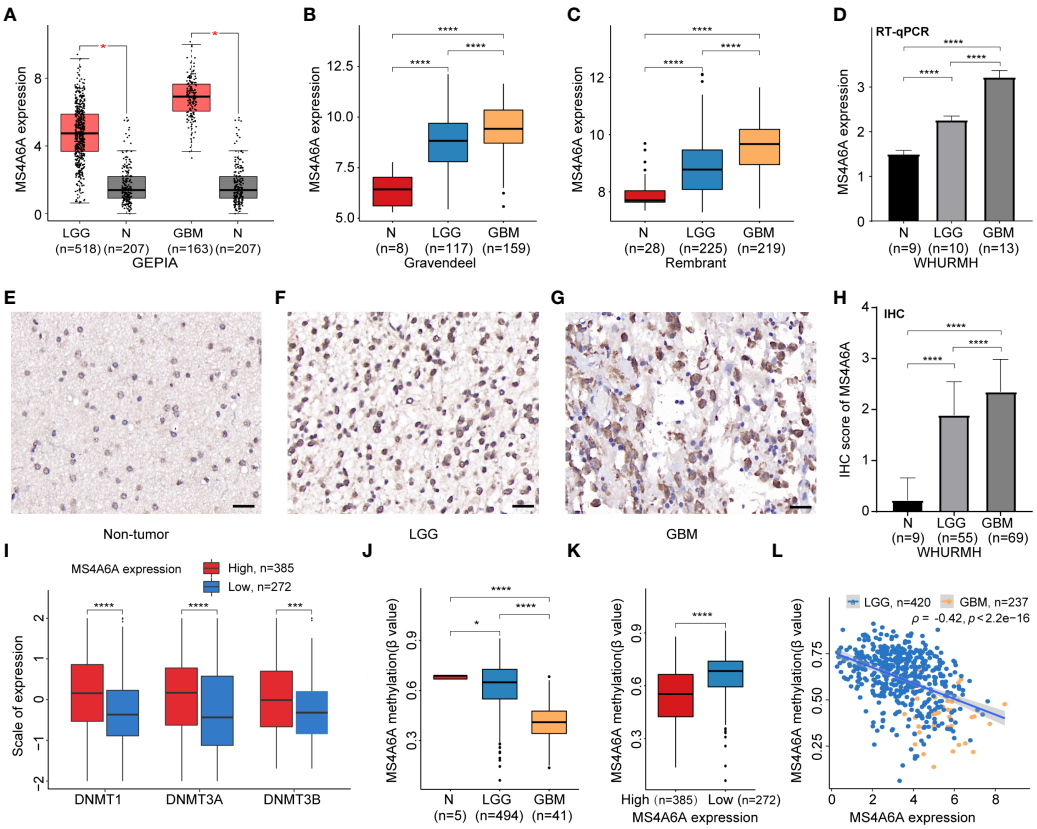


FIGURE 1
Expression and methylation analysis of MS4A6A in glioma.MS4A6A is upregulated in glioma explored based on public data **(A-C)** and validated by RT-PCR **(D)**; representative IHC staining images of normal control **(E)**, LGG **(F)**, and GBM **(G)**; scale bar, 20 µm. GBM and LGG samples had higher IHC scores than normal samples **(H)**. DNA methyltransferases are upregulated in the high MS4A6A expression group; the expression profiles were Z score normalized **(I)**. The MS4A6A methylation level correlates negatively with glioma WHO grade **(J)** and demonstrated differences between subgroups according to MS4A6A expression **(K)**. MS4A6A methylation has a negative impact on its mRNA expression **(L)**. *p*-values were obtained from the Wilcoxon test **(A–C, I–K)** and *t*-test **(D–H)** (bar plots show means ± SD; ns, $p > 0.05$, *$p < 0.05$; ***$p < 0.001$; ****$p < 0.0001$).

and Figures S3C, D). Univariate and multivariate Cox regression analyses of clinicopathological covariates and MS4A6A expression showed MS4A6A to constitute an index that can independently assess glioma outcomes in the CGGA1 (HR: 1.765, $p < 0.001$), CGGA2 (HR: 2.626, $p < 0.001$), TCGA (HR: 1.415, $p < 0.001$), Rembrandt (HR: 1.809, $p < 0.001$), and Gravendeel (HR: 1.613, $p < 0.001$) sets (Table 1 and Table S4). In addition, patients with low MS4A6A had favorable outcomes when they received adjuvant therapy (Figures S4A–D).

Association of MS4A6A expression with clinical subgroup

The prognostic ability of MS4A6A expression was further evaluated in gliomas with distinct clinical and pathological parameters in CGGA1, CGGA2, and TCGA cohorts. We found that MS4A6A expression had no correlation with sex or MGMTp status in glioma. However, 1p19q deletion, IDH wild-type or WHO IV correlated significantly with higher MS4A6A expression (Figures S5A–C). Elevated expression of MS4A6A was found in glioma patients with a mean age > 43 years (Figures S5A–C), demonstrating the tight association of MS4A6A expression with the aging process. Moreover, according to K-M plots, the survival differences were still obvious after grouping by MS4A6A expression and clinicopathologic subgroups (log-rank test, $p < 0.001$; Figures 4A–F, Figures S6A–F and Figures S7A–F), demonstrating that the MS4A6A expression level might play an important role in glioma OS classification.

Functional enrichment analysis of MS4A6A-related DEGs

To further explore the potential functions of MS4A6A in glioma, GO and KEGG pathway enrichment analyses were

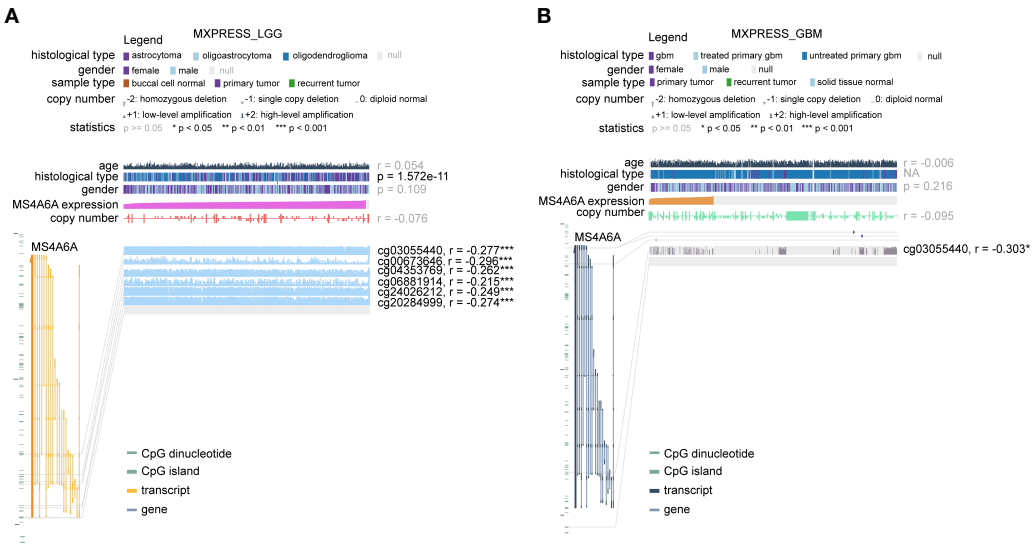


FIGURE 2
The DNA methylation level of MS4A6A in LGG **(A)** and GBM **(B)** correlates negatively with the MS4A6A expression level using data from the MEXPRESS database. ***P < 0.001.

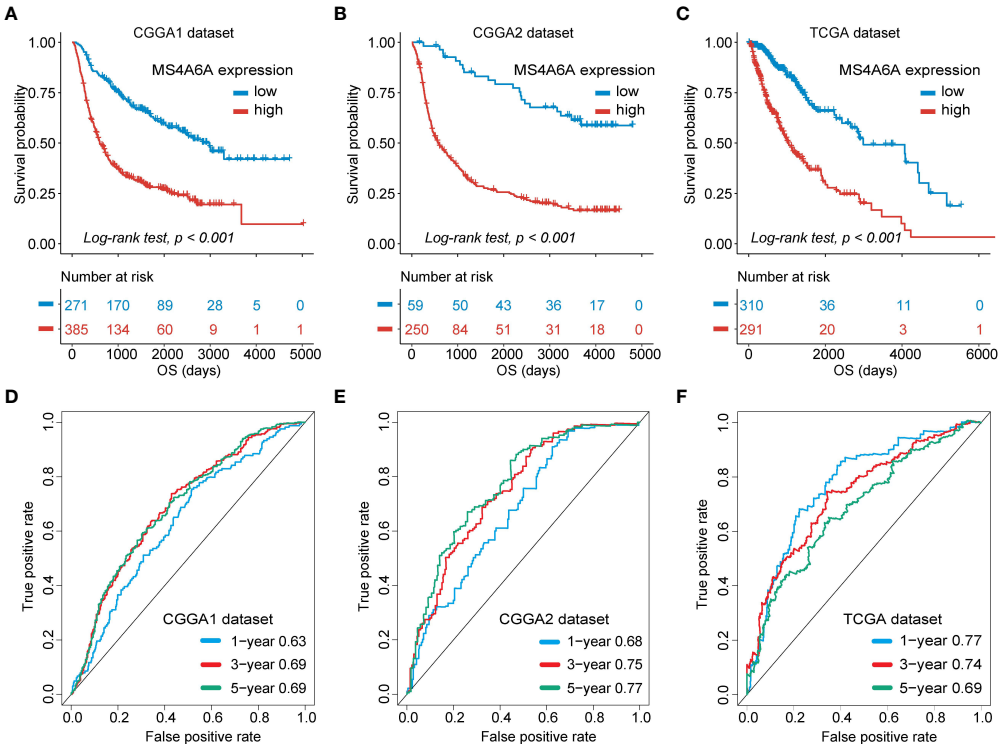


FIGURE 3
Survival analysis of MS4A6A expression and prediction accuracy assessment.Kaplan–Meier curves of survival differences between MS4A6A subgroups in the CGGA1 set **(A)**, CGGA2 set **(B)**, and TCGA set **(C)**. ROC curves calculating the predictive accuracy of MS4A6A in the CGGA1 set **(D)**, CGGA2 set **(E)**, and TCGA set **(F)** for OS at 1, 3, and 5 years.

10.3389/fimmu.2022.865020

TABLE 1 Cox regression analysis of the clinical variables, and survival in the CGGA1, CGGA2 and TCGA cohorts.

	CGGA1			CGGA2			TCGA		
	HR	95% CI	*P*	HR	95% CI	*P*	HR	95% CI	*P*
Univariate Cox regression analysis									
Grade	3.791	3.089-4.654	< 0.001	4.888	3.636-6.571	< 0.001	10.884	7.783-15.221	< 0.001
Gender	1.061	0.868-1.297	0.563	0.924	0.702-1.216	0.572	1.092	0.824-1.447	0.541
Age	1.026	1.018-1.035	< 0.001	1.033	1.02-1.046	< 0.001	1.074	1.062-1.086	< 0.001
IDH status	3.093	2.510-3.812	< 0.001	2.777	2.099-3.674	< 0.001	8.840	6.561-11.91	< 0.001
1p19q status	3.733	2.691-5.177	< 0.001	5.887	3.608-9.606	< 0.001	3.820	2.449-5.957	< 0.001
MGMTp status	1.257	1.01-1.566	0.041	1.196	0.909-1.573	0.202	3.223	2.419-4.294	< 0.001
MS4A6A	2.409	1.938-2.993	< 0.001	4.168	2.668-6.511	< 0.001	3.314	2.449-4.484	< 0.001
Multivariate Cox regression analysis									
Grade	2.152	1.594-2.905	< 0.001	2.529	1.799-3.554	< 0.001	2.257	1.506-3.383	< 0.001
Age	1.009	1-1.018	0.043	1.014	1.001-1.026	0.035	1.052	1.039-1.066	< 0.001
IDH status	1.472	1.09-1.987	0.012	1.013	0.704-1.459	0.943	2.645	1.667-4.196	< 0.001
1p19q status	2.021	1.337-3.056	0.001	3.573	2.096-6.09	< 0.001	2.140	1.286-3.562	0.003
MGMTp status	1.105	0.870-1.404	0.412	1.101	0.820-1.479	0.522	1.187	0.838-1.682	0.334
MS4A6A	1.618	1.206-2.17	0.001	2.634	1.627-4.264	< 0.001	1.415	1.000-2.004	0.041

conducted based on DEGs between groups divided by MS4A6A expression. We found that expression of 1,494 genes was dysregulated, including 1,376 upregulated and 118 downregulated genes (Table S5). In addition, CD68 (CD68 molecule) and HLA-DRA (major histocompatibility complex, class II, DR alpha) were upregulated in the high MS4A6A expression group (Figure 5A). GO analysis of the upregulated genes indicated involvement in immune activation-related

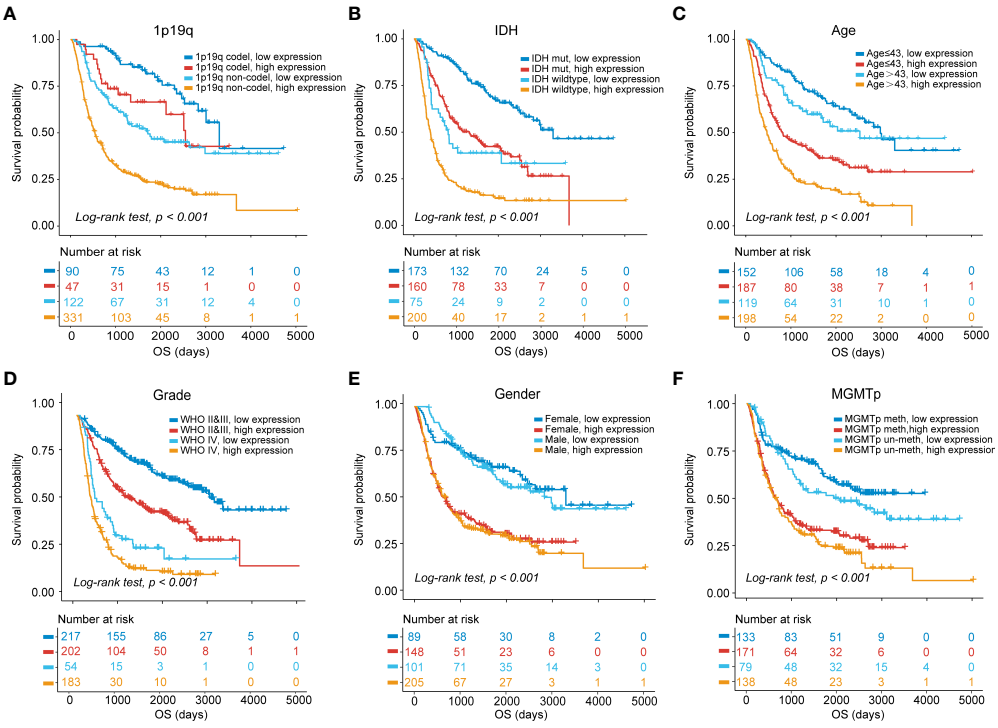


FIGURE 4
OS stratification analysis.Kaplan–Meier curves of gliomas in the CGGA1 cohort based on the combined effects of MS4A6A expression and 1p19q status **(A)**, IDH status **(B)**, age **(C)**, grade **(D)**, sex **(E)**, and MGMTp status **(F)**.

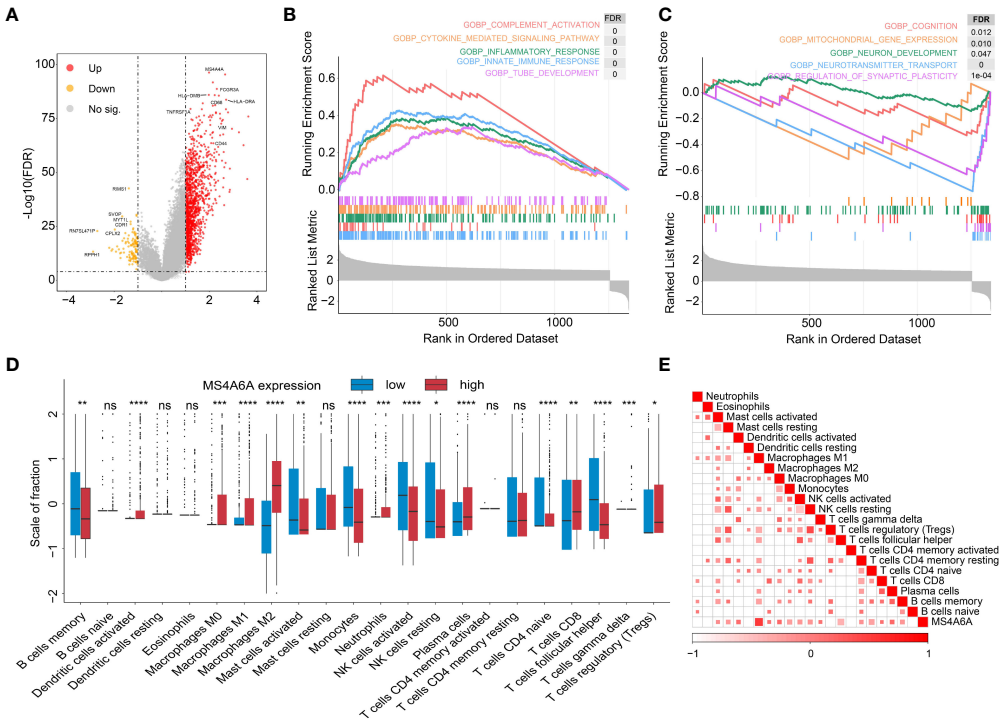


FIGURE 5
Functional annotation of MS4S6A-related genes and correlation between MS4A6A expression and immune infiltrates.Volcano plot of differentially expressed genes (DEGs) between high and low MS4A6A expression groups **(A)**. GSEA of upregulated **(B)** and downregulated **(C)** DEGs. Box plots of 22 immune cell infiltration levels between the high and low MS4A6A groups **(D)**. Correlation between MS4A6A expression and TILs (tumor-infiltrating lymphocytes) **(E)** (ns, $p > 0.05$, *$p < 0.05$; **$p < 0.01$; ***$p < 0.001$; ****$p < 0.0001$).

processes, such as the MHC protein complex, regulation of mononuclear cell proliferation and antigen processing and presentation, and oncogenic processes, such as extracellular matrix remodeling. KEGG analysis demonstrated that genes with overexpression are mainly enriched in immunosuppressive and carcinogenic pathways, such as the IL-17 and p53 signaling pathways (Table S6 and Figure S8A). Furthermore, GO analysis of downregulated genes showed enrichment of glutamatergic synapse and GABA receptor activity, and KEGG analysis revealed that downregulated genes are associated with cognition (Table S7 and Figure S8B). PPI networks are composed of proteins interacting with each other, and we used the STRING online tool to illustrate potential proteins related to MS4A6A. We found that MS4A6A might be coexpressed with ABCA7 (ATP Binding Cassette Subfamily A Member 7), BIN1 (Bridging Integrator 1), C1orf162 (Chromosome 1 Open Reading Frame 162), CD163 (CD163 Molecule), CD2AP (CD2-Associated Protein), CD33 (CD33 Molecule), FGL2 (Fibrinogen Like 2), MS4A4E (Membrane Spanning 4-Domains A4E), and PICALM (Phosphatidylinositol Binding Clathrin Assembly Protein) (Figure S8C). CD163, a phenotypic marker of M2 macrophages, has been applied to differentiate M2 from M1 macrophages, and interactions between CD163 and MS4A6A might indicate the role of MS4A6A in inducing macrophage infiltration. Finally, GSEA was conducted for glioma samples, and GOBP: innate immune response and GOBP: Toll-like signaling pathway were enriched in the MS4A6A high expression group (Figures 5B, C). For an in-depth understanding of enrichment differences between MS4A6A subgroups of gliomas in the same WHO grade group, we conducted enrichment analysis on DEGs between MS4A6A LGG and in GBM subgroups (Tables S8, S9). The results showed processes including GO: myeloid leukocyte activation and GO: lymphocyte mediated immunity to be significantly enriched in the MS4A6A high expression subgroup in LGG and GBM, respectively (Tables S10, S11). These findings show that MS4A6A elevation in glioma might be involved in modulating immune suppression by inducing myeloid leukocyte infiltration, independent of glioma grade.

Insight into the role of MS4A6A in immune infiltrates in the GIME

It has been demonstrated that immune cells in the tumor microenvironment play a role in carcinogenesis and cancer development. To estimate the possible correlation of MS4A6A

with TILs in the GIME, we first carried out correlation analysis on deconvoluted data from the CIBERSORT website and found a strong correlation between the infiltrative levels of macrophages and MS4A6A (Figures 5D, E). Using the calculated data from the ESTIMATE database, patients in the MS4A6A^{high} group had statistically higher immune scores than those in the MS4A6A^{low} subgroup in the cohorts TCGA-GBM and TCGA-LGG (Figure S8D, E, Wilcoxon test, $p < 0.001$, respectively). As shown in Figure S8F, the MS4A6A expression level based on the TIMER database in GBM was significantly related to infiltration of B cells (ρ = 0.378, p = 1.13e-15), CD8+ T cells (ρ = −0.362, p = 2.26e-14), CD4+ T cells (ρ = 0.147, p = 2.60e-03), macrophages (ρ = 0.319, p = 2.37e-11), neutrophils (ρ = 0.371, p = 4.04e-15), and dendritic cells (ρ = 0.378, p = 1.30e−15); for LGG, the MS4A6A expression level was also associated with infiltration of B cells (ρ = 0.445, p = 1.16e-24), CD8+ T cells (ρ = 0.233, p = 2.73e-07), CD4+ T cells (ρ = 0.691, p = 6.04e-69), macrophages (ρ = 0.741, p = 2.03e-83), and neutrophils (ρ = 0.668, p = 8.98). After adjustment based on glioma purity, MS4A6A remained notably related to the majority of signatures of immune cells, particularly macrophages (GBM: CD68: ρ = 0.623, $p < 0.001$; LGG: CD68: ρ = 0.805, $p < 0.001$) and M2 macrophages (GBM: CD163: ρ = 0.591, $p < 0.001$; LGG: CD163: ρ = 0.750, $p < 0.001$) (Table 2). Additionally, there was a high degree of correlation between MS4A6A and the molecular signatures of exhausted T cells, for example, a strong correlation of MS4A6A expression with HAVCR2 (hepatitis A virus cellular receptor 2) expression (GBM: ρ = 0.660, $p < 0.001$; LGG: ρ = 0.714, $p < 0.001$) (Table 2), demonstrating the pivotal role played by MS4A6A in HAVCR2-modulated T-cell exhaustion.

TABLE 2 Correlation analysis between MS4A6A expression and related markers of immune cells using data in TIMER database.

Description	Gene markers	GBM		LGG	
		Cor	*P*	Cor	*P*
B cell	CD19	0.316	***	0.375	**
	CD79A	0.405	***	0.42	***
T cell (general)	CD3D	0.582	***	0.543	***
	CD3E	0.544	***	0.595	***
CD8+ T cell	CD2	0.605	***	0.613	***
	CD8A	0.243	**	0.163	***
	CD8B	0.393	***	0.24	***
Monocyte	CD86	0.752	***	0.738	***
	CSF1R	0.59	***	0.568	***
TAM	CCL2	0.406	***	0.466	***
	CD68	0.623	***	0.805	***
	IL10	0.74	***	0.601	***
M1 Macrophage	NOS2	-0.017	ns	-0.233	***
	IRF5	0.392	***	0.669	***
M2 Macrophage	CD163	0.591	***	0.750	***
	VSIG4	0.737	***	0.651	***
	MS4A4A	0.884	***	0.893	***
Neutrophils	CEACAM8	-0.228	**	0.011	ns
	ITGAM	0.398	***	0.593	ns
	CCR7	0.501	***	0.436	ns
Natural killer cell	KIR2DL1	0.184	*	0.043	ns
	KIR2DL3	0.025	ns	0.226	***
	KIR3DL1	0.066	ns	0.071	ns
	KIR3DL2	0.099	ns	0.232	ns
	KIR3DL3	0.084	ns	-0.022	ns
	KIR2DS4	0.118	ns	0.242	ns
Dendritic cell	CD1C	0.384	***	0.511	***
	THBD	0.356	***	0.352	***
	NRP1	0.208	*	0.387	***
	IL3RA	0.029	ns	0.118	**
	ITGAX	0.151	ns	0.484	***
Th1	TBX21	0.29	***	0.372	***
	STAT4	0.245	**	-0.276	***
	STAT1	0.191	*	0.428	***
	IFNG	0.186	*	0.252	***
	TNF	0.23	**	0.227	***
Th2	GATA3	0.175	*	0.42	***
	STAT6	0.265	**	0.348	***
	STAT5A	0.228	**	0.602	***
	IL13	-0.122	ns	-0.015	ns
Tfh	BCL6	-0.153	ns	0.169	ns
	IL21	0.03	ns	0.085	ns
Th17	IL17A	-0.169	*	-0.005	ns
Treg	FOXP3	0.121	ns	-0.126	ns
	CCR8	0.462	***	0.227	ns
	STAT5B	-0.199	*	0.075	ns
	TGFB1	0.319	***	0.608	***

(Continued)

MS4A6A correlates with macrophage infiltration validated by scRNA-seq

To better illustrate the role played by MS4A6A in immune infiltration in the GIME, scRNA-seq analysis was performed. First, based on the six datasets (GSE102130, GSE103224, GSE138794, GSE89567, GSE131928_Smart-seq2, and GSE131928_10X) from the TISCH database, we found MS4A6A to be exclusively expressed in the monocyte/macrophage cluster (Figures S9A–G). For further analysis of the main macrophage subpopulations in which MS4A6A is involved, 10 scRNA-seq glioma samples were introduced (Figure S10A). A total of 16,158 cells were separated into 16 main clusters by UMAP for nonlinear dimension reduction on the top 10 principal components from PCA (Figures S10B, C), with a parameter resolution of 0.10 (Figure S10D). Table S12 demonstrates the profiles of DEGs between each cluster. Sixteen clusters of cells were identified, namely astrocyte, oligodendrocyte precursor cell, neuron, radial glial cell (RGC), bone marrow-derived M2b macrophage (BMDM M2b), oligodendrocyte cell, bone marrow-derived M2c macrophage (BMDM M2c),

10.3389/fimmu.2022.865020

TABLE 2 Continued

Description	Gene markers	GBM		LGG	
		Cor	*P*	Cor	*P*
T cell exhaustion	PDCD1	0.362	***	0.568	***
	CTLA4	0.45	***	0.359	***
	HAVCR2	0.66	***	0.714	***
	GZMB	0.373	***	0.342	***

LGG, low grade glioma; TAM, tumor-associated macrophage; Th, T helper cell; Tfh, Follicular helper T cell; Treg, regulatory T cell; Cor, R value of Spearman's correlation; None, correlation without adjustment; Purity, correlation adjusted by purity. ns, P > 0.05; *P < 0.05; **P < 0.01; ***P < 0.001.

oligodendroglioma stem cell, cancer-associated fibroblast (CAF), MHC^{lo} meningeal border-associated macrophage (MHC^{lo} meningeal BAM), microglia, neoplastic cell (mesenchymal), cancer stem cell (proneural), glial cell, Schwann cell, and endothelial cell (Figure 6A), based on markers retrieved from the CellMarker database and previous findings (13, 14, 28–34). These results confirm that a resolution of 0.10 is biologically valid. The expression profiles of the corresponding markers in all cell clusters are displayed in Table S13 and visualized in Figure 6B. We subsequently analyzed the expression level of MS4A6A in the divided clusters, showing that MS4A6A is mainly expressed in macrophages, including BMDM M2b, BMDM M2c, and MHC^{lo} meningeal BAMs (Figure 6B). The three clusters are differentiated cells that have been confirmed to be immunosuppressive cells in the glioma microenvironment (35, 36). We visualized the correlation of MS4A6A/CD68 and MS4A6A/CD163 expression using the blend function of the Seurat R package, which confirmed the expression feature of MS4A6A to be quite dominant in macrophages (Figure 6C). Representative IF staining images for CD68/MS4A6A and CD163/MS4A6A confirmed these coexpression and colocalization features in macrophages (Figure 6D).

Correlation between MS4A6A expression and the cancer somatic genome

Recently, many studies have revealed that cancers with an elevated tumor burden mutation (TMB) may show an increased treatment response to anticancer immunotherapeutic strategies (37, 38). Admittedly, MS4A6A expression values and TMB values increase with glioma WHO grade; however, there is no direct research on the relationship of both factors to date. Hence, we made efforts to detect inherent relationships between TMB and MS4A6A expression. As a result, patients with higher MS4A6A expression had significantly increased TMB values

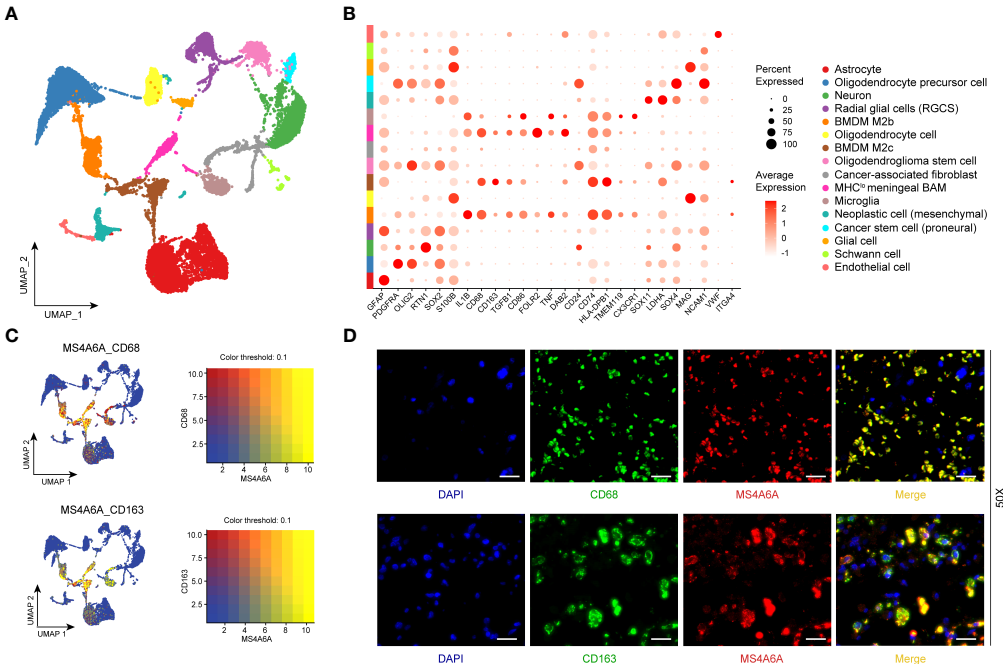


FIGURE 6
Single-cell RNA-seq analysis and immunofluorescent **(IF)** staining.UMAP plot mapping assigned cell types across glioma samples (*N* = 10). Each cell type is defined by a specific color **(A)**. Dot plot of gene expression of marker genes selected in each subcluster. Rows depict cell types, and columns describe signatures **(B)**. UMAP plots illustrate the coexpression patterns of MS4A6A, CD68, and CD163 **(C)** in scRNA-seq samples. Representative immunofluorescent If staining images reveal colocalization of MS4A6A/CD68 and MS4A6A/CD163 in glioma tissues. Scale bar, 20 μm **(D)**. Abbreviations: BMDM: bone marrow-derived macrophages; BAM: border-associated macrophages.

that samples with lower MS4A6A expression (Wilcoxon test, $p < 0.001$, Figure 7A) and TMB showed a positive correlation with MS4A6A expression ($\rho = 0.34$, $p < 2.2e\text{-}16$, Figure 7B). Then, the R package Survminer was selected to acquire the optimal threshold value of TMB to group glioma cases. In terms of the identified interactions of TMB with MS4A6A expression, the synergistic effects of both factors on glioma outcomes were assessed. Based on OS stratification analysis, MS4A6A expression remained an independent prognostic predictor of glioma even when TMB values interfered with (log rank test, $p < 0.001$, Figure 7C). These findings demonstrate that MS4A6A might serve as a predictor to select gliomas responsive to antitumor immunotherapy. Further analysis identified the correlation of MS4A6A and immunotherapy-associated signatures, such as immune checkpoint-CD274 (PD-L1), T-cell markers CD3D and CD3E, markers of cytotoxic T lymphocyte (CTL) activation (GZMA and GZMB), and major histocompatibility complex class II (MHC) molecules, such as HLA-DRA and HLA-DRB5 (39–41) (Figures 7D, E). The purpose of anticancer immunotherapy is to promote the activity of CTLs within tumors for the development and establishment of an efficient and durable antitumor immune response (42), and recent research demonstrates that PD-L1 expression and MHC II positivity can predict a favorable outcome when PD-1 blockade is applied (40). The positive correlation of the above markers indicates that MS4A6A expression may be an indicator for immunotherapy. In addition, analysis was conducted on the landscape of somatic alterations between the MS4A6A expression groups using the R package maftools. Genes with the top 20 highest variations in the high MS4A6A expression group and low MS4A6A expression group were detected, as displayed in Figures 8A, B, respectively. We noticed that TP53 and IDH showed the highest mutation rate in the high MS4A6A expression group (46%, Figure 8A), with IDH having the highest mutation frequency in the low MS4A6A expression group (80%, Figure 8B). In addition, 17 molecules were differentially altered between the MS4A6A subgroups based on Fisher's exact test (Figure 8C and Table S14). Among them, IDH and IDH2 were significantly enriched in the low MS4A6A expression group and PTEN and EGFR in the high MS4A6A expression group (Figure 8C). Oncogenic genes are typically symbiotic or demonstrate strong exclusivity in their mutation patterns. We found that IDH1 exhibited a mutually exclusive mutation pattern with that of PTEN and

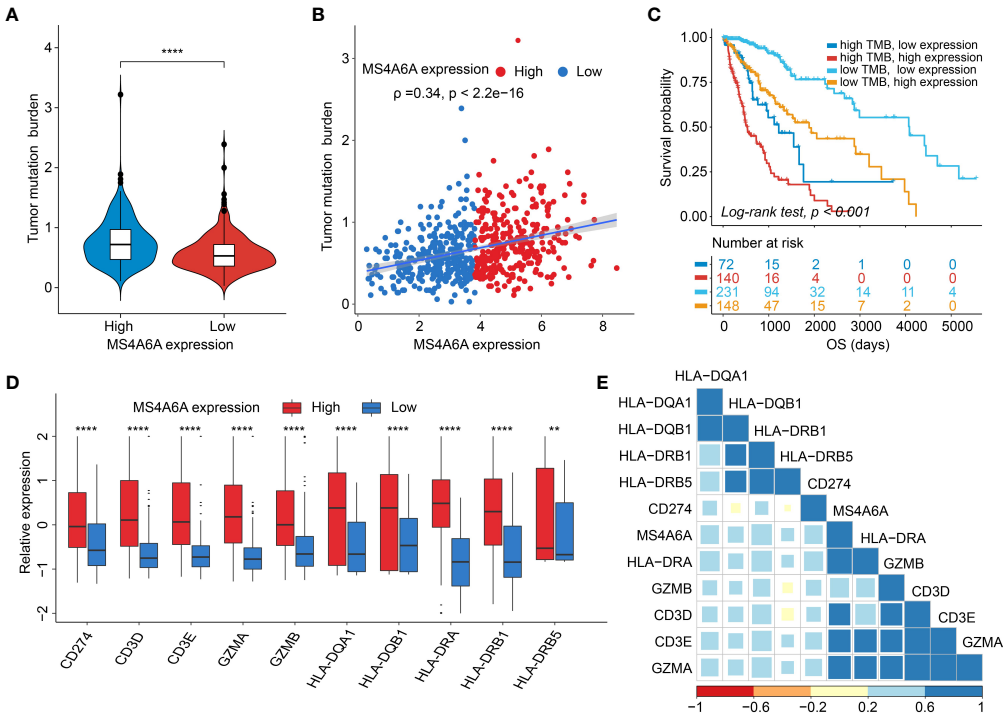


FIGURE 7
Correlation between the MS4A6A and immunotherapy-related markers.There were TMB differences after grouped by MS4A6A expression **(A)**. Dotplot of correlation of MS4A6A expression with TMB values **(B)**. Kaplan–Meier plot of gliomas OS in the TCGA set stratified by TMB and MS4A6A **(C)**. Box plots of expression features of T cell-inflamed markers between MS4A6A subgroups **(D)**. Corplot of correlation of MS4A6A expression with T cell-inflamed signatures **(E)** (**$p < 0.01$; ****$p < 0.0001$).

EGFR and concurrent mutant feature with IDH2 mutation, which might help to explain why patients with higher MS4A6A expression had unfavorable outcomes (Figure 8D).

Discussion

In our research, based on comprehensive examination and identification, aging-related MS4A6A is not only able to accurately predict an unfavorable prognosis of glioma but is also associated with malignant features, such as IDH status, 1p19q status, and WHO grade. Additionally, the functions of DEGs were systemically explored, and IL-17 and Toll-like receptor (TLR) signaling pathways were associated with high MS4A6A expression. Additionally, the PPI network demonstrated that CD33, ABCA7, and CD163 might interact with MS4A6A, which may explain why MS4A6A participates in the induction of macrophage infiltration and influences the outcomes of immunotherapy.

Overall, analysis of epigenetic modifications has provided exceptional insight into the tumorigenesis and pathology of brain tumors (43, 44). In methylation analysis, we found lower methylation of MS4A6A in glioma tissues, and this decreased tendency correlated negatively with WHO grade. Importantly, MS4A6A-associated methylation sites (cg20284999, cg24026212, cg06881914, cg04353769, cg00673646, cg03055440, and cg03055440) correlated negatively with expression of the gene. DNA methyltransferases DNMT3B, DNMT3A, and DNMT1 were comparatively overexpressed in the MS4A6A high expression subgroup, which might be the reason for MS4A6A hypomethylation in glioma tissues, leading to insight into upregulated mechanisms of MS4A6A in glioma. Moreover, integrated research of CGGA1 data revealed that MS4A6A expression can independently act as a prognosis-predicting biomarker for glioma, whereby patients with higher MS4A6A expression have poorer outcomes. The above findings were validated in CGGA2, TCGA, Gravendeel, and Rembrandt glioma cohorts. Furthermore, ROC analysis revealed AUC values of approximately 0.70 for 1-, 3-, and 5-year OS,

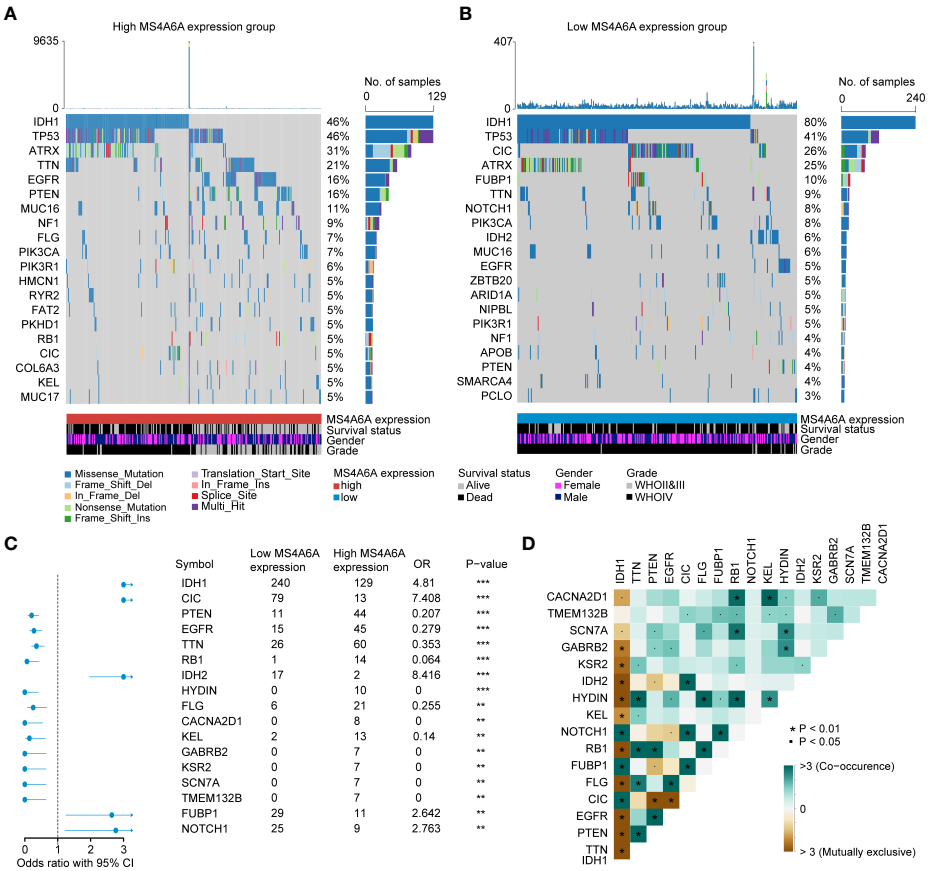


FIGURE 8
Correlation between the TIMEscore and somatic variants.The oncoPrint plots of gene mutant frequency in high **(A)** and low **(B)** MS4A6A expression group. Forest plot of differentially mutated genes after divided by MS4A6A **(C)**. Corplot of mutually exclusive or co-occurring genes, tested by pairwise Fisher's exact test **(D)** (*$p < 0.05$; **$p < 0.01$; ***$p < 0.001$).

highlighting the strong potential of MS4A6A in clinical assessment of OS. By analyzing interactions of MS4A6A expression with clinicopathological features, we confirmed that the potential marker is markedly downregulated in patients with 1p19q codeletion, IDH mutant status, or WHO grade II/III and upregulated in those aged > 43. These findings show the high possibility of applying MS4A6A expression to stratify glioma clinical and pathological characteristics.

1p19q codeletion has been considered a marker for response to adjuvant chemotherapy and a powerful prognostic predictive marker for LGG (45–47), which might explain why the patients in our research with 1p19q codeletion and lower MS4A6A expression had favorable outcomes after receiving chemotherapy. Regarding IDH mutation, a strong prognosis-predicting and therapeutic response assessment indicator of gliomas (48), our findings revealed a higher mutation frequency in the low MS4A6A expression group, with exclusive mutant features with PTEN and EGFR alterations, which have been identified as crucial changes in glioma genesis and progression (49, 50). Recent research has revealed lower overall levels of TILs in IDH-mutant gliomas than in IDH wild-type gliomas, with decreases in macrophages, T cells, B cells, and dendritic cells (51), consistent with our findings presented in Figure 5D and Figures S5A–C.

Exploration of the functions of MS4A6A was conducted through GO and KEGG analyses. We identified that MS4A6A might be involved in immune-related biological processes such as antigen processing and presentation and pathways such as the IL-17 signaling pathway and TLR signaling pathway. IL-17 might be involved in anticancer immunosuppression by enhancing the immunosuppressive effect of mesenchymal stem cells (MSCs) (52). IL-17 can also mediate specific γδ T-cell subset recruitment, which promotes immunosuppressive myeloid populations, enhancing cancer progression (53). In addition, IL-17 can promote the proliferation and migration of glioma cells by activating the PI3K/Akt1/NF-κB-p65 pathway (54). Myeloid cells secrete TLRs and produce high levels of immunosuppressive molecules, such as TGF-β, IL-10, and COX-2, to suppress cytotoxic T lymphocyte (CTL) activity (55, 56). The findings above show that MS4A6A overexpression might act as a factor in GIME remodeling, leading to immunosuppression. To gain insight into the immune-related processes of MS4A6A independent of glioma WHO grade, enrichment analysis of MS4A6A in LGG and GBM was conducted separately; in both glioma subgroups, immune-associated processes, such as myeloid leukocyte activation, were enriched in the MS4A6A high expression group. These findings demonstrate that elevated MS4A6A expression might exert a critical role in modulating the antitumor immune response, independent of glioma WHO grade. To explore the protein level of MS4A6A, the PPI network revealed that MS4A6A might interact with the macrophage-related protein CD163 and the glioma progression-related marker fibrinogen-like protein 2 (FGL2). FGL2 upregulation in glioma has been validated as an immune suppressor and is involved in malignant progression (57). CD163 is a classic and distinctive biomarker for macrophage infiltration and is involved in glioma progression and poor survival (58). Furthermore, functional annotation of MS4A6A-related genes using GSEA confirmed the tight correlation of MS4A6A with the innate immune response. Using infiltrative data of immune cells from the TIMER, ESTIMATE, and CIBERSORT algorithms and scRNA-seq analysis, we found that MS4A6A expression is related to macrophage infiltration, including polarized BMDM M2b, BMDM M2c, and MHC^{lo} meningeal BAMs. M2b (Th2 cell activation and immunoregulation) and M2c (immunoregulation, matrix deposition, and tissue remodeling) macrophages are two distinct subsets of alternative macrophage activation (59). Accumulating evidence shows that the tumor microenvironment is complicated and sophisticated, consisting of various cell types roughly divided into malignant and nonmalignant cells and influencing carcinogenesis, tumor growth, and response to clinical interventions (39). A considerable percentage of nonneoplastic cells are TAMs, creating a supporting stromal environment essential for tumor cell growth and invasion (59, 60) by releasing a great variety of chemokines and cytokines, such as TGF-β (transforming growth factor-β), MMP-2 (matrix metalloproteinase-2), and VEGF (vascular endothelial growth factor). Thus, by promoting malignant behaviors, high TAM infiltration results in unfavorable outcomes in glioma, which might be the reason why MS4A6A negatively influences patient prognosis.

Overall, the immune system acts as a modulator of the balance between activation, tolerance, and exhaustion of T cells and tumor pathology by a variety of molecules of coinhibition and costimulation, which are referred to as immune checkpoints (61, 62), such as PD-1 and PD-L1, the dysregulation of which may contribute to evasion of anticancer T-cell immunity (63). Moreover, studies have revealed that blocking this PD-1/PD-L1 signal leads to durable responses and prolonged survival of various tumors (64–66). To gain deep insight into whether stratification based on MS4A6A expression impacts the glioma response to immunotherapy, we first explored and validated the high degree of correlation between MS4A6A and checkpoints at the transcriptome level. Further investigation confirmed a tendency toward a higher TMB in the high MS4A6A expression group. Our findings demonstrate that MS4A6A expression may act as an indicator to assess patients who may benefit from anticancer immunotherapy.

Conclusion

In summary, great efforts have been made to explore the biology of MS4A6A in glioma. We comprehensively analyzed mechanisms of MS4A6A dysregulation in glioma, highlighting its negative influence on clinical outcomes and further illustrating the

differences in macrophage infiltration in association with MS4A6A expression. Our findings show that the features of the inflammatory microenvironment and expression of immune checkpoints might differ based on the MS4A6A expression level and may be relevant to the formulation and conduction of clinical trials to investigate the therapeutic value of MS4A6A in glioma.

Data availability statement

The original contributions presented in the study are included in the article/Supplementary Material. Further inquiries can be directed to the corresponding author.

Ethics statement

The studies involving human participants were reviewed and approved by the Institutional Ethical Boards of Wuhan University Renmin Hospital (WHURMH). Written informed consent to participate in this study was provided by the participants' legal guardian/next of kin. Written informed consent was obtained from the individual(s), and minor(s)' legal guardian/next of kin, for the publication of any potentially identifiable images or data included in this article.

Author contributions

CZ, LH, YT, YX, YL, QS, ZS and ST performed the data analysis and QC, DT, CZ, and WZ drafted the manuscript. All authors contributed to the article and approved the submitted version.

Funding

This work was supported by The National Natural Science Foundation of China (No. 81572489) and the Medical Discipline Construction Project of Pudong Health Committee of Shanghai (PWYgy 2021-07) and the Outstanding Leaders Training Program of Pudong Health Bureau of Shanghai (PWR12018-07).

Conflict of interest

The authors declare that the research was conducted in the absence of any commercial or financial relationships that could be construed as a potential conflict of interest.

Publisher's note

All claims expressed in this article are solely those of the authors and do not necessarily represent those of their affiliated organizations, or those of the publisher, the editors and the reviewers. Any product that may be evaluated in this article, or claim that may be made by its manufacturer, is not guaranteed or endorsed by the publisher.

Supplementary material

The Supplementary Material for this article can be found online at: https://www.frontiersin.org/articles/10.3389/fimmu.2022.865020/full#supplementary-material

References

1. Weller M, Wick W, Aldape K, Brada M, Berger M, Pfister SM, et al. Glioma. *Nat Rev Dis Primers* (2015) 16:1–15017. doi: 10.1038/nrdp.2015.17

2. Wen PY, Packer RJ. The 2021 WHO classification of tumors of the central nervous system: Clinical implications. *Neuro-Oncology* (2021) 23(8):1215–7. doi: 10.1093/neuonc/noab120

3. Lapointe S, Perry A, Butowski NA. Primary brain tumours in adults. *Lancet* (2018) 392(10145):432–46. doi: 10.1016/S0140-6736(18)30990-5

4. Wu W, Klockow JL, Zhang M, Lafortune F, Chang E, Jin L, et al. Glioblastoma multiforme (GBM): An overview of current therapies and mechanisms of resistance. *Pharmacol Res* (2021) 171:105780. doi: 10.1016/j.phrs.2021.105780

5. Ye L, Xu Y, Wang L, Zhang C, Hu P, Tong S, et al. Downregulation of CYP2E1 is associated with poor prognosis and tumor progression of gliomas. *Cancer Med* (2021) 10(22):8100–811. doi: 10.1002/cam4.4320

6. Zhang C, Wang L, Liu H, Deng G, Xu P, Tan Y, et al. ADPRH is a prognosis-related biomarker and correlates with immune infiltrates in low grade glioma. *J Cancer* (2021) 12(10):2912–20. doi: 10.7150/jca.51643

7. Zhang H, He J, Dai Z, Wang Z, Liang X, He F, et al. PDIA5 is correlated with immune infiltration and predicts poor prognosis in gliomas. *Front Immunol* (2021) 12:628966. doi: 10.3389/fimmu.2021.628966

8. Hollingworth P, Harold D, Sims R, Gerrish A, Lambert JC, Carrasquillo MM, et al. Common variants at ABCA7, MS4A6A/MS4A4E, EPHA1, CD33 and CD2AP are associated with alzheimer's disease. *Nat Genet* (2011) 43(5):429–35. doi: 10.1038/ng.803

9. Mhatre SD, Tsai CA, Rubin AJ, James ML, Andreasson KI. Microglial malfunction: The third rail in the development of alzheimer's disease. *Trends Neurosci* (2015) 38(10):621–36. doi: 10.1016/j.tins.2015.08.006

10. Martinez FO, Gordon S, Locati M, Mantovani A. Transcriptional profiling of the human monocyte-to-Macrophage differentiation and polarization: New molecules and patterns of gene expression. *J Immunol (Baltimore Md 1950)* (2006) 177(10):7303–11. doi: 10.4049/jimmunol.177.10.7303

11. Karch CM, Jeng AT, Nowotny P, Cady J, Cruchaga C, Goate AM. Expression of novel alzheimer's disease risk genes in control and alzheimer's disease brains. *PloS One* (2012) 7(11):e50976–6. doi: 10.1371/journal.pone.0050976

12. Guo MM, Chang LS, Huang YH, Wang FS, Kuo HC. Epigenetic regulation of macrophage marker expression profiles in Kawasaki disease. *Front Pediatr* (2020) 8:129. doi: 10.3389/fped.2020.00129

13. Friebel E, Kapolou K, Unger S, Núñez NG, Utz S, Rushing EJ, et al. Single-cell mapping of human brain cancer reveals tumor-specific instruction of tissue-invading leukocytes. *Cell* (2020) 181(7):1626–1642.e1620. doi: 10.1016/j.cell.2020.04.055

14. Pombo Antunes AR, Scheyltjens I, Lodi F, Messiaen J, Antoranz A, Duerinck J, et al. Single-cell profiling of myeloid cells in glioblastoma across species and disease stage reveals macrophage competition and specialization. *Nat Neurosci* (2021) 24(4):595–610. doi: 10.1038/s41593-020-00789-y

15. Ochocka N, Segit P, Walentynowicz KA, Wojnicki K, Cyranowski S, Swatler J, et al. Single-cell RNA sequencing reveals functional heterogeneity of glioma-associated brain macrophages. *Nat Commun* (2021) 12(1):1151. doi: 10.1038/s41467-021-21407-w

16. Hussain SF, Yang D, Suki D, Aldape K, Grimm E, Heimberger AB. The role of human glioma-infiltrating Microglia/Macrophages in mediating antitumor immune responses. *Neuro Oncol* (2006) 8(3):261–79. doi: 10.1215/15228517-2006-008

17. Raychaudhuri B, Rayman P, Huang P, Grabowski M, Hambardzumyan D, Finke JH, et al. Myeloid derived suppressor cell infiltration of murine and human gliomas is associated with reduction of tumor infiltrating lymphocytes. *J neuro-oncol* (2015) 122(2):293–301. doi: 10.1007/s11060-015-1720-6

18. Ma J, Hou X, Li M, Ren H, Fang S, Wang X, et al. Genome-wide methylation profiling reveals new biomarkers for prognosis prediction of glioblastoma. *J Cancer Res Ther* (2015) 11 Suppl 2:C212–215. doi: 10.4103/0973-1482.168188

19. Yang Ja, Yang Q. Identification of core genes and screening of potential targets in glioblastoma multiforme by integrated bioinformatic analysis. (2021) 10:615976. doi: 10.3389/fonc.2020.615976

20. Xiong Y, Wei Y, Gu Y, Zhang S, Lyu J, Zhang B, et al. DiseaseMeth version 2.0: A major expansion and update of the human disease methylation database. *Nucleic Acids Res* (2017) 45(D1):D888–d895. doi: 10.1093/nar/gkw1123

21. Koch A, De Meyer T, Jeschke J, Van Criekinge W. MEXPRESS: Visualizing expression, DNA methylation and clinical TCGA data. *BMC Genomics* (2015) 16 (1):636. doi: 10.1186/s12864-015-1847-z

22. Wu T, Hu E, Xu S, Chen M, Guo P, Dai Z, et al. Clusterprofiler 4.0: A universal enrichment tool for interpreting omics data. *Innovation (New York NY)* (2021) 2(3):100141. doi: 10.1016/j.xinn.2021.100141

23. Szklarczyk D, Gable AL, Nastou KC, Lyon D, Kirsch R, Pyysalo S, et al. The STRING database in 2021: Customizable protein-protein networks, and functional characterization of user-uploaded Gene/Measurement sets. *Nucleic Acids Res* (2021) 49(D1):D605–d612. doi: 10.1093/nar/gkaa1074

24. Chen B, Khodadoust MS, Liu CL, Newman AM, Alizadeh AA. Profiling tumor infiltrating immune cells with CIBERSORT. *Methods Mol Biol* (2018) 1711:243–59. doi: 10.1007/978-1-4939-7493-1_12

25. Li B, Severson E, Pignon J-C, Zhao H, Li T, Novak J, et al. Comprehensive analyses of tumor immunity: Implications for cancer immunotherapy. *Genome Biol* (2016) 17(1):174. doi: 10.1186/s13059-016-1028-7

26. Yoshihara K, Shahmoradgoli M, Martínez E, Vegesna R, Kim H, Torres-Garcia W, et al. Inferring tumour purity and stromal and immune cell admixture from expression data. *Nat Commun* (2013) 4(1):2612. doi: 10.1038/ncomms3612

27. Zhang X, Lan Y, Xu J, Quan F, Zhao E, Deng C, et al. CellMarker: A manually curated resource of cell markers in human and mouse. *Nucleic Acids Res* (2018) 47(D1):D721–8. doi: 10.1093/nar/gky900%J Nucleic Acids Research

28. Van Hove H, Martens L, Scheyltjens I, De Vlaminck K, Pombo Antunes AR, De Prijck S, et al. A single-cell atlas of mouse brain macrophages reveals unique transcriptional identities shaped by ontogeny and tissue environment. *Nat Neurosci* (2019) 22(6):1021–35. doi: 10.1038/s41593-019-0393-4

29. Liu Z, Jin YQ, Chen L, Wang Y, Yang X, Cheng J, et al. Specific marker expression and cell state of schwann cells during culture *in vitro*. *PloS One* (2015) 10(4):e0123278. doi: 10.1371/journal.pone.0123278

30. Hegde S, Leader AM, Merad M. MDSC: Markers, development, states, and unaddressed complexity. *Immunity* (2021) 54(5):875–84. doi: 10.1016/j.immuni.2021.04.004

31. Sahai E, Astsaturov I, Cukierman E, DeNardo DG, Egeblad M, Evans RM, et al. A framework for advancing our understanding of cancer-associated fibroblasts. *Nat Rev Cancer* (2020) 20(3):174–86. doi: 10.1038/s41568-019-0238-1

32. Young KF, Gardner R, Sariana V, Whitman SA, Bartlett MJ, Falk T, et al. Can quantifying morphology and TMEM119 expression distinguish between microglia and infiltrating macrophages after ischemic stroke and reperfusion in Male and female mice? *J Neuroinflamm* (2021) 18(1):58. doi: 10.1186/s12974-021-02105-2

33. Wang Y, Zhao M, Liu S, Guo J, Lu Y, Cheng J, et al. Macrophage-derived extracellular vesicles: Diverse mediators of pathology and therapeutics in multiple diseases. *Cell Death Dis* (2020) 11(10):924. doi: 10.1038/s41419-020-03127-z

34. Wang LX, Zhang SX, Wu HJ, Rong XL, Guo J. M2b macrophage polarization and its roles in diseases. *J leukocyte Biol* (2019) 106(2):345–58. doi: 10.1002/jlb.3ru1018-378rr

35. Ying W, Cheruku PS, Bazer FW, Safe SH, Zhou B. Investigation of macrophage polarization using bone marrow derived macrophages. *J visualized experiments JoVE* (2013) 76:50323. doi: 10.3791/50323

36. Andersen BM, Faust Akl C, Wheeler MA, Chiocca EA, Reardon DA, Quintana FJ. Glial and myeloid heterogeneity in the brain tumour microenvironment. *Nat Rev Cancer* (2021) 21(12):786–802. doi: 10.1038/s41568-021-00397-3

37. Nanda R, Chow LQM, Dees EC, Berger R, Gupta S, Geva R, et al. Pembrolizumab in patients with advanced triple-negative breast cancer: Phase ib KEYNOTE-012 study. *J Clin Oncol* (2016) 34(21):2460–7. doi: 10.1200/JCO.2015.64.8931

38. Hellmann MD, Ciuleanu TE, Pluzanski A, Lee JS, Otterson G, Audigier-Valette C, et al. Abstract CT077: Nivolumab (Nivo) + ipilimumab (Ipi) vs platinum-doublet chemotherapy (PT-DC) as first-line (1L) treatment (Tx) for advanced non-small cell lung cancer (NSCLC): Initial results from CheckMate 227. *Cancer Res* (2018) 78(13 Supplement):CT077–7. doi: 10.1158/1538-7445.am2018-ct077

39. Sampson JH, Gunn MD, Fecci PE, Ashley DM. Brain immunology and immunotherapy in brain tumours. *Nat Rev Cancer* (2020) 20(1):12–25. doi: 10.1038/s41568-019-0224-7

40. Roemer MGM, Redd RA, Cader FZ, Pak CJ, Abdelrahman S, Ouyang J, et al. Major histocompatibility complex class II and programmed death ligand 1 expression predict outcome after programmed death 1 blockade in classic Hodgkin lymphoma. *J Clin Oncol* (2018) 36(10):942–50. doi: 10.1200/jco.2017.77.3994

41. Rompré-Brodeur A, Shinde-Jadhav S, Ayoub M, Piccirillo CA, Seuntjens J, Brimo F, et al. PD-1/PD-L1 immune checkpoint inhibition with radiation in bladder cancer: *In situ* and abscopal effects. *Mol Cancer Ther* (2020) 19(1):211–20. doi: 10.1158/1535-7163.Mct-18-0986

42. Borst J, Ahrends T, Bąbała N, Melief CJM, Kastenmüller W. CD4(+) T cell help in cancer immunology and immunotherapy. *Nat Rev Immunol* (2018) 18 (10):635–47. doi: 10.1038/s41577-018-0044-0

43. Riemenschneider MJ, Jeuken JW, Wesseling P, Reifenberger G. Molecular diagnostics of gliomas: State of the art. *Acta neuropathol* (2010) 120(5):567–84. doi: 10.1007/s00401-010-0736-4

44. Filbin MG, Suvà ML. Gliomas genomics and epigenomics: Arriving at the start and knowing it for the first time. *Annu Rev Pathol* (2016) 11:497–521. doi: 10.1146/annurev-pathol-012615-044208

45. Omuro A, DeAngelis LM. Glioblastoma and other malignant gliomas: A clinical review. *JAMA* (2013) 310(17):1842–50. doi: 10.1001/jama.2013.280319

46. Morris PG, Lassman AB. Medical oncology: Optimizing chemotherapy and radiotherapy for anaplastic glioma. *Nat Rev Clin Oncol* (2010) 7(8):428–30. doi: 10.1038/nrclinonc.2010.98

47. Lv L, Zhang Y, Zhao Y, Wei Q, Zhao Y, Yi Q. Effects of 1p/19q codeletion on immune phenotype in low grade glioma. (2021) 15(274):704344. doi: 10.3389/fncel.2021.704344

48. Han S, Liu Y, Cai SJ, Qian M, Ding J, Larion M, et al. IDH mutation in glioma: Molecular mechanisms and potential therapeutic targets. *Br J Cancer* (2020) 122(11):1580–9. doi: 10.1038/s41416-020-0814-x

49. Vaubel RA, Tian S, Remonde D, Schroeder MA, Mladek AC, Kitange GJ, et al. Genomic and phenotypic characterization of a broad panel of patient-derived xenografts reflects the diversity of glioblastoma. *Clin Cancer Res* (2020) 26 (5):1094–104. doi: 10.1158/1078-0432.Ccr-19-0909

50. Smith JS, Tachibana I, Passe SM, Huntley BK, Borell TJ, Iturria N, et al. PTEN mutation, EGFR amplification, and outcome in patients with anaplastic astrocytoma and glioblastoma multiforme. *J Natl Cancer Inst* (2001) 93(16):1246–56. doi: 10.1093/jnci/93.16.1246

51. Amankulor NM, Kim Y, Arora S, Kargl J, Szulzewsky F, Hanke M, et al. Mutant IDH1 regulates the tumor-associated immune system in gliomas. *Genes Dev* (2017) 31(8):774–86. doi: 10.1101/gad.294991.116

52. Han X, Yang Q, Lin L, Xu C, Zheng C, Chen X, et al. Interleukin-17 enhances immunosuppression by mesenchymal stem cells. *Cell Death Differentiation* (2014) 21(11):1758–68. doi: 10.1038/cdd.2014.85

53. Rei M, Pennington DJ, Silva-Santos B. The emerging protumor role of γδ T lymphocytes: Implications for cancer immunotherapy. *Cancer Res* (2015) 75 (5):798–802. doi: 10.1158/0008-5472.Can-14-3228

54. Wang B, Zhao CH, Sun G, Zhang ZW, Qian BM, Zhu YF, et al. IL-17 induces the proliferation and migration of glioma cells through the activation of PI3K/Akt1/NF-κb-P65. *Cancer Lett* (2019) 447:93–104. doi: 10.1016/j.canlet.2019.01.008

55. Veglia F, Sanseviero E, Gabrilovich DI. Myeloid-derived suppressor cells in the era of increasing myeloid cell diversity. *Nat Rev Immunol* (2021) 21(8):485–98. doi: 10.1038/s41577-020-00490-y

56. Gabrilovich DI, Nagaraj S. Myeloid-derived suppressor cells as regulators of the immune system. *Nat Rev Immunol* (2009) 9(3):162–74. doi: 10.1038/nri2506

57. Latha K, Yan J, Yang Y, Gressot LV, Kong L-Y, Manyam G, et al. The role of fibrinogen-like protein 2 on immunosuppression and malignant progression in glioma. *J Natl Cancer Inst* (2019) 111(3):292–300. doi: 10.1093/jnci/djy107

58. Gieryng A, Pszczolkowska D, Walentynowicz KA, Rajan WD, Kaminska B. Immune microenvironment of gliomas. *Lab Invest* (2017) 97(5):498–518. doi: 10.1038/labinvest.2017.19

59. Hambardzumyan D, Gutmann DH, Kettenmann H. The role of microglia and macrophages in glioma maintenance and progression. *Nat Neurosci* (2016) 19 (1):20–7. doi: 10.1038/nn.4185

60. Rossi ML, Hughes JT, Esiri MM, Coakham HB, Brownell DB. Immunohistological study of mononuclear cell infiltrate in malignant gliomas. *Acta neuropathol* (1987) 74(3):269–77. doi: 10.1007/bf00688191

61. Keir ME, Butte MJ, Freeman GJ, Sharpe AH. PD-1 and its ligands in tolerance and immunity. *Annu Rev Immunol* (2008) 26:677–704. doi: 10.1146/annurev.immunol.26.021607.090331

62. Sun C, Mezzadra R, Schumacher TN. Regulation and function of the PD-L1 checkpoint. *Immunity* (2018) 48(3):434–52. doi: 10.1016/j.immuni.2018.03.014

63. Ribas A. Tumor immunotherapy directed at PD-1. *New Engl J Med* (2012) 366(26):2517–9. doi: 10.1056/NEJMe1205943

64. Ferris RL, Blumenschein GJr., Fayette J, Guigay J, Colevas AD, Licitra L, et al. Nivolumab for recurrent squamous-cell carcinoma of the head and neck. *N Engl J Med* (2016) 375(19):1856–67. doi: 10.1056/NEJMoa1602252

65. Economopoulou P, Agelaki S, Perisanidis C, Giotakis EI, Psyrri A. The promise of immunotherapy in head and neck squamous cell carcinoma. *Ann Oncol* (2016) 27(9):1675–85. doi: 10.1093/annonc/mdw226

66. Garon EB, Rizvi NA, Hui R, Leighl N, Balmanoukian AS, Eder JP, et al. Pembrolizumab for the treatment of non-small-cell lung cancer. *New Engl J Med* (2015) 372(21):2018–28. doi: 10.1056/NEJMoa1501824

frontiers | Frontiers in Immunology

TYPE Original Research
PUBLISHED 11 August 2022
DOI 10.3389/fimmu.2022.877076

Check for updates

OPEN ACCESS

EDITED BY
Giulia Accardi,
University of Palermo, Italy

REVIEWED BY
Xing Niu,
China Medical University, China
Kun Fang,
First Affiliated Hospital of Harbin Medical University, China

*CORRESPONDENCE
Weimin Zhong
zhongweimin63@gmail.com
Dongna Ma
m_dongna@163.com

SPECIALTY SECTION
This article was submitted to Cancer Immunity and Immunotherapy, a section of the journal Frontiers in Immunology

RECEIVED 16 February 2022
ACCEPTED 21 July 2022
PUBLISHED 11 August 2022

CITATION
Zhu M, Huang C, Wu X, Gu Y, Hu X, Ma D and Zhong W (2022) Aging-based molecular classification and score system in ccRCC uncovers distinct prognosis, tumor immunogenicity, and treatment sensitivity.
Front. Immunol. 13:877076.
doi: 10.3389/fimmu.2022.877076

COPYRIGHT
© 2022 Zhu, Huang, Wu, Gu, Hu, Ma and Zhong. This is an open-access article distributed under the terms of the Creative Commons Attribution License (CC BY). The use, distribution or reproduction in other forums is permitted, provided the original author(s) and the copyright owner(s) are credited and that the original publication in this journal is cited, in accordance with accepted academic practice. No use, distribution or reproduction is permitted which does not comply with these terms.

Aging-based molecular classification and score system in ccRCC uncovers distinct prognosis, tumor immunogenicity, and treatment sensitivity

Maoshu Zhu[1], Chaoqun Huang[1], Xinhong Wu[1], Ying Gu[2], Xiaoxu Hu[3], Dongna Ma[4]* and Weimin Zhong[1]*

[1]Department of Central Laboratory, the Fifth Hospital of Xiamen, Xiamen, China, [2]Department of Pharmacy, Xiang'an Hospital of Xiamen University, School of Medicine, Xiamen University, Xiamen, China, [3]Affiliated Primary School to Renmin University of China, Beijing, China, [4]Key Laboratory of the Ministry of Education for Coastal and Wetland Ecosystems, College of the Environment and Ecology, Xiamen University, Xiamen, China

Objective: Aging is a complex biological process and a major risk factor for cancer development. This study was conducted to develop a novel aging-based molecular classification and score system in clear cell renal cell carcinoma (ccRCC).

Methods: Integrative analysis of aging-associated genes was performed among ccRCC patients in the TCGA and E-MTAB-1980 cohorts. In accordance with the transcriptional expression matrix of 173 prognostic aging-associated genes, aging phenotypes were clustered with the consensus clustering approach. The agingScore was generated to quantify aging phenotypes with principal component analysis. Tumor-infiltrating immune cells and the cancer immunity cycle were quantified with the ssGSEA approach. Immunotherapy response was estimated through the TIDE algorithm, and a series of tumor immunogenicity indicators were computed. Drug sensitivity analysis was separately conducted based on the GDSC, CTRP, and PRISM analyses.

Results: Three aging phenotypes were established for ccRCC, with diverse prognosis, clinical features, immune cell infiltration, tumor immunogenicity, immunotherapeutic response, and sensitivity to targeted drugs. The agingScore was developed, which enabled to reliably and independently predict ccRCC prognosis. Low agingScore patients presented more undesirable survival outcomes. Several small molecular compounds and three therapeutic targets, namely, *CYP11A1*, *SAA1*, and *GRIK4*, were determined for the low agingScore patients. Additionally, the high agingScore patients were more likely to respond to immunotherapy.

10.3389/fimmu.2022.877076

Conclusion: Overall, our findings introduced an aging-based molecular classification and agingScore system into the risk stratification and treatment decision-making in ccRCC.

KEYWORDS

clear cell renal cell carcinoma, aging phenotypes, prognosis, tumor immunogenicity, treatment sensitivity

Introduction

Renal cell carcinoma (RCC) affects more than 400,000 people in the world annually (1). The age of diagnosis is around 60, and men are diagnosed twice as often as women (2). RCC has a few histological subtypes, with around 70% of individuals diagnosed with clear cell renal cell carcinoma (ccRCC) (1). Although ccRCC can be detected early and successfully treated with surgery or ablation regimens, over one-third of cases develop or progress to metastatic disease that is almost uniformly lethal (3). ccRCC is highly immune infiltrated, but there is extensive immune heterogeneity within and between patients (4). Immune checkpoint blockade (ICB) and combined strategies have favorably prolonged the survival of ccRCC patients (5–7). Tumor-infiltrating cells enable to influence the balance of antitumor immune response and immune escape in ccRCC, and T-cell exhaustion within the tumor microenvironment (TME) is responsible for the low response rate of ICB (4). Patients who respond to ICB present remarkable enrichment of tissue-resident T-cell populations, with enrichment of tumor-associated macrophages in resistant patients (4). Nevertheless, predicting which patients will respond to ICB remains a fundamental issue. Additionally, the drivers and resistors of ICB responses are still not fully elucidated.

Cancer is regarded as an aging-related degenerative malignancy, and aging is an independent risk factor of cancer (8). The mechanisms by which aging results in cancer progression remain being explored. Many aging-related cellular events (genomic instability, inflammatory response, immunity, etc.) are hallmarks of cancer (9). Despite the widespread study of the aging microenvironment in cancers, few studies focused on the overall characteristics of the transcriptional landscape of aging-associated genes in ccRCC. Previously, several aging-associated genes have been determined to be linked to unfavorable survival outcomes of RCC (9). Additionally, experimental evidence demonstrates that aging-associated genes participate in RCC progression. The molecular characteristics that reflect ccRCC ontogeny and development are being increasingly defined. Herein, on the basis of molecular and clinical information of ccRCC patients, we comprehensively evaluated aging phenotypes and their interactions with the tumor immune landscape. Three different aging phenotypes were characterized, which presented different prognosis and immunologic mechanisms, demonstrating the critical role of the aging process in remodeling tumor immune landscape in ccRCC individuals. Thereafter, aging phenotypes were individually quantified *via* generating the agingScore. Altogether, our findings might assist risk stratification and guide treatment decision-making for ccRCC.

Abbreviations: RCC, renal cell carcinoma; ccRCC, clear cell renal cell carcinoma; ICB, immune checkpoint blockade; TME, tumor microenvironment; RNA-seq, RNA sequencing; TCGA, The Cancer Genome Atlas; KIRC, kidney renal clear cell carcinoma; KIRP, kidney renal papillary cell carcinoma; RMA, robust multiarray average; CAN, copy number alteration; HAGR, Human Ageing Genomic Resources; CDF, cumulative distribution function; PCA, principal component analysis; ssGSEA, single-sample gene-set enrichment analysis; GSVA, gene set variation analysis; MSigDB, Molecular Signatures Database; GO, Gene Ontology; KEGG, Kyoto Encyclopedia of Genes and Genomes; EMT, epithelial–mesenchymal transition; pan-FTBRS, pan-fibroblast TGFβ response signature; GSVA, gene set variation analysis; TIDE, Tumor Immune Dysfunction and Exclusion; CTLs, cytotoxic T lymphocytes; SubMap, Subclass Mapping; GDSC, Genomics of Drug Sensitivity in Cancer; IC_{50}, half maximal inhibitory concentration; CCLs, cancer cell lines; CCLE, Cancer Cell Line Encyclopedia; CTRP, Cancer Therapeutics Response Portal; SNPs, single-nucleotide polymorphisms; SNV, single nucleotide variation; TMB, tumor mutation burden; CTAs, cancer/testis antigens; DEGs, differentially expressed genes; OS, overall survival; ROC, receiver operating characteristic; DFS, disease-free survival; DSS, disease-specific survival; PFS, progression-free survival; AUC, area under the curve; HR, hazard ratio; CI, confidence interval.

Materials and methods

Publicly available datasets and processing

For the discovery cohort, RNA sequencing (RNA-seq) data of The Cancer Genome Atlas-kidney renal clear cell carcinoma (TCGA-KIRC) cohort (n = 529) were obtained *via* the UCSC

Xena project (https://xenabrowser.net/datapages/). For the verification cohorts, RNA-seq profiles of the TCGA-kidney renal papillary cell carcinoma (TCGA-KIRP) (n = 286) were also obtained from the UCSC Xena Portal, while the microarray data of the E-MTAB-1980 cohort (n = 240) were downloaded from the ArrayExpress database (https://www.ebi.ac.uk/arrayexpress/) (10). RNA-seq data were further transformed to log2 (TPM+1), which had higher similarity with microarray profiling and higher comparability between samples. The corresponding clinical information was collected from the UCSC and ArrayExpress databases (Supplementary Table 1). The microarray data were adjusted for background and normalized by quantile utilizing the robust multiarray average (RMA) approach from the affy package (11). For the TCGA-KIRC project, the somatic mutational data as well as the copy number alteration (CNA) data were acquired from the TCGA portal (https://portal.gdc.cancer.gov/). Figure 1 depicts the work procedure of this study. We collected 307 aging-associated genes from the Human Ageing Genomic Resources (HAGR; https://genomics.senescence.info/), which is a collection of online resources for exploring the biology of human aging (12).

Establishment of aging phenotypes

The optimum number of clusters was determined in the TCGA-KIRC cohort *via* the ConsensusClusterPlus package based on the expression profiling of prognostic aging-associated genes generated from the univariate Cox regression models (13). Eighty percent of the samples were subsampled in each iteration, and each subsample was divided into at most k (maximum k value = 9) groups *via* the k-means algorithm through the Euclidean distance. This analysis was repeated 1,000 times. Thereafter, the perfect clustering result was determined by considering consistent cumulative distribution function (CDF) graphs. Afterward, the results were illustrated as

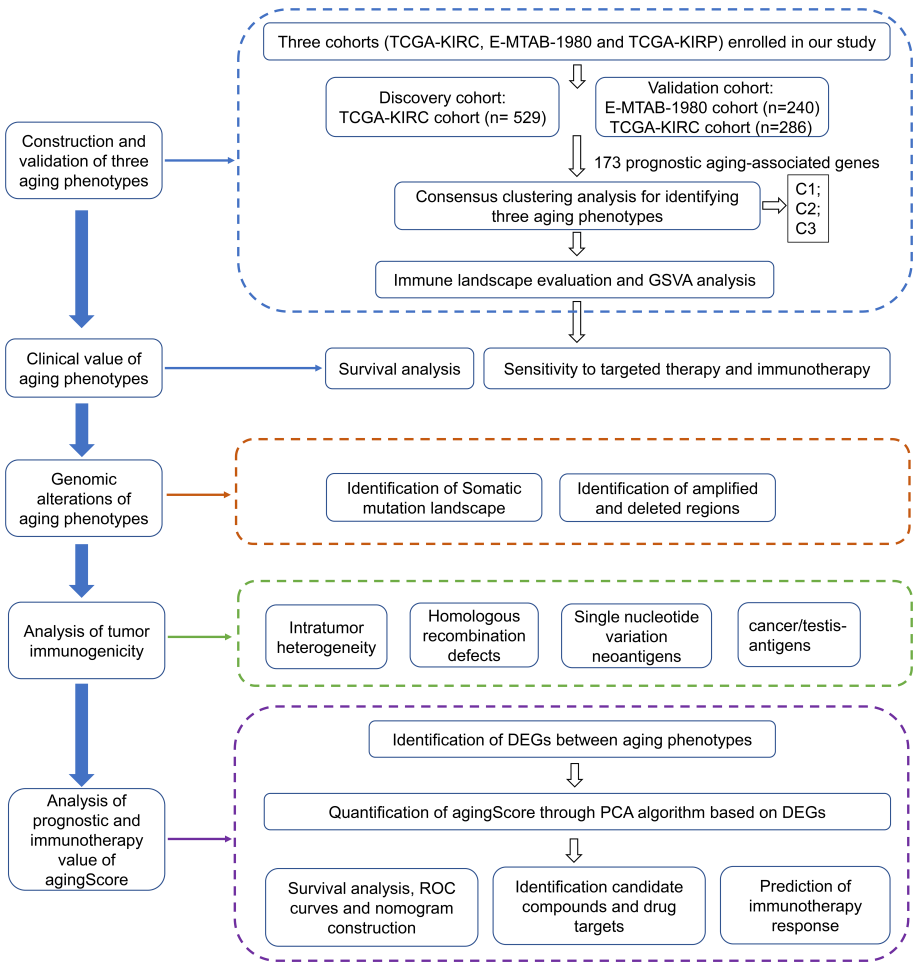


FIGURE 1
The workflow of our study.

consensus matrix heatmaps generated by the heatmap package. The reproducibility of the clusters was evaluated in the E-MTAB-1980 cohort.

Functional and pathway enrichment analysis

The single-sample gene set enrichment analysis (ssGSEA) algorithm from the gene set variation analysis (GSVA) software (14) was implemented to ascertain the hallmark pathways and evaluate the differences in biological significance among aging phenotypes. The hallmark gene set was collected from the Molecular Signatures Database (MSigDB) to run the GSVA. Through the clusterProfiler package (15), functional annotation of aging phenotype-associated genes was carried out. P <0.05 was regarded as significant enrichment in Gene Ontology and Kyoto Encyclopedia of Genes and Genomes (KEGG). The known pathways were acquired, consisting of epithelial–mesenchymal transition (EMT1, 2, 3), immune checkpoint, antigen processing machinery, $CD8^+$ T effector signature, angiogenesis signature, and pan-fibroblast TGFβ response signature (pan-FTBRS) (16–18). The activities of the above biological processes were computed *via* the ssGSEA approach.

Generation of tumor-infiltrating immune cells

Through the ssGSEA, the infiltrations of 28 immune cell types were quantified in accordance with the 782 metagenes utilizing the GSVA package (14). Tumor purity as well as stromal and immune scores was computed *via* the ESTIMATE package with default parameters (19).

Cancer immunity cycle

The cancer immunity cycle can reflect the anti-tumor immune response and comprises seven steps, as previously described (20). The activities of the above steps were quantified *via* the ssGSEA approach.

Immunotherapy response

Through the tumor immune dysfunction and exclusion (TIDE) algorithm, the response to immunotherapy was predicted in accordance with the tumor immune escape mechanisms: inducing T-cell dysfunction within tumors with enhanced infiltrations of cytotoxic T lymphocytes (CTLs) as well as preventing the infiltrations of T cells within tumors with reduced CTLs [21]. The expression similarity between phenotypes and the patients who differently responded to immunotherapy was evaluated with the Subclass Mapping (SubMap) approach that employed the GSEA algorithm to infer the commonality between groups (21). P <0.05 suggested a significant similarity between groups.

Drug sensitivity analysis

Through the pRRophetic package (22), a ridge regression analysis was conducted in accordance with the Genomics of Drug Sensitivity in Cancer (GDSC) cell line expression data (23). The half maximal inhibitory concentration (IC_{50}) value was estimated to reflect the sensitivity to agents. The expression profiling and somatic mutational data of human cancer cell lines (CCLs) were retrieved from the Cancer Cell Line Encyclopedia (CCLE) database (https://portals.broadinstitute.org/ccle/) (24). CERES scores can be utilized for measuring the dependency of target genes in certain CCLs. A negative score represents that the cell line grows slower when the specific gene is knocked out, and a positive score represents that the cell line grows faster when the specific gene is knocked out. The CERES scores of CRISPR-knockdown screening of over 18,000 genes across over 700 cell lines were acquired from the dependency map (DepMap) database (https://depmap.org/portal/). Drug sensitivity data of CCLs were required from the Cancer Therapeutics Response Portal (CTRP; https://portals.broadinstitute.org/ctrp) containing 481 agents over 835 CCLs as well as from the PRISM project (https://depmap.org/portal/prism/) containing 1,448 agents over 482 CCLs. The two datasets offer the area under the dose–response curve (AUC) measures of drug sensitivity. A lower AUC value indicates a higher sensitivity to an agent. Since the CCLs in the two projects were required from the CCLE project, expression profiling in CCLE was utilized for further CTRP and PRISM analysis.

Analysis of single-nucleotide polymorphisms and CNAs

The maftools package was applied for analyzing somatic variants, and overall mutation status was illustrated across three phenotypes (25). Through the GISTIC (version 2.0) software, the amplified and deleted CNAs in the tumor were quantified with the input of "SNP6" files (26).

Evaluation of tumor immunogenicity indicators

Immune checkpoints with therapeutic potential were collected from the study of Auslander et al. (27). Single

nucleotide variation (SNV) neoantigens were calculated *via* NetMHCpan (version 3.0) (28) in accordance with human leukocyte antigen (HLA) types required from RNA-seq utilizing OptiType (version 1.2) (29). Tumor mutation burden (TMB) was quantified following the total count of non-synonymous mutations (30). Homologous recombination defects score was computed through three DNA-based genomic instability: large (>15 Mb) non-arm-level regions with loss of heterozygosity, telomeric allelic instability, and large-scale state conversion with breaks between adjacent segments >10 Mb (31). Intratumor heterogeneity and cancer/testis antigens (CTAs) were also involved.

Analysis of aging phenotype-associated genes

The limma package was applied for determining the differentially expressed genes (DEGs) between phenotypes (32). The threshold was set as adjusted P <0.05 as well as at least 1.5-fold changes in expression. The Venn plot directly depicted the number of DEGs among phenotypes.

Generation of the aging gene signature

For quantifying the aging phenotypes of individual patients, a scoring system was generated for assessing all individuals, named as agingScore. Univariate Cox regression analysis was conducted to determine the prognostic implication of DEGs. The DEGs with P <0.05 were utilized to compute the agingScore *via* the PCA algorithm. The principal components (PCs) PC1 and PC2 acted as the scoring system (33, 34). The formula of the agingScore was as follows: aging Score = $\sum_{i}^{j} PCi + PCj$ where i and j indicate the ranking and the total number of the prognostic DEGs, respectively. The advantage of this approach is to focus the score on the set with the largest well-related (or anti-correlated) genes in the set while reducing the contribution of genes that are not tracked with other set members.

Analysis of post-transcriptional features correlated to agingScore

In the TCGA-KIRC cohort, differentially expressed miRNAs or mRNAs were screened between high and low agingScore groups in accordance with FDR <0.05 and at least 1.5-fold changes. The targeted mRNAs were then predicted through the miRbase database (http://www.mirbase.org/) (35). Analysis of KEGG pathways enriched by the miRNA-targeted mRNAs was carried out.

Statistical analysis

The dissimilarity of the clusters was verified through principal component analysis (PCA). Student's t-test or the Wilcoxon rank sum test was applied to evaluate the difference between two groups, while one-way analysis of variance or the Kruskal–Wallis test was implemented to estimate the difference between three groups. The Benjamini–Hochberg approach was implemented to correct multiple tests. Kaplan–Meier analysis was implemented to compare the overall survival (OS), disease-free survival (DFS), disease-specific survival (DSS), and progression-free survival (PFS) between groups utilizing survival and survminer packages. The difference in OS was computed with the log-rank test. The receiver operating characteristic (ROC) curves of OS, DFS, DSS, and PFS were conducted and the AUC values were calculated with the survivalROC package. Univariate Cox regression analysis was implemented to identify the significant associations of agingScore and clinical features with OS, DFS, DSS, and PFS. Hazard ratio (HR), 95% confidence interval (CI), and the P-value of each variable were separately computed. Multivariable Cox regression analysis was utilized to assess whether agingScore was independent of other clinical features. In accordance with the multivariate Cox regression results, a nomogram was generated to provide a visualized risk prediction after each factor was assigned a score *via* the rms package. The time-dependent concordance index (C-index) was computed with the pec package. A calibration diagram was drawn to estimate the calibration capacity of the nomogram. Correlation analysis was implemented with Pearson's or Spearman's correlation test. All statistical P-values were two-sided, with P <0.05 as statistically significant. All analyses were conducted with the R software (version 4.0.2).

Results

The landscape of prognosis and clinical features of the three aging phenotypes in ccRCC

Among 307 aging-associated genes, univariate Cox regression determined 173 genes significantly linked to clinical outcomes among 529 ccRCC patients in the TCGA-KIRC cohort (Supplementary Table 2), which were included for consensus clustering analysis. Through applying the ConsensusClusterPlus approach, three aging phenotypes were achieved, termed as C1, C2, and C3 in accordance with the selection of k = 3 as the optimal k value (Figures 2A–D). Thereafter, PCA affirmed the remarkable difference among the three phenotypes (Figure 2E). Patients

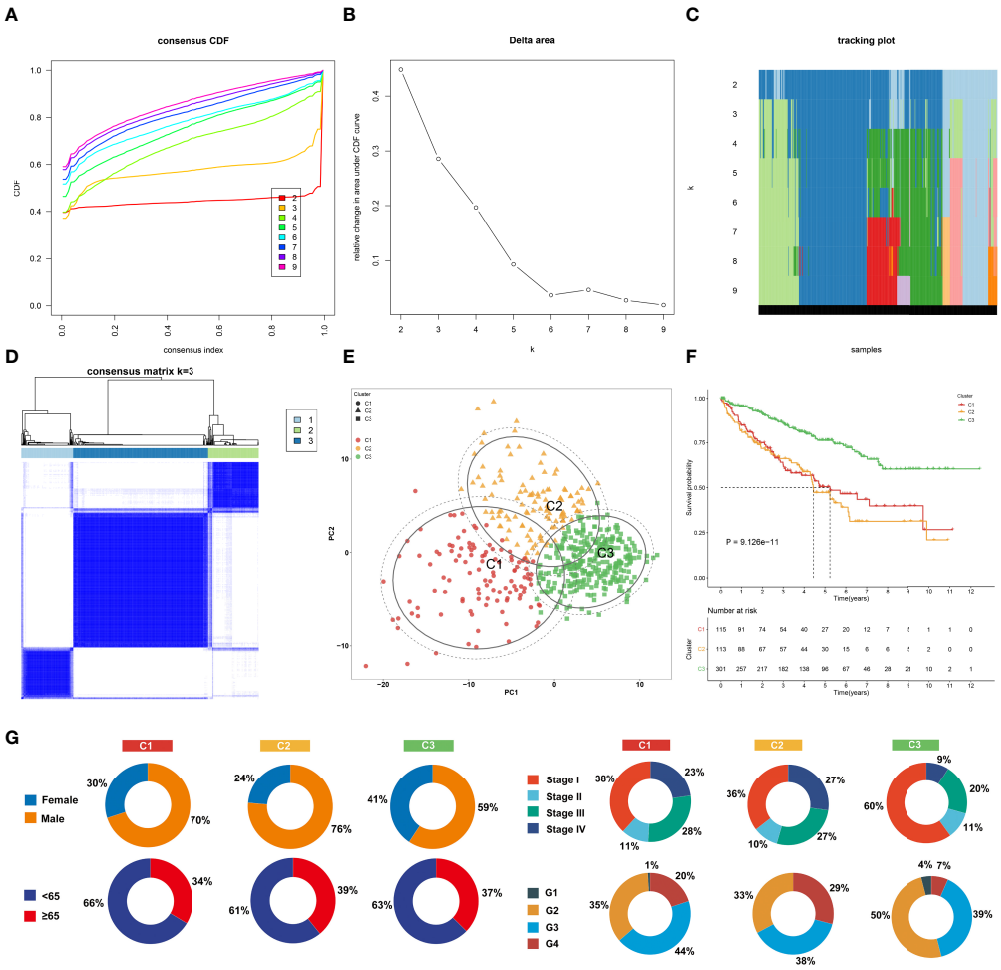


FIGURE 2
The landscape of prognosis and clinical features of the three aging phenotypes in The Cancer Genome Atlas-kidney renal clear cell carcinoma (TCGA-KIRC) cohort. **(A)** The cumulative distribution functions (CDFs) of the consensus matrix for k = 2~9 marked by colors. **(B)** Relative alterations in area under the CDFs for k = 2~9. **(C)** Tracking plot for the classification of the TCGA-KIRC dataset into diverse subtypes for k = 2~9. **(D)** Classification of the TCGA-KIRC cohort into three clusters when k = 3. **(E)** PCA of the RNA expression profiling of prognostic aging-associated genes. **(F)** Kaplan–Meier analysis for overall analysis (OS) among the three phenotypes. **(G)** Pie plots of the distribution of clinical features across the three phenotypes.

with the C3 phenotype presented the best OS outcomes, followed by C1 and C2 (Figure 2F). Figure 2G illustrates the distribution of clinical features among the three phenotypes. Because the E-MTAB-1980 cohort possessed relatively complete prognostic information as well as a large sample size, it was employed for validating the repeatability of this classification. Similarly, consensus clustering analysis was implemented on the cohort, and the three different aging phenotypes were clearly clustered (Supplementary Figures 1A–E). The remarkable difference in OS outcomes was noted among the phenotypes (Supplementary Figure 1F), affirming the reliability of this classification for ccRCC.

The immune landscape of the three aging phenotypes

To uncover the molecular mechanisms underlying the aging phenotypes, we focused on the TCGA-KIRC dataset that had relatively complete omics data and clinical characteristics. The activity status of the hallmark pathways was firstly computed across the three aging phenotypes. In Figure 3A, oxidative phosphorylation, peroxisome, reactive oxygen species pathway, and DNA repair presented relatively high activities in the C1 phenotype; the C2 phenotype had relatively high activities of immune pathways (IL2–STAT5 signaling, inflammatory

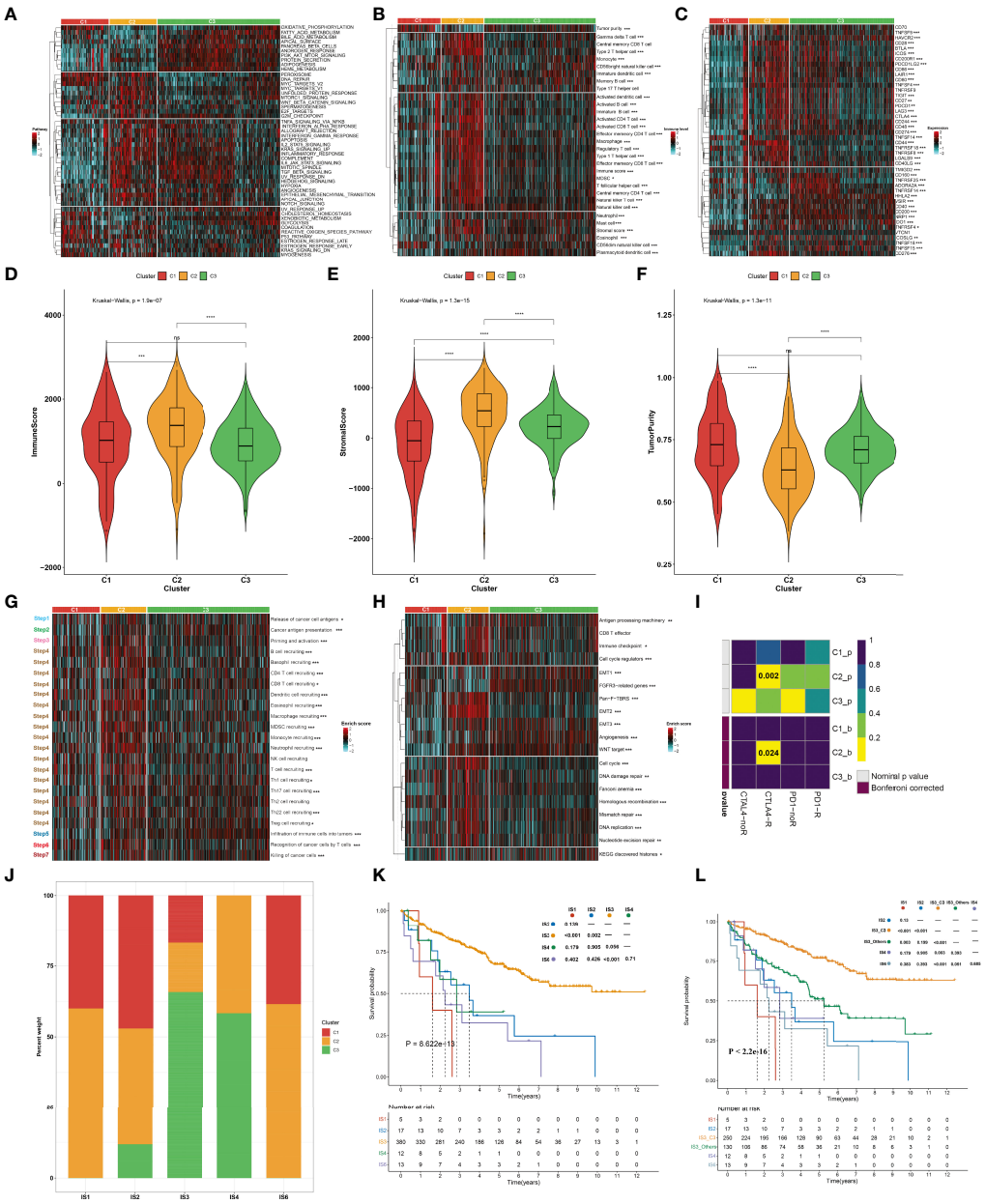


FIGURE 3
Immune landscape and antitumor immune responses of the three aging phenotypes in the TCGA-KIRC cohort. **(A)** Heatmap depicting the activities of hallmark pathways across the three aging phenotypes. Activated and inhibited hallmark pathways are colored by red and cyan, respectively. **(B)** Heatmap of the relative abundance of tumor-infiltrating immune cell populations across the three aging phenotypes. The high and low enrichment levels are colored red and cyan, respectively. **(C)** Heatmap of the RNA expression of immune checkpoint molecules across the three aging phenotypes. The high and low expression levels of immune checkpoints are marked by red and cyan, respectively. **(D–F)** Box plots of the differences in **(D)** immune and **(E)** stromal scores as well as **(F)** tumor purity across the three aging phenotypes. **(G)** Heatmap of the activation states of the seven steps within the cancer immunity cycle across the three aging phenotypes. Activated and inhibited steps are colored red and cyan, respectively. **(H)** Heatmap of the activities of known biological processes across the three aging phenotypes. Activated or inactivated processes are colored red or cyan. **(I)** Prediction of the response to anti-PD-1 and anti-CTLA4 among the three aging phenotypes. R, response; noR, non-response. **(J)** Distribution of the three aging phenotypes across known immune subtypes. **(K)** Kaplan–Meier analysis for OS of the TCGA-KIRC cohort stratified by immune subtypes. **(L)** Kaplan–Meier analysis for OS of the TCGA-KIRC cohort stratified by immune subtypes and aging phenotypes. Ns, no significance; *$P < 0.05$; **$P < 0.01$; ***$P < 0.001$; ****$P < 0.0001$.

response, complement, etc.) as well as stromal pathways (WNT beta-catenin signaling, angiogenesis, etc.); and the C3 phenotype presented features of activation of metabolism pathways (fatty acid metabolism, bile acid metabolism, etc.). Extrinsic immune evasion mechanisms were evaluated in accordance with the absence of leukocytes as well as the presence of immunosuppressive cell populations. As illustrated in Figure 3B, the C1 phenotype presented deficient immune cell infiltrations and immune-mediated elimination, which can be characterized as the immune-deserted type; the C2 phenotype was recognized as the immune-excluded type which had relatively high stromal score and infiltrations of immunosuppressive cells [type 1 helper cells, type 2 helper cells, regulatory T cells, myeloid-derived suppressor cells (MDSCs), T follicular helper cells, etc.]; and the C3 phenotype was recognized as immune-inflamed characterized by the immune-active cells ($CD4^+$ T cells, $CD8^+$ T cells, etc.). Therefore, we speculated that the C1 and C3 phenotypes probably reflected the deficiency of recruitment or activation of innate immune cell populations, thereby triggering the failure of adaptive antitumor immune responses. Moreover, the C2 phenotype had a higher expression of co-stimulatory and co-inhibitory immune checkpoint molecules in comparison to the other phenotypes (Figure 3C), indicating that the C2 phenotype might upregulate the immune checkpoint molecules to escape the immune elimination following immune activation. Through the ESTIMATE approach, we estimated the overall levels of immune and stromal cells as well as tumor purity. Not surprisingly, the C2 phenotype presented higher immune and stromal scores as well as lower tumor purity compared with the other phenotypes (Figures 3D–F).

Antitumor immune responses of the three aging phenotypes

The activities of the cancer immunity cycle were computed to reflect antitumor immune responses. In Figure 3G, most steps within the cancer immunity cycle showed higher activity status in the C2 phenotype in comparison to the other phenotypes. It was also noted that the C2 phenotype was characterized by stromal activation (EMT, pan-F-TBRS, etc.) as well as cell cycle progression (cell cycle, DNA replication, etc.), as illustrated in Figure 3H. It was predicted that the C2 phenotype responded to anti-CTAL4 therapy (Figure 3I). A previous study has defined six major immune subtypes (ISs) across pan-cancer in TCGA: IS1 (wound healing), IS2 (IFN-γ dominant), IS3 (inflammatory), IS4 (lymphocyte depleted), IS5 (immunologically quiet), and IS6 (TGF-β dominant) (36). We sought to comprehend the interaction of aging phenotypes with immune subtypes. Overall, the IS1, IS2, and IS6 subtypes tended to have more C1 and C2 aging phenotypes, with more C3 aging phenotype in the IS3 and IS4 subtypes (Figure 3J). Among five immune subtypes, ccRCC patients in the IS3 subtype presented the best OS outcomes, with the worst outcomes for those in the IS1 subtype (Figure 3K). Interestingly, the C3 patients were significantly enriched in the IS3 subtype (16.84% in C1, 17.37% in C2, 65.79% in C3). Although both C3 and IS3 showed a favorable prognosis, nearly 34% of IS3 patients had C1 and C2 phenotypes, which resulted in a poor prognosis. Thus, we explored whether aging-related clusters could further categorize patients into distinct survival groups. By performing a log-rank test, IS3 belonging to the C3 phenotype showed a more favorable prognosis compared to the other phenotypes (Figure 3L). These results indicated that aging-related genes could provide an additional characterization from a preexisting molecular classification of ccRCC.

Sensitivity to known targeted drugs of the three aging phenotypes

Considering that targeted treatment remains the preferred therapeutic regimen against advanced RCC, the sensitivity to axitinib, pazopanib, sorafenib, and sunitinib across the three aging phenotypes was assessed on the basis of the GDSC cell line expression data. The C2 phenotype presented higher sensitivity to axitinib (Figure 4A) and pazopanib (Figure 4B), the C3 phenotype was more sensitive to sorafenib (Figure 4C), and the C1 phenotype had higher sensitivity to sunitinib (Figure 4D).

Genomic alterations of the three aging phenotypes

The somatic mutation landscape was determined in the TCGA-KIRC cohort. Among the three aging phenotypes, *VHL* (48%) and *PBRM1* (41%) were the most frequent mutated genes (Figure 4E). Additionally, the mutated genes were evenly distributed across the three aging phenotypes. Further analysis was conducted to delineate the significant focal copy number alterations *via* GISTIC 2.0. Figure 4F illustrates the distinct focal amplifications and deletions of CNVs in each phenotype. In comparison to the C1 phenotype, a higher TMB score was investigated in the C2 phenotype (Figure 4G). The diverse genomic alteration preferences across the three phenotypes might result in distinct ccRCC progression.

Intrinsic immune evasion mechanisms of the three aging phenotypes

The intrinsic immune evasion mechanisms underlying the three aging phenotypes were evaluated in accordance with a series of indicators associated with tumor immunogenicity. The C3 phenotype had a higher intratumor heterogeneity compared with the C1 and C2 phenotypes (Figure 4H). Genomic instability was evaluated according to homologous recombination defects.

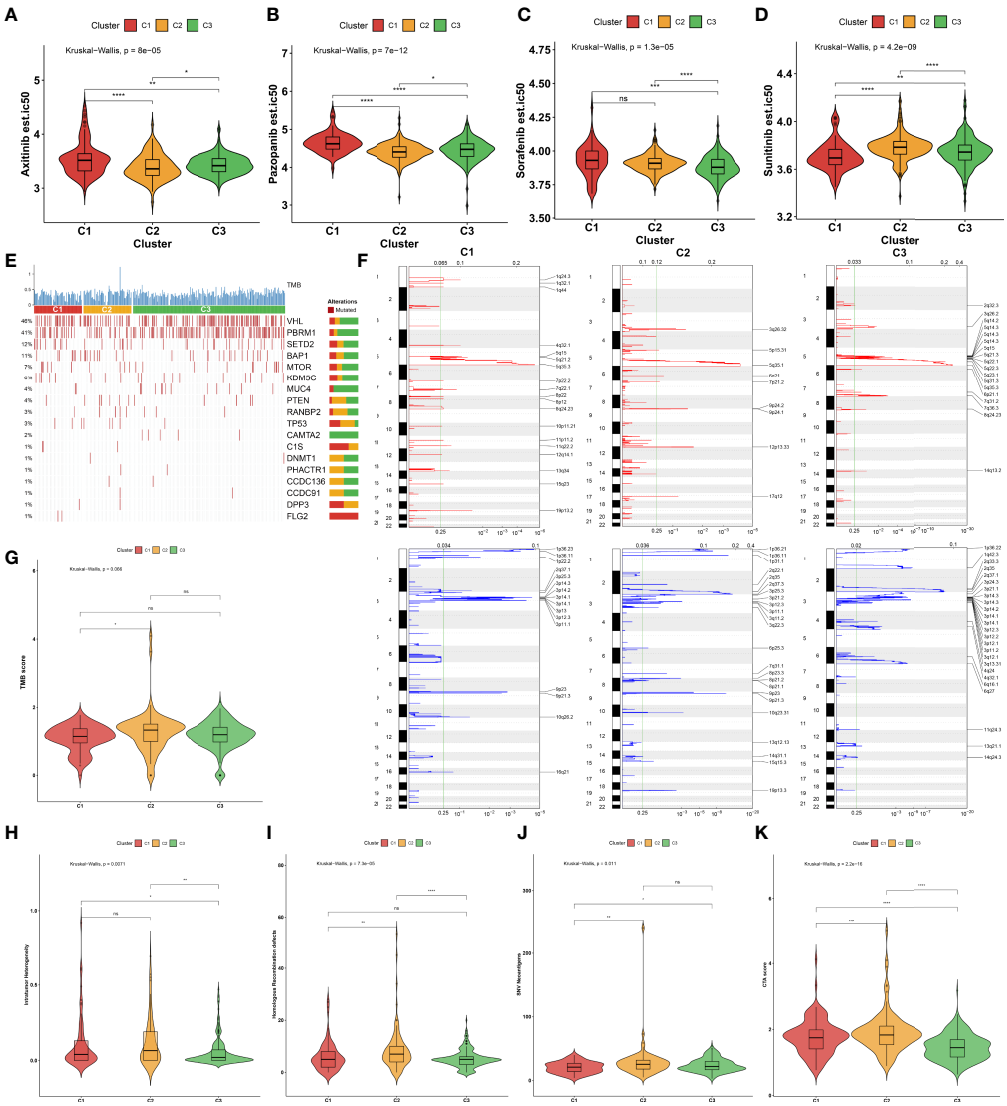


FIGURE 4
Sensitivity to known targeted drugs, genomic alterations, and intrinsic immune evasion mechanisms of the three aging phenotypes in the TCGA-KIRC cohort. **(A–D)** Box plots of the differences in sensitivity to **(A)** axitinib, **(B)** pazopanib, **(C)** sorafenib, and **(D)** sunitinib across the three aging phenotypes. **(E)** Waterfall plot of tumor somatic mutation across the three aging phenotypes. The top bar plot shows TMB. Each column represents an individual patient. Numbers and bar graphs depict the mutational frequencies as well as the proportions of mutation types. **(F)** Somatic copy number alterations across the three aging phenotypes. The *y*-axis indicates the chromosome positions, while the *x*-axis depicts the focal deletion or amplification identified by a horizontal blue or red bar. The green line indicates the significance threshold of FDR <0.25. (**G–K**) Box plots of the differences in **(G)** TMB score, **(H)** intratumor heterogeneity, **(I)** homologous recombination defects, **(J)** SNV neoantigens, and **(K)** CTA score across the three aging phenotypes. Ns, no significance; *$P < 0.05$; **$P < 0.01$; ***$P < 0.001$; ****$P < 0.0001$.

The C2 phenotype presented higher homologous recombination defects in comparison to the other phenotypes (Figure 4I). In contrast to the C1 phenotype, increased SNV neoantigens were investigated in the C2 and C3 phenotypes (Figure 4J). Moreover, the C3 phenotype had a lower overall expression of CTAs in comparison to the C1 and C2 phenotypes (Figure 4K). Overall, the above elements associated with tumor immunogenicity had remarkable differences in the three aging phenotypes.

Identification of aging phenotype-associated genes and generation of an agingScore system for ccRCC

In total, 450 aging phenotype-associated genes were identified by comparing the differential expression between aging phenotypes (Figure 5A; Supplementary Table 3). Further analysis demonstrated their roles in vessel morphogenesis and

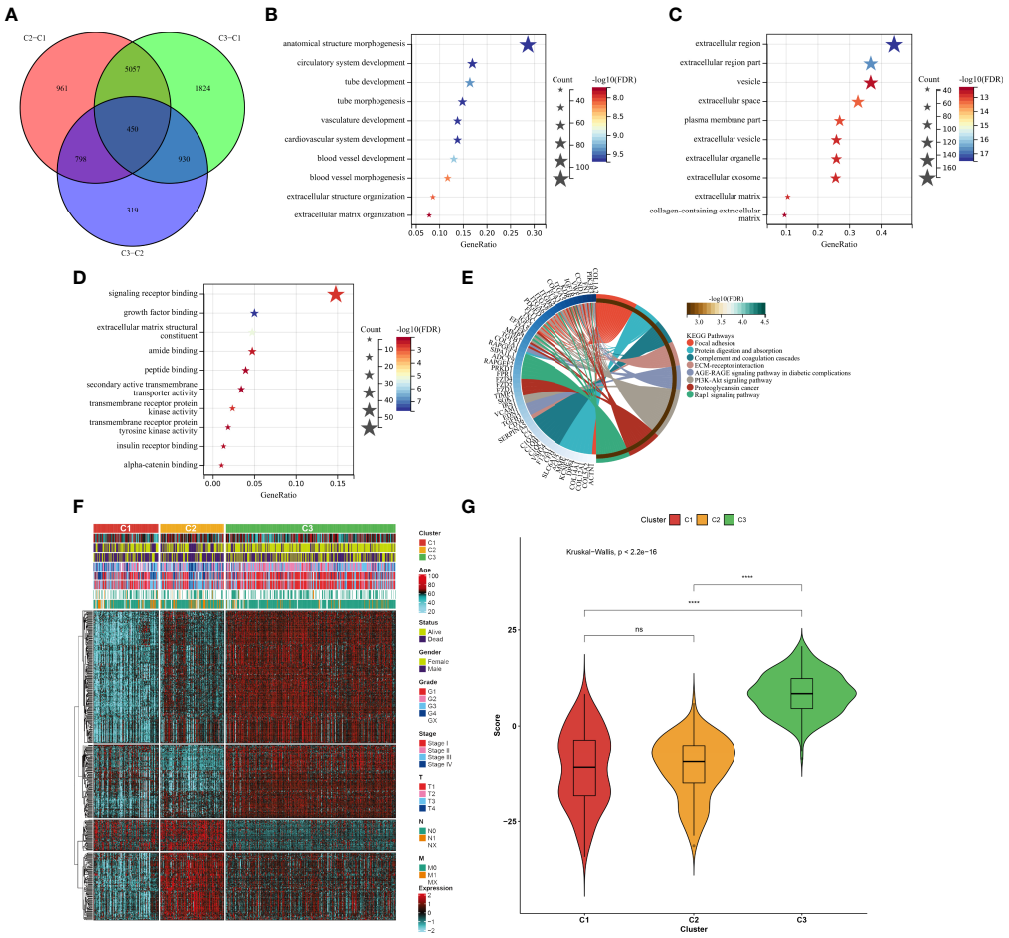


FIGURE 5
Identification of the aging phenotype-associated genes and generation of an agingScore system for ccRCC. **(A)** Venn diagram for the aging phenotype-associated genes *via* comparing the aging phenotypes. **(B–D)** The major **(B)** biological processes, **(C)** cellular components, or **(D)** molecular components enriched by aging phenotype-associated genes. **(E)** The major KEGG pathways enriched by aging phenotype-associated genes. **(F)** Distribution of the expression patterns of the aging phenotype-associated genes and clinical features across the three aging phenotypes. **(G)** Box plots of the distribution of agingScore among the three aging phenotypes. Ns, no significance; ****$P < 0.0001$.

development, extracellular components, and signaling receptor binding (Figures 5B–D). Additionally, these aging phenotype-associated genes were involved in mediating tumorigenic pathways (ECM–receptor interaction, PI3K–Akt signaling pathway, proteoglycans in cancer, Rap1 signaling pathway, etc.; Figure 5E). As illustrated in Figure 5F, there was widespread heterogeneity in the aging phenotype-associated genes among the three aging phenotypes. Univariate Cox regression determined 261 prognostic aging phenotype-associated genes in the TCGA-KIRC cohort (Supplementary Table 4). With the PCA approach, we computed an agingScore system for ccRCC. The C3 phenotype presented a higher agingScore in comparison to the C1 and C2 phenotypes (Figure 5G). In accordance with the median value of agingScore, we stratified the TCGA-KIRC, E-MTAB-1980, or TCGA-KIRP cohort into high and low agingScore populations. A high agingScore presented more favorable OS outcomes in comparison to a low agingScore in the TCGA-KIRC cohort (Figure 6A), E-MTAB-1980 cohort (Figure 6B), and TCGA-KIRP cohort (Figure 6C). Additionally, in the TCGA-KIRC cohort, a high agingScore was linked to better DFS (Figure 6D), DSS (Figure 6E), and PFS (Figure 6F), affirming the prognostic implication of the agingScore in ccRCC.

Validation of the predictive performance of the agingScore in ccRCC prognosis

The ROC diagram was drawn to verify the efficacy of this agingScore in predicting ccRCC prognosis. The AUC values of

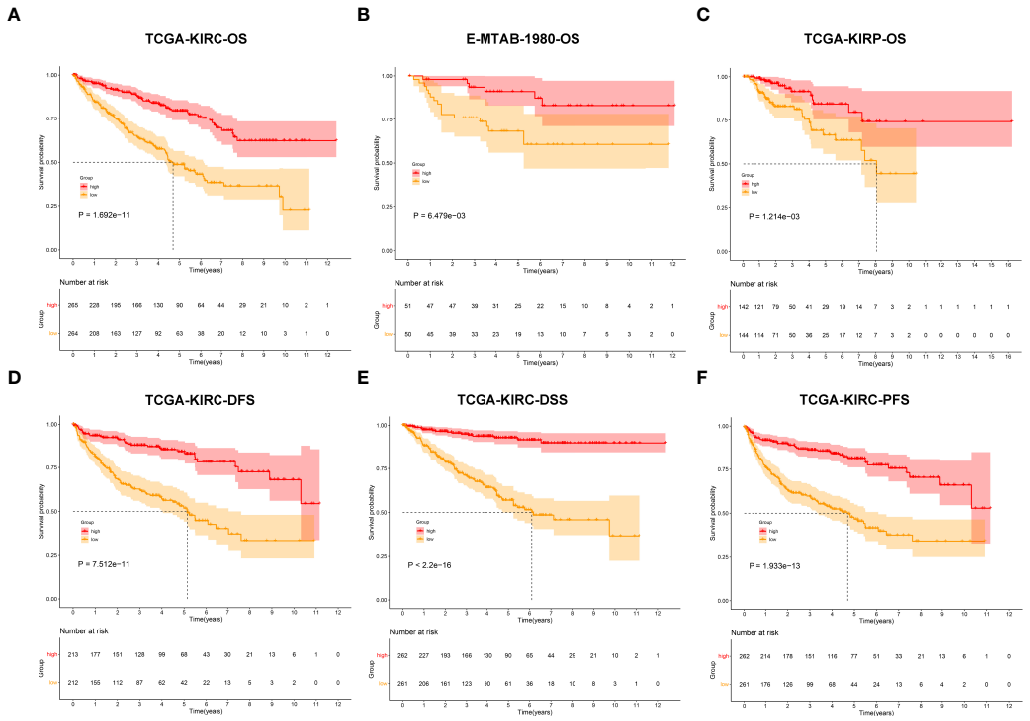


FIGURE 6
Analysis of the prognostic implication of the agingScore. **(A–C)** Kaplan–Meier analysis for OS between the high and low agingScore groups in the **(A)** TCGA-KIRC cohort, **(B)** E-MTAB-1980 cohort, and **(C)** TCGA-KIRP cohort. (**D–F**) Kaplan–Meier analysis for **(D)** DFS, **(E)** DSS, and **(F)** PFS between the high and low agingScore groups in the TCGA-KIRC cohort.

the 1-, 3-, and 5-year OS were 0.77, 0.61, and 0.61 in the TCGA-KIRC cohort and 0.70, 0.76, and 0.73 in the E-MTAB-1980 cohort (Figures 7A, B). Moreover, in the TCGA-KIRC cohort, the AUC values of the 1-, 3-, and 5-year DFS were 0.65, 0.68, and 0.69, respectively (Figure 7C); the AUC values of the 1-, 3-, and 5-year DSS were 0.75, 0.75, and 0.76, respectively (Figure 7D); and the AUC values of the 1-, 3-, and 5-year PFS were 0.69, 0.71, and 0.73, respectively (Figure 7E). Overall, the agingScore was a reliable prognostic indicator of ccRCC. In both the TCGA-KIRC and E-MTAB-1980 cohorts, the agingScore was an independent protective factor of ccRCC patients' OS (Figures 7F, G). Additionally, the agingScore was independently predictive of ccRCC patients' DFS, DSS, and PFS (Figures 7H–J).

Construction of an agingScore-based nomogram for ccRCC prognosis

To facilitate the clinical application of the agingScore, we conducted a personalized nomogram model. This nomogram for OS prediction was conducted by incorporating the following independent prognostic factors: age, stage, grade, and agingScore. In Figure 7K, the 1-, 3-, and 5-year OS for ccRCC individuals from the TCGA-KIRC cohort can be evaluated by this personalized nomogram model (C-index = 0.782). As illustrated in the calibration diagram, a favorable overlap was found between the nomogram-predicted and the observed 1-, 3-, and 5-year OS of ccRCC patients (Figure 7L). Overall, the nomogram had a good prediction performance in ccRCC prognosis.

Identification of agingScore-related candidate compounds and drug targets

On the basis of the GDSC cell line data, we computed the associations of the AUCs of the GDSC-derived compounds with agingScore. Figure 8A illustrates the agingScore-related GDSC-derived compounds. The above compounds were involved in the tumorigenic pathways (apoptosis regulation, DNA replication, cell cycle, EGFR signaling, etc.; Figure 8B). The AUCs of six CTRP-derived compounds (leptomycin B, CR-1-31B, SR-II-138A, paclitaxel, ouabain, and methotrexate) were positively correlated to agingScore (Figure 8C). The low agingScore group presented lower AUCs of the above compounds in comparison to the high agingScore group, demonstrating that patients with low agingScore were more likely to be sensitive to the above

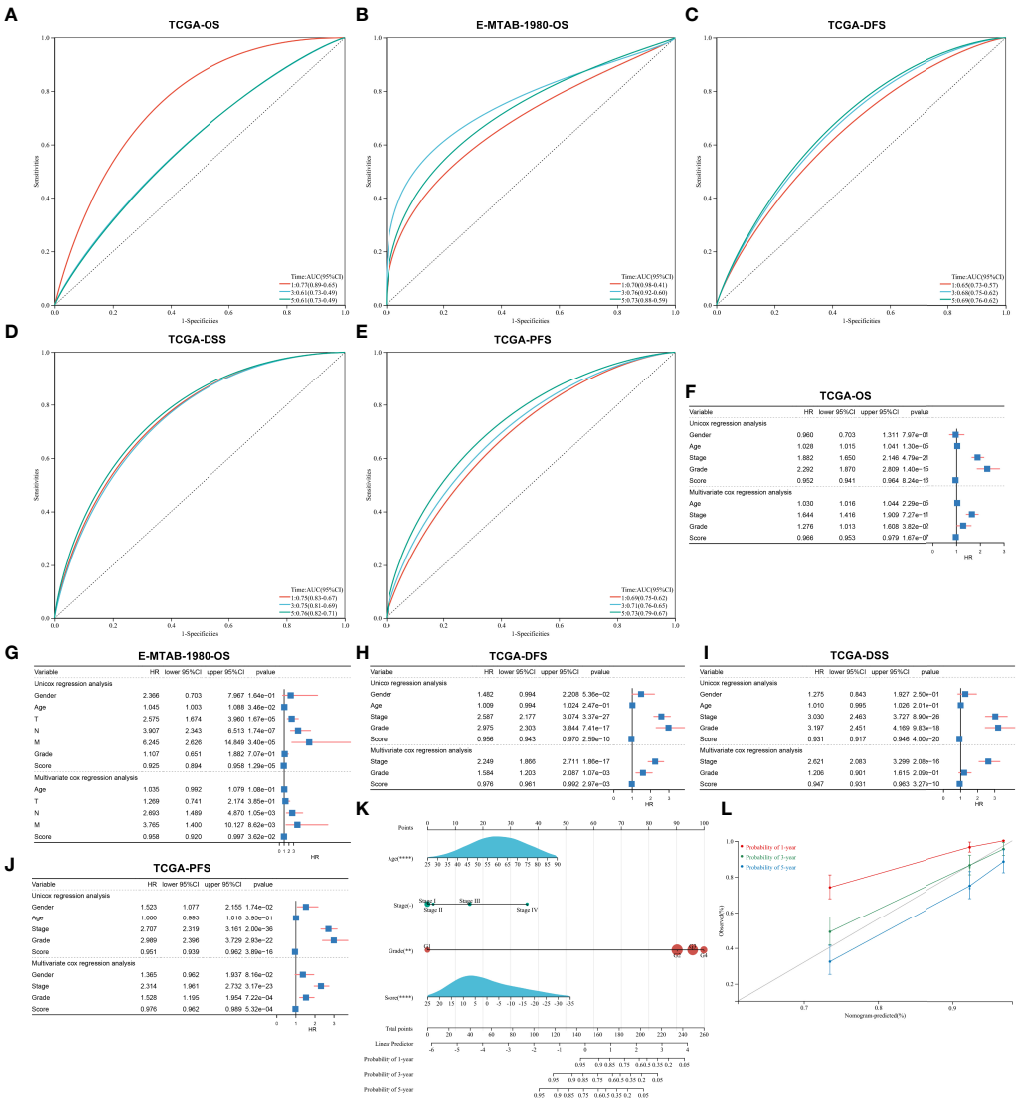


FIGURE 7
Validation of the predictive performance of the agingScore and generation of an agingScore-based nomogram for ccRCC prognosis. **(A, B)** ROC diagram of the 1-, 3-, and 6-year OS in the TCGA-KIRC cohort and the E-MTAB-1980 cohort. **(C–E)** ROC curves of the 1-, 3-, and 5-year DFS, DSS, and PFS in the TCGA-KIRC cohort. **(F, G)** Univariate and multivariate Cox regression models of agingScore as well as clinical features with OS in the TCGA-KIRC and E-MTAB-1980 cohorts. **(H–J)** Univariate and multivariate Cox regression analyses of agingScore and clinical features with DFS, DSS, and PFS in the TCGA-KIRC cohort. **(K)** Generation of an agingScore-based nomogram comprised of independent predictive indicators in the TCGA-KIRC cohort. (**L**) Calibration diagram for the nomogram-estimated and actual 1-, 3-, and 5-year OS in the TCGA-KIRC cohort.

compounds. Additionally, we determined the positive associations of the AUCs of eight PRISM-derived compounds (combretastatin-A-4, cabazitaxel, vincristine, PHA-793887, romidepsin, gemcitabine, dolastatin-10, and YM-155) with agingScore (Figure 8D). Lower AUCs were found in the low agingScore group, indicating higher sensitivity to the above compounds. Through Spearman's correlation analysis between the CERES score of drug targets and agingScore, 261 targets were screened ($P < 0.05$, and correlation coefficient > 0.82; Figure 8E). Additionally, Spearman's correlation analysis of druggable protein expression with agingScore was carried out. As a result, 242 protein targets were determined based on $P < 0.05$ and correlation coefficient ≤0.1 (Figure 8F). Three genes, namely, *CYP11A1*, *SAA1*, and *GRIK4*, were determined as potential therapeutic targets through the above analysis, indicating that suppressing the functions of the above genes in low agingScore individuals could present desirable therapeutic effects. Moreover, *CYP11A1* and *GRIK4* expression was validated in normal and kidney tissues by immunohistochemistry from the Human Protein Atlas (Figure 8G).

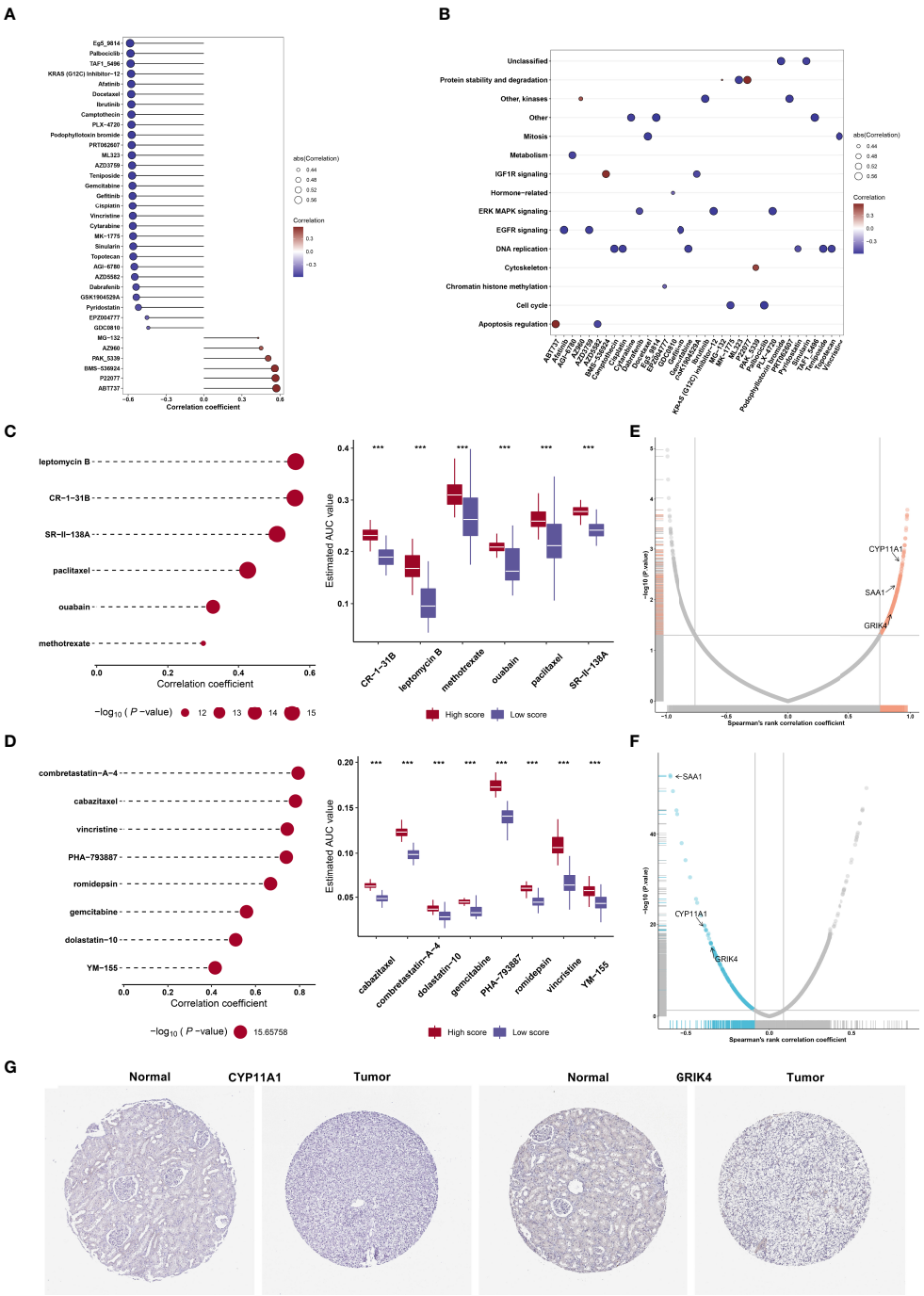


FIGURE 8
Identification of agingScore-related candidate compounds and drug targets. **(A)** Spearman's correlation analysis of GDSC-derived compounds and agingScore. **(B)** Mechanisms involving GDSC-derived compounds. **(C)** Spearman's correlation analysis of six CTRP-derived compounds and agingScore as well as differential analysis of drug responses between the high and low agingScore groups. **(D)** Spearman's correlation analysis of eight PRISM-derived compounds and agingScore as well as differential analysis of drug responses between groups. A lower AUC value implies higher drug sensitivity. ***$P < 0.001$. **(E)** Volcano plot of Spearman's correlation between agingScore and CERES score of drug targets. The red dot represents the significantly positive correlation ($P < 0.05$, and Spearman's correlation coefficient>0.82). **(F)** Volcano plot of Spearman's correlation between agingScore and protein expression of drug targets. The blue dot indicates a significant negative correlation ($P < 0.05$, and Spearman's correlation coefficient ≤ 0.1). **(G)** Immunohistochemistry of the expression of *CYP11A1* and *GRIK4* in normal and kidney cancer tissues. Bar, 200 μm.

Association between agingScore and antitumor immune responses

As illustrated in Figure 9A, the low agingScore group presented relatively high infiltrations of immunosuppressive cells (MDSCs, type 1 helper cells, type 2 helper cells, T follicular helper cells, etc.) as well as immune active cells ($CD4^+$ T cells, $CD8^+$ T cells, etc.) in comparison to the high agingScore group, indicating that tumors with high agingScore lacked recruitment or activation of innate immune cell populations. Moreover, the high agingScore group showed a higher expression of most co-stimulatory and co-inhibitory immune checkpoint molecules than the low agingScore group (Figure 9B), indicating that high agingScore might upregulate the immune checkpoint molecules to escape the immune elimination after immune activation. In Figure 9C, agingScore was positively linked with cancer antigen presentation, $CD8^+$ T cell recruiting, NK cell recruiting, infiltration of immune cells into tumors, and killing of cancer cells. Additionally, agingScore was positively linked with stromal activation (EMT, FGFR3-related genes, angiogenesis, and WNT target) and antigen-processing machinery and was negatively linked with cell cycle progression. With the TIDE algorithm, patients who responded to immunotherapy had relatively higher agingScore both in the TCGA-KIRC cohort (Figure 9D) and the E-MTAB-1980 cohort (Figure 9E). Therefore, individuals with high agingScore had a higher probability to respond to immunotherapy.

Post-transcriptional features correlated to agingScore

In the TCGA-KIRC cohort, we identified 5 upregulated miRNAs and 55 downregulated miRNAs in the high agingScore group in comparison to the low agingScore group in accordance with FDR <0.05 and at least 1.5-fold changes (Figure 10A). Additionally, 2,921 mRNAs were upregulated and 476 mRNAs were downregulated in the high agingScore group compared with the low agingScore group according to FDR <0.05 and at least 1.5-fold changes (Figure 10B). Thereafter, the targeted differentially expressed mRNAs of the above miRNAs were predicted (Supplementary Table 5), and enrichment analysis of the signaling pathways of their target genes was conducted. The tumorigenic pathways especially were enriched by the miRNA-targeted mRNAs in the high agingScore group, containing pathways in cancer; miRNAs in cancer; FoxO, PI3K-Akt, ErbB, and Notch signaling pathways; focal adhesion; and Th1 and Th2 cell differentiation (Figure 10C). These results indicated that agingScore was related to post-transcriptional mechanisms and tumorigenic pathways.

Discussion

Over the past decade, high-throughput analysis has greatly advanced our understanding of ccRCC biology, allowing us to recapitulate critical events in ccRCC initiation and progression (2). The increase in understanding of the molecular profiles as well as genetic alterations has translated into novel targets or biomarkers, which affect ccRCC decision-making, thereby shedding a novel insight into prolonging patients' clinical outcomes (1). Considering the unique molecular and clinical features of ccRCC, tailoring specialized management is of importance (36). Our study categorized ccRCC into three clinically and therapeutically relevant subtypes in accordance with the expression profiles of prognostic aging-associated genes (12). Additionally, agingScore was generated and presented a favorable performance in prognostication as well as immunotherapeutic responses. Our findings proposed a precise prognostic prediction approach for ccRCC patients with similar biological patterns with more precise prognostication.

ccRCC is a highly heterogeneous tumor among individual patients, encompassing different malignancies with different pathologic characteristics and molecular pathways, which makes it nearly impossible to determine a therapy that fits all ccRCC cases (4). Intratumor heterogeneity, a common feature of ccRCC, is linked to patterns of metastatic spread and prognosis after surgery, complicating the assessment of prognostic indicators (37). Hence, finding tailored therapeutic regimens for subpopulations is significant for maximizing therapeutic efficiency. In accordance with the expression profiling of 173 prognostic aging-associated genes, 529 ccRCC patients in the TCGA-KIRC cohort were classified into three aging phenotypes, which was affirmed in the E-MTAB-1980 cohort. The successful development of new immunotherapy and immunotherapy-based combination therapy requires an in-depth understanding of ccRCC immunobiology. Many chromosomal alterations are linked to the response or resistance to ICB in advanced ccRCC, and the crosstalk of somatic alterations with immune infiltrations impacts the response to ICB (38). It has been demonstrated that previous genomic correlations of ICB responses in solid tumors (TMB and PD-L1 status, etc.) cannot predict ccRCC, suggesting the important role of the immune microenvironment in modulating clinical benefits (39–41). Most ccRCC presents a moderate TMB, but high infiltration of intratumoral $CD8^+$ T cells is linked to an unfavorable prognosis. Three aging phenotypes were characterized by diverse prognosis, clinical features, immune cell infiltration, tumor immunogenicity, immunotherapeutic response, and sensitivity to targeted drugs (axitinib, pazopanib, sorafenib, and sunitinib), indicating the roles of the aging process in ccRCC progression. Additionally, the interactions of the aging phenotypes with the TME reflected that aging processes seem to mediate immune cell subpopulations in ccRCC tumors.

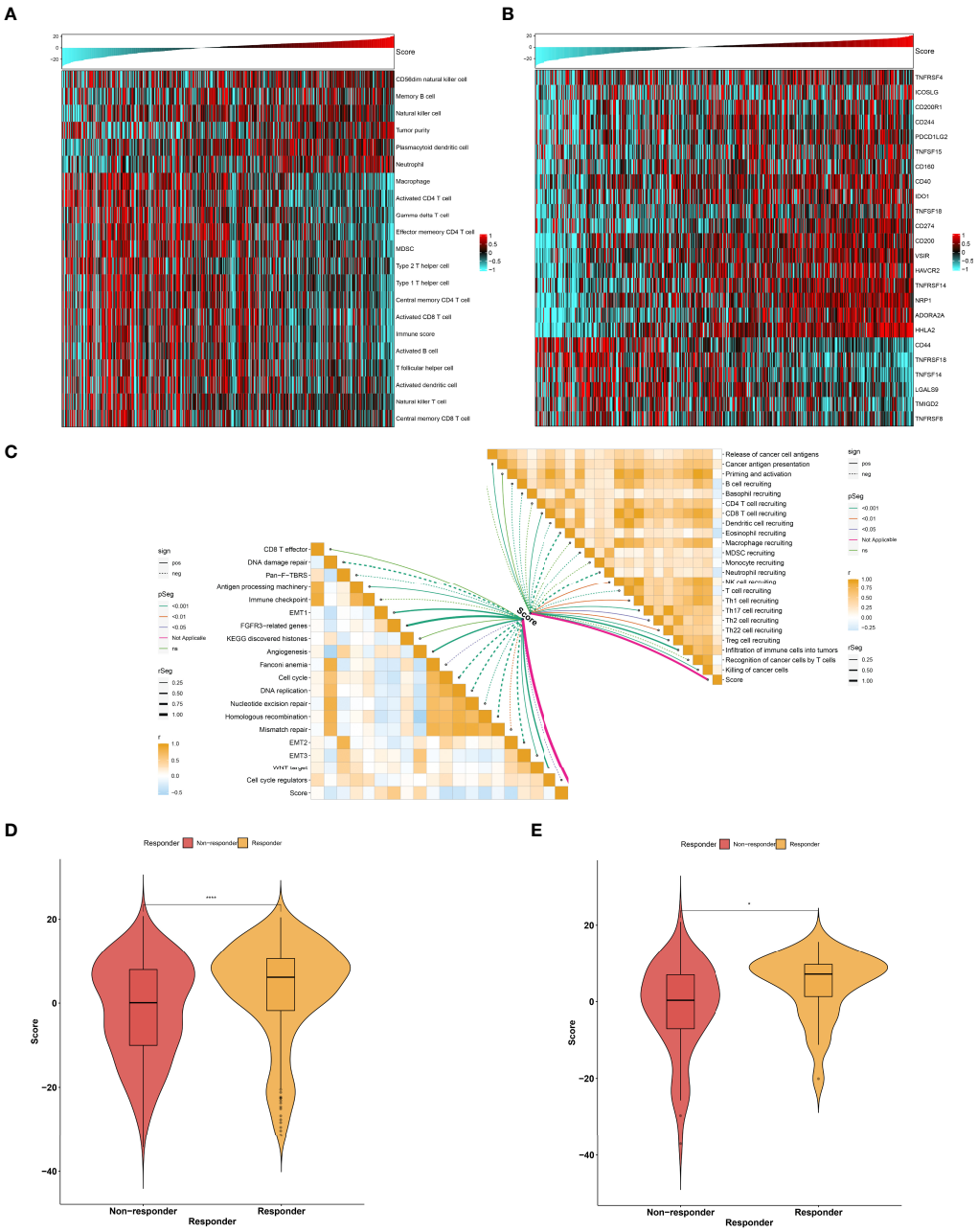


FIGURE 9
Association between agingScore and antitumor immune responses. **(A)** Landscape of immune cell infiltrations in the high as well as low agingScore groups in the TCGA-KIRC dataset. **(B)** Distribution of the expression of immune checkpoint molecules in the high and low agingScore groups in the TCGA-KIRC cohort. **(C)** Association of agingScore with activities of cancer immunity cycle and known biological processes in the TCGA-KIRC dataset. Solid lines represent positive correlations, while dashed lines represent negative correlations. **(D)** Prediction of response to immunotherapy in the TCGA-KIRC dataset. **(E)** Validation of the response to immunotherapy in the high and low agingScore groups in the E-MTAB-1980 cohort. *$P < 0.05$; ****$P < 0.0001$.

We generated the agingScore system, which enabled us to reliably and independently predict ccRCC prognosis. Patients with low agingScore presented undesirable prognosis in contrast to those with high agingScore. Recently, Chen et al. defined cellular senescence score for delineating the cellular senescence landscape across pan-cancer, which correlated to genomic and immune features, immunotherapeutic responses, and clinical outcomes (42). The nomogram is a useful and easy-to-use tool used by doctors to predict outcomes, plan personalized therapy, and determine follow-up or imaging

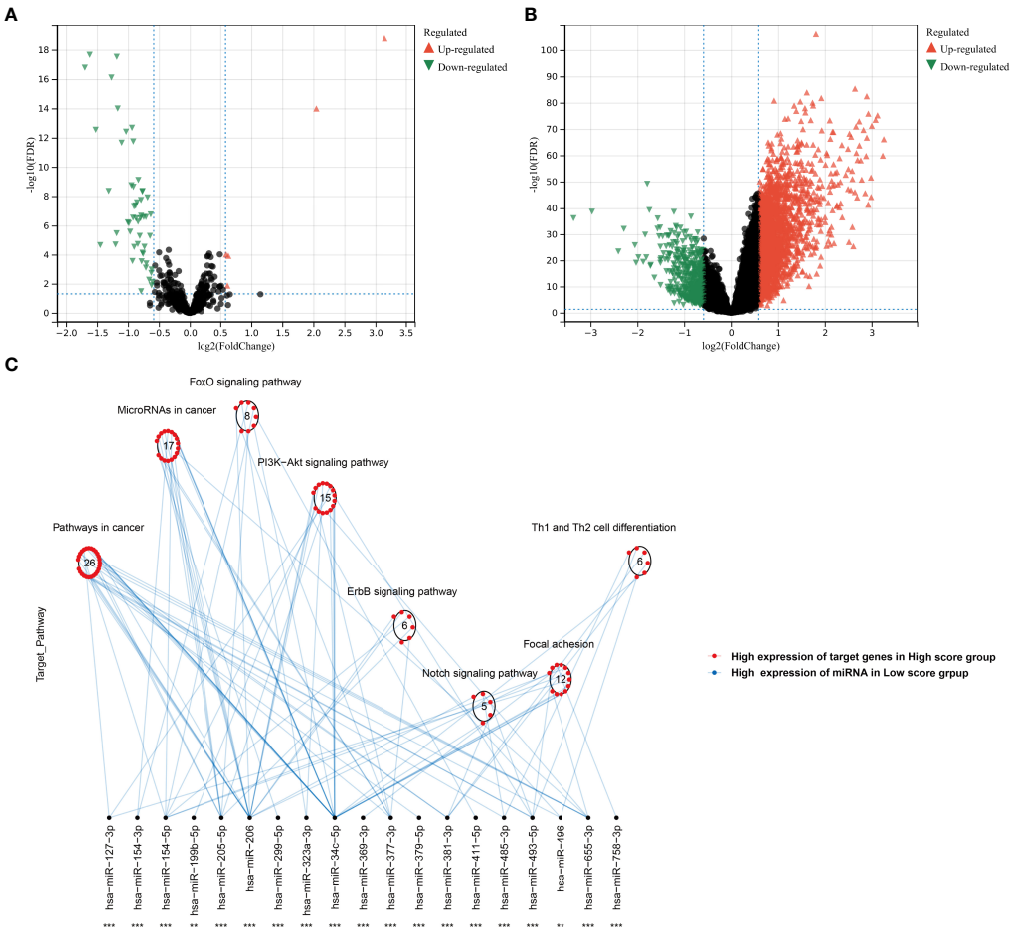


FIGURE 10
Analysis of post-transcriptional features correlated to agingScore in the TCGA-KIRC cohort. **(A)** Volcano diagram of differentially expressed miRNAs between the high and low agingScore groups. **(B)** Volcano diagram of differentially expressed RNAs between the high and low agingScore groups. Red represents upregulation, while green represents downregulation. **(C)** Differences in miRNA-targeted signaling pathways between the high and low agingScore groups. The red dot indicates the high expression of targeted mRNAs in the high agingScore group, while the blue dot indicates the high expression of miRNAs in the low agingScore group.

intervals (43). Previous research has conducted several nomogram models for ccRCC (44, 45). Regrettably, few nomograms have been applied in clinical practice. Herein, we developed the nomogram to estimate the personalized OS probability of ccRCC subjects, comprising age, stage, grade, and agingScore. Calibration plots confirmed the favorable overlap between this model-estimated and investigated OS probabilities of ccRCC. Hence, the agingScore-based nomogram may provide individualized prognosis estimates for ccRCC subjects. The agingScore was remarkably linked to tumorigenic pathways, immune cell infiltration, and tumor immunogenicity. Additionally, high agingScore patients were responsive to immunotherapy. Several small molecular compounds were determined for the low agingScore patients. Proteins showing an enhanced negative association with agingScore could possess therapeutic potential for patients with low agingScore (46). Nevertheless, most human proteins are undruggable because they are short of distinct active sites where small molecule agents can bind to as well as reside in cells that are inaccessible to biological agents. Hence, it is of importance to speculate on the potential druggable therapeutic targets for low agingScore patients with undesirable survival outcomes. Through Spearman's correlation analysis of agingScore with the CERES score of drug targets and the expression level of druggable proteins, we determined the three genes, namely, *CYP11A1*, *SAA1*, and *GRIK4*, as promising therapeutic targets for low agingScore patients.

Collectively, our findings offered a novel insight into personalized prognostication methods as well as threw light on combining tailored risk stratification with precision treatment. Nevertheless, our analysis still possessed several limitations. At first, the number of datasets with available RNA-seq or

microarray profiles remained limited. The three aging subtypes and agingScore needed to be verified with a larger sample size. Secondly, the relationships between drug targets and small molecular compounds lacked verification, thereby reducing the persuasiveness of our conclusion. Thirdly, our results were obtained from *in-silico* analysis, and more experimental and clinical verification was required to facilitate the clinical application of our findings.

Conclusion

Our findings revealed the interactions between aging-associated genes in ccRCC and remodeling of the TME, providing a novel insight into the molecular drivers underlying ccRCC initiation and development. Collectively, our study offered opportunities for ccRCC prevention, early detection, and prognostication as well as therapy.

Data availability statement

The datasets presented in this study can be found in online repositories. The names of the repository/repositories and accession number(s) can be found in the article/Supplementary Material.

Author contributions

DM and WZ designed the study. MZ, CH, XW, YG, and XH collected the clinical information and gene expression data. MZ and CH analyzed the data and wrote the manuscript. All authors have read, revised, and approved the final manuscript.

Funding

This study was supported by the Xiamen Medical and Health Guidance Project (3502Z202147ZD1264, 3502Z20214ZD1258, and 3502Z20214ZD1263), Fujian Provincial Science and Technology Plan Project (2021D008, 2021D010, 2021D012, and 2022D030), and Fujian Health Scientific Research Personnel Training Program (No. 2019-ZQNB-34).

Conflict of interest

The authors declare that the research was conducted in the absence of any commercial or financial relationships that could be construed as a potential conflict of interest.

Publisher's note

All claims expressed in this article are solely those of the authors and do not necessarily represent those of their affiliated organizations, or those of the publisher, the editors and the reviewers. Any product that may be evaluated in this article, or claim that may be made by its manufacturer, is not guaranteed or endorsed by the publisher.

Supplementary material

The Supplementary Material for this article can be found online at: https://www.frontiersin.org/articles/10.3389/fimmu.2022.877076/full#supplementary-material

SUPPLEMENTARY FIGURE 1
Validation of three aging phenotypes across ccRCC in the E-MTAB-1980 dataset. **(A)** The CDFs of consensus matrix for k=2~9 identified by colors. **(B)** Relative alteration in area under CDFs for k=2~9. **(C)** Tracking plot for classification of TCGA-KIRC dataset into diverse subtypes for k=2~9. **(D)** Classification of the E-MTAB-1980 cohort into three clusters when k=3. **(E)** PCA of the RNA expression profiling of prognostic aging-associated genes. **(F)** Kaplan-Meier analysis for OS among three phenotypes.

SUPPLEMENTARY TABLE 1
Clinical information of TCGA-KIRC, TCGA-KIRP, and E-MTAB-1980 cohorts.

SUPPLEMENTARY TABLE 2
Univariate Cox regression analysis of 173 prognostic aging-associated genes in TCGA-KIRC dataset.

SUPPLEMENTARY TABLE 3
The list of aging phenotype-associated genes in TCGA-KIRC cohort.

SUPPLEMENTARY TABLE 4
The information of prognostic aging phenotype-associated genes in TCGA-KIRC cohort.

SUPPLEMENTARY TABLE 5
The list of targeted differentially expressed mRNAs of differentially expressed miRNAs.

References

1. Bray F, Ferlay J, Soerjomataram I, Siegel RL, Torre LA, Jemal A. Global cancer statistics 2018: GLOBOCAN estimates of incidence and mortality worldwide for 36 cancers in 185 countries. *CA Cancer J Clin* (2018) 68(6):394–424. doi: 10.3322/caac.21492

2. Wei G, Sun H, Dong K, Hu L, Wang Q, Zhuang Q, et al. The thermogenic activity of adjacent adipocytes fuels the progression of ccRCC and compromises anti-tumor therapeutic efficacy. *Cell Metab* (2021) 33(10):2021–39.e8. doi: 10.1016/j.cmet.2021.08.012

3. Jonasch E, Walker CL, Rathmell WK. Clear cell renal cell carcinoma ontogeny and mechanisms of lethality. *Nat Rev Nephrol* (2021) 17(4):245–61. doi: 10.1038/s41581-020-00359-2

4. Krishna C, DiNatale RG, Kuo F, Srivastava RM, Vuong L, Chowell D, et al. Single-cell sequencing links multiregional immune landscapes and tissue-resident T cells in ccRCC to tumor topology and therapy efficacy. *Cancer Cell* (2021) 39 (5):662–77.e6. doi: 10.1016/j.ccell.2021.03.007

5. Banchereau R, Leng N, Zill O, Sokol E, Liu G, Pavlick D, et al. Molecular determinants of response to PD-L1 blockade across tumor types. *Nat Commun* (2021) 12(1):3969. doi: 10.1038/s41467-021-24112-w

6. Motzer RJ, Escudier B, McDermott DF, George S, Hammers HJ, Srinivas S, et al. Nivolumab versus everolimus in advanced renal-cell carcinoma. *N Engl J Med* (2015) 373(19):1803–13. doi: 10.1056/NEJMoa1510665

7. Motzer RJ, Robbins PB, Powles T, Albiges L, Haanen JB, Larkin J, et al. Avelumab plus axitinib versus sunitinib in advanced renal cell carcinoma: biomarker analysis of the phase 3 JAVELIN renal 101 trial. *Nat Med* (2020) 26 (11):1733–41. doi: 10.1038/s41591-020-1044-8

8. Aunan JR, Cho WC, Søreide K. The biology of aging and cancer: A brief overview of shared and divergent molecular hallmarks. *Aging Dis* (2017) 8(5):628–42. doi: 10.14336/ad.2017.0103

9. Oh E, Kim JH, Um J, Jung DW, Williams DR, Lee H. Genome-wide transcriptomic analysis of non-tumorigenic tissues reveals aging-related prognostic markers and drug targets in renal cell carcinoma. *Cancers (Basel)* (2021) 13(12):3045. doi: 10.3390/cancers13123045

10. Sato Y, Yoshizato T, Shiraishi Y, Maekawa S, Okuno Y, Kamura T, et al. Integrated molecular analysis of clear-cell renal cell carcinoma. *Nat Genet* (2013) 45(8):860–7. doi: 10.1038/ng.2699

11. Gautier L, Cope L, Bolstad BM, Irizarry RA. Affy–analysis of affymetrix GeneChip data at the probe level. *Bioinformatics* (2004) 20(3):307–15. doi: 10.1093/bioinformatics/btg405

12. de Magalhães JP, Costa J, Toussaint O. HAGR: the human ageing genomic resources. *Nucleic Acids Res* (2005) 33(Database issue):D537–43. doi: 10.1093/nar/gki017

13. Wilkerson MD, Hayes DN. ConsensusClusterPlus: a class discovery tool with confidence assessments and item tracking. *Bioinformatics* (2010) 26 (12):1572–3. doi: 10.1093/bioinformatics/btq170

14. Hänzelmann S, Castelo R, Guinney J. GSVA: gene set variation analysis for microarray and RNA-seq data. *BMC Bioinf* (2013) 14:7. doi: 10.1186/1471-2105-14-7

15. Yu G, Wang LG, Han Y, He QY. clusterProfiler: an r package for comparing biological themes among gene clusters. *Omics* (2012) 16(5):284–7. doi: 10.1089/omi.2011.0118

16. Şenbabaoğlu Y, Gejman RS, Winer AG, Liu M, Van Allen EM, de Velasco G, et al. Tumor immune microenvironment characterization in clear cell renal cell carcinoma identifies prognostic and immunotherapeutically relevant messenger RNA signatures. *Genome Biol* (2016) 17(1):231. doi: 10.1186/s13059-016-1092-z

17. Rosenberg JE, Hoffman-Censits J, Powles T, van der Heijden MS, Balar AV, Necchi A, et al. Atezolizumab in patients with locally advanced and metastatic urothelial carcinoma who have progressed following treatment with platinum-based chemotherapy: a single-arm, multicentre, phase 2 trial. *Lancet* (2016) 387 (10031):1909–20. doi: 10.1016/s0140-6736(16)00561-4

18. Mariathasan S, Turley SJ, Nickles D, Castiglioni A, Yuen K, Wang Y, et al. TGFβ attenuates tumour response to PD-L1 blockade by contributing to exclusion of T cells. *Nature* (2018) 554(7693):544–8. doi: 10.1038/nature25501

19. Yoshihara K, Shahmoradgoli M, Martínez E, Vegesna R, Kim H, Torres-Garcia W, et al. Inferring tumour purity and stromal and immune cell admixture from expression data. *Nat Commun* (2013) 4:2612. doi: 10.1038/ncomms3612

20. Chen DS, Mellman I. Oncology meets immunology: the cancer-immunity cycle. *Immunity* (2013) 39(1):1–10. doi: 10.1016/j.immuni.2013.07.012

21. Hoshida Y, Brunet JP, Tamayo P, Golub TR, Mesirov JP. Subclass mapping: identifying common subtypes in independent disease data sets. *PloS One* (2007) 2 (11):e1195. doi: 10.1371/journal.pone.0001195

22. Geeleher P, Cox N, Huang RS. pRRophetic: an r package for prediction of clinical chemotherapeutic response from tumor gene expression levels. *PloS One* (2014) 9(9):e107468. doi: 10.1371/journal.pone.0107468

23. Yang W, Soares J, Greninger P, Edelman EJ, Lightfoot H, Forbes S, et al. Genomics of drug sensitivity in cancer (GDSC): a resource for therapeutic biomarker discovery in cancer cells. *Nucleic Acids Res* (2013) 41(Database issue): D955–61. doi: 10.1093/nar/gks1111

24. Ghandi M, Huang FW, Jané-Valbuena J, Kryukov GV, Lo CC, McDonald ER3rd, et al. Next-generation characterization of the cancer cell line encyclopedia. *Nature* (2019) 569(7757):503–8. doi: 10.1038/s41586-019-1186-3

25. Mayakonda A, Lin DC, Assenov Y, Plass C, Koeffler HP. Maftools: efficient and comprehensive analysis of somatic variants in cancer. *Genome Res* (2018) 28 (11):1747–56. doi: 10.1101/gr.239244.118

26. Mermel CH, Schumacher SE, Hill B, Meyerson ML, Beroukhim R, Getz G. GISTIC2.0 facilitates sensitive and confident localization of the targets of focal somatic copy-number alteration in human cancers. *Genome Biol* (2011) 12(4):R41. doi: 10.1186/gb-2011-12-4-r41

27. Auslander N, Zhang G, Lee JS, Frederick DT, Miao B, Moll T, et al. Robust prediction of response to immune checkpoint blockade therapy in metastatic melanoma. *Nat Med* (2018) 24(10):1545–9. doi: 10.1038/s41591-018-0157-9

28. Nielsen M, Andreatta M. NetMHCpan-3.0; improved prediction of binding to MHC class I molecules integrating information from multiple receptor and peptide length datasets. *Genome Med* (2016) 8(1):33. doi: 10.1186/s13073-016-0288-x

29. Szolek A, Schubert B, Mohr C, Sturm M, Feldhahn M, Kohlbacher O. OptiType: precision HLA typing from next-generation sequencing data. *Bioinformatics* (2014) 30(23):3310–6. doi: 10.1093/bioinformatics/btu548

30. Chalmers ZR, Connelly CF, Fabrizio D, Gay L, Ali SM, Ennis R, et al. Analysis of 100,000 human cancer genomes reveals the landscape of tumor mutational burden. *Genome Med* (2017) 9(1):34. doi: 10.1186/s13073-017-0424-2

31. Thorsson V, Gibbs DL, Brown SD, Wolf D, Bortone DS, Yang T-HO, et al. The immune landscape of cancer. *Immunity* (2018) 48(4):812–30.e14. doi: 10.1016/j.immuni.2018.03.023

32. Ritchie ME, Phipson B, Wu D, Hu Y, Law CW, Shi W, et al. Limma powers differential expression analyses for RNA-sequencing and microarray studies. *Nucleic Acids Res* (2015) 43(7):e47. doi: 10.1093/nar/gkv007

33. Gao Y, Wang H, Li H, Ye X, Xia Y, Yuan S, et al. Integrated analyses of m(1) A regulator-mediated modification patterns in tumor microenvironment-infiltrating immune cells in colon cancer. *Oncoimmunology* (2021) 10 (1):1936758. doi: 10.1080/2162402x.2021.1936758

34. Zhang B, Wu Q, Li B, Wang D, Wang L, Zhou YL. m(6)A regulator-mediated methylation modification patterns and tumor microenvironment infiltration characterization in gastric cancer. *Mol Cancer* (2020) 19(1):53. doi: 10.1186/s12943-020-01170-0

35. Kozomara A, Birgaoanu M, Griffiths-Jones S. miRBase: from microRNA sequences to function. *Nucleic Acids Res* (2019) 47(D1):D155–d62. doi: 10.1093/nar/gky1141

36. Miao D, Margolis CA, Gao W, Voss MH, Li W, Martini DJ, et al. Genomic correlates of response to immune checkpoint therapies in clear cell renal cell carcinoma. *Science* (2018) 359(6377):801–6. doi: 10.1126/science.aan5951

37. Au L, Hatipoglu E, Robert de Massy M, Litchfield K, Beattie G, Rowan A, et al. Determinants of anti-PD-1 response and resistance in clear cell renal cell carcinoma. *Cancer Cell* (2021) 39(11):1497–518.e11. doi: 10.1016/j.ccell.2021.10.001

38. Braun DA, Hou Y, Bakouny Z, Ficial M, Sant' Angelo M, Forman J, et al. Interplay of somatic alterations and immune infiltration modulates response to PD-1 blockade in advanced clear cell renal cell carcinoma. *Nat Med* (2020) 26 (6):909–18. doi: 10.1038/s41591-020-0839-y

39. Snyder A, Makarov V, Merghoub T, Yuan J, Zaretsky JM, Desrichard A, et al. Genetic basis for clinical response to CTLA-4 blockade in melanoma. *N Engl J Med* (2014) 371(23):2189–99. doi: 10.1056/NEJMoa1406498

40. Riaz N, Havel JJ, Makarov V, Desrichard A, Urba WJ, Sims JS, et al. Tumor and microenvironment evolution during immunotherapy with nivolumab. *Cell* (2017) 171(4):934–49.e16. doi: 10.1016/j.cell.2017.09.028

41. Havel JJ, Chowell D, Chan TA. The evolving landscape of biomarkers for checkpoint inhibitor immunotherapy. *Nat Rev Cancer* (2019) 19(3):133–50. doi: 10.1038/s41568-019-0116-x

42. Wang X, Ma L, Pei X, Wang H, Tang X, Pei JF, et al. Comprehensive assessment of cellular senescence in the tumor microenvironment. *Brief Bioinform* (2022) 23(3):bbac118. doi: 10.1093/bib/bbac118

43. Gittleman H, Lim D, Kattan MW, Chakravarti A, Gilbert MR, Lassman AB, et al. An independently validated nomogram for individualized estimation of survival among patients with newly diagnosed glioblastoma: NRG oncology RTOG 0525 and 0825. *Neuro Oncol* (2017) 19(5):669–77. doi: 10.1093/neuonc/now208

44. Qi-Dong X, Yang X, Lu JL, Liu CQ, Sun JX, Li C, et al. Development and validation of a nine-Redox-Related long noncoding RNA signature in renal clear cell carcinoma. *Oxid Med Cell Longev* (2020) 2020:6634247. doi: 10.1155/2020/6634247

45. Yin X, Wang Z, Wang J, Xu Y, Kong W, Zhang J. Development of a novel gene signature to predict prognosis and response to PD-1 blockade in clear cell renal cell carcinoma. *Oncoimmunology* (2021) 10(1):1933332. doi: 10.1080/2162402x.2021.1933332

46. Yang C, Huang X, Li Y, Chen J, Lv Y, Dai S. Prognosis and personalized treatment prediction in TP53-mutant hepatocellular carcinoma: an in silico strategy towards precision oncology. *Brief Bioinform* (2021) 22(3):bbaa164. doi: 10.1093/bib/bbaa164

frontiers | Frontiers in Immunology

TYPE Original Research
PUBLISHED 27 October 2022
DOI 10.3389/fimmu.2022.905057

Check for updates

OPEN ACCESS

EDITED BY
Elena Ciaglia,
University of Salerno, Italy

REVIEWED BY
You Lang Zhou,
Affiliated Hospital of Nantong University, China
Jo A. Van Ginderachter,
Vrije University Brussel, Belgium

*CORRESPONDENCE
Kuntang Shen
shen.kuntang@zs-hospital.sh.cn

†These authors have contributed equally to this work

SPECIALTY SECTION
This article was submitted to Cancer Immunity and Immunotherapy, a section of the journal Frontiers in Immunology

RECEIVED 26 March 2022
ACCEPTED 11 October 2022
PUBLISHED 27 October 2022

CITATION
Zhang Q, Sun X, Sun J, Lu J, Gao X, Shen K and Qin X (2022) RNA m^{5}C regulator-mediated modification patterns and the cross-talk between tumor microenvironment infiltration in gastric cancer.
Front. Immunol. 13:905057.
doi: 10.3389/fimmu.2022.905057

COPYRIGHT
© 2022 Zhang, Sun, Sun, Lu, Gao, Shen and Qin. This is an open-access article distributed under the terms of the Creative Commons Attribution License (CC BY). The use, distribution or reproduction in other forums is permitted, provided the original author(s) and the copyright owner(s) are credited and that the original publication in this journal is cited, in accordance with accepted academic practice. No use, distribution or reproduction is permitted which does not comply with these terms.

RNA m^{5}C regulator-mediated modification patterns and the cross-talk between tumor microenvironment infiltration in gastric cancer

Qiang Zhang[1,2†], Xiangfei Sun[1†], Jianyi Sun[1†], Jiangshen Lu[1], Xiaodong Gao[1], Kuntang Shen[1*] and Xinyu Qin[1]

[1]Department of General Surgery, Zhongshan Hospital, Fudan University, Shanghai, China, [2]Department of Gastrointestinal Surgery, the Second People's Hospital of Lianyungang Affiliated to Kangda College, Nanjing Medical University, Lianyungang, Jiangsu, China

The effect of immunotherapy strategy has been affirmed in the treatment of various tumors. Nevertheless, the latent role of RNA 5-methylcytosine (m^{5}C) modification in gastric cancer (GC) tumor microenvironment (TME) cell infiltration is still unclear. We systematically explore the m^{5}C modification patterns of 2,122 GC patients from GEO and TCGA databases by 16 m^{5}C regulators and related these patterns to TME characteristics. LASSO Cox regression was employed to construct the m^{5}Cscore based on the expression of regulators and DEGs, which was used to evaluate the prognosis. All the GC patients were divided into three m^{5}C modification clusters with distinct gene expression characteristics and TME patterns. GSVA, ssGSEA, and TME cell infiltration analysis showed that m^{5}C clusters A, B, and C were classified as immune-desert, immune-inflamed, and immune-excluded phenotype, respectively. The m^{5}Cscore system based on the expression of eight genes could effectively predict the prognosis of individual GC patients, with AUC 0.766. Patients with a lower m^{5}Cscore were characterized by the activation of immunity and experienced significantly longer PFS and OS. Our study demonstrated the non-negligible role of m^{5}C modification in the development of TME complexity and inhomogeneity. Assessing the m^{5}C modification pattern for individual GC patients will help recognize the infiltration characterization and guide more effective immunotherapy treatment.

KEYWORDS

5-methylcytosine (m^{5}C), RNA methylation modification, tumor microenvironment, immune, prognosis, m^{5}Cscore

Introduction

As a global disease, gastric cancer (GC) is the fifth most diagnosed malignancy and the third most common cause of cancer-related death, with 784,000 deaths worldwide in 2018 (1). Although the incidence and mortality rates of GC have declined in several countries, regions seriously threatened by GC, such as China and other East Asian countries, still bear severe health and economic burden. In China, 562,000 newly diagnosed GC patients were recorded, accounting for nearly half of the new cases worldwide (2). The 5-year survival rate of GC is 35.9% in China due to the late stage at diagnosis, notably lower than 71.5% in South Korea and 65% in Japan (3, 4). Due to the complexity of the pathogenic mechanism and the lack of specific biomarkers of GC, the effects of treatment strategies such as surgery, chemotherapy, and radiotherapy are not satisfactory.

RNA 5-methylcytosine (m^5C) is an important kind of RNA methylation modification; there have been more than 150 RNA modifications identified to date (5). Traditionally, DNA m^5C has been proven to be the most dominant DNA modification in mammals and functions by adding a methyl group at the carbon-5 position of the cytosine base (6). RNA m^5C modification, as the third layer of epigenetics, can be found in but not limited to mRNA, noncoding RNA, and tRNA (7–13). Like other RNA epigenetic modifications, such as N6-methyladenosine (m^6A), m^5C is a dynamic reversible process that can be regulated by "writers", "erasers", and "readers", namely, the methyltransferases, demethylases, and binding proteins (14). The methylation formation of m^5C modification is catalyzed by methyltransferases composed of the SUN/NOL1/NOP2 domain family of proteins (NSUN1, NSUN2, NSUN3, NSUN4, NSUN5, NSUN6, and NSUN7) and DNA methyltransferase homologues (DNMT1, DNMT2, DNMT3A, and DNMT3B) (15–17). At the same time, the demethylation process is regulated by the erasers consisting of enzymes of the ten-eleven translocation (TET) family members, including TET1, TET2, and TET3 (18, 19). Additionally, the whole methylation process is mediated by a cluster of special RNA-binding proteins, including ALYREF and YBX1 (8, 20). An increasing number of studies validate that the dynamic modification of m^5C and its regulators is involved in a series of physiological and pathological processes, including RNA stability, gene expression, and protein synthesis. As for tumor malignant biological behaviors, it has been reported that m^5C and its regulators play essential roles in the pathogenesis of leukemia (21), hepatocellular carcinoma (HCC) (22), glioblastoma multiforme (GBM) (12), and bladder cancer (20), indicating the promising prospect of m^5C modification in cancer treatment.

Recently, immunotherapy, anti-PD-L1 antibody, and anti-PD-1 antibody have increased the overall survival rate of some advanced GC patients who were treated with two or more lines of chemotherapy (23). The efficiency of immunotherapy depends on the status of EB virus infection, microsatellite instability (MSI)/mismatch repair (MMR), and the expression of PD-L1. However, the dominant population of immunotherapy is still challenging to identify because of the heterogeneity of GC. Hence, to better analyze the heterogeneity and immunophenotype of patients with GC, it is essential to improve long-term survival. Consistently, epigenetic and genetic variations of malignant cells are the only factors participating in the tumor progression, which is a complex multistep process. Notwithstanding, numerous studies have proved that the tumor microenvironment (TME), where tumor cells survive and grow, is crucial in tumorigenesis and development. The composition of TME is rather complicated, including not only the tumor part but also the stromal cells, macrophages, bone marrow-derived cells (BMDCs), distant recruited cells, secreted factors, and neovascularization (24). The detailed types of cells and cytokines in the TME are complex, including cancer-associated fibroblasts (CAFs), myeloid cells, lymphocytes, chemokines, cytokines, and growth factors. Among these cells, tumor-associated macrophages (TAMs), tumor-associated neutrophils (TANs), myeloid-derived suppressor cells (MDSCs), Tie2-expressing monocytes, and dendritic cells together constitute the tumor-associated myeloid cells (TAMCs) (25). The cross-talk between cancer cells and TME components promotes tumor proliferation and angiogenesis, avoids hypoxia, inhibits apoptosis, and mediates immune tolerance. With the gradual deepening of the understanding of the complexity and diversity of TME, increasing data depict its essential role in immune escape and immunotherapy. Moreover, the TME cell infiltration pattern can predict the response to the immune checkpoint blockade (ICB), which is promising in the tumor treatment strategies (26). Accordingly, particular tumor immunophenotypes are supposed to be validated *via* thoroughly parsing the TME landscape complexity and heterogeneity (27). As GC is characterized by tumor heterogeneity, it is urgent to identify the dominant population of immunotherapy by the landscape TME cell infiltration.

Lately, m^5C modification is related to the TME-infiltrating immune cells, and the mechanisms are more complicated than expected. In systemic lupus erythematosus (SLE), abnormal m^5C mRNAs were identified as relevant to critical immune pathways in CD4+ T cells (28). Another study reported that the eraser TET1 is downregulated *via* NF-κB signaling pathway activation in breast cancer cells (29). Interestingly, Andries and colleagues found that m^5C-modified mRNA promoted protein expression by the increased ability of the mRNA to elude downstream innate immune signaling and activation of endosomal Toll-like receptor 3 (TLR3) (30). During virus infection, m^5C RNA methyltransferases, such as NSUN family proteins, were employed to modify viral RNA and change antiviral host responses (31). All these latest findings reveal the fact that m5C modification and regulators may have a further effect on the TME, and previous studies focus only on one or two m^5C regulators due to the limitation of technologies.

In the present study, the genomic and clinical data of 1,983 GC samples were employed to thoroughly estimate the m^5C modification patterns and the correlation between m^5C modification and TME features. Three different m^5C modification patterns and the specific TME cell infiltration peculiarities were identified. Three immunophenotypes, immune-inflamed, immune-excluded, and immune-desert phenotype, were related to the three m^5C clusters. Subsequently, a scoring system based on the m^5C modification pattern was established for individual GC patients.

Materials and methods

The detailed materials and methods can be found in the supplementary files (32–37).

Results

Blueprint of genetic variation of m^5C regulators in GC

In the process of dynamic modification, methyltransferases and demethylases work together to keep the balance of the RNA m^5C modification with the help of the readers. The ideograph of RNA m^5C modification is shown in Figure 1A. Firstly, the characteristics of somatic mutations and copy number variations (CNVs) of the 16 m^5C regulators were summarized in GC. Among all the 433 samples from TCGA, 83 (19.17%) patients experienced mutations of m^5C regulators. We found that the three demethylases exhibited the highest mutation rates, while the readers (YBX1 and ALYREF) hardly showed any mutations (Figure 1B). Moreover, a significant mutation co-occurrence pattern was identified between NSUN2 and NSUN3 (Figure S1B). For CNV analysis, the most prevalent CNV alternation in the regulators was the amplification in copy number, except for NSUN3, TET2, and NSUN7, which were characterized by a high frequency of CNV deletion (Figure 1C). In Figure 1D, the detailed locations of CNV alternation of each m^5C regulator are recorded on the chromosomes. Notably, we could thoroughly determine GC patients from normal samples based on the expression of the 16 m^5C regulators (Figure 1E). To further ascertain the relation between the above genetic alternations and the expression of m^5C regulators, we explored the expression of regulators in both GC and normal tissues. We found that CNVs might be the main factors leading to the abnormal expression of the m^5C regulators. Regulators with amplificated CNV tended to highly expressed in tumor samples (e.g., DNMT1, ALYREF, and NSUN5), and *vice versa* (e.g., NSUN7 and NSUN6) (Figures 1C, F). The assessment disclosed the heterogeneity of expressional and genetic alternation patterns in m^5C regulators between GC and normal tissues, hinting that the aberrant expression of m^5C regulators played an essential role in the tumorigenesis and development of GC.

m^5C methylation modification patterns mediated by 16 regulators

A meta-cohort including five GEO datasets (GSE57303, GSE84437, GSE34942, GSE62254, and GSE15459) with full OS and other clinical data was used to identify the expression pattern of 16 regulators. The prognostic values of 16 m^5C regulators were analyzed through a univariate Cox regression model (Figure S1C and Figure 2A). We found that the readers ALYREF and YBX1 were favorable prognosis factors for GC patients. The cross-talk between 16 regulators and prognostic significance for patients was revealed in the m^5C regulator network (Figures 2A, B). We noticed that a significant correlation was shown in both the same and different functional category regulators. Interestingly, the correlation of expression is consistent in regulators from the same functional category. However, we found that the relationship in writers is much complicated, such as DNMT1, which is remarkably negatively correlated with NSUN6 and NSUN7 (Figure 2B). In addition, the expression of the readers ALYREF and YBX1 was almost significantly correlated with other regulators. According to the expression of 16 m^5C regulators, we further explored the m^5C modification patterns *via* the ConsensusClusterPlus package, and identified three different modification patterns by the unsupervised clustering method, including 308 patients in m^5C cluster A, 334 patients in m^5C cluster B, and 417 patients in m^5C cluster C (Figures S2A–D and Table S3). The heatmap of the 16 m^5C regulators in 1,059 GC patients is depicted in Figure 2C. The expression of 16 regulators in three m^5C clusters was remarkably different. LogRank analysis showed that the prognosis of patients in m^5C cluster B was better than the other two clusters (Figure 2D).

TME cell infiltration characteristics in distinct m^5C modification patterns

To better understand the biological characteristics among the distinct m^5C modification clusters, the GSVA enrichment method was conducted. In Figure 2E, m^5C cluster A is related to the immune suppression process, while m^5C cluster B is notably enriched in immune full activation pathways, including cytokine–cytokine receptor interaction, natural killer cell-mediated cytotoxicity, antigen processing and presentation, Toll-like receptor signaling pathway, and chemokine signaling pathway. m^5C cluster C is enriched in carcinogenic and stromal activation pathways, such as ECM receptor interaction, TGF beta signaling pathway, adhesion and gap junction, mTOR, and

10.3389/fimmu.2022.905057

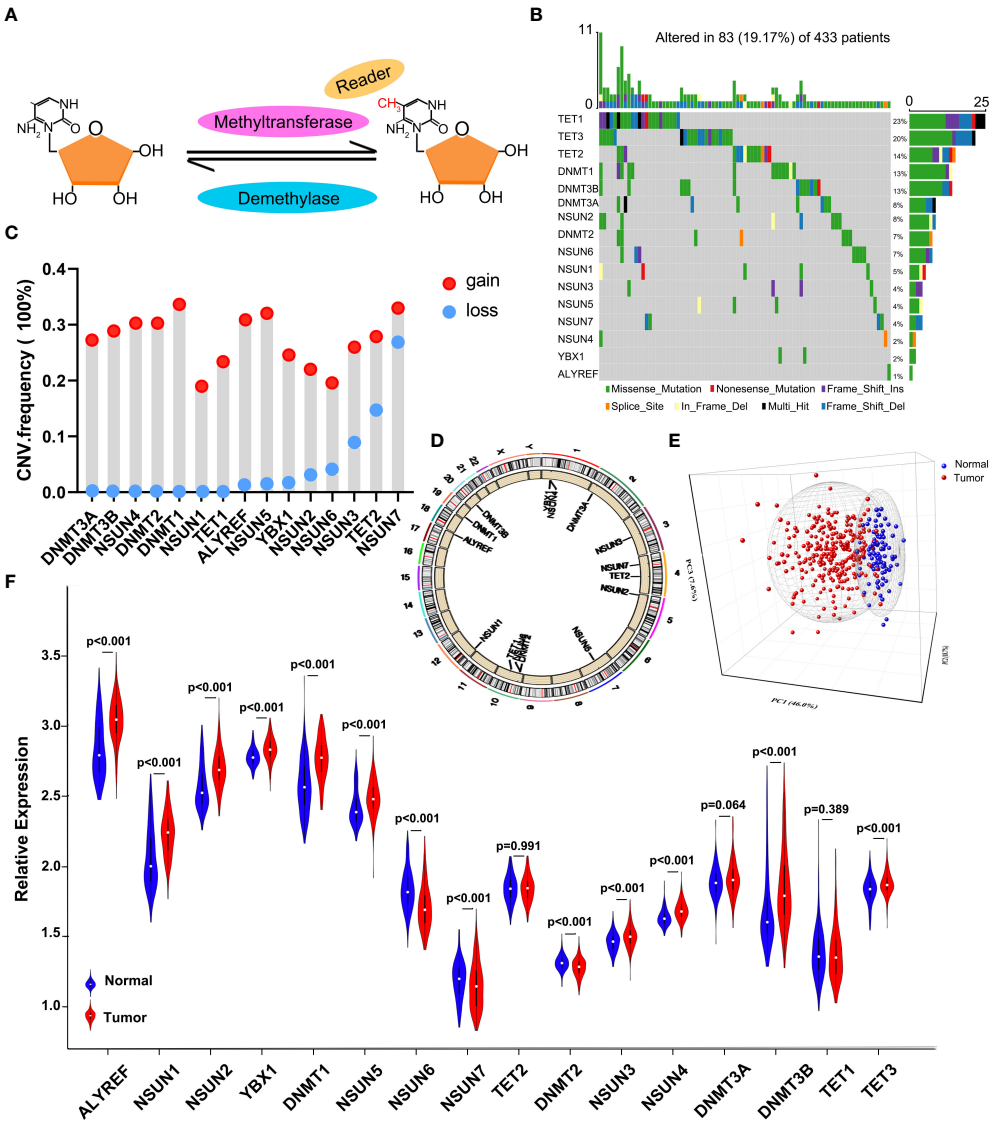


FIGURE 1
The landscape of genetic and expression alternation of m^{5}C regulators in GC. **(A)** Diagram of the dynamic reversible process of m^{5}C RNA methylation regulated by different types of regulators. **(B)** The mutation frequency of 16 m^{5}C regulators in 433 GC patients from the TCGA-STAD cohort. Each column represents individual patients. The upper bar plot indicates TMB. The numbers on the right show the mutation frequency of specific regulators and the right bar plot represents the proportion of each variant type. The colors of each variant type are listed at the bottom. **(C)** The CNV mutation frequency of m^{5}C regulators in the GSE62717 dataset. The height of the column represents the variation frequency. Amplification frequency, red dot; deletion frequency, blue dot. **(D)** The location of CNV mutation of 16 m^{5}C regulators on 23 chromosomes in the GSE62717 dataset. **(E)** PCA indicates that the expression of 16 m^{5}C regulators can distinguish GC tumors from normal samples in the GSE2269 cohort. Tumors and normal samples are marked with blue and red, separately. **(F)** The differential expression of 16 m^{5}C regulators between normal and tumor samples. Tumor, red; normal, blue.

MAPK signaling pathways (Figure 2F). Interestingly, TME immune cell infiltration analysis subsequently showed that m^{5}C cluster C was rich in resting and naïve immune cells, such as dendritic cells, CD4 memory T cells, mast cells, B cells, and other innate immune cells, by the CIBERSORT method. On the contrary, m^{5}C cluster B is characterized by specific immune cell enrichment (Figure 3A, Figure S2E, and Table S4). The correlation of specific m^{5}C regulators and immune cell is shown in Figure S2F. To further reveal the TME features, the single-sample GSEA (ssGSEA) analysis of all the 1,059 cases was conducted. In addition to immune cells, more details about immune functions and pathways can be summarized *via* the ssGSEA method. As shown in Figure 3B, three distinct immune patterns under three m^{5}C clusters are identified (Table S5).

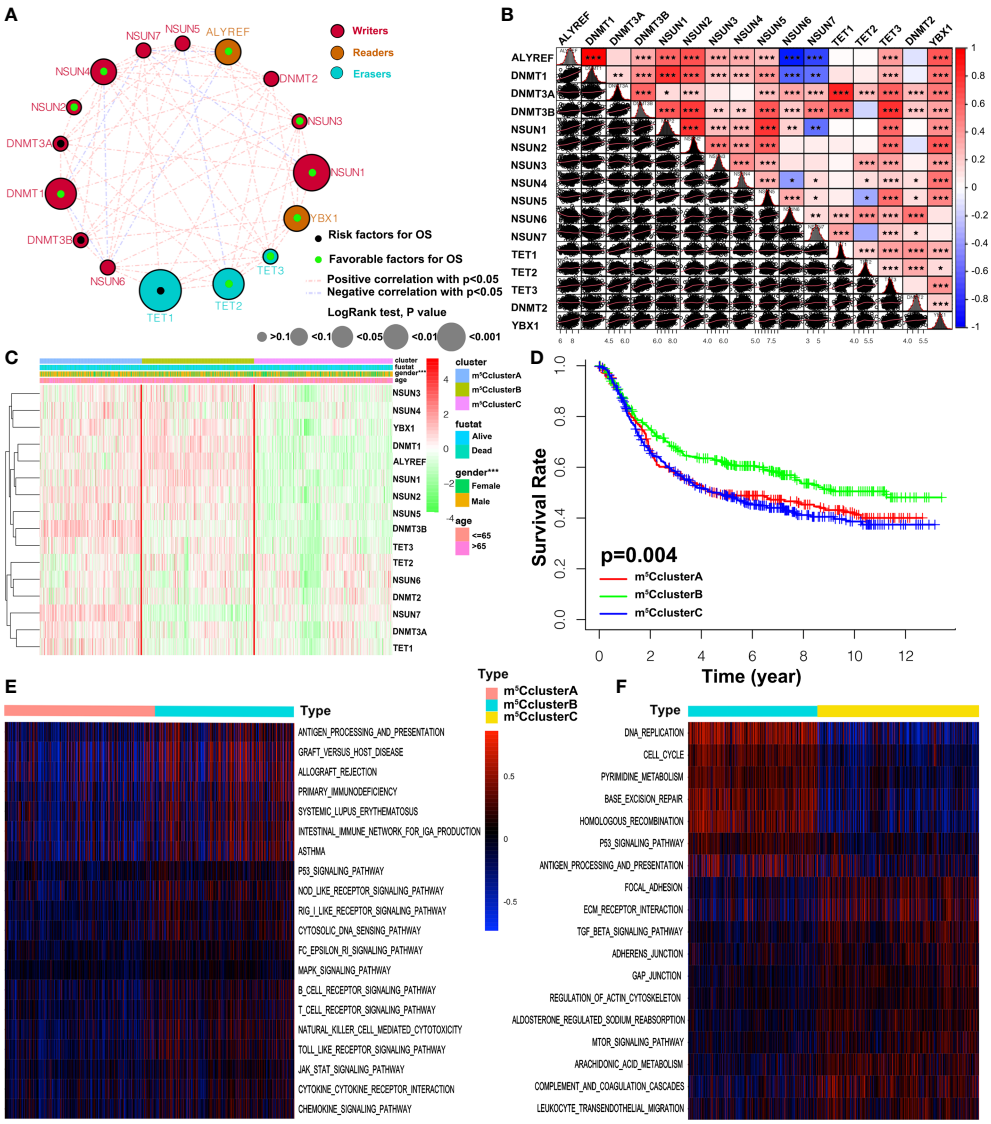


FIGURE 2
m^{5}C methylation modification patterns and biological characteristics. **(A)** The interaction between 16 m^{5}C regulators in GC. The size of the circles represents the effect of a specific regulator on the prognosis, and the values calculated *via* the Log-rank method were $p > 0.1$, $p < 0.1$, $p < 0.05$, $p < 0.01$, and $p < 0.001$, respectively. Black dots, favorable factors; green dots, risk factors. The lines between two regulators show the interaction. Negative correlation and positive correlation are marked with blue and red. **(B)** The expression correlation of the 16 m^{5}C regulators in GC. Each cell in the lower left corner represents the expression of two regulators, and the red line is the trend line. Cells in the upper right corner show the statistic result. The asterisks represent the *p*-value (*$p < 0.05$, **$p < 0.01$, and ***$p < 0.001$). **(C)** Unsupervised clustering of 16 m^{5}C regulators in the five independent gastric cancer cohorts. The m^{6}A clusters and basic clinical information are used as patient annotations. Each column represents patients and each row represents m^{5}C regulators. **(D)** Overall survival of three m^{5}C modification clusters based on the GC patients from five GEO cohorts. Log-rank *p*-value 0.004 indicates a significant prognostic difference among three m^{5}C clusters. **(E, F)** GSVA enrichment analysis revealing the activation states of biological pathways in distinct m^{5}C clusters. The heatmap is employed to visualize the biological processes, and blue represents inhibited pathways and yellow represents activated pathways.

Combined with the survival results above, we were surprised to find that m^{5}C cluster A belonged to the immune-desert phenotype, characterized by immunological suppression; m^{5}C cluster B was classified as immune-inflamed phenotype, which features immune activation and immune cell infiltration; m^{5}C cluster C was labeled as immune-excluded phenotype, characterized by stromal activation and innate immune cell infiltration (Figures 2D and 3A, B). These results demonstrated that the interaction among the writers, erasers, and readers might play fundamental roles in distinct m5C modification patterns and TME cell infiltration characteristics of individual GC patients.

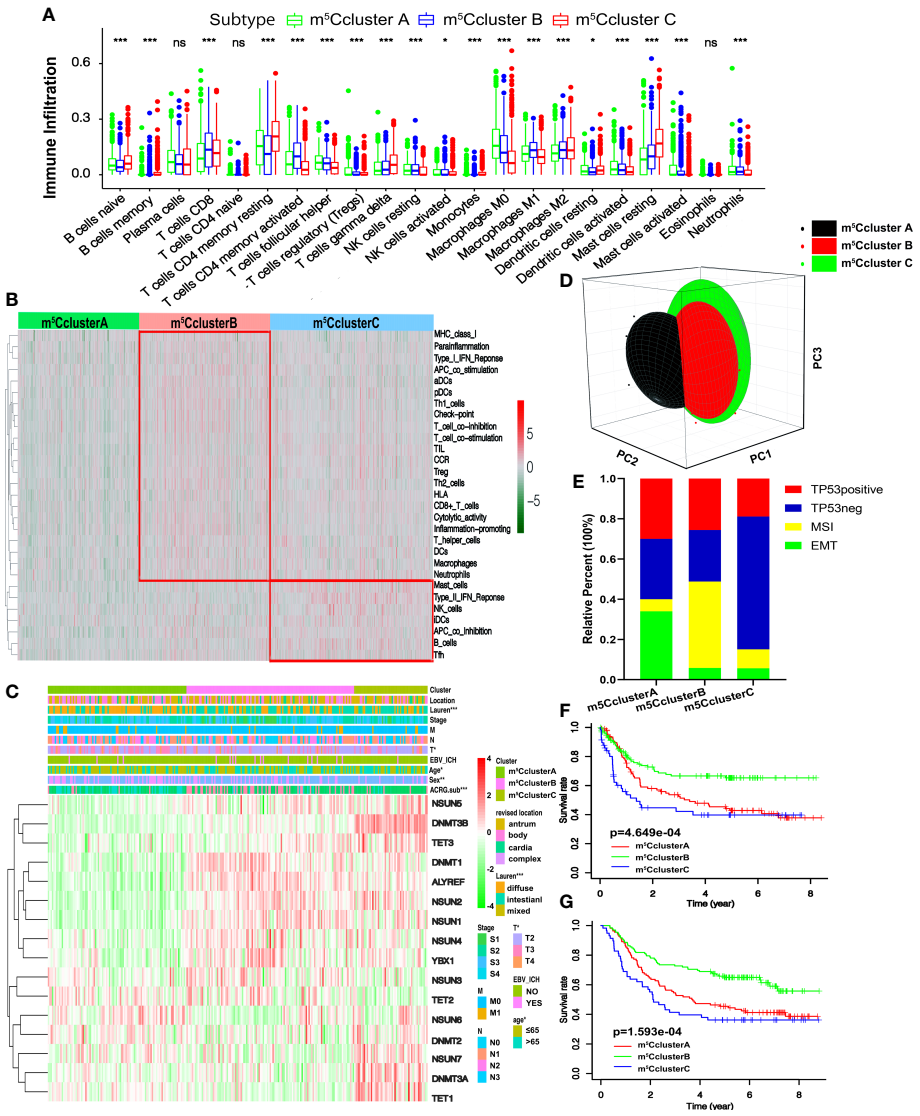


FIGURE 3
TME cell infiltration traits and transcriptome characteristics in three m^{5}C modification clusters. **(A)** The enrichment of TME-infiltrating cell in distinct m^{5}C clusters. The lower and upper ends of the boxes represent interquartile range of values. The dots represent outliers and the lines in the boxes show the median value. **(B)** The heatmap of TME-infiltrating cells in three m^{5}C patterns. **(C)** Unsupervised clustering of 16 m^{5}C regulators in the ACRG cohort. The m^{5}C cluster, location, Lauren types, tumor stage, EBV status, sex, age, and ACRG molecular subtypes are used as patient annotations. High and low expression of regulators is marked with red and green, respectively. **(D)** PCA shows that the expression of 16 m^{5}C regulators can divide the ACRG cohort into three distinct m^{5}C clusters. **(E)** The relative percent of four molecular subtypes in distinct m^{5}C clusters. **(F)** Recurrence-free survival of three m^{5}C modification clusters based on the GC patients from the ACRG cohort. **(G)** Overall survival of three m^{5}C modification clusters based on the GC patients from the ACRG cohort (ns, not significant: *$p < 0.05$; **$p < 0.01$; ***$p < 0.001$).

m^{5}C methylation modification patterns in the ACRG cohort

We focused on the ACRG cohort, a group of 300 GC participants with complete clinicopathological information, to further reveal the biological behaviors and the features of m^{5}C modification patterns. Like the meta-cohort datasets, the ACRG cohort is divided into three distinct m^{5}C modification clusters as well by the unsupervised clustering method (Figures S3A–D and Figures 3C, D). The heatmap based on the expression of 16 m^{5}C regulators shows that m^{5}C cluster A exhibits a high expression of TET2 and NSUN6 and is downregulated in other regulators; m^{5}C cluster B is characterized by the upregulated readers and five writers including NSUN1–4 and DNMT1; m^{5}C cluster C shows high levels of two erasers and four writers (Figure 3C). We found that patients in m^{5}C cluster A were rich in the diffuse

subtype and tended to have poor differentiation. Intestinal subtype was more likely to be observed in m^5C cluster B and C modification pattern. GC patients with diffuse histological and EMT molecular subtypes were related to poorer survival; on the contrary, MSI was linked to a better prognosis. Consequently, patients with an m^5C cluster pattern were markedly linked to high malignancy, stromal activation, and poor prognosis (Figure 3C). Moreover, Figure 3E shows that patients in m^5C cluster A are also significantly related to EMT molecular subtypes, while the MSI subtypes are featured by m^5C cluster B modification. The survival results revealed that patients in m^5C cluster B are related to a favorable prognosis, while m^5C clusters A and C show a shorter survival time (Figure 3F). Notably, we also found that the relapse-free survival (RFS) of m^5C cluster B is better than the other two clusters (Figure 3G). The findings above demonstrate that most GC patients with EMT molecular subtypes were divided into m^5C cluster A and related to stromal activation; most patients with MSI instead of the EMT subtype were in m^5C cluster B and characterized by immune activation.

Immunomodulatory effect of m^5C modification on the TME

Subsequently, four gene clusters belonging to distinct immune processes were used to reveal the role of m^5C modification on the immune regulation of the TME. Chemokines and cytokines with different functions were selected from the published literature. The essential members of human leukocyte antigen (HLA), the major histocompatibility complex (MHC) of human beings, present antigen and mediate immune response. CD8A, CXCL9, CXCL10, GZMA, GZMB, IFNG, PRF1, TBX2, and TNF are related to immune activation. CD80, CD86, HAVCR2, CTLA-4, LAG3, IDO1, PD-1, PD-L1, PD-L2, TNFRSF9, and TIGIT are supposed to correlate with immune checkpoints. ACTA2, CLDN3, COL4A1, SMAD9, TGRB1, TGFBR2, TWIST1, VIM, and ZEB1 are considered to associate with TGF-β and EMT pathways (24, 38). In Figure 4A, HLA-I molecules, including HLA-A, B, C, E, F, and G, are remarkably highly expressed in m^5C cluster B, which means stronger antigen presentation and tumor-killing ability. We noted that HLA-II molecules, such as HLA-DPB2, HLA-DQA1, HLA-DQB2, and HLA-DQA1, were upregulated in m^5C cluster A. HLA-G is reported to suppress the immune response and leads to long-term immune escape and tolerance (39). Meanwhile, we also found that the expression of genes related to TGF-β and EMT pathways was remarkably upregulated in m^5C cluster A, which added the evidence of stromal activation, while m^5C cluster B exhibited overexpression of mRNAs relevant to immune activation (Figures 4B–D). Immune checkpoint analysis showed that all the genes, including CTLA-4, PD-1, and PD-L1, were upregulated in m^5C cluster B (Figure 4C). The results above demonstrate that m^5C modification patterns are significantly related to TME immune regulation and may play crucial roles in immunotherapy. However, these findings were only based on the 16 m^5C modification regulators.

Considering the heterogeneity and complexity of m^5C methylation modification, we tried to identify the DEGs under different m^5C clusters using the limma package. Finally, 229 m^5C phenotype-related DEGs were found and showed a distinct expression pattern under three m^5C clusters (Figures 4E, F). The GO and KEGG enrichment analysis of the 229 DEGs showed that (Figures S3E, F) the DEGs were rich in immune-related biological processes and pathways, including CD8+ αβT cell activation, negative regulation of the immune system process, NOD-like receptor signaling pathway, and TNF signaling pathways.

Generation of m^5Cscore and capability to predict prognosis

We established a scoring system that depended on the expression of DEGs and m^5C regulators to quantify the individual m^5C modification pattern; we termed this m^5Cscore. The univariate Cox regression method was employed to determine the DEGs that were significantly related to the survival of GC patients in ACRG (Table S6). Ninety-nine genes were involved in the LASSO Cox regression algorithm to generate the m5Cscore signature, and eight genes were selected, including seven DEGs (RBPMS2, TNFRSF11A, NBEA, INHBB, RGN, DFNA5, and TPD52L1) and one writer (DNMT3A) (Figures 5A, B). The m5Cscore of each GC patient and prognostic information is summarized in Table S7. The alluvial diagram shows the attribute changes of individual GC patients (Figure 5C). Log-rank results depict that the OS of patients with a low m^5Cscore is remarkably higher than patients with a high m^5Cscore under the cutoff value of 9.92 (Figures 5D, E). The area under the curve (AUC) is 0.766, quantified by the pROC package (Figure 5F). Univariate and multivariate analysis demonstrates that age, N stage, M stage, and m^5Cscore are the independent factors of prognosis (Figures 5G, H). Meanwhile, we found that m^5Cscores significantly differed in distinct ACRG molecular subtypes. Patients in the EMT subgroup showed the highest m^5Cscore compared to the other molecular groups (Figure 6A). Additionally, patients in m^5C cluster B showed the lowest m^5Cscore compared to other clusters (Figure 6B). In Figure S3G–I, GC patients with a high m^5Cscore show a significantly higher stromal score and a lower tumor purity score. The results added to the evidence that a low m^5Cscore was significantly related to immune activation and a high m^5Cscore was correlated with stromal activation. m^5Cscore could be a better marker to estimate the m^5C modification of individual GC patients. Notably, patients with a low m^5Cscore and who received adjuvant chemotherapy showed significant treatment advantages (Figure 6C). The result also demonstrated that the prediction value of m^5Cscore was not affected by chemotherapy, and a low m^5Cscore showed obvious survival advantage, regardless of whether patients received chemotherapy or not (Figure 6C).

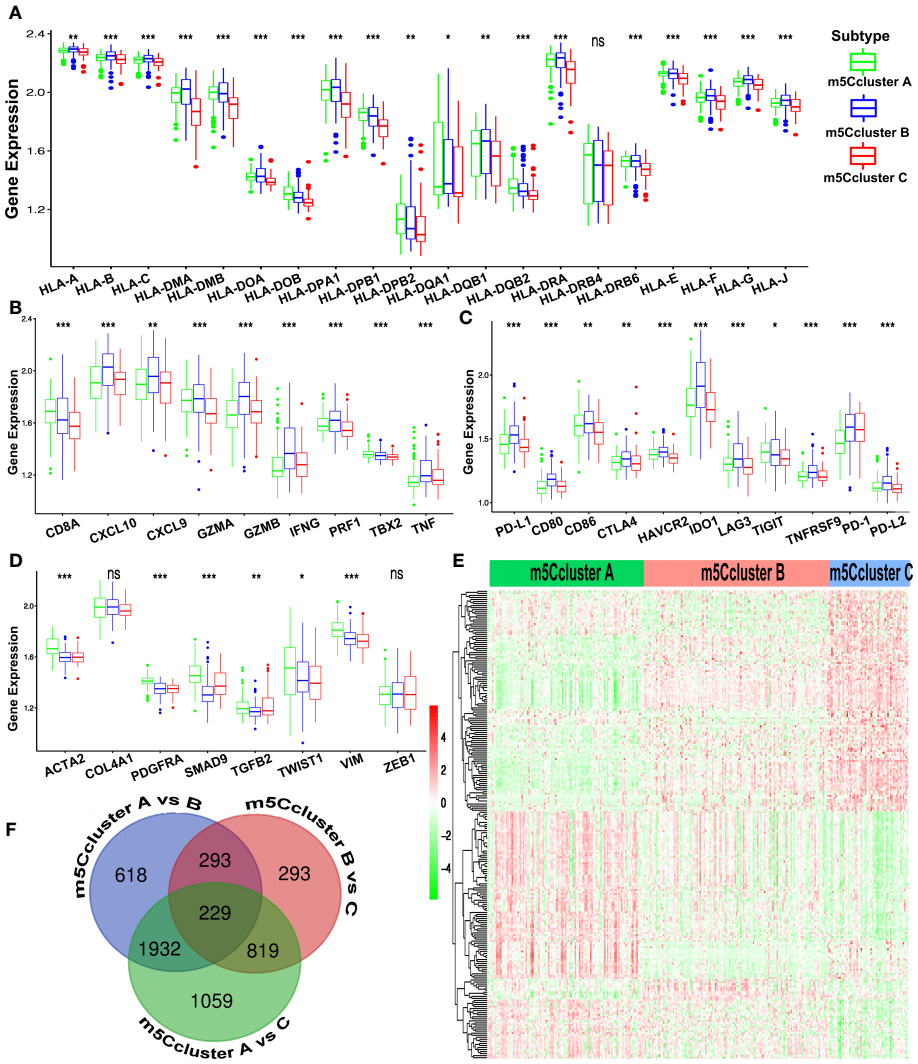


FIGURE 4
Immune characteristics of the different m^{5}C patterns from the ACRG cohort. **(A)** The expression of the HLA alleles of GC patients of distinct m^{5}C clusters. **(B)** Difference in the immune-activation-related gene expression among three m^{5}C clusters. **(C)** Difference in the immune-checkpoint-related gene expression among three m^{5}C clusters. **(D)** Difference in the TGF-β–EMT-related gene expression among three m^{5}C clusters. **(E)** The Venn diagram shows the 229 DEGs from the pairwise comparison of three m^{5}C clusters. **(F)** The heatmap of DEGs of the distinct m^{5}C clusters reveals three expression patterns. (ns, not significant; *p < 0.05; **p < 0.01; ***p < 0.001).

Moreover, older patients, intestinal histological subtype, and early GC patients were notably related to a low m^{5}Cscore, which demonstrated that these GC patients were characterized by the m^{5}C cluster B and immune-inflamed phenotype, with a better prognosis (Figure 6D).

Validation of m^{5}C modification in TCGA and other datasets

Data from the TCGA-STAD cohort and GEO were used for external and internal validation to determine the role of m^{5}C modification and the prognostic value of m^{5}Cscore. m^{5}Cscore was employed to evaluate the individual m^{5}C modification of the single patients in the TCGA dataset, among which 267 patients have a low m^{5}Cscore and 69 patients have a high m^{5}Cscore. Combined with the prognosis information, we revealed that patients with a low m^{5}Cscore had a better prognosis (Figure 6E). ROC curve analysis showed that the AUC was 0.898, which was even higher than that in the training cohort (Figure 6F). We also noticed that patients with a high m^{5}Cscore and without chemotherapy experienced the worst prognosis, while patients with a low m^{5}Cscore and chemotherapy showed a favorable prognosis (Figure 6G). As shown in Figures 6H, I, patients in the

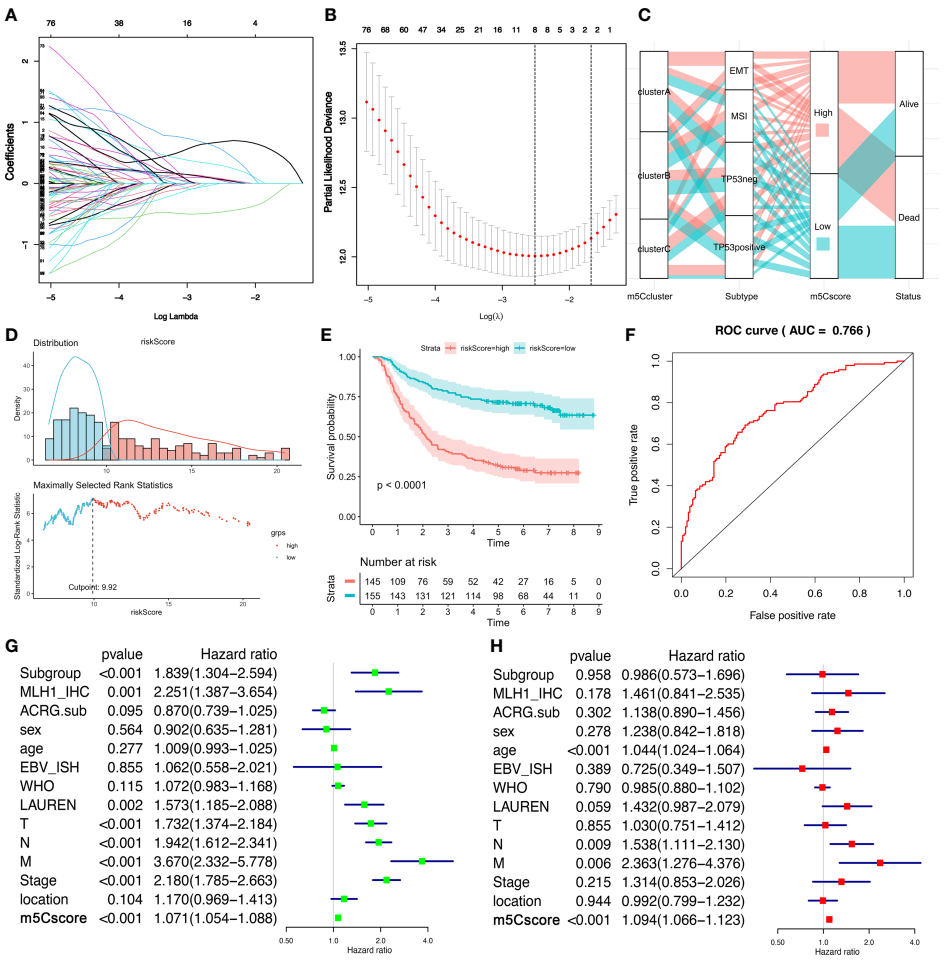


FIGURE 5
The generation of the m^{5}Cscore system in the ACRG cohort. **(A, B)** The LASSO regression model and verification. **(A)** The longitudinal, lower transverse, and upper transverse coordinates are the correlation coefficient, Log Lambda (penalty coefficient), and the number of non-zero coefficients in the model. The lines with different colors show the trajectories of related variables changing with Log Lambda in the model. **(B)** The upper transverse, lower transverse, and longitudinal coordinates represent the format of the factor, the Log Lambda (penalty coefficient), and the error of cross-verification. The point with the smallest cross-verification error corresponds to the number of factors involved in the LASSO regression model. **(C)** Alluvial diagram demonstrates the changes of m^{6}A clusters, molecular subtypes, m^{5}Cscores, and status. **(D)** The distribution of the m^{5}Cscore of each patient from the ACRG cohort. The cutoff point of m^{5}Cscore is 9.92. **(E)** Kaplan–Meier curves show that the m^{5}Cscore is significantly related to the overall survival of GC patients in the ACRG cohort, of which 145 patients were in the high-m^{5}Cscore group and 155 patients were in the low-m^{5}Cscore group ($p < 0.0001$, Log-rank test). **(F)** The predictive value of m^{5}Cscore in the ACRG cohort. AUC, 0.766. **(G)** Univariate Cox regression analysis for m^{5}Cscore in the ACRG cohort shown by the forest plot. **(H)** Multivariate Cox regression analysis for m^{5}Cscore in the ACRG cohort shown by the forest plot.

high-m^{5}Cscore group exhibit less extensive tumor mutation burden than patients in the low-m^{5}Cscore group, with alternation rates of 88.41% and 92.88%, respectively. TMB analysis demonstrated that a high m^{5}Cscore was significantly related to lower TMB, and showed a notable negative correlation (Figures 6H, I). Furthermore, the mean TMB of patients with a high or low m5Cscore was 2.31 and 1.26 mutations per MB. The violin plot also demonstrated that the TMB of patients in the high-m5Cscore group was significantly higher than that of patients in the low-m5Cscore group, and the *p*-value was 0.012 (Figure S3J).

Next, to further validate the stability of the m^{5}Cscore system, the m^{5}Cscore model was applied to other independent GC cohorts to confirm the prognostic value. Figures 7A–C show that GC patients with a low m^{5}Cscore have a better prognosis in GSE57303, GSE84437, and GSE 15459. Moreover, we combined all the five GEO datasets together and found that the m^{5}Cscore model was validated (Figure 7D). The ROC curve was drawn, and all AUCs were over 0.6 (Figure 7E). In addition, GSE26253, a new GEO dataset, was used to evaluate the predictive value of recurrence-free survival. Figure 7F confirms the ability of

10.3389/fimmu.2022.905057

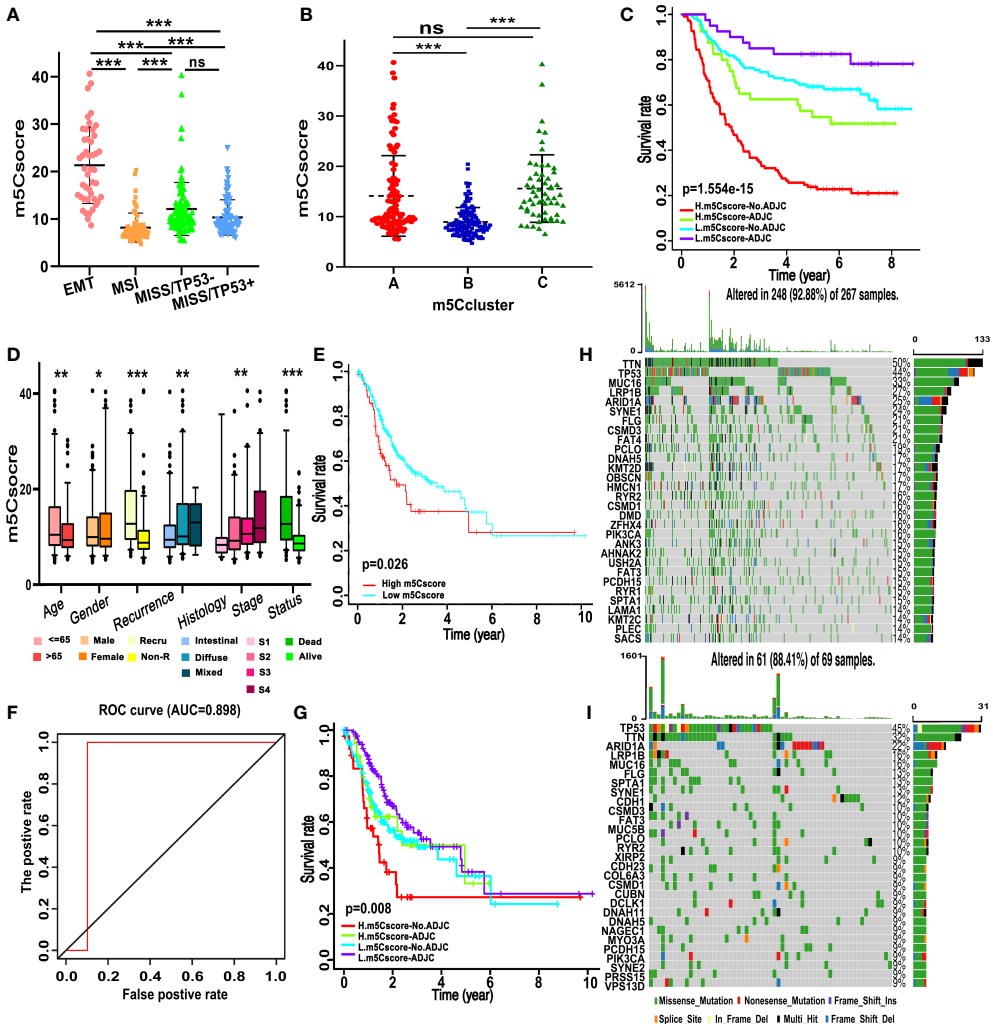


FIGURE 6
Traits of m^{5}C modification in different molecular subgroups and somatic tumor mutation. **(A)** Differences in m^{5}Cscore between different ACRG molecular subgroups. **(B)** Differences in m^{5}Cscore between distinct m^{5}C clusters. **(C)** Survival analyses for subgroup GC patients stratified by both adjuvant chemotherapy treatment and m^{5}Cscore using the Kaplan–Meier method. L, low; H, high; ADJC, adjuvant chemotherapy. **(D)** Differences in m^{5}Cscore among clinicopathological groups. **(E)** Kaplan–Meier curves show that the m^{5}Cscore is significantly correlated to the overall survival of patients in the TCGA-STAD cohort. **(F)** The predictive value of m^{5}Cscore in the TCGA-STAD cohort. AUC, 0.898. **(G)** Survival analyses for subgroup GC patients divided by adjuvant chemotherapy treatment and m^{5}Cscore using Kaplan–Meier curves in the TCGA-STAD cohort. **(H,I)** The waterfall plot of tumor somatic mutation based on those with high m^{5}Cscore **(H)** and low m^{5}Cscore **(I)** in the TCGA-STAD cohort. Each column represents each GC patient. The upper and right bar plots show TMB and the proportion of each variant type. The number on the right indicated the mutation frequency in each gene. (ns, not significant; *p < 0.05; **p < 0.01; ***p < 0.001).

m^{5}Cscore to predict RFS, which means the underlying potential mechanisms exist between m^{5}C modification and tumor relapse to be elucidated.

Discussion

Growing evidence revealed that aberrant RNA m^{5}C methylation modification played a crucial role in tumorigenesis, progression, and patient prognosis by means of dynamic RNA epigenetic modification. In the current study, we analyzed that m^{5}C regulators in GC explored the correlation between TME and m^{5}C modification, as well as established an m^{5}Cscore system to evaluate the prognosis of GC patients *via* the data from GEO datasets and the TCGA-STAD cohort. The m^{5}Cscore model was further validated by internal and external datasets. These findings added clues for understanding the m^{5}C modification of individual GC patients.

Sixteen m^{5}C methylation regulators were involved in the analysis, including methyltransferases, demethylases, and RNA

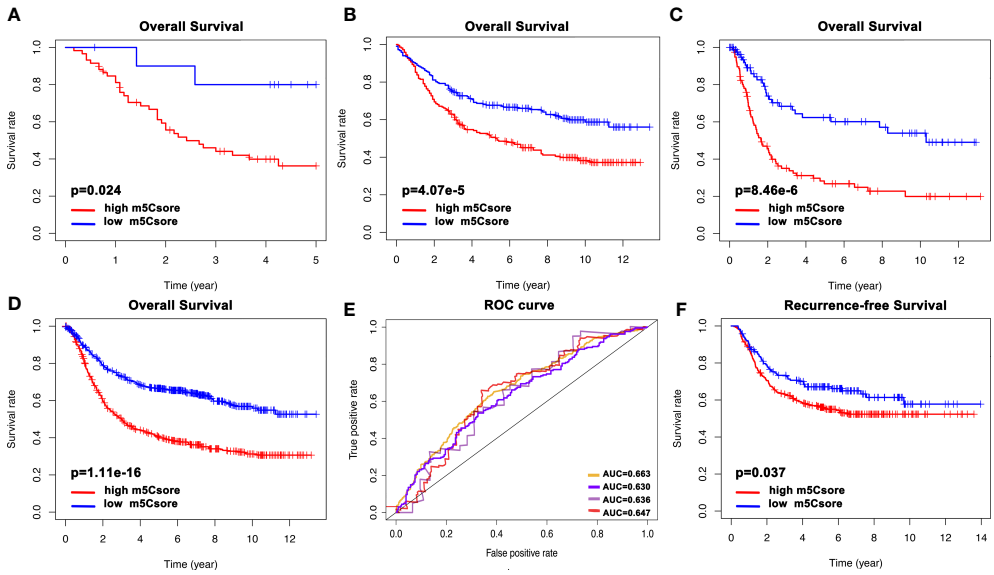


FIGURE 7
The validation of the m^{5}Cscore system of individual GC patients from internal and external cohorts. **(A)** Overall survival analysis of m^{5}Cscore in the GSE57303 cohort. **(B)** Overall survival analysis of m^{5}Cscore in the GSE84437 cohort. **(C)** Overall survival analysis of m^{5}Cscore in the GSE15459 cohort. **(D)** Overall survival analysis of m^{5}Cscore in all five GEO cohorts. **(E)** The predictive value of m^{5}Cscore in the four validation cohorts. The orange line represents all five GEO datasets with AUC 0.663; the purple line represents the GSE84437 cohort with AUC 0.630; the gray line represents the GSE57303 cohort with AUC 0.636; the red line represents the GSE15459 cohort with AUC 0.647. **(F)** Recurrence-free survival analysis of m^{5}Cscore in the GSE26253 cohort.

binding proteins. Although the exact number of m^{5}C regulators and detailed mechanisms of m^{5}C methylation are far from clear, the existing evidence has validated the essential function of m^{5}C modification on different types of RNA, physiological, and pathological processes (7, 14). Among all the regulators, 13 regulators are significantly aberrantly expressed with 10 genes upregulated and 3 downregulated in GC samples. NSUN7 and DNMT2 are the only low-expression regulators out of the 11 methyltransferases. Sato et al. reported that NSUN7 was upregulated in low-grade glioma with an unknown mechanism (40). However, in GC, we suppose that the low expression of NSUN7 is caused by the loss of CNV frequency. Mei and colleagues found that NSUN2 was overexpressed in GC, which is consistent with our results, and they further validated that NSUN2 promotes GC cell proliferation *via* repressing p57(Kip2) in an m^{5}C-dependent manner (41). In correlation analysis, we noticed that the methyltransferases tended to be related to each other, indicating the underlying interaction of mediating the m^{5}C methylation modification. As for the readers, ALYREF and YBX1 were remarkably overexpressed in GC patients. Research on bladder cancer, breast cancer, HCC, and oral squamous cell carcinoma revealed that ALYREF and YBX1 were upregulated as well (22, 42–44). Intriguingly, high expression of ALYREF and YBX1 are also significantly correlated with the favorable prognosis of GC patients. All three erasers are notably related to the OS of GC patients despite the fact that only TET3 is significantly abnormally expressed in tumor samples.

Based on the expression of 16 m^{5}C methylation regulators, three m^{5}C modification patterns were distinguished. The three m^{5}C modification clusters were characterized by different TME cell infiltration patterns. m^{5}C cluster A was included in the immune-desert phenotype, characterized by immunosuppression; m^{5}C cluster B belonged to the immune-inflamed phenotype, showing the activation of adaptive immunity; m^{5}C cluster C was classified as immune-excluded phenotype, characterized by stroma and immunity activation. The GSVA analysis also revealed that m^{5}C cluster B is enriched in cytokine–cytokine receptor interaction, natural killer cell-mediated cytotoxicity, antigen processing and presentation, Toll-like receptor signaling pathway, and chemokine signaling pathway. These results added to the evidence that the immune-inflamed phenotype, also known as a hot tumor, is characterized by immune cell infiltration and immune-related signal pathway stimulation in TME (45, 46). Additionally, we found that the immune checkpoints in m^{5}C cluster B were notably overexpressed than the other two m^{5}C clusters, which indicated that patients in m^{5}C cluster B might benefit from immunotherapy. In the immune-excluded phenotype, TGF-β and EMT pathways are activated and abate the efficiency of immunotherapy (47). However, we observed the activation of TGF-β and EMT pathways in m^{5}C cluster A, which was

classified as the immune-desert phenotype. The anomaly may be due to the limited number of TGF-β and EMT pathway-related genes, which requires more data analysis and illustrates the complexity of m^5C methylation modification. In survival analysis, m^5C cluster B showed the most favorable prognosis, which is consistent with the above-mentioned immune-inflamed phenotype.

The m^5Cscore system was established based on the expression of eight genes *via* the LASSO Cox regression method, namely, DNMT3A, RBPMS2, TNFRSF11A, NBEA, INHBB, RGN, DFNA5, and TPD52L1. Among all the genes calculated in the m^5Cscore system, only DNMT3A is an m^5C modification regulator; TNFRSF11A, INHBB, and DFNA5 are involved in TNF-related pathways (48–50); TPD52L1 participates in cell proliferation and calcium signaling; and RBPMS2, as an RNA binding protein, is involved in the regulation of cell differentiation and proliferation (51, 52). m^5Cscore is a reliable marker to evaluate the prognosis of GC patients with an AUC of 0.766 in the ACRG training set and 0.898 in the TCGA validation set. m^5Cscore was verified by other GEO datasets as well. Inevitably, m^5Cscore is distinct in different m^5C clusters, in which m^5C cluster B had the lowest m^5Cscore. We noticed that GC patients with the EMT molecular subtype show the highest m^5Cscore, demonstrating poor prognosis. Furthermore, GC patients with a high m^5Cscore tend to have a shorter RFS, indicating that m^5C methylation may play an essential role in tumor recurrence.

Conclusion

In summary, we revealed the potential regulatory mechanisms of m^5C methylation modification on the GC TME. The characteristics of distinct m^5C modification patterns might lead to the complexity and heterogeneity of individual GC TME. A far-reaching understanding of specific m^5C modification patterns in GC will contribute to identifying TME cell infiltration and guiding clinical immunotherapy treatments.

Data availability statement

The datasets presented in this study can be found in online repositories. The names of the repository/repositories and accession number(s) can be found in the article/Supplementary Material.

Ethics statement

The study complied with the principles set forth in the Declaration of Helsinki. Access to the deidentified linked dataset was obtained from the TCGA and GEO databases in accordance with the database policy. For analyses of deidentified data from the TCGA and GEO databases, institutional review board approval and informed consent were not required.

Author contributions

All authors searched the literature, designed the study, interpreted the findings, and revised the manuscript. QZ, JS, XS and KS carried out data management and statistical analysis and drafted the manuscript. JL, XG, KS and XQ helped with cohort identification and data management. QZ, JS, XS and KS performed project administration. All authors contributed to the article and approved the submitted version.

Funding

This work was supported by grants from the National Natural Science Foundation of China (82003184) and the Health Science and Technology Project of Lianyungang (201914).

Acknowledgments

The authors thank all individuals who participated in this study and donated samples.

Conflict of interest

The authors declare that the research was conducted in the absence of any commercial or financial relationships that could be construed as a potential conflict of interest.

Publisher's note

All claims expressed in this article are solely those of the authors and do not necessarily represent those of their affiliated organizations, or those of the publisher, the editors and the reviewers. Any product that may be evaluated in this article, or claim that may be made by its manufacturer, is not guaranteed or endorsed by the publisher.

Supplementary material

The Supplementary Material for this article can be found online at: https://www.frontiersin.org/articles/10.3389/fimmu.2022.905057/full#supplementary-material

References

1. Smyth EC, Nilsson M, Grabsch HI, van Grieken NC, Lordick F. Gastric cancer. *Lancet* (2020) 396(10251):635–48. doi: 10.1016/S0140-6736(20)31288-5

2. Collaborators GBDSC. The global, regional, and national burden of stomach cancer in 195 countries, 1990-2017: a systematic analysis for the global burden of disease study 2017. *Lancet Gastroenterol Hepatol* (2020) 5(1):42–54. doi: 10.1016/S2468-1253(19)30328-0

3. Matsuda T, Ajiki W, Marugame T, Ioka A, Tsukuma H, Sobue T, et al. Population-based survival of cancer patients diagnosed between 1993 and 1999 in Japan: a chronological and international comparative study. *Japanese J Clin Oncol* (2011) 41(1):40–51. doi: 10.1093/jjco/hyq167

4. Hong S, Won YJ, Park YR, Jung KW, Kong HJ, Lee ES, et al. Cancer statistics in Korea: Incidence, mortality, survival, and prevalence in 2017. *Cancer Res Treat* (2020) 52(2):335–50. doi: 10.4143/crt.2020.206

5. Boccaletto P, Machnicka MA, Purta E, Piatkowski P, Baginski B, Wirecki TK, et al. MODOMICS: a database of RNA modification pathways. 2017 update. *Nucleic Acids Res* (2018) 46(D1):D303–D7. doi: 10.1093/nar/gkx1030

6. Bestor TH. Cloning of a mammalian DNA methyltransferase. *Gene* (1988) 74 (1):9–12. doi: 10.1016/0378-1119(88)90238-7

7. Garcia-Vilchez R, Sevilla A, Blanco S. Post-transcriptional regulation by cytosine-5 methylation of RNA. *Biochim Biophys Acta Gene Regul Mech* (2019) 1862(3):240–52. doi: 10.1016/j.bbagrm.2018.12.003

8. Yang X, Yang Y, Sun BF, Chen YS, Xu JW, Lai WY, et al. 5-methylcytosine promotes mRNA export - NSUN2 as the methyltransferase and ALYREF as an m (5)C reader. *Cell Res* (2017) 27(5):606–25. doi: 10.1038/cr.2017.55

9. Van Haute L, Lee SY, McCann BJ, Powell CA, Bansal D, Vasiliauskaite L, et al. NSUN2 introduces 5-methylcytosines in mammalian mitochondrial tRNAs. *Nucleic Acids Res* (2019) 47(16):8720–33.

10. Sharma S, Yang J, Watzinger P, Kotter P, Entian KD. Yeast Nop2 and Rcm1 methylate C2870 and C2278 of the 25S rRNA, respectively. *Nucleic Acids Res* (2013) 41(19):9062–76. doi: 10.1093/nar/gkt679

11. Xue S, Xu H, Sun Z, Shen H, Chen S, Ouyang J, et al. Depletion of TRDMT1 affects 5-methylcytosine modification of mRNA and inhibits HEK293 cell proliferation and migration. *Biochem Biophys Res Commun* (2019) 520(1):60–6. doi: 10.1016/j.bbrc.2019.09.098

12. Cheray M, Etcheverry A, Jacques C, Pacaud R, Bougras-Cartron G, Aubry M, et al. Cytosine methylation of mature microRNAs inhibits their functions and is associated with poor prognosis in glioblastoma multiforme. *Mol Cancer* (2020) 19 (1):36. doi: 10.1186/s12943-020-01155-z

13. David R, Burgess A, Parker B, Li J, Pulsford K, Sibbritt T, et al. Transcriptome-wide mapping of RNA 5-methylcytosine in arabidopsis mRNAs and noncoding RNAs. *Plant Cell* (2017) 29(3):445–60. doi: 10.1105/tpc.16.00751

14. Xue C, Zhao Y, Li L. Advances in RNA cytosine-5 methylation: detection, regulatory mechanisms, biological functions and links to cancer. *biomark Res* (2020) 8:43. doi: 10.1186/s40364-020-00225-0

15. Reid R, Greene PJ, Santi DV. Exposition of a family of RNA m(5)C methyltransferases from searching genomic and proteomic sequences. *Nucleic Acids Res* (1999) 27(15):3138–45. doi: 10.1093/nar/27.15.3138

16. Goll MG, Kirpekar F, Maggert KA, Yoder JA, Hsieh CL, Zhang X, et al. Methylation of tRNAAsp by the DNA methyltransferase homolog Dnmt2. *Sci (New York NY)* (2006) 311(5759):395–8. doi: 10.1126/science.1120976

17. Schaefer M, Pollex T, Hanna K, Tuorto F, Meusburger M, Helm M, et al. RNA Methylation by Dnmt2 protects transfer RNAs against stress-induced cleavage. *Genes Dev* (2010) 24(15):1590–5. doi: 10.1101/gad.586710

18. Traube FR, Carell T. The chemistries and consequences of DNA and RNA methylation and demethylation. *RNA Biol* (2017) 14(9):1099–107. doi: 10.1080/15476286.2017.1318241

19. Huang Y, Wang G, Liang Z, Yang Y, Cui L, Liu CY. Loss of nuclear localization of TET2 in colorectal cancer. *Clin Epigenet* (2016) 8:9. doi: 10.1186/s13148-016-0176-7

20. Chen X, Li A, Sun BF, Yang Y, Han YN, Yuan X, et al. 5-methylcytosine promotes pathogenesis of bladder cancer through stabilizing mRNAs. *Nat Cell Biol* (2019) 21(8):978–90. doi: 10.1038/s41556-019-0361-y

21. Cheng JX, Chen L, Li Y, Cloe A, Yue M, Wei J, et al. RNA Cytosine methylation and methyltransferases mediate chromatin organization and 5-azacytidine response and resistance in leukaemia. *Nat Commun* (2018) 9 (1):1163. doi: 10.1038/s41467-018-03513-4

22. Li D, Li K, Zhang W, Yang KW, Mu DA, Jiang GJ, et al. The m6A/m5C/m1A regulated gene signature predicts the prognosis and correlates with the immune status of hepatocellular carcinoma. *Front Immunol* (2022) 13:918140. doi: 10.3389/fimmu.2022.918140

23. Smyth EC, Cervantes A. Immunotherapy is not for all comers in chemotherapy-refractory advanced gastric cancer. better predictive biomarkers are needed. *Ann Oncol* (2018) 29(10):2027–8. doi: 10.1093/annonc/mdy331

24. Zhang B, Wu Q, Li B, Wang D, Wang L, Zhou YL. m(6)A regulator-mediated methylation modification patterns and tumor microenvironment infiltration characterization in gastric cancer. *Mol Cancer* (2020) 19(1):53. doi: 10.1186/s12943-020-01170-0

25. Pitt JM, Marabelle A, Eggermont A, Soria JC, Kroemer G, Zitvogel L. Targeting the tumor microenvironment: removing obstruction to anticancer immune responses and immunotherapy. *Ann Oncol* (2016) 27(8):1482–92. doi: 10.1093/annonc/mdw168

26. Ali HR, Chlon L, Pharoah PD, Markowetz F, Caldas C. Patterns of immune infiltration in breast cancer and their clinical implications: A gene-Expression-Based retrospective study. *PloS Med* (2016) 13(12):e1002194. doi: 10.1371/journal.pmed.1002194

27. Binnewies M, Roberts EW, Kersten K, Chan V, Fearon DF, Merad M, et al. Understanding the tumor immune microenvironment (TIME) for effective therapy. *Nat Med* (2018) 24(5):541–50. doi: 10.1038/s41591-018-0014-x

28. Guo G, Wang H, Shi X, Ye L, Yan K, Chen Z, et al. Disease activity-associated alteration of mRNA m(5) c methylation in CD4(+) T cells of systemic lupus erythematosus. *Front Cell Dev Biol* (2020) 8:430. doi: 10.3389/fcell.2020.00430

29. Collignon E, Canale A, Al Wardi C, Bizet M, Calonne E, Dedeurwaerder S, et al. Immunity drives TET1 regulation in cancer through NF-kappaB. *Sci Adv* (2018) 4(6):eaap7309. doi: 10.1126/sciadv.aap7309

30. Andries O, Mc Cafferty S, De Smedt SC, Weiss R, Sanders NN, Kitada T. N (1)-methylpseudouridine-incorporated mRNA outperforms pseudouridine-incorporated mRNA by providing enhanced protein expression and reduced immunogenicity in mammalian cell lines and mice. *J Control Release* (2015) 217:337–44. doi: 10.1016/j.jconrel.2015.08.051

31. Wnuk M, Slipek P, Dziedzic M, Lewinska A. The roles of host 5-methylcytosine RNA methyltransferases during viral infections. *Int J Mol Sci* (2020) 21(21): 8176. doi: 10.3390/ijms21218176

32. Colaprico A, Silva TC, Olsen C, Garofano L, Cava C, Garolini D, et al. TCGAbiolinks: an R/Bioconductor package for integrative analysis of TCGA data. *Nucleic Acids Res* (2016) 44(8):e71. doi: 10.1093/nar/gkv1507

33. Wilkerson MD, Hayes DN. ConsensusClusterPlus: a class discovery tool with confidence assessments and item tracking. *Bioinformatics* (2010) 26 (12):1572–3. doi: 10.1093/bioinformatics/btq170

34. Charoentong P, Finotello F, Angelova M, Mayer C, Efremova M, Rieder D, et al. Pan-cancer immunogenomic analyses reveal genotype-immunophenotype relationships and predictors of response to checkpoint blockade. *Cell Rep* (2017) 18 (1):248–62. doi: 10.1016/j.celrep.2016.12.019

35. Ritchie ME, Phipson B, Wu D, Hu Y, Law CW, Shi W, et al. Limma powers differential expression analyses for RNA-sequencing and microarray studies. *Nucleic Acids Res* (2015) 43(7):e47. doi: 10.1093/nar/gkv007

36. Xiang ZJ, Wang Y, Ramadge PJ. Screening tests for lasso problems. *IEEE Trans Pattern Anal Mach Intell* (2017) 39(5):1008–27. doi: 10.1109/TPAMI.2016.2568185

37. Engebretsen S, Bohlin J. Statistical predictions with glmnet. *Clin Epigenet* (2019) 11(1):123. doi: 10.1186/s13148-019-0730-1

38. Zeng D, Li M, Zhou R, Zhang J, Sun H, Shi M, et al. Tumor microenvironment characterization in gastric cancer identifies prognostic and immunotherapeutically relevant gene signatures. *Cancer Immunol Res* (2019) 7 (5):737–50. doi: 10.1158/2326-6066.CIR-18-0436

39. Amiot L, Vu N, Samson M. Biology of the immunomodulatory molecule HLA-G in human liver diseases. *J Hepatol* (2015) 62(6):1430–7. doi: 10.1016/j.jhep.2015.03.007

40. Sato K, Tahata K, Akimoto K. Five genes associated with survival in patients with lower-grade gliomas were identified by information-theoretical analysis. *Anticancer Res* (2020) 40(5):2777–85. doi: 10.21873/anticanres.14250

41. Mei L, Shen C, Miao R, Wang JZ, Cao MD, Zhang YS, et al. RNA Methyltransferase NSUN2 promotes gastric cancer cell proliferation by repressing p57(Kip2) by an m(5)C-dependent manner. *Cell Death Dis* (2020) 11 (4):270. doi: 10.1038/s41419-020-2487-z

42. Yamashita T, Higashi M, Momose S, Morozumi M, Tamaru JI. Nuclear expression of y box binding-1 is important for resistance to chemotherapy including gemcitabine in TP53-mutated bladder cancer. *Int J Oncol* (2017) 51 (2):579–86. doi: 10.3892/ijo.2017.4031

43. Campbell TM, Castro MAA, de Oliveira KG, Ponder BAJ, Meyer KB. ERalpha binding by transcription factors NFIB and YBX1 enables FGFR2 signaling

to modulate estrogen responsiveness in breast cancer. *Cancer Res* (2018) 78 (2):410–21. doi: 10.1158/0008-5472.CAN-17-1153

44. Saito Y, Kasamatsu A, Yamamoto A, Shimizu T, Yokoe H, Sakamoto Y, et al. ALY as a potential contributor to metastasis in human oral squamous cell carcinoma. *J Cancer Res Clin Oncol* (2013) 139(4):585–94. doi: 10.1007/s00432-012-1361-5

45. Chen DS, Mellman I. Elements of cancer immunity and the cancer-immune set point. *Nature* (2017) 541(7637):321–30. doi: 10.1038/nature21349

46. Turley SJ, Cremasco V, Astarita JL. Immunological hallmarks of stromal cells in the tumour microenvironment. *Nat Rev Immunol* (2015) 15(11):669–82. doi: 10.1038/nri3902

47. Mariathasan S, Turley SJ, Nickles D, Castiglioni A, Yuen K, Wang Y, et al. TGFbeta attenuates tumour response to PD-L1 blockade by contributing to exclusion of T cells. *Nature* (2018) 554(7693):544–8. doi: 10.1038/nature25501

48. Luo J, Yang Z, Ma Y, Yue Z, Lin H, Qu G, et al. LGR4 is a receptor for RANKL and negatively regulates osteoclast differentiation and bone resorption. *Nat Med* (2016) 22(5):539–46. doi: 10.1038/nm.4076

49. Zou G, Ren B, Liu Y, Fu Y, Chen P, Li X, et al. Inhibin b suppresses anoikis resistance and migration through the transforming growth factor-beta signaling pathway in nasopharyngeal carcinoma. *Cancer Sci* (2018) 109(11):3416–27. doi: 10.1111/cas.13780

50. Hu L, Chen M, Chen X, Zhao C, Fang Z, Wang H, et al. Chemotherapy-induced pyroptosis is mediated by BAK/BAX-caspase-3-GSDME pathway and inhibited by 2-bromopalmitate. *Cell Death Dis* (2020) 11(4):281. doi: 10.1038/s41419-020-2476-2

51. Byrne JA, Nourse CR, Basset P, Gunning P. Identification of homo- and heteromeric interactions between members of the breast carcinoma-associated D52 protein family using the yeast two-hybrid system. *Oncogene* (1998) 16(7):873–81. doi: 10.1038/sj.onc.1201604

52. Notarnicola C, Rouleau C, Le Guen L, Virsolvy A, Richard S, Faure S, et al. The RNA-binding protein RBPMS2 regulates development of gastrointestinal smooth muscle. *Gastroenterology* (2012) 143(3):687–97.e9. doi: 10.1053/j.gastro.2012.05.047

frontiers | Frontiers in Immunology

TYPE Original Research
PUBLISHED 27 October 2022
DOI 10.3389/fimmu.2022.907182

Check for updates

OPEN ACCESS

EDITED BY
Elena Ciaglia,
University of Salerno, Italy

REVIEWED BY
Zongsheng He,
Daping Hospital, China
Keehoon Jung,
Seoul National University, South Korea

*CORRESPONDENCE
Quan Cheng
chengquan@csu.edu.cn
Hao Zhang
zhsw@hospital.cqmu.edu.cn

†These authors have contributed equally to this work

SPECIALTY SECTION
This article was submitted to Cancer Immunity and Immunotherapy, a section of the journal Frontiers in Immunology

RECEIVED 29 March 2022
ACCEPTED 12 September 2022
PUBLISHED 27 October 2022

CITATION
Guo A, Zhang J, Tian Y, Peng Y, Luo P, Zhang J, Liu Z, Wu W, Zhang H and Cheng Q (2022) Identify the immune characteristics and immunotherapy value of CD93 in the pan-cancer based on the public data sets. *Front. Immunol.* 13:907182. doi: 10.3389/fimmu.2022.907182

COPYRIGHT
© 2022 Guo, Zhang, Tian, Peng, Luo, Zhang, Liu, Wu, Zhang and Cheng. This is an open-access article distributed under the terms of the Creative Commons Attribution License (CC BY). The use, distribution or reproduction in other forums is permitted, provided the original author(s) and the copyright owner(s) are credited and that the original publication in this journal is cited, in accordance with accepted academic practice. No use, distribution or reproduction is permitted which does not comply with these terms.

Identify the immune characteristics and immunotherapy value of CD93 in the pan-cancer based on the public data sets

Aiyuan Guo[1†], Jingwei Zhang[2,3†], Yuqiu Tian[4], Yun Peng[2,5], Peng Luo[6], Jian Zhang[6], Zaoqu Liu[7], Wantao Wu[8], Hao Zhang[9*] and Quan Cheng[2,3,10*]

[1]Department of Dermatology, The Third Xiangya Hospital, Central South University, Changsha, China, [2]Department of Neurosurgery, Xiangya Hospital, Central South University, Changsha, China, [3]National Clinical Research Center for Geriatric Disorders, Xiangya Hospital, Central South University, Changsha, China, [4]Department of Infectious Disease, Zhuzhou Central Hospital, Zhuzhou, China, [5]Teaching and Research Section of Clinical Nursing, Xiangya Hospital of Central South University, Changsha, China, [6]Department of Oncology, Zhujiang Hospital, Southern Medical University, Guangzhou, China, [7]Department of Interventional Radiology, The First Affiliated Hospital of Zhengzhou University, Zhengzhou, China, [8]Department of Oncology, Xiangya Hospital, Central South University, Changsha, China, [9]Department of Neurosurgery, The Second Affiliated Hospital, Chongqing Medical University, Chongqing, China, [10]Clinical Diagnosis and Therapy Center for Glioma of Xiangya Hospital, Central South University, Changsha, China

CD93 is a transmembrane receptor that is mainly expressed on endothelial cells. A recent study found that upregulated CD93 in tumor vessels is essential for tumor angiogenesis in several cancers. However, the underlying mechanisms are largely unexplored. Our present research systematically analyzed the characteristics of CD93 in tumor immunotherapy among 33 cancers. CD93 levels and co-expression of CD93 on cancer and stromal cells were detected using public databases and multiple immunofluorescence staining. The Kaplan-Meier (KM) analysis identified the predictive role of CD93 in these cancer types. The survival differences between CD93 mutants and WT, CNV groups, and methylation were also investigated. The immune landscape of CD93 in the tumor microenvironment was analyzed using the SangerBox, TIMER 2.0, and single-cell sequencing. The immunotherapy value of CD93 was predicted through public databases. CD93 mRNA and protein levels differed significantly between cancer samples and adjacent control tissues in multiply cancer types. CD93 mRNA expression associated with patient prognosis in many cancers. The correlation of CD93 levels with mutational status of other gene in these cancers was also analyzed. CD93 levels significantly positively related to three scores (immune, stromal, and extimate), immune infiltrates, immune checkpoints, and neoantigen expression.. Additionally, single-cell sequencing revealed that CD93 is predominantly co-expressed on tumor and stromal cells, such as endothelial cells, cancer-associated fibroblasts (CAFs), neutrophils, T cells, macrophages, M1 and M2 macrophages. Several

immune-related signaling pathways were enriched based on CD93 expression, including immune cells activation and migration, focal adhesion, leukocyte transendothelial migration, oxidative phosphorylation, and complement. Multiple immunofluorescence staining displayed the relationship between CD93 expression and CD8, CD68, and CD163 in these cancers. Finally, the treatment response of CD93 in many immunotherapy cohorts and sensitive small molecules was predicted from the public datasets. CD93 expression is closely associated with clinical prognosis and immune infiltrates in a variety of tumors. Targeting CD93-related signaling pathways in the tumor microenvironment may be a novel therapeutic strategy for tumor immunotherapy.

KEYWORDS

CD93, pan-cancer, immunotherapy, macrophages, T cells, tumor microenvironment

Introduction

Cancer remains the second most common cause of death in the United States and remains a significant global public health threat until now (1). Uncontrolled cell proliferation is mainly due to the accumulation of genetic and epigenetic alterations, leading to cancer formation (2, 3). Cancer occurs due to the synergistic action of multiple carcinogens, such as chemical and physical carcinogens, viruses, and bacteria (4, 5). There are only a few options for cancer treatment, including surgery, chemotherapy, targeted drug therapy, radiation and hormone therapy, stem cell transplant, clinical trials, and immunotherapy (6–8). Despite rapid improvements in early diagnosis and treatment in past decades, five-year survival rates for many cancer types remain unsatisfied (9). The past decades have witnessed tremendous developments in cancer immunotherapy, one of the most promising fields for the future of cancer treatment. Immunotherapy functions by inducing the immune system to target the tumor and stroma cells *via* various xenoantigens, ultimately enhancing the innate anti-tumor immune responses (10, 11). In particular, checkpoint inhibitors in the tumor microenvironment (TME) have been shown improve prognosis for patients with advanced malignancies, including melanoma, lymphoma, lung and bladder cancers (12, 13). A large number of immune checkpoints have been discovered through public databases according to the rapid development of high-throughput sequencing technology (14–16). Validating the effectiveness of these immune checkpoints through preclinical and clinical studies will help significantly improve the prognosis of cancer patients.

Recent evidence indicated CD93 act as anew immune checkpoint for immunotherapy in the TME (17–19). CD93 is a transmembrane protein from the Group XIV C-Type lectin family (20). It contains a short cytoplasmic tail, a C-type lectin domain, a unique transmembrane like and a highly glycosylated mucin like as well as a series of epidermal growth factor like structural domains (21). CD93 plays a vital role in endothelial cell-cell adhesion, cell migration, cell polarization, and phagocytosis (22). Endothelial cell migration is essential for angiogenesis and promotes the formation of new blood vessels under physiological and pathological conditions (23, 24). In addition, CD93 can regulate β_1 integrin activation and fibronectin fibril formation, thereby mediating angiogenesis during tumorigenesis and growth. CD93 is expressed by various cell types, such as myeloid lineage, platelets, monocytes, microglia, and endothelial cells (25). CD93 expression levels in tumor blood vessels are associated with poor survival in patients with high-grade astrocytic glioma (21). Similarly, CD93-deficient glioma mice had significantly slower intracranial tumor growth and improved survival than wild-type mice. In addition, recent papers have shown that CD93 is a prognostic marker for many malignant cancers and is involved in immune responses in the TME during cancer immunization (26, 27). However, the specific mechanisms of CD93 in tumor immunity remain largely undiscovered. Thus, a comprehensive assessment of the predictive value of CD93 in other cancers and the co-expression and role of CD93 on tumor and stromal cells in the TME require further elaboration.

Therefore, in this paper, we systematically checked the prognostic and immune role of CD93 in pan-cancer based on public databases like TCGA, CCLE, and GTEX. Meanwhile, the survival difference between CD93 mutant and WT, CNV groups, and methylation were explored. Moreover, the co-expression of CD93 on various cell types in the TME were verified through the online dataset, single-cell sequencing analysis, and multiple fluorescent staining. Furthermore, the immunotherapy effectiveness and sensitive drugs targeting CD93 in these cancers were predicted.

Materials and methods

Data collection and preparation

The transcriptomic data of CD93 in pan-cancer cohorts were obtained from The Cancer Genome Atlas (TCGA; http://cancergenome.nih.gov) (28) and Genotype Tissue-Expression (GTEX; https://gtexportal.org/home/) (29) databases. The cell lines data were collected from the Cancer Cell Line Encyclopedia (CCLE; https://sites.broadinstitute.org/ccle/) (30) dataset. The single-cell sequencing data were collected from the Gene Expression Omnibus (GEO; https://www.ncbi.nlm.nih.gov/geo/) database, including BLCA (GSE145137), BRCA (GSE75688 and GSE118389), CHOL (GSE125449), COAD (GSE81861), HNSC (GSE103322), KIRC (GSE121636 and GSE171306), LIHC (GSE125449), OV (GSE118828), PRAD (GSE137829), SKCM (GSE72056), and STAD (GSE183904). The Single Cell Portal platform was used to collect the scRNA-seq dataset of GBM (SCP50 and SCP393, http://singlecell.broadinstitute.org). The Genome Sequence Archive (GSA) database was used to collect the scRNA-seq dataset of PAAD (CRA001160, https://ngdc.cncb.ac.cn/gsa/browse/CRA001160). The BioProject (#PRJNA591860) database was applied to collect the scRNA-seq dataset of LUAD.

CD93 prognostic and immune role identification

The Kaplan-Meier (KM) curve was applied to analyze the overall survival (OS) and disease-specific survival (DSS). The immune landscapes of CD93 were analyzed by the SangerBox (http://sangerbox.com/) and immunedeconv package. The immune score is a sophisticated tissue-based assay that defines the score by precisely quantifying and identifying T lymphocytes infiltrating the tumor in specific regions. The stromal score, which captures the presence of stroma in the TME, uses expression data for specific gene signatures associated with the stromal component of the TME to predict levels of infiltrating stromal cells. Estimated scores are used to infer tumor purity in the TME. These scores were calculated by the SangerBox using the ESTIMATE algorithm. The correlation between CD93 levels and other gene mutation status in these cancers was analyzed by the MuTarget dataset (https://www.mutarget.com/analysis?type=target) (31). The Gene set variation analysis algorithm (GSVA) (32), Kyoto Encyclopedia of Genes and Genomes database (KEGG; https://www.genome.jp/kegg/) (33, 34), and HALLMARK database were applied to identified enriched signaling pathways. The survival difference between mutant and WT, CNV groups, and methylation were analyzed by the GSCA dataset. The TIDE (http://tide.dfci.harvard.edu) and TISMO (http://tismo.cistrome.org) websites were used to analyze the immunotherapy and gene treatment responses of CD93 in these cancers.. The Gene Set Cancer Analysis (GSCA; http://bioinfo.life.hust.edu.cn/GSCA/#/), CCLE, and CellMiner (https://discover.nci.nih.gov/cellminer/) (35) datasets were used to predict the sensitive small molecule drugs. The correlation of CD93 expression with treatment response in breast cancer, OV, GBM, and colorectal cancer was predicted by the ROC Plotter (http://www.rocplot.org/site/index) (36, 37).

Single-cell sequencing analysis

The R package (Seurat) were applied for BRCA and STAD data integration and quality control (38). Dimensionality reduction using Principal Component Analysis (PCA). Visualization of CD93 expression by R packages (Vlnplot, Dimplot, and Featureplot). The FindClusters function was applied to cluster the cells together. Identification of tumor cells by the R package (infercnv and copycat). Visualization of dimensionality reduction with UMAP functions.

Multiple immunofluorescence staining

Multiple immunofluorescence staining was performed as previously described (39, 40). The primary Abs were CD8 (Mouse, 1:3000, Proteintech), CD68 (Rabbit, 1:3000, AiFang biological), CD93 (Rabbit, 1:200, Thermo Fisher), and CD163 (Rabbit, 1:3000, Proteintech). PV6001 (horseradish peroxidase-conjugated secondary antibody, ZSGB-BIO, China) was the secondary antibody, and the tyramide signal was amplified to TSA [FITC-TSA, CY3-TSA, 594-TSA, and 647-TSA (Servicebio, China)]. Image analysis and positive cell quantification were performed by Caseviewer (C.V 2.3, C.V 2.0) and Pannoramic viewer (P.V 1.15.3). Negative controls excluded the primary Ab. We obtained the tissue microarray (HOrg-C110PT-01) from the Outdo Biotech company (Shanghai, China), and the ethics were approved.

Statistical analysis

The R package calculated the optimal cutoff of CD93 (survminer). A student's t-test (normally distributed data) and Kruskal-Wallis's test (non-normally distributed data) compared CD93 expression in the cancer and corresponding samples, respectively. Meanwhile, the log-rank test was applied to explore the prognostic role of CD93. All tests were bilateral, and $P< 0.05$ was set as statistically significant.

Expression and prognostic value of CD93

The flow chart designed in this paper is shown in Figure 1. Firstly, we used the CCLE, TCGA, and GTEX databases to

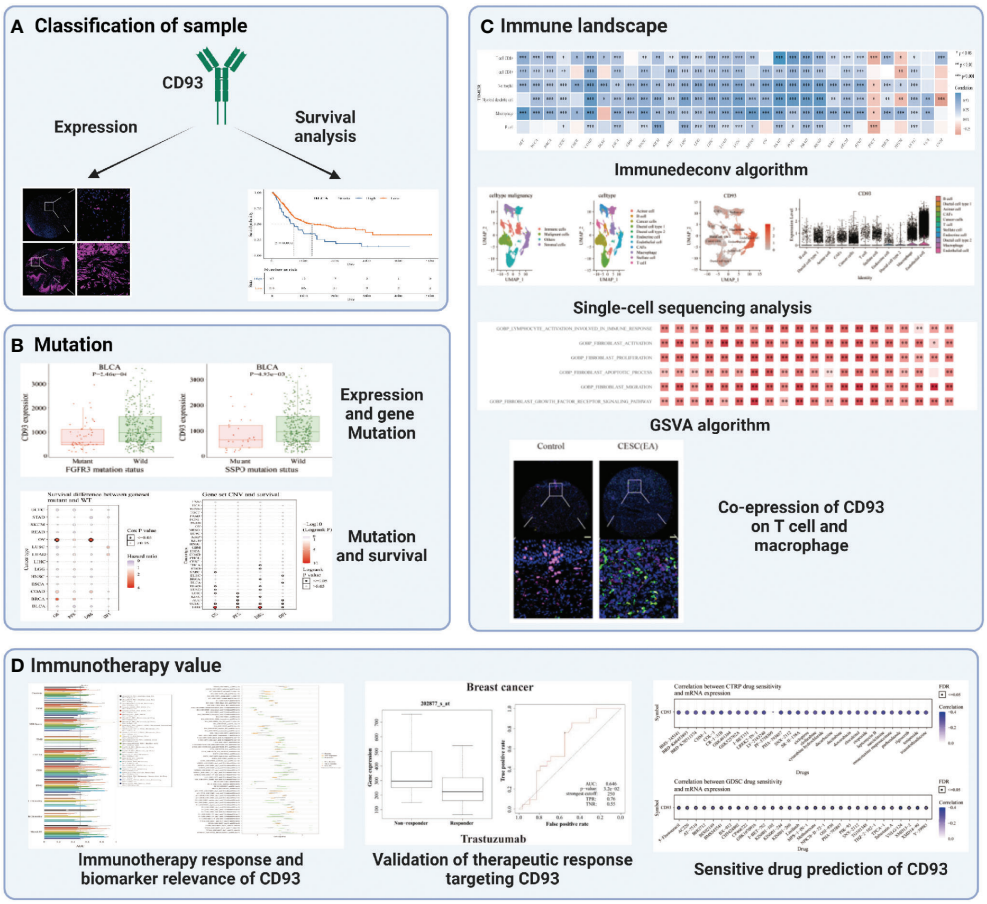


FIGURE 1
The flow chart of this study. *p < 0.05, **p < 0.01, ***p < 0.001.

explore the CD93 levels in the cancers and their counterparts. Data from the CCLE database showing CD93 expression in tumor cell lines, of which the top three cell lines were AML, B cell ALL, and leukemia (Figure 2A). Elevated mRNA levels of CD93 in tumor samples compared to normal controls in GBM, PAAD, STAD, CHOL, LGG, LIHC, KIRC, acute myeloid leukemia (LAML), HNSC, TGCT, and SKCM (Figure 2B; P<0.05). Conversely, decreased mRNA levels of CD93 in tumor samples compared to normal controls in COAD, KIRP, ACC, CESC, UCEC, BRCA, BLCA, LUAD, PRAD, KICH, THCA, LUSC, and UCS (Figure 2B; P<0.05). Meanwhile, we verified the protein levels of CD93 in our tumor microarrays through immunofluorescence staining (Figure 2C). Data showed that CD93 protein levels were upregulated in the tumor samples compared to control (pericancerous) samples in penile squamous cell carcinoma (PSCC), laryngeal squamous cell carcinoma (LSCC), and TGCT. Meanwhile, CD93 protein levels were decreased in the tumor samples than in control samples in THCA, UTUC, BLCA, and CESC. The CD93 protein levels were also expressed in ovarian serous papillary adenocarcinoma (OPV) and OV.

In addition, the prognostic role of CD93 in these cancers was explored using the KM algorithm. Results show that CD93 has a good value in predicting OS (Supplementary Figure 1A) and DSS (Supplementary Figure 1B) in multiple cancers. Low CD93 mRNA levels were associated with longer OS in BLCA, CESC, COAD, ESCA, GBM, UCEC, UVM, KIRP, LAML, LGG, LIHC, READ, LUSC, MESO, OV, STAD, and THCA (Supplementary Figure 1C; P<0.05). Conversely, low CD93 mRNA levels were associated with shorter OS in PCPG, LUAD, SARC, HNSC, and KIRC (Supplementary Figure 1C; P<0.05). In addition, low CD93 mRNA levels related to better DSS in BLCA, COAD, ESCA, LGG, LUSC, KIRP, MESO, OV, UCEC, and UVM, and related to poor DSS in HNSC, LUAD, KIRC, SARC, and PCPG

10.3389/fimmu.2022.907182

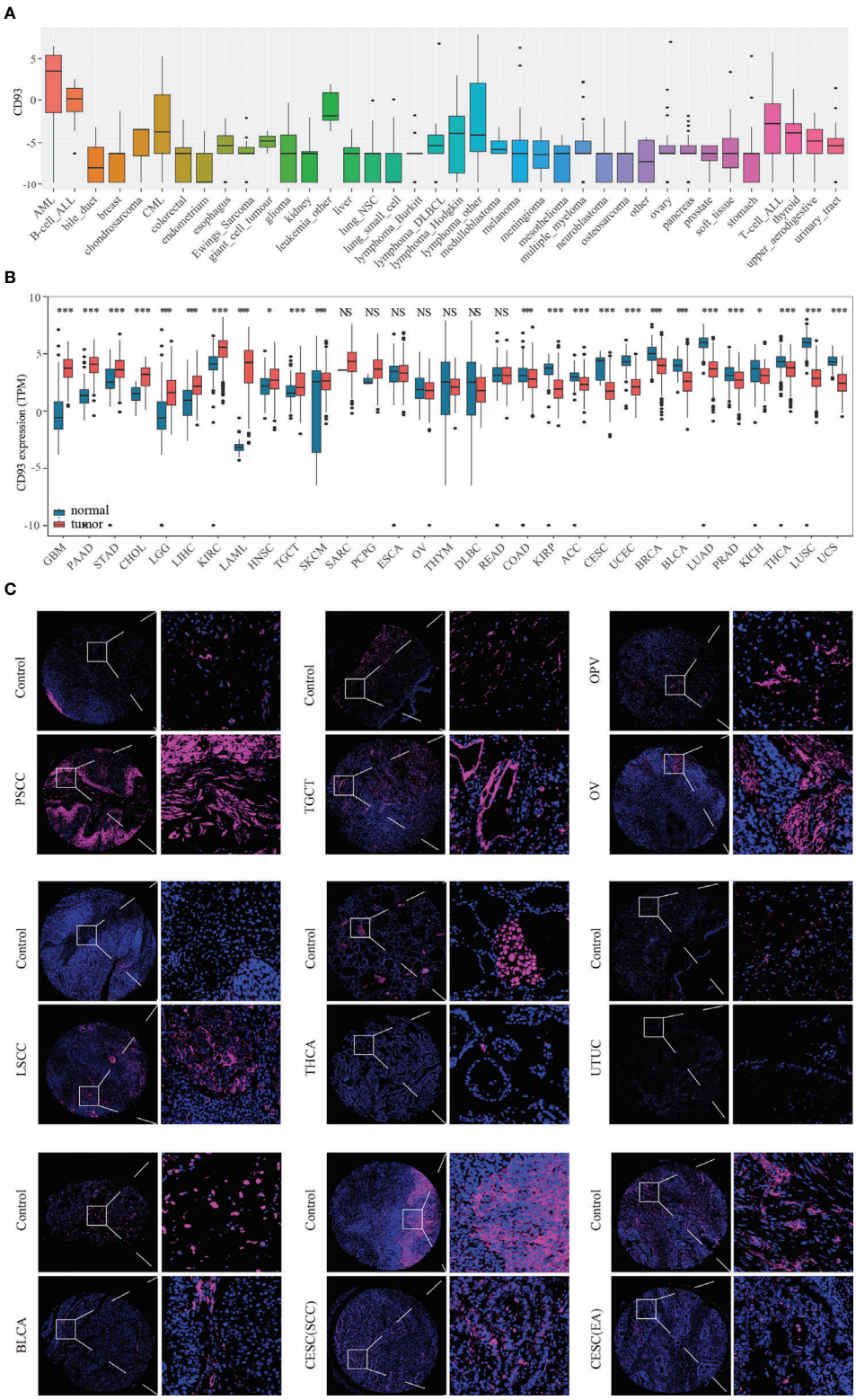


FIGURE 2
CD93 levels in tumor samples and counterparts. CD93 mRNA expression in cancer cell lines from the CCLE dataset **(A)**. CD93 mRNA expression in cancer and normal samples from the TCGA and GETX datasets **(B)**. CD93 protein expression in cancer and control samples in tumor microarrays **(C)**. *p < 0.05, ***p < 0.001, NS, no significant differences.

(Supplementary Figure 2A; P<0.05). A summary of CD93 expression in pan-cancer and its association with prognosis is shown in Supplementary Figure 2B.

Mutation analysis of CD93 in pan-cancer

Furthermore, we analyzed the survival difference between CD93 genome mutants and the WT group in these cancers through progression-free survival (PFS), disease-free interval (DFI), OS, and DSS analysis (Figure 3A). The DSS and OS in the CD93 mutant group significantly differ from the WT group in OV (Figure 3A and Table S1; P<0.05). CD93 copy number variation (CNV) and survival analysis results showed significant differences in OS for LGG, UCEC, READ, LIHC, SARC, and LUAD (P<0.05); in PFS for LGG, UCEC, ACC, LIHC, and KIRC (P<0.05); in DSS for LGG, UCEC, LUAD, KIRC, THCA, STAD, READ and BRCA (P<0.05); in DFI for ACC, UCEC, DLBC, LGG and BLCA (Figure 3B and Table S2; P<0.05). CD93 RNA expression is associated with methylation in almost every type of cancer except OV (Figure 3C and Table S3; P<0.05). CD93 high methylation group showed a significant difference with the low methylation group in DSS and OS for UVM, KIRP, LGG, SKCM, and KIRC (Figure 3D and Table S4; P<0.05).

The MuTarget dataset showed that CD93 expression was associated with several gene mutational states in CESC, including MUC4, TENM1, PLXNC1, LATS1, and CACNA1C. The wild group of these genes has more CD93 expression than the mutant group (Figure 4A; P<0.01). In COAD, the mutant group of KIAA1217, GLG1, PAM, PFAS, and NCOR1 has more CD93 expression than the wild group (Figure 4B; P<0.001). In LGG, the mutant group of EGFR, HMCN1, PTEN, and LRP2 has more CD93 expression than the wild group, while the wild group of IDH1 has more CD93 expression than the mutant group (Figure 4C; P<0.01). In LUAD, the wild group of ZNF804B, SLITRK3, NELL1, HERC2, and IFT172 has more CD93 expression than the mutant group (Figure 4D; P<0.01). In LUSC, the wild group of CTNND2, JAK2, LAMA5, and RASGRP3 has more CD93 expression than the mutant group, while the mutant group of CHD5 has more CD93 expression than the wild group (Figure 4E; P<0.01). In SKCM, the wild group of PKHD1, KIAA1551, CAPN13, and CASR has more CD93 expression than the mutant group, while the mutant group of MARVELD2 has more CD93 expression than the wild group (Figure 4F; P<0.01). In STAD, the wild group of PKD1, HDAC4, GABRG2, TRRAP, and TRPA1 has more CD93 expression than the mutant group (Figure 4G; P<0.01). In UCEC, the wild group of LPCAT4, MRO, IRS4, ZNF251, and CCDC18 has more CD93 expression than the mutant group (Figure 4H; P<0.001). In BLCA, the wild group of FGFR3, SSPO, and KHDRBS2 has more CD93 expression than the mutant group, while the mutant group of KDM5B has more CD93 expression than the wile group (Supplementary Figure 3A; P<0.01). In SARC, the wild group of AHNAK and CCDC168 has more CD93 expression than the mutant group (Supplementary Figure 3B; P<0.01). In LIHC, the wild group of CTNNB1, KMT2D, and AXIN1 has more CD93 expression than the mutant group, while the mutant group of COL6A3 has more CD93 expression than the wile group (Supplementary Figure 3C; P<0.01). In OV, the mutant group of AOC2, DNAH11, ZNF835, and PLEKHG1 has more CD93 expression than the wild group (Supplementary Figure 3D; P<0.01). In HNSC, the wild group of AJUBA has more CD93 expression than the mutant group (Supplementary Figure 3E; P<0.01). In multiple myeloma, the wild group of SLC22A3, PTOV1, GRM2, and NBPF10 has more CD93 expression than the mutant group, while the mutant group of CXXC1 has more CD93 expression than the wile group (Supplementary Figure 3F; P<0.001).

Immune characteristics of CD93 in the tumor microenvironment

Next, to clarify the immune characteristics of CD93 in the TME in these cancers, we explored the relationship between CD93 expression and three scores (immune, estimate, and stromal) in 33 cancers using the ESTIMATE algorithm through the SangerBox website. CD93 expression positively correlated with immune scores in almost all cancers, except DLBC, KIRC, TGCT, THCA, and THYM (Supplementary Figure 4; P<0.05). CD93 levels were strongly correlated with estimate scores for almost all cancers except TGCT and THCA (Supplementary Figure 5; P<0.01). High CD93 expression was strongly associated with high stromal scores in all cancers (Supplementary Figure 6; P<0.01). In addition, six immune infiltration algorithms were applied, including EPIC, TIMER, QUANTIAEQ, xCell, MCPCOUNTER, and CIBERSORT (Supplementary Figure 7) to analyze the correlation between CD93 and stromal cells in these cancers. The results indicated that CD93 was closely associated with these stromal cells in the TME of these cancers. Results indicated that CD93 is closely related to these stromal cells in the TME in these cancers. Especially, high CD93 levels were positively correlated with the expression of endothelial cells, T cells ($CD8^+$ and $CD4^+$), neutrophils, myeloid dendritic cells, macrophages, B cells, T cell regulatory (Tregs), M1 and M2 macrophages, monocytes, and hematopoietic stem cells in almost all cancers. On the contrary, the expression of $CD4^+$ T cell (Th1 and central memory), T cell follicular helper, B cell plasma, and activated NK cell was negatively correlated with CD93 levels.

Neoantigens, a group of tumor-specific antigens generated by tumor cell mutations in the TME, have the potential to become valuable targets for tumor immunotherapy (41, 42). The expression of neoantigens kept a close correlation with CD93 levels in BRCA, STAD, CESC, THCA, and LGG (Supplementary Figure 8; P<0.05). Moreover, we studied the correlation between

10.3389/fimmu.2022.907182

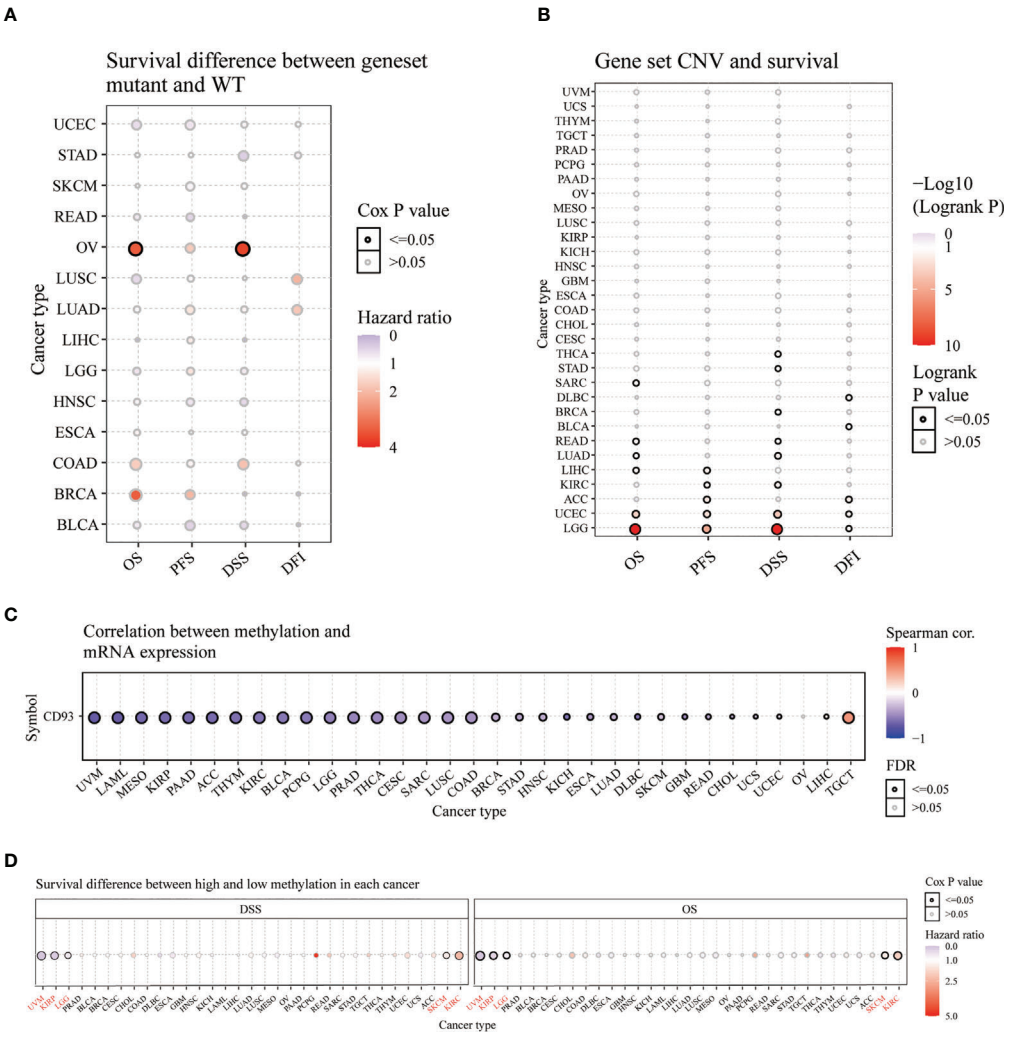


FIGURE 3
Survival analysis of CD93 in pan-cancer from the GSCA database. Survival difference between CD93 mutant and WT **(A)**. CD93 CNV and survival **(B)**. Correlation between CD93 methylation and mRNA expression **(C)**. Survival difference between CD93 high and low methylation **(D)**.

CD93 and other classical immune checkpoints in these cancers. Results showed that CD93 expression was closely associated with the levels of several immune checkpoints in many cancers, including NRP1, LAIR1, CD28, CD200R1, HAVCR2, CD276, VSIR, and CD86 (Supplementary Figure 9; P<0.05).

Functional analysis based on CD93 expression

Many immune-related pathways based on the GSVA algorithm were significantly positively correlated with CD93 expressions in these cancers, such as lymphocyte activation involved in immune response, fibroblast activation and proliferation, fibroblast migration, fibroblast growth factor receptor signaling pathway, T cell extravasation, response to macrophage colony-stimulating factor, macrophage cytokine production, macrophage and macrophage-derived foam cell differentiation (Figure 5A; P<0.05). These signaling pathways play an irreplaceable role in tumor immunity in the TME, especially in the infiltration and activation of T cells, CAFs, macrophages, and mast cells. Additionally, the top three negatively enriched pathways were focal adhesion, vascular smooth muscle contraction, and leukocyte transendothelial migration (Figure 5B; P<0.001), while the top four positively enriched pathways were Huntington's disease, proteasome, Parkinson's disease, and oxidative phosphorylation analyzed from the KEGG database (Figure 5C; P<0.01). KRAS signaling up, UV response DN, and complement were the top three negatively enriched pathways (Figure 5D; P<0.001), while

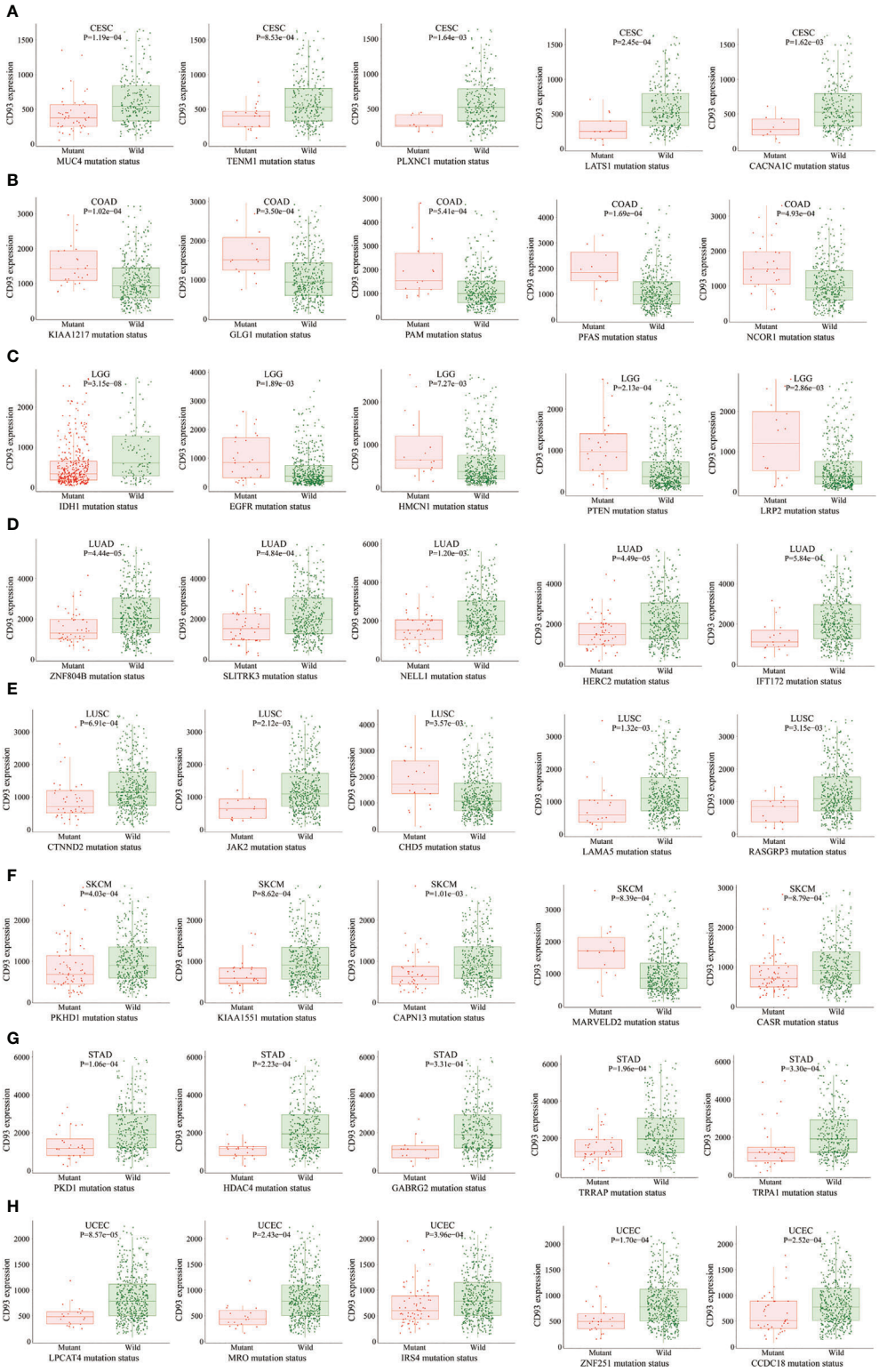


FIGURE 4
The correlation between CD93 expression and gene mutation status. CESC **(A)**, COAD **(B)**, LGG **(C)**, LUAD **(D)**, LUSC **(E)**, SKCM **(F)**, STAD **(G)**, and UCEC **(H)**.

DNA repair, MYC targets V2, MYC targets V1, and oxidative phosphorylation were the top four positively enriched pathways analyzed from the HALLMARK database (Figure 5E; P<0.05).

Relationship between CD93 and tumor and stromal cells analyzed by the single-cell sequencing and multiplex immunofluorescence staining

Then, we investigated the relationship between CD93 and tumor and stromal cells in the TME of these cancers, including GBM, HNSC, KIRC, LUAD, PAAD, PRAD, BLCA, BRCA, CHOL, COAD, LIHC, OV, SKCM, and STAD (Figure 6 and Supplementary Figure 10). Interestingly, microglial cells, M1 and M2 macrophages, macrophages, B cells, NK cells, astrocyte, neurons, neoplastic, oligodendrocyte, CAFs, T cells, endothelial cells, monocyte, neutrophils, smooth muscle cells, epithelial, cancer cells, stellate cells, endocrine cells, acinar cells, ductal cell type 1, TEC, and HPC-like were found to express CD93 in these cancers.

Furthermore, we performed multiplex immunofluorescence staining to identify the relationship between CD93 and CD8 (marker for T cells), CD68 (marker for macrophages), and CD163 (marker for M2 macrophages) in these cancers. CD8 is labeled in pink, CD68 is labeled in red, CD163 is labeled in green, CD93 is labeled in rose red, and DAPI is labeled in blue (Figure 7M). WHOIII gliomas have higher CD93 expression than WHOII gliomas (Figure 7A). CD93 was found to be closely related to CD8 in GBM (Figure 7B), UTUC (Figure 7C), and PRAD (Figure 7L). CD93 was found to be closely related to CD68 in UTUC (Figure 7C), THCA (Figure 7F), CESC (SCC) (Figure 7G), PSCC (Figure 7I), OPV, and OV (Figure 7J), TGCT (Figure 7K), and PRAD (Figure 7L). In addition, CD163 was found to be closely related to CD93 expression in BLCA (Figure 7D), CESC (Figures 7G, H), and TGCT (Figure 7K). LSCC expressed more CD93 levels than the control (Figure 7E). Interestingly, CD93 protein levels appear to be higher in GBM than in LGG.

Prediction of tumor immunotherapy value based on CD93 expression

Finally, to systematically clarify the underlying value of CD93 as an immunotherapy target in these cancers, we predicted the immunotherapy response and sensitive drugs from the public databases (Figure 8). Based on the predictive role of classical biomarkers for response outcomes and OS in human immunotherapy cohorts, we calculated the biomarker correlation of CD93 by comparing it to these classical biomarkers. Of the total 25 immunotherapy cohorts, CD93 alone showed an AUC above 0.5 in 8 immunotherapy cohorts (Figures 8A, C). The predictive value of CD93 was higher than the B. Clonality with AUC value above 0.5 in seven immunotherapy cohorts. CD93 had the same predictive value as the TMB with an AUC value above 0.5 in 8 immunotherapy cohorts. The predictive value of CD93 was lower than the T.Clonality, MSI score, IFNG, and CD8, TIDE, and CD274, with AUC values above 0.5 in 9, 13, 17, 18, 18, and 21 immunotherapy cohorts, respectively. CD93 significantly predicted immunotherapy response in 4 immunotherapy cohorts, where responders were more likely to have high CD93 levels (Figures 8B, D). The ROC Plotter dataset analyzed the prediction of response to therapy targeting CD93 in breast, OV, GBM, and colorectal cancer. Results showed that the AUC of treatment with trastuzumab in breast cancer was 0.646 (Supplementary Figure 11A; P<0.05). The AUC of treatment with capecitabine in colorectal carcinoma was 0.677 (Supplementary Figure 11B; P<0.05). Therapeutic responses of CD93 in mechanistic follow-up experiments in the core dataset, immunotherapy dataset, CRISPR Screen dataset, and immune-suppressive cell types were predicted from the TIDE website (Figure 8E).

Then, we predicted the sensitive small molecule drugs through CTRP (Figure 8F) and GDSC (Figure 8G) datasets. The top five sensitive drugs were BRD-K30748066, isoliquiritigenin, teniposide, PHA-793887, and CR-1-31B based on CD93 expression from the CTRP dataset (Table S5; P<0.05). The top five sensitive drugs were VNLG/124, XMD14-99, CH5424802, TG101348, and 5-Fluorouracil based on CD93 expression from the GDSC dataset (Table S5; P<0.0001). The top three sensitive compounds were PF2341066, PD-0332991, and L-685458 based on CD93 expression from the CCLE dataset (Table S6; P<0.05). Triostin a, sb-253226, toxin. delta.53l, pederin, and euserotin were top-five sensitive compounds based on CD93 expression from the CellMiner dataset. In contrast, 2-[(3,4-dicloro) anilino]-3-phenyl-5,7-diamino quinoxaline, janus red, juncusol deriv (compound 1), 1,4-benzenediamine (9ci), n-butyl-n'-phenyl-, and 1-benzyl-3-hexadecyl-2-methylimidazolium chloride were top-five sensitive compounds based on CD93 methylation from the CellMiner dataset (Table S6; P<0.05). These small molecules have been found to play anti-tumor roles in several cancers. For example, CR-1-31B, a synthetic rocaglate and a potent eIF4A inhibitor, significantly reduced the growth and apoptosis of neuroblastoma and gallbladder tumor cells (43, 44). PHA-793887, a novel and potent inhibitor of CDK, showed promising efficacy in the human ovarian A2780, colon HCT-116, and pancreatic BX-PC3 cancer xenograft models (45, 46). VNLG/124 exhibited potent anti-proliferative effects in both hormone-insensitive/drug-resistant breast cancer cell lines and the hormone-insensitive PC-3 prostate cancer cell lines (47). Computational models for drug sensitivity prediction indicated XMD14-99 could act as a kinase inhibitor to exert efficacy in several cancer cell lines (47). Excitingly, our results indicated that CD93 expression is associated with prognosis. These results

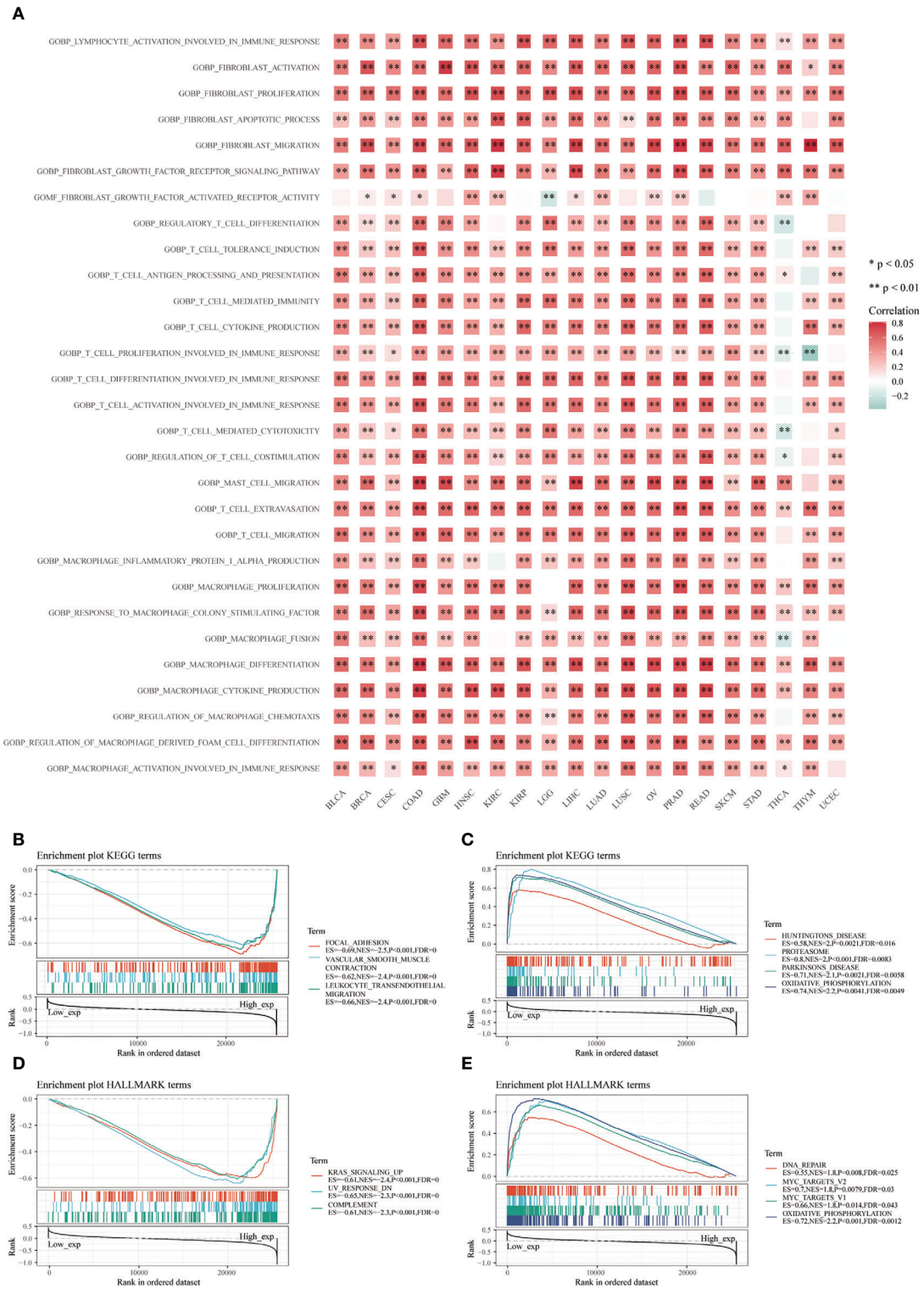


FIGURE 5
Functional analysis based on CD93 expression. Correlation analysis of CD93 from the GSVA algorithm **(A)**. Top three negative **(B)** and top four positive **(C)** enriched pathways using the KEGG database. The top three negative **(D)** and four positive **(E)** enriched pathways using the HALLMARK database.

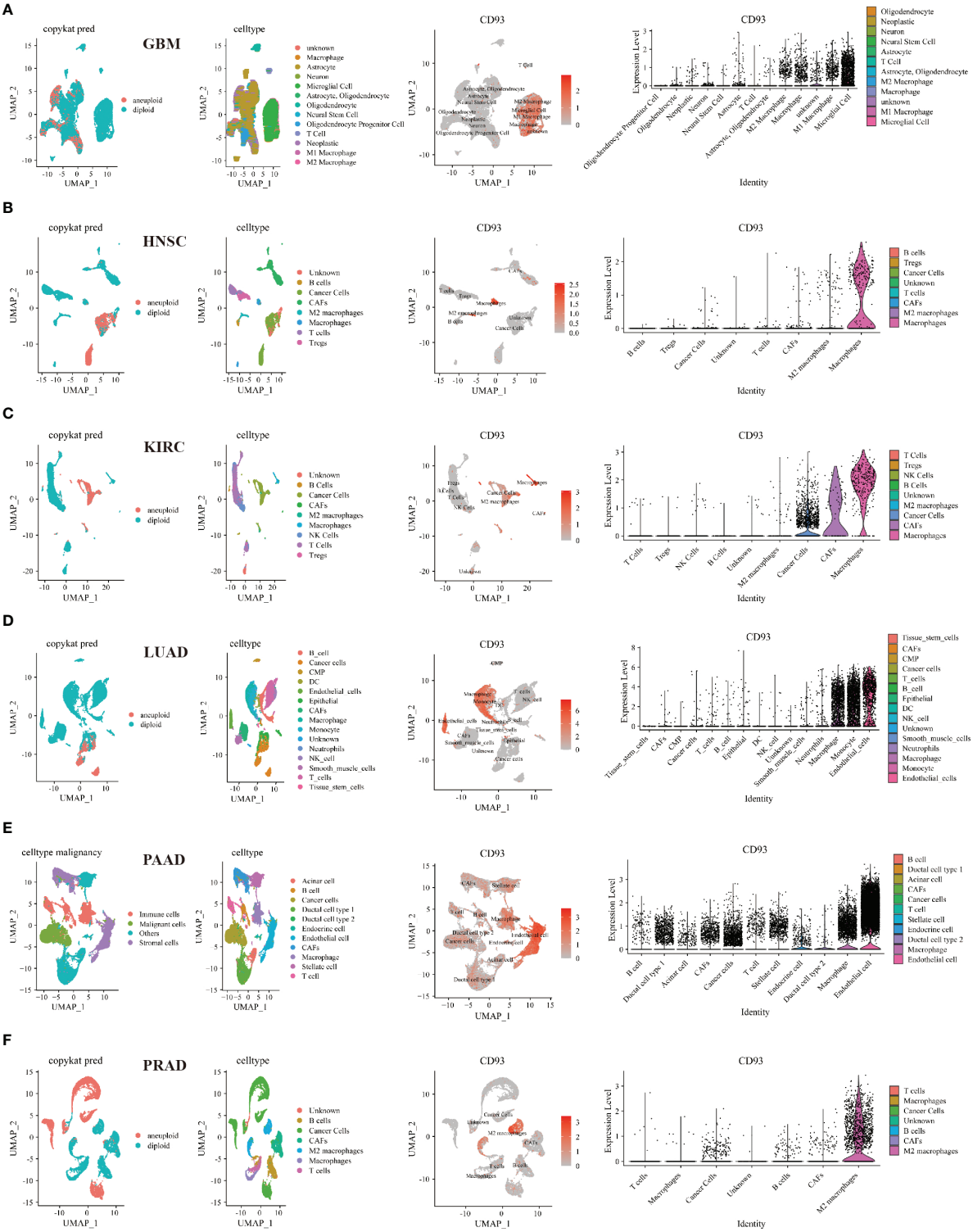


FIGURE 6
Single-cell sequencing analyzing the co-expression of CD93 on tumor and stromal cells in the TME. Co-expression of CD93 on tumor and stromal cells in GBM **(A)**, HNSC **(B)**, KIRC **(C)**, LUAD **(D)**, PAAD **(E)**, and PRAD **(F)**.

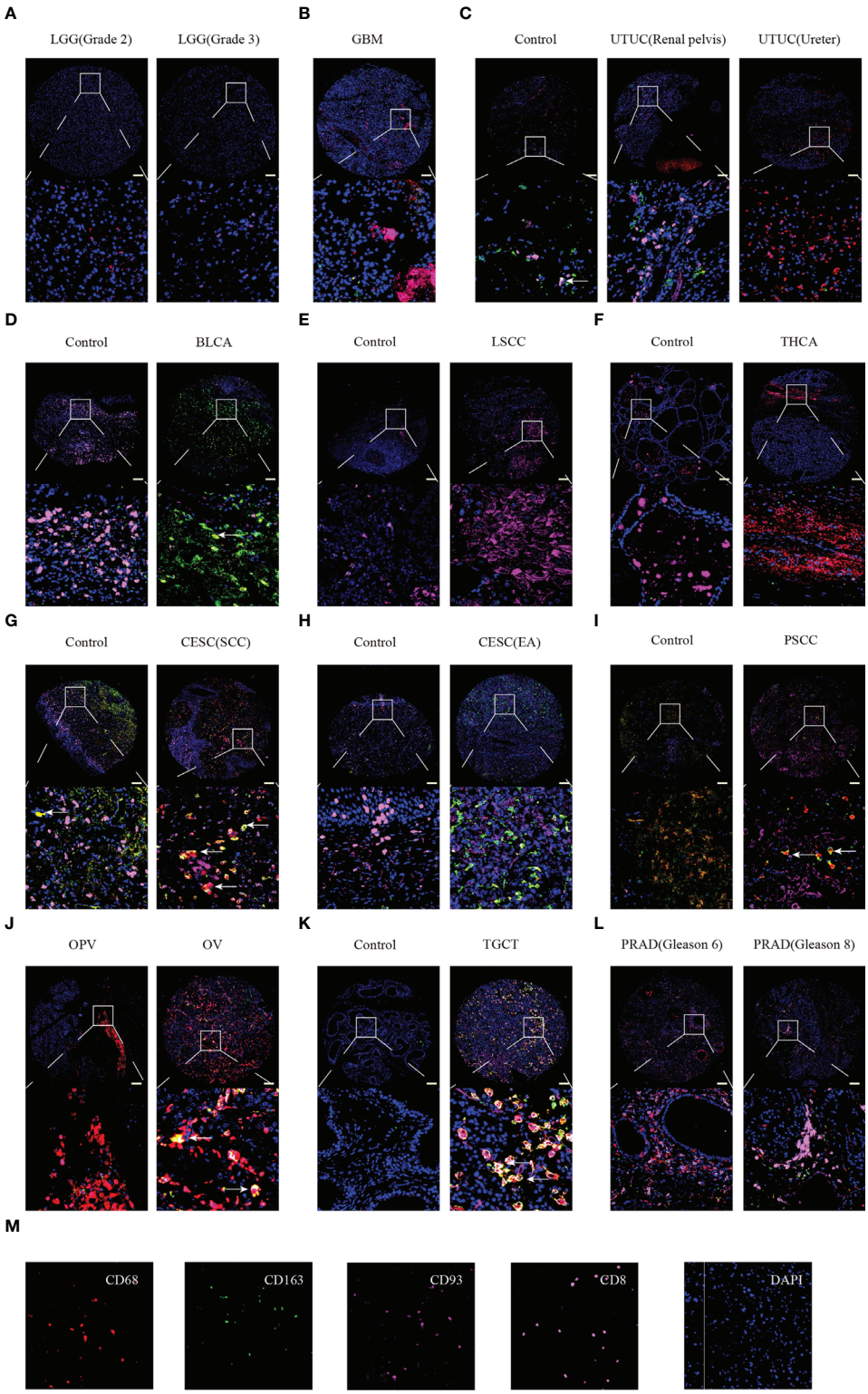


FIGURE 7
Multiplex immunofluorescence staining identified the relationship between CD93 expression and CD8, CD68, and CD163 in tumor and normal samples. LGG **(A)**, GBM **(B)**, UTUC **(C)**, BLCA **(D)**, LSCC **(E)**, THCA **(F)**, CESC **(G, H)**, PSCC **(I)**, OPV and OV **(J)**, TGCT **(K)**, and PRAD **(L)**. Staining for CD8, CD163, CD93, CD9, and DAPI **(M)**. Scale bar=100um.

10.3389/fimmu.2022.907182

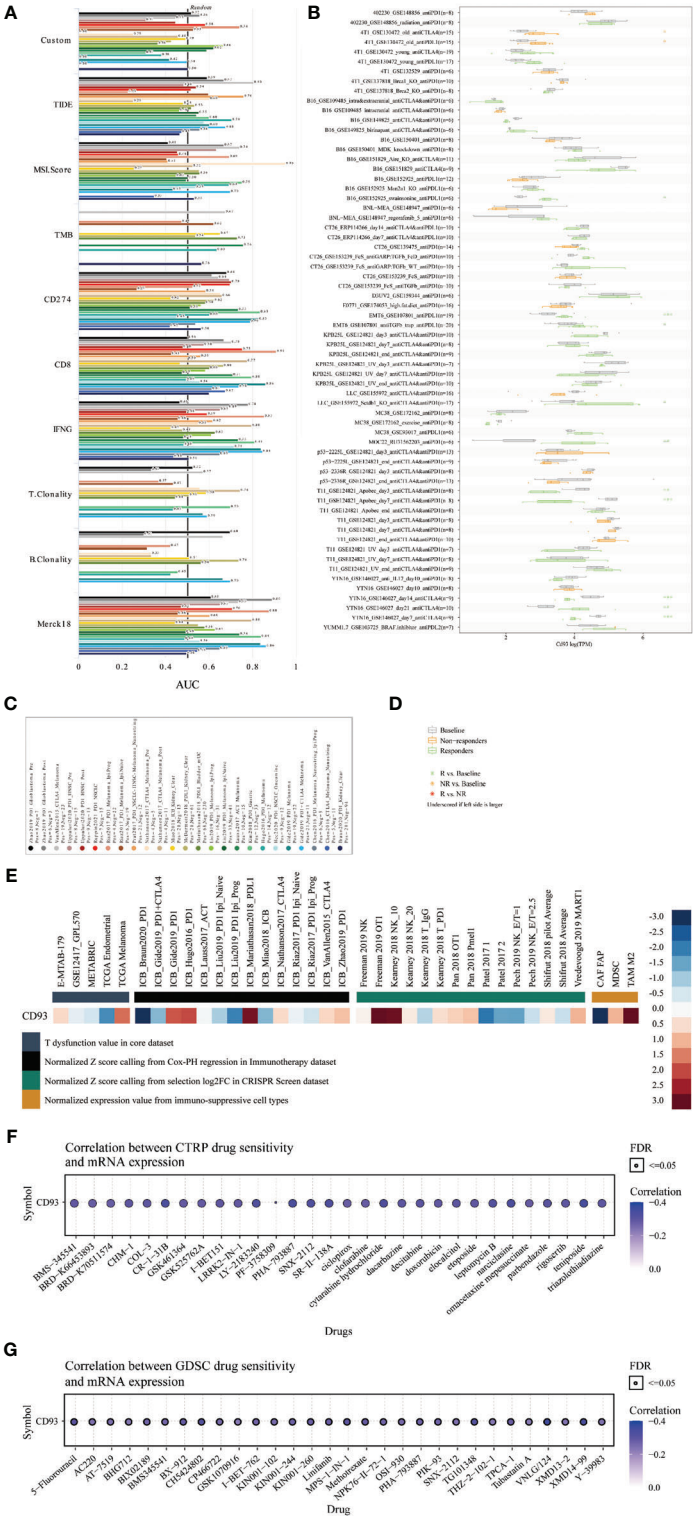


FIGURE 8
Immunotherapy value and sensitive drug prediction of CD93 based on the public datasets. Immunotherapy response **(A)** and biomarker relevance **(B)** of CD93 in immunotherapy cohorts. Notes for the immunotherapy response **(C)** and biomarker relevance **(D)** of CD93.Therapeutic responses of CD93 in mechanistic follow-up experiments in the given datasets **(E)**. Sensitive small compounds predicted from the CTRP **(F)** and GDSC **(G)** websites based on CD93 levels.

provide a theoretical basis for our preclinical and clinical cancer experiments targeting CD93 expression in the TME. However, there are also some limitations in our study. First, due to the relatively small samples of certain cancer types on the tissue microarray, it is difficult for us to quantify and perform statistical analyses. Second, the exact relationship between CD93 and tumor immunity and related signaling pathways in these cancers were not revealed through *in vivo* and *in vitro* study, more validated experiments are needed in the future.

Discussion

The previous study has demonstrated the critical role of CD93 in tumor vascularization and upregulated CD93 in tumor vessels as a potential malignant biomarker in several cancers. Given that the molecular characteristics of CD93 in pan-cancer remain unexplored, we performed large-scale single-cell and bulk sequencing analysis to identify the prognostic value and immune features of CD93 in these cancers. In our paper, we observed the mRNA expression of CD93 in 38 cancer cell lines, 31 cancer samples, and counterparts based on public databases. By combining TCGA and GTEX datasets, CD93 levels were higher in GBM, PAAD, STAD, CHOL, LGG, LIHC, KIRC, LAML, HNSC, TGCT, and SKCM than in normal controls. CD93 levels were lower in COAD, KIRP, ACC, CESC, UCEC, BRCA, BLCA, LUAD, PRAD, KICH, THCA, LUSC, and UCS than in controls. At the same time, the immunofluorescence staining showed that CD93 protein was upregulated in PSCC, LSCC, and TGCT than control samples while downregulated in THCA, UTUC, BLCA, and CESC than control samples. CD93 protein levels appear to be higher in GBM than in LGG. In addition, CD93 can serve as a stable prognostic biomarker in almost all cancers except ACC, BRCA, CHOL, DLBC, PAAD, PRAD, SKCM, and UCS. The survival difference between CD93 mutants and WT, CNV of CD93 and survival, the correlation between CD93 methylation and mRNA levels, and the survival difference between CD93 low and high methylation in pan-cancer were analyzed.

The pathological process of tumor formation, growth, and migration is regulated by genetic mutations in tumor cells and the dynamic interactions of the components in the TME (48, 49). Cancer cells, stromal cells, vascular system and extracellular matrix such as fibronectin, laminin, enzymes, and glycoproteins together form a complex and interconnected tumor microenvironment (50, 51). The tumor stromal cells are composed of CAFs, adipocytes, endothelial cells, pericytes, and immune cells, including M1 and M2 macrophages, T cells, B cells, neutrophils, microglia, monocyte, and NK cells (52, 53). These stromal cells play a crucial role in developing tumor, metastasis, immune infiltration, and chemoresistance by producing growth factors, cytokines, chemokines, pro-tumorigenic and anti-tumorigenic factors (54, 55). For example, CAFs are essential for the TME to remodel the extracellular matrix and mediate leukocyte infiltration (56). Increasing evidence showed that activated CAFs could regulate tumor cell invasion and growth by secreting soluble factors (exosomes, HGF and GAS6) and depleting metabolic factors (lactate, amino acid, alanine, and aspartate) (57). Meanwhile, CAFs induced the infiltration and activation of macrophages, endothelial cells, and T cells by producing VEGF, TGFβ, IL-6, CCL2, and CXCL12. Cancer-associated endothelial cells play an irreplaceable role in tumor cell growth and migration. A study in breast cancer treatment found that cancer-associated endothelial cells contribute to the production of CXCL1/2 and S100A8/9, which eventually led to breast cancer cell survival and drug resistance (58). Macrophages have the function of phagocytosing and digesting foreign antigens, and play a crucial role in clearing away cellular debris and tumor cells (59). Tumor-associated macrophages (M2) lose their ability to kill tumors due to the absence of phagocytosis, which eventually leads to the spread of tumor cells to other tissues and organs (60). The intratumoral T cells, a significant component of the infiltrated immune cells in the TME, comprises $CD4^+$, $CD8^+$, naïve, memory, effector, and regulatory T cells. These different T cell subtypes are essential mediators of anti-tumor immunity, recognizing and responding to tumor-expressed antigens (61).

In current paper, we observed the co-expression of CD93 on tumor and stromal cells based on bulk and large-scale single-cell sequencing and tumor chips. Many stromal cells expressed high CD93 levels in the tumor microenvironment of pan-cancer, such as endothelial cells, B cells, T cells, neutrophils, myeloid dendritic cells, macrophages, monocyte, and hematopoietic stem cell. Notably, CD93 expression significantly correlated with these scores (immune, stromal, and estimate) in almost all cancers. Moreover, large-scale single-cell sequencing analysis demonstrated that macrophages, astrocytes, CAFs, T cells, B cells, endothelial cells, neutrophils, and cancer cells are the primary cells that expressed CD93 in the TME. Furthermore, the relationship between CD8, CD68, and CD163 in these cancers was verified by multiplex immunofluorescence staining. Furthermore, the functional signaling analysis indicated that many tumor immune-related pathways were enriched according to CD93 expression, such as immune cells (fibroblast, macrophages, and T cells) activation and migration, focal adhesion, leukocyte transendothelial migration, oxidative phosphorylation, and complement. These results invariably illustrate the pivotal role of CD93 in tumor immunity.

Immunotherapy, focusing on inhibiting immune checkpoints, has undoubtedly been the highest achievement of cancer treatment in the last decade. The programmed death 1 (PD-1)/programmed cell death-ligand 1 (PD-L1) and cytotoxic T-lymphocyte–associated antigen 4 (CTLA-4)/B7 are two classical immune checkpoint signaling pathways, which negatively mediate T cell immunity during the activation and proliferation of T cells under pathological conditions. Targeting

PD1/PD-L1 and CTLA-4/B7 with specific inhibitors has demonstrated exciting preclinical and clinical efficacy in several cancers. This paper studied the correlation between CD93 and other classical immune checkpoints in pan-cancer. Data showed that the many immune checkpoints positively correlate with CD93 expression in many cancers, particularly NRP1, LAIR1, VSIR, and CD86. Predicting the immunotherapy value and the optimal individualized therapeutic drugs from public databases and computational models has been increasingly attractive in recent years (62–64). Biomarker correlations for CD93 were calculated in more than 20 immunotherapy cohorts to validate its predictive value. Out of a total of 25 immunotherapy cohorts, eight immunotherapy cohorts had AUC values above 0.5. The predictive value of CD93 was higher than the B.Clonality with AUC value above 0.5 in 7 immunotherapy cohorts. CD93 had the same predictive value as the TMB with an AUC value above 0.5 in 8 immunotherapy cohorts. Moreover, the predictive value of CD93 was lower than the T.Clonality, MSI score, IFNG and CD8, TIDE and CD274, with AUC values above 0.5 in 9, 13, 17, 18, 18 and 21 immunotherapy cohorts, respective. GDSC and CTRP are free, publicly available databases of over 500 small molecule compounds based on the therapeutic response of over 1000 genetically characterised human cancer cell lines. Ultimately, we discovered a lot of sensitive small molecules according to CD93 levels from the public datasets, such as CR-1-31B, PHA-793887, SR-II-138A, cytarabine hydrochloride, narciclasine, VNLG/124, XMD14-99, TG101348, CH5424802, and 5-Fluorouracil. These data will provide theoretical support for future clinical trials targeting CD93 in these cancers.

Conclusion

In this project, we comprehensively analyzed the prognostic value and immune profile of CD93 in pan-cancer using large-scale single-cell and bulk sequencing analysis. CD93 is highly involved in tumor immunity and may act as a novel immune checkpoint in immunotherapy of these cancers. Therefore, therapeutic strategies that block CD93 in the tumor microenvironment are expected to benefit patients with malignancies.

Data availability statement

The original contributions presented in the study are included in the article/Supplementary Material. Further inquiries can be directed to the corresponding authors.

Author contributions

Original Draft, Methodology, Validation, Visualization: JWZ and HZ. Data Curation, Validation: AG, WW, YP, PL, and JZ. Investigation: ZL and YT. Conceptualization, Methodology, Supervision, Project Administration, and Funding Acquisition: HZ, and QC. All authors contributed to the article and approved the submitted version.

Funding

This work was supported by the Hunan Provincial Health Committee Foundation of China (NO.202204044869), Hunan Provincial Natural Science Foundation of China (NO.2020JJ5850).

Acknowledgments

The author express gratitude to the public databases, websites, and softwares used in the paper. We are grateful to the High Performance Computing Center of Central South University for partial support of this work.

Conflict of interest

The authors declare that the research was conducted in the absence of any commercial or financial relationships that could be construed as a potential conflict of interest.

Publisher's note

All claims expressed in this article are solely those of the authors and do not necessarily represent those of their affiliated organizations, or those of the publisher, the editors and the reviewers. Any product that may be evaluated in this article, or claim that may be made by its manufacturer, is not guaranteed or endorsed by the publisher.

Supplementary material

The Supplementary Material for this article can be found online at: https://www.frontiersin.org/articles/10.3389/fimmu.2022.907182/full#supplementary-material

References

1. Siegel RL, Miller KD, Fuchs HE, Jemal A. Cancer statistic. *CA Cancer J Clin* (2022) 72(1):7–33. doi: 10.3322/caac.21708

2. Takeshima H, Ushijima T. Accumulation of genetic and epigenetic alterations in normal cells and cancer risk. *NPJ Precis Oncol* (2019) 3:7. doi: 10.1038/s41698-019-0079-0

3. Lu J, Ding J, Liu Z, Chen T. Retrospective analysis of the preparation and application of immunotherapy in cancer treatment (Review). *Int J Oncol* (2022) 60 (2):12. doi: 10.3892/ijo.2022.5302

4. Anand P, Kunnumakkara AB, Sundaram C, Harikumar KB, Tharakan ST, Lai OS, et al. Cancer is a preventable disease that requires major lifestyle changes. *Pharm Res* (2008) 25(9):2097–116. doi: 10.1007/s11095-008-9661-9

5. Loeb LA, Harris CC. Advances in chemical carcinogenesis: a historical review and prospective. *Cancer Res* (2008) 68(17):6863–72. doi: 10.1158/0008-5472.CAN-08-2852

6. Pucci C, Martinelli C, Ciofani G. Innovative approaches for cancer treatment: current perspectives and new challenges. *Ecancermedicalscience* (2019) 13:961. doi: 10.3332/ecancer.2019.961

7. Matthews HK, Bertoli C, de Bruin RAM. Cell cycle control in cancer. *Nat Rev Mol Cell Biol* (2022) 23(1):74–88. doi: 10.1038/s41580-021-00404-3

8. Waldman AD, Fritz JM, Lenardo MJ. A guide to cancer immunotherapy: From T cell basic science to clinical practice. *Nat Rev Immunol* (2020) 20(11):651–68. doi: 10.1038/s41577-020-0306-5

9. Xie YH, Chen YX, Fang JY. Comprehensive review of targeted therapy for colorectal cancer. *Signal Transduct Target Ther* (2020) 5(1):22. doi: 10.1038/s41392-020-0116-z

10. Whiteside TL. The tumor microenvironment and its role in promoting tumor growth. *Oncogene* (2008) 27(45):5904–12. doi: 10.1038/onc.2008.271

11. Giraldo NA, Sanchez-Salas R, Peske JD, Vano Y, Becht E, Petitprez F, et al. The clinical role of the TME in solid cancer. *Br J Cancer* (2019) 120(1):45–53. doi: 10.1038/s41416-018-0327-z

12. Bondhopadhyay B, Sisodiya S, Chikara A, Khan A, Tanwar P, Afroze D, et al. Cancer immunotherapy: a promising dawn in cancer research. *Am J Blood Res* (2020) 10(6):375–85.

13. Taefehshokr N, Baradaran B, Baghbanzadeh A, Taefehshokr S. Promising approaches in cancer immunotherapy. *Immunobiology* (2020) 225(2):151875. doi: 10.1016/j.imbio.2019.11.010

14. Yi R, Lin A, Cao M, Xu A, Luo P, Zhang J. ATM Mutations benefit bladder cancer patients treated with immune checkpoint inhibitors by acting on the tumor immune microenvironment. *Front Genet* (2020) 11:933. doi: 10.3389/fgene.2020.00933

15. Zhang J, Zhou N, Lin A, Luo P, Chen X, Deng H, et al. ZFHX3 mutation as a protective biomarker for immune checkpoint blockade in non-small cell lung cancer. *Cancer Immunol Immunother* (2021) 70(1):137–51. doi: 10.1007/s00262-020-02668-8

16. Zhang H, He J, Dai Z, Wang Z, Liang X, He F, et al. PDIA5 is correlated with immune infiltration and predicts poor prognosis in gliomas. *Front Immunol* (2021) 12:628966. doi: 10.3389/fimmu.2021.628966

17. Lugano R, Vemuri K, Yu D, Bergqvist M, Smits A, Essand M, et al. CD93 promotes beta1 integrin activation and fibronectin fibrillogenesis during tumor angiogenesis. *J Clin Invest* (2018) 128(8):3280–97. doi: 10.1172/JCI97459

18. Maas SLN, Abels ER, Van De Haar LL, Zhang X, Morsett L, Sil S, et al. Glioblastoma hijacks microglial gene expression to support tumor growth. *J Neuroinflamm* (2020) 17(1):120. doi: 10.1186/s12974-020-01797-2

19. Riether C, Radpour R, Kallen NM, Burgin DT, Bachmann C, Schurch CM, et al. Metoclopramide treatment blocks CD93-signaling-mediated self-renewal of chronic myeloid leukemia stem cells. *Cell Rep* (2021) 34(4):108663. doi: 10.1016/j.celrep.2020.108663

20. Khan KA, McMurray JL, Mohammed F, Bicknell R. C-type lectin domain group 14 proteins in vascular biology, cancer and inflammation. *FEBS J* (2019) 286 (17):3299–332. doi: 10.1111/febs.14985

21. Langenkamp E, Zhang L, Lugano R, Huang H, Elhassan TE, Georganaki M, et al. Elevated expression of the c-type lectin CD93 in the glioblastoma vasculature regulates cytoskeletal rearrangements that enhance vessel function and reduce host survival. *Cancer Res* (2015) 75(21):4504–16. doi: 10.1158/0008-5472.CAN-14-3636

22. Fantone S, Tossetta G, Di Simone N, Tersigni C, Scambia G, Marcheggiani F, et al. CD93 a potential player in cytotrophoblast and endothelial cell migration. *Cell Tissue Res* (2022) 387(1):123–30. doi: 10.1007/s00441-021-03543-3

23. Lamalice L, Le Boeuf F, Huot J. Endothelial cell migration during angiogenesis. *Circ Res* (2007) 100(6):782–94. doi: 10.1161/01.RES.0000259593.07661.1e

24. Ma Q, Reiter RJ, Chen Y. Role of melatonin in controlling angiogenesis under physiological and pathological conditions. *Angiogenesis* (2020) 23(2):91–104. doi: 10.1007/s10456-019-09689-7

25. Ikewaki N, Kulski JK, Inoko H. Regulation of CD93 cell surface expression by protein kinase c isoenzymes. *Microbiol Immunol* (2006) 50(2):93–103. doi: 10.1111/j.1348-0421.2006.tb03774.x

26. Tong W, Wang G, Zhu L, Bai Y, Liu Z, Yang L, et al. Pan-cancer analysis identified CD93 as a valuable biomarker for predicting patient prognosis and immunotherapy response. *Front Mol Biosci* (2021) 8:793445. doi: 10.3389/fmolb.2021.793445

27. Zhang Z, Zheng M, Ding Q, Liu M. CD93 correlates with immune infiltration and impacts patient immunotherapy efficacy: A pan-cancer analysis. *Front Cell Dev Biol* (2022) 10:817965. doi: 10.3389/fcell.2022.817965

28. Cancer Genome Atlas Research, Weinstein JN, Collisson EA, Mills GB, Shaw KR, Ozenberger BA, et al. The cancer genome atlas pan-cancer analysis project. *Nat Genet* (2013) 45(10):1113–20. doi: 10.1038/ng.2764

29. Consortium GT. The genotype-tissue expression (GTEx) project. *Nat Genet* (2013) 45(6):580–5. doi: 10.1038/ng.2653

30. Barretina J, Caponigro G, Stransky N, Venkatesan K, Margolin AA, Kim S, et al. The cancer cell line encyclopedia enables predictive modelling of anticancer drug sensitivity. *Nature* (2012) 483(7391):603–7. doi: 10.1038/nature11003

31. Nagy A, Gyorffy B. muTarget: A platform linking gene expression changes and mutation status in solid tumors. *Int J Cancer* (2021) 148(2):502–11. doi: 10.1002/ijc.33283

32. Hanzelmann S, Castelo R, Guinney J. GSVA: Gene set variation analysis for microarray and RNA-seq data. *BMC Bioinf* (2013) 14:7. doi: 10.1186/1471-2105-14-7

33. Kanehisa M, Goto S. KEGG: kyoto encyclopedia of genes and genomes. *Nucleic Acids Res* (2000) 28(1):27–30. doi: 10.1093/nar/28.1.27

34. Kanehisa M, Sato Y, Kawashima M, Furumichi M, Tanabe M. KEGG as a reference resource for gene and protein annotation. *Nucleic Acids Res* (2016) 44 (D1):D457–462. doi: 10.1093/nar/gkv1070

35. Shankavaram UT, Varma S, Kane D, Sunshine M, Chary KK, Reinhold WC, et al. CellMiner: a relational database and query tool for the NCI-60 cancer cell lines. *BMC Genomics* (2009) 10:277. doi: 10.1186/1471-2164-10-277

36. Fekete JT, Gyorffy B. ROCplot.org: Validating predictive biomarkers of chemotherapy/hormonal therapy/anti-HER2 therapy using transcriptomic data of 3,104 breast cancer patients. *Int J Cancer* (2019) 145(11):3140–51. doi: 10.1002/ijc.32369

37. Menyhart O, Fekete JT, Gyorffy B. Gene expression-based biomarkers designating glioblastomas resistant to multiple treatment strategies. *Carcinogenesis* (2021) 42(6):804–13. doi: 10.1093/carcin/bgab024

38. Butler A, Hoffman P, Smibert P, Papalexi E, Satija R. Integrating single-cell transcriptomic data across different conditions, technologies, and species. *Nat Biotechnol* (2018) 36(5):411–20. doi: 10.1038/nbt.4096

39. Sanchez K, Kim I, Chun B, Pucilowska J, Redmond WL, Urba WJ, et al. Multiplex immunofluorescence to measure dynamic changes in tumor-infiltrating lymphocytes and PD-L1 in early-stage breast cancer. *Breast Cancer Res* (2021) 23 (1):2. doi: 10.1186/s13058-020-01378-4

40. Parra ER, Uraoka N, Jiang M, Cook P, Gibbons D, Forget MA, et al. Validation of multiplex immunofluorescence panels using multispectral microscopy for immune-profiling of formalin-fixed and paraffin-embedded human tumor tissues. *Sci Rep* (2017) 7(1):13380. doi: 10.1038/s41598-017-13942-8

41. Peng M, Mo Y, Wang Y, Wu P, Zhang Y, Xiong F, et al. Neoantigen vaccine: an emerging tumor immunotherapy. *Mol Cancer* (2019) 18(1):128. doi: 10.1186/s12943-019-1055-6

42. Zhang Z, Lu M, Qin Y, Gao W, Tao L, Su W, et al. Neoantigen: A new breakthrough in tumor immunotherapy. *Front Immunol* (2021) 12:672356 doi: 10.3389/fimmu.2021.672356

43. Cao Y, He Y, Yang L, Luan Z. Targeting eIF4A using rocaglate CR131B sensitizes gallbladder cancer cells to TRAILmediated apoptosis through the translational downregulation of cFLIP. *Oncol Rep* (2021) 45(1):230–8. doi: 10.3892/or.2020.7856

44. Chan K, Robert F, Oertlin C, Kapeller-Libermann D, Avizonis D, Gutierrez J, et al. eIF4A supports an oncogenic translation program in pancreatic ductal adenocarcinoma. *Nat Commun* (20195151) 10(1):5151. doi: 10.1038/s41467-019-13086-5

45. Brasca MG, Albanese C, Alzani R, Amici R, Avanzi N, Ballinari D, et al. Optimization of 6,6-dimethyl pyrrolo[3,4-c]pyrazoles: Identification of PHA-793887, a potent CDK inhibitor suitable for intravenous dosing. *Bioorg Med Chem* (2010) 18(5):1844–53. doi: 10.1016/j.bmc.2010.01.042

46. Tamura K. Development of cell-cycle checkpoint therapy for solid tumors. *Jpn J Clin Oncol* (2015) 45(12):1097–102. doi: 10.1093/jjco/hyv131

47. Gediya LK, Khandelwal A, Patel J, Belosay A, Sabnis G, Mehta J, et al. Design, synthesis, and evaluation of novel mutual prodrugs (hybrid drugs) of all-trans-retinoic acid and histone deacetylase inhibitors with enhanced anticancer

activities in breast and prostate cancer cells *in vitro*. *J Med Chem* (2008) 51 (13):3895–904. doi: 10.1021/jm8001839

48. Baghban R, Roshangar L, Jahanban-Esfahlan R, Seidi K, Ebrahimi-Kalan A, Jaymand M, et al. Tumor microenvironment complexity and therapeutic implications at a glance. *Cell Commun Signal* (2020) 18(1):59. doi: 10.1186/s12964-020-0530-4

49. Wu T, Dai Y. Tumor microenvironment and therapeutic response. *Cancer Lett* (2017) 387:61–8. doi: 10.1016/j.canlet.2016.01.043

50. Jahanban-Esfahlan R, Seidi K, Banimohamad-Shotorbani B, Jahanban-Esfahlan A, Yousefi B. Combination of nanotechnology with vascular targeting agents for effective cancer therapy. *J Cell Physiol* (2018) 233(4):2982–92. doi: 10.1002/jcp.26051

51. Anderson NM, Simon MC. The tumor microenvironment. *Curr Biol* (2020) 30(16):R921–5. doi: 10.1016/j.cub.2020.06.081

52. Cheng HS, Lee JXT, Wahli W, Tan NS. Exploiting vulnerabilities of cancer by targeting nuclear receptors of stromal cells in tumor microenvironment. *Mol Cancer* (2019) 18(1):51. doi: 10.1186/s12943-019-0971-9

53. Spees JL, Lee RH, Gregory CA. Mechanisms of mesenchymal stem/stromal cell function. *Stem Cell Res Ther* (2016) 7(1):125. doi: 10.1186/s13287-016-0363-7

54. Plava J, Cihova M, Burikova M, Matuskova M, Kucerova L, Miklikova S. Recent advances in understanding tumor stroma-mediated chemoresistance in breast cancer. *Mol Cancer* (2019) 18(1):67. doi: 10.1186/s12943-019-0960-z

55. Arango Duque G, Descoteaux A. Macrophage cytokines: Involvement in immunity and infectious diseases. *Front Immunol* (2014) 5:491. doi: 10.3389/fimmu.2014.00491

56. Xing F, Saidou J, Watabe K. Cancer associated fibroblasts (CAFs) in tumor microenvironment. *Front Biosci (Landmark Ed)* (2010) 15(1):166–79. doi: 10.2741/3613

57. Sahai E, Astsaturov I, Cukierman E, DeNardo DG, Egeblad M, Evans RM, et al. A framework for advancing our understanding of cancer-associated fibroblasts. *Nat Rev Cancer* (2020) 20(3):174–86. doi: 10.1038/s41568-019-0238-1

58. Acharyya S, Oskarsson T, Vanharanta S, Malladi S, Kim J, Morris PG, et al. A CXCL1 paracrine network links cancer chemoresistance and metastasis. *Cell* (2012) 150(1):165–78. doi: 10.1016/j.cell.2012.04.042

59. Zhou J, Tang Z, Gao S, Li C, Feng Y, Zhou X. Tumor-associated macrophages: Recent insights and therapies. *Front Oncol* (2020) 10:188. doi: 10.3389/fonc.2020.00188

60. Pan Y, Yu Y, Wang X, Zhang T. Tumor-associated macrophages in tumor immunity. *Front Immunol* (2020) 11:583084. doi: 10.3389/fimmu.2020.583084

61. Zhang Z, Liu S, Zhang B, Qiao L, Zhang Y, Zhang Y, et al. And exhaustion in cancer. *Front Cell Dev Biol* (2020) 8:17. doi: 10.3389/fcell.2020.00017

62. Fu J, Li K, Zhang W, Wan C, Zhang J, Jiang P, et al. Large-Scale public data reuse to model immunotherapy response and resistance. *Genome Med* (2020) 12 (1):21. doi: 10.1186/s13073-020-0721-z

63. Ekins S, Bradford J, Dole K, Spektor A, Gregory K, Blondeau D, et al. A collaborative database and computational models for tuberculosis drug discovery. *Mol Biosyst* (2010) 6(5):840–51. doi: 10.1039/b917766c

64. Masoudi-Sobhanzadeh Y, Omidi Y, Amanlou M, Masoudi-Nejad A. Drug databases and their contributions to drug repurposing. *Genomics* (2020) 112 (2):1087–95. doi: 10.1016/j.ygeno.2019.06.021

frontiers | Frontiers in Immunology

TYPE Original Research
PUBLISHED 06 February 2023
DOI 10.3389/fimmu.2023.911368

Check for updates

OPEN ACCESS

EDITED BY
Giulia Accardi,
University of Palermo, Italy

REVIEWED BY
Zheng Liu,
Virginia Commonwealth University, United States
Enrico Capobianco,
Jackson Laboratory, United States

*CORRESPONDENCE
Bin Liu
l_bin@mails.jlu.edu.cn

†These authors have contributed equally to this work and share first authorship

SPECIALTY SECTION
This article was submitted to Cancer Immunity and Immunotherapy, a section of the journal Frontiers in Immunology

RECEIVED 02 April 2022
ACCEPTED 23 January 2023
PUBLISHED 06 February 2023

CITATION
Tu J, Wang D, Zheng X and Liu B (2023) Single-cell RNA datasets and bulk RNA datasets analysis demonstrated *C1Q*+ tumor-associated macrophage as a major and antitumor immune cell population in osteosarcoma.
Front. Immunol. 14:911368.
doi: 10.3389/fimmu.2023.911368

COPYRIGHT
© 2023 Tu, Wang, Zheng and Liu. This is an open-access article distributed under the terms of the Creative Commons Attribution License (CC BY). The use, distribution or reproduction in other forums is permitted, provided the original author(s) and the copyright owner(s) are credited and that the original publication in this journal is cited, in accordance with accepted academic practice. No use, distribution or reproduction is permitted which does not comply with these terms.

Single-cell RNA datasets and bulk RNA datasets analysis demonstrated *C1Q*+ tumor-associated macrophage as a major and antitumor immune cell population in osteosarcoma

Jihao Tu†, Duo Wang†, XiaoTian Zheng and Bin Liu*

Department of Hand and Foot Surgery, The First Hospital of Jilin University, Changchun, Jilin, China

Background: Osteosarcoma is the most frequent primary bone tumor with a poor prognosis. Immune infiltration proved to have a strong impact on prognosis. We analyzed single-cell datasets and bulk datasets to confirm the main immune cell populations and their properties in osteosarcoma.

Methods: The examples in bulk datasets GSE21257 and GSE32981 from the Gene Expression Omnibus database were divided into two immune infiltration level groups, and 34 differentially expressed genes were spotted. Then, we located these genes among nine major cell clusters and their subclusters identified from 99,668 individual cells in single-cell dataset GSE152048 including 11 osteosarcoma patients. Especially, the markers of all kinds of myeloid cells identified in single-cell dataset GSE152048 were set to gene ontology enrichment. We clustered the osteosarcoma samples in the TARGET-OS from the Therapeutically Applicable Research to Generate Effective Treatments dataset into two groups by complete component 1q positive macrophage markers and compared their survival.

Results: Compared with the low-immune infiltrated group, the high-immune infiltrated group showed a better prognosis. Almost all the 34 differentially expressed genes expressed higher or exclusively among myeloid cells. A group of complete component 1q-positive macrophages was identified from the myeloid cells. In the bulk dataset TARGET-OS, these markers and the infiltration of complete component 1q-positive macrophages related to longer survival.

Conclusions: Complete component 1q-positive tumor-associated macrophages were the major immune cell population in osteosarcoma, which contributed to a better prognosis.

KEYWORDS

tumor-associated macrophages, osteosarcoma, immune infiltration, biomarker, single-cell sequencing technology

1 Introduction

Osteosarcoma (OS) represents the most frequent and primary bone sarcoma, which primarily affects children, adolescents, and young adults (1). The standard therapy for OS, comprising surgery and chemotherapy, was established in the 1980s and resulted in long-term survival in >60% of patients presenting with localized disease (2); however, limited therapeutic progress has been made since that time.

Infiltrating immune and stromal cells are essential for OS progression (1). The immune infiltration level was considered an important factor in response to immunotherapy and prognosis. Analyses of the tumor microenvironment (TME) of OS consistently demonstrate an immune cell infiltration consisting of both macrophages and T cells (1, 3, 4). Primary OS is demonstrated as "immune deserts," devoid of T cells and NK cells (5, 6). Instead, myeloid cells were observed in large quantities (7). In the OS microenvironment, tumor-associated macrophages (TAMs) play a critical role in immunoreaction (8). However, among contradictory conclusions, it is still not clear if these myeloid cells or the TAMs contribute to tumor growth or tumor limitation.

In the analysis of the public dataset GSE150248, we found that TAMs were an essential population in the TME of OS. Generally, macrophages are considered as a plastic cell type because they can be polarized into different phenotypes. M1-type macrophages (M1) and M2-type macrophages (M2) are two major kinds of them. M1 can be induced by pathogen-associated patterns such as lipopolysaccharides and interferon-γ. M1 highly expresses interleukin 6 (*IL-6*), *IL-1β*, and tumor necrosis factor, which facilitate a proinflammatory response. M2 can be induced by *IL-4* and *IL-13*, which turn on the expression of anti-inflammatory cytokines, such as *IL-10* and *ARG1*. These are considered immune suppression and pro-tumor signals (9). Reprograming M2-like TAMs to M1-like TAMs exerts a synergistic effect in radiotherapy and overcoming chemoresistance in breast cancer (10–12). Macrophages can also be divided by where they were produced. TAMs are proved to be of dichotomous origin, from *in situ* proliferation marked by *FOLR2* and the differentiation of circulating monocytes marked by *TREM2* (13–15). It is reported that the M1 or M2 paradigm is an oversimplification, Tissue-resident macrophages are far more complex cells with a full range of identities and activation states (16). In human breast cancer, tissue-resident *FOLR2*+ macrophages instead of M1 or M2 are proved to associate with *CD8*+ T-cell infiltration and better prognosis (17).

Complete component 1q (*C1Q*), one of the three first components of the classical pathway, modulates both inflammation and repair progress (18). *C1Q* is a marker of a particular subpopulation of tissue-resident macrophages and TAMs, which often expresses *CD206*, *HLA-DR*, *SEPP1*, *FOLR2*, and *APOE* (19). In cancer, *C1Q* is usually regarded as a cancer-promoting factor (15, 20). In the classical pathway, *C1Q* generates the C5a production, which was proved as an immunosuppression and angiogenesis factor in cancer progression (21–23). *C1Q* can function as a pattern recognition receptor to apoptotic cells and extracellular vesicles before a non-inflammatory clearance by macrophages. In this case, macrophages produce M2 markers such as *IL-10* and *TGFβ* (24).

Here, we explored the immune-related genes of OS. Especially, we mapped these genes among all the cell populations through a combination of bulk-sequencing and single-cell sequencing technology. We found that *C1Q*+ TAMs are the main immune cells in the OS TME. In detail, *C1Q* is an obvious immune-related gene expressed exclusively by myeloid cells. Moreover, this research found that *C1Q*, different from its pro-tumor characteristic in other cancers (15), seems to be an antitumor factor in OS. *C1Q*+ TAMs promote *CD8*+ T-cell dysfunction and tumor growth in the Lewis lung carcinoma mouse model (25). However, we noticed that *C1Q*+ TAMs act as an antitumor cell population in OS.

2 Materials and methods

2.1 Datasets for analysis and derivation of the gene list

Clinical and transcriptome data of OS patients were downloaded from the Therapeutically Applicable Research to Generate Effective Treatments (TARGET) database (https://ocg.cancer.gov/programs/target) and the Gene Expression Omnibus (GEO) database (https://www.ncbi.nlm.nih.gov/geo/). Dataset TARGET-OS contains 88 samples with both complete survival information and expression profiles. Dataset GSE21257 contains 53 OS samples with survival information and expression profiles. Dataset GSE32981 contains 23 samples with only expression profiles. Specific clinical information of 88 samples in the TARGET database and 53 samples in the GSE21257 dataset is separately listed in Supplementary Tables S7, S8. Dataset GSE152048, a single-cell dataset, contains tumor samples from 11 OS patients (five men and six women, 11–38 years old). There are eight osteoblastic OS lesions, including six primary, one recurrent, and one lung metastatic lesions, and three chondroblastic OS lesions including one primary, one recurrent, and one lung metastasis site. The workflow of this research is provided in Figure 1.

2.2 Samples clustered into high- and low-immune infiltrated groups and their immune cell scores evaluated

The samples in datasets GSE21257 and GSE32981 were clustered into high- and low-immune infiltrated groups by R. We used identified immune metagenes (26) and function hclust(x, method = "complete") and cutree(x, k = 2) to divide the samples into two groups. Then, the overall survival was compared between two groups by the R package survival (https://CRAN.R-project.org/package=survival) and survminer (https://CRAN.R-project.org/package=survminer). The grouping of samples in dataset TARGET-OS was almost the same, except that the immune metagenes were replaced by *C1Q*+ TAM markers with a fold change larger than 0.25. Based on the normalized expression matrix, immune scores across OS specimens from the GSE21257 dataset were estimated using single-sample gene set enrichment analysis (ssGSEA). This algorithm infers the overall infiltration levels of immune cells in tumor tissues using gene expression signatures. The Kaplan–Meier overall survival curves

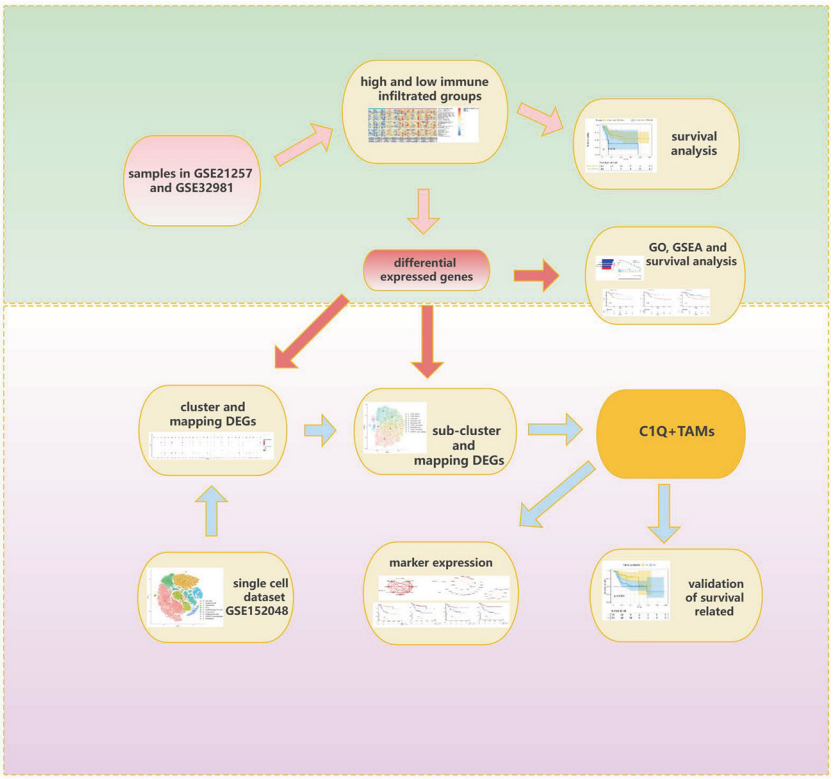


FIGURE 1
Workflow of this research.

were examined between groups, and the prognosis was compared by log-rank test.

2.3 Differential expression analysis, functional enrichment analysis, and gene set enrichment analysis

The limma, edgeR, and DESeq2 packages were applied for differential expression analysis (27–29). |Fold change (FC)| > 1.5 and adjusted $p < 0.05$ were set as the criteria of differentially expressed gene (DEG) identification. The enrichment analysis of DEGs was carried out *via* the clusterProfiler package, including Gene Ontology (GO) (30). Terms with adjusted $p < 0.05$ were significantly enriched. Gene set enrichment analysis (GSEA) evaluates microarray data at the level of gene sets. The DEGs identified from GSE21257 were used as the gene sets (30).

2.4 Single-cell data processing

Single-cell dataset GSE152048 was processed with the Seurat package (version 4.1.0; http://satijalab.org/seurat/). Each of the 11 samples generated a Seurat object by function Read10×. Next, we filtered out the cells with less than 300 expressed genes or with mitochondrial gene expression accounting for more than 10% of total expressed genes. The top 3,000 highly variable genes were picked up for the principal component analysis. Further, the doublets in each Seurat object were cleared out by the DoubletFinder package (version 2.0.3) (31). We integrated the 11 Seurat objects into one combined Seurat object by base function merge(). The batch effects were removed by the Harmony package (version 1.0). Functions FindNeighbors(x, reduction = "harmony"), FindClusters(x, resolution = 0.1), and FindAllMarkers(x) were applied to the cell clustering and cluster annotation. Fold change (FC) > 0.25 and adjusted $p < 0.05$ were set as the criteria of DEGs or markers between cell groups. 2D maps of the identified clusters were generated with the distributed Stochastic Neighbor Embedding or Uniform Manifold Approximation and Projection method. A similar procedure was applied during the subclustering analysis.

2.5 Cell–cell communication analysis with CellPhoneDB 2

CellPhoneDB 2 is a repository of ligand–receptor complexes and a statistical tool to predict the cell-type specificity of cell–cell communication *via* molecular interactions (32). The repository includes subunit architecture for both ligands and receptors, to accurately represent heteromeric complexes. We used CellPhoneDB 2 to calculate the interaction pairs between *C1Q*+ TAMs and the rest of the 13 clusters that gained after clustering and subclustering. Interaction pairs with a p-value less than 0.05 returned by CellPhoneDB 2 were picked up to draw an interaction bubble plot.

CellPhoneDB 2 was used in the python 3.7 environment; the rest of the analysis was presented using R version 4.1.2 (http://www.R-project.org) and its appropriate packages.

3 Results

3.1 High-immune infiltrated group showed a better prognosis in osteosarcoma

After clustering, 40 and 13 samples of dataset GSE21257 were divided into high- and low-immune infiltrated groups, respectively (Figure 2A). Then, we calculated the immune infiltration scores of these two groups by ssGSEA. The high-immune infiltrated group indeed showed a higher immune cell score, but it is kind of strange that all kinds of immune cell scores were lower in the low-immune infiltrated group (Figure 2B); especially, the low-immune infiltrated group indeed showed some highly expressed genes. Maybe it was one kind of immune cell that caused the highly expressed genes in both two groups. The high-immune infiltrated group had a better prognosis (Figure 2C). We performed a similar analysis progress, dividing samples and then calculating the immune scores using ssGSEA, on GSE32981 (Figure S1). There were 20 and 3 samples in GSE32981 that were divided into high- and low- immune infiltrated groups (Figure S1A). The high-immune infiltration group also showed a higher immune score (Figure S1B). A step further, DEGs between high-and low-immune infiltrated groups were respectively collected in datasets GSE21257 and GSE32981. The high-immune infiltrated group of GSE21257 got 146 higher expressed genes and 261 lower expressed genes. As for GSE32981, it got 110 higher expressed genes and 14 lower expressed genes. In a total of 240 higher expressed genes, 34 overlapped genes were picked up. We found no intersections between 275 lower expressed genes. Moreover, just like the survival plot depending on immune-related grouping, almost all of these 34 genes were bound up with better overall survival (Figures 2F, S2). GO biological process enrichment showed that those 34 gene genes were involved in the process of leukocyte and T-cell proliferation (Figure 2D). Further GSEA of DEG analyses showed the hallmarks of complement signaling, cytokine–cytokine receptor interaction, osteoclast differentiation, phagocytosis, and viral protein interaction with cytokine and cytokine receptor were highly enriched (Figure 2E).

3.2 Macrophages are the main immune cell population in osteosarcoma

To explore the source of higher expressed genes, we analyzed the cell population of OS with the single-cell sequencing dataset GSE152048. After initial quality control assessment and doublet removal, we obtained single-cell transcriptomes from a total of

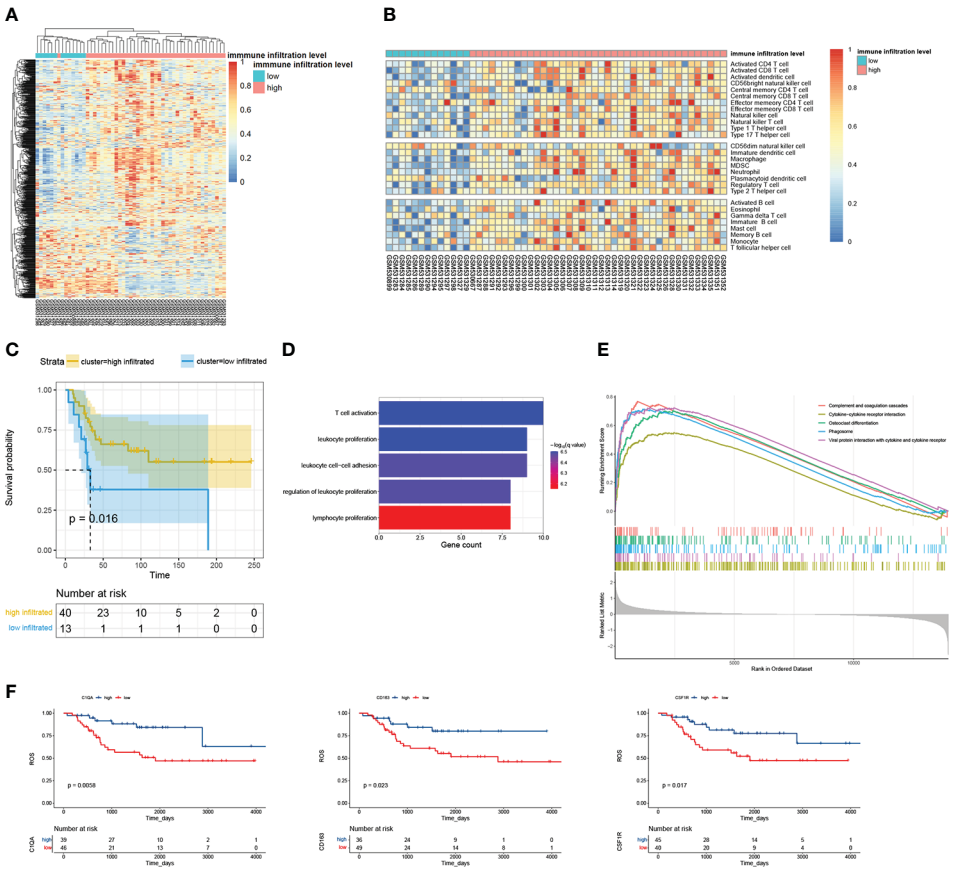


FIGURE 2
The overview of analyzing GSE21257. **(A)** There were 53 examples clustered into two groups by immune metagenes. **(B)** The score of 28 kinds of immune cells calculated by ssGSEA. The 53 examples were ordered by their immune groups instead of getting clustered. **(C)** The survival plot of high- and low- immune infiltrated groups. **(D)** Biological process enrichment of the 34 overlapped DEGs. **(E)** GSEA of the 34 overlapped genes; the top 5 terms were selected. All p-values are 1e-10, and all p.adjust are 1.447826e-09. **(F)** The survival plot of overlapped genes.

99,668 cells. These cells were clustered into nine groups. They are as follows: (0) 37,939 OS cells highly express *SPP1*, *COL2A1*, *SOX9*, and *ACAN*; (1) 21,067 myeloid cells highly express *CD74*, *CD14*, and *FCGR3A*; (2) 13,667 fibroblasts highly express *COL1A1* and *LUM*; (3) 8,089 TILs including T and NK cells highly express *IL7R*, *CD3D*, and *NKG7*; (4) 7,699 proliferating OS cells highly express *TOP2A*, *PCNA*, and *MKI67*; (5) 7,307 osteoclasts highly express *MMP9* and *CTSK*; (6) 3,646 endothelial cells highly express *vWF*, (7) 129 *FABP4+* macrophages highly express *FCGR3A* and *FABP4*; and (8) 125 myoblasts highly express MYPL (Figures 3A–D). The violin plots show the expression level of one representative marker gene of each cell group, sequentially, except *C1QA*. It is more convenient to compare the expression of markers by dot plot (Figures 3B, C). *COL1A1*, a marker of fibroblasts and OS cells, is mainly expressed in fibroblasts and also in OS cells. In addition, *ACAN* is mainly expressed in OS cells but also in fibroblasts. First, seven clusters are distributed evenly among 11 patients (Figure 3D). The *FABP4+* macrophage group and myoblast group, with very little cell number, consist mainly of cells in sample BC17. It is worth noting that the *FABP4+* macrophages have an unusually high number of detected genes. We also calculated the DEGs in each cell group and the GO terms these genes enriched (Table S1). The markers in myeloid cells were enriched in immune response, myeloid cell activation, and myeloid cell differentiation (Table S2). We tried to match the 34 higher expressed DEGs to the certain cell groups identified here. The dot plot showed that these genes were largely expressed by myeloid cells and *FABP4+* macrophages (Figure 3E).

3.3 *C1QA* and other overlapped DEGs were mainly expressed by *C1Q+* TAMs

As DEGs were expressed by myeloid cells and *FABP4+* macrophages, we took the myeloid cell group to a subcluster analysis similar to the previous step. Myeloid cells were divided into nine clusters when the resolution was set as 0.5. We identified

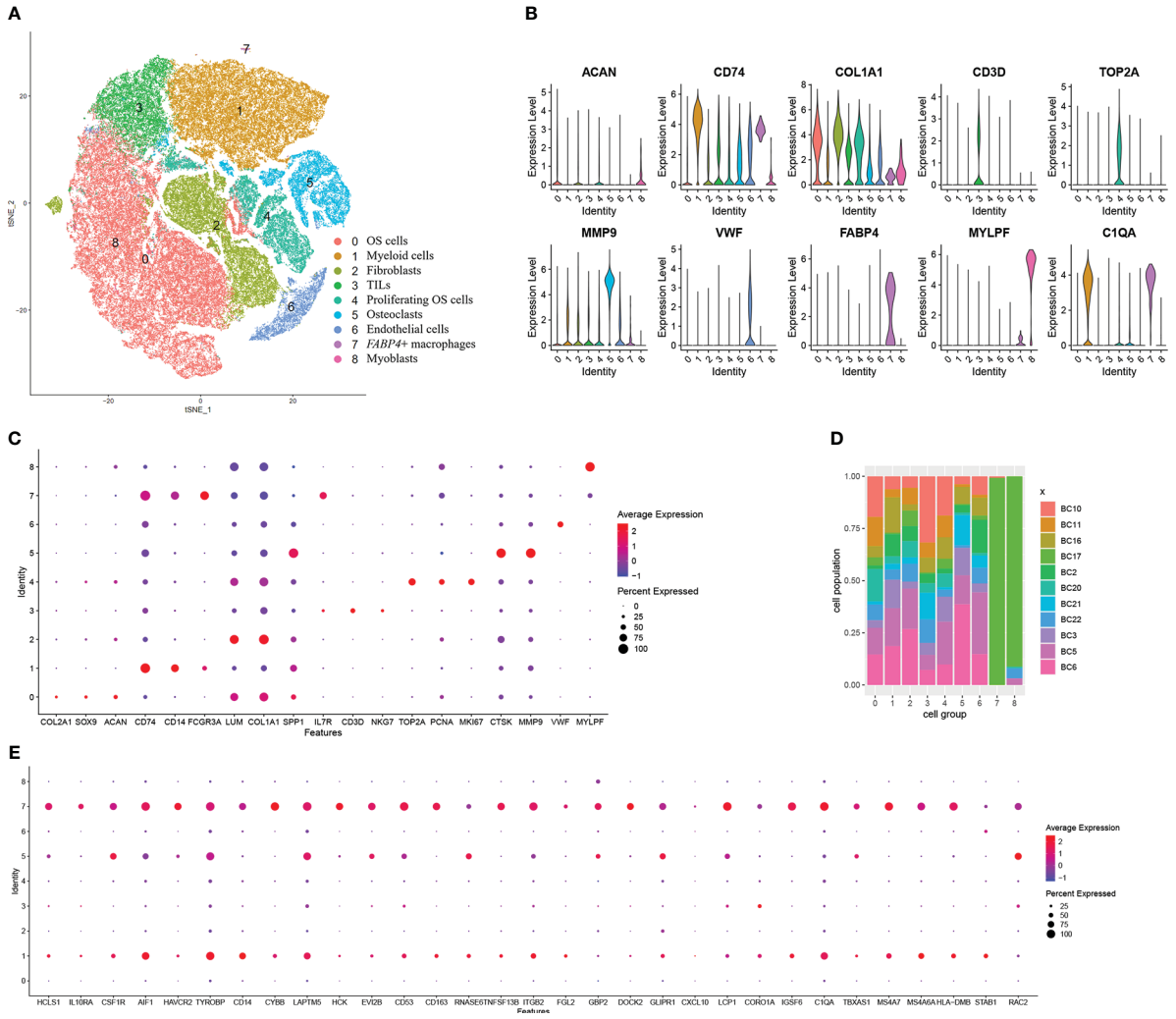


FIGURE 3
Single-cell transcriptomic analysis reveals the transcriptome of cells in the microenvironment of OS. **(A)** The t-distributed stochastic neighbor embedding (t-SNE) plot of the nine identified main cell types in OS lesions. **(B)** Violin plots showed the normalized expression levels of eight representative canonical markers across the nine clusters. **(C)** Representative marker expression in nine clusters of cells. Dot size indicates the proportion of cells expressing markers. Dot color shows the average expression level of the markers. **(D)** Distribution of the nine clusters among 11 patients with OS. **(E)** Dot plot of the 34 overlapped DEGs showing their expressing proportion and level among nine clusters.

six cell groups from the nine clusters (Figures 4A–D). They are (1) 9,601 C1Q+ TAMs with high *C1Q* expression in clusters 0 and 1; (2) 3,516 monocytes with low *C1Q* expression and high *G0S2* and *S100A9* expression in cluster 2; (3) 1,072 *C1Q*+ osteoclasts with high *C1Q*, *MMP9*, and *CTSK* expression in cluster 5; (4) 609 *C1Q*+ fibroblasts with high *C1Q*, *COL1A1*, and *LUM* expression in cluster 7; (5) 79 *FABP4*+ macrophages with high FABP4 expression in cluster 8; and (6) 7,418 unknown cells in clusters 3, 4, and 6 (Figures 4A–D). The violin plot shows that *CD14*, *CD74*, and *C1Q* are expressed in all groups (Figure 4B). *C1Q* expresses the highest in *C1Q*+ TAMs and lower in monocytes and *C1Q*+ osteoclasts (Figure 4C, Table S3). Osteoclasts and fibroblasts identified previously barely express *C1Q* (Figure 3B). Then, we call these two groups of cells *C1Q*+ fibroblasts and *C1Q*+ osteoclasts since they express both *C1Q* and individual markers. They can also be special kinds of macrophages. The unknown cells have inconspicuous markers with a low fold change and uncertain gene ontology biological process (Tables S3, 4). The *FABP4*+ macrophages came from all 11 patients, a very small amount of which came from BC17 (Figure 4D). Figure 3D shows that the *FABP4*+ macrophage group mainly came from BC17. We consider that the two *FABP4*+ macrophage groups identified in twice clustering are the same. We compared marker genes of these cell groups and 34 DEGs obtained previously. There are 15 DEGs including *C1QA* found to be *C1Q*+ TAM markers Figure 4E, Table S3, 6 DEGs found to be monocyte markers. The GO enrichment of *C1Q*+ macrophage markers showed antigen processing and presentation and neutrophil activation (Figure 4F). We also set other cell groups to the GO analysis (Table S4).

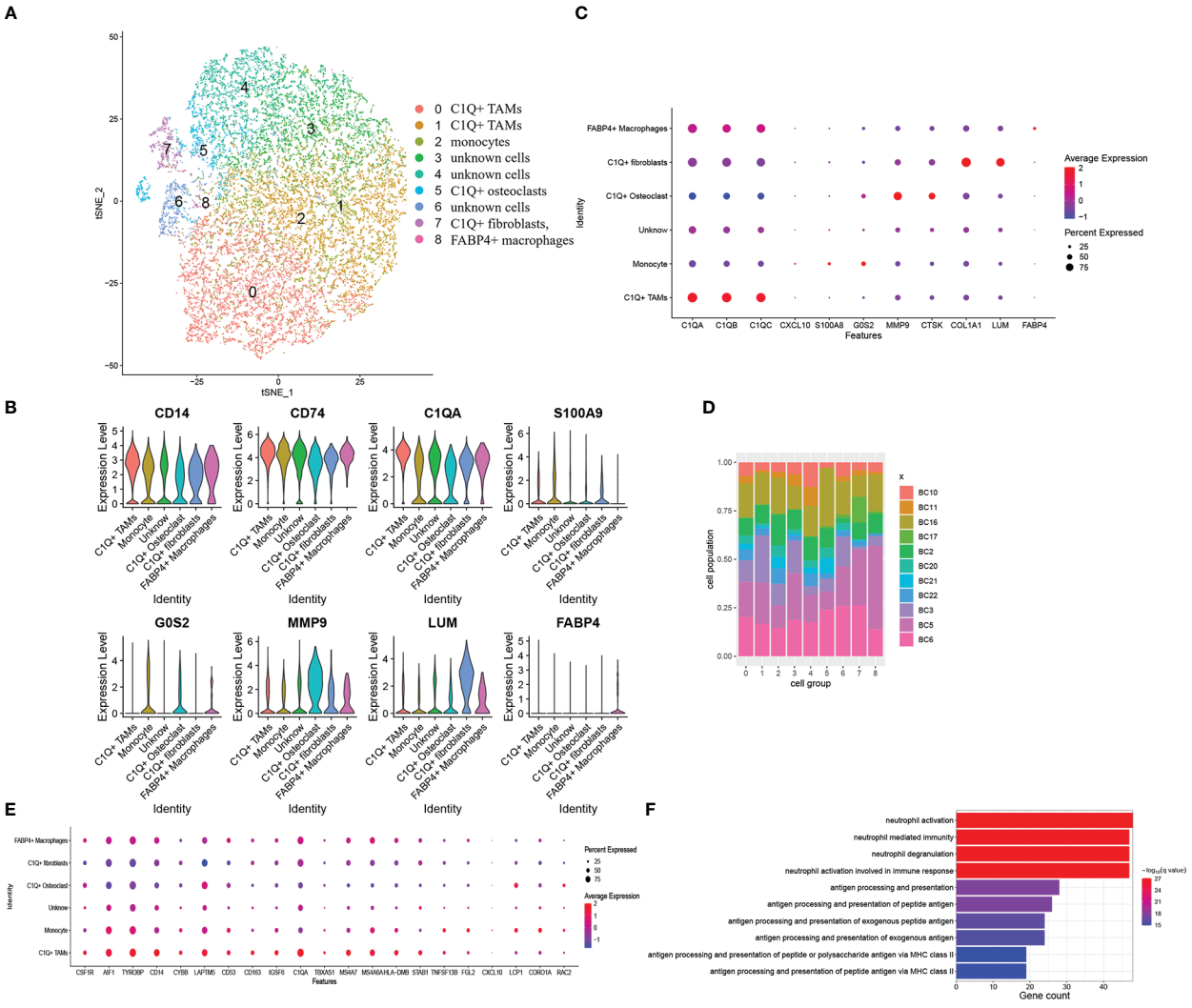


FIGURE 4
Myeloid cells subclustered and DEGs combined with these six cell groups. **(A)** The t-SNE plot of the nine identified clusters or six cell groups. **(B)** Violin plots showed the normalized expression levels of representative markers across the six cell groups **(C)** Representative markers expression in six cell groups. Dot size and color delivered the same meaning as the previous dot plot **(D)** Distribution of the nine clusters among 11 patients with OS. **(E)** Dot plot of the overlapped DEGs, which represented as C1Q+ TAM markers. The plot showed expressing proportion and level among six cell groups of these DEGs. **(F)** Biological process enrichment of *C1Q*+ TAM markers.

10.3389/fimmu.2023.911368

3.4 *C1Q*+ TAM markers were better prognosis related and highly co-expressed

C1Q+ TAMs have 219 markers, we found that 5 of 10 top markers with the highest fold change were related to a better prognosis. They are *C1QA*, *C1QB*, *FOLR2*, *LGMN*, and *APOE* (Figure 5A). Similarly, we divided examples of dataset TARGET-OS into two groups by the result of the hierarchical cluster using the highly expressed markers of *C1Q*+ TAMs (Figure 5B). Moreover, the group with high *C1Q*+ macrophage marker expression showed a better overall survival (Figure 5C), which indicated that *C1Q*+ TAM infiltration plays an antitumor role. We calculated the co-expression coefficients between the 219 markers. We select *C1QA*, *C1QB*, and *C1QC* as a benchmark. The correlation coefficients among the three were 0.97, 0.97, and 0.98 in dataset TARGET-OS. In *C1Q*+ TAMs, it was 0.44. However, when we separated these *C1Q*+ TAMs by patients, the correlation coefficients of *C1Q*+ TAM markers from each patient evenly vary between 0.5 and 0.8 except BC2, BC3, and BC5 (Table S5). The difference could come from the heterogeneity of different patients' TAMs and also the gene co-expressed between *C1Q*+ TAMs and other cells since other myeloid cells also express *C1QA/B/C*. We calculated the coefficients of the TAM markers for each patient, picked up the obvious co-expression genes, and drew the mean coefficients by Cytoscape (Figure 5D, Table S6). *CD74*, *HLA-D*, complement1, and apolipoprotein took the dominant role. Furthermore, we explored the cell–cell interactions and the ligand–receptor pairs between *C1Q*+ TAMs and other cell groups gained from the first clustering and subclustering (Figure 5E). Cell–cell interaction analysis by cellphone showed that *C1Q*+ TAMs mostly acted on endothelial cells. The ligand–receptor pairs are *CCL2/CCL8-ACKR1*, *CXCL1/5/8-ACKR1*, *VEGFA-KDR/FLT1*, *TNF-FLT4*, and *CCR1–CCL14*. We noticed that *C1Q*+ TAMs express higher *CCL2* and lower *VEGFA* and *CXCL8* (Table S3).

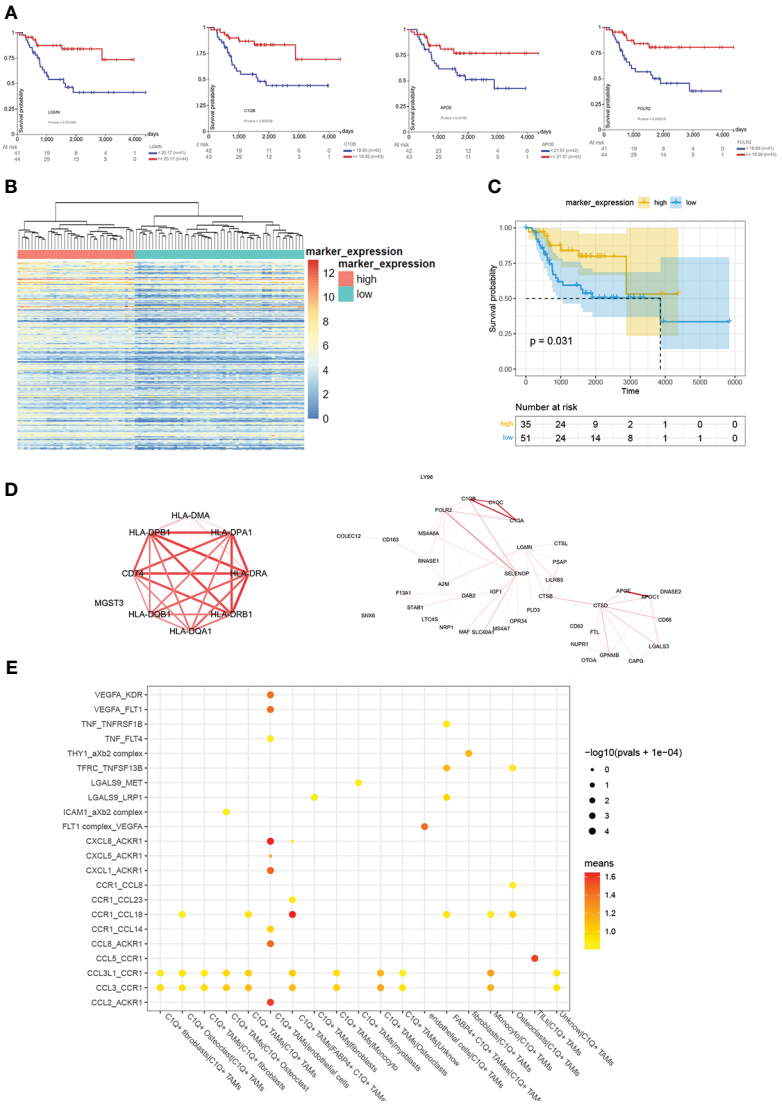


FIGURE 5
Overview of analyzing C1Q+ TAMs group and its marker. **(A)** The survival plots of *C1QA*, *C1QB*, *FOLR2*, *LGMN*, and *APOE*. **(B)** Cluster 88 examples in TARGET-OS into two groups by *C1Q*+ TAM markers with a fold change larger than 0.25. **(C)** The survival plot of high- and low- *C1Q*+ TAM infiltration groups. **(D)** The co-expression among *C1Q*+ TAM markers. The larger co-expression coefficient gets redder and wider lines. **(E)** Bubble plots show ligand–receptor pairs between *C1Q*+ TAMs and other cell groups.

4 Discussion

The authors of dataset GSE21257 found that TAMs were associated with reduced metastasis and longer survival in high-grade osteosarcoma (33). We had similar findings, combining bulk datasets with a single-cell dataset. We reported more details about these TAMs in OS. Unlike many other kinds of tumors (15), we found that higher expressed *C1Q* was related to a better prognosis and the *C1Q*+ TAMs in OS were identified as an antitumor factor.

In the analysis of bulk datasets GSE21275 and GSE32981, we divided the examples into high- and low- immune infiltrated groups according to their hierarchical cluster results. Although the high-immune infiltrated groups showed that no kind of immune cell was lower infiltrated compared to the low-immune infiltrated groups, it showed better overall survival. Moreover, most of the DEGs were related to a better prognosis. These results portrayed an antitumor image of immune infiltration in OS. Next, we tried to identify immune components that play the most important role in the OS TME.

In order to minimize the error caused by the analysis method, we performed the differential expressing twice more using R packages edgeR and DESeq2 (Figure S3). We also mapped these DEGs in GSE152048 (Figure S4). They were mostly expressed by myeloid cells and C1Q+ TAMs. Then, we thought that the difference of the immune microenvironment is mainly caused by C1Q+ TAMs.

The analysis of GSE152048 showed that TAMs were the main immune cell population in OS. Further research showed that the DEGs gained from bulk datasets were enriched in *C1Q*+ TAMs, the markers of *C1Q*+ TAMs were related to a better prognosis, and the infiltration of *C1Q*+ TAMs went with better overall survival. These results indicated strongly that *C1Q*+ TAMs were just the main immune cell population against OS.

Although *C1Q* is regarded as a cancer-promoting factor (20), it has multiple regulatory effects on the immune system including inflammation and repair progress (18). *C1Q* could function as a pattern recognition receptor to opsonize apoptotic cells and extracellular vesicles. The extracellular vesicle-combined *C1Q* induces *IL-10* and *TGF-β* production in macrophages (24). Moreover, *IL-10* and *TGF-β* are known as immunosuppressive mediators and tumor promoters (34, 35). High-mobility group box 1 (*HMGB1*) and *HMGB1* plus *C1Q* can respectively regulate inflammatory macrophage polarization. *HMGB1* plus *C1Q* induced an anti-inflammatory phenotype by inhibiting *IRF5*, a regulator of pro-inflammatory macrophage polarization (36), when *HMGB1* singly induced a pro-inflammatory phenotype by upregulating IRF5 (37). As the trigger of the classical pathway of complement, C1 can produce C3a and C5a through cascade reaction. C3a and C5a can modulate the immune microenvironment toward a pro-tumor or antitumor response. Tumor type and local concentrations of the anaphylatoxins matter in this regulation (38).

Some research depicted the possible ways that *C1Q*+ TAMs promote or limit tumors. In colorectal cancer, the RNA N+6-methyladenosine (m6A) program can regulate *C1Q*+ TAMs, which express multiple immunomodulatory ligands to modulate tumor-infiltrating *CD8*+ T cells. A low *METTL14-m+6A* level induces high levels of *EBI3*, a cytokine subunit, and finally leads to dysfunctional T cells (25). In clear-cell renal cell carcinoma, high densities of *C1Q*-producing TAMs contributed to the immunosuppressed microenvironment, in which a high expression of immune checkpoints was detected (39).

TAMs with different phenotypes could exert conversely on OS. M1 induced by interferon γ could secrete *HSPA1L* to promote OS cell apoptosis *via IRAK1* and *IRAK4 in vitro*. *HSPA1L* can be upregulated by *LGALS3BP* secreted by OS cells binding to *LGALS3* on M1 (40). M1 was thought to produce iNOS, oxygen intermediates, colony-stimulating factors, tumor necrosis factors, and interleukins to promote inflammation and to suppress OS. However, specific blockage of cytokines, nitric oxide, or reactive oxygen species did not inhibit the antitumor effect (41). M1 markers were found to enrich at the tumor interface region, whereas M2 markers were found to present throughout the whole tumor in OS pulmonary metastases (7). M2 could be recruited by *IL34* and promote osteosarcoma growth (42). *IL10*-polarized M2 could suppress OS in the presence of the anti-EGFR cetuximab (41). M2 enhanced metastasis of OS cells to the lungs in mice, and all-trans retinoic acid inhibited this metastasis *via* inhibiting the M2 polarization (43). *GNG12* was a highly effective biomarker for osteosarcoma; high *GNG12* related to a better prognosis and lower M1 and M2 scores (44). the Rab22a-NeoF1 fusion protein promotes M2 polarization by activating *STAT3* and subsequently facilitates lung metastases (45). In lung metastases, M2 correlated with curtailed patient survival could be induced by exosomes (4). Systemic administration of PLX3397, a *CSF1R* inhibitor, significantly suppressed the primary tumor growth and lung metastasis. After treatment, both M1 and M2 were depleted and the infiltration of *CD8*+T cells increased (46). Especially, *CD163*+ TAMs were reported to be crucial better prognostic biomarkers in OS (47). *CD163* was also a marker of *C1Q*+ TAMs (Table S3). We tried to find if there was a certain subtype of TAMs such as M1 and M2 among the *C1Q*+ TAMs as previous research summarized several conditions of macrophages and their markers (48–50). The difference in the direction of polarization macrophages has long been found, but we could not identify subclusters from *C1Q*+ TAMs; the markers of M1 and M2 did not show an obvious difference among them (Figure S5). Combined with the findings in bulk data, the samples were grouped according to immune-related genes, and then the immune cells of the two groups were scored. There were no immune cells with a high score in the low-immune infiltrated group. These genes include antitumor and pro-tumor genes, and cells also include antitumor and pro-tumor cells. If there were enough tumor-suppressor immune cells except TAMs in OS, the low-immune infiltrated group should have at least one main immune cell with high score. Bulk data suggest that immunosuppressive cells in OS are not easy to be observed. In the single-cell dataset, the classical M2 macrophages and M1 macrophages could not be clearly distinguished. There might be only one major immune cell in OS. They are *C1Q*+ TAMs, which suppress tumors. We noticed that some other researchers had worked on the TAM population in human breast cancer, which was defined by *APOE*, *APOC*, and *C1Q* expression. They found that a subset of *FOLR2*+ TAMs correlates with increased survival in patients with breast cancer. The *C1Q*+ TAMs and *FLOR2*+ TAMs described by our research and Nalio Ramos et al. are very similar. Both of them are defined by markers such as *APOE*, *FLOR2*, *CCL18*, *F13A1*, *MRC1*,

SLC40A1, and *SELENOP* (*SEPP1*) (17). They described *FOLR2*+ TAMs as tissue-resident macrophages, whereas they failed to recognize M1- or M2-polarized macrophages in their dataset.

We tried to explain the tumor-limiting function of C1Q+TAMs by cell–cell interaction. Cellphone analysis suggested that C1Q+ TAMs act mainly on endothelial cells by the ACKR1-related pathway (Figure 5E). ACKR1 or DARC is a receptor for chemokines on erythrocytes and endothelial cells. It is not clear how ACKR1 expression contributes to the development and outcome of human diseases. At first, *ACKR1* was regarded as a neutralizer of chemokine instead of a signal transmitter, but now it is reported that chemokines retain their biological activity after binding to *DARC* [spice] (51, 52). When overexpressed in endothelial cells, *ACKR1* decreased the pro-angiogenic properties of chemokines (53). Further research about the interaction between TAMs and endothelial cells is required.

Some other subclusters of myeloid cells are also worth paying attention. We detected *FABP4*+ macrophages just like previous authors did (54). They have a small amount of 208 cells. The mean number of detected genes of these *FABP4*+ macrophages roared over 3,000, whereas the mean number of the rest was lower than 2,000. We thought that these cells were homologous doublets. The subcluster monocytes highly expressed *S100A8* and *S100A9*. *S100A8* and *S100A9*, molecular markers promoting pre-metastatic niche formation, can cause an expansion of myeloid-derived suppressor cells, thereby contributing to an immunocompromise (55, 56). There were 1,072 myeloid cells identified as *C1Q*+ osteoclasts, whereas there were 7,307 normal osteoclasts. Osteoclasts are multinucleated members of the monocyte/macrophage family, working as skeletal remodelers. OS cells mediated bone destruction by activated osteoclasts and obtained higher OS aggressiveness (57). However, in advanced OS, osteoclasts were proved to prevent metastatic osteosarcomas (58). Osteoclasts can secrete *C1Q* just like Kupffer cells in the liver and microglia in the brain. In turn, *C1Q* strongly promotes osteoclasts derived from monocytes (59). We noticed that there were *CD74+LUM+C1Q*+ cells. It might be a distinct TAM-induced extracellular matrix molecular signature (19). In the orthotopic colorectal cancer model, monocyte-derived TAMs promote tumor development by remodeling its extracellular matrix composition and structure (19).

5 Conclusion

This analysis revealed that a higher immune infiltration level improves the overall survival of OS patients and most of the high expression of immune infiltration-related genes links to better survival. Especially, we report *C1Q* as an antitumor factor in osteosarcoma. *C1Q*+ TAMs, marked by high *C1QA/B/C*, *APOE/C*, *FLOR2*, *SLC40A1*, *SEPP1*, and *MRC1* expression, contribute to a better prognosis in OS patients. *C1Q*+ TAMs are the major immune cells in the OS TME. This study provided the image of how immune cells influence prognosis in osteosarcoma and *C1Q*+ TAMs that can be therapeutic target cells to improve the osteosarcoma treatment.

Data availability statement

Publicly available datasets were analyzed in this study. This data can be found here: TARGET-OS: https://portal.gdc.cancer.gov/repository GSE21257:https://www.ncbi.nlm.nih.gov/geo/query/acc.cgi?acc=GSE21257 GSE32981:https://www.ncbi.nlm.nih.gov/geo/query/acc.cgi?acc=GSE32981 GSE152048:https://www.ncbi.nlm.nih.gov/geo/query/acc.cgi?acc=GSE152048.

Ethics statement

Ethical review and approval was not required for the study on human participants in accordance with the local legislation and institutional requirements. Written informed consent for participation was not required for this study in accordance with the national legislation and the institutional requirements.

Author contributions

BL, JT, DW, and XZ designed this research. JT collected and analyzed datasets. DW drafted this manuscript. XZ adapted the manuscript for final submission. All authors contributed to the article and approved the submitted version.

Funding

This work was supported by the Funds of Jilin Provincial Finance Department (grant no. JLSCZD2019-002).

Conflict of interest

The authors declare that the research was conducted in the absence of any commercial or financial relationships that could be construed as a potential conflict of interest.

Publisher's note

All claims expressed in this article are solely those of the authors and do not necessarily represent those of their affiliated organizations, or those of the publisher, the editors and the reviewers. Any product that may be evaluated in this article, or claim that may be made by its manufacturer, is not guaranteed or endorsed by the publisher.

Supplementary material

The Supplementary Material for this article can be found online at: https://www.frontiersin.org/articles/10.3389/fimmu.2023.911368/full#supplementary-material

References

1. Zheng D, Yang K, Chen X, Li Y, Chen Y. Analysis of immune-stromal score-based gene signature and molecular subtypes in osteosarcoma: Implications for prognosis and tumor immune microenvironment. *Front Genet* (2021) 12:699385. doi: 10.3389/fgene.2021.699385

2. Isakoff MS, Bielack SS, Meltzer P, Gorlick R. Osteosarcoma: Current treatment and a collaborative pathway to success. *J Clin* (2015) 33(27):3029–35. doi: 10.1200/JCO.2014.59.4895

3. Corre I, Verrecchia F, Crenn V, Redini F, Trichet V. The osteosarcoma microenvironment: A complex but targetable ecosystem. *Cells* (2020) 9(4). doi: 10.3390/cells9040976

4. Wolf-Dennen K, Gordon N, Kleinerman ES. Exosomal communication by metastatic osteosarcoma cells modulates alveolar macrophages to an M2 tumor-promoting phenotype and inhibits tumoricidal functions. *Oncoimmunology* (2020) 9 (1):1747677. doi: 10.1080/2162402X.2020.1747677

5. Majzner RG, Simon JS, Grosso JF, Martinez D, Pawel BR, Santi M, et al. Assessment of programmed death-ligand 1 expression and tumor-associated immune cells in pediatric cancer tissues. *Cancer* (2017) 123(19):3807–15. doi: 10.1002/cncr.30724

6. Koirala P, Roth ME, Gill J, Piperdi S, Chinai JM, Geller DS, et al. Immune infiltration and PD-L1 expression in the tumor microenvironment are prognostic in osteosarcoma. *Sci Rep* (2016) 6(1):30093. doi: 10.1038/srep30093

7. Ligon JA, Choi W, Cojocaru G, Fu W, Hsiue EH-C, Oke TF, et al. Pathways of immune exclusion in metastatic osteosarcoma are associated with inferior patient outcomes. *J Immunother Cancer* (2021) 9(5):e001772. doi: 10.1136/jitc-2020-001772

8. Chen C, Xie L, Ren T, Huang Y, Xu J, Guo W. Immunotherapy for osteosarcoma.: Fundamental mechanism, rationale, and recent breakthroughs. *Cancer Lett* (2021) 500:1–10. doi: 10.1016/j.canlet.2020.12.024

9. Wang N, Wang S, Wang X, Zheng Y, Yang B, Zhang J, et al. Research trends in pharmacological modulation of tumor-associated macrophages. *Clin Transl Med* (2021) 11(1):e288–8. doi: 10.1002/ctm2.288

10. Xie R, Ruan S, Liu J, Qin L, Yang C, Tong F, et al. Furin-instructed aggregated gold nanoparticles for re-educating tumor associated macrophages and overcoming breast cancer chemoresistance. *Biomaterials* (2021) 275:120891. doi: 10.1016/j.biomaterials.2021.120891

11. Figueiredo P, Lepland A, Scodeller P, Fontana F, Torrieri G, Tiboni M, et al. Peptide-guided resiquimod-loaded lignin nanoparticles convert tumor-associated macrophages from M2 to M1 phenotype for enhanced chemotherapy. *Acta biomaterialia* (2021) 133:231–43. doi: 10.1016/j.actbio.2020.09.038

12. Cai Z, Lim D, Liu G, Chen C, Jin L, Duan W, et al. Valproic acid-like compounds enhance and prolong the radiotherapy effect on breast cancer by activating and maintaining anti-tumor immune function. *Front Immunol* (2021) 12:646384–4. doi: 10.3389/fimmu.2021.646384

13. Zhu Y, Herndon JM, Sojka DK, Kim K-W, Knolhoff BL, Zuo C, et al. Tissue-resident macrophages in pancreatic ductal adenocarcinoma originate from embryonic hematopoiesis and promote tumor progression. *Immunity* (2017) 47(2):323–338.e326. doi: 10.1016/j.immuni.2017.07.014

14. Bugatti M, Bergamini M, Missale F, Monti M, Laura A, Pezzali I, et al. A population of TIM4+FOLR2+ macrophages localized in tertiary lymphoid structures correlates to an active immune infiltrate across several cancer types. *Cancer Immunol Res* (2022) 10(11):1340–53. doi: 10.1158/2326-6066.CIR-22-0271

15. Revel M, Sautès-Fridman C, Fridman W-H, Roumenina LT. C1q+ macrophages: Passengers or drivers of cancer progression. *Trends Cancer* (2022) 8(7):517–26. doi: 10.1016/j.trecan.2022.02.006

16. Blériot C, Chakarov S, Ginhoux F. Determinants of resident tissue macrophage identity and function. *Immunity* (2020) 52(6):957–70. doi: 10.1016/j.immuni.2020.05.014

17. Nalio Ramos R, Missolo-Koussou Y, Gerber-Ferder Y, Bromley CP, Bugatti M, Núñez NG, et al. Tissue-resident FOLR2+ macrophages associate with CD8+ t cell infiltration in human breast cancer. *Cell* (2022) 185(7):1189–1207.e1125. doi: 10.1016/j.cell.2022.02.021

18. Baldwin WMIII, Valujskikh A, Fairchild RL. C1q as a potential tolerogenic therapeutic in transplantation. *Am J Transplant* (2021) 21(11):3519–23. doi: 10.1111/ajt.16705

19. Afik R, Zigmond E, Vugman M, Klepfish M, Shimshoni E, Pasmanik-Chor M, et al. Tumor macrophages are pivotal constructors of tumor collagenous matrix. *J Exp Med* (2016) 213(11):2315–31. doi: 10.1084/jem.20151193

20. Bulla R, Tripodo C, Rami D, Ling GS, Agostinis C, Guarnotta C, et al. C1q acts in the tumour microenvironment as a cancer-promoting factor independently of complement activation. *Nat Commun* (2016) 7:10346. doi: 10.1038/ncomms10346

21. Markiewski MM, DeAngelis RA, Benencia F, Ricklin-Lichtsteiner SK, Koutoulaki A, Gerard C, et al. Modulation of the antitumor immune response by complement. *Nat Immunol* (2008) 9(11):1225–35. doi: 10.1038/ni.1655

22. Afshar-Kharghan V. The role of the complement system in cancer. *J Clin Invest* (2017) 127(3):780–9. doi: 10.1172/JCI90962

23. Reis ES, Mastellos DC, Ricklin D, Mantovani A, Lambris JD. Complement in cancer: Untangling an intricate relationship. *Nat Rev Immunol* (2018) 18(1):5–18. doi: 10.1038/nri.2017.97

24. Bohlson SS, O'Conner SD, Hulsebus HJ, Ho M-M, Fraser DA. Complement, C1q, and C1q-related molecules regulate macrophage polarization. *Front Immunol* (2014) 5. doi: 10.3389/fimmu.2014.00402

25. Dong L, Chen C, Zhang Y, Guo P, Wang Z, Li J, et al. The loss of RNA N6-adenosine methyltransferase Mettl14 in tumor-associated macrophages promotes CD8+ t cell dysfunction and tumor growth. *Cancer Cell* (2021) 39(7):945–957.e910. doi: 10.1016/j.ccell.2021.04.016

26. Charoentong P, Finotello F, Angelova M, Mayer C, Efremova M, Rieder D, et al. Pan-cancer immunogenomic analyses reveal genotype-immunophenotype relationships and predictors of response to checkpoint blockade. *Cell Rep* (2017) 18(1):248–62. doi: 10.1016/j.celrep.2016.12.019

27. Ritchie ME, Phipson B, Wu D, Hu Y, Law CW, Shi W, et al. Limma powers differential expression analyses for RNA-sequencing and microarray studies. *Nucleic Acids Res* (2015) 43(7):e47–7. doi: 10.1093/nar/gkv007

28. Love MI, Huber W, Anders S. Moderated estimation of fold change and dispersion for RNA-seq data with DESeq2. *Genome Biol* (2014) 15(12):550. doi: 10.1186/s13059-014-0550-8

29. Robinson MD, McCarthy DJ, Smyth GK. EdgeR: @ a bioconductor package for differential expression analysis of digital gene expression data. *Bioinf (Oxford England)* (2010) 26(1):139–40. doi: 10.1093/bioinformatics/btp616

30. Subramanian A, Tamayo P, Mootha VK, Mukherjee S, Ebert BL, Gillette MA, et al. Gene set enrichment analysis. a knowledge-based approach for interpreting genome-wide expression profiles. *Proc Natl Acad Sci U.S.A.* (2005) 102(43):15545–50. doi: 10.1073/pnas.0506580102

31. McGinnis CS, Murrow LM, Gartner ZJ. DoubletFinder.: Doublet detection in single-cell rna sequencing data using artificial nearest neighbors. *Cell Syst* (2019) 8 (4):329–337.e324. doi: 10.1016/j.cels.2019.03.003

32. Vento-Tormo R, Efremova M, Botting RA, Turco MY, Vento-Tormo M, Meyer KB, et al. Single-cell reconstruction of the early maternal-fetal interface in humans. *Nature* (2018) 563(7731):347–53. doi: 10.1038/s41586-018-0698-6

33. Buddingh EP, Kuijjer ML, Duim RAJ, Bürger H, Agelopoulos K, Myklebost O, et al. Tumor-infiltrating macrophages are associated with metastasis suppression in high-grade osteosarcoma: A rationale for treatment with macrophage activating agents. *Clin Cancer Res* (2011) 17(8):2110–9. doi: 10.1158/1078-0432.CCR-10-2047

34. Locati M, Curtale G, Mantovani A. Diversity, mechanisms, and significance of macrophage plasticity. *Annu Rev Pathol* (2020) 15:123–47. doi: 10.1146/annurev-pathmechdis-012418-012718

35. Batlle E, Massagué J. Transforming growth factor-β signaling in immunity and cancer. *Immunity* (2019) 50(4):924–40. doi: 10.1016/j.immuni.2019.03.024

36. Hedl M, Yan J, Witt H, Abraham C. IRF5 is required for bacterial clearance in human M1-polarized macrophages, and IRF5 immune-mediated disease risk variants modulate this outcome. *J Immunol* (2019) 202(3):920–30. doi: 10.4049/jimmunol.1800226

37. Liu T, Xiang A, Peng T, Doran AC, Tracey KJ, Barnes BJ, et al. HMGB1-C1q complexes regulate macrophage function by switching between leukotriene and specialized proresolving mediator biosynthesis. *Proc Natl Acad Sci U.S.A.* (2019) 116 (46):23254–63. doi: 10.1073/pnas.1907490116

38. Roumenina LT, Daugan MV, Petitprez F, Sautès-Fridman C, Fridman WH. Context-dependent roles of complement in cancer. *Nat Rev Cancer* (2019) 19(12):698–715. doi: 10.1038/s41568-019-0210-0

39. Roumenina LT, Daugan MV, Noé R, Petitprez F, Vano YA, Sanchez-Salas R, et al. Tumor cells hijack macrophage-produced complement C1q to promote tumor growth. *Cancer Immunol Res* (2019) 7(7):1091–105. doi: 10.1158/2326-6066.CIR-18-0891

40. Li J, Zhao C, Li Y, Wen J, Wang S, Wang D, et al. Osteosarcoma exocytosis of soluble LGALS3BP mediates macrophages toward a tumoricidal phenotype. *Cancer Lett* (2022) 528:1–15. doi: 10.1016/j.canlet.2021.12.023

41. Pahl JHW, Kwappenberg KMC, Varypataki EM, Santos SJ, Kuijjer ML, Mohamed S, et al. Macrophages inhibit human osteosarcoma cell growth after activation with the bacterial cell wall derivative liposomal muramyl tripeptide in combination with interferon-γ. *J Exp Clin Cancer Res* (2014) 33(1):27–7. doi: 10.1186/1756-9966-33-27

42. Ségaliny AI, Mohamadi A, Dizier B, Lokajczyk A, Brion R, Lanel R, et al. Interleukin-34 promotes tumor progression and metastatic process in osteosarcoma through induction of angiogenesis and macrophage recruitment. *Int J Cancer* (2015) 137(1):73–85. doi: 10.1002/ijc.29376

43. Zhou Q, Xian M, Xiang S, Xiang D, Shao X, Wang J, et al. All-trans retinoic acid prevents osteosarcoma metastasis by inhibiting m2 polarization of tumor-associated macrophages. *Cancer Immunol Res* (2017) 5(7):547–59. doi: 10.1158/2326-6066.CIR-16-0259

44. Yuan J, Yuan Z, Ye A, Wu T, Jia J, Guo J, et al. Low GNG12 expression predicts adverse outcomes: A potential therapeutic target for osteosarcoma. *Front Immunol* (2021) 12:758845–5. doi: 10.3389/fimmu.2021.758845

45. Zhong L, Liao D, Li J, Liu W, Wang J, Zeng C, et al. Rab22a-NeoF1 fusion protein promotes osteosarcoma lung metastasis through its secretion into exosomes. *Signal Transduct Target Ther* (2021) 6(1):59–9. doi: 10.1038/s41392-020-00414-1

46. Fujiwara T, Yakoub MA, Chandler A, Christ AB, Yang G, Ouerfelli O, et al. CSF1/CSF1R signaling inhibitor pexidartinib (PLX3397) reprograms tumor-associated macrophages and stimulates t-cell infiltration in the sarcoma microenvironment. *Mol Cancer Ther* (2021) 20(8):1388–99. doi: 10.1158/1535-7163.MCT-20-0591

47. Gomez-Brouchet A, Illac C, Gilhodes J, Bouvier C, Aubert S, Guinebretiere JM, et al. CD163-positive tumor-associated macrophages and CD8-positive cytotoxic lymphocytes are powerful diagnostic markers for the therapeutic stratification of osteosarcoma patients: An immunohistochemical analysis of the biopsies fromthe french OS2006 phase 3 trial. *Oncoimmunology* (2017) 6(9):e1331193. doi: 10.1080/2162402X.2017.1331193

48. Wang C, Ma C, Gong L, Guo Y, Fu K, Zhang Y, et al. Macrophage polarization and its role in liver disease. *Front Immunol* (2021) 12:803037–7. doi: 10.3389/fimmu.2021.803037

49. Mohapatra S, Pioppini C, Ozpolat B, Calin GA. Non-coding RNAs regulation of macrophage polarization in cancer. *Mol Cancer* (2021) 20(1):24–4. doi: 10.1186/s12943-021-01313-x

50. Zhou K, Cheng T, Zhan J, Peng X, Zhang Y, Wen J, et al. Targeting tumor-associated macrophages in the tumor microenvironment. *Oncol Lett* (2020) 20(5):234–4. doi: 10.3892/ol.2020.12097

51. Rot A. Contribution of duffy antigen to chemokine function. *Cytokine Growth Factor Rev* (2005) 16(6):687–94. doi: 10.1016/j.cytogfr.2005.05.011

52. Groblewska M, Litman-Zawadzka A, Mroczko B. The role of selected chemokines and their receptors in the development of gliomas. *Int J Mol Sci* (2020) 21(10). doi: 10.3390/ijms21103704

53. Du J, Luan J, Liu H, Daniel TO, Peiper S, Chen TS, et al. Potential role for duffy antigen chemokine-binding protein in angiogenesis and maintenance of homeostasis in response to stress. *J leukocyte Biol* (2002) 71(1):141–53. doi: 10.1189/jlb.71.1.141

54. Zhou Y, Yang D, Yang Q, Lv X, Huang W, Zhou Z, et al. Single-cell RNA landscape of intratumoral heterogeneity and immunosuppressive microenvironment in advanced osteosarcoma. *Nat Commun* (2020) 11(1):6322–2. doi: 10.1038/s41467-020-20059-6

55. Heinemann AS, Pirr S, Fehlhaber B, Mellinger L, Burgmann J, Busse M, et al. In neonates S100A8/S100A9 alarmins prevent the expansion of a specific inflammatory monocyte population promoting septic shock. *FASEB J* (2017) 31(3):1153–64. doi: 10.1096/fj.201601083R

56. Zhao F, Hoechst B, Duffy A, Gamrekelashvili J, Fioravanti S, Manns MP, et al. S100A9 a new marker for monocytic human myeloid-derived suppressor cells. *Immunology* (2012) 136(2):176–83. doi: 10.1111/j.1365-2567.2012.03566.x

57. Alfranca A, Martinez-Cruzado L, Tornin J, Abarrategi A, Amaral T, de Alava E, et al. Bone microenvironment signals in osteosarcoma development. *Cell Mol Life Sci* (2015) 72(16):3097–113. doi: 10.1007/s00018-015-1918-y

58. Endo-Munoz L, Cumming A, Rickwood D, Wilson D, Cueva C, Ng C, et al. Loss of osteoclasts contributes to development of osteosarcoma pulmonary metastases. *Cancer Res* (2010) 70(18):7063–72. doi: 10.1158/0008-5472.CAN-09-4291

59. Teo BHD, Bobryshev Yuri V, Teh Boon K, Wong Siew H, Lu J. Complement C1q production by osteoclasts and its regulation of osteoclast development. *Biochem J* (2012) 447(2):229–37. doi: 10.1042/BJ20120888

Frontiers in Immunology

Explores novel approaches and diagnoses to treat immune disorders.

The official journal of the International Union of Immunological Societies (IUIS) and the most cited in its field, leading the way for research across basic, translational and clinical immunology.

Discover the latest Research Topics

See more →



Frontiers

Avenue du Tribunal-Fédéral 34
1005 Lausanne, Switzerland
frontiersin.org

Contact us

+41 (0)21 510 17 00
frontiersin.org/about/contact